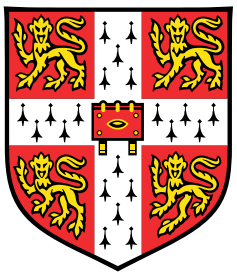
Uncovering gravitational wave signatures of modified theories of gravity and exotic matter



Tamara Evstafyeva

Supervisor: Prof. Ulrich Sperhake

Advisor: Dr. Michalis Agathos

Department of Applied Mathematics and Theoretical Physics
University of Cambridge

This dissertation is submitted for the degree of
Doctor of Philosophy

Newnham College August 2024

Declaration

This thesis is the result of my own work and includes nothing which is the outcome of work done in collaboration except as declared in the preface and specified in the text. It is not substantially the same as any work that has already been submitted, or is being concurrently submitted, for any degree, diploma or other qualification at the University of Cambridge or any other University or similar institution except as declared in the preface and specified in the text. It does not exceed the prescribed word limit for the relevant Degree Committee.

This thesis contains work that appears in the following publications:

- **Evstafyeva, T.**, Agathos, M. and Ripley, J.L., 2023. *Measuring the ringdown scalar polarization of gravitational waves in Einstein-scalar-Gauss-Bonnet gravity*. Physical Review D, 107(12), p.124010.
- **Evstafyeva, T.**, Sperhake, U., Helfer, T., Croft, R., Radia, M., Ge, B.X. and Lim, E.A., 2023. *Unequal-mass boson-star binaries: initial data and merger dynamics*. Classical and Quantum Gravity, 40(8), p.085009.
- **Evstafyeva, T.**, Roşca-Mead, R., Sperhake, U. and Brügmann, B., 2023. *Boson stars in massless and massive scalar-tensor gravity*. Physical Review D, 108(10), p.104064.
- **Evstafyeva, T.**, Sperhake, U., Romero-Shaw, I. and Agathos, M., 2024. *Gravitational-wave data analysis with high-precision numerical relativity simulations of boson star mergers*. Physical Review Letters, DOI 10.1103/PhysRevLett.133.131401.

Although not included and discussed in this thesis, I have also co-authored the following publications:

- Croft, R., Helfer, T., Ge, B.X., Radia, M., **Evstafyeva, T.**, Lim, E.A., Sperhake, U. and Clough, K., 2023. *The gravitational afterglow of boson stars*. Classical and Quantum Gravity, 40(6), p.065001.
- Saló, L.A., Brady, S.E., Clough, K., Doneva, D., **Evstafyeva, T.**, Figueras, P., Rossi, L. and Yao, S., 2023. GRFolres: *A code for modified gravity simulations in strong gravity*. Journal of Open Source Software, 9(98), 6369.

Abstract

The observation of the first gravitational-wave (GW) event almost a decade ago opened a new promising window to our scientific endeavours in understanding the deepest mysteries of our Universe and its history. Using the foundations of general relativity (GR), we are now in the position of being able to model coalescence and merger of binary black holes and neutron stars, and understand how their modelled data fit within the manifold of our GW observations. A key ingredient in source modelling of binary systems is numerical relativity (NR), allowing us to resolve the merger regime and forming the foundation of this thesis.

Despite the success of GR, many proposals of modified theories gravity and exotic compact objects have been put forward to address experimental data, theoretical inconsistencies of the theory of general relativity, and merely human curiosity of 'what if?'. In the pursuit of addressing all of the open questions, we now find ourselves presented with an elaborate list of possible extensions to GR and the Standard Model of particle physics. Whilst we have not found any modification to gravity to be statistically preferred, with the rise of future GW detectors and increased number of events, we may be in position to even further constrain and test our theoretical proposals. However, in order to achieve this, we require accurate modelling of the phenomena we wish to study and understand its implications for GW observations. The goal of this thesis is to pave the path towards achieving this goal, by bringing together numerical relativity and GW analysis for certain modified theories of gravity and classes of exotic compact objects. We assume that the reader has some introductory knowledge about the theory of general relativity, numerical and statistical methods. However, we do review the key theoretical points and tools that have facilitated our studies.

We start our discussion with the numerical study of binary black holes in Einstein-scalar-Gauss-Bonnet (EsGB) theory of gravity in the decoupling limit. An interesting feature of this theory is that black holes can posses scalar hair and the resulting gravitational-wave signals – scalar polarisation. By focusing on the ringdown and modelling the scalar content of the theory, we forecast the ability of present and future GW detectors to measure it. We find that the ringdown scalar polarisation is undetectable with the current GW detectors, but that scalar ringdown of a limited number of binary configurations could be in principle measured with the design sensitivity of the next generation detectors.

We next move to the discussion of a specific class of exotic compact objects – boson stars (BSs). We first devise the numerical methods required to construct these objects as single spacetimes in spherical symmetry in GR. We then extend their study to massless and massive scalar-tensor (ST) theories of gravity. We perform a systematic study of the whole parameter space and study their stability. Overall, we find that similar to neutron stars, boson stars in ST theory can undergo spontaneous scalarisation, which may result in smoking-gun effects for future observations. However, BSs turn out to be less susceptible to scalarisation than neutron stars.

By focusing on GR and moving away from the study of single boson-star spacetimes, we then consider them in the binary context. By focusing on head-on collisions, we devise a suitable method for constructing initial data for boson-star binaries of arbitrary mass ratio, allowing us to circumvent spurious and unphysical effects that arise from methods commonly employed in the literature. We explore the parameter space of head-on boson-star collisions and find that in certain regimes their GW signals exhibit conspicuous features of tidal deformation, posing a direct way of differentiating them from black holes.

Finally, we apply our numerical infrastructure to inspiralling quasi-circular boson-star systems. We construct for the first time high-precision numerical relativity waveforms that we make publicly available. Further, we use our numerically simulated signals as injections into detector noise and assess the ability of standard binary black hole and neutron star waveform approximants to recover them. We find strong biases in the parameter estimation and show that even with the sensitivity of present GW detectors, certain binary boson-star systems, if present in the detector band, are likely to leave non-Gaussian residuals, signalling the presence of ‘new’ physics.

Given applications of gravitational wave analysis to numerical relativity presented in this thesis, we also include a brief guide on how to prepare numerical relativity waveforms as injections into detector noise. Our tools and methods may be applied to any theory of gravity and/or exotic compact objects, as long as one is able to model their resulting GW signals.

Acknowledgements

I would like to thank my family, friends, mentors and collaborators for the support and time they have provided me with during the last four years, and without whom this work would not have been possible.

Firstly, I am extremely grateful to my supervisor, Ulrich Sperhake for his advice and guidance on my projects and life in academia in general. I would like to especially thank you for connecting me with such a wide network of your collaborators and giving me a chance to work across a diverse range of topics. I have not only immensely benefited from our discussions on various research ideas but also from your invaluable mentorship. Thank you also for introducing me to the best practices of research and numerical relativity.

During my PhD I have enjoyed working with the GRChombo collaboration (currently known as the GRTL collaboration), whose numerical relativity code I have been using for my research purposes. I would like to thank the entire Collaboration for their ongoing work on the code and their extremely friendly and welcoming attitude to the newcomers. I have enjoyed every biannual meeting we had and in particular the GRChombo quizzes. I would like to express my gratitude to Eugene Lim, Thomas Helfer and Bo-Xuan Ge for their support of my work and our fruitful discussions on boson stars.

I would like to thank all my friends at Department of Applied Mathematics and Theoretical Physics and in particular my officemates, Iain Davies and William Biggs, with whom we embarked on our PhD journeys together. I am grateful to Miren Radia, Robin Croft and Amelia Drew, who helped me immensely in starting with the GRChombo code and shared their experiences. I am also thankful to Priscilla Canizares for her support and mentorship.

I am eternally grateful to my family for their unconditional love and support, and especially my parents, who have been my ultimate role models of resilience and hard work. Without your support and unwavering encouragement, my education and move to the UK would not have been possible. I am grateful to my grandparents, who spent time with me during my write-up in the summer, shared lots of stories from their university times and played our favourite card games with me. The location of the write-up of this work was inspired by my grandad, who wrote his top-secret thesis in the same village near Saratov region, allegedly, in 2 weeks. Finally, my time in Cambridge would not have been the same

without Michael. Thank you for your encouragements during the difficult times and your continued support. My PhD life would not have been as tasty without you cooking me all of my meals.

The simulations presented in this thesis used the following resources:

- The Cambridge Service for Data Driven Discovery (CSD3), part of which is operated by the University of Cambridge Research Computing Service on behalf of the Science and Technology Facilities Council (STFC) DiRAC HPC Facility. The DiRAC component of CSD3 was funded by BEIS capital funding via STFC capital grants ST/P002307/1 and ST/R002452/1 and STFC operations grant ST/R00689X/1.
- The DiRAC@Durham facility managed by the Institute for Computational Cosmology on behalf of the STFC DiRAC HPC Facility. The equipment was funded by BEIS capital funding via STFC capital grants ST/P002293/1, ST/R002371/1 and ST/S002502/1, Durham University and STFC operations grant ST/R000832/1.
- The DiRAC Data Intensive service (DIaL2 / DIaL3) at the University of Leicester, managed by the University of Leicester Research Computing Service on behalf of the STFC DiRAC HPC Facility. The DiRAC service at Leicester was funded by BEIS, UKRI and STFC capital funding and STFC operations grants. The equipment was funded by BIS National E-Infrastructure capital grant ST/K000373/1 and STFC DiRAC Operations grant ST/K0003259/1.
- The Fawcett supercomputer at DAMTP funded by STFC Consolidated Grant ST/P000673/1.
- The Hawk supercomputer in Cardiff funded by STFC grants ST/I006285/1 and ST/V005618/1.
- The LIGO Lab supercomputers funded by National Science Foundation Grants PHY-0757058 and PHY-0823459.

To my grandparents, Tamara, professor in botanical biology, Slava, cosmodrome engineer, Natalia, magnetics engineer and Yuri, doctor of radioelectronics . . .



Donguz village surrounded by the bosonic cloud.

Table of contents

xi

List of figures xix

List of tables xxxiii

Nomenclature xxxvii

1 The bigger picture: The quest towards understanding gravity 3
- 1.1 Theory of general relativity . . . 3
- 1.2 History of tests of GR . . . 4
- 1.3 Challenging our understanding . . . 5
  - 1.3.1 Modifying gravity . . . 6
  - 1.3.2 Modifying the nature of compact objects . . . 9
  - 1.3.3 How to test gravity theories beyond the GR and SM paradigm? . . . 10

2 Numerical Relativity 13
- 2.1 Introduction . . . 13
- 2.2 3+1 decomposition of spacetime and ADM formalism . . . 14
- 2.3 BSSN formulation . . . 16
- 2.4 CCZ4 formulation . . . 18
- 2.5 Gauge conditions . . . 19
  - 2.5.1 Lapse condition . . . 20
  - 2.5.2 Shift condition . . . 21
- 2.6 Initial Data . . . 21
  - 2.6.1 Brill-Lindquist initial data . . . 22
  - 2.6.2 Puncture initial data . . . 23
- 2.7 GRChombo code . . . 24
  - 2.7.1 Overview . . . 24

2.7.2 Basics of Adaptive Mesh Refinement . . . 25
2.7.3 Tagging criteria . . . 26
2.7.4 Boundary Conditions . . . 28
2.7.5 Gravitational waves . . . 29

Appendices **35**
Appendix 2.A BSSN equations . . . 35
Appendix 2.B CCZ4 equations . . . 36
Appendix 2.C York–Lichnerowicz conformal decomposition . . . 37

3 Gravitational wave data analysis for numerical relativists in fundamental physics **41**
3.1 Introduction . . . 41
3.2 Gravitational wave detectors . . . 42
3.2.1 Present and future GW detectors . . . 42
3.2.2 Gravitational wave polarisations . . . 43
3.2.3 Antenna response functions . . . 44
3.2.4 Detector noise and matched filtering . . . 45
3.3 Bayesian inference and parameter estimation . . . 47
3.3.1 Bayes theorem . . . 47
3.3.2 Parameter Estimation . . . 50
3.4 Numerical relativity injections . . . 54
3.4.1 Preparing your NR data . . . 54
3.4.2 Disentangling the frames . . . 54
3.4.3 Using LALSUITE to transform NR data . . . 57

4 Binary black hole mergers in Einstein-scalar-Gauss-Bonnet gravity **59**
4.1 Introduction . . . 59
4.2 Theoretical background . . . 61
4.2.1 Formulation of 4-derivative scalar-tensor (4∂ST) gravity . . . 61
4.2.2 Polarisation content . . . 62
4.2.3 Perturbative equations of motion . . . 63
4.2.4 Current observational constraints . . . 66
4.3 Numerical set-up . . . 67
4.3.1 Numerical Relativity code and evolution equations . . . 67
4.3.2 Grid setup and initial data . . . 68
4.3.3 Extraction of physical quantities . . . 69
4.3.4 Numerical results: scalar waveforms . . . 71

4.4 Modelling the Scalar Ringdown Waveform . . . 74
4.5 Observational Prospects . . . 79
4.5.1 Measurability of the scalar ringdown . . . 79
4.6 Bayesian Inference on the Scalar Ringdown Signal . . . 85
4.6.1 Analysis Set-up . . . 86
4.6.2 Results . . . 88
4.7 Conclusion . . . 91

Appendices **93**
Appendix 4.A Convergence testing and error estimation . . . 93
4.A.1 Gravitational and scalar waveforms . . . 93
4.A.2 GW Energy and angular momentum flux convergence . . . 96
Appendix 4.B Code Validation . . . 96
Appendix 4.C Quasi-normal modes of a Kerr black hole in GR . . . 98

5 Boson stars in general relativity **99**
5.1 Introduction . . . 99
5.2 History of boson stars . . . 100
5.3 Formulation . . . 101
5.4 Equilibrium, Spherically Symmetric Solutions . . . 103
5.4.1 Equations of motions . . . 103
5.4.2 Boundary conditions . . . 105
5.4.3 Asymptotic behaviour . . . 106
5.4.4 Computing solutions . . . 108
5.5 Diagnostics . . . 110
5.6 Examples of boson-star solutions . . . 110
5.7 Conversion to isotropic coordinates . . . 112

6 Boson stars in massless and massive scalar-tensor gravity **115**
6.1 Introduction . . . 115
6.2 Theory and formulation . . . 117
6.2.1 Scalar-tensor action . . . 117
6.2.2 Spherically symmetric solutions . . . 118
6.2.3 The field equations in spherical symmetry . . . 119
6.2.4 Choice of model . . . 121
6.2.5 Numerics and Diagnostics . . . 122
6.3 Scalarised boson stars . . . 123

6.3.1 A prototypical example . . . 123
6.3.2 Scalar mass and the onset of scalarisation . . . 126
6.3.3 Dependence on the bosonic potential . . . 130
6.3.4 Dependence on α_0 . . . 136
6.3.5 Thin-shell models . . . 137
6.4 Stability . . . 139
6.5 Conclusions . . . 141

Appendices **145**
Appendix 6.A Asymptotic Behaviour . . . 145
Appendix 6.B Numerics . . . 147
Appendix 6.C Boson-star families . . . 150

7 Head-on collisions of boson stars **157**
7.1 Introduction . . . 157
7.2 Theoretical framework . . . 159
7.3 The 3+1 decomposition and boosted stars . . . 159
7.4 Computational infrastructure . . . 161
7.4.1 Lean . . . 162
7.4.2 GRChombo . . . 162
7.4.3 Convergence testing . . . 162
7.5 Boson-star binary initial data construction . . . 162
7.5.1 Revisiting the initial data construction for equal-mass binaries . . . 163
7.5.2 Construction of the generalised unequal-mass initial data . . . 164
7.6 Set-up and exploration of the parameter space . . . 166
7.6.1 Equal-mass binaries . . . 166
7.6.2 Unequal-mass binaries . . . 167
7.7 Results: time evolutions of off-phase BS binaries . . . 170
7.7.1 Equal-mass collisions . . . 170
7.7.2 Unequal-mass collisions . . . 173
7.7.3 Scalar field profiles . . . 174
7.7.4 Gravitational waveforms . . . 176
7.7.5 Energy radiated by unequal-mass binaries . . . 179
7.8 Conclusion . . . 180

Appendices **183**
Appendix 7.A Choice of conformal factor . . . 183

Appendix 7.B Improved superposition in the limits $R_A, R_B \to 0$ or $R_A, R_B \to \infty$. 185
7.B.1 The limit $R_A, R_B \to 0$ . . . 185
7.B.2 The limit $R_A, R_B \to \infty$ . . . 186
Appendix 7.C Gravitational radiation and numerical uncertainties . . . 187
7.C.1 Extraction of physical quantities . . . 187
7.C.2 LEAN code . . . 187
7.C.3 GRCHOMBO code . . . 188
Appendix 7.D Constraint violations in the (R_A, R_B) parameter space . . . 189

8 Gravitational-wave data analysis with high-precision numerical relativity simulations of boson star mergers 191
8.1 Introduction . . . 191
8.2 Theory . . . 192
8.3 NR Simulations . . . 193
8.3.1 Numerical set-up . . . 193
8.3.2 Waveforms . . . 195
8.4 Parameter Estimation . . . 196
8.4.1 Set-up . . . 196
8.4.2 Diagnostics . . . 198
8.5 Results: `A17` families . . . 199
8.5.1 `A17` ($\delta\phi = 0, \varepsilon = 1$) . . . 200
8.5.2 `A17-p180` ($\delta\phi = \pi, \varepsilon = 1$) . . . 201
8.5.3 `A17-d090` ($\delta\phi = \pi/2, \varepsilon = 1$) . . . 201
8.5.4 `A17-e1` ($\delta\phi = 0, \varepsilon = -1$) . . . 202
8.5.5 Interpretation . . . 202
8.6 Results: `A147` family . . . 204
8.7 Conclusions . . . 205

Appendices 207
Appendix 8.A Tagging criterion and adaptive-mesh-refinement parameters . . . 207
Appendix 8.B Convergence tests . . . 210
Appendix 8.C Black-hole and boson-star signals . . . 212
Appendix 8.D Injections . . . 214

9 Conclusions and outlook 219

References 223

List of figures

1 *Donguz village surrounded by the bosonic cloud.* xi

2.1 Foliation of a 4-dimensional spacetime into 3-dimensional spatial hypersurfaces Σ_t, and a time-like normal $\boldsymbol{n}$. Note that each spatial hypersurface is in fact a 3-dimensional volume, which is represented here as a 2-dimensional surface for illustrative purposes. 16

2.2 Illustrations adapted from Smarr and York [1]. *Left panel*: Kruskal–Szekeres diagram representing the evolution of a Schwarzschild spacetime with an event horizon at $r = 2M$ and a singularity at $r = 0$. The axes correspond to transformed time and radial coordinates of the Schwarzschild spacetime such that $U = -1/2\exp(-\tilde{t} + r)\exp(-4M)$ and $V = 1/2\exp(\bar{t} + r)\exp(-4M)$, where $\bar{t} = t + 2M\ln|r - 2M|$ and $\tilde{t} = t - 2M\ln|r - 2M|$. Time evolution using geodesic slicing, depicted by the curves transitioning from blue to red, shows that hypersurfaces hit the BH singularity in finite proper time, $\tau = \pi M$. *Right panel*: A sketch of coordinate shearing and stretching. On the one hand, a small sphere being transported along a normal vector is transformed into an ellipsoid. On the other hand, introducing a non-trivial shift vector helps to reduce the distortion of its shape and excessive coordinate shearing. 20

2.3 2D snapshots in the $x - y$ plane. The finer AMR grids are shown around two compact objects (boson stars that we will encounter later in Chapters 5–8) and a conformal factor χ is illustrated via the colour gradient. *Left*: A fill-ratio of $\varepsilon_{\rm FR} = 0.7$ is used. The inner refinement levels have sharper edges and a less box-like structure. *Right*: A fill-ratio of $\varepsilon_{\rm FR} = 1$ is now used. Unlike the $\varepsilon_{\rm FR} = 0.7$, the inner refinement levels now have a distinct box-like structure. 26

2.4 Illustration of the tagging criterion $C_{\rm pos}$ of Eq. (2.40) in the $x-y$ plane being triggered around a compact object of mass m_1 (orange blob) . Assuming we have 7 additional AMR levels on top of the base level $l=0$, we show how the grids are likely to be resolved around the compact object in question. . . 29

3.2.1 Definition of the propagation angles (θ,ϕ) and the polarisation angle ψ in the detector frame. Note that $\{\hat{\boldsymbol{d}}_x,\hat{\boldsymbol{d}}_y,\hat{\boldsymbol{d}}_z\}$ denote the Cartesian basis in the detector frame, whilst $\{\boldsymbol{\ell},\boldsymbol{m},\boldsymbol{k}\}$ is the basis at the source, where $\boldsymbol{k}$ is taken to be in the direction of propagation. 45

3.3.1 Shapes (from left to right) of uniform, uniform in cosmological comoving volume, uniform in cosine and sine priors for an arbitrary variable X. 47

3.3.2 Example of individual mass posterior distributions from a parameter estimation run in BILBY. 51

3.4.1 Definition of the wave frame defined by the basis vectors $(\boldsymbol{X},\boldsymbol{Y},\boldsymbol{Z})$ and the NR frame $(\hat{\boldsymbol{x}},\hat{\boldsymbol{y}},\hat{\boldsymbol{z}})$ in Cartesian coordinates (dark blue) and $(\hat{\boldsymbol{r}},\hat{\boldsymbol{\theta}},\hat{\boldsymbol{\phi}})$ in spherical coordinates (light blue). Note that the spherical basis $(\hat{\boldsymbol{r}},\hat{\boldsymbol{\theta}},\hat{\boldsymbol{\phi}})$ is related to the $(\boldsymbol{\ell},\boldsymbol{m},\boldsymbol{k})$ basis we defined in Section 3.2.3 via the polarisation angle. The Figure is partly adapted from Ref. [2]. 56

3.4.2 Implementation of scalar polarisation reconstruction in LALSUITE. Similar approach can be taken for vector-x and vector-y polarisations. 57

4.2.1 The classification of the six polarisations encoded in the four Newman-Penrose scalars. The shapes represent displacement that each mode induces on a sphere of test particles. The wave is assumed to propagate in the z-direction indicated by the icons/arrows in the right corners. 63

4.2.2 Range of validity of our EsGB theory, taking into account theoretical constraints on the dimensionless coupling β_0/m_1^2 and experimental constraint on the conformal factor a_0. The vertical dashed line separates the maximally allowed value of a_0 (to the left) from the observationally ruled out values (shaded grey region to the right). The two horizontal lines indicate the two theoretical constraints on the value of β_0/m_1^2. The upper line at $\beta_0/m_1^2=0.3$ represents the maximum coupling allowed before naked singularities appear in static solutions to the theory, while the line at $\beta_0/m_1^2=0.2$ represents the upper bound before the theory suffers a breakdown in hyperbolicity. See Sections 4.2.3 and 4.2.4 for more discussion. 66

4.3.1 Scalar waveforms for $l \geq 1$ for mass ratios of $q = 1/2, 2/3, 1$ extracted at $R_{\rm ext} = 110$. For unequal mass cases, the scalar field amplitude is more pronounced. The waveforms have been aligned so that the amplitude peaks of the scalar field coincide at $\hat{t} = 0$, and we set $\beta_0/m_1^2 = 1$ for convenience (recall that since we are using an order-reduction scheme, there is no restriction on the value of β_0/m_1^2 in our evolution). In our analysis, we choose a physically allowed value of β_0/m_1^2 and re-scale the scalar waveforms using Eq. (4.21). 72

4.3.2 Scalar $l = 0$ mode for binary mass ratios of $q = 1, 2/3, 1/2$, extracted at $R_{\rm ext} = 110$. 73

4.3.3 Scalar $l = 2, m = 2$ mode for mass ratios of $q = 1, 2/3, 1/2$. The inset shows the zoom-in on the ringdown portion of the signal. Within the inset, the blue dotted line indicates the time where the amplitudes of the $q = 2/3$ and $q = 1/2$ waveforms become smaller in amplitude than the $q = 1$ waveform. 73

4.3.4 *Left*: Scalar energy flux computed using Eq. (4.37). Here we set $\beta_0/m_1^2 = 0.01$. *Right*: Gravitational wave energy flux computed using Eq. (4.32). . . 74

4.4.1 Convergence of the estimated amplitudes with decreasing variance $\sigma^2 = \{0.005, 0.004, 0.003, 0.002, 0.001, 0.0008, 0.0005\}$ of Eq. (4.43) for the (22) mode of `BBH-12` run. The variance value estimated as 4% from the peak amplitude takes the value of $\sigma^2 = 0.003$ in our fit for this configuration. We have verified that the same convergence holds qualitatively for the $N = 1$ mode fit too. 78

4.5.1 Scalar antenna pattern for various choices of polar and azimuthal angles. Yellow regions indicate the maximum response from the detector from the incoming scalar-polarised GW. 81

4.5.2 Contour plot of network SNR in the $M_{\rm fin} \times q$ plane for the scalar ringdown of a BBH at 1 Gpc as observed by the Virgo, Livingston and Hanford network of detectors at design sensitivity. Here the couplings $a_0, \beta_0/m_1^2$ are fixed to their maximally allowed values as described in Section 4.5.1. NR data are available along horizontal lines of $q = \{1/2, 2/3, 1\}$, based on which SNR values are estimated by interpolation on the plane. 83

4.5.3 Contour plot of the SNR in the $M_{\rm fin} \times q$ plane for the scalar ringdown of a BBH at 1 Gpc as observed by the Einstein Telescope. The couplings $a_0, \beta_0/m_1^2$ are fixed to their maximally allowed values as described in Section 4.5.1. The top left panel shows the total SNR, while the individual scalar mode SNRs are shown in the remaining three panels. NR data are available along horizontal lines of $q = \{1/2, 2/3, 1\}$, based on which SNR values are estimated by interpolation on the plane. 84

4.5.4 Same as Fig. 4.5.3, except here the Gauss-Bonnet coupling $\sqrt{\beta_0} = 1.18\,\mathrm{km}$ is fixed and the plot is given on a logarithmic scale. For more discussion see Section 4.5.1. 86

4.6.1 Reconstructed waveforms for (11) (top) and (22) (bottom) modes for the scalar field for an injection into the Einstein Telescope. The left panel illustrates zero-noise injections and the right panel Gaussian-noise injections. The yellow line shows the recovered damped sinusoid model for each of the modes (see the main text for the details), the dashed purple and pink lines show the trigger-time (defined as the reference time in the reference detector) and ringdown start time respectively. For more discussion see Section 4.6.2. 89

4.6.2 Joint posterior distributions for the amplitudes and phases recovered for the (11) and (22) modes. The upper panel shows the parameters for the zero-noise injections and the lower panel for the Gaussian noise injections. The upper and lower limits on the estimated parameters lie within the 90% confidence interval. Parameter estimation from both injections clearly demonstrates that noise does not bias the recovered amplitudes and phases significantly. For more discussion see Section 4.6.2. 90

4.A.1 Convergence of $\Psi_{4,22}$ extracted at $R_{\rm ext} = 110M$ for the `BBH-11` configuration. *Top*: Convergence of the amplitude, $\Psi^A_{4,lm}$. The difference for medium/high resolutions is rescaled according to second and third orders of convergence. The inset shows an interval around the merger. *Bottom*: Convergence of the phase, $\Psi^\phi_{4,lm}$. The difference for medium/high resolutions is rescaled according to second, third and fourth orders of convergence. 94

4.A.2 *Left:* Convergence of the amplitude of φ_{22} extracted at $R_{\rm ext} = 110M$ for the `BBH-11` configuration. The difference for medium/high resolutions is rescaled from second to fourth orders of convergence. *Right:* Same as left but for the `BBH-12` configuration. 94

4.A.3 Convergence of $\Psi_{4,22}$ extracted at $R_{\rm ext} = 110M$ for the `BBH-12` configuration. *Top*: Convergence of the amplitude, $\Psi^{A}_{4,lm}$. *Bottom*: Convergence of the phase, $\Psi^{\phi}_{4,lm}$. 95

4.A.4 *Left*: Convergence of the energy flux extracted at $R_{\rm ext} = 110M$ for `BBH-11`. The difference for medium/high resolutions is rescaled according to third and forth orders of convergence. *Right*: Same as left but the diagnostic quantity is the angular momentum flux in the z-direction extracted at $R_{\rm ext} = 110M$ for `BBH-11`. 96

4.B.1 Self convergence of the $L1$-norm normalised over the total volume for the Gauss-Bonnet term. The difference for medium/high resolutions is rescaled according to the second order convergence. 97

4.B.2 Comparison of the $L1$-norm of the scalar field profile normalised over total volume for numeric and analytic solutions. 97

5.3.1 Four example cases of the BS scalar potential function $V(A)$, where $A \coloneqq |\varphi|$, defined in Eqs. (5.5–5.7). Here we set $\mu = 1$ for simplicity, however the BS solution can be rescaled appropriately for any value of μ following scaling arguments of Eqs. (5.17) and (5.20). The non-interacting potential for mini BSs is recovered for $\sigma_0 \to \infty$ or $\lambda_4 = 0$. Note the false vacuum state for solitonic potentials and the systematic increase of $V(A)$ from small σ_0 to the mini-BS limit and larger λ_4. 103

5.6.1 Behaviour of BS models with the mini BS potential of Eq. (5.5) (top) and a solitonic potential (5.7) with $\sqrt{G}\sigma_0 = 0.2$ (bottom). In the left (right) figures we show families of BS models of ground ($n = 0$) and excited ($n = 1$ and $n = 2$) states in the mass-radius (mass-central-amplitude) planes. 111

6.3.1 BS models in ST gravity with $\mu_\varphi = 0.05$, $\alpha_0 = 0$ and $\beta_0 = -11$ for a solitonic potential with $\sigma_0 = 0.2$. Each point in these mass-radius diagrams represents a BS model. The location of the point represents the star's mass $M_{\rm ADM}$ and radius $R_{\rm J}$, and the colour coding in the respective panels displays the central gravitational scalar $|\varphi|_{\rm ctr}$, the maximum (over radius) gravitational scalar magnitude $|\varphi|_{\rm max}$, the central BS scalar amplitude $A_{\rm ctr}$ and the frequency ω. The four circles labeled 1 to 4 mark the models displayed in more detail in Fig. 6.3.2. 124

6.3.2 Radial profiles of the BS scalar amplitude A, the gravitational scalar φ, the mass function m and the trace T of the energy momentum tensor for four selected models marked 1 to 4 in Fig. 6.3.1. The pair of models $1,2$ represents one scalarised and one GR star with equal compactness $C = 0.117$ and amplitudes $A_{\rm ctr}$ as indicated in the legend. Likewise, $3,4$ represent a scalarised and GR model with $C = 0.240$ each. As indicated by the dashed curves for GR and the solid lines for scalarised models, the scalarisation tends to push the BS scalar $A(r)$ towards larger radii and results in larger masses. In the region of strongest scalarisation in φ, the energy momentum tensor has negative trace T. 125

6.3.3 *Top*: Mass radius diagram for four values of the scalar mass. The scalarised branches decrease in size for larger μ_φ. *Bottom*: The maximal value of the gravitational scalar, $|\varphi|_{\rm max}$, is shown as a function of the central BS scalar amplitude $A_{\rm ctr}$ for the same BS families. Note that for $\alpha_0 = 0$, the models for positive and negative φ are degenerate and we plot both extrema, $\pm|\varphi|_{\rm max}$, to illustrate the loop structure. Again the loops shrink for larger μ_φ, but we also notice a split into two separate loops at $\mu_\varphi = 0.1$. For $\mu_\varphi = 0.15$, the second loop containing highly compact models with large $A_{\rm ctr}$ is no longer present. 127

6.3.4 The threshold value of β_0 for the onset of scalarisation; for $\beta_0 \leq \beta_{0,\rm thr}$, scalarised BS models exist. 128

6.3.5 *Upper panels*: Radial profiles of the BS scalar amplitude A, the gravitational scalar φ and the trace of the energy-momentum tensor T for the BS Models 1 and 2 indicated by a circle and a triangle, respectively, in the panels below. The models with $\lambda_4 = 0$ (left) have frequencies $\omega_1 = 0.8518$ and $\omega_2 = 0.7729$, whilst for models 1 and 2 with $\lambda_4 = 50$ (right) we have $\omega_1 = 0.8303$ and $\omega_2 = 0.7572$. Note that the trace of the energy-momentum tensor has been scaled for presentation purposes. As supported by the analysis in the main text, T becomes negative at small radii for models with a gravitational scalar peaking at the origin. *Lower panels*: Mass-radius plots with the colour bar indicating the central amplitude of the BS scalar field. The star marks the threshold at which the gravitational scalar starts to peak off centre; we ubiquitously observe that φ peaks at $r = 0$ for less compact stars ($A_{\rm ctr}$ is lower than for the threshold case, i.e. dark blue colour) and φ peaks off centre for more compact stars (large $A_{\rm ctr}$, i.e. cyan colour). We exemplify this with models 1 (less compact with φ peaking at $r = 0$) and 2 (more compact with φ peaking off-center) for each of the potentials (left with $\lambda_4 = 0$ and right with $\lambda_4 = 50$). 129

6.3.6 Maximum of the gravitational scalar field as a function of the central bosonic amplitude for various potentials considered in this work. We remark that repulsive potentials result in more strongly scalarised solutions than any other potential considered here. 133

6.3.7 Flow-chart showing the dependence of the gravitational scalar profile φ on the BS parameters, $A_{\rm ctr}$ and $V(A)$, and the ST parameters, μ_φ and β_0. As discussed in the main text, the sign of $\partial_r \kappa$ determines the behaviour of φ at the origin. If $\partial_r \kappa > 0$, φ peaks away from $r = 0$, whilst for $\partial_r \kappa < 0$, φ peaks at $r = 0$. The two source terms, denoted by I and II in the diagram, play the leading role in determining the sign of $\partial_r \kappa$ at $r = 0$. By the boxes' colours we mark how the ST and BS parameters tend to impact the φ profiles – blue for peaking at the origin and pink for peaking off centre. 134

6.3.8 *Top:* The threshold $\beta_{0,\mathrm{thr}}$ for the onset of scalarisation as a function of μ_φ for different BS potentials $V(A)$ as given in Eq. (6.17) with the indicated parameter values σ_0 and λ_4. The lines represent quadratic fits with the given coefficients. The case $\lambda_4 = 100$, $\mu_\varphi = 1.5$ exhibits one minor anomaly: here, the $\times$ symbol marks the disappearance of stable scalarised models, but extremely compact unstable BSs are still found up to the β_0 value marked by the filled circle. Only the former ($\times$) data point is used in the fit. *Bottom:* The threshold $\beta_{0,\mathrm{thr}}$ for the onset of strong scalarisation is shown for the different types of potentials and three values of the gravitational scalar mass $\mu_\varphi = 0,\ 0.1$ and 0.3. The horizontal axis represents σ_0 for the solitonic potential on the left and λ_4 for the repulsive potential on the right. 135

6.3.9 *Left*: BS models in ST gravity with $\mu_\varphi = 0$, $\beta_0 = -7$ and varying α_0 for a solitonic potential with $\sigma_0 = 0.2$. The branches obtained for each value of α_0 are presented in different shades of one colour to differentiate between positive and negative central gravitational field amplitudes. For $\alpha_0 = 0.01$, for instance, dark green denotes models where $\varphi_{\mathrm{ctr}} < 0$ and light green those with $\varphi_{\mathrm{ctr}} > 0$. For reference, we also plot the solutions for $\alpha_0 = 0$ which are shown in grey. *Right*: Dependence of the BS solutions on β_0 for $\alpha_0 = 0.01$, $\mu_\varphi = 0$ and a solitonic potential with $\sigma_0 = 0.2$. The inset highlights the self-intersecting $\varphi_{\mathrm{ctr}} > 0$ branch with ∞ shape for the sequence of models with $\beta_0 = -10$. 137

6.3.10 *Left*: Mass-radius diagram for solitonic BS models with $\mu_\varphi = 0$, $\alpha_0 = 0$, $\beta_0 = -12$ and $\sigma_0 = 0.2$. *Right:* Frequency ω as a function of the central BS scalar amplitude A_{ctr} for the same family of models. The colour represents the maximal gravitational scalar in both panels. 138

6.3.11 Radial profiles of the scalar functions $A(r)$, $\varphi(r)$ and the mass $m(r)$ for a scalarised BS with $A_{\mathrm{ctr}} = 0.148$ and a GR model with $A_{\mathrm{ctr}} = 0.177$, corresponding to the minimal frequencies $\omega = 0.1476$ and $\omega = 0.4283$ and marked by circles in Fig. 6.3.10. For presentation purposes, the scalar fields A and φ have been amplified by a factor 10. 139

6.4.1 Mass-radius diagram for BS solutions for $\mu_\varphi = 0.05$, $\alpha_0 = 0$, $\beta_0 = -11$ and a solitonic potential with $\sigma_0 = 0.2$. Stable models are determined by identifying among the set of all stars with equal Noether charge Q_{BS} the BS with the strongest binding energy $E_{\mathrm{b}} = M_{\mathrm{ADM}} - Q_{\mathrm{BS}}$. These stable models are displayed in light (copper) colour and the remaining unstable stars in dark (black). 140

6.4.2 Stability of other BS models considered in this work. From left to right: (i) repulsive potential with $\lambda_4 = 50$, massless φ, $\alpha_0 = 0$, $\beta_0 = -7$; (ii) solitonic potential with $\sigma_0 = 0.2$, massive φ with $\mu_\varphi = 0.05$, $\alpha_0 = 0.01$, $\beta_0 = -10$; (iii) mini potential with $\lambda_4 = 0$, massless φ, $\alpha_0 = 0$, $\beta_0 = -7$. As in Fig. 6.4.1, light (copper) colour denotes stable BS models and dark (black) unstable ones. Note that for $\alpha_0 \neq 0$ (center and right panels) we always have two separate scalarised branches, either of which may self-intersect: one closed loop and one open branch with two loose ends. For the mini BS in the right panel, these two branches almost touch, yet remain separate as shown in the inset. 141
6.C.1 Boson-star families in the mass-radius plane for fixed ST parameters $\alpha_0 = 0$, $\beta_0 = -10$, $\mu_\varphi = 0$ and BS potential functions $V(A)$ as given in Eq. (6.17). The parameters σ_0 or λ_4 are specified in each panel for the corresponding BS family. The mini-BS case is recovered in either of the limits $\sigma_0 \to \infty$ or $\lambda_4 = 0$. The colour bar marks the degree of scalarisation in terms of the maximum of $|\varphi(r)|$. 151
6.C.2 Same as Fig. 6.C.1 but with $|\varphi|_{\rm ctr}$ colour coded. 152
6.C.3 Same as Fig. 6.C.1 but with $A_{\rm ctr}$ colour coded. 153
6.C.4 Same as Fig. 6.C.1 but with ω colour coded. 154
6.C.5 Same as Fig. 6.C.1 but with the stability coded in colour, light (copper) for stable BSs and black for unstable models. 155

7.6.1 *Left:* Real parts of the (20)-mode of the Newman-Penrose scalar Ψ_4 for binary sequence `q1-d11-p000`, obtained for plain superposition, the equal-mass fix and our improved method. The waveforms have been shifted by $t_{\rm peak}$, the time at which the maximum GW amplitude is reached. *Right:* Maximum of the scalar field amplitude for the same binary configuration. Notably, plain superposition leads to formation of a BH well before the equal-mass fix, therefore resulting in an altered gravitational waveform. Here we indicate the merger time by the vertical lines. 168

7.6.2 *Left:* Log plot of the $L2$-norm of the Hamiltonian constraint violations (normalised by the central energy density $16\pi\rho_{\rm ctr}$ of the heavier star) across the simulation grid for the binary configuration `q075-d12-p000`. The grey region indicates the parameter space of $(R_{\rm A}, R_{\rm B})$ where constraint violations diverge. The values of constraint violations have been interpolated onto the full domain using the runs performed indicated by the yellow circles. *Right:* A zoom-in on the region $(R_{\rm A}, R_{\rm B}) \in [(0,100)\times(0,100)]$. Asymmetries in the constraint violations are visible across the diagonal $R_{\rm A} = R_{\rm B}$, demonstrating the non-trivial dependence of the constraints on the choice of radial parameters. In the equal-mass case, we have verified that the constraint violations are symmetric under exchange A $\leftrightarrow$ B, as expected. The results for the remaining mass ratios are displayed in Figure 7.D.1. 169

7.6.3 Log-scaled Hamiltonian constraint $\mathscr{H}$ (normalised by the central energy density $16\pi\rho_{\rm ctr}$ of the heavier star) and the x-component of the momentum constraint $\mathscr{M}_x$ (normalised by the central momentum density $8\pi j_{x,\rm ctr}$ of the heavier star) computed along the collision axis of the binary of mass ratio $q = 0.5$ and initial separation $d/M = 14.8$. 170

7.7.1 Radiated energy $E_{\rm rad}$ as a function of the phase off-set parameter $\delta\phi$ for equal-mass BS binary head-on collisions `q1-dX-pX` of Table 7.6.2 starting from different separations d/M using plain superposition (left panel) and the equal-mass fix (right panel). The single error bar displayed at $\delta\phi = \pi/2$ in the right panel indicates our numerical uncertainty which is very similar for all data points. 171

7.7.2 *Left:* The radiated energy $E_{\rm rad}$ is shown as a function of the phase offset parameter $\delta\phi$ as in Fig. 7.7.1, but now for BS binary configurations starting from initial separation $d/M = 11.2$ with different velocities. For $v = 0.18$, the radiated energy closely matches the teal coloured curve of the $d/M = 22.3$, $v = 0.1$ binary as predicted by a Newtonian calculation of the infall velocity. *Right:* The radiated energy is shown as a function of time for BS binaries with a phase offset $\delta\phi = \pi$. Again, starting a BS binary from $d/M = 11.2$ with a larger velocity, as obtained from a Newtonian calculation, the energy functions for $v = 0.1$ but larger initial separation are recovered. The initial separation d is given in units of M, even though this factor has been omitted in the legends for presentation purposes. 173

7.7.3 Evolution of the central scalar field $|\varphi_c|$ of the two BSs for the mass ratio $q = 0.5$ using plain superposition (left) and the improved method (right). The results for the heavy star B are shown as solid and those for the light star A as dotted curves, and the colour encodes the initial separation. For each configuration, the phase offset $\delta\phi$ has been chosen to maximise the GW radiation; cf. Table 7.7.1. The vertical dashed lines mark the time of formation of a common apparent horizon. The inset shows the early evolution of $|\varphi_c|$ for the heavy star B up to the point of divergence; plain superposition results in significant oscillations of $|\varphi_c|$. For $d/M = 14.8$ and 29.7, these oscillations trigger a premature collapse of the heavy star into a BH (signalled by the rapid drop of $|\varphi_c|$ to zero) well before a common apparent horizon forms. 175

7.7.4 20-modes of the Newman-Penrose scalar Ψ_4 of binary configurations with $q = 0.75$ (upper) and $q = 0.38$ (lower) with varying initial separation, d. For each mass ratio, initial separation and superposition method, we choose the phase off-set parameter that maximises the GW energy; cf. Table 7.7.2. The straight line shows the waveform obtained for our improved method, whilst the dashed line shows that for plain superposition. As we increase the separation, both superpositions give comparable results. This is most notable in the case of smaller mass ratio $q = 0.38$, where good agreement is already reached at smaller distances $d/M \gtrsim 32.4$. 177

7.7.5 20-modes and 30-modes of the Newman-Penrose scalar Ψ_4 for the improved binary configuration $q = 0.38$ with initial separation $d/M = 64.8$ and different phase off-set parameters $\delta\phi$. The prominent feature of certain off-set parameters (e.g. $\delta\phi = 60^\circ, 90^\circ$) is that they result in fainter GW signals with more complex structure and $\ell = 3$ modes become comparable in amplitude to the $\ell = 2$ ones. This is unlike the head-on BH case of the same mass ratio, where $\ell = 3$ mode is roughly 5 times smaller than the $\ell = 2$ mode [3]. . . . 178

7.7.6 Radiated energy as a function of the phase off-set parameter $\delta\phi$ for binary collisions of $q = 0.75, 0.5, 0.38$. The left panels show the results for plain superposition (7.27) and the right panels those for our improved superposition. 179

7.C.1 Convergence analysis of the GW energy computed with the LEAN code for the collision and merger of the BS binary `q05_d29_p000` of Table 7.6.2. The upper panel shows the differences in the energy results obtained for different resolutions, measured here in terms of the grid spacing on the innermost refinement level. The high-resolution difference has been rescaled by $Q_1 = 0.8$ and $Q_4 = 1.57$ corresponding to first and fourth-order convergence. While the small contribution due to noisy junk radiation converges only at first order, the total radiated energy exhibits convergence close to fourth order. The bottom panel displays the radiated energy as a function of time for the three resolutions as well as a fourth-order Richardson extrapolation. 188

7.C.2 Convergence analysis of the GW energy computed with at $R_{ex} = 120$ for the GRCHOMBO simulation of BS binary `q075_d12_p000` of Table 7.6.2. The difference between high and medium resolutions has been rescaled by factors Q_1 to Q_4 corresponding to convergence of first to fourth order. At early times, the order of convergence fluctuates between second and third, whilst at later times it settles to just below second order of convergence. . . 189

7.D.1 The logarithm of the $L2$-norm of the Hamiltonian constraint violations is shown for the binary configurations `q05-d14-p000` (upper) and `q038-d16-p000` (lower panels). For each case, the right panel shows a zoom-in on the region $(R_A, R_B) = [(0,100) \times (0,100)]$. The grey region indicates the parameter space of (R_A, R_B), where constraint violations are too large; note that this region increases in size for smaller mass ratios. 190

8.3.1 Plus polarizations of the 22 IMR mode for the `A17-d14` and `A147-d19` binaries of Table 8.3.1. 195

8.3.2 *Left*: Comparison of the plus polarizations of the 22 IMR mode for the `A17-d12`, `A17-d12-p180` and `A17-d12-e1` binaries of Table 8.3.1. *Right*: The same as the left panel but showing the amplitude of the strain. Note the difference in the strength of the chirp across all of the runs. 196

8.4.1 Null distribution of the SNR of Gaussian noise and the residual SNR in the Hanford (H1) and Livingston (L1) detectors, computed from the `IMRPhenomXP` approximant evaluated at the source parameters of the maximum of the joint log-likelihood. *Left*: Example of a Gaussian residual for a `A147-d19` binary of $M_{tot}^{inj} = 72.4 M_\odot$ at $d_L = 500$Mpc. *Right*: Example of a *non*-Gaussian residual for a `A147-d19` binary of $M_{tot}^{inj} = 75.8 M_\odot$ at $d_L = 250$Mpc. 198

8.5.1 Injection of an `A17-d12` binary of $M_{\rm inj}^{\rm tot} = 72.4 M_\odot$ at $d_{\rm L} = 500$Mpc and its recovery using the `IMRPhenomXP` waveform approximant with fixed (variable) spins in the top (bottom) panels. As expected, the inference with variable spins is able to match the injected GW signal better, especially in the merger and the ringdown. This is in particular manifested in the increase of the recovered SNR, e.g. in Hanford we find a SNR of 32.7 for variable spins and 31.4 for fixed. Note the SNR of the injection in Hanford is 32.9. 201

8.5.2 *Left:* Comparison of key PE results for `A17-d12` and `A17-d12-e1` injections. We use `IMRPhenomXP` for recovery of a BS binary with $M_{\rm tot}^{\rm inj} = 72.4 M_\odot$, $d_{\rm L} = 500$Mpc and allow all binary parameters to be sampled over. The 1, 1.5, 2-sigma contours are shown. *Right*: PE results for an `A17-d12` injection with $M_{\rm tot}^{\rm inj} = 4.96 M_\odot$, $d_{\rm L} = 31.25$Mpc and recovery with `IMRPhenomPv2_NRTidal` with all parameters being sampled over. The dotted vertical lines show the 90% confidence interval. We note that the 90% confidence interval, within which the recovered tidal deformability Λ_2 is contained, is wider than that of the Λ_1 parameter. 202

8.5.3 PE results obtained for four BS families and injections with total mass $M_{\rm tot}^{\rm inj} \in [5, 105] M_\odot$ and luminosity distance $d_L = (M_{\rm tot}^{\rm det}/80\,M_\odot)500\,$Mpc. For each injection, we display the median values of the recovered component masses m_1, m_2 normalised by their injected values (large and small circles) and the effective spin (crosses with 90 % confidence interval). The recoveries are obtained for fixed (blue) or variable spins (red symbols). The dashed lines mark the injected values, 1 for the masses and 0 for $\chi_{\rm eff}$. The recovered parameters deviate from these values non-randomly; cf. the main text. By repeating selected injections with different $d_{\rm L}$, we have verified that the displayed trends are robust under variations of the SNR. 203

8.5.4 *Top:* The recovery of a high-mass `A147-d19` binary injection using `IMRPhenomXP` results in $m_1 \sim 70 M_\odot$, $m_2 \sim 65 M_\odot$, $a_1 \sim 0.98$ and $a_2 \sim 0.60$. *Bottom:* The recovery of a low-mass `A147-d19` binary injection using `IMRPhenomPv2_NRTidal` yields maximum-joint-log-likelihood estimates $m_1 \sim 3.7 M_\odot$, $m_2 \sim 1.3 M_\odot$, $a_1 \sim 0.96$, $a_2 \sim 0.63$, $\Lambda_1 \sim 3000$ and $\Lambda_2 \sim 11000$. 204

8.A.1 We compare results of `A147-d17` binary evolutions with tagging using grid variables (left) and tagging using a 'moving-boxes' approach (right). From top to bottom we show the real part of the (22)-mode of Ψ_4, the positions of the stars and the maximum of the central amplitude of the scalar field. . . . 208

8.B.1 Convergence test of the compact configurations `A17-d12` and `A17-d14` of Table 8.3.1. The difference between high and medium resolutions has been re-scaled by factors Q_2 to Q_4, corresponding to convergence of second to fourth order. 210

8.B.2 Convergence test of the configuration `A147-d19` of Table II in the main document for the GW strain (upper) and phase (lower panel). The difference between high and medium resolutions has been scaled by factors Q_4 and Q_7, corresponding to fourth- and seventh-order convergence. 211

8.C.1 Comparison of amplitude (left) and phase (right) of the dominant (22)-modes obtained for the in-phase BS (`A17-d15`), dephased (`A17-d15-p090`), anti-phase (`A17-d15-p180`), anti-BS (`A17-d15-e1`) and BH binaries. Both amplitude and phase have been aligned such that the peak amplitudes coincide in time. The anti-BS signal exhibits the best agreement with the BH waveform, whereas the in-phase and anti-phase configurations result in the largest deviations from the BH signal. 213

List of tables

3.3.1 Binary black hole source parameters and their priors typically employed in parameter estimations pipelines. Here 'Sin' and 'Cos' denote uniform priors in cosine and sine correspondingly (note the order here!), whilst 'Comoving' refers to the uniform prior in cosmological comoving volume. The 'max' and 'min' subscripts are used to denote the lower and upper bounds on the priors. 49

4.2.1 Summary of current constraints on the EsGB coupling parameter β_0, the dimensionless parameter β_0/m_1^2 and the conformal coupling a_0. Our conventions for β_0 and a_0 are given in Eq. (4.3). 67

4.3.1 Two puncture initial data used for three binary BH configurations considered in this Chapter. Here $M_{\rm fin}$ and $j_{\rm fin}$ denote the final mass and final spin of the remnant BHs respectively, which were calculated from balance arguments given in Eqs. (4.30) and (4.31). Assuming the validity of the balance arguments, we estimate 0.01% error in the final mass and 0.05% error in the final spin when compared to their Richardson-extrapolated values. In Appendix 4.A.2 we present convergence plots for the radiated energy and angular momentum. 69

4.4.1 Estimated amplitudes from the $N = 1$ mode and $N = 2$ mode fits summarized by Eqs. (4.41)-(4.42). As in Fig. 4.3.1, we set $\beta_0/m_1^2 = 1$ for convenience. The dash indicates that a specific fit could not describe the data accurately. In all cases with an $N = 2$ mode fit, A_1 represents the amplitude of the scalar Kerr QNM. For the (11) mode, A_2 is the amplitude of the scalar Kerr overtone, while for all other modes, A_2 represents the amplitude of gravitational Kerr QNM. The upper and lower limits on the estimated parameters lie within the 90% confidence interval and the central value is the median. 79

4.4.2 Estimated gravitational amplitudes of the $N = 1$ mode fit of Eq. (4.38), where the fundamental gravitational QNMs are kept fixed. The upper and lower limits on the estimated parameters lie within the 90% confidence interval. . 80
4.5.1 Distance and final BH mass range targeted with each of the detectors considered in this study. 82
4.C.1 QNMs of the remnant Kerr BH in GR, used in the fitting procedure described in Section 4.4. 98

6.3.1 Summary of threshold values of β_0 for the onset of scalarisation for different potentials in the massless case. 132
6.3.2 The minimum value of σ_0 where we find BS models with a gravitational scalar peaking at $r = 0$ is listed for solitonic BS families with $\alpha_0 = 0$ as well as the specified values of μ_φ and β_0. A gravitational scalar φ reaching its global extremum at the origin is easier to obtain for smaller μ_φ and for larger β_0. 133

7.6.1 Solitonic BS models with $\sqrt{G}\sigma_0 = 0.2$ considered in this work. $A(0)$ denotes the central scalar field amplitude, $M_{\rm BS}$ the mass of the BS, ω the frequency of the ground state solution, r_{99} the areal radius containing 99% of the BS mass, and $\max(m(r)/r)$ our measure of compactness. Note that for this potential the maximum mass of a BS is $\mu M_{BS} = 0.7212$. 166
7.6.2 Binary initial data configurations considered in this work. Each run has a suffix `dX-pX`, where `dX` is a wildcard for the initial separation and `pX` is a wildcard for the off-phase parameter in degrees, $\frac{180^\circ}{\pi}\delta\phi \in [0^\circ, 360^\circ)$. In our convention, the off-phase parameter, $\delta\phi$, is added to star A, whilst for star B it remains zero. Here $v_x^{\rm J}$ for $\mathrm{J} \in \{\mathrm{A},\mathrm{B}\}$ denote the initial boost velocities with associated Lorentz factors $\gamma_{\rm J}$, $d = ||x^i_{\rm A} - x^i_{\rm B}||$ is the initial separation and $M = \gamma_{\rm A} M^{\rm A}_{\rm BS} + \gamma_{\rm B} M^{\rm B}_{\rm BS}$ is the total mass of the binary. 167
7.6.3 Choice of radial parameters $(R_{\rm A}, R_{\rm B})$ for the unequal-mass binaries considered in this work. 169
7.7.1 Choices of dephasing parameters $\delta\phi$ maximising the GW energy for `q05-dX-pX` binary configuration. 175
7.7.2 Choices of dephasing parameters $\delta\phi$ maximising the GW energy for `q075-dX-pX` and `q038-dX-pX` binary configurations. 176
7.A.1 A list of the conformal factor functions used in our discussion of binary initial-data construction. Note that in the main text we fix $n = 4$ in the newly defined conformal factor, so that $\gamma_{ij} = \lambda_{\rm new}\tilde{\gamma}_{ij}$. 184

8.2.1 Summary of the solitonic BS models considered in this Chapter. We start by listing the central amplitude $A_{\rm ctr}$, the mass of the BS m, the frequency of the ground state solution ω, the areal radius containing 99% of the BS mass r_{99} and the compactness C. 193
8.3.1 Summary of the BS binaries evolved in the centre-of-mass frame with initial boost velocity $v_{x,\rm ini}$ in the x-direction, impact parameter b in the y-direction and separation d in the x-direction. The dephased, anti-phase and anti-BS binaries are labelled as `p090`, `p180`, `e1`. $E_{l=2}$ is the GW energy contained in the $l=2$ modes. 194
8.5.1 Recovery results for a range of BS injections from Table 8.3.1 using the `IMRPhenomXP` approximant with spins fixed to zero. We contrast the injected ($\rho^{\rm inj}_{\rm net}$) and recovered ($\rho^{\rm rec}_{\rm net}$) network SNRs and report the recovered chirp-masses $\mathscr{M}^{\rm rec}_{\rm c}$, mass-ratios $q^{\rm rec}$ at maximum-joint-log-likelihood. 200
8.D.1 List of all our injections for the BS families listed in Table 8.3.1. We report the injected component masses, m_1 and m_2, luminosity distance d_L and the corresponding SNR values for the H1 and L1 detectors. The recovery is performed using the specified approximants and samplers initialised with N_s sampling points. The recovered values for the masses, luminosity distance, the dimensionless spins a_1 and a_2, the effective and precession spin parameters $\chi_{\rm eff}$, $\chi_{\rm p}$ and the tidal deformability parameters Λ_1, Λ_2 are given in the form of median values with 90% confidence intervals. We additionally list the recovered optimal SNR and Bayes evidence factors $\log(\mathscr{B}^{\rm S}_{\rm N})$ and mark residuals consistent (inconsistent) with Gaussian noise by a ✓(✗) symbol. . 215

Nomenclature

Roman Symbols

$\mathbf{R}$	Four-dimensional Riemann tensor
${}^{(3)}\mathbf{R}$	Three-dimensional (spatial) Riemann tensor
$\mathbf{g}$	Four-dimensional metric
$\mathbf{n}$	Unit normal to spatial hypersurfaces
$\mathbf{K}$	Extrinsic curvature
$\hat{\mathbf{L}}$	Unit vector of orbital angular momentum
h	Gravitational-wave strain
$E_{\rm rad}$	Gravitational-wave energy
$\mathrm{J}_{\rm rad}$	Radiated angular momentum
$R_{\rm ext}, R_{\rm ex}$	Extraction radius
$n_{\rm B}$	Number of cells in the buffer region

Greek Symbols

$\boldsymbol{\gamma}$	Three-dimensional (spatial) metric
$\boldsymbol{\eta}$	Minkowski metric
α	Lapse
$\boldsymbol{\beta}$	Shift
χ, ψ	Conformal factor

Ψ_4 The 4th Newman-Penrose scalar

Y_{lm} Spherical harmonics

${}_{-2}Y_{lm}$ Spin weighted $s = -2$ spherical harmonics

Σ_t Spatial hypersurface at time t

ι Inclination angle

$\varepsilon_{\rm FR}$ Fill ratio

$d_{\rm L}$ Luminosity distance

z Redshift

Acronyms / Abbreviations

ADM Arnowitt-Deser-Misner

AMR Adaptive Mesh Refinement

BBH Binary Black Hole

BH Black Hole

BS Boson Star

BBS Binary Boson Star

BSSN(OK) Baumgarte-Shapiro-Shibata-Nakamura (-Oohara-Kojima)

CCZ4 Conformal and Covariant Z4

CE Cosmic Explorer

CPU Central Processing Unit

CWB Coherent Wave Burst

DM Dark Matter

ECO Exotic Compact Object

EFT Effective Field Theory

ESA European Space Agency

EsGB Einstein-scalar-Gauss-Bonnet

ET Einstein Telescope

GR General Relativity

IMR Inspiral-merger-ringdown

LAL LIGO Scientific Collaboration Algorithm Library

LIGO Laser Interferometer Gravitational-Wave Observatory

LISA Laser Interferometer Space Antenna

LVK LIGO-Virgo-KAGRA

MCMC Markov Chain Monte Carlo

ML Machine Learning

MPI Message Passing Interface

NASA National Aeronautics and Space Administration

NR Numerical Relativity

NS Neutron Star

PN Post Newtonian

PSD Power Spectral Density

SIMD Single instruction, multiple data

SM Standard Model

SNR Signal-to-Noise Ratio

ST Scalar-tensor

SXS Simulating eXtreme Spacetimes

QNM Quasinormal Mode

ΛCDM Λ Cold Dark Matter

Units and conventions

The biggest fear of every physicist is probably sorting out units and converting between various conventions. In every Chapter we will specify what units we are using; generally we will either use *geometric*, $G = c = 1$, or *natural*, $c = \hbar = 1$, units. We remind the reader that in geometric units $L = M = T$, where L denotes the length scale, M – the mass scale and T – the time scale; whilst in natural units we have that $E = T^{-1} = M = L^{-1}$, where E is the energy scale. It is therefore convenient to measure everything in units of mass in geometric units and in units of energy (or mass) in natural units.

We use a plus signature $(-+++)$ and the Riemann tensor is $R^{\alpha}{}_{\mu\beta\nu} = \partial_\beta \Gamma^{\alpha}_{\mu\nu} - ....$ We use Greek letters $\mu, \nu, ...$ running from $0, 1, 2, 3$ for spacetime indices and Latin letters $i, j, ...$ running from $1, 2, 3$ for spatial indices. We sometimes denote vectors and tensors in index-free notation using bold symbols such as $\boldsymbol{\beta}$ and $\mathbf{T}$. Purely spatial tensors will be denoted with the superscript ${}^{(3)}$ in front of them, e.g. ${}^{(3)}R_{ij}$.

Chapter 1

The bigger picture: The quest towards understanding gravity

> I consider the theory of relativity to be an example showing how a fundamental scientific discovery, sometimes even against the resistance of its creator, gives birth to further fruitful developments, following its own autonomous course.
>
> *Wolfgang Pauli*

1.1 Theory of general relativity

In 1915, Einstein published his famous theory of general relativity (GR) [4], which is now regarded as one of the main pillars of modern physics. Einstein's theory presented a radical new conception of space and time and how gravity couples to matter. The space-time is described as a $4D$ Lorentzian manifold[1] $\mathscr{M}$, equipped with a metric $g_{\mu\nu}$ mediating gravity. The theory can be elegantly formulated in terms of the Einstein-Hilbert action,

$$S = \int \sqrt{-g}\frac{1}{2\kappa}(R-2\Lambda)\,\mathrm{d}^4x + S_{\mathrm{M}}, \tag{1.1}$$

where $\sqrt{-g}$ is the volume form, $\kappa = 8\pi G/c^4$, R is the Ricci scalar, Λ is the cosmological constant and S_{M} is the matter action. Varying the action with respect to the metric, results in

[1] A Lorentzian manifold is a pair $(\mathscr{M},\mathbf{g})$ where $\mathscr{M}$ is an N-dimensional smooth manifold and $\mathbf{g}$ is a Lorentzian metric. The metric associates to each point $p \in \mathscr{M}$ a scalar product g_p on the tangent space $T_p\mathscr{M}$. Here g_p is a non-degenerate symmetric bilinear form $(\cdot,\cdot)$ such that $\exists$ basis $e_1, e_2, \ldots$ with $(e_i,e_j) = -1$ if $i = j = 1$, $(e_i,e_j) = 1$ if $i = j \geq 2$ and $(e_i,e_j) = 0$ otherwise.

the Einstein field equations,

$$R_{\mu\nu} - \frac{1}{2} g_{\mu\nu} R + \Lambda g_{\mu\nu} = \kappa T_{\mu\nu}, \tag{1.2}$$

where $R_{\mu\nu}$ is the Ricci tensor and $T_{\mu\nu}$ is the energy-momentum tensor,

$$T_{\mu\nu} = -\frac{2}{\sqrt{-g}} \frac{\delta S_{\rm M}}{\delta g^{\mu\nu}}. \tag{1.3}$$

We will assume that $\Lambda = 0$ for the rest of this thesis and in this Chapter we will employ geometric units $G = c = 1$, so that the Einstein-Hilbert action and the equations of motion reduce to

$$\boxed{S = \int \sqrt{-g} \frac{1}{16\pi} R \mathrm{d}^4 x + S_{\rm M} \implies R_{\mu\nu} - \frac{1}{2} g_{\mu\nu} R = 8\pi T_{\mu\nu}.} \tag{1.4}$$

The formulation of the Einstein's equations led to an array of predictions, including black holes and gravitational waves, and resulted in more profound understanding of the history of our cosmos, including modelling of the early universe and the Big Bang. At the beginning the opinions on the framework of general relativity separated into two distinct groups [5]. One the one hand, it was widely referred to as 'one of the greatest examples of the power of speculative thought' – a model with 'logical simplicity' of its axioms. On the other hand, the theory faced a lot of criticism as many found its Riemannian and nonlinear character 'incomprehensible'. Due to a lack of observational evidence supporting the validity of GR, many critics emphasized why would anyone even try finding solutions to such an 'ephemeral set' of equations. As even harshly pointed out by the French physicist Bouasse: 'the experimental physicists will have the last word: we accept the theories that we find convenient; we reject those which we cannot understand and that are for this reason useless'. Despite all the criticism, many remained optimistic about Einstein's ideas. Four years later British missions to Sobral, led by Davidson and Crommelin, and to Principe, led by Eddington, confirmed Einstein's prediction of light deflection [6, 7]. This marked the first step for devising a programme for testing the validity of GR and its subsequent success.

1.2 History of tests of GR

In his original work, Einstein proposed three *classical* tests: (i) the perihelion advance of Mercury's orbit, (ii) the deflection of light by the Sun, and (iii) the gravitational redshift of

light. Later on further modern tests have been devised, including the Shapiro time delay [8, 9], gravitational lensing [10] and Post-Newtonian tests of gravity [11]. More recently, in 2015 (precisely one century after Einstein's theoretical prediction) the international collaboration consisting of the Laser Interferometer Gravitational-Wave Observatory (LIGO), Virgo and Kamioka gravitational wave detectors (KAGRA) reported the first direct observation of gravitational waves (GWs) [12]. The signal GW150914 was detected independently by the two LIGO detectors, capturing the gravitational waves from a coalescence of two stellar black holes (BHs) of masses $\sim 36M_{\odot}$ and $\sim 29M_{\odot}$. To the present date, LIGO and Virgo have detected over 100 GW events from merging BHs and neutron stars (NSs) [13, 14]. With current sensitivity of GW detectors no deviations from GR have been found so far [15–19].

Even though GR had impressive success in passing all of these tests, we cannot fully rule out that in strong-field tests, such as observations of GWs, we simply have not yet detected deviations from GR, which if they exist may be small. With the future generation of GW detectors we will be in a position to even more accurately constrain our alternative hypotheses to Einstein's theory of gravity. It is important to highlight however that Einstein's theory never disproved the Newton's law of gravity, but rather showed it to be *incomplete*. Presently, GR is undergoing similar tests, as many believe that even Einstein's theory may be incomplete, especially in the strong-field, high curvature regimes. This is motivated by a plethora of theoretical dilemmas we discuss in the following Sections.

1.3 Challenging our understanding

Before beginning the discussion of the current challenges encountered in the formulation of GR, let us travel back in time to one of the proposed classical tests of Einstein – the perihelion advance of Mercury's orbit. This first test dates back to the observations of the 19th century by Urbain Le Verrier, who remarked that Mercury's precessing orbit does not behave as predicted by Newton's gravity. Back in 1846, Neptune was the first planet to be discovered mathematically as an explanation for Uranus' deviation from its predicted orbit. Inspired by this hypothesis Le Verrirer suggested that the anomalous orbit of Mercury could be due to a hypothetical planet nearby that he named Vulcan. Unfortunately, his hypothesis was proved to be incorrect once Einstein formulated his theory of general relativity and tests have been carried out to verify Mercury's precessing orbit. However, this history lesson serves as a great example of revolutionary theory – a truly modified theory of gravity, an alternative to Newtonian thinking – superseding our classical understanding of physics. In the present world, we find ourselves in the same position: now general relativity is regarded as one of the most important classical field theories, yet for the reasons we will discuss below,

we are not fully satisfied with it and are in fact on the search for a complete theory of gravity, where GR is one of its limits. So why is the theory of general relativity not enough?

One of the fundamental theoretical reasons to believe that the range of validity of GR may be restricted is its inconsistency with quantum field theory, which does not describe gravitational attraction on microscopic scales. GR is furthermore non-renormalisable in a quantum-field theory sense [20]. The as yet unknown theory that unites the two is usually called *quantum gravity*, example candidates of which include string theory and loop quantum gravity [21]. Additionally, cosmological and astrophysical observations suggest the existence of *dark matter* and *dark energy* [22, 23]. Dark matter makes up as much as $\sim 27\%$ of the mass of the Universe, and its gravity affects everything around it, whilst dark energy constitutes $\sim 68\%$ of the Universe's energy and causes the rate of expansion of our universe to accelerate over time. On the one hand, it still remains unclear what is the particle nature of dark matter [24]. On the other hand, despite numerous suggested candidates[2], there is a well-known approach to model dark energy within GR and it is achieved by adding a cosmological constant Λ, which we already encountered in Eq. (1.1). The cosmological constant forms the basis of the widely accepted standard cosmological model – the ΛCDM model, where 'CDM' stands for cold dark matter. However, many researchers find the inclusion of Λ unsatisfactory as in order to fit the data one needs such fine-tuning that Λ is very small with respect to the Planck length ($l_p^2\Lambda \sim 10^{-122}$, where $l_p \approx 10^{-35}$m is the Planck length). Further, theoretical estimates of the vacuum energy density in quantum field theory predict Λ values of at least 40 orders of magnitude larger than what is observed [28] – this is known to be the largest discrepancy in physics. The above considerations and inconsistencies led scientists to look for modifications of GR – *modified theories of gravity*, which we discuss in Section 1.3.1 – and modifications to the Standard Model (SM) of particle physics – *new matter*, discussed in Section 1.3.2.

1.3.1 Modifying gravity

There are systematic ways in which one may arrive at a modified theory of gravity, and they usually originate from violating one the conditions of Lovelock's theorem [29]. His theorem proves the uniqueness of the Einstein tensor, $G_{\mu\nu} \coloneqq R_{\mu\nu} - 1/2 g_{\mu\nu} R$, assuming it is symmetric and divergence-free and given: (i) the equations of motions are of second order, (ii) the metric $g_{\mu\nu}$ is the only geometric field and there are no extra degrees of freedom (iii) theory is local, Lorentz invariant and limited to 4 dimensions. Modifications of gravity

[2] We note however that many modified theories of gravity proposed as dark energy candidates have been ruled out following the detection of the binary neutron star merger GW170817 and its associated electromagnetic counterpart [25–27].

therefore typically lead to at least one violation of the above assumptions. As you can imagine the ways of violating the above assumptions open many possibilities of how one may modify GR, leading to a whole zoo of modified theories of gravity. Generally, we can break these theories into different classes by (see Refs. [30, 31] for complete reviews):

1. *Introducing extra degrees of freedom*: The simplest modification one can make to a gravity theory is to add a scalar field. Examples of the most widely studied theories include scalar-tensor theories [32, 33]. A popular class of such theories is the Hordenski gravity [34], representing the most general four dimensional scalar–tensor theory with second-order field equations and one scalar field. Furthermore, theories to include vector, tensor and even higher rank fields have also been formulated [35, 36].

2. *Formulating theories with higher-derivative equations*: Having higher than second order equations of motion may be undesirable as they are prone to Ostrogradsky instabilities [37], manifested through *ghost fields* admitting physical states with negative energy. In some cases it is possible to formulate theories that do exhibit some basic stability properties, such as $f(R)$ theories of gravity [38]. These theories have attracted interest as alternatives to the ΛCDM model and have been proposed as explanations for the late-time accelerating expansion of the Universe [39–41]. They have also been devised to model inflation, with the Starobinsky cosmological model [42] being one of the famous proposals. $f(R)$ theories divide in many sub-classes, depending on which variational approach one adopts, for example one may have *metric variation*, assuming the Levi-Civita connection, or even the *Palatini approach*, where the action is varied with respect to the metric and connection $\Gamma^{\rho}_{\mu\nu}$ independently [43]. Gravity theories with higher order curvature invariants (e.g. with terms like $R^3, R^3_{\mu\nu}$) tend to also lead to higher order equations of motion prone to Ostrogradsky instability. Field redefinitions are necessary to circumvent the instability, however its remedy does not always guarantee well-posedness[3]; methods of *fixing the equations* have been developed to tackle this problem (see Refs. [44, 45] for more details). Recently, Ref. [46] proposed a novel way to reformulate higher-derivative theories in vacuum so that they admit a well-posed initial value formulation. By introducing regularising terms from field redefinitions, the authors show how one may rewrite the resulting equations of motion as a system of second-order nonlinear wave equations for a wide class of theories of gravity with higher order curvature invariants.

3. *Introducing extra dimensions*: Classically, we study GR in $D = 4$ dimensions. Theories introducing extra spatial or even temporal directions have also been proposed. One

[3]We will briefly discuss the notion of well-posedness in Section 1.3.3.

of the first such examples is Kaluza–Klein theory initially formulated in the attempt to unify gravity with electrodynamics [47]. String theory is another candidate, which requires, at least 10 dimensions. However, a few phenomenological issues arise: we clearly observe gravity effects in three spatial and one temporal dimensions, so where do all other dimensions go? Despite a few interpretations in the literature proposing that extra dimensions must be small and compact [48] or adopting the braneworld paradigm [49], it is still not clear how these proposals would fit within the experimental missions of testing the nature of gravity.

4. *Stepping away from Riemannian geometry*: An even more exotic way of modifying gravity is to consider non-Riemannian geometries. Examples include teleparallel [50] and non-commutative gravity [51].

Examples of modified theories of gravity

In GR, the gravitational force is mediated by a massless spin-2 field, the metric tensor $g_{\mu\nu}$. As we previously suggested, the most common and simplest way to modify GR is to add a scalar field, ϕ, thus resulting in so-called *scalar-tensor* theories. A typical example of such a theory is given by the action

$$S_{\rm st} = \int \mathrm{d}^4x\sqrt{-g}\left[\frac{F(\phi)}{16\pi}R - \frac{1}{2}\frac{1}{M_{\rm pl}^2}g^{\mu\nu}\partial_\mu\phi\partial_\nu\phi - U(\phi)\right] + S_{\rm M}[g_{\mu\nu},\Psi], \tag{1.5}$$

where $M_{\rm pl}$ denotes the Planck mass, $U(\phi)$ the potential of the scalar field and Ψ the matter fields. Note that the scalar field ϕ is non-minimally coupled to the Ricci scalar, such a coupling corresponds to the *Jordan frame*. As we will see in Chapter 6, it is possible with the use of appropriate transformations to reduce this action so that scalar field is minimally coupled. After such a transformation, the action is said to be in the *Einstein frame*. Despite numerous discussions in the literature on the meaning of Jordan and Einstein frames [52, 53], we will refer to the Jordan frame as the physical frame (for example, that of a GW detector), since the matter content moves according to the geometry of the Jordan (physical) metric, $g_{\mu\nu}$, as clearly seen from the $S_{\rm M}[g_{\mu\nu},\Psi]$ term.

It is also possible to couple a scalar field to higher order curvature invariants. Adding higher-order curvature invariants (such as R^2, $R_{\mu\nu}R^{\mu\nu}, R^3, R\Box R$ and so on) has become a popular choice in modified theories of gravity since it has been shown by Stelle that adding quadratic curvature invariants leads to renormalisability [54]. In this discussion, for simplicity we will focus only on quadratic terms, however we note that one may also go to higher orders (see e.g. Ref. [55] for sixth order and Ref. [56, 57] for eighth order curvature terms). Let us

now discuss what are these quadratic curvature invariants and then show why it is necessary to couple a scalar field to them.

Curvature modifications to GR are typically treated with the effective-field theory (EFT) approach [58], where one defines an energy scale referred to as a *cutoff*, beyond which the EFT loses its validity[4]. The EFT approach therefore focuses on observables within the low-energy approximation. In the framework of gravity, we regard the Einstein-Hilbert term as the leading term in the expansions containing higher order curvature invariants suppressed by some scale. At second order, there are only four independent curvature invariants, so that an even-parity alternative theory of gravity with all possible quadratic algebraic curvature invariants can be then written as follows [31, 59]

$$\begin{aligned} S_{\rm q} &= \tfrac{1}{16\pi}\int\sqrt{-g}\mathrm{d}^4x[R+X-V(\phi)+g_2(\phi)X^2+\beta_1(\phi)R^2+\beta_2(\phi)R_{\mu\nu}R^{\mu\nu} \\ &\quad +\beta_3(\phi)R_{\mu\nu\rho\sigma}R^{\mu\nu\rho\sigma}+\beta_4(\phi)^*RR]+S_{\rm M}, \end{aligned} \tag{1.6}$$

where $X=-(1/2)\nabla_\mu\phi\nabla^\mu\phi$, $V(\phi)$ is the scalar-field potential, $\beta_i(\phi)$, $i\in\{1,2,3,4\}$ and $g_2(\phi)$ are the coupling constants. Here ${}^*RR := \frac{1}{2}R_{\mu\nu\rho\sigma}\varepsilon^{\nu\mu\lambda\kappa}R^{\rho\sigma}{}_{\lambda\kappa}$, where $\varepsilon^{\nu\mu\lambda\kappa}$ is the 4D Levi-Civita tensor, is the *Pontryagin scalar* originating from loop quantum gravity and forms the basis of Chern-Simons gravity theories [60]. Another scalar hidden in this action is the *Gauss-Bonnet scalar* $R^2_{\rm GB}=R^2-4R^2_{\mu\nu}+R^2_{\mu\nu\rho\sigma}$. With the choice $\beta_1=\phi$, $\beta_2=-4\phi=-4\phi$, $\beta_4=0$ and $g_2=0$, action (1.6) reduces to Einstein-scalar-Gauss-Bonnet (EsGB) gravity that we will encounter in Chapter 4. Addition of Pontryagin and the Gauss-Bonnet scalars with no scalar field couplings to the Einstein-Hilbert action does not yield any modifications to the field equations, as both scalars are topological invariants and therefore can be absorbed in the boundary term. The coupling to a scalar field in this case is therefore necessary to obtain a modified theory of gravity. Generally, the action (1.6) yields higher order field equations likely to cause Ostrogradsky instability. Luckily this is not the case for the EsGB gravity, which in fact falls under the umbrella of Horndeski gravity theories.

1.3.2 Modifying the nature of compact objects

In the classical picture, we always assume that ordinary matter cannot form a massive and ultracompact object (e.g. object containing a light ring), so BH formation past a certain limit is inevitable. For example, NSs with compactness $M/R\sim 1/3$, where M is the mass and R is the radius of the star, cannot sustain masses larger than $\sim 3M_\odot$ [61]. A lack of direct observations of the event (or apparent) horizon led many to theorise about the existence of ultracompact and horizonless objects – *exotic compact objects* (ECOs), also referred to

[4] As past this cutoff one starts to encounter ultraviolet divergences from loop integrals.

as *BH mimickers* as they are proposed as replacements to the BH paradigm. The lack of a horizon implies that these ECOs are expected to leave distinct GW imprints that could be differentiated from BH signatures. Examples of exotic compact objects include *boson stars* [62], which will be the main characters of our Chapters 5-8, *Proca stars* [63], *gravastars* [64, 65] and many more (see Ref. [19] for a complete review). It is important to note that typically the construction of exotic compact objects, e.g. boson stars, entails assumption of 'new' particles prevalent in theories beyond the Standard Model of particle physics. As we will see later, these objects can co-exist with GR, in the sense that no additional curvature terms or scalar fields mediating the gravity sector will be necessary. However, the mere addition of a scalar field to the Einstein-Hilbert action modelling a new bosonic particle will be enough to construct a compact object with a different anatomy to that of a BH. Therefore, we do not necessarily associate exotic compact objects with modified theories of gravity, but rather regard them as a manifestation of theories beyond the Standard Model of particle physics.

Similar to the Lovelock theorem used as a recipe for modifying gravity, there is a theorem by Buchdhal placing restrictions on the compactness of exotic compact objects [66, 67]. The theorem states that the maximum compactness of a self-gravitating object is $M/R = 4/9$. We note that this threshold is lower than that of a BH, e.g. for a spherically symmetric BH, we commonly define its compactness by $1/2$, which is the ratio of the Schwarzschild mass to the Schwarzschild radius. The statement however holds under the following assumptions: (i) the object is spherically symmetric, (ii) GR is the ultimate theory of gravity, (iii) the matter sector is described by a perfect fluid, which is either isotropic or mildly anisotropic (i.e. the tangential pressure is allowed to be smaller than the radial pressure), (iv) the radial pressure and energy density are non-negative, (v) the energy density decreases as one moves away from the centre of the object. In the case of gravastars and fuzzballs it is possible to get to compactness values arbitrarily close to the BH case[5], whilst for perfect fluids and boson stars it is harder to evade the Buchdhal's limit [19, 71].

1.3.3 How to test gravity theories beyond the GR and SM paradigm?

Having introduced ample varieties of how one may modify the nature of gravity and challenge our classical beliefs, it may seem rather overwhelming. How do we navigate in this zoo of modified theories of gravity and exotic compact objects, and synergise our, most likely, wild theoretical ideas with the real GW data that we observe?

[5]Gravastars are modelled with an anisotropic internal effective fluid [68] and are supported by a negative pressure, whilst fuzzballs arise from the description of the BH interior in string theory and are not spherically symmetric [69, 70]. Both objects therefore evade the Buchdhal's limit.

To answer the first part of the question we have to define a few simple criteria for deeming a given modified theory of gravity or exotic compact object as viable and worthy of studying. We require that the alternative theory in question:

1. *Satisfies current observational constraints:* The theory must be consistent with all the predictions from the solar system and binary pulsars tests [72, 73]. There must therefore be a limit in which the theory would reduce to that of general relativity.

2. *Has well-posed formulation*[6]*:* Classical field theories described by a set of partial differential equations (PDEs) and requiring prescription of boundary and initial conditions, rely on the notion of well-posedness to guarantee mathematical consistency. The meaning of the well-posedness translates to the solutions of the system of equations in question being unique and continuously dependent on the initial data. Formally, the latter condition translates into the following inequality for the solution u

$$||u(t,x^i)|| \leq Ae^{kt}||u(0,x^i)||, \tag{1.7}$$

   where A and k are some constants and $||\cdot||$ denotes a suitable norm. Well-posedness of the initial value problem in GR was proved in the late 90s by Choquet Bruhat [74, 75] and later proved in several modified theories of gravity [76–78]. Proof of the well-posedness relies on the principal part of the governing PDEs: when the principal symbol is diagonalisable (i.e. contains a complete set of independent eigenvectors) and has real eigenvalues, the equations are referred to as *strongly hyperbolic*. Strong hyperbolicity in turn implies well-posedness (see Ref. [79] for a review).

3. *Has stable solutions:* The theory must possess solutions that are stable to small perturbations. We refer to the solution $u(t)$ as *stable* if every other solution $v(t)$ close enough to $u(t)$ at $t = 0$ remains close to it during the evolution. Formally, this translates to the following definition: $\forall\varepsilon > 0$, $\exists\delta > 0$ such that $|v(t) - u(t)| < \varepsilon$ when $|v(0) - u(0)| < \delta$.

Finally, to answer the second part of the question, we will focus on GW-inspired tests that are most relevant to this thesis. Examples of tests include searches for violations of the 'no-hair' theorem, stating that the mass and spin are the only two properties of astrophysical black holes in general relativity, extra polarisation content, deviation of the speed of gravity from the speed of light (see Refs. [17, 80] for the full list of LIGO-Virgo-KAGRA analyses). However, in order to devise the above mentioned tests, we need to model GWs and understand the

[6]Well-posed initial value formulation is required in order to solve the resulting field equations numerically. Whilst some effective field theories of gravity may be ill-posed, the full theory may not.

key dynamical parts of a binary merger. In the limits of large separation and slow velocities ($v/c \ll 1$) (i.e. the early inspiral), the gravitational waveforms are typically provided by the perturbative post-Newtonian (PN) expansion [81, 82]. For the last orbits and merger, where the fields are particularly strong and the distances between the bodies are small, the PN expansion breaks down. The late inspiral and merger parts can realistically only be resolved through numerical relativity (NR) simulations, which will form the base of this thesis. After the two objects eventually merge and settle down to a single compact object, one may describe the system using the linearised (perturbation) theory. This end-part of the signal is what we call the *ringdown*. For binary systems, where one of the objects is much more massive than the other, self-force calculations may be used [83] (with second-order calculations being still under development [84]) and are expected to supersede the numerical relativity simulations in accuracy and speed.

All of the above methods may be combined to construct GW signals consisting of the inspiral, merger and ringdown, thereby allowing us to construct appropriate tests that separate into two distinct groups: *theory agnostic* or *bottom-up approach* and *theory dependent* or *top-down approach*. The former group introduces generic parameters that may represent a typical deviation from GR, a great example of such a test is the parameterised post-Einsteinian approach (for details see Section 5.3.4 of Ref. [85]). The latter group focuses on a specific gravity theory and then makes predictions that are tested using observations. The main drawback of such an approach is that one has to choose a theory – given the lack of a particular alternative to GR and many proposed modifications, this choice is highly non-trivial. Having said that, theory dependent modelling can inform theory independent tests and the possible parametrised modification one may wish to look for. If, say, we observe a deviation from GR using generic parametrisations, a top-down approach would be necessary to weed out the theories leading to such an observed deviation.

Chapter 2

Numerical Relativity

2.1 Introduction

To date, numerical relativity (NR) is the only tool capable of solving the Einstein field equations in the merger regime. Therefore, our understanding of gravity and physics relies on the robustness and accuracy of our numerical simulations. Numerical relativity plays an important role in GW analysis and in particular in the construction of hybrid waveforms [86], matching Post-Newtonian calculations to the merger of NR simulations. NR is a relatively young field in physics, as only recently it has become possible to evolve complex binary systems for a long duration and with high accuracy. However, its roots date back to the 1960s and the work by Hahn and Lindquist [87], who performed short numerical simulations of two mouths of a wormhole. Numerous attempts to evolve a binary system had been carried out by various groups for almost 50 years, until 2005, when Frans Pretorius evolved the very first orbiting black hole binary through merger [88], followed by the moving puncture breakthrough a year later [89, 90]. Since then binary evolutions of merging black holes and neutron stars (NSs) became a day-to-day task with the largest number of simulations being produced by the Simulating eXtreme Spacetimes (SXS) Collaboration, e.g. with one of their longer GW signals having ~ 350 wave cycles [91]. Nowadays applications of NR in fact extend beyond modelling GWs from BHs and NSs in GR and 4 dimensions; active research is ongoing in the fields of modified theories of gravity [92–95], exotic compact objects [96], higher dimensional BHs [97–100] and cosmic strings [101]. With computer hardware undergoing major developments and improvements, we are in the firm position of leveraging the computational power to modelling the strong field regime and resolving physics of interest. As an example, take the recent general-relativistic neutrino-radiation magneto-hydrodynamic simulation of a binary neutron star system of Ref. [102], consuming 85 million CPU hours.

By now you are probably very impressed with the recent advances in numerical relativity, but how do we make this possible? Reviewing the basics of NR and common pitfalls will be the primary aims of this Chapter. We will start by reviewing the Arnowitt–Deser–Misner (ADM) evolution equations [103, 104] arising in the $3+1$ decomposition in Section 2.2. We note that an alternative to the $3+1$ decomposition is the *generalised harmonic formulation* (see e.g. Ref. [105]), utilising generalised harmonic coordinates, as first suggested in Ref. [106], and used in the breakthrough simulation of Pretorius. Next, in Section 2.3 we will review necessary modifications to the ADM formulation making it well-posed and stable. In Section 2.4 we will describe the numerical scheme that is usually employed for damping constraint violations that may arise during time evolution. In Sections 2.5 and 2.6 we will present the common recipes for choosing a suitable gauge and prescribing constraint satisfying initial data. Finally, in Section 2.7 we will review the numerical relativity code GRCHOMBO which will be used in the subsequent Chapters of this thesis.

2.2 3+1 decomposition of spacetime and ADM formalism

Let us assume that the spacetime $(\mathscr{M}, g_{\mu\nu})$ can be foliated into a family of non-intersecting space-like hypersurfaces Σ_t with time-like unit normal $\boldsymbol{n}$ so that $\mathscr{M} = \bigcup \Sigma_t$. To avoid ambiguity in our definitions we use Greek letters $\{\alpha, \beta, ...\}$ for indices of 4-dimensional quantities, extending from 0 to 3, whilst Latin letters $\{a, b, ...\}$ for indices running from 1 to 3. We therefore additionally introduce spatial coordinates $x^i(t)$ that label the points on a spatial slice Σ_t at some coordinate time t and refer to the coordinate system (t, x^i) as *adapted* coordinates (i.e. adapted to the spacetime split). Within the slices, the proper distance is given by a 3-dimensional spatial metric γ_{ij}

$$\mathrm{d}l^2 = \gamma_{ij}\mathrm{d}x^i\mathrm{d}x^j. \tag{2.1}$$

Further, we define the *lapse function* α and a *shift vector* $\boldsymbol{\beta}$

$$\alpha := \sqrt{-||\boldsymbol{dt}||^2}^{-1} > 0, \tag{2.2}$$

$$\boldsymbol{\beta} := \boldsymbol{\partial}_t - \alpha\boldsymbol{n}, \tag{2.3}$$

where $\boldsymbol{n} = -\alpha\boldsymbol{dt} > 0$ is the time-like unit normal to spatial hypersurfaces and is therefore the 4-velocity of the *normal observers*. We note that the lapse function α relates the proper

time τ measured by normal observers to the coordinate time t as

$$\mathrm{d}\tau = \alpha \mathrm{dt}. \tag{2.4}$$

The lapse encodes our freedom to slice the time-evolution as we want, while the shift vector tells us how to propagate the coordinate system (x^i) from Σ_t to Σ_{t+dt} (see Fig. 2.1). We now use the space projection operator

$$\perp^{\mu}{}_{\nu} \equiv \delta^{\mu}{}_{\nu} + n^{\mu} n_{\nu}, \tag{2.5}$$

to obtain the spatial projection of the spacetime metric

$$\gamma_{\mu\nu} \equiv (\perp g)_{\mu\nu} = \perp^{\alpha}{}_{\mu} \perp^{\beta}{}_{\nu} g_{\alpha\beta} = g_{\mu\nu} + n_{\mu} n_{\nu}. \tag{2.6}$$

With our definitions of the lapse (2.2), the shift vector (2.3) and the spatial metric (2.6), we find that the spacetime metric in adapted coordinates can be written as

$$\mathrm{d}s^2 = -\alpha^2 \mathrm{d}t^2 + \gamma_{ij}(\mathrm{d}x^i + \beta^i \mathrm{d}t)(\mathrm{d}x^j + \beta^j \mathrm{d}t). \tag{2.7}$$

We also define the projections of the energy-momentum tensor $T_{\mu\nu}$, which can be decomposed into the *energy density* $\rho = n^{\alpha} n^{\beta} T_{\alpha\beta}$, the *momentum density* $j_{\mu} = - \perp^{\alpha}{}_{\mu} n^{\nu} T_{\alpha\nu}$ and the *stress tensor* $S_{\mu\nu} = \perp^{\alpha}{}_{\mu} \perp^{\beta}{}_{\nu} T_{\alpha\beta}$ so that

$$T_{\mu\nu} = \rho n_{\mu} n_{\nu} + n_{\mu} j_{\nu} + n_{\nu} j_{\mu} + S_{\mu\nu}. \tag{2.8}$$

The remaining ingredient we require is a way of describing the embedding of slices Σ_t in the spacetime $\mathscr{M}$. This is because on each slice Σ_t, the 3-dimensional Riemann tensor ${}^{(3)}R^{m}{}_{ijk}$ only contains information about the intrinsic geometry. For this purpose we introduce the *extrinsic curvature* K_{ij} [107]

$$K_{\alpha\beta} = - \perp^{\mu}{}_{\alpha} \nabla_{\mu} n_{\beta}. \tag{2.9}$$

By combining the Gauss-Codazzi-Ricci relations [108] with the Einstein equations (1.4), we arrive at the decomposed $3+1$ equations of Arnowitt, Deser and Misner (ADM) [103], as reformulated by York [104]; cf. also [108]. The formulation consists of two evolution equations

$$\partial_t \gamma_{ij} = \mathscr{L}_{\beta} \gamma_{ij} - 2\alpha K_{ij}, \tag{2.10}$$

$$\partial_t K_{ij} = \mathscr{L}_{\beta} K_{ij} - D_i D_j \alpha + \alpha \left({}^{(3)}R_{ij} - 2K_{ik}K^{k}_{j} + K K_{ij} \right) + 4\pi\alpha \left[\gamma_{ij} (S - \rho) - 2S_{ij} \right], \tag{2.11}$$

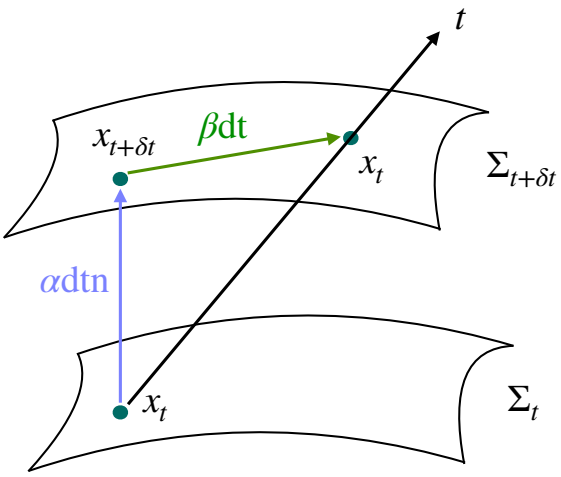


Fig. 2.1 Foliation of a 4-dimensional spacetime into 3-dimensional spatial hypersurfaces Σ_t, and a time-like normal $\boldsymbol{n}$. Note that each spatial hypersurface is in fact a 3-dimensional volume, which is represented here as a 2-dimensional surface for illustrative purposes.

where $S = \gamma^{ij} S_{ij}$ and D_i is the Levi-Civita connection associated with the metric $\boldsymbol{\gamma}$, and two constraint equations

$$ {}^{(3)}R + K^2 - K_{ij}K^{ij} - 16\pi\rho = 0, \tag{2.12} $$

$$ D_i(K^i_j - K) - 8\pi j_i = 0. \tag{2.13} $$

Here $\mathscr{L}$ denotes a Lie derivative and therefore $\mathscr{L}_\beta$ corresponds to the Lie derivative with respect to $\boldsymbol{\beta}$. The constraint equations in Eqs. (2.12) and (2.13) are referred to as the *Hamiltonian* and *momentum* constraints respectively and have to be satisfied throughout the evolution. We note that in Eq. (2.12) ${}^{(3)}R$ denotes the trace part of the spatial Ricci tensor ${}^{(3)}R_{ij}$, i.e. ${}^{(3)}R = \gamma^{ij}{}^{(3)}R_{ij}$. The gravitational fields (γ_{ij}, K_{ij}) are not *free* data and have to be specified on some initial hypersurface Σ_0 so that they satisfy the constraint equations (2.12)-(2.13). We will discuss initial data construction in more detail in Section 2.6. In fact, by the Cauchy-Kovalevskaya theorem, at later times the constraints are preserved by the dynamical evolution equations. Of course, in numerical evolutions this is not exactly the case due to numerical errors.

2.3 BSSN formulation

The ADM evolution equations introduced in the previous Section are unfortunately ill-posed [109], as the equations can be shown to be only *weakly hyperbolic*. Further modifications

can be applied to the ADM formalism in order to obtain well-posed equations and stability. This was first achieved in Baumgarte-Shapiro-Shibata-Nakamura (BSSN) formulation [110–112]. Let us now briefly outline the key differences between BSSN and ADM formulations. First, note that the evolution equations are in fact non-unique: one can always add arbitrary multiples of the constraints equations (which are zeros) to obtain new evolution equations that are just as valid. The BSSN formalism utilises this freedom, thereby changing the principal part of the equations. Additionally, BSSN applies conformal decomposition, allowing for improved stability, and introduces an additional dynamical variable, $\tilde{\Gamma}^i$ defined in Eq. (2.19), also contributing to the overall hyperbolicity of the formulation [113, 114]. The resulting BSSN equations have the same physical solutions as in the ADM formalism, but different mathematical properties, including well-posedness. Let us now discuss the BSSN variables in more detail below.

From now on, for clarity, all conformal quantities will be marked by a tilde. We start by conformally rescaling the spatial metric using

$$\boxed{\tilde{\gamma}_{ij} = \chi \gamma_{ij}, \quad \text{where } \chi = \det(\gamma_{ij})^{-\frac{1}{3}} \text{ and } \det\tilde{\gamma}_{ij} = 1.} \tag{2.14}$$

Here χ is called the *conformal factor*[1] and its advantage is that near most singularities $\chi \to 0$, whilst $\det(\gamma_{ij}) \to \infty$, thereby keeping $\tilde{\gamma}_{ij}$ regular. For example, in the case of the Schwarzschild spacetime, the definition for the conformal factor follows directly from its line-element in isotropic coordinates

$$\mathrm{d}s^2 = -\left(\frac{1-\frac{M}{2R}}{1+\frac{M}{2R}}\right)\mathrm{d}t^2 + \left(1+\frac{M}{2R}\right)^4\left(\mathrm{d}R^2 + R^2\mathrm{d}\Omega^2\right), \tag{2.15}$$

where $\chi = [1+M/(2R)]^{-4} \to 0$ when $R \to 0$. The covariant derivative associated with the conformal metric $\tilde{\gamma}_{ij}$ will be denoted by $\tilde{D}$. We impose the metric compatibility condition (in the same way as for the 4D Riemannian connection in GR)

$$\tilde{D}_i \tilde{\gamma}_{jk} = 0. \tag{2.16}$$

Given a tensor $\boldsymbol{T}$, the covariant derivative D_i is therefore related to the conformal covariant derivative $\tilde{D}_i$ the following way,

$$D_k T^{i_1\ldots i_p}{}_{j_1\ldots j_q} = \tilde{D}_k T^{i_1\ldots i_p}{}_{j_1\ldots j_q} + \sum_{r=1}^{p} C^{i_r}{}_{kl} T^{i_1\ldots l\ldots i_p}{}_{j_1\ldots j_q} - \sum_{r=1}^{q} C^{l}{}_{kj_r} T^{i_1\ldots i_p}{}_{j_1\ldots l\ldots j_q}, \tag{2.17}$$

[1] Note that some texts also use $\tilde{\gamma}_{ij} = \chi^2\gamma_{ij}$, or $\tilde{\gamma}_{ij} = \psi^{-4}\gamma_{ij}$, or $\tilde{\gamma}_{ij} = e^{-\phi}\gamma_{ij}$.

where $C^k_{ij} := \Gamma^k_{ij} - \tilde{\Gamma}^k_{ij}$ and $\tilde{\Gamma}^k_{ij}$ is the Christoffel symbol associated with the conformal metric, $\tilde{\boldsymbol{\gamma}}$.

Next, we decompose the extrinsic curvature into its trace K and a traceless part $\tilde{A}_{ij} = \chi A_{ij}$

$$K_{ij} = \frac{1}{\chi}\left(\tilde{A}_{ij} + \frac{1}{3}\tilde{\gamma}_{ij}K\right), \tag{2.18}$$

so that $K = \gamma^{ij}K_{ij}$ and $\tilde{\gamma}^{ij}\tilde{A}_{ij} = 0$. We also introduce an auxiliary variable in the form of a *conformal connection* $\tilde{\Gamma}^i$,

$$\tilde{\Gamma}^i := \tilde{\gamma}^{jk}\tilde{\Gamma}^i_{jk}, \tag{2.19}$$

where $\tilde{\Gamma}^i_{jk}$ are the Christoffel symbols associated with the conformal metric $\tilde{\gamma}_{ij}$. The evolution equations can then be derived from the ADM evolution equations (2.10)-(2.11) and we present them in Appendix 2.A.

2.4 CCZ4 formulation

The covariant and conformal Z4 (CCZ4) formulation inherits features from the strongly hyperbolic BSSN formulation, however additionally introduces constraint damping terms, controlled by coefficients κ_1 and κ_2, and a four-vector Z^μ to the Einstein field equations [115, 116]

$$R_{\mu\nu} + 2\nabla_{(\mu}Z_{\nu)} - \kappa_1\left[2n_{(\mu}Z_{\nu)} - (1+\kappa_2)g_{\mu\nu}n_\alpha Z^\alpha\right] = -8\pi\left(T_{\mu\nu} - \frac{1}{2}Tg_{\mu\nu}\right), \tag{2.20}$$

where $T = g^{\mu\nu}T_{\mu\nu}$ is the trace of the stress-energy tensor. Solutions satisfying $Z_\mu = 0$ therefore correspond to solutions of the Einstein field equations, whilst $Z_\mu \neq 0$ measures the deviations from them. The constraint-propagation of the system can be derived by taking the divergence of (2.20) and applying the conservation of the energy-momentum tensor and the Bianchi identities, which leads to

$$\nabla^\nu\nabla_\nu Z_\mu + R_{\mu\nu}Z^\nu = -\kappa_1\nabla^\nu\left(2n_{(\mu}Z_{\nu)} + \kappa_2 g_{\mu\nu}n_\alpha Z^\alpha\right). \tag{2.21}$$

We note that the Z^μ vector obeys a wave equation, which is inherently hyperbolic and guarantees that any deviation from the Einstein field equations, if present, can propagate away from the computational domain (or even may fall into the BH). It has been shown in Ref. [117] that as long as $\kappa_1 > 0$, $\kappa_2 > -1$, constraint violations are damped. This is a very desirable effect for numerics as throughout evolution, we can accumulate constraint violations from various channels, such as finite discretisation, inaccurate boundary conditions

and initial data. Having said that, it is important to emphasise that one should always aim to have accurate enough initial data to guarantee a physical evolution, as initially constraint-violating data might never reach the space of constraint-satisfying data. Checking physical quantities throughout the evolution is therefore crucial to ensuring that the system being evolved is what we intended it to be initially.

For the newly defined vector Z^μ, we further define the following time and spatial projections of Z^μ

$$\Theta := -n_\mu Z^\mu \quad \text{and} \quad \Theta_\mu := \perp Z_\mu := \perp^\alpha{}_\mu Z_\alpha. \tag{2.22}$$

A 3+1 decomposition of the tensorial equation (2.20) and a lengthy calculation results in evolution equations summarised in Appendix 2.B. In this work we set, $\kappa_2 = 0$, $\kappa_3 = 1$ and following Ref. [118], $\alpha\kappa_1 = 0.1$.

2.5 Gauge conditions

In order to determine the foliation of our spacetime, we have to define appropriate gauge conditions, i.e. suitable equations for the lapse α and shift β. The choice of gauge plays a crucial role in numerical simulations as it affects the stability and accuracy of the evolution. In particular, the gauge choice becomes important in evolutions of black hole spacetimes, where one has a singularity and therefore has to navigate through all the pathologies that may arise because of it. Below we will briefly describe some of the issues that one may encounter and motivate the gauge choice that will be employed in the subsequent Chapters.

The simplest gauge choice is to impose $\alpha = 1$, also referred to as *geodesic slicing*, and a vanishing shift, $\beta^i = 0$. With $\beta^i = 0$ coordinate observers coincide with normal observers, whilst with $\alpha = 1$ coordinate time coincides with the proper time. Unfortunately, such a choice of gauge is inappropriate, as for instance in a Schwarzschild spacetime, the geodesic slices eventually fall into a singularity (cf. the left panel of Fig. 2.2). We therefore, need a gauge with *singularity avoiding* properties. Additionally, $\beta^i = 0$ can cause *slice stretching*, depicted in the right panel of Fig. 2.2. This pathology is manifested in the coordinate lines in the neighbourhood of the singularity falling inside the BH horizon. We therefore, want to impose a shift condition that minimises the hypersurface stretching and shearing.

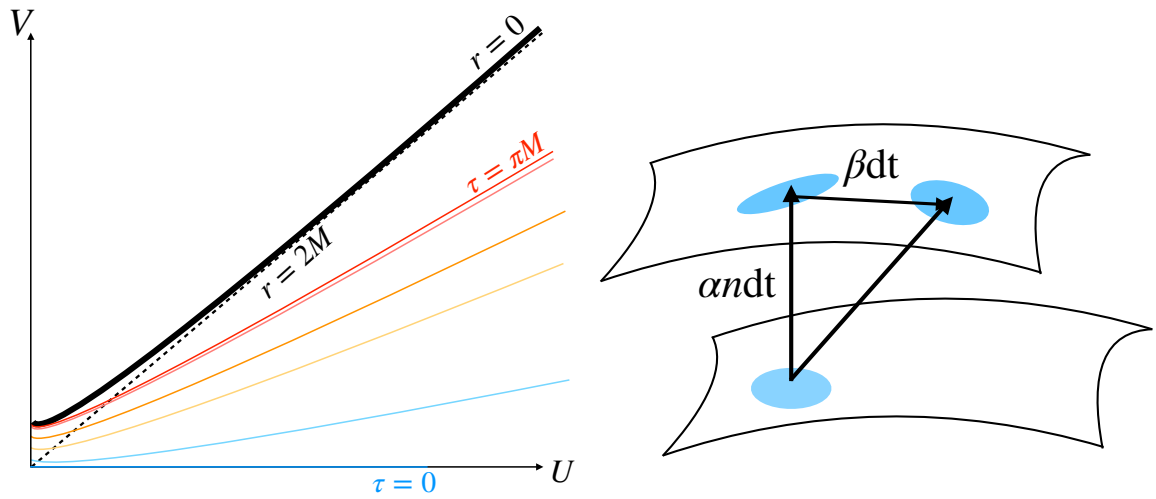


Fig. 2.2 Illustrations adapted from Smarr and York [1]. *Left panel*: Kruskal–Szekeres diagram representing the evolution of a Schwarzschild spacetime with an event horizon at $r = 2M$ and a singularity at $r = 0$. The axes correspond to transformed time and radial coordinates of the Schwarzschild spacetime such that $U = -1/2\exp(-\tilde{t}+r)\exp(-4M)$ and $V = 1/2\exp(\bar{t}+r)\exp(-4M)$, where $\bar{t} = t + 2M\ln|r-2M|$ and $\tilde{t} = t - 2M\ln|r-2M|$. Time evolution using geodesic slicing, depicted by the curves transitioning from blue to red, shows that hypersurfaces hit the BH singularity in finite proper time, $\tau = \pi M$. *Right panel*: A sketch of coordinate shearing and stretching. On the one hand, a small sphere being transported along a normal vector is transformed into an ellipsoid. On the other hand, introducing a non-trivial shift vector helps to reduce the distortion of its shape and excessive coordinate shearing.

2.5.1 Lapse condition

The most famous choice for the lapse slicing condition widely used in 3+1 NR codes belongs to the *Bona-Maso* family of slicing conditions [119],

$$\partial_t \alpha - \beta^i \partial_i \alpha = -\alpha^2 f(\alpha) K, \tag{2.23}$$

where $f(\alpha)$ is some positive function of the lapse. In this work, we will be using the choice $f(\alpha) = 2/\alpha$ corresponding to the *1+log slicing*, which has been shown to posses singularity avoidance properties and guarantee the stability of BH spacetime evolutions. An alternative method would be to excise the computational region containing a BH singularity (see e.g. Ref.[120]).

In the CCZ4 formulation, 1+log slicing takes a slightly modified version of [116],

$$\partial_t \alpha = \beta^i \partial_i \alpha - 2\alpha(K - 2\Theta). \tag{2.24}$$

2.5.2 Shift condition

In order to circumvent the spurious effects of slice stretching, we employ a *Gamma driver* shift condition given by[2]

$$\partial_t \beta^i = b_1 \beta^j \partial_j \beta^i + b_2 B^i, \tag{2.25}$$

$$\partial_t B^i = b_1 \left(\beta^j \partial_j B^i - \beta^k \partial_k \hat{\Gamma}^i \right) + \partial_t \hat{\Gamma}^i - \eta B^i, \tag{2.26}$$

where $\hat{\Gamma}^i$ is the CCZ4 modified conformal connection function defined in Eq. (2.76) and b_1, b_2, and η are freely specifiable constants. In this work we set $b_1 = 1$, $b_2 = 3/4$ and $\eta = 1$. The name of this shift condition stems from the fact that this gauge "freezes Gamma", i.e. drives $\partial_t \hat{\Gamma}^i$ to zero as the physics of the spacetime evolve towards quiescence.

Together, 1+log slicing and Gamma driver conditions, are often referred to as a *moving puncture gauge*, which allows BHs to move through the computational without contaminating the numerical evolution. Before the moving puncture gauge, *static puncture evolution* methods were commonly used to handle infinities associated with puncture initial data. However, the gauge kept BHs fixed, limiting the success of such methods modelling the dynamics of binary black holes. The idea of evolving the two punctures was arrived at independently by the two groups, Brownsville [89] and Goddard [90]. A non-zero shift at the positions of the punctures is precisely what allows them to move and their positions $x^i_{\rm p}$ can be found by the integrating the following equation out

$$\frac{\mathrm{d}x^i_{\rm p}}{\mathrm{d}t} = -\beta^i(x^j_{\rm p}). \tag{2.27}$$

2.6 Initial Data

Let us recall that in our $3+1$ decomposition we also obtained constraint equations given by Eqs. (2.12)–(2.13). These constraints have to be satisfied initially for a given physical system, which requires prescription of *constraint satisfying* initial data for the spatial metric γ_{ij} and the extrinsic curvature K (and any additional dynamical fields if present in the theory). The initial data may be constructed analytically for systems with symmetries, e.g. Brill-Lindquist initial data for N BHs at the moment of time symmetry, or with the use of initial condition solvers [121–123]. The key challenge of computing initial data is the fact that we have 12 degrees of freedom from the spatial metric and the extrinsic curvature, but only 4 differential equations to solve. This means that one must fix 8 degrees of freedom as free-data

[2] Note that for BSSN formulation, we would replace $\hat{\Gamma}^i$ with $\tilde{\Gamma}^i$ in Eq. (2.26).

(to be chosen initially at the start of the simulation), and solve only for the remaining 4 variables. There is no direct recipe for identifying what is physical to assume to be free data, however a common way of dealing with this issue is to use the York–Lichnerowicz conformal decomposition that we review in more detail in Appendix 2.C.

2.6.1 Brill-Lindquist initial data

The Brill-Lindquist initial data construction relies on the York–Lichnerowicz conformal decomposition (see Section 3.2 of Ref. [124] for more details or Appendix 2.C), which conformally rescales the spatial metric

$$\gamma_{ij} = \psi^4 \tilde{\gamma}_{ij}. \tag{2.28}$$

We assume BH spacetime at the moment of time symmetry, which corresponds to imposing $K_{ij} = 0$, as well as $\rho = 0$ and $j^i = 0$. The momentum constraint in Eq. (2.13) is then trivially satisfied. Simplifying the problem further by assuming conformal flatness, i.e. $\tilde{\gamma}_{ij} = \eta_{ij}$, where η_{ij} is the flat metric, we find that the Hamiltonian constraint reduces to a simple wave equation in Laplace spacetime

$$D_\eta^2 \psi = 0, \tag{2.29}$$

where by D_η^2 we denote the flat-spacetime Laplacian operator. Asymptotic flatness requires $\psi = 1$ at infinity, which implies that the conformal factor solution to Eq. (2.29) takes the following form

$$\tilde{\psi}_{\rm BL} = 1 + \frac{C}{r}, \tag{2.30}$$

where C is a constant and r is the coordinate radius. The physical metric in spherical coordinates therefore reduces to

$$ds^2 = \left(1 + \frac{C}{r}\right)^4 \left[dr^2 + r^2 d\Omega^2\right]. \tag{2.31}$$

From the form of the metric it is clear that by choosing $M = 2C$, where M denotes the mass of the BH corresponds to the Schwarzschild solution in isotropic coordinates. The solution (2.30) can be generalised to N static BHs with bare masses m_i, located at points $\boldsymbol{r}_i$, via

$$\psi_{\rm BL} = 1 + \sum_{i=1}^{N} \frac{m_i}{2\,|\boldsymbol{r} - \boldsymbol{r}_i|}. \tag{2.32}$$

2.6.2 Puncture initial data

It is also possible to apply the York–Lichnerowicz conformal decomposition to more astrophysically motivated initial data, such as BHs that have angular and linear momenta. Imposing maximal slicing condition (i.e $K = 0$), we find that the momentum constraint equation can be shown to reduce to the wave-like equation

$$\tilde{D}_j \left(\tilde{L}\tilde{V}\right)^{ij} = 0, \tag{2.33}$$

where $\tilde{L}$ and $\tilde{V}^i$ are defined in Appendix 2.C. The above equation has analytic solution for $\tilde{V}^i$ and subsequently $\tilde{A}_{ij}$ (see Ref.[107] and Section 3.4.2 of Ref.[124] for more details) and is known as the *Bowen-York* solution.

Solving the Hamiltonian constraint is harder and we have to do that numerically. We start with the ansatz that the solution should be a modification of the previously discussed Brill-Lindquist solution of Section 2.6.1,

$$\psi = \psi_{\rm BL} + u, \tag{2.34}$$

where $D^2_\eta \psi_{\rm BL} = 0$ in the punctured domain, i.e. $\mathscr{R}^3 \backslash \{\boldsymbol{r}_i\}$. The Hamiltonian constraint equation we now have to solve is

$$\Delta u + (\psi_{\rm BL} + u)^{-7} \tilde{A}_{ij}\tilde{A}^{ij} = 0, \tag{2.35}$$

where asymptotic flatness implies that $u - 1 = \mathscr{O}(r^{-1})$ for large distances from the punctures. The existence and uniqueness of solutions to Eq. (2.35) has been established in Ref. [125]. Solving for u can be done using a variety of methods, see e.g. Ref. [126] for spectral implementation. Solving for the Hamiltonian equation (2.35) is what we refer to as *puncture initial data*. We are typically used to thinking of a Kerr solution when working under stationary and axisymmetric assumptions, however we note that this initial data corresponds to a distorted Kerr BH [127, 128]. Numerical evolution of puncture initial data *relaxes* to an approximately Kerr form and produces an initial burst of GW radiation, also known as *junk radiation*.

2.7 GRChombo code

2.7.1 Overview

GRCHOMBO is a numerical relativity code written in C++, facilitating fully non-linear studies of various single and binary spacetimes relevant to gravitational wave physics and cosmology. The code is built on CHOMBO [129], which is an adapative mesh refinement (AMR) library, allowing for resolving the physical elements of the system of interest with higher resolution. The code was originally developed by Katy Clough, Pau Figueras, Hal Finkel, Markus Kunesch, Eugene A. Lim and Saran Tunyasuvunakool [130] and many additional features that are now available in the public release have been implemented since (see e.g. Refs. [131, 132]). Use of templating and classes allows the users to create their own *examples*, targeting their own physical systems of interest, e.g. binary black holes [133, 134, 134–137], oscillatons [138, 139], axion stars [140], boson stars [141–143], Proca stars [144], superradiance [145], inflationary scenarios [146–148], cosmic strings [101, 149, 150], warp drives [151] and many more. For a comprehensive review of the code structure see Refs. [152, 153]. Since the original development of GRCHOMBO, a few standalone extensions have been developed and made open-source, like TWOPUNCTURES initial data solver, GRFOLRES enabling evolutions of binary black holes in modified theories of gravity [154] and GRDZHADZHA allowing for time evolutions on fixed backgrounds [155]. The GRCHOMBO code was compared to the LEAN code[3] in Ref. [153], where both codes demonstrated excellent agreement in the context of long and high-precision binary black hole evolutions in GR.

Simulating physical systems in GR and beyond is a computationally expensive task so that parallelisation becomes of paramount importance. The computational domain is therefore split into many *boxes* (or more precisely cuboids) of typically 8, 16, 32 or 64 gridpoints in length. These boxes are shared between a number of processes across multiple nodes using Message Passing Interface (MPI). Additionally, GRCHOMBO makes use of OpenMP threading over the y and z direction of the boxes within each MPI process. The x-direction on the other hand supports 'Single instruction, multiple data' (SIMD) vector intrinsics.

[3] LEAN is based on the CACTUS computational toolkit [156] and employs mesh refinement in the form of moving boxes as provided by CARPET [157].

2.7.2 Basics of Adaptive Mesh Refinement

The grid in GRCHOMBO comprises a hierarchy of cell-centered Cartesian meshes comprising $L+1$ refinement levels, where the grid spacing on level l, Δx_l, is half of the resolution of the next outer one, Δx_{l-1}, so that

$$\Delta x_l = \frac{\Delta x_0}{2^l}, \tag{2.36}$$

where $l = 0, 1, ..., L$. In order to devise how big or small the refinement levels are and where they are placed, we use a *tagging criterion*. On a given refinement level l, for each cell with indices $I = (i, j, k)$ and Cartesian coordinates $\left(x_i, y_j, z_k\right)$, we evaluate a tagging criterion, $C(I)$ (examples of which we will consider in Section 2.7.3)[4], and define a user-specified threshold τ. If $C(I) > \tau$ then the cell I is tagged for refinement. The evaluation of the tagging criterion happens at the initial grid generation and then subsequently at every regridding, the frequency of which is user-specifiable on every refinement level $l < L$. A regridding on some level $l = l'$ triggers regridding on all finer levels $l' \leq l < L$. In simulations that we will present in the next Chapters, we enforce regridding only every few timesteps on the coarser levels (e.g. $l = 0$ or $l = 1$), as having less frequent regridding not only reduces the computational cost of the simulation, but also avoids introducing numerical errors and noise due to interpolation.

We have mentioned before that our computational domain is split into boxes, however we have not been very specific on how this is done. Partitioning into boxes requires an efficient algorithm, as poorly split computational domain can significantly increase the wall time of the simulation. In GRCHOMBO we utilise the *Berger-Rigoutsos* grid generation algorithm [158], discussed in more detail in Section 2.2.2. of Ref. [153]. To ensure proper load-balancing, the algorithm requires that:

- the size of the boxes does not exceed the maximum allowed box size that is specified by the user (we usually set the maximum size of the box to be 16, although other values are also possible and depend on the nature of the simulation),
- the partition is efficient in the sense that the proportion of tagged cells to all cells in a given box does not exceed a *fill-ratio*, $\varepsilon_{\text{FR}} \leq 1$, which is user-specifiable (we usually set $\varepsilon_{\text{FR}} = 0.7$). A higher fill ratio will require a larger quantity of smaller boxes to cover the whole grid, which may be computationally expensive to handle. The effect of a larger fill-ratio (e.g $\varepsilon_{\text{FR}} = 1$) is a more box-like structure of the AMR grids, which we juxtapose with the $\varepsilon_{\text{FR}} = 0.7$ choice in Fig. 2.3.

A fairly common issue of AMR is when the refinement levels end up clustering nearby each other. This often introduces undesired noise upon interpolation and even reflections off

[4]The choice of the tagging criterion is often motivated by the physics we are simulating.

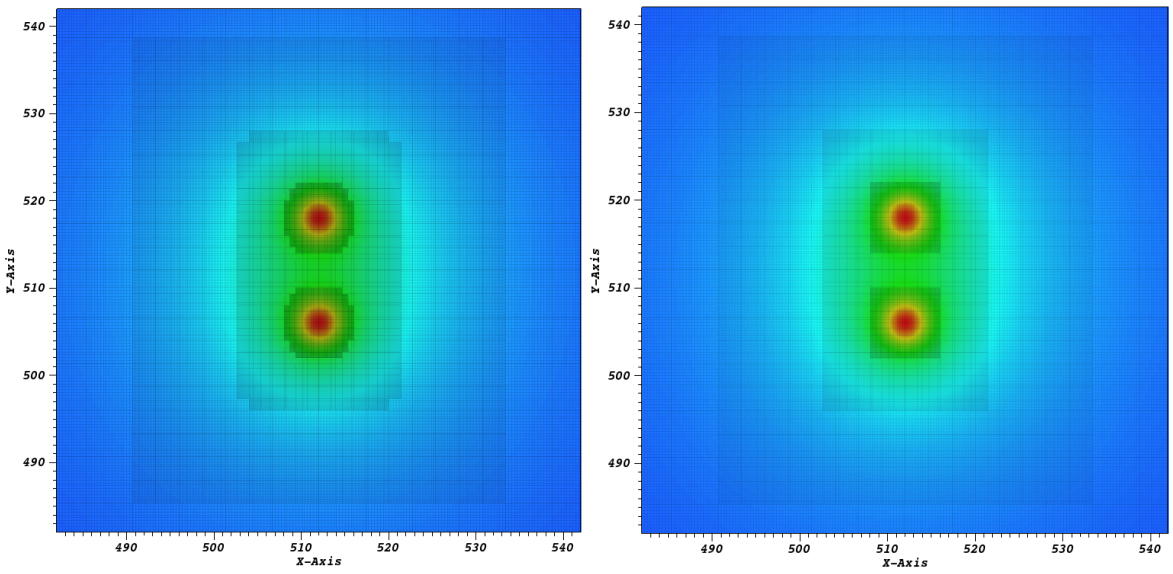


Fig. 2.3 2D snapshots in the $x-y$ plane. The finer AMR grids are shown around two compact objects (boson stars that we will encounter later in Chapters 5–8) and a conformal factor χ is illustrated via the colour gradient. *Left*: A fill-ratio of $\varepsilon_{\rm FR} = 0.7$ is used. The inner refinement levels have sharper edges and a less box-like structure. *Right*: A fill-ratio of $\varepsilon_{\rm FR} = 1$ is now used. Unlike the $\varepsilon_{\rm FR} = 0.7$, the inner refinement levels now have a distinct box-like structure.

the refinement levels that do not fully dissipate and as a result contaminate the numerical evolution. For this purpose, GRCHOMBO uses a parameter that controls the size of *buffer regions* between AMR levels, denoted by $n_{\rm B}$, and specifies the number of cells between the levels. Typically the parameter uses the buffer of $n_{\rm B} = 8$ cells, however in some of our simulations (e.g. Chapter 8) we set it to $n_{\rm B} = 64$. We note that $n_{\rm B}$ *does not* shrink the size of the finer levels, but rather expands the coarser ones.

2.7.3 Tagging criteria

Grid variable type of tagging

A classical way to tag cells in GRCHOMBO is to use grid variables or their derived quantities, e.g. their first or second derivatives as they are likely to be changing rapidly. Let us denote an arbitrary grid variable by F; an easy example for F would be to choose the conformal factor χ, previously defined in Eq. (2.14). Near the BH the gradients of the conformal factor are likely to grow and these are the regions we need to spend most resolution on. A suitable criterion for any grid variable F may then be defined via

$$C = \sqrt{\sum_{ij} \left(\partial_i \partial_j F\right) \left(\partial_i \partial_j F\right)} \Delta x_l. \tag{2.37}$$

We note that it is necessary to scale the gradients of the variables with the spatial resolution on the given level, Δx_l, as otherwise the criterion may be continuously triggered and cause unlimited regridding. A more sophisticated version of Eq. (2.37), incorporating second and first derivatives of some variable F is to use their ratio,

$$C = \sqrt{\frac{\sum_{i,j} \left(\partial_i \partial_j F\right) \left(\partial_i \partial_j F\right)}{\sum_k \left(\partial_k F\right) \left(\partial_k F\right) + \varepsilon}} \Delta x_l, \tag{2.38}$$

where ε is a small constant, specified by the user, as to avoid divisions by zero.

Depending on the numerical simulation of interest, it may be useful to define tagging criterion (2.37) for several evolution or diagnostic variables. For example, if the physical problem has the conformal factor χ and a real scalar field φ in the evolution, we may define two tagging criteria using Eq. (2.37) or Eq. (2.38): C_χ with $F = \chi$ and C_φ with $F = \varphi$. Then, the final tagging criterion may defined by taking the maximum, i.e. $C = \max\left(\mathrm{C}_\chi, \mathrm{C}_\varphi\right)$.

Tagging for extraction zones

In numerical simulations, we typically extract a physical quantity on a spherical shell (e.g. gravitational radiation). This is usually done at a fixed *extraction radius*, R_{ext}, far away from the center of the domain. Therefore, it can happen that in the extraction zone, the quantity of interest is not well resolved. We can ensure that sufficient resolution is used around the extraction sphere labelled by i, by choosing the desired extraction level $l_{\mathrm{ext,i}}$ for each of the extraction radii $R_{\mathrm{ext,i}}$ and using the following criteria

$$C_{\mathrm{ext,i}} = \begin{cases} 100, & \text{if } r < 1.2 R_{\mathrm{ext,i}} \text{ and } l < l_{\mathrm{ext,i}}, \\ 0, & \text{otherwise.} \end{cases} \tag{2.39}$$

Here we use a fudge number of 100 in the criterion near the extraction zones; this is just some arbitrary large number to ensure that the cells are tagged in that region. The combined criterion can then be found via a maximum measure of all criteria for each of the spherical shells, $C_{\mathrm{ext}} = \max_i(C_{\mathrm{ext},i})$.

A là moving boxes tagging

Grid variable tagging often results in tagged regions, which are 'LEGO' spheres, rather than boxes. As we are dealing with a Cartesian cuboid domain, it may be more natural to impose the tagging to be box-like. In this Section, we follow the discussion of Ref. [153] and review how this can be achieved for binary systems, whose components' positions, $\boldsymbol{x}_p^{(1)}$ and $\boldsymbol{x}_p^{(2)}$,

can be tracked throughout the evolution. The tagging criterion is split into 3 parts and is defined via $C = \max\left(\mathrm{C}_{\chi}, \mathrm{C}_{\mathrm{ex}}, \mathrm{C}_{\mathrm{pos}}\right)$. The first part, C_{χ}, tags the cells based on Eq. (2.37) with $F = \chi$, whilst the second one, C_{ext}, is the criterion ensuring sufficient resolution near the extraction zones as previously discussed in Section 2.7.3. Finally, the most non-trivial component of the tagging C_{pos} is split into two parts – the inspiral C_{insp} and the merger C_{merg} tagging criteria, defined as

$$C_{\mathrm{pos}} = \begin{cases} C_{\mathrm{insp}}, & \text{if } d \geq M + b, \\ C_{\mathrm{merg}}, & \text{if } d < M + b, \end{cases} \tag{2.40}$$

where $d = \sqrt{\left|\boldsymbol{x}_p^{(1)} - \boldsymbol{x}_p^{(2)}\right|}$ denotes the separation between the two objects, $M = m_1 + m_2$ is the total mass of the binary and b is a buffer parameter we typically set to $b = 1.2$. The individual 'inspiral' and 'merger' components are defined as follows

$$C_{\mathrm{insp}} = \begin{cases} 100, & \text{if } R_1 < (m_1 + b)2^{\min(L-l-1,2)} \text{ or } R_2 < (m_2 + b)2^{\min(L-l-1,2)}, \\ 0 & \text{otherwise}, \end{cases} \tag{2.41}$$

$$C_{\mathrm{merg}} = \begin{cases} 100, & \text{if } R_{\mathrm{com}} < (M + b)2^{\min(L-l-1,2)}, \\ 0 & \text{otherwise}, \end{cases} \tag{2.42}$$

where $R_i = \max(|x - x_p^{(i)}|, |y - y_p^{(i)}|, |z - z_p^{(i)}|)$ and $R_{\mathrm{com}} = \max(|x - x_{\mathrm{com}}|, |y - y_{\mathrm{com}}|, |z - z_{\mathrm{com}}|)$ with $(x_{\mathrm{com}}, y_{\mathrm{com}}, z_{\mathrm{com}})$ denoting the coordinates in the centre-of-mass frame. The factors of powers of 2 in Eqs. (2.41)-(2.42) enable us to ensure that coarser refinement levels are twice the size of the finer levels, therefore replicating the structure of *moving boxes* style of refinement. The factors may look daunting, but all they do is provide proper box-like refinement around the binary objects; we break-down their effects in Fig. 2.4. Most importantly, we note that C_{insp} tags the cells so that the refinement boxes are positioned around the binary objects individually, whilst boxes in C_{merg} are centered around the centre of mass coordinates.

2.7.4 Boundary Conditions

Our numerical relativity simulations are limited to a finite domain, which is truncated at some artificial boundary, typically far away from the binary evolution. Prescription of appropriate boundary conditions becomes necessary in this case, such that the initial value problem is well-posed and any spurious ingoing reflections arising at the boundary are minimised. In

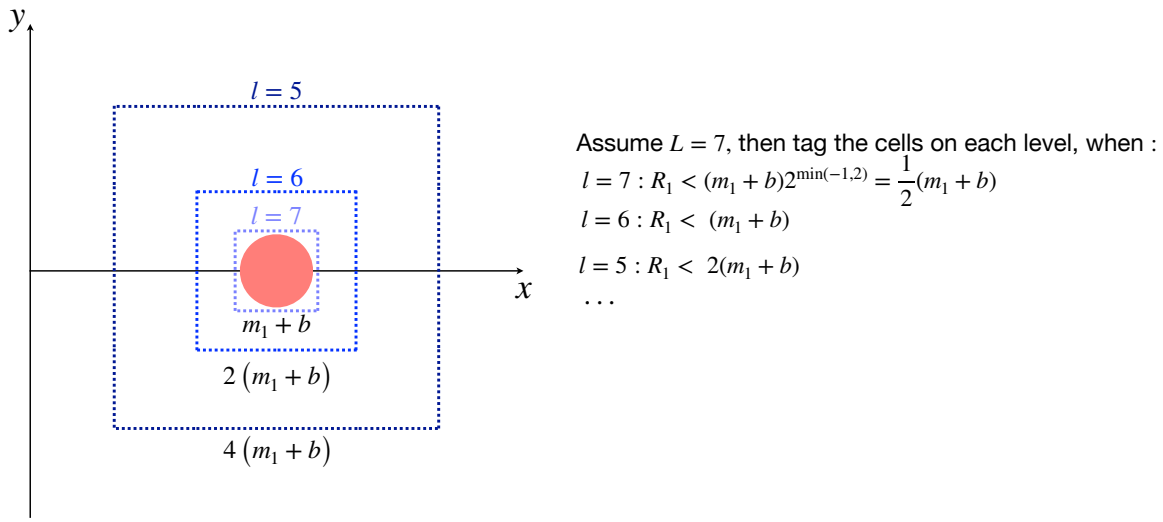


Fig. 2.4 Illustration of the tagging criterion $C_{\rm pos}$ of Eq. (2.40) in the $x-y$ plane being triggered around a compact object of mass m_1 (orange blob) . Assuming we have 7 additional AMR levels on top of the base level $l=0$, we show how the grids are likely to be resolved around the compact object in question.

the generalised harmonic formulation absorbing boundary conditions have been proposed for this purpose (see Refs. [159, 160]). In finite differencing codes, like GRCHOMBO, using BSSN and CCZ4 evolution formulations, we impose *Sommerfeld* (i.e. outgoing radiation) boundary conditions. For some evolution variable v we assume a $\mathcal{O}(r^{-n})$ fall-off, where n is an integer. Mathematically, we can write this as $v = v_\infty + u(t-r)/r^n$, where v_∞ is some background constant value that the evolution variable reaches at large enough radii. The outgoing radiation boundary can then be written as

$$\partial_t u + \partial_r u = 0 \implies \partial_t v + n\frac{v-v_\infty}{r} + \frac{x^i}{r}\partial_i v = 0. \tag{2.43}$$

The outgoing radiation boundary condition is non-exact and may introduce spurious reflections at the boundary, thanks to the non-linearity of our evolution equations. However, having a computational boundary far away from the evolution domain usually ensures that physical quantities are not significantly affected by the spurious modes.

2.7.5 Gravitational waves

Overview

In this Section we will briefly recap the main results of most GR courses, concerning GWs in GR. The reader may be already aware that GWs are derived from linearised theory of

GR in vacuum using the transverse-traceless gauge (see Refs. [161–163] for a complete introduction to this field). GWs correspond to small perturbations of $\mathscr{O}(\varepsilon)$ around Minkowski background, denoted by h_{ij} and satisfying the wave equation

$$\left(\frac{\partial^2}{\partial t^2}+\nabla^2\right)h_{ij}=0. \tag{2.44}$$

Now let us have a closer look at the physical effect of such a GW, h_{ij}, passing by the array of some test particles. The relative motion of the test particles is well described by the *geodesic deviation* equation

$$\frac{D^2}{d\tau^2}\xi^\mu = R^\mu{}_{\nu\rho\sigma}U^\nu U^\rho \xi^\sigma, \tag{2.45}$$

where U^μ is the 4-velocity of the particles, ξ^μ is their separation vector and $D/d\tau$ denotes the covariant differentiation with respect to U^μ. Working in a local inertial (i.e. freely falling) frame[5], we find that the Christoffel symbols vanish. Furthermore, assuming that the test particles are slowly moving[6] and noting that both the Riemann tensor and the change in the separation vector are $\mathscr{O}(\varepsilon)$, the 4-velocity can be taken as $U^\mu=(1,0,0,0)$ [164] and Eq. (2.45) reduces to

$$\frac{\mathrm{d}^2}{\mathrm{dt}^2}\xi^i=\frac{1}{2}\xi^j\frac{\mathrm{d}^2}{\mathrm{dt}^2}h^i{}_j, \tag{2.46}$$

where we have used the fact that $\tau=t$ to leading order, and that $R_{0i0j}=1/2\partial_0\partial_0 h_{ij}$ in the transverse-traceless gauge. Assuming h_{ij} is small, we integrate Eq. (2.46) and to leading order find

$$\xi^j(t)=\xi^j(0)+\frac{1}{2}h^{jk}\left(t-\boldsymbol{k}\cdot\boldsymbol{r}\right)\xi_k(0). \tag{2.47}$$

It follows that the displacement vector $\xi^j(t)$ is driven by h^{jk} – the metric perturbation. This metric perturbation can be decomposed into *plus* and *cross polarisations*, h_+ and $h_\times$ respectively, via $h_{ij}=h_+e^+_{ij}+h_\times e^\times_{ij}$, where e^+_{ij} and $e^\times_{ij}$ are the polarisation matrices we will discuss in more detail in Chapter 3.

Gravitational waves in numerical relativity

As we have seen in the previous Section 2.7.5, the relative, tidal acceleration between the test particles as a GW passes by is determined by the geodesic deviation equation, which is sourced by the Riemann tensor. If we were to measure a *plane*, *null* wave propagating to us on Earth, it would be characterised by the linearised Riemann components as functions of retarded time. The properties of these waves would depend on the symmetries of the

[5] We choose such coordinates that $g_{\mu\nu}=\eta_{\mu\nu}=\mathrm{diag}(-1,1,1,1)$ and $\partial_\rho g_{\mu\nu}=0$.

[6] Meaning we can express U^μ as a vector in the time direction plus corrections of $\mathscr{O}(\varepsilon)$.

Riemann tensor. For example, in vacuum there are six algebraically independent components of the Riemann tensor, corresponding to six polarisations [165]. One of these components corresponds to the modes we will be extracting in our simulations – the plus h_+ and cross $h_\times$ polarisations.

We start by splitting the Riemann tensor into its irreducible parts, consisting of the combinations of the Ricci tensor, Ricci scalar and the Weyl tensor, defined as follows in 4-dimensions

$$C_{\mu\nu\rho\sigma} = R_{\mu\nu\rho\sigma} - \left(g_{\mu[\rho}R_{\sigma]\nu} - g_{\nu[\rho}R_{\sigma]\mu}\right) + \frac{1}{3}g_{\mu[\rho}g_{\sigma]\nu}R. \tag{2.48}$$

We then construct an orthonormal basis $\{e^\mu_{(0)}, e^\mu_{(1)}, e^\mu_{(2)}, e^\mu_{(3)}\}$ in NR (typically using Gram-Schmidt orthonormalisation), satisfying $g_{\alpha\beta}e^\alpha_{(a)}e^\beta_{(b)} = \eta_{(a)(b)}$ and the null tetrad consisting of ingoing and outgoing null vectors, k^μ and l^μ respectively, a complex null vector m^μ and its conjugate $\bar{m}^\mu$. The null tetrad $(l^\mu, k^\mu, m^\mu, \bar{m}^\mu)$ is then related to the $\{e^\mu_{(0)}, e^\mu_{(1)}, e^\mu_{(2)}, e^\mu_{(3)}\}$ tetrad the following way

$$l^\mu = \frac{1}{\sqrt{2}}\left(e^\mu_{(0)} + e^\mu_{(1)}\right), \tag{2.49}$$

$$k^\mu = \frac{1}{\sqrt{2}}\left(e^\mu_{(0)} - e^\mu_{(1)}\right), \tag{2.50}$$

$$m^\mu = \frac{1}{\sqrt{2}}\left(e^\mu_{(2)} + ie^\mu_{(3)}\right), \tag{2.51}$$

$$\bar{m}^\mu = \frac{1}{\sqrt{2}}\left(e^\mu_{(2)} - ie^\mu_{(3)}\right). \tag{2.52}$$

The outgoing gravitational radiation is captured by one of the *Weyl Newman Penrose* scalars, defined by the projection of the Weyl tensor $C_{\alpha\beta\gamma\sigma}$ onto the null tetrad

$$\Psi_4 \coloneqq C_{\alpha\beta\gamma\sigma}k^\alpha\bar{m}^\beta k^\gamma\bar{m}^\sigma. \tag{2.53}$$

In order to compute Ψ_4 we have to choose the null tetrad. In GRCHOMBO we use the *quasi-Kinnersley* tetrad proposed in Ref. [166] (see Section 2.4.4 of Ref. [131] for more details on the implementation).

Far away from the source, the GW is a plane wave and the metric perturbations are directly related to Ψ_4 defined in Eq. (2.53)

$$\Psi_4 = \partial_t^2\left(h_+ - ih_\times\right). \tag{2.54}$$

By the peeling theorem, in an asymptotically flat spacetime we have that $\Psi_4 \sim O(r^{-1})$ at future null infinity [167, 168]. The gravitational radiation is therefore described by $r\Psi_4$, ideally evaluated in the limit $r \to \infty$ or at some large extraction radius $R_{\rm ext}$.

Extraction techniques

In our simulations we often decompose Ψ_4 into its respective spherical harmonic modes. We use spin weighted $s = -2$ spherical harmonics ${}_{-2}Y^{lm}$ defined by [124, 169]

$$ {}_sY^{lm}(\theta,\phi) = (-1)^s \sqrt{\frac{2l+1}{4\pi}} d^l_{m(-s)}(\theta) e^{im\phi}, \tag{2.55} $$

where d^l_{ms} are the Wigner functions defined as

$$ d^l_{ms}(\theta) = \sum_{t=\max(0,m-s)}^{\min(l+m,l-s)} \frac{(-1)^t \sqrt{(l+m)!(l-m)!(l+s)!(l-s)!}}{(l+m-t)!(l-s-t)!t!(t+s-m)!} \left(\frac{\cos\theta}{2}\right)^N \left(\frac{\sin\theta}{2}\right)^M, \tag{2.56} $$

where $N = 2l+m-s-2t$ and $M = 2t+s-m$. The multipolar modes of Ψ_4 on a two-sphere S^2 are then given by

$$ \Psi_{lm}(t,r) = \oint_{S^2} \Psi_4(t,r,\theta,\phi)\, {}_{-2}Y^{*lm}(\theta,\phi) \mathrm{d}\Omega, \tag{2.57} $$

so that the original scalar may be retrieved via

$$ \Psi_4(t,r,\theta,\phi) = \sum_{l=2}^{\infty} \sum_{m=-l}^{m=l} \Psi_{lm}(t,r)\, {}_{-2}Y^{lm}(\theta,\phi). \tag{2.58} $$

The computation of the strain modes h_{lm}, according to Eq. (2.54), requires double integration in time, i.e.

$$ h^{lm}(t) = h^{lm}_+ - i h^{lm}_\times(t) = \int^t \mathrm{d}t' \int^{t'} \mathrm{d}t'' \Psi^{lm}. \tag{2.59} $$

Whilst such integration may look easy to perform, in practice it can be challenging: it has been found that random noise present in the Ψ^{lm} modes can lead to drifts in the waveform and consequent accuracy issues [170]. A remedy for this is to perform the integration in the frequency domain, which reduces the time integration to division by the frequency ω

$$ \tilde{h}^{lm}_+(\omega) - i\tilde{h}^{lm}_\times(\omega) = -\frac{\tilde{\Psi}^{lm}(\omega)}{\omega^2}. \tag{2.60} $$

It is clear to see that when ω is small, the division by ω^2 becomes problematic in a numerical sense and we run into a problem of growing modes. In our approach we choose a *frequency cut-off*, ω_0, so that [170]

$$\tilde{h}_+^{lm}(\omega) - i\tilde{h}_\times^{lm}(\omega) = \begin{cases} -\frac{\tilde{\Psi}^{lm}(\omega)}{\omega^2}, & \text{for } w \geq \omega_0 \\ -\frac{\tilde{\Psi}^{lm}(\omega)}{\omega_0^2}, & \text{for } w < \omega_0. \end{cases} \tag{2.61}$$

The choice of ω_0 is rather arbitrary and requires some form of fine-tuning. In practice we pick a set of ω_0 values for comparison: when ω_0 is too high, the physical low-frequency modes are significantly suppressed, whilst for very low values of ω_0 we start to see drifts. Finding the middle, 'golden' value of ω_0 therefore requires some experimentation. For other possible filters for computing the strain in the frequency domain, see Refs. [171, 172].

Appendix

Appendix 2.A BSSN equations

Baumgarte-Shapiro-Shibata-Nakamura (BSSN) equations

$$\partial_t \chi = \beta^m \partial_m \chi + \frac{2}{3}\chi(\alpha K - \partial_m \beta^m), \tag{2.62}$$

$$\partial_t \tilde{\gamma}_{ij} = \beta^m \partial_m \tilde{\gamma}_{ij} + 2\tilde{\gamma}_{m(j}\partial_{i)}\beta^m - \frac{2}{3}\tilde{\gamma}_{ij}\partial_m \beta^m - 2\alpha \tilde{A}_{ij}, \tag{2.63}$$

$$\partial_t K = \beta^m \partial_m K - \chi \tilde{\gamma}^{ml} D_m D_l \alpha + \alpha \left[\tilde{A}^{mn}\tilde{A}_{mn} + \frac{1}{3}K^2 + 4\pi(S+\rho) \right], \tag{2.64}$$

$$\begin{aligned} \partial_t \tilde{A}_{ij} = {} & \beta^m \partial_m \tilde{A}_{ij} + 2\tilde{A}_{m(j}\partial_{i)}\beta^m - \frac{2}{3}\tilde{A}_{ij}\partial_m \beta^m - 2\alpha \tilde{A}_{im}\tilde{A}^m{}_j + \alpha \tilde{A}_{ij} K \\ & + \chi \left[-D_i D_j \alpha + \alpha(\tilde{R}_{ij} + R^{\chi}_{ij} - 8\pi S_{ij}) \right]^{\mathrm{TF}}, \end{aligned} \tag{2.65}$$

$$\begin{aligned} \partial_t \tilde{\Gamma}^i = {} & \beta^m \partial_m \tilde{\Gamma}^i + \frac{2}{3}\tilde{\Gamma}^i \partial_m \beta^m - \tilde{\Gamma}^m \partial_m \beta^i + \tilde{\gamma}^{mn}\partial_m \partial_n \beta^i + \frac{1}{3}\tilde{\gamma}^{im}\partial_m \partial_n \beta^n \\ & - 2\tilde{A}^{im}\partial_m \alpha + 2\alpha \left(\tilde{\Gamma}^i_{mn}\tilde{A}^{mn} - \frac{2}{3}\tilde{\gamma}^{im}\partial_m K - \frac{3}{2}\tilde{A}^{im}\frac{\partial_m \chi}{\chi} - 8\pi \tilde{\gamma}^{im} j_m \right), \end{aligned} \tag{2.66}$$

where $[..]^{\mathrm{TF}}$ denotes the trace-free part, and $\tilde{R}_{ij}$ and R^{χ}_{ij} are parts of the spatial Ricci tensor ${}^{(3)}R_{ij}$ so that

$$\begin{aligned} {}^{(3)}R_{ij} &= \tilde{R}_{ij} + R^{\chi}_{ij}, \\ \tilde{R}_{ij} &= -\frac{1}{2}\tilde{\gamma}^{km}\partial_k \partial_m \tilde{\gamma}_{ij} + \tilde{\gamma}_{m(i}\partial_{j)}\tilde{\Gamma}^m + \tilde{\Gamma}^m \tilde{\Gamma}_{(ij)m} + \tilde{\gamma}^{mn}\left[2\tilde{\Gamma}^k_{m(i}\tilde{\Gamma}_{j)kn} + \tilde{\Gamma}^k_{im}\tilde{\Gamma}_{kjn} \right], \\ R^{\chi}_{ij} &= \frac{1}{2\chi}\left[\tilde{D}_i \tilde{D}_j \chi - \frac{1}{2\chi}\tilde{D}_i \chi \tilde{D}_j \chi \right] + \frac{\tilde{\gamma}_{ij}}{2\chi}\left[\tilde{\gamma}^{mn}\tilde{D}_m \tilde{D}_n \chi - \frac{3}{2\chi}\tilde{\gamma}^{mn}\tilde{D}_m \chi \tilde{D}_n \chi \right]. \end{aligned} \tag{2.67}$$

Finally, we note that in Eqs. (2.65)-(2.66) we have

$$D_i D_j \alpha = \partial_i \partial_j \alpha - \tilde{\Gamma}^k_{ij} \partial_k \alpha + \frac{1}{2\chi} \left(\partial_{(i} \alpha \partial_{j)} \chi - \tilde{\gamma}_{ij} \tilde{\gamma}^{kl} \partial_k \alpha \partial_l \chi \right). \tag{2.68}$$

Appendix 2.B CCZ4 equations

Covariant and conformal Z4 (CCZ4) equations

$$\partial_t \chi = \beta^m \partial_m \chi + \frac{2}{3} \chi (\alpha K - \partial_m \beta^m), \tag{2.69}$$

$$\partial_t \tilde{\gamma}_{ij} = \beta^m \partial_m \tilde{\gamma}_{ij} + 2 \tilde{\gamma}_{m(i} \partial_{j)} \beta^m - \frac{2}{3} \tilde{\gamma}_{ij} \partial_m \beta^m - 2\alpha \tilde{A}_{ij}, \tag{2.70}$$

$$\begin{aligned} \partial_t K = {} & \beta^m \partial_m K - D^m D_m \alpha + \alpha \Big[{}^{(3)}R + 2 D^m \Theta_m + K(K - 2\Theta) \\ & - 3\kappa_1 (1 + \kappa_2) \Theta + 4\pi (S - 3\rho) \Big], \end{aligned} \tag{2.71}$$

$$\begin{aligned} \partial_t \tilde{A}_{ij} = {} & \beta^m \partial_m \tilde{A}_{ij} + 2 \tilde{A}_{m(i} \partial_{j)} \beta^m - \frac{2}{3} \tilde{A}_{ij} \partial_m \beta^m - 2\alpha \tilde{A}_{im} \tilde{A}^m{}_j + \alpha \tilde{A}_{ij} (K - 2\Theta) \\ & + \chi \left[-D_i D_j \alpha + \alpha \left({}^{(3)}R_{ij} + 2 D_{(i} \Theta_{j)} - 8\pi S_{ij} \right) \right]^{\mathrm{TF}}, \end{aligned} \tag{2.72}$$

$$\begin{aligned} \partial_t \hat{\Gamma}^i = {} & \beta^m \partial_m \hat{\Gamma}^i + \tilde{\gamma}^{mn} \partial_m \partial_n \beta^i + \frac{1}{3} \tilde{\gamma}^{ik} \partial_k \partial_m \beta^m + \frac{2}{3} \partial_m \beta^m \left(\tilde{\Gamma}^i + 2\kappa_3 \frac{\Theta^i}{\chi} \right) \\ & - 2\partial_m \alpha (\tilde{A}^{im} + \Theta \tilde{\gamma}^{im}) - \tilde{\Gamma}^m \partial_m \beta^i + 2\alpha \tilde{A}^{mn} \tilde{\Gamma}^i_{mn} - 3\alpha \tilde{A}^{im} \frac{\partial_m \chi}{\chi} - 2 \frac{\alpha}{\chi} \kappa_1 \Theta^i \\ & - \frac{4}{3} \frac{\alpha}{\chi} K \Theta^i + 2\alpha \tilde{\gamma}^{im} \left(\partial_m \Theta - \frac{2}{3} \partial_m K \right) - 2\kappa_3 \frac{\Theta^m}{\chi} \partial_m \beta^i - 16\pi \alpha \tilde{\gamma}^{im} j_m, \end{aligned} \tag{2.73}$$

$$\begin{aligned} \partial_t \Theta = {} & \beta^m \partial_m \Theta + \frac{\alpha}{2} \Big[{}^{(3)}R + 2 D_m \Theta^m - \tilde{A}^{mn} \tilde{A}_{mn} + \frac{2}{3} K^2 - 2K\Theta \\ & - 2\Theta^m \frac{\partial_m \alpha}{\alpha} - \kappa_1 (4 + 2\kappa_2) \Theta - 16\pi \rho \Big], \end{aligned} \tag{2.74}$$

$$\begin{aligned} \partial_t \Theta_i = {} & \beta^m \partial_m \Theta_i + \Theta_m \partial_i \beta^m + \alpha \Big(D_m K^m{}_i - D_i K - 2 K_{im} \Theta^m + D_i \Theta \\ & - \Theta \frac{\partial_i \alpha}{\alpha} - \kappa_1 \Theta_i - 8\pi j_i \Big). \end{aligned} \tag{2.75}$$

In Eq. (2.73), we have defined a *modified conformal connection function*, $\hat{\Gamma}^i$ defined by

$$\hat{\Gamma}^i := \tilde{\Gamma}^i + 2\frac{\Theta^i}{\chi}. \tag{2.76}$$

Furthermore, in Eq. (2.72), we have utilised a modified version of the Ricci tensor

$$\begin{aligned}
&{}^{(3)}R_{ij} + 2D_{(i}\Theta_{j)} = \hat{R}_{ij} + R^{\chi}_{ij} + R^{Z}_{ij}, \\
&\hat{R}_{ij} = -\frac{1}{2}\tilde{\gamma}^{km}\partial_k\partial_m\tilde{\gamma}_{ij} + \tilde{\gamma}_{m(i}\partial_{j)}\hat{\Gamma}^m + \hat{\Gamma}^m\tilde{\Gamma}_{(ij)m} + \tilde{\gamma}^{mn}\left[2\tilde{\Gamma}^k_{m(i}\tilde{\Gamma}_{j)kn} + \tilde{\Gamma}^k_{im}\tilde{\Gamma}_{kjn}\right], \\
&R^{Z}_{ij} = \frac{\Theta^m}{\chi^2}\left[\tilde{\gamma}_{jm}\partial_i\chi + \tilde{\gamma}_{im}\partial_j\chi - \tilde{\gamma}_{ij}\partial_m\chi\right],
\end{aligned} \tag{2.77}$$

where $\hat{R}_{ij}$ is essentially $\tilde{R}_{ij}$ but with $\tilde{\Gamma}^i$ in Eq. (2.67) replaced by $\hat{\Gamma}^i$. Note the additional constraint parameter κ_3 in Eq. (2.73) – this term proved to be necessary for stable numerical evolutions of BHs [116]. In this work we set, $\kappa_3 = 1$. We remark that the elliptic constraint equations previously seen in the BSSN formalism are now replaced by the hyperbolic equations for Θ and Θ_i. This poses a great advantage for numerics, whereby we avoid solving the computationally expensive constraint equations at every time-step.

Appendix 2.C York–Lichnerowicz conformal decomposition

In the same spirit as the BSSN formalism, the York–Lichnerowicz conformal decomposition begins with a conformal rescaling of the spatial metric

$$\gamma_{ij} = \psi^4\tilde{\gamma}_{ij}, \tag{2.78}$$

and a split of the extrinsic curvature into its trace and trace-free components, K and A_{ij}, respectively

$$K^{ij} = A^{ij} - \frac{1}{3}\gamma^{ij}K. \tag{2.79}$$

Upon such a decomposition, the constraint equations become

$$8\tilde{D}^2\psi - \tilde{R}\psi + \psi^5\left(A_{ij}A^{ij} - \frac{2}{3}K^2\right) + 16\pi\psi^5\rho = 0, \tag{2.80}$$

$$D_jA^{ij} - \frac{2}{3}D^iK - 8\pi j^i = 0. \tag{2.81}$$

Next, in order to transform the momentum constraint equation into 3 equations with 3 unknowns, we will use the fact that any symmetric traceless tensor X^{ij} can be split into transverse and longitudinal parts.

$$\tilde{B}^{ij} = \tilde{B}^{ij}_{*} + (\tilde{L}\tilde{W})^{ij}, \tag{2.82}$$

where $\tilde{B}^{ij}_{*}$ is transverse so that $D_j\tilde{B}^{ij}_{*} = 0$, $\tilde{W}^i$ is a vector to be determined and $\tilde{L}$ is a linear operator associated with the conformal metric $\tilde{\gamma}_{ij}$,

$$\left(\tilde{L}\tilde{W}\right)^{ij} := \tilde{D}^i\tilde{W}^j + \tilde{D}^j\tilde{W}^i - \frac{2}{3}\tilde{\gamma}^{ij}\tilde{D}_k\tilde{W}^k. \tag{2.83}$$

A natural trace-free symmetric quantity to apply decomposition (2.83) on is $\tilde{A}^{ij}$. However, we first need to define the conformal version of A^{ij}, which we achieve in the following way,

$$\tilde{A}^{ij} = \psi^{10}A^{ij}. \tag{2.84}$$

We then split $\tilde{A}^{ij}$ into transverse and longitudinal parts,

$$\tilde{A}^{ij} = \tilde{A}^{ij}_{*} + (\tilde{L}\tilde{W})^{ij}. \tag{2.85}$$

Now, we use a little'trick', which may seem unnatural at first however it will eventually help us in simplifying the momentum constraint equation. First, we start by rearranging Eq. (2.85) but for now replace $\tilde{A}^{ij}$ with some arbitrary symmetric and trace-free tensor $\tilde{M}^{ij}$ that we will be able to choose freely

$$\tilde{M}^{ij}_{*} = \tilde{M}^{ij} - \left(\tilde{L}\tilde{Y}\right)^{ij}, \tag{2.86}$$

where $\tilde{Y}^i$ is the vector ultimately to be determined. Taking into account that $\tilde{M}^{*}_{ij}$ is transverse, $\tilde{Y}^i$ then satisfies the following relation

$$\tilde{D}_j\tilde{M}^{ij} = \tilde{D}_j\left(\tilde{L}\tilde{Y}.\right)^{ij} \tag{2.87}$$

Now, defining $\tilde{V}^i := \tilde{W}^i - \tilde{Y}^i$ and taking $\tilde{A}^{ij}_{*} = \tilde{M}^{ij}_{*}$, we arrive at

$$\tilde{A}^{ij} = \tilde{M}^{ij} + \left(\tilde{L}\tilde{V}\right)^{ij}, \tag{2.88}$$

so that the Hamiltonian and momentum equation become

$$8\tilde{D}^2\psi - \tilde{R}\psi + \psi^{-7}\tilde{A}_{ij}\tilde{A}^{ij} - \frac{2}{3}\psi^5 K^2 + 16\pi\psi^5\rho = 0, \tag{2.89}$$

$$\tilde{D}_j\left(\tilde{L}\tilde{V}\right)^{ij} + \tilde{D}_j\tilde{M}^{ij} - \frac{2}{3}\psi^6\tilde{D}^i K - 8\pi\psi^{10}j^i = 0. \tag{2.90}$$

Provided free-data $\tilde{\gamma}_{ij}$, $\tilde{M}^{ij}$, K, ρ and j, equations (2.89)–(2.90) are solved for ψ and $\tilde{V}^i$. We now have a system of 4 constraint equations and 4 unknowns. For puncture initial data, we choose $\tilde{M}^{ij} = 0$, therefore significantly simplifying the momentum constraint to Eq. (2.33) – this is where our trick of Eq. (2.86) comes in handy.

Chapter 3

Gravitational wave data analysis for numerical relativists in fundamental physics

3.1 Introduction

In this Chapter we would like to bring together the tools used for GW analysis with numerical relativity waveforms, and present the basic introductory material required for a numerical relativist to be able to prepare and inject their simulation data into GW analysis pipelines. This may be of particular interest to groups who study the effects of modified theories of gravity and/or exotic compact objects on GW observations and would like to understand the response of parameter estimation pipelines to their simulated GW signals as well as potential modelling biases related to their theories of interest. In Section 3.2, we start with a status review of current and future GW detectors and describe the principles of matched filtering techniques used for GW detection. In Section 3.3 we discuss the fundamentals of Bayesian inference and methods involved in inferring the source parameters following a GW detection (or NR injection). Finally, in Section 3.4 we review the steps of data preparation required to perform numerical relativity injections into detector noise. Our discussion covers injections of conventional plus and cross GW polarisations of GR, as well as scalar polarisation modes.

3.2 Gravitational wave detectors

3.2.1 Present and future GW detectors

The network of first GW detectors consisted of 2 LIGO detectors in the US, the Virgo detector in Italy, the GEO600 detector in Germany and the TAMA300 detector in Japan. After some hardware upgrades the Advanced LIGO detectors made the observation of the first binary black hole (BBH) event GW150914 in engineering mode of their first observing run [12]. In 2016 LIGO-Virgo entered their second observing run (O2), followed by the O3 run in 2019 and just recently by the O4 run in 2024. In the second observing run, LIGO-Virgo detected the first binary neutron star signal GW170817. By the end of the third observing run, during which the first two binary black hole neutron star mergers were detected (GW200115 and GW200105) [173], LIGO and Virgo were joined by the Japanese KAGRA interferometer. Current GW detectors are able to detect gravitational waves in the frequency range of $10 - 10^4$Hz; lower frequency signals are harder to probe due to *seismic* and *Newtonian* noise[1] [174], whilst the higher frequency band is limited by *shot* noise (i.e. fluctuations in the photon number) [175]. The present detectors are L-shaped and use laser interferometry to sense the motion of test masses at the ends of the arms as the GW passes through. Gravitational waves change the relative displacement of the interferometers' arms, resulting in the strain

$$h = \frac{\Delta L}{L} \sim 10^{-21}, \tag{3.1}$$

where L is the length of the detector arm and ΔL is the length change.

In the next years, the ensemble of GW detectors awaits new additions. For example, by 2030, the LIGO India interferometer [176] is expected to become operational. The next generation detectors are also planned to be built, including the Cosmic Explorer [177, 178] (CE) with longer arm lengths increasing its sensitivity and the Einstein Telescope (ET) [179]. Last but not least, GW science is going to space: the Laser Interferometer Space Antenna (LISA) [180–182] detector, adopted by the European Space Agency (ESA) and the National Aeronautics and Space Administration (NASA) is expected to begin its construction in 2025, promising to extend our detection range into lower frequency band of $10^{-4} - 10^{-1}$Hz. The LISA Pathfinder mission was completed in 2017, testing the in-flight technologies required for GW detection in space and demonstrating its feasibility [183]. On the other hand, another space-based detector DECIGO [184] proposed for 2030s by Japan will be sensitive in the

[1] Seismic noise is generated by the ground vibrations that can happen anywhere on the Earth, whilst Newtonian noise – by the small fluctuations of the Earth's gravitational field.

frequency band of $0.1 - 10$Hz, therefore filling in the gap between the sensitivity bands of LIGO and LISA.

3.2.2 Gravitational wave polarisations

At large distances, a GW coming from a source can be interpreted as a plane wave travelling along a unit vector $\boldsymbol{k}$, which points from the source to the observer. Let us fix our coordinate axes so that

$$\boldsymbol{k} = \begin{pmatrix} 0 \\ 0 \\ 1 \end{pmatrix}, \tag{3.2}$$

and the components of the GW – i.e. the metric perturbation – are

$$\boxed{h_{ij} = h_+ e^+_{ij} + h_\times e^\times_{ij},} \tag{3.3}$$

where h_+ and $h_\times$ are the plus and cross polarisations, both functions of $(t - \boldsymbol{k}\cdot\boldsymbol{r})$, and

$$(e_+)_{ij} \coloneqq \boldsymbol{e}_+ = \begin{pmatrix} 1 & 0 & 0 \\ 0 & -1 & 0 \\ 0 & 0 & 0 \end{pmatrix}, \qquad (e_\times)_{ij} \coloneqq \boldsymbol{e}_\times = \begin{pmatrix} 0 & 1 & 0 \\ 1 & 0 & 0 \\ 0 & 0 & 0 \end{pmatrix} \tag{3.4}$$

are the polarisation matrices. In this case, when the wave is propagating in the z-direction, we can see from Eq. (2.47) that only displacement in ξ^1 and ξ^2 directions of the test particles is triggered (but not in ξ^3). In a general setting, we can always construct polarisation matrices $(e_+)_{ij}$ and $(e_\times)_{ij}$ as long as we are provided with the orthonormal basis $(\boldsymbol{\ell}, \boldsymbol{m}, \boldsymbol{k})$, where $\boldsymbol{\ell}, \boldsymbol{m}$ lie in the plane perpendicular to $\boldsymbol{k}$

$$\boldsymbol{e}_+ = \boldsymbol{\ell}\boldsymbol{\ell}^T - \boldsymbol{m}\boldsymbol{m}^T, \tag{3.5}$$

$$\boldsymbol{e}_\times = \boldsymbol{\ell}\boldsymbol{m}^T + \boldsymbol{m}\boldsymbol{\ell}^T. \tag{3.6}$$

In modified theories of gravity, additional polarisation content may be encoded in the forms of *vector-x*, *vector-y*, *breathing* and *longitudinal* modes (cf. Fig. 4.2.1) whose respective

polarisation matrices are

$$\boldsymbol{e}_x = \boldsymbol{\ell}\boldsymbol{k}^T + \boldsymbol{k}\boldsymbol{\ell}^T, \tag{3.7}$$

$$\boldsymbol{e}_y = \boldsymbol{m}\boldsymbol{k}^T + \boldsymbol{k}\boldsymbol{m}^T, \tag{3.8}$$

$$\boldsymbol{e}_b = \boldsymbol{\ell}\boldsymbol{\ell}^T + \boldsymbol{m}\boldsymbol{m}^T, \tag{3.9}$$

$$\boldsymbol{e}_l = \boldsymbol{k}\boldsymbol{k}^T. \tag{3.10}$$

As we will see in Chapter 4, the polarisation content can be classified in terms of Newman-Penrose scalars, one of which is Ψ_4, we already encountered in Section 2.7.5 of Chapter 2. For a comprehensive discussion on testing GR via GW polarisations see Refs. [185–188].

3.2.3 Antenna response functions

Note that h_{ij} describes GWs as a tensor on a Minkowski background, whilst the inputs and outputs of the GW detector are in fact scalar quantities. When a gravitational wave travels to the detector, it records a time series of the following form

$$h(t) = D^{ij}h_{ij}(t) = \sum_A D^{ij}e^A_{ij}h_A(t), \tag{3.11}$$

where A denotes the polarisation symbol, e.g. $+$ and $\times$ in GR, and D^{ij} is a constant tensor depending on the geometry of the detector. For LIGO-Virgo-KAGRA that are *differential arm detectors*, the detector tensor is given by

$$D^{ij} = \frac{1}{2}\left(d^i_x d^j_x - d^i_y d^j_y\right), \tag{3.12}$$

where d^i_x and d^i_y are the unit spatial vectors along each of detector arms. By defining the *detector pattern* or *antenna response* functions via

$$F_A = D^{ij}e^A_{ij}, \tag{3.13}$$

the strain of Eq. (3.11) in the *detector frame* can then be written as

$$\boxed{h(t) = h_+(t)F_+(\theta,\phi,\psi) + h_\times(t)F_\times(\theta,\phi,\psi),} \tag{3.14}$$

where (θ,ϕ) define the direction of the propagation and ψ is the polarisation angle that we define below. We typically choose $\boldsymbol{\ell}$ to lie on the intersection of the equatorial plane of the source with the plane of sky. Different orientation of $\boldsymbol{\ell}$, obtained through the rotation of

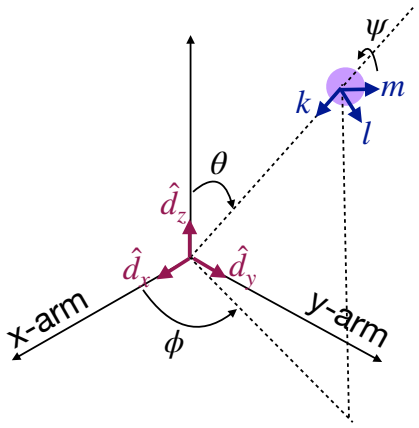


Fig. 3.2.1 Definition of the propagation angles (θ,ϕ) and the polarisation angle ψ in the detector frame. Note that $\{\hat{\boldsymbol{d}}_x,\hat{\boldsymbol{d}}_y,\hat{\boldsymbol{d}}_z\}$ denote the Cartesian basis in the detector frame, whilst $\{\boldsymbol{\ell},\boldsymbol{m},\boldsymbol{k}\}$ is the basis at the source, where $\boldsymbol{k}$ is taken to be in the direction of propagation.

the unit vectors around the direction of propagation, can be incorporated by including the polarisation angle ψ (see Fig. 3.2.1). We will see an example of defining the $(\boldsymbol{\ell},\boldsymbol{m},\boldsymbol{k})$ basis in Section 3.4.2, which will constitute what we call a *wave frame*. The antenna response function are then written as follows

$$F_+ = \frac{1}{2}\left(1+\cos^2\theta\right)\cos2\phi\cos2\psi - \cos\theta\sin2\phi\sin2\psi, \tag{3.15}$$

$$F_\times = \frac{1}{2}\left(1+\cos^2\theta\right)\cos2\phi\sin2\psi + \cos\theta\sin2\phi\cos2\psi, \tag{3.16}$$

$$F_x = -\sin\theta\left(\cos\theta\cos2\phi\cos\psi - \sin2\phi\sin\psi\right), \tag{3.17}$$

$$F_y = -\sin\theta\left(\cos\theta\sin2\phi\cos\psi + \sin2\phi\cos\psi\right), \tag{3.18}$$

$$F_b = -\frac{1}{2}\sin^2\theta\cos2\phi, \tag{3.19}$$

$$F_s = \frac{1}{2}\sin^2\theta\cos2\phi. \tag{3.20}$$

3.2.4 Detector noise and matched filtering

The GW detectors are not perfect machines that can just register any GW signal. Often, noise effects and artifacts from the surroundings contaminate our GW measurements and therefore have to be taken into account, when searching for GW signatures. The GW detector output

can be assumed as[2]

$$d(t) = h(t) + n(t), \tag{3.21}$$

where $h(t)$ is the pure GW signal and $n(t)$ is the noise. We assume the noise is *stationary* so that the average over many of its possible realisations is given by

$$\langle \tilde{n}^*(f)\tilde{n}(f')\rangle = \frac{1}{2}\delta(f-f')S_n(f), \tag{3.22}$$

where $\tilde{n}(f)$ is the noise in the frequency domain, $\tilde{n}^*(f)$ its conjugate and $S_n(f)$ is the *single-sided noise* or *power spectral density* (PSD). Note that here $S_n(f)$ has dimensions Hz^{-1}.

The problem of GW detection is that the noise is often louder than the incoming GW signal and we are confronted with the task of somehow 'filtering out' $h(t)$. This becomes possible if we know the form of the strain $h(t)$ as well as the typical magnitude of variations of the noise. Typically $h(t)$ is either given by one of the parametrised waveform approximants (see Table 12 of Ref. [180] for a representative set of frequency and time domain BBH approximants) or a numerically simulated signal.

In our quest for filtering through the noise, we define a *filter function* $K(t)$ so that

$$\hat{d} = \int_{-\infty}^{\infty} \mathrm{d}t\, d(t)K(t). \tag{3.23}$$

We then look for $K(t)$ such that it maximises the signal-to-noise ratio (SNR), defined as the ratio of the expected values of $\hat{d}$ when the GW signal is present and the root mean squared value of $\hat{d}$ when there is no signal. Such filter function in the Fourier domain can be found to be [161]

$$\tilde{K}(f) \sim \frac{\tilde{h}(f)}{S_n(f)}. \tag{3.24}$$

The signal-to-noise-ratio, ρ, then takes the following form

$$\rho^2 = 4\int_0^{\infty} \mathrm{d}f \frac{|\tilde{h}(f)|^2}{|S_n(f)|}. \tag{3.25}$$

The technique of maximising the SNR is referred to as *matched filtering*, as the filter K is chosen to 'match' the GW signal. Matched filtering is one of the methods used to search for GW signals in the data. An alternative unmodelled method is to use wavelets in the

[2]Note that here we are ignoring the calibration error function.

reconstruction of the GW signal, as done in the *Coherent Wave Burst* (CWB) pipeline [189, 190] which detected the first BBH event GW150914.

3.3 Bayesian inference and parameter estimation

3.3.1 Bayes theorem

When a signal has been triggered as detected either by the matched filtering or CWB pipelines, we can study the 'morphology' of the signal in more detail. In particular, using Bayesian inference, we can infer the parameters of the sources, $\theta = \{\theta_i\}$, the signal is coming from. The central equation of this Section is Bayes theorem

$$p(\theta|d) = \frac{\mathscr{L}(d|\theta)\pi(\theta)}{\mathscr{Z}}, \quad \mathscr{Z} = \int \mathrm{d}\theta \mathscr{L}(d|\theta)\pi(\theta), \tag{3.26}$$

where $\mathscr{L}(d|\theta)$ is the *likelihood function*, $\pi(\theta)$ is the *prior*, encoding our knowledge about the possible distribution of the parameters θ, and $\mathscr{Z}$ is the *evidence*. Formally, the evidence is a completely marginalised[3] likelihood function and is simply a normalisation factor of Eq. (3.26).

Prior

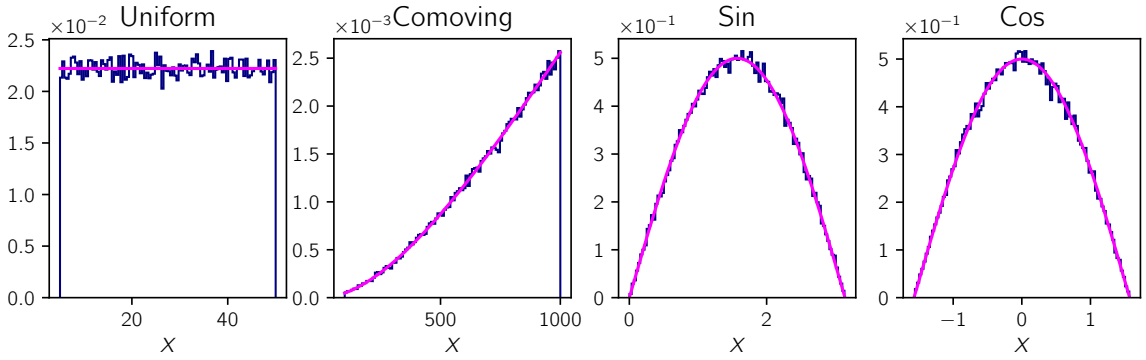


Fig. 3.3.1 Shapes (from left to right) of uniform, uniform in cosmological comoving volume, uniform in cosine and sine priors for an arbitrary variable X.

Let us now provide an example of suitable prior functions. The GW signal coming from a black hole binary is characterized by 15 source parameters. They can be separated into

[3]Marginalisation is a powerful technique in the context of high-dimensional posterior distributions. By marginalising, i.e. by integrating over the 'nuisance' parameters, we can isolate the probability distribution for a single parameter we are interested in.

intrinsic $\{m_1, m_2, \phi_c, a_1, a_2, \theta_1, \theta_2, \phi_{12}, \phi_{JL}\}$ and *extrinsic* $\{t_c, \alpha, \delta, \iota, d_L, \psi\}$ parameters that we describe in more detail in Table 3.3.1. Typical prior choices include: *uniform*, *uniform in sine*, *uniform in cosine* and *uniform in comoving volume* (see Fig. 3.3.1). One the one hand, a simple uniform prior usually highlights our ignorance about how a certain source parameter should be distributed. For example, the individual component masses, m_1 and m_2, are often characterised by such priors under the constraint that $m_1 \geq m_2$. On the other hand, if we have some astrophysically motivated knowledge that a parameter is isotropically distributed, we may revert to using uniform priors in sine or cosine. For example, it is expected that binaries formed via dynamical interactions in stellar clusters are expected to have spin directions isotropically distributed [191]. However, this is not the only available choice and the impact of the spin prior choice on the parameter estimation is, in fact, a hot topic in gravitational wave astronomy, see Refs. [192, 193] for further discussions. Finally, uniform in comoving volume prior is typically used for the luminosity distance, d_L, allowing us to capture the effect of an increasing distribution of BBHs events, as we move further away. We report typical prior choices employed in gravitational wave analysis in Table 3.3.1.

Table 3.3.1 includes the individual component masses, m_1 and m_2, and imposes a uniform prior on them. Realistically, most analyses would sample the chirp mass, $\mathscr{M}$, defined via

$$\mathscr{M} = \frac{(m_1 m_2)^{3/5}}{(m_1 + m_2)^{1/5}}, \tag{3.27}$$

as it is the leading term in the frequency evolution in the Post-Newtonian (PN) expansion and so is much better constrained. The second parameter we typically choose to sample is the mass ratio, $q := m_2/m_1 \leq 1$.

Likelihood

The likelihood function is in principle a freely specifiable function. As the likelihood portrays the probability of the data given the source parameters, it therefore encodes the description of the measurement. A typical choice for a single GW detector is a Gaussian likelihood function, which also allows us to implicitly introduce the noise parameter related to our measurements and impose the assumption of Gaussian detector noise

$$\mathscr{L}(d|\theta) = \frac{1}{2\pi\sigma^2} \exp\left(-\frac{1}{2}\frac{|d-\mu(\theta)|^2}{\sigma^2}\right). \tag{3.28}$$

Above σ denotes the detector noise and $\mu(\theta)$ a waveform template. The analysis usually takes place in the Fourier domain and the noise is represented by the PSD $S_n(f)$, which we

Symbol	Description	Units	Prior
m_1, m_2	Individual component masses	$M_\odot$	Uniform$[M_{\rm min}, M_{\rm max}]$
ϕ_c	Reference phase of the binary	rad	Uniform$[0, 2\pi]$
a_1, a_2	Dimensionless spin magnitudes	–	Uniform$[0, 0.99]$
θ_1, θ_2	Tilt angles, corresponding to $\theta_i = a_i \cos(\alpha_i)$, where $i \in \{1,2\}$ and α_i is the angle between the spin and orbital angular momentum	rad	Sin$[0, \pi]$
ϕ_{12}	Difference between the azimuthal angles of the individual spin projections onto the orbital plane	rad	Uniform$[0, 2\pi]$
ϕ_{JL}	Difference between total and orbital momentum azimuthal angles	rad	Uniform$[0, 2\pi]$
ι	Inclination angle defined as the angle between the line of sight and the orbital angular momentum. When $\iota = 0^\circ$, the binary is *face-on*, and when $\iota = 90^\circ$, it is *edge-on*	rad	Sin$[0, \pi]$
t_c	Time of coalescence at geocenter	s	Uniform$[t_{c,\rm min}, t_{c,\rm max}]$
α	Right ascension (sky position)	rad	Uniform$[0, 2\pi]$
δ	Declination (sky position)	rad	Cos$[-\pi/2, \pi/2]$
d_L	Luminosity distance of the source	Mpc	Comoving$[d_{L,\rm min}, d_{L,\rm max}]$
ψ	Polarisation angle	rad	Uniform$[0, 2\pi]$

Table 3.3.1 Binary black hole source parameters and their priors typically employed in parameter estimations pipelines. Here 'Sin' and 'Cos' denote uniform priors in cosine and sine correspondingly (note the order here!), whilst 'Comoving' refers to the uniform prior in cosmological comoving volume. The 'max' and 'min' subscripts are used to denote the lower and upper bounds on the priors.

have previously seen in Eq. (3.22). The likelihood function for a frequency bin i can be written as

$$\hat{\mathscr{L}}(d_i|\theta) = \frac{1}{2\pi S_{n,i}(f)} \exp\left(-2\delta f \frac{|\hat{d}_i - \hat{\mu}_i(\theta)|^2}{S_{n,i}(f)}\right), \tag{3.29}$$

where δf is the frequency resolution. As the signal is usually spread over N bins[4], the total likelihood is merely a product of all individual likelihood functions in each of the frequency bins

$$\mathscr{L}(d|\theta) = \prod_{i=1}^{N} \mathscr{L}(d_i|\theta). \tag{3.30}$$

[4]Here we work under the assumption that the noise in each frequency bin is a collection of independent and identically distributed random variables.

For multiple independent detectors, denoted by j, the likelihood function is given via

$$\mathscr{L}(d|\theta) = \prod_j \prod_{i=1}^{N} \mathscr{L}(d_{i,j}|\theta). \tag{3.31}$$

Evidence

Equation (3.28) has a freedom in specifying the waveform template $\mu(\theta)$. Therefore depending on the choice of the waveform approximant, we will obtain different likelihood estimates and subsequently different evidence factors $\mathscr{Z}$. In fact, the evidence is a useful diagnostic when (i) comparing two competing models, referred to as *model selection*, or (ii) inferring whether provided data stream actually contains a GW signal or is pure noise. In the latter case, we denote the noise evidence by $\mathscr{Z}_N$ and the signal evidence by $\mathscr{Z}_S$, where

$$\mathscr{Z}_N = \mathscr{L}(d|0), \tag{3.32}$$

$$\mathscr{Z}_S = \int \mathrm{d}\theta \mathscr{L}(d|\theta)\pi(\theta). \tag{3.33}$$

Computing the ratio between the two evidence factors gives us the *Bayes factor*

$$\mathscr{B}^S_N := \frac{\mathscr{Z}_S}{\mathscr{Z}_N}. \tag{3.34}$$

In reality we often work with the log-Bayes factor, $\log \mathscr{B}^{\mathrm{S}}_{\mathrm{N}}$. A positive (negative) log-Bayes factor would indicate that the signal (noise) model is preferred. In model selection, the correct statistic for comparison to use is the *odds*

$$\mathscr{O}^Y_X = \frac{\mathscr{Z}_X}{\mathscr{Z}_Y}\frac{\pi_X}{\pi_Y}, \tag{3.35}$$

where X and Y denote two competing models and π_X/π_Y encode the prior odds. Typically, the relative likelihood of models A and B is taken to be equal and so the prior odds are set to unity, therefore reducing the odds in Eq. (3.35) to the Bayes factor in Eq. (3.34).

3.3.2 Parameter Estimation

The problem of computing the posterior, $p(\theta|d)$ – i.e. the probability density of source parameters θ given some data stream – is an inverse problem. In the context of GWs, this is a high-dimensional and computationally complex problem – recall that our typical BBH signal in Section 3.3.1 was described by 15 parameters. A typical way to estimate $p(\theta|d)$ is to use stochastic samplers, either utilising *Markov chain Monte Carlo sampling* (MCMC) [194]

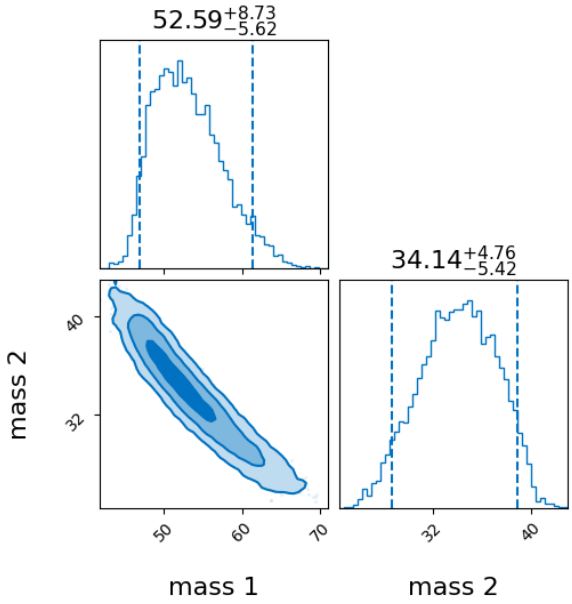


Fig. 3.3.2 Example of individual mass posterior distributions from a parameter estimation run in BILBY.

or *nested sampling* [195] (see Refs. [196, 197] for detailed reviews). Parameter estimation pipelines widely used in the analysis of GW events from LIGO-Virgo-KAGRA observing runs include LALINFERENCE [198] and BILBY [199].

A typical result of a parameter estimation pipeline is presented in the form of a *corner* plot in Fig. 3.3.2, where for simplicity we focus only on the mass parameters. The plot illustrates the posterior distributions for the two component masses m_1 and m_2, where the skewness of the posterior contours relative to the $m_1 = m_2$ line underlines that an unequal-mass system is inferred. The central values presented on the plot correspond to median values, whilst the dashed lines represent 90% *credible intervals*, defined as regions of the parameter space containing 90% of the posterior probability. Formally, symmetric credible intervals are constructed from a cumulative distribution function $P(x) = \int \mathrm{d}x' p(x')$ and the X% credible interval is defined as the set of X for which the following inequalities hold,

$$\frac{1}{2}\left(1 - \frac{X}{100}\right) < P(X) < \frac{1}{2}\left(1 + \frac{X}{100}\right). \tag{3.36}$$

MCMC

The goal of MCMC is to draw independent samples from the posterior distribution by using *particles* or *walkers* undergoing a random walk through the parameter space. Once a number

N of walkers is randomly initialised from the prior $\pi(\theta)$, the samples are produced iteratively so that the current sample, θ, determines the next sample, θ'. Such an iteration when repeated many times produces a Markov chain. One of the most widely used algorithms for generating the Markov chain is the Metropolis–Hastings algorithm [200], which utilises a *proposal distribution* for generating a proposed sample θ' and some criterion for either accepting or rejecting the proposed moves. The algorithm terminates after some user-specifiable condition is met, typically corresponding to some number of samples representative enough of the posterior distribution. In the context of GW analysis, we sample from $\mathscr{L}(d|\theta)\pi(\theta)$, which is proportional to the posterior. Therefore, in most classical MCMC implementations, we are *only* able to draw samples proportional to the posterior; otherwise, the computation of the normalisation factor, the evidence, would be required. Having said that, there are some proposed methods of computing the evidence within the MCMC algorithm (see Refs. [201, 202]).

Whilst MCMC is a powerful tool for approximating high-dimensional posterior distributions, there are some subtleties that should be taken into account:

- The early-time behaviour of the walkers depends on the way they are initialised, especially if the walkers have been initialised in the regions of low-probability density. A *burn-in*, when a certain number of initial samples are not included, is required to ensure that the walkers have settled into a stable state.

- The set of nearby samples in the Markov chain are correlated, often leading to misleading estimation of the posterior width. In order to reflect the posterior accurately, we usually select samples separated by the autocorrelation length of the chain, a method we refer to as *thinning*.

- Sometimes MCMC algorithms may fail to approximate very complex multimodal distributions, where high probability regions are separated by very low probabilities. Initialising the sampling with many walkers usually allows us to circumvent this problem.

Examples of implementations of MCMC algorithms include EMCEE [203], BILBY-MCMC [204] and PTEMCEE [205].

Nested sampling

Unlike MCMC algorithms, nested sampling calculates the evidence. The calculation of the evidence relies on the fact that its multidimensional integral in Eq. (3.26) can be transformed into a 1D integral over the prior volume. Computation of the evidence then becomes possible

with the use of standard numerical methods, like the trapezium rule. The algorithm starts by first drawing a number of points from the prior, n_{live}, in a similar manner as we initialised our 'walkers' in the MCMC method, and evaluating the likelihood at those points. The points with the lowest likelihood value are removed and added to a set of so-called dead points, which are then replaced with new samples of higher likelihood. Repetition of these steps therefore leads to a sequence of nested (or possibly disjoint) samples of increasing likelihood. The process is repeated until a termination criterion, e.g. until the evidence estimate does not change by more than ~ 0.1 (or some other plausible threshold). The posterior samples are then produced by resampling the sets of dead and current live points and weighing the samples used to compute the evidence by their posterior probabilities.

We list some of the limitations of nested sampling below:

- The computation of the evidence is sensitive to the size of the prior volume that we need to integrate over. Therefore, broad or poorly informed priors can significantly increase the run time of the algorithm.

- In classical implementations of nested samplers, the sampling is *static*, i.e the number of live point, n_{live} is usually constant. Increasing n_{live} on the one hand improves the accuracy of the evidence and posterior estimations, yet on the other hand significantly slows down the sampling. The workaround is the so-called *dynamic nested sampling*, where the number of live points is allowed to vary during the run-time [206].

Examples of nested samplers used in GW parameter estimation include DYNESTY [207], CPNEST [208] and MULTINEST [209].

Other approaches

In the era of rapid developments in machine learning (ML) techniques, ML has also found its place in GW analysis. Samplers based on normalising flows [210–212] have been introduced to speed up the sampling provided by conventional samplers, using solely MCMC or nested sampling, see e.g. NESSAI [213, 214] and FLOWMC [215]. In the algorithms described in the previous Sections you may have noticed that at each position of either the walkers or the live points, evaluation of the likelihood is required. In the context of GW analysis, $\mathcal{O}(10^4)$ samples would entail millions of evaluations of the likelihood function. This is often computationally challenging, and depending on the signal duration and the waveform model $\mu(\theta)$ of interest, the typical inference time can take up to a month, if not more. ML algorithms relaxing the need of Gaussian likelihood evaluations therefore demonstrate superiority to standard techniques. Several independent parameter estimation pipelines have

been developed to facilitate rapid and real time parameter estimation of GW signals; examples include DINGO [216], approximating the posterior distribution by means of normalising flows, and PEREGRINE [217], allowing for simulation-based inference where the Bayes theorem is reduced to a classification problem.

3.4 Numerical relativity injections

Say you have simulated your favourite binary system and have extracted the GW strain as per our discussion in Section 2.7.5. You therefore now have the multipoles $h^{lm}_{+/\times}(t)$ extracted at different radii, $R_{\rm ext}$. How can we inject a numerically simulated signal into the GW detector and register its response? A comprehensive guide on NR injections can be found in Ref. [2] (also see Ref. [218]). However, here we review a few steps in more detail and explain how the preparation of NR data can be done via the LIGO Scientific Collaboration Algorithm Library (LALSuite).

3.4.1 Preparing your NR data

The first, perhaps the most trivial step, is to appropriately scale your data with the total mass ($M = m_1 + m_2$, where m_1 and m_2 are the individual mass components)[5] so that it is independent of the mass scale, and cut the junk radiation at the beginning of the waveform. It will be convenient to work with the amplitude $\mathscr{A}$ and phase ϕ of the strain where

$$R_{\rm ext}h^{lm}_{+}(t) - iR_{\rm ext}h^{lm}_{\times}(t) = \mathscr{A}^{lm}(t)e^{i\phi^{lm}(t)} := H_{lm}(t), \tag{3.37}$$

where one chooses an extraction radius with sufficiently small error as, for example, determined in Section 4.A.1. Be aware that higher harmonic modes may be more strongly contaminated with numerical noise and/or errors from reflections off the boundaries and as such they must be checked before performing the injections.

3.4.2 Disentangling the frames

Most data analysis pipelines rely on the strain given in a *wave frame*, which establishes the relationship between the binary and the observer. The goal of this Section will be to define this wave frame and relate it to the NR frame, which is specific to our simulations. This means that when we extract the strain from our NR simulations, we will need to perform appropriate transformations on it in order to have the data ready to be used in the wave frame.

[5] One may also use the ADM mass.

The process is two-stage and involves: (i) establishing the relation between the wave frame and the properties of the binary at a reference time, and (ii) devising the relation between the NR frame and the wave frame.

The NR frame is usually just a generic coordinate system, with Cartesian basis-vectors

$$\hat{\boldsymbol{x}}, \hat{\boldsymbol{y}}, \hat{\boldsymbol{z}}. \tag{3.38}$$

As, we extract the strain on spherical shells, the Cartesian basis translates to the spherical basis-vectors $(\hat{\boldsymbol{r}}, \hat{\boldsymbol{\theta}}, \hat{\boldsymbol{\phi}})$, where $\hat{\boldsymbol{\theta}}$ and $\hat{\boldsymbol{\phi}}$ are the unit vectors of the polar and azimuthal directions respectively. Using this basis in the polarisation matrices definitions of Eq. (3.5) and Eq. (3.3), we find that the NR strain can be decomposed the following way

$$h_+(t) = \left(\hat{\boldsymbol{\theta}}_i \hat{\boldsymbol{\theta}}_j - \hat{\boldsymbol{\phi}}_i \hat{\boldsymbol{\phi}}_j\right) h^{ij}(t), \tag{3.39}$$

$$h_\times(t) = \left(\hat{\boldsymbol{\theta}}_i \hat{\boldsymbol{\phi}}_j + \hat{\boldsymbol{\phi}}_i \hat{\boldsymbol{\theta}}_j\right) h^{ij}(t). \tag{3.40}$$

The wave frame on the other hand consists of the basis vectors $(\boldsymbol{X}, \boldsymbol{Y}, \boldsymbol{Z})$ and relies on defining several quantities[6] describing the binary system (cf. also Fig. 3.4.1):

1. $\hat{\boldsymbol{n}}_{12}$ – a unit vector pointing from the second body to the first one in the binary,
2. $\hat{\boldsymbol{L}}$ – unit direction of the orbital angular momentum of the binary,
3. ι – the angle between the line of sight and the orbital angular momentum.

As the binary is dynamically changing, some of the above quantities will be defined only at some particular reference time-point, which we denote by $\overset{(ref)}{=}$. It then can be shown that the wave frame basis in terms of the binary quantities is given by [2]

$$\boldsymbol{X} \overset{(ref)}{=} -\cos\iota \hat{\boldsymbol{L}} \times \hat{\boldsymbol{n}}_{12} + \sin\iota \hat{\boldsymbol{L}}, \tag{3.41}$$

$$\boldsymbol{Y} \overset{(ref)}{=} \hat{\boldsymbol{n}}_{12}, \tag{3.42}$$

$$\boldsymbol{Z} \overset{(ref)}{=} \sin\iota \hat{\boldsymbol{L}} \times \hat{\boldsymbol{n}}_{12} + \cos\iota \hat{\boldsymbol{L}}, \tag{3.43}$$

where quantities like $\hat{\boldsymbol{L}}$ and $\hat{\boldsymbol{n}}_{12}$ are extracted directly from NR simulations. From Fig. 3.4.1, we can clearly see that $\boldsymbol{Z} = \hat{\boldsymbol{r}}$ is the direction of the propagation, whilst the remaining NR

[6] Note that an additional angle, Φ, between the line of ascending node (the intersection of the orbital plane with the XY axes) and $\hat{n}_{12}$, is often introduced. This angle denotes the reference orbital phase, and for simplicity in this work we take it as $\Phi = 0$, meaning that the line of ascending node coincides with $\hat{n}_{12}$.

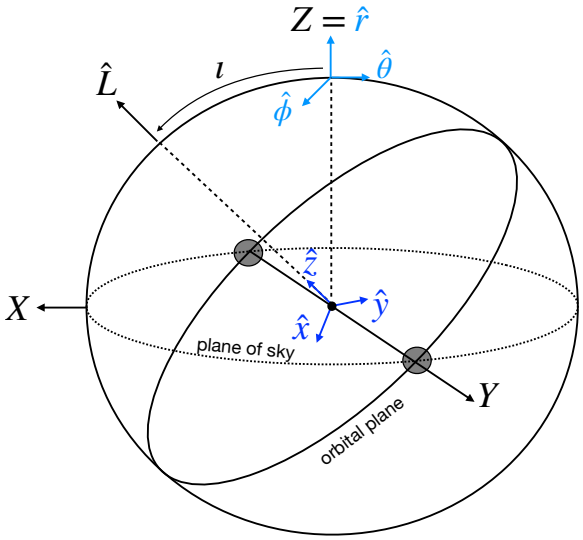


Fig. 3.4.1 Definition of the wave frame defined by the basis vectors $(\boldsymbol{X},\boldsymbol{Y},\boldsymbol{Z})$ and the NR frame $(\hat{\boldsymbol{x}},\hat{\boldsymbol{y}},\hat{\boldsymbol{z}})$ in Cartesian coordinates (dark blue) and $(\hat{\boldsymbol{r}},\hat{\boldsymbol{\theta}},\hat{\boldsymbol{\phi}})$ in spherical coordinates (light blue). Note that the spherical basis $(\hat{\boldsymbol{r}},\hat{\boldsymbol{\theta}},\hat{\boldsymbol{\phi}})$ is related to the $(\boldsymbol{\ell},\boldsymbol{m},\boldsymbol{k})$ basis we defined in Section 3.2.3 via the polarisation angle. The Figure is partly adapted from Ref. [2].

basis angles $(\hat{\boldsymbol{\theta}},\hat{\boldsymbol{\phi}})$ have to be rotated into $(\boldsymbol{X},\boldsymbol{Y})$ using[7]

$$\boldsymbol{X} = \cos\alpha\hat{\boldsymbol{\theta}} - \sin\alpha\hat{\boldsymbol{\phi}}, \tag{3.44}$$

$$\boldsymbol{Y} = \sin\alpha\hat{\boldsymbol{\theta}} + \cos\alpha\hat{\boldsymbol{\phi}}, \tag{3.45}$$

where, by taking the product of Eq. (3.42) with $\hat{\boldsymbol{\theta}}$, the angle α can be found via

$$\sin\alpha = \hat{\boldsymbol{n}}_{12}\cdot\hat{\boldsymbol{\theta}}. \tag{3.46}$$

As we obtain spherical data from our NR simulations, we need to convert them into strain by using spin-weighted spherical harmonics, ${}^{s}Y_{lm}$ with weight $s=-2$. In particular, given a source with total mass of $M_{\rm tot}$ and at luminosity distance d_L, the strain is given by

$$h_+ - ih_\times = \frac{M_{\rm tot}}{d_L}\sum_{l=2}^{\infty}\sum_{m=-l}^{l} H_{lm}(t)\,{}^{-2}Y_{lm}(\theta,\phi). \tag{3.47}$$

[7]Here angle α is equivalent to the polarisation angle ψ we discussed earlier in Section 3.2.3.

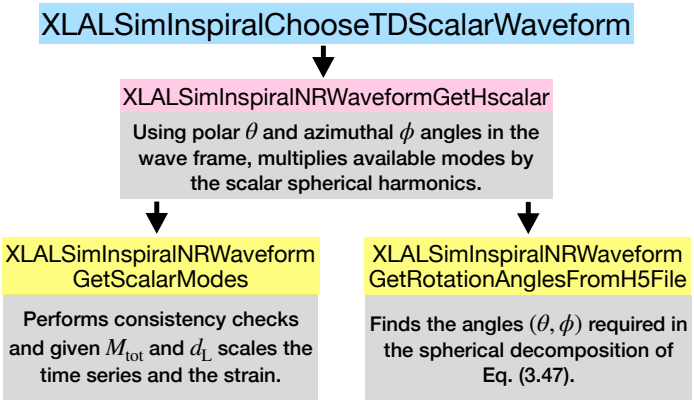


Fig. 3.4.2 Implementation of scalar polarisation reconstruction in LALSUITE. Similar approach can be taken for vector-x and vector-y polarisations.

Using Eq. (3.39)-(3.40), the strain polarisations in the wave frame are then found according to

$$h_{+}^{\rm W}(t) = \cos(2\alpha)h_{+}(t) - \sin(2\alpha)h_{\times}(t), \tag{3.48}$$

$$h_{\times}^{\rm W}(t) = \sin(2\alpha)h_{+}(t) + \cos(2\alpha)h_{\times}(t). \tag{3.49}$$

3.4.3 Using LALSUITE to transform NR data

If you are feeling brave enough, you can create your own programme translating the strain in the NR frame to the wave frame as per the prescription in Section 3.4.2. Alternatively, you can use built-in functions inside of LALSUITE. Whether you are injecting the conventional plus and cross polarisations or any additional polarisation content from a modified theory of gravity, the logic of using LALSUITE is the same.

For plus and cross polarisations one can directly call XLALSIMINSPIRALCHOOSETDWAVEFORM function, which (i) performs the rotation of the NR frame into the wave frame (ii) scales the strain as per Eq. (3.47) and the time series by $tM_{\rm tot}$. However, for any additional, beyond-GR polarisations, the functions have to be tailored to your needs. As this is what we in fact end up doing for the purposes of the next Chapter 4, here we briefly outline the steps required to handle scalar polarisation reconstruction.

The task of reconstructing the scalar polarised modes simplifies significantly, as in the absence of plus and cross polarisations, we no longer need to apply a rotation of the strain as in Eq. (3.47) and this directly follows from the polarisation matrices' definition of the breathing and/or longitudinal modes in Eqs. (3.9)-(3.10). Therefore, our only remaining task is the scaling of the strain with $M_{\rm tot}$ and d_L, and multiplication by the spin-weighted spherical

harmonics as in Eq. (3.47), but with the harmonics being now of spin weight $s = 0$ nature. In Fig. 3.4.2 we show a summary of our implementation.

Chapter 4

Binary black hole mergers in Einstein-scalar-Gauss-Bonnet gravity

The content presented in this Chapter contains material that appears in the co-authored publication Ref. [219] with M.Agathos and J.L.Ripley. I have implemented the Einstein-scalar-Gauss-Bonnet evolution in the decoupling limit and performed all of the numerical relativity and data analysis runs. The goals, the content of the study and the interpretation of the results were devised in collaboration with the co-authors of the paper.

4.1 Introduction

General relativity (GR) has passed all observational tests to date [220, 221] and so far observations of gravitational wave signals in LIGO [222] and Virgo [223] data have been consistent with its predictions [15–19, 80]. Nevertheless, there has been an increasing amount of work that tests the predictions of non-GR theories of gravity (*modified theories of gravity*) with gravitational wave measurements of binary black hole (BH) and neutron star (NS) mergers [224–228]. These *model-dependent* tests of GR have allowed for remarkably strong constraints to be placed on a wide array of modified gravity theories.

Here we focus on the gravitational wave implications for black hole binaries in Einstein scalar Gauss-Bonnet (EsGB) gravity. EsGB gravity can be motivated from effective field theory (EFT)-styled arguments [59, 229], and has been shown to appear in the low-energy limits of heterotic string theories [230–232]. What makes EsGB interesting from a phenomenological point of view is that black holes in the theory can have scalar hair [233, 234] (for a review, see Ref. [235]). Because of this, binary black hole (BBH) systems can emit scalar radiation [236]. From a theoretical point of view, EsGB gravity is a Horndeski the-

ory [237], and as such, has second order equations of motion, circumventing the Ostrogradsky instability. In addition, the theory has been shown to have a well-posed initial value problem in the weak coupling limit [229] which allows for numerical relativity simulations of the full theory [78, 92, 238, 239]. [1]

In this Chapter, we focus on the leading order effects of EsGB on the gravitational waveform emitted during the ringdown stage of BBH mergers. It is expected that the strongest constraints on most modified theories of gravity will come from the inspiral, due to the cumulative dephasing of the signal from the GR predicted waveform, over a large number of observed cycles [85, 243]. Nevertheless, correctly modeling the ringdown is crucial to understanding the properties of the remnant black hole formed from binary coalescence, and to performing consistency tests with theory-specific estimates of the final black hole properties inferred from the inspiral and merger [244]. While the dephasing of the inspiral can be a common feature of many different theories of modified gravity and the theory-specific details can be difficult to model at high accuracy (see Ref. [226, 245] for perturbative approaches in EsGB), a spectroscopic analysis of the ringdown signal may reveal characteristic features that will help narrow down the origin of an observed deviation from GR.

Working in the decoupling limit of EsGB gravity, we extract first-order tensorial and scalar waveforms and focus on the ringdown portion of the signal. We study the quasi-normal mode (QNM) spectrum of the resulting scalar and tensor waveforms and numerically compute the amplitudes of the excited modes. Unlike most previous studies on EsGB gravity, we study the impact of the radiated scalar field on the *scalar polarisation* measured by the gravitational wave detectors through the presence of a non-minimal scalar field coupling to the metric tensor in the matter field action (without such a coupling, gravitational waves would not have a scalar polarisation component in EsGB gravity [246]). While there has been work on model-independent tests of the polarisation of gravitational waveforms [185, 186, 247, 248], we present the first model-dependent analysis of the feasibility of measuring a non-tensor polarisation from black hole binaries with current and future gravitational wave detectors (we note though that Ref. [249] considers model-dependent tests with stochastic gravitational wave backgrounds). Ultimately, we find the scalar polarisation – given current constraints on the EsGB gravity and weak-field tests of general relativity – is unobservable with current gravitational wave detectors, although there is a higher chance that it could be measured with next-generation detectors.

[1] It is, however, not guaranteed that dynamical spacetimes will preserve the weak coupling of their initial data during their evolution, and local pathologies may form [240–242].

This Chapter is organized as follows. In Section 4.2.1 we present the theoretical framework of EsGB gravity in the Einstein frame. In Section 4.2.2, we review how to extract the polarisation content of gravitational waves (GWs), and show how the conformal scalar field coupling can give rise to a scalar polarisation in gravitational waves. Next, we review and justify the application of the decoupling limit for solving the equations of motion of EsGB gravity in Section 4.2.3. For reference, we present a summary of current observational and theoretical constraints on the couplings of the theory we consider in Section 4.2.4. In Sections 4.3.1–4.3.3 we review our numerical set-up and the diagnostics we use to extract physical quantities from our simulations. In Section 4.3.4, we present the scalar waveforms measured from our numerical relativity (NR) simulations. We analyse the QNM spectrum of our resulting scalar waveforms in Section 4.4 and compute their signal-to-noise ratio (SNR) in Section 4.5.1 to assess the measurability of the scalar signal. We then move on to a full Bayesian data analysis of our simulated signals by performing NR injections of the scalar waveform into simulated current and future-generation detector noise using a tailored ringdown pipeline in Section 4.6. We finish with concluding remarks in Section 4.7.

4.2 Theoretical background

4.2.1 Formulation of 4-derivative scalar-tensor (4∂ST) gravity

The general action for Einstein scalar Gauss-Bonnet gravity is

$$S = \frac{c^4}{16\pi G}\int \mathrm{d}^4x\sqrt{-g}\left[R + X - V(\varphi) + \bar{\alpha}(\varphi)X^2 + \alpha_{\rm GB}\beta(\varphi)\mathscr{R}_{GB}\right] + S_{\rm M}[\psi_{\rm M}, A^2(\varphi)g_{\mu\nu}], \tag{4.1}$$

where $V(\varphi)$ is the scalar field potential, $\alpha_{\rm GB}$ is a coupling constant, $\bar{\alpha}(\varphi)$, $\beta(\varphi)$ are arbitrary coupling functions of the scalar field, $X \equiv -\frac{1}{2}(\nabla\varphi)^2$, $S_{\rm M}$ is the action functional for the matter fields (which we denote schematically with $\psi_{\rm M}$), $A^2(\varphi)$ is the conformal coupling of matter to the metric, and $\mathscr{R}_{\rm GB}$ is the Gauss-Bonnet scalar

$$\mathscr{R}_{GB} \equiv \frac{1}{4}\varepsilon^{\mu\nu\alpha\beta}\varepsilon^{\rho\sigma\gamma\delta}R_{\mu\nu\rho\sigma}R_{\alpha\beta\gamma\delta}. \tag{4.2}$$

If $A \neq 1$, the scalar field couples directly to matter. This coupling generally leads to violations of the strong-equivalence principle (barring the presence of *screening* mechanisms [250]), as the effective gravitational field felt by matter fields will depend on the value of the scalar field φ. Weak field tests of gravity have strongly constrained violations of the strong-equivalence

principle, which can be translated to constraints on the strength of the coupling A [220, 251]. In geometric units, the coupling parameter $\alpha_{\rm GB}$ has dimensions length squared, L^2. It is then natural to expect strong constraints on the scalar Gauss-Bonnet coupling will come from regions of high spacetime curvature [31, 85, 243].

In this work we examine a subset of theories for which $V = \bar{\alpha} = 0$. We assume the beyond-GR corrections give only relatively small deviations to the background GR solution. Therefore, we impose that $|\varphi|, |\alpha_{\rm GB}|, |\beta| \ll 1$ and to leading order we have

$$S = \frac{c^4}{16\pi G}\int \mathrm{d}^4x\sqrt{-g}\left[R - \frac{1}{2}(\nabla\varphi)^2 + \beta_0\varphi\mathscr{R}_{\rm GB}\right] + S_{\rm M}\left[\psi_{\rm M}, (1+a_0\varphi)\, g_{\mu\nu}\right], \tag{4.3}$$

where we have Taylor expanded β and A in φ, set $A(0) = 1, A'(0) \equiv a_0/2$, and $\beta_0 \equiv \alpha_{\rm GB}\beta'(0)$. We have discarded the term $\beta(0)$ as the Gauss-Bonnet scalar is a total derivative in four spacetime dimensions, so it does not contribute to the equations of motion.

4.2.2 Polarisation content

In alternative metric theories of gravity, there may exist up to six polarisations associated with additional degrees of freedom: tensorial (plus and cross), vector (x and y) and scalar (breathing and longitudinal) [165]. Because of their symmetries, the breathing and longitudinal modes are fully degenerate to networks of quadrupolar antennas [252], so we will refer to them jointly as the scalar polarisation. The scalar polarisation state is generally a mixture of the transverse breathing and longitudinal polarisations. In the massless limit, the longitudinal polarisation disappears, while the breathing one persists [253]. Since the scalar field we consider is massless, we only study the breathing polarisation in this work.

The six polarisation states are encoded in six "electric" components of the Riemann tensor, R_{i0j0} (i, j spatial), which can be written in terms of the following Newman-Penrose scalars [165]

$$\Psi_2 = \frac{1}{6}R_{z0z0}, \tag{4.4}$$

$$\Psi_3 = \frac{1}{2}\left(-R_{x0z0} + iR_{y0z0}\right), \tag{4.5}$$

$$\Psi_4 = R_{y0y0} - R_{x0x0} + 2iR_{x0y0}, \tag{4.6}$$

$$\Phi_{22} = -(R_{x0x0} + R_{y0y0}). \tag{4.7}$$

In Fig. 4.2.1 we illustrate the form of the different polarisation states. Perturbing the metric and scalar field, the Jordan frame metric $\hat{g}_{\mu\nu} = (1+a_0\varphi)g_{\mu\nu}$ that couples to the matter fields

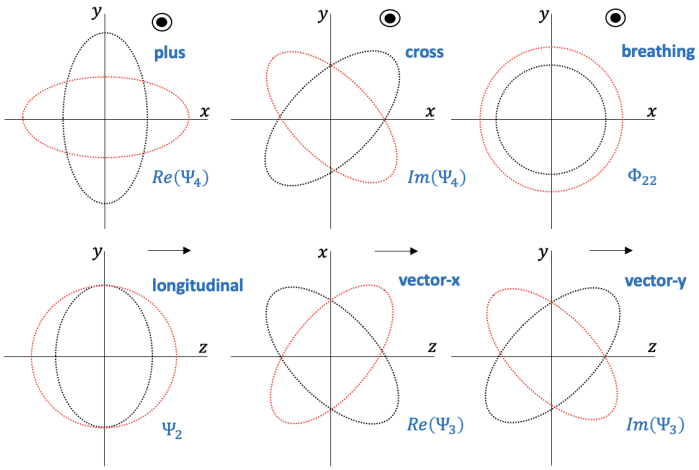


Fig. 4.2.1 The classification of the six polarisations encoded in the four Newman-Penrose scalars. The shapes represent displacement that each mode induces on a sphere of test particles. The wave is assumed to propagate in the z-direction indicated by the icons/arrows in the right corners.

(such as a gravitational wave detector) in the wave zone is

$$\hat{g}_{\mu\nu} = \eta_{\mu\nu} + h_{\mu\nu} + a_0 \eta_{\mu\nu} \varphi + \ldots, \tag{4.8}$$

where $\eta_{\mu\nu}$ is the Minkowski metric. The tensorial perturbation $h_{\mu\nu}$ gives the plus and cross polarisations, while the coupling constant a_0, along with a nonzero value of φ, gives a new scalar breathing-mode polarisation to gravitational waves[2] [249, 254].

4.2.3 Perturbative equations of motion

Unless otherwise stated, in this section we work in geometric units $G = c = 1$. Our discussion roughly follows that of Refs. [255, 256]. We start with the full equations of motion derived from the action (4.3)

$$G_{\mu\nu} = T_{\mu\nu} - \beta_0 C^{\rm GB}_{\mu\nu}, \tag{4.9}$$

$$\Box\varphi = -\beta_0 \mathscr{R}_{\rm GB}, \tag{4.10}$$

[2]We note that if $a_0 = 0$, then gravitational waves have no scalar polarisation in EsGB gravity [246].

where

$$T_{\mu\nu} = \nabla_\mu\varphi\nabla_\nu\varphi - \frac{1}{2}g_{\mu\nu}\nabla_\rho\varphi\nabla^\rho\varphi, \tag{4.11}$$

$$C^{\rm GB}_{\mu\nu} = 2g_{\rho(\mu}g_{\nu)\alpha}\varepsilon^{\kappa\alpha\tau\eta}\nabla_\lambda({}^*R^{\rho\lambda}{}_{\tau\eta}\nabla_\kappa\varphi). \tag{4.12}$$

Note that above ${}^*R^{\rho\lambda}{}_{\tau\eta}$ denotes the dual Riemann tensor defined via

$${}^*R^{\rho\lambda}{}_{\tau\eta} = \varepsilon^{\rho\lambda\mu\nu}R_{\mu\nu\lambda\tau}. \tag{4.13}$$

We expand the metric and the scalar field as

$$\varphi = \sum_{k=0}^{\infty}\frac{1}{k!}\delta^k\varphi^{(k)}, \tag{4.14}$$

$$g_{\mu\nu} = g^{(0)}_{\mu\nu} + \sum_{k=1}^{\infty}\frac{1}{k!}\delta^k h^{(k)}_{\mu\nu}, \tag{4.15}$$

where δ is a book-keeping parameter for our perturbative expansion. By considering the equations of motion order by order in δ, one finds that up to $\mathscr{O}(\delta)$ [256]

$$\varphi^{(0)} = 0, \qquad g^{(0)}_{\mu\nu} = g^{\rm GR}_{\mu\nu}, \tag{4.16}$$

$$\varphi^{(1)} = \varphi^{(1)}, \qquad h^{(1)}_{\mu\nu} = 0. \tag{4.17}$$

We note that the zeroth-order equations of motion are the Einstein field equations minimally coupled to a massless scalar field. The choice of $\varphi^{(0)} = 0$ in the zeroth order solution of Eq. (4.16) is therefore motivated by the fact that asymptotically flat black holes cannot carry scalar hair [257], which if initially present would be radiated away at late times, and that a cosmological value of φ for EsGB gravity has been constrained by measurements of the speed of gravitational waves [225, 258]. Using Eqs. (4.16) and (4.17), the equations of motion to $\mathscr{O}(\delta)$ reduce to

$$G^{(0)}_{\mu\nu} = 0, \tag{4.18}$$

$$\Box^{(0)}\varphi^{(1)} = -\mathscr{R}^{(0)}_{GB}\beta_0. \tag{4.19}$$

We note that there is no back-reaction of the scalar field on the background geometry, however at $\mathscr{O}(\delta^2)$ the metric will be corrected by the backreaction of the scalar field $\varphi^{(0)}$ on the spacetime [259, 260].

We reintroduce dimensions by choosing the characteristic length scale of the system to be L, and introduce a dimensionless coordinate $\hat{x} = Lx$. By redefining $x \to \hat{x}$, we acquire a factor of L^{-2} in front of the wave operator and a factor of L^{-4} in front of the Gauss-Bonnet scalar, leading to

$$\hat{\Box}^{(0)}\varphi^{(1)} = -\beta_0 L^{-2}\hat{\mathscr{R}}^{(0)}_{GB}. \tag{4.20}$$

We then may re-scale the scalar field

$$\varphi^{(1)} = \left(\frac{\beta_0}{L^2}\right)\hat{\varphi}, \tag{4.21}$$

so that

$$\hat{\Box}^{(0)}\hat{\varphi} = -\hat{\mathscr{R}}^{(0)}_{GB}. \tag{4.22}$$

This implies that a solution with a given β_0/L^2 parametrises a family of solutions with different L and β_0. Further, Eq. (4.21) naturally introduces the choice for the dimensionless parameter δ, that we use to parametrize the weak-coupling of our solutions. Since we are interested in binary black hole systems and the corrections become larger for smaller masses, we choose $L = m_1$, which is the mass of the smaller black hole in our binary black hole configuration. We then define

$$\delta \equiv \frac{\beta_0}{m_1^2} \ll 1. \tag{4.23}$$

By combining Eqs. (4.21) and (4.8), we note that the scalar GW amplitude is then controlled by the couplings of our theory via $a_0\beta_0/m_1^2$. The dimensionless EsGB parameter δ plays an important role in EsGB gravity. Depending on the coupling β_0 chosen in the theory, a stationary BH solution of mass m_1 cannot exist above a certain threshold $\max\left(\beta_0/m_1^2\right) = \delta_{\rm thr} > \delta$. This threshold is controlled by the regularity of the scalar field on the horizon and the finite radius singularity being hidden behind it for sufficiently small β_0. If the coupling becomes too large, a naked singularity emerges from within the horizon in solutions to the full theory. For instance, in the spherically-symmetric case of shift-symmetric EsGB, $\delta_{\rm thr} \sim 0.3$ [234]. Hyperbolicity constraints on the theory suggest a somewhat more stringent bound of $\delta_{\rm thr} \sim 0.2$ [261]. In Fig. 4.2.2, we outline schematically the range of validity of our EsGB theory in the parameter space of $a_0 \times \beta_0/m_1^2$, taking into consideration the observational constraints on a_0 from Table 4.2.1 and theoretical constraints on β_0/m_1^2. The contour lines therefore represent possible scalar GW amplitude values.

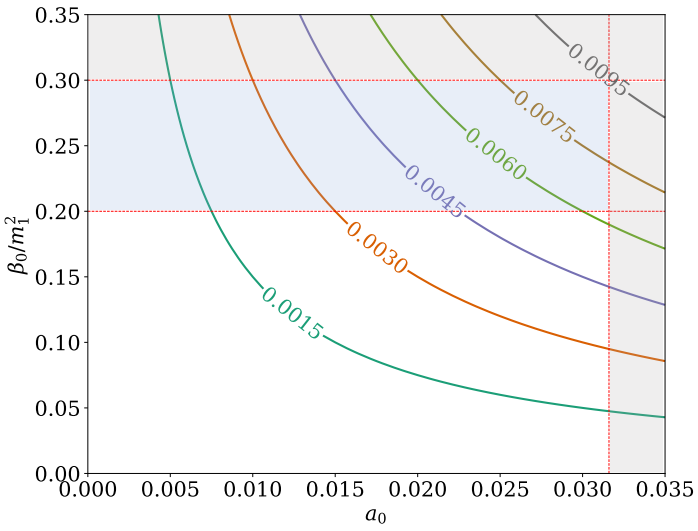


Fig. 4.2.2 Range of validity of our EsGB theory, taking into account theoretical constraints on the dimensionless coupling β_0/m_1^2 and experimental constraint on the conformal factor a_0. The vertical dashed line separates the maximally allowed value of a_0 (to the left) from the observationally ruled out values (shaded grey region to the right). The two horizontal lines indicate the two theoretical constraints on the value of β_0/m_1^2. The upper line at $\beta_0/m_1^2 = 0.3$ represents the maximum coupling allowed before naked singularities appear in static solutions to the theory, while the line at $\beta_0/m_1^2 = 0.2$ represents the upper bound before the theory suffers a breakdown in hyperbolicity. See Sections 4.2.3 and 4.2.4 for more discussion.

4.2.4 Current observational constraints

Here we discuss current experimental tests and observational bounds on the parameters a_0 and β_0. The EsGB coupling β_0 has been most strongly constrained through the analysis of inspiral and merger of binary systems of compact objects using GW data released by the LIGO-Virgo-KAGRA (LVK) Collaboration [226]. Weak-field tests of GR also place a constraint on the coupling, but do not constrain it as significantly [262], as the Gauss-Bonnet coupling does not lead to much scalarisation of stellar solutions [236]. This being said, as we are considering $a_0 \neq 0$, stars can scalarise in the theory we consider. In this work, we use the first constraint on a_0, obtained from the Viking relativity experiment on verification of signal retardation by solar gravity [263][3], $a_0^2 \lesssim 10^{-3}$. Table 4.2.1 references the studies constraining

[3]We note however that the most stringent constraint of $a_0^2 \lesssim 10^{-5}$ is known to be from the Cassini measurements of the Shapiro time delay [220, 264]. Here we use a weaker constraint from the Viking experiment to see how well in principle the scalar polarisation could be measured by present GW detectors.

Coupling $\sqrt{\beta_0}$		
Study	**References**	**Constraint**
Solar system constraints	[262]	$\mathcal{O}(10^7)$ km
GW150914 ppE	[266]	$\lesssim 72.85$ km
EsGB constraints from LIGO/Virgo events and ParSpec formalism	[267]	$\lesssim 35$ km
EsGB constraints from EOB waveform model and ParSpec formalism	[268]	$\lesssim 35$ km
X-ray binary orbital decay	[269]	$\lesssim 14.1$ km
LIGO SNR 30 detections (projection)	[270]	$\mathcal{O}(1-10)$ km
Second order EdGB simulations for GW150914	[259]	$\lesssim 15.6$ km
Compact star stability	[271]	$\lesssim 7.6$ km
First order EdGB scalar simulations for GW151226	[272]	$\lesssim 3.8$ km
EsGB constraints from BHBH GW events	[227]	$\lesssim 1.7$ km
EsGB constraints from BHNS GW events (GW200105, GW200115 and GW190814)	[226]	$\lesssim 1.18$ km
Coupling a_0		
Viking relativity experiment on signal retardation	[263, 273]	$\sqrt{10^{-3}}$
VBLI measurement of solar gravitational deflection	[274]	$\sqrt{10^{-4}}$
Cassini Shapiro time delay	[220, 264]	$\sqrt{10^{-5}}$
Theoretical constraints on β_0/m_1^2		
Shift-symmetric EsGB in spherical symmetry	[234]	$\lesssim 0.3$
Scalarised black holes in the full dynamical EdGB gravity	[261]	$\lesssim 0.2$

Table 4.2.1 Summary of current constraints on the EsGB coupling parameter β_0, the dimensionless parameter β_0/m_1^2 and the conformal coupling a_0. Our conventions for β_0 and a_0 are given in Eq. (4.3).

the EsGB coupling[4] β_0 and the conformal coupling a_0. We additionally summarize theoretical constraints on the dimensionless coupling β_0/m_1^2 as discussed in Section 4.2.3.

4.3 Numerical set-up

4.3.1 Numerical Relativity code and evolution equations

Here we describe our numerical set-up to solve Eqs. (4.18)–(4.19). For our simulations, we use a modified version of GRCHOMBO [130, 275, 276]. The metric and the scalar field are evolved with the method of lines using fourth order finite difference stencils and Runge Kutta time integration. We use the covariant and conformal Z4 (CCZ4) formulation [116] with the moving puncture gauge [89, 90] for evolving the Einstein equations (4.18) (cf. Sections 2.5

[4] If one assumes that both objects in GW190814 are BHs, then an even more stringent constraint on the EsGB coupling can be found [265]. However, in this work we take a conservative approach, by quoting the constraints from GW190814 that assume the secondary object is a neutron star.

and 2.4). The evolution equations for the scalar field (4.19) read

$$\partial_t \varphi = \alpha\Pi + \beta^i \partial_i \varphi, \tag{4.24}$$

$$\begin{aligned}\partial_t \Pi &= \alpha K \Pi + \beta^i \partial_i \Pi \\ &\quad + \tilde{\gamma}^{km}\left(\chi\alpha\partial_k\partial_m\varphi + \chi\partial_m\alpha\partial_k\varphi - \frac{1}{2}\alpha\partial_m\chi\partial_k\varphi\right) \\ &\quad - \chi\alpha\tilde{\gamma}^{jj}\tilde{\Gamma}^k_{ij}\partial_k\varphi + \alpha\left(\beta_0\mathscr{R}_{\rm GB}\right),\end{aligned} \tag{4.25}$$

where $\Pi \equiv 1/\alpha(\partial_t\varphi - \beta^m\partial_m\varphi)$, α is the lapse function, β^i is the shift vector, $\tilde{\gamma}_{ij} \equiv \chi\gamma_{ij}$ is the conformally re-scaled metric constituent of the conformal factor $\chi = \det(\gamma_{ij})^{-1/3}$ and physical spatial metric γ_{ij}. We rewrite the Gauss-Bonnet scalar in terms of the gravito-electric, E_{ij}, and gravito-magnetic, B_{ij}, counterparts [256]

$$\mathscr{R}^{GB} = 8(E^{kl}E_{kl} - B_{kl}B^{kl}), \tag{4.26}$$

which in CCZ4 variables take the form of [276]

$$\begin{aligned}E_{ij} &= \left[{}^{(3)}R_{ij} - K^s{}_i K_{js} + K_{ij}(K-\Theta) + D_{(i}\Theta_{j)}\right]^{TF}, \\ B_{kl} &= \varepsilon_{ks(i}D^s K_{j)}{}^k.\end{aligned} \tag{4.27}$$

Here ${}^{(3)}R_{ij}$ is the 3D Ricci tensor, K_{ij} is the extrinsic curvature, $\Theta = -n_\mu Z^\mu$ is the projection of the CCZ4 vector Z^μ onto the time-like unit normal n^μ, $[..]^{\rm TF}$ denotes the trace-free part and D_i is the covariant derivative compatible with the physical metric γ_{ij}. In the case of $\Theta = 0$, we recover the Baumgarte-Shapiro-Shibata-Nakamura-Oohara-Kojima (BSSNOK) formulation [111, 112, 277].

4.3.2 Grid setup and initial data

For the results presented in this Chapter we set up a computational domain of size $L = 1024M$, where $M = m_1 + m_2$ is the sum of the individual mass components. We use a grid spacing of $\Delta x = 2M$ in the outermost refinement level with 8 additional refinement levels. In this set-up we roughly have 64 points covering the smallest BH in the most asymmetric run (mass ratio 1:2). At the outer boundary, we use Sommerfeld boundary conditions and we take advantage of the bitant symmetry to evolve only half of the grid. We estimate the discretisation error for the amplitudes of Ψ_4 and φ to be $\lesssim 2\%$ and for the phase of Ψ_4 to be $\lesssim 0.15$ radians. We further estimate the finite radius extraction error to be $\lesssim 2\%$ and thus a total error budget

Run	q	m_1	m_2	$\mathbf{P}_1$	$\mathbf{P}_2$	$M_{\rm fin}$	$j_{\rm fin}$	$j_{\rm fin}/M_{\rm fin}$
BBH-11	1	0.5	0.5	(-0.0013 -0.11 0.0)	(0.0013 0.11 0.0)	0.9511	0.69	0.7255
BBH-23	2/3	0.4	0.6	(-0.0012 -0.108 0.0)	(0.0012 0.108 0.0)	0.9549	0.67	0.7016
BBH-12	1/2	0.33	0.67	(-0.0011 -0.1001 0.0)	(0.0011 0.1001 0.0)	0.9611	0.62	0.6451

Table 4.3.1 Two puncture initial data used for three binary BH configurations considered in this Chapter. Here $M_{\rm fin}$ and $j_{\rm fin}$ denote the final mass and final spin of the remnant BHs respectively, which were calculated from balance arguments given in Eqs. (4.30) and (4.31). Assuming the validity of the balance arguments, we estimate 0.01% error in the final mass and 0.05% error in the final spin when compared to their Richardson-extrapolated values. In Appendix 4.A.2 we present convergence plots for the radiated energy and angular momentum.

of $\lesssim 4\%$. See Figs. 4.A.1–4.A.3 of Appendix 4.A.1 for a quantitative illustration of the convergence of the code.

For our initial data, we consider two non-spinning black holes with initial masses m_1 and m_2 (we assume $m_2 > m_1$), initial linear momenta $\mathbf{P}_1$ and $\mathbf{P}_2$ and initial separation D. We prescribe quasi-circular initial data for a black hole binary by using puncture initial data [125] of Bowen-York [107] type provided by the spectral initial data solver TwoPunctures [126, 133] (cf. also Section 2.6.2).

We have investigated the effects of different initial separations (as well as initial momenta) on the eccentricity and found that $D = 8M$ (resulting in 4 orbits) gave us an eccentricity estimator of no more than 0.012 for all of the configurations considered here (we used Eq. (20) of Ref. [278] to calculate the eccentricity).

The initial data for the scalar field is chosen to be $\varphi = 0$ and $\partial_t \varphi = 0$. The authors in Ref. [256] found that using an initially vanishing scalar or superposing two hairy solutions gave indistinguishable scalar waveforms after sufficiently long evolution (see Fig. 4 of Ref. [256]). Moreover, this choice of initial data solves the exact constraint equations of EsGB gravity [92, 239]. We therefore do not investigate any other forms of initial data for the scalar field. We further pick three configurations for black holes of different mass ratios $q = m_1/m_2$, $(q \leq 1)$ summarized in Table 4.3.1.

4.3.3 Extraction of physical quantities

To order $\mathscr{O}(\delta)$, the metric sector of our spacetime is determined by the Einstein equations of GR (see Eq. (4.18)), so that the gravitational waveform, h_+ and $h_\times$, will be no different from GR. To calculate gravitational radiation we use the Newman-Penrose formalism [279, 280], and determine the outgoing gravitational radiation by computing the complex scalar Ψ_4. By interpolating the real and imaginary parts of Ψ_4 onto a sphere of fixed radius $R_{\rm ext} = 110M$, we

decompose them in terms of spin-weighted spherical harmonics Y^s_{lm} with $s=-2$ [281, 282]

$$\Psi_{4,lm}(t,R)=\int_{S^2}\Psi_4(t,R,\theta,\phi)^{-2}Y^*_{lm}(\theta,\phi)\mathrm{d}\Omega, \tag{4.28}$$

where $\mathrm{d}\Omega=\sin\theta\mathrm{d}\theta\mathrm{d}\phi$. By a similar decomposition into spherical harmonics Y_{lm} and integrating over the sphere, we construct the scalar waveform

$$\varphi_{lm}(t,R)=\int_{S^2}\varphi(t,R,\theta,\phi)Y^*_{lm}(\theta,\phi)\mathrm{d}\Omega. \tag{4.29}$$

In what follows, we use the subscript "rad" to denote quantities calculated from the start of our simulation, which includes spurious "junk" radiation. Otherwise, we consider quantities from $t=R_{\rm ext}+50M$. The mass and spin of the final BH are estimated from balance arguments [283]

$$M_{\rm fin}=M_{\rm ADM}-E^{\rm GW}_{\rm rad}, \tag{4.30}$$

$$j_{\rm fin}=\frac{L-J^z_{\rm rad}}{M^2_{\rm fin}}, \tag{4.31}$$

where $E^{\rm GW}_{\rm rad}$ denotes the total radiated energy of GWs, $J^z_{\rm rad}$ is the radiated angular momentum in the z-direction (by symmetry) and $L=P_yD$. In the above balance arguments the radiated energy and angular momentum are determined through [284, 285]

$$E^{\rm GW}_{\rm rad}(t)=\lim_{r\to\infty}\frac{r^2}{16\pi}\int_{t_0}^{t}\mathrm{d}t'\oint_{S^2}\mathrm{d}\Omega\left|\int_{-\infty}^{t'}dt''\Psi_4\right|^2, \tag{4.32}$$

$$\mathbf{J}_{\rm rad}(t)=-\lim_{r\to\infty}\frac{r^2}{16\pi}\mathrm{Re}\left\{\int_{\rm t_0}^{\rm t'}\mathrm{dt}'\left[\oint_{\rm S^2}\left(\int_{-\infty}^{\rm t'}\mathrm{dt}''\Psi_4^*\right)\mathbf{J}\left(\int_{-\infty}^{\rm t'}\mathrm{dt}''\int_{-\infty}^{\rm t''}\mathrm{dt}'''\Psi_4\right)\mathrm{d}\Omega\right]\right\}, \tag{4.33}$$

where $\mathbf{J}$ is the angular momentum operator for spin weight $s=-2$

$$\mathbf{J}=\left(\mathrm{Re}\mathbf{J}_+,\mathrm{Im}\mathbf{J}_+,\frac{\partial}{\partial\phi}\right), \tag{4.34}$$

$$\mathbf{J}_+=\mathrm{e}^{\mathrm{i}\phi}\left(\mathrm{i}\frac{\partial}{\partial\theta}-\cot\theta\frac{\partial}{\partial\phi}+2\mathrm{icosec}\theta\right). \tag{4.35}$$

Apart from tensor energy, we expect some of the scalar field energy to be emitted too. Since the scalar field is of order $\varphi\sim\delta$, the radiated energy must be of order $E^\varphi\sim\delta^2$. The

energy flux of the scalar field through a 2-sphere of radius R is given via

$$\frac{\mathrm{d}E^{\varphi}}{\mathrm{d}t} = \int_{S^2_R} T^{(\varphi)}_{ab} n^a \mathrm{d}S^b, \tag{4.36}$$

where n^a is the time-like unit normal and $T^{(\varphi)}_{ab} = T_{ab} - \beta_0 C^{\mathrm{GB}}_{ab}$ represents the RHS of the modified Einstein's equations (4.9). Assuming that a spherical surface is located in the radiation zone of an asymptotically flat spacetime and φ behaves as outgoing radiation in the radiation zone, to leading order we find that $T^{(\varphi)}_{ab} = T_{ab}$. Then, to leading order Eq. (4.36) reads

$$\frac{\mathrm{d}E^{\varphi}_0}{\mathrm{d}t} = -\int_{S^2} r^2 T^r_t d\Omega = \int_{S^2} [\dot{\varphi}(t-r)]^2 \mathrm{d}\Omega, \tag{4.37}$$

where the dot denotes time differentiation. We therefore integrate Eq. (4.37) to find the total radiated scalar energy to leading order.

4.3.4 Numerical results: scalar waveforms

In this section we present our numerical results. The initial data for the simulations are listed in Table 4.3.1. We find good agreement with numerical results of Ref. [272], which made use of the same decoupling approximation as we do. We show scalar waveforms for $l \geq 1$ modes in Fig. 4.3.1 and for the $l = 0$ mode in Fig. 4.3.2, where we align the waveforms so that the amplitude peaks of the scalar field coincide at $\hat{t} = 0$ and choose $\beta_0/m_1^2 = 1$ for convenience.

For equal-mass binaries we have only even l-modes present in the waveform, as equal-mass non-spinning binaries are symmetric under parity transformations ($\vec{r} \to -\vec{r}$). Since $Y^m_{l=\mathrm{odd}}(\vartheta, \varphi)$ is antisymmetric and the EsGB coupling is invariant under parity, there must be no emission from odd l-modes for equal-mass binaries. On the other hand, in the unequal-mass case, odd l-modes are present and the dipole emission dominates all other higher modes of the scalar waveform for EsGB gravity (it enters at -1PN order) [236, 245, 286]. In Fig. 4.3.2, we see that the $l = 0$ mode looks unlike the other modes and is roughly constant before merger time (this is consistent with leading order PN theory [236, 272]). After merger it settles to almost the same value for all the mass ratios, since the remnant BHs formed have quite similar final masses and spins, and thus the same amount of remnant scalar hair. Overall, from Figs. 4.3.1 and 4.3.2, at fixed β_0/m_1^2, the scalar field radiation becomes stronger for more extreme unequal-mass binaries, especially in the inspiral and merger portions of the signal. End state BHs with smaller spin (i.e. BHs formed from more extreme mass ratios) have faster damping times than BHs with higher spin. As a result, the scalar waves in the ringdown of the (22) mode are more pronounced at late times for black holes produced from more symmetric-mass-ratio ($q \sim 1$) progenitors. To illustrate this point, we align the

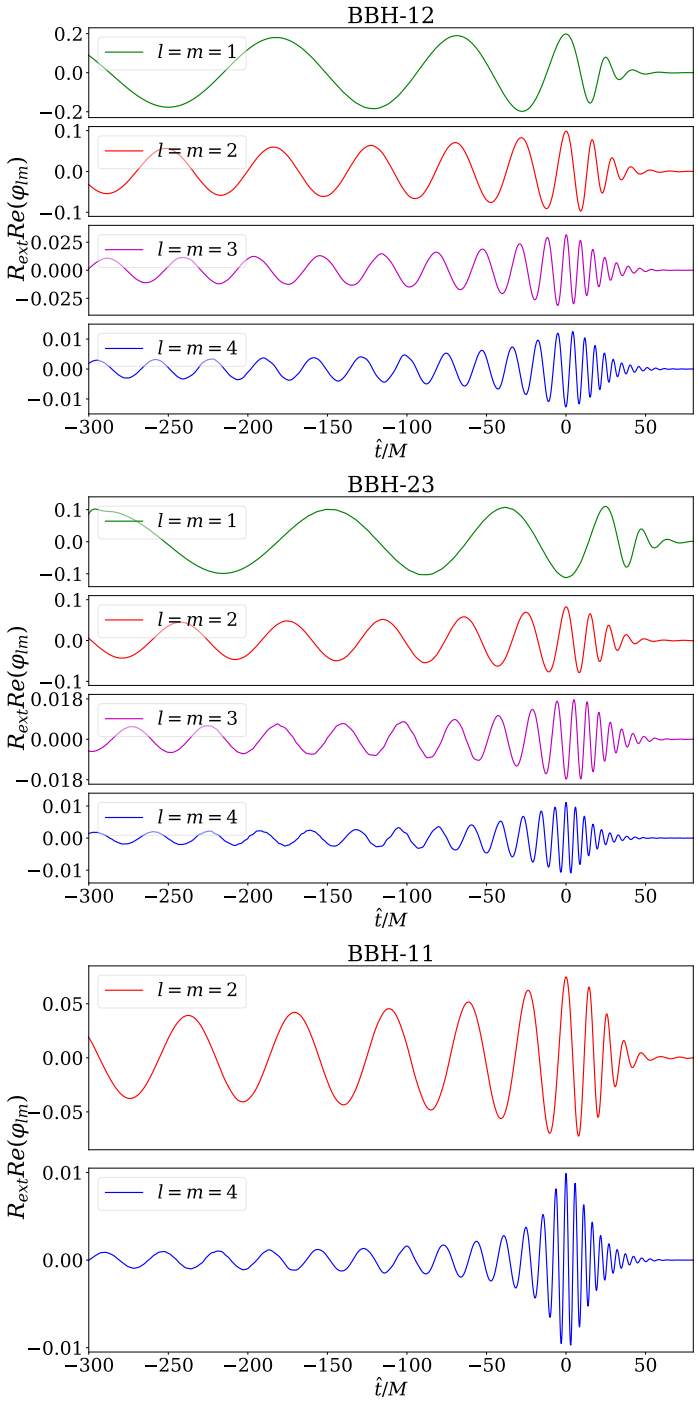


Fig. 4.3.1 Scalar waveforms for $l \geq 1$ for mass ratios of $q = 1/2, 2/3, 1$ extracted at $R_{\rm ext} = 110$. For unequal mass cases, the scalar field amplitude is more pronounced. The waveforms have been aligned so that the amplitude peaks of the scalar field coincide at $\hat{t} = 0$, and we set $\beta_0/m_1^2 = 1$ for convenience (recall that since we are using an order-reduction scheme, there is no restriction on the value of β_0/m_1^2 in our evolution). In our analysis, we choose a physically allowed value of β_0/m_1^2 and re-scale the scalar waveforms using Eq. (4.21).

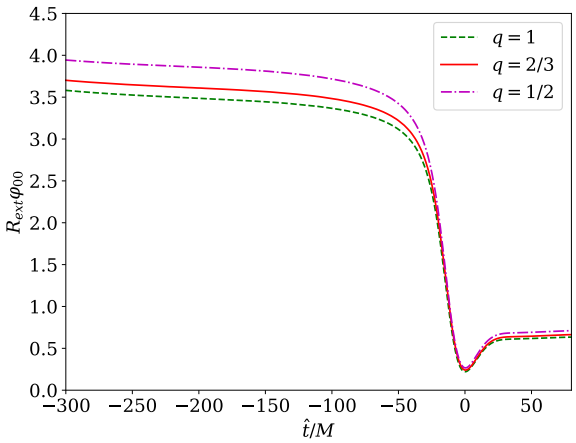


Fig. 4.3.2 Scalar $l = 0$ mode for binary mass ratios of $q = 1, 2/3, 1/2$, extracted at $R_{\rm ext} = 110$.

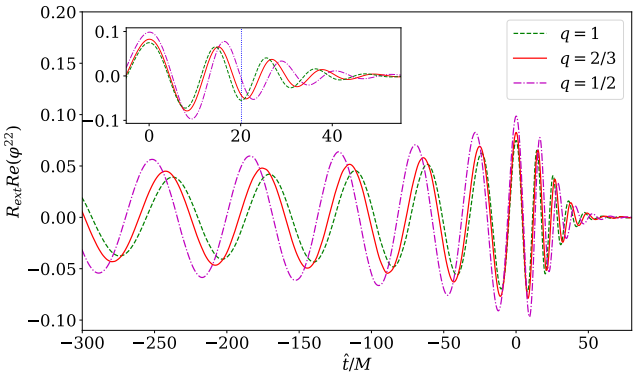


Fig. 4.3.3 Scalar $l = 2, m = 2$ mode for mass ratios of $q = 1, 2/3, 1/2$. The inset shows the zoom-in on the ringdown portion of the signal. Within the inset, the blue dotted line indicates the time where the amplitudes of the $q = 2/3$ and $q = 1/2$ waveforms become smaller in amplitude than the $q = 1$ waveform.

(22) modes in the amplitude peak of the scalar field for different mass ratios in Fig. 4.3.3, and zoom-in on the ringdown, where the amplitude for more symmetric-mass-ratio binaries becomes larger than for more asymmetric systems later in time.

Finally, the scalar energy flux, as computed from Eq. (4.37), is shown in Fig. 4.3.4. We see that it is dominated by the contribution from $l = 0$ mode, which is larger for more unequal-mass-ratio binaries, as expected from PN theory [236, 272]. This is unlike the tensorial gravitational energy flux, where the strongest flux comes from the equal-mass binary. This can be explained by the fact that to leading order the total radiated gravitational energy $E^{\rm GW}_{\rm rad} \sim \eta^2$, where $\eta = q/(1+q)^2$ is the symmetric mass ratio [287]. We note that the scalar energy flux measured here using Eq. (4.37) is a second-order effect and so is

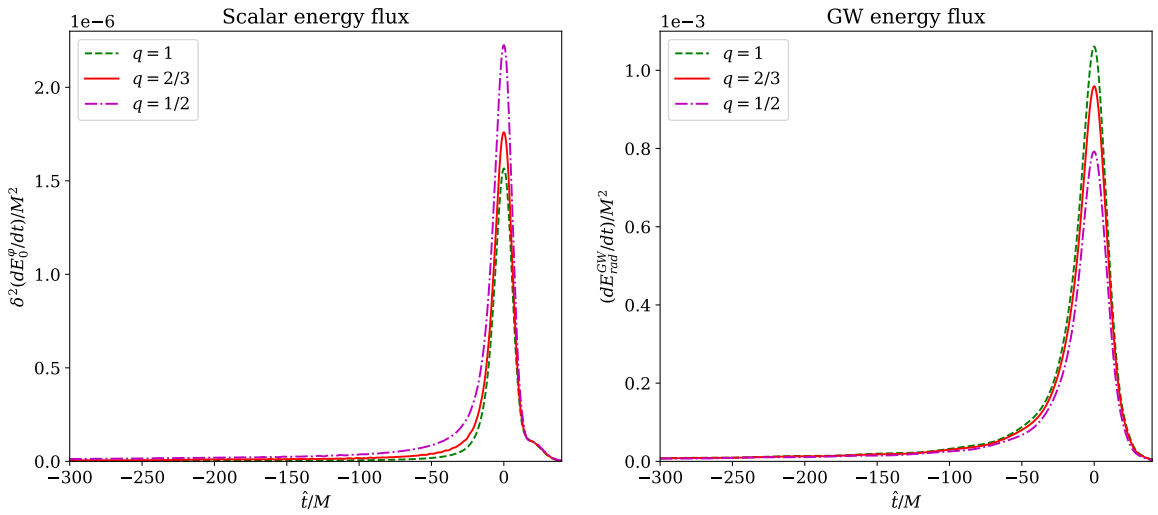


Fig. 4.3.4 *Left*: Scalar energy flux computed using Eq. (4.37). Here we set $\beta_0/m_1^2 = 0.01$. *Right*: Gravitational wave energy flux computed using Eq. (4.32).

significantly suppressed—at merger, it accounts for much less than 1% of the gravitational energy flux.

4.4 Modelling the Scalar Ringdown Waveform

When exploring the GW phenomenology of astrophysical systems in modified gravity, a key aim is to obtain an accurate waveform model for the signal (here the scalar ringdown) and to be in a position to observe the effects in question and infer information on the underlying theory from the observed GW data. In this section we model the scalar ringdown based on the NR data of Section 4.3.4. The gravitational waves emitted by the remnant BH formed by a merger, known as the ringdown signal, can be approximated as a superposition of damped sinusoids [288]. In GR, each mode of the tensorial ringdown signals can then be written as

$$h^{lm} = \sum_{J=1}^{N} H_J e^{-i(\omega_J^{\rm GR}(t-t_0)+p_J)}, \tag{4.38}$$

where t_0 is the start time of the ringdown, $J = (lmn)$ is the mode number, H_J and p_J are real amplitude and phase of mode J at $t = t_0$, (which depend on the binary configuration and dynamics near merger), and ω_J are the complex frequencies of the N most dominant QNMs.

In a similar fashion, the scalar ringdown signal can be written as,

$$\varphi_{lm} = \sum_{J=1}^{N} A_J e^{-i(\omega_J^{\varphi}(t-t_0)+p_J)}, \tag{4.39}$$

where A_J now denote scalar real amplitudes and ω_J^{φ} – the complex frequencies of the scalar mode. For a mode J corresponding to a given set of QNM indices (lmn), we write the real and imaginary parts as

$$\omega_{\rm QNM} = \omega_{lmn} - \frac{i}{\tau_{lmn}}. \tag{4.40}$$

The integers (lm) describe the angular properties of the emission, while n is the overtone number [289]. Modes with $n = 0$ are referred to as the *fundamental modes*, while those with $n \geq 1$ as *overtones*, which (at least in GR) have lower frequencies and damping times than their corresponding fundamental modes. We have denoted the total number of quasinormal modes with which we model the ringdown signal by N.

The no-hair theorem of GR states that the damping times, τ^{lmn}, and frequencies, ω^{lmn}, for gravitational wave perturbations around astrophysical (non-charged) BHs in GR, are uniquely determined by the mass and spin of the final black hole. The excitation coefficients also depend on the initial conditions of the perturbation [289], in our case the progenitor parameters. For modified theories of gravity, the QNM spectrum of BH spacetimes generally depends on the theory in question, and so observations of the ringdown signal can provide a way to discriminate between GR and possible modified theories of gravity. Unlike GR [290], for alternative theories of gravity there is typically no set of separable master equations for linearised perturbations of black holes. Instead, the calculation of QNMs has relied on either the assumption of spherical symmetry [291, 292], the slow spin approximation [293, 294][5], or on numerical fits of time-domain waveforms computed from NR simulations [256, 296]. In this work we focus on the last method by performing numerical fits to the scalar and tensor waveforms.

In our analysis, we take a similar approach of modeling the scalar ringdown as a superposition of damped sinusoids given by Eq. (4.39), except our QNM frequencies no longer correspond to just scalar QNMs of GR. We note that the operator acting on φ in its equation of motion consists of the background GR metric in the decoupling approximation we use (see Eq. (4.19)). Therefore, the homogeneous solution of the beyond-GR scalar perturbation equation around a BH spacetime should contain the same scalar QNMs as the corresponding Kerr BH in GR, $\omega_{lmn}^{\rm Kerr,scalar}$. However, our equation is non-homogeneous as we also have

[5] Although there has been recent work on extending the Teukolsky formalism to modified gravity theories to compute their quasinormal modes for fast-rotating black hole solutions [295].

the Gauss-Bonnet scalar evaluated on the background GR metric, acting as a source term. Particular solutions to the scalar equation introduce additional frequencies into the ringdown QNM spectrum [256, 296]. The spectrum of these "driven" modes by the source term for $l \geq 2$ has been shown to coincide with the quasinormal modes for tensor perturbations for Kerr, $\omega_{lmn}^{\rm Kerr,grav}$; while for $l = 1$ the "driven" mode has been fitted empirically [256].

Can our scalar ringdown waveforms be modeled by the gravitational and/or scalar QNMs of a Kerr black hole in GR as the above findings suggest? To address this question we perform one-mode ($N = 1$) and two-mode ($N = 2$) fits, whilst keeping the QNMs fixed to their values in GR. These fixed values employed in our analysis can be found in Table 4.C.1 of Appendix 4.C. For one-mode fits, we utilize Eq. (4.41), where we check whether just one QNM fixed to either $\omega_{lmn}^{\rm Kerr,scalar}$ or $\omega_{lmn}^{\rm Kerr,grav}$ describes the data well. Next, we perform a two-mode fit using Eq. (4.42), where we fix $\omega_{lmn}^{\rm Kerr,scalar}$ and $\omega_{lmn}^{\rm Kerr,grav}$ simultaneously. We note that for the $l = 1$ ringdown modes fitted with the $N = 2$ mode fit we take a conservative approach and only use a fundamental scalar QNM and its first overtone.

$$Re(\varphi_{N=1}^{lm}) = \begin{cases} A_1^{lm0} e^{-(t-t_0)/\tau_{lm0}} \cos[\omega_{lm0}(t-t_0) + p_1^{lm0}], \quad \omega_{\rm QNM} \in \left\{ \omega_{\rm QNM}^{\rm Kerr,scalar}, \omega_{\rm QNM}^{\rm Kerr,grav} \right\} & l,m > 1 \\ A_1^{lm0} e^{-(t-t_0)/\tau_{lm0}^{\rm Kerr,\ scalar}} \cos[\omega_{lm0}^{\rm Kerr,\ scalar}(t-t_0) + p_1^{lm0}] & l = m = 1, \end{cases} \tag{4.41}$$

$$Re(\varphi_{N=2}^{lm}) = \begin{cases} A_1^{lm0} e^{-(t-t_0)/\tau_{lm0}^{\rm Kerr,scalar}} \cos[\omega_{lm0}^{\rm Kerr,scalar}(t-t_0) + p_1^{lm0}] \\ \qquad + A_2^{lm0} e^{-(t-t_0)/\tau_{lm0}^{\rm Kerr,grav}} \cos[\omega_{lm0}^{\rm Kerr,grav}(t-t_0) + p_2^{lm0}] & l,m > 1 \\ A_1^{lm0} e^{-(t-t_0)/\tau_{lm0}^{\rm Kerr,scalar}} \cos[\omega_{lm0}^{\rm Kerr,scalar}(t-t_0) + p_1^{lm0}] + \\ \qquad A_2^{lm0} e^{-(t-t_0)/\tau_{lm1}^{\rm Kerr,scalar}} \cos[\omega_{lm1}^{\rm Kerr,scalar}(t-t_0) + p_2^{lm1}] & l = m = 1. \end{cases} \tag{4.42}$$

Equations (4.41)–(4.42) fit to the real parts of the scalar multipoles, as their imaginary parts will have the same amplitudes and phases. We make use of all scalar mode waveforms presented in Section 4.3.4, and therefore perform the fitting on the $(lm) = (11), (22), (33), (44)$ modes.

We sample the parameter space using `emcee` [203]. Dropping the (lmn) indices in Eqs. (4.41)–(4.42) and keeping just the mode number $N \in [1,2]$, we use uniform priors in our inference, namely $\log A_i \in [-3,1]$ and $p_i \in [0, 2\pi]$ for $i \in [1,N]$. We compute the frequencies ω_{lmn} with the `qnm` package [297] using our final spin calculations from Table 4.3.1.

There is an ongoing debate around when is the optimal time to begin fitting quasinormal ringdown (see e.g. Ref. [298]), as different start times can give different answers for the mode

fits, and have also caused some controversy regarding the confidence of a subdominant QNM observation in GW data [299]. While overtones are typically quick to decay, they can play an important role as we approach the time of merger [300–305]. To avoid the intricacies of having to account for overtones, as well as nonlinear effects in the early ringdown [306, 307], we take a conservative approach and start the ringdown analysis $t_0 = 16M$ after the time of the peak amplitude of the scalar mode[6]. By starting too early we risk including nonlinear effects from the merger and by starting too late the SNR of the signal may be significantly lower. In our analysis, the damped sinusoid model is most accurate as an approximation in the late ringdown and so we sacrifice on the strength of the signal. The end time of our analysis is determined by the point in the late ringdown when the signal becomes very faint and the numerical noise becomes more significant. The point when this happens varies on the mode by mode basis, with higher modes being prone to numerical noise earlier than others. However, the typical length of our ringdown varies in the range of $\sim 15-30M$.

In the optimization process, we use a least-squares likelihood in the time domain, with a flat noise spectral density

$$L(d;\boldsymbol{\theta}) \propto \sum_i \exp\left\{-\frac{[\varphi_{\vec{\theta}}(t_i)-d(t_i)]^2}{2\sigma^2}\right\}, \tag{4.43}$$

where $d(t_i)$ is the time sequence of numerical data, σ^2 is the variance and $\boldsymbol{\theta} = \{A_i, p_i\}$. We estimate the variance by taking our total error budget percentage (i.e. 4%) from the peak of the amplitude for each mode. As such, the error we account for through the variance parameter varies on a mode by mode basis. This choice for error estimation in our analysis assumes that the total NR error is not correlated in time. In reality, this is not likely to be an accurate assumption to make as in certain regions of the waveform we may in fact be over- or under-estimating the allowed deviation of the data from the true values. Ideally, our likelihood function should contain some sort of correction to account for such correlation of the data with time. However, this is out of scope of this work and we leave this for future study. We have verified the robustness of our choice of variance in the likelihood function of Eq. (4.43) by gradually decreasing its value and assessing its effect on the estimation of the modes' amplitudes. As expected, with decreasing variance, the amplitudes converge to some fixed values with smaller error bars, representing an ideal scenario where our NR error is very small. These idealised values provide the relative error we make in our fitting procedure when estimating amplitudes using our actual total NR error budget percentage to calculate a fixed variance. Fig. 4.4.1 shows this convergence of A_i for $i \in [1,2]$ of the (22) mode of the

[6]We have investigated the choice of other start times ranging from $10M$ to $16M$ and found similar results on the estimated parameters.

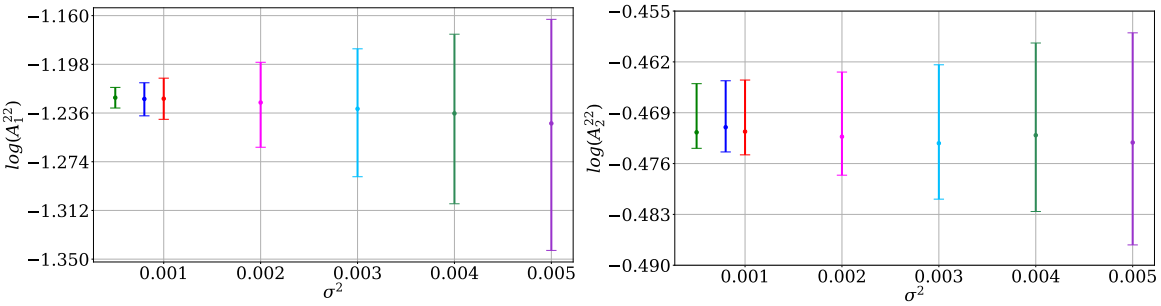


Fig. 4.4.1 Convergence of the estimated amplitudes with decreasing variance $\sigma^2 = \{0.005, 0.004, 0.003, 0.002, 0.001, 0.0008, 0.0005\}$ of Eq. (4.43) for the (22) mode of `BBH-12` run. The variance value estimated as 4% from the peak amplitude takes the value of $\sigma^2 = 0.003$ in our fit for this configuration. We have verified that the same convergence holds qualitatively for the $N = 1$ mode fit too.

`BBH-12` configuration, where the fixed variance of $\sigma^2 = 0.003$ used in the fitting procedure results in median amplitudes lying within the error bars of the smallest variance.

In Table 4.4.1 we summarize the results of our fits. We note that we fixed the dimensionless coupling β_0/m_1^2 to unity for convenience there. Therefore, when choosing a different value for the coupling, appropriate rescaling to the amplitudes has to be done according to Eq. (4.21). We find that that the ratio of amplitudes of scalar Kerr QNMs to gravitational Kerr QNMs varies on a mode-by-mode basis for $l > 1$ modes. In the case of the $l = 1$ mode fit, the amplitude of the overtone $n = 1$ dominates the amplitude of its fundamental mode as also found in the analysis of gravitational ringdown in Ref. [301]. Unless indicated by a dash in Table 4.4.1, we find that for certain modes a $N = 1$ mode fit is able to describe the data accurately enough. This happens in the cases where the amplitude of one of the modes in the $N = 2$ mode fit is dominant, or when the frequencies of the $N = 2$ mode fit lie close to each other.

We additionally fit the amplitudes of our gravitational waveforms in Table 4.4.2, where we use $(lm) = (11), (22), (33), (44), (55), (66)$ modes in the fitting procedure. We find that the $N = 1$ mode fit of Eq. (4.38) is sufficient to describe the data. Since the Einstein equations to leading order remain unchanged (see Eq. (4.18)), we have fixed the frequency of the $N = 1$ mode fit to the fundamental gravitational Kerr QNM of GR.

In summary, the leading order QNMs of the scalar and tensor components of the ringdown waveform in EsGB gravity are accurately described by QNMs of GR. The next correction in δ to the scalar QNM spectrum would depend on the nature of the coupling to the Gauss-Bonnet term, while the correction to the gravitational QNM spectrum would happen at $\mathscr{O}(\delta^2)$. In the case of sub-leading corrections to the scalar QNMs, for EdGB gravity with exponential coupling, $\beta(\varphi) = e^{\varphi}$, the next correction will come from second order in δ,

Run	(lm) mode	$N=2$		$N=1$, $\omega_{lm}^{\rm Kerr,grav}$ fixed	$N=1$, $\omega_{lm}^{\rm Kerr,scalar}$ fixed
		$\log_{10}A_1$	$\log_{10}A_2$	$\log_{10}A_1$	$\log_{10}A_1$
BBH-11	22	$-0.81^{+0.26}_{-0.02}$	$-0.67^{+0.01}_{-0.09}$	–	–
	44	$-1.62^{+0.04}_{-0.48}$	$-2.41^{+0.77}_{-0.39}$	–	$-1.58^{+0.01}_{-0.34}$
BBH-23	11	$-0.50^{+0.01}_{-0.02}$	$0.07^{+0.08}_{-0.04}$	–	–
	22	$-0.89^{+0.03}_{-0.03}$	$-0.61^{+0.01}_{-0.02}$	–	–
	33	$-1.34^{+0.03}_{-0.09}$	$-1.39^{+0.03}_{-0.07}$	–	–
	44	$-1.76^{+0.04}_{-0.16}$	$-2.59^{+0.46}_{-0.28}$	–	$-1.72^{+0.01}_{-0.58}$
BBH-12	11	$-0.10^{+0.01}_{-0.01}$	$0.69^{+0.18}_{-0.12}$	–	–
	22	$-1.23^{+0.05}_{-0.05}$	$-0.47^{+0.01}_{-0.01}$	$-0.48^{+0.01}_{-0.01}$	–
	33	$-1.30^{+0.17}_{-0.05}$	$-1.29^{+0.04}_{-0.07}$	$-1.09^{+0.01}_{-0.13}$	$-1.03^{+0.01}_{-0.01}$
	44	$-1.90^{+0.46}_{-0.12}$	$-1.40^{+0.03}_{-0.11}$	$-1.40^{+0.01}_{-0.32}$	–

Table 4.4.1 Estimated amplitudes from the $N=1$ mode and $N=2$ mode fits summarized by Eqs. (4.41)-(4.42). As in Fig. 4.3.1, we set $\beta_0/m_1^2=1$ for convenience. The dash indicates that a specific fit could not describe the data accurately. In all cases with an $N=2$ mode fit, A_1 represents the amplitude of the scalar Kerr QNM. For the (11) mode, A_2 is the amplitude of the scalar Kerr overtone, while for all other modes, A_2 represents the amplitude of gravitational Kerr QNM. The upper and lower limits on the estimated parameters lie within the 90% confidence interval and the central value is the median.

while for shift-symmetric Gauss-Bonnet gravity with coupling $\beta(\varphi)=\varphi$, at the third order in δ [260]. Given the smallness of δ, we expect any kind of deviation from GR in the scalar QNM spectrum in Gauss-Bonnet gravity to be very small.

4.5 Observational Prospects

4.5.1 Measurability of the scalar ringdown

Having formulated a model for the scalar polarisation component of the EsGB ringdown waveform, we now make a first attempt to assess the measurability of its presence in compact binary coalescence observations by the current and future networks of GW detectors. Returning to Eq. (4.8), we recall that the second term predicts an additional scalar contribution, whose strength is controlled by the magnitude of the conformal coupling a_0 defined in Section 4.2.2 and the amplitude of the scalar field φ, which may be re-scaled using the dimensionless parameter β_0/m_1^2 according to Eq. (4.21). Therefore, the choice of the re-scaling applied to the amplitude of the scalar field will affect the strength of the scalar polarisation, and our choices of the re-scaling will be detailed in the following Sections. However, before making predictions on the strength of the scalar signal, it is necessary to make the conversion

Run	(lm) mode	$\log_{10}A_1$
BBH-11	22	$-0.81^{+0.01}_{-0.01}$
	44	$-1.62^{+0.01}_{-0.01}$
	66	$-2.36^{+0.01}_{-0.01}$
BBH-23	22	$-1.04^{+0.01}_{-0.01}$
	33	$-1.58^{+0.003}_{-0.003}$
	44	$-1.75^{+0.01}_{-0.01}$
	55	$-1.93^{+0.01}_{-0.25}$
	66	$-2.51^{+0.01}_{-0.02}$
BBH-12	22	$-1.03^{+0.01}_{-0.01}$
	33	$-1.34^{+0.01}_{-0.01}$
	44	$-1.74^{+0.002}_{-0.001}$
	55	$-1.91^{+0.01}_{-0.01}$
	66	$-2.29^{+0.02}_{-0.03}$

Table 4.4.2 Estimated gravitational amplitudes of the $N = 1$ mode fit of Eq. (4.38), where the fundamental gravitational QNMs are kept fixed. The upper and lower limits on the estimated parameters lie within the 90% confidence interval.

to physical units. The scalar polarisation now takes the form of

$$h_{\rm S} = \frac{M_{\rm fin}}{D_L} a_0 \varphi, \tag{4.44}$$

where $M_{\rm fin}$ is the final BH mass and D_L is its luminosity distance from the Earth. We note that φ is the sum of all (lm)-modes and is dependent on the inclination angle ι, which is defined as the angle between orbital angular momentum and the line-of-sight

$$\varphi = \sum_{lm} \varphi^{lm} Y_{lm}(\iota). \tag{4.45}$$

In our analysis we set $\iota = 60^\circ$. As we discussed in Section 4.2.2, each polarisation has a distinct geometrical imprint on a GW detector. We therefore begin with projecting the scalar strain, $h_{\rm S}$, onto the detector D located at $\mathbf{x}_D$

$$h_{\rm D}(t) = h_{\rm S}(t, \mathbf{x}_{\rm D}) F^{\rm S}. \tag{4.46}$$

Here $F^{\rm S}$ is the response, or antenna pattern, of a detector D to scalar polarisation. It can be given in terms of the polar angle θ and the azimuthal angle ϕ in the detector frame (i.e. θ

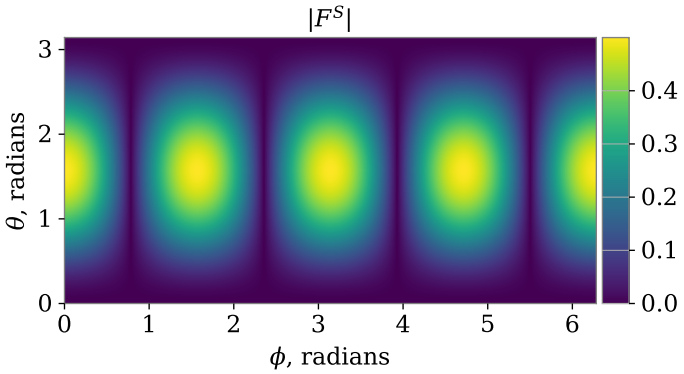


Fig. 4.5.1 Scalar antenna pattern for various choices of polar and azimuthal angles. Yellow regions indicate the maximum response from the detector from the incoming scalar-polarised GW.

and ϕ measured with respect to detector arms along the x and y-axes) in the following form

$$F^{\rm S}(\theta,\phi) = -\frac{1}{2}\sin^2\theta\cos 2\phi. \tag{4.47}$$

Note the absence of dependence on the polarisation angle ψ that defines the orientation of the source projected on the celestial sphere; this is a direct consequence of the spin-0 nature of the scalar field, in contrast with the tensorial GWs that behave as a spin-2 field. The response to scalar polarisation depends on the polar and azimuthal angles at which the GW comes in with respect to the detector frame. Figure 4.5.1 illustrates the change of the antenna pattern for various angles. We position the source at an optimal sky location for one of the detectors (LIGO Hanford in particular), that is straight down one of its arms, i.e. $\theta = \frac{\pi}{2}$, $\phi = 0$. For a given GW detector, we then compute the squared SNR of the scalar signal defined via

$$\rho^2 = \int_0^\infty \frac{4|\tilde{h}_{\rm D}(f)|^2}{S_n(f)} df, \tag{4.48}$$

where $\tilde{h}_{\rm D}$ is the signal in the Fourier domain and $S_n(f)$ is the noise power spectral density (PSD) of the detector, which we set to the predicted noise curve of (i) the current network of LIGO (Hanford and Livingston) and Virgo detectors at design sensitivity [308, 309] and (ii) the Einstein Telescope (ET) [310] in the ET-D configuration [311]. We list luminosity distance and the range of masses chosen for each of the detectors in Table 4.5.1.

In the computation of the SNR from Eq. (4.48), the signal is weighted by the noise PSD curve in the frequency domain. Having a frequency of the scalar waveform close to the minima of the PSD would therefore increase the integrand of SNR for a fixed amplitude of the waveform. However, for varying mass, the amplitude is not fixed but scales according

Detector	D_L/Gpc	$M_{\rm fin}/M_\odot$
LIGO/Virgo	1	[100, 1000]
ET	1	[10, 1000]

Table 4.5.1 Distance and final BH mass range targeted with each of the detectors considered in this study.

to Eq. (4.44). Further, the amplitude of the scalar signal is affected by the mass ratio: as suggested by our NR simulations from Section 4.3.4, the amplitude increases for more asymmetric binaries (recall that the scalar amplitude scales with β_0/m_1^2, where the scaling is the largest for asymmetric binaries, where the mass of one of the progenitors is smaller).

We now move on to estimate the actual signal strength for two different scenarios with respect to the values of the coupling parameters in EsGB.

Maximally allowed couplings

Our prior for the range allowed for the couplings a_0 and β_0/m_1^2 is controlled by the theoretical and observational constraints described in Section 4.2.4. In this Section we make the 'optimistic' choice of $\max(\beta_0/m_1^2) = \varepsilon_{\rm thr} \approx 0.2$ and $a_0^{\rm max} = \sqrt{10^{-3}} \approx 0.0316$ to be maximally allowed values for our couplings (i.e. the blue region of Fig. 4.2.2 is where the theory can be said to be no longer predictive) and investigate in more detail the dependence of the SNR of the scalar ringdown signal on the total mass $M_{\rm fin}$ and mass ratio q of the progenitors. Following common practice [312, 313], we assume SNR ≥ 8 is required for a detection.

Figure 4.5.2 shows the network SNR for the current LIGO (Livingston and Hanford) and Virgo detector network, calculated via quadrature, $\rho_{\rm network} = \sqrt{\sum_j \rho_j^2}$, where ρ_j represents the SNR in a single detector. Here the values of numerically calculated SNR span three horizontal lines of constant $q = \{1/2, 2/3, 1\}$ and are interpolated on the parameter space of $M_{\rm fin} \times q$. The typical scalar signal is weaker than its tensorial counterpart by at least three orders of magnitude, and the choice of maximally allowed couplings results in increased SNR for larger masses. The largest network SNR of 1.8 is produced from for the smallest mass ratio of $q = 1/2$ and the final BH mass of $M_{\rm fin} = 1000 M_\odot$. We note, however, that our choice of $t_0 = 16M$ to be the ringdown start-time reduces the strength of the signal. As seen in Section 4.4, the amplitudes for highly asymmetric mass ratios become significantly damped at later times. Therefore, one may expect larger SNR, if an earlier ringdown start-time was chosen.

The strength of the signal significantly improves in the ET, which we illustrate in Fig. 4.5.3. Here we further disentangle contributions of each mode to the total SNR by

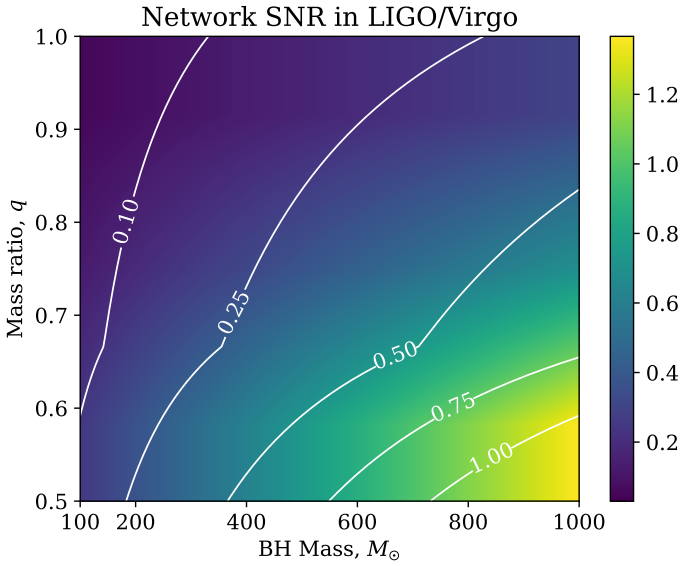


Fig. 4.5.2 Contour plot of network SNR in the $M_{\rm fin} \times q$ plane for the scalar ringdown of a BBH at 1 Gpc as observed by the Virgo, Livingston and Hanford network of detectors at design sensitivity. Here the couplings $a_0, \beta_0/m_1^2$ are fixed to their maximally allowed values as described in Section 4.5.1. NR data are available along horizontal lines of $q = \{1/2, 2/3, 1\}$, based on which SNR values are estimated by interpolation on the plane.

plotting SNR for the strongest individual modes, i.e. $(lm) = (11), (22), (33)$. We observe that some cross-terms between modes may contribute destructively in the integrand of SNR (see Eq. (4.48)) and as such, the total SNR is not simply a sum in quadrature of the individual modes' contributions. We find that the strongest total SNR calculated from all modes is recovered from the most extreme mass ratio considered in our simulations, $q = 1/2$. This is as expected since its modes' amplitudes are significantly larger than for milder mass ratios. Assuming a luminosity distance of $D_L = 1$Gpc for the `BBH-12` configuration, the total SNR of the scalar ringdown is weak for BHs with masses $M_{\rm fin} \lesssim 50 M_\odot$ and falls below the detectability threshold. However, taking the parameters of the GW151226 event with $q \sim 1/2$, $D_L = 440$ Mpc and $M_{\rm fin} \sim 20.8 M_\odot$ [314], we find the SNR in ET to be around 7.15. Interestingly, the SNR of individual modes has a more complicated structure and there are several competing factors contributing to their strength. First, the final BH mass determines where the QNM frequencies lie in relation to the high-sensitivity region of the detector's noise curve. Second, the hierarchy and relative amplitudes of the scalar modes are determined by the mass ratio of the progenitor (e.g. with odd-m modes vanishing for symmetric binaries). Third, higher modes are less long-lived for more extreme mass ratios, meaning that at later ringdown start times these modes become significantly damped. Finally, the inclination angle contributes an additional l-dependent geometric factor to the relative mode amplitudes as

seen by the observer. As such, in our simulated analysis, the SNR of the (22) mode is the strongest for $q = 2/3$ and (11) and (33) modes are the strongest for the $q = 1/2$ one.

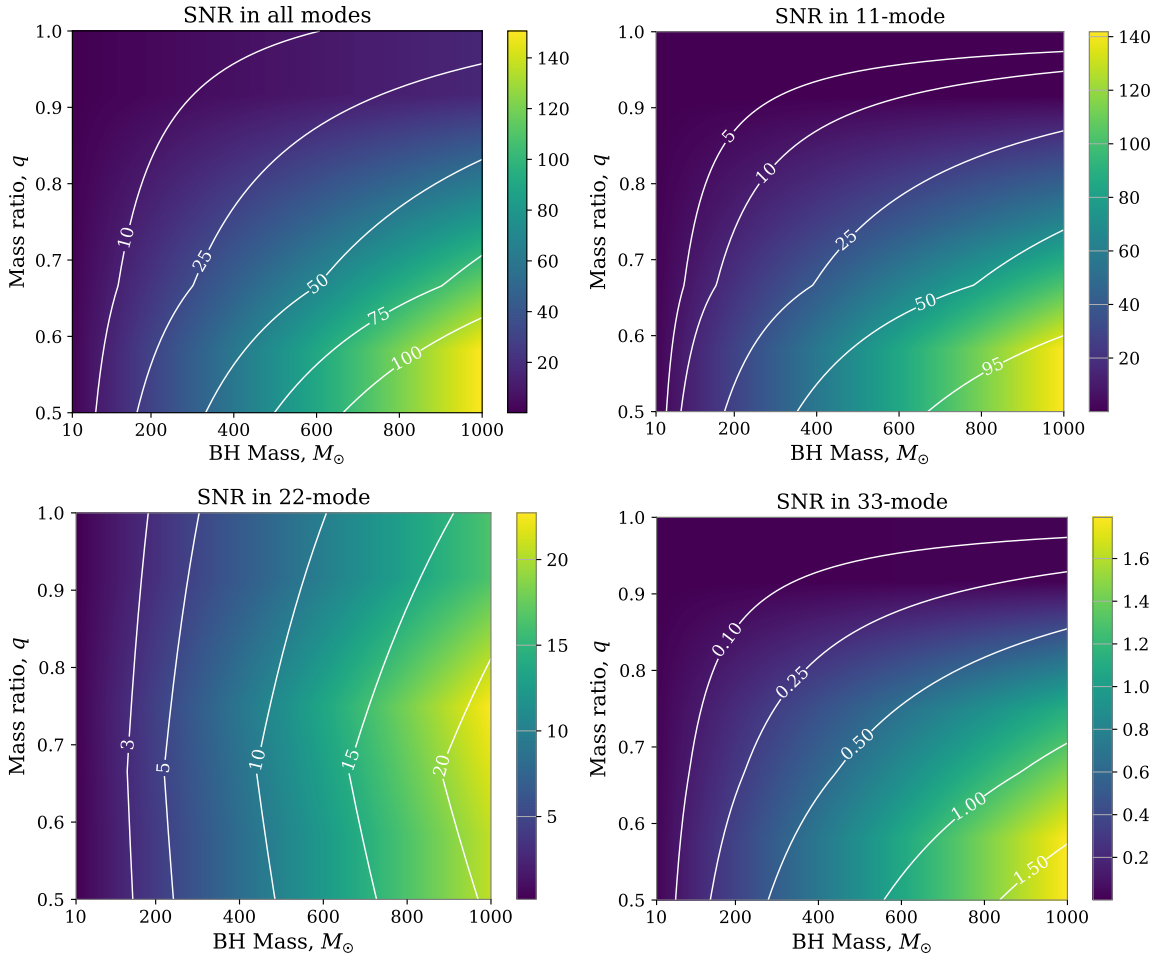


Fig. 4.5.3 Contour plot of the SNR in the $M_{\rm fin} \times q$ plane for the scalar ringdown of a BBH at 1 Gpc as observed by the Einstein Telescope. The couplings $a_0, \beta_0/m_1^2$ are fixed to their maximally allowed values as described in Section 4.5.1. The top left panel shows the total SNR, while the individual scalar mode SNRs are shown in the remaining three panels. NR data are available along horizontal lines of $q = \{1/2, 2/3, 1\}$, based on which SNR values are estimated by interpolation on the plane.

Imposing the most pessimistic constraint, $\sqrt{\beta_0} = 1.18\,\mathrm{km}$

So far we have explored the strength of the signal in the optimistic scenario, where the strength of the EsGB dimensionless parameter is set at the limit of the theoretical bound and appears to be strong enough for certain binary configurations. Constraints on the EsGB coupling β_0 coming from data analyses of astrophysical observations (see Table 4.2.1) further

limit the range of the coupling and therefore are expected to significantly lower the strength of the scalar signal. We now follow the analysis of Ref. [226] on GW signals from the inspiral of BBH and BH-NS binaries and set the value of the EsGB coupling to their quoted 90% combined upper bound, i.e. $\sqrt{\beta_0} = 1.18\,\mathrm{km}$. This result is based on an analytically approximated inspiral model, where the leading-order correction to the waveform at -1PN (i.e. $\delta\Psi \propto (\beta_0^2/M^4)v^{-7}$) is inferred[7] and mapped to a bound on β_0. Higher-order corrections to an incomplete 2PN level can vary the resulting bounds by more than 10%, depending on the binary parameters, therefore this value should not be considered as a robust upper bound at 90% confidence. Nevertheless, we expect that the upcoming fourth observing run (O4) of the LVK Collaboration [309] will probe this value range with much higher confidence.

In this scenario the SNR of the scalar ringdown becomes significantly suppressed, which we demonstrate in Fig. 4.5.4 on a logarithmic scale. Unlike the previous case, where we bounded a_0 and β_0/m_1^2, here, smaller values of the final BH mass and more asymmetric mass ratios yield a stronger scalar polarisation signal, as expected. In particular, the largest SNR of 0.42 is observed for a binary of mass ratio $q = 1/2$ with the smallest final mass of $M_{\mathrm{fin}} = 10M_\odot$. Unless the source is observed at very small luminosity distance of $D_{\mathrm{L}} \sim 52.5\,\mathrm{Mpc}$, the scalar ringdown signal of this binary configuration will not be detectable even with third generation detectors. Our predictions are less pessimistic for lower-mass binaries at even higher mass-ratios, however, in this work we do not consider BH-NS binaries or BHs with masses lower than $5M_\odot$.

4.6 Bayesian Inference on the Scalar Ringdown Signal

We now perform full Bayesian inference on a hypothetical scalar signal present in the bands of the LVK detector network and ET. We model the data stream in each detector as

$$d(t) = h(t) + n(t), \tag{4.49}$$

where $h(t)$ is the signal as described in Section 4.4 and $n(t)$ is a realisation of detector noise. Although we use continuum-appropriate notation, in practice the above are realized as discrete time series with a sampling rate of 4096 Hz, which is sufficient for our purposes in this work.

[7] Here $v = (\pi M f)^{1/3}$ is the relative velocity of the binary constituents (cf. Ref. [226] and references therein).

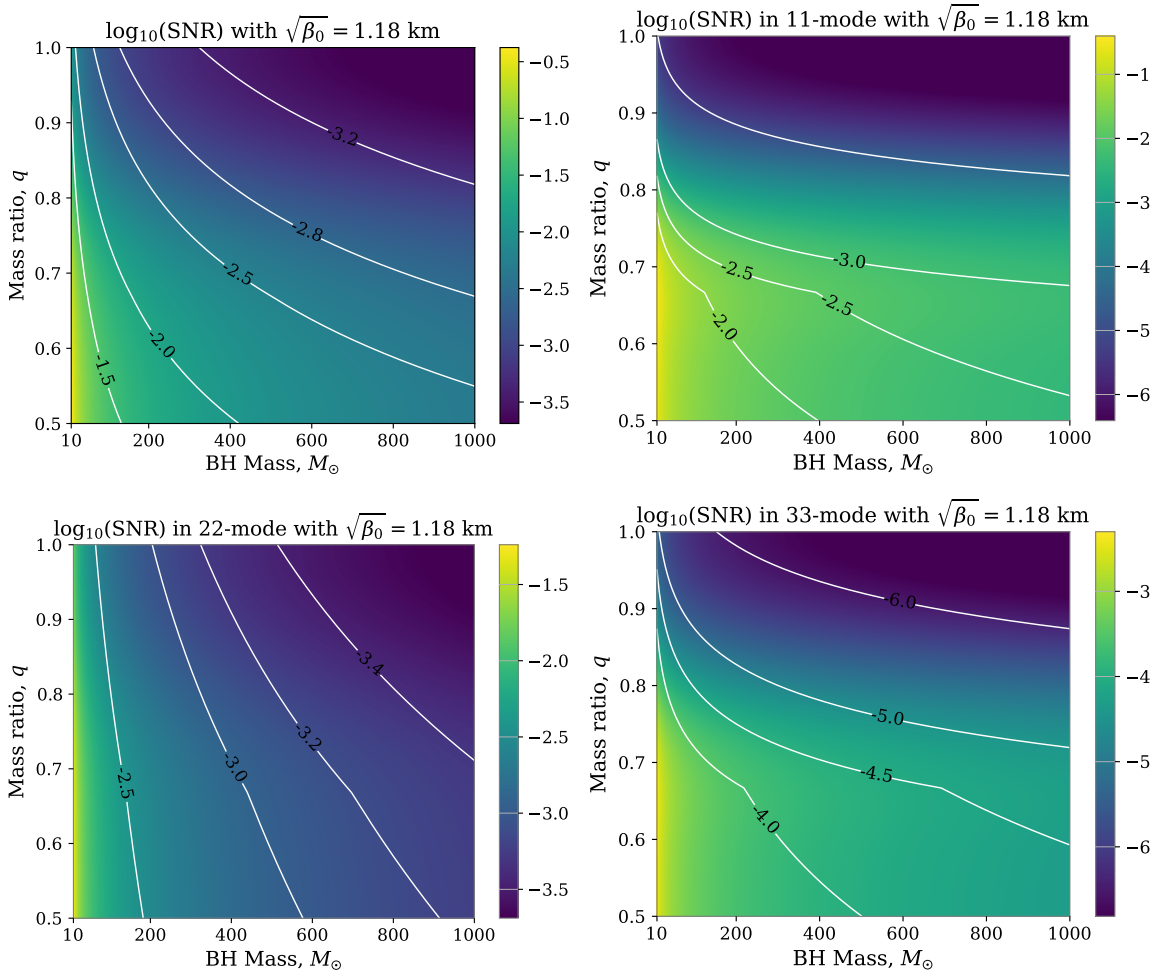


Fig. 4.5.4 Same as Fig. 4.5.3, except here the Gauss-Bonnet coupling $\sqrt{\beta_0} = 1.18\,\mathrm{km}$ is fixed and the plot is given on a logarithmic scale. For more discussion see Section 4.5.1.

4.6.1 Analysis Set-up

Before delving into the details of our analysis, let us first describe the simplifications performed here. First, we assume that the GR part of the signal is well-modeled and has been successfully reconstructed and removed from the data, without being particularly interested in the details of that part of the analysis. In practice this means that we have reduced the problem of performing an apples-to-apples comparison between GR and EsGB to the problem of searching for the presence of our EsGB scalar-ringdown signal in the residual data. This, in turn, makes use of the decoupling-limit assumption, that is, GW generation is driven by GR dynamics and therefore the tensorial ringdown signals in GR and EsGB are identical. Furthermore, we factorise the analysis of multiple QNMs into individual analyses for each (lm) pair, here performed using $N = 1$ or $N = 2$ modes for each pair that can capture the

presence of a "gravity-led" mode (or even an unusually strong overtone). This simplification assumes that the frequency content of e.g. the $l = m = 1$ and $l = m = 2$ modes that are studied here can be separated into disjoint regions in the frequency domain, as was done in recent searches for subdominant modes [299]. Although this latter assumption may not always hold, prior information on the final BH parameters, and hence on the expected scalar spectrum, will always be available from the analysis of the much louder tensorial signal ("+" and "×" polarisations), thus allowing for the scalar analysis set-up to be adapted accordingly. Details related to the above considerations will not be discussed here, but are left to be explored in future work.

We thus define our two competing hypotheses as follows:

1. $\mathscr{H}_0$: is our null hypothesis, corresponding to the data consisting of pure Gaussian noise, according to the PSD of each detector in our network.

2. $\mathscr{H}_1$: is our scalar-ringdown signal hypothesis, corresponding to the presence of a scalar signal in addition to noise in our data, where the scalar model is described in Section 4.4 and is parametrized by the real QNM amplitudes and phases (A_k^{lm}, p_k^{lm}), while the complex mode frequencies are fixed to their expected values (see details in Eqs. (4.41)–(4.42)).

Our first task is then to infer whether our hypothetical scalar signal could be identified as being present in the data – according to Eq. (4.49), where $h(t) = h_S(t;\vec{\theta})$ is consistent with our scalar signal model – or the data is consistent with pure noise, i.e. $h(t) = 0$. For scalar signals that are detected with confidence against the noise hypothesis, our analysis will also estimate the parameters $\vec{\theta}$ of our scalar ringdown model as posterior probability distributions on the model parameter space $p(\vec{\theta}|d,\mathscr{H}_1)$. To accomplish this, we inject our NR scalar waveforms $h_S(t)$ into data streams of simulated Gaussian noise and perform time-domain ringdown analysis using the `pyring` pipeline [315–317], which relies on a PYTHON implementation of the nested sampling algorithm [195] called `cpnest` [208]. The built-in calculation of the evidences $P(d|\mathscr{H}_i)$ in nested sampling, by statistically integrating each likelihood function $p(d|\vec{\theta},\mathscr{H}_i)$ over the respective parameter space Σ_i, enables model selection between the signal and noise hypotheses, by means of the Bayes factor,

$$\mathscr{B}^{\rm S}_{\rm N} = \frac{P(d|\mathscr{H}_1)}{P(d|\mathscr{H}_0)} = \frac{\int_{\Sigma_1} p(d|\vec{\theta}_1,\mathscr{H}_1)p(\vec{\theta}_1|\mathscr{H}_1)\mathrm{d}\vec{\theta}_1}{\int_{\Sigma_0} p(d|\vec{\theta}_0,\mathscr{H}_0)p(\vec{\theta}_0|\mathscr{H}_0)\mathrm{d}\vec{\theta}_0}. \tag{4.50}$$

Since $\mathscr{H}_0$ here is the noise hypothesis, its parameter space is the empty set and the integral in the denominator reduces to a product of noise likelihoods $p(d|\mathscr{H}_0) \propto \exp\{-\frac{1}{2}\sum_{i,j} d_i C^{-1}_{ij} d_j\}$,

one for each detector, where C_{ij} is the two-point autocovariance matrix that characterizes the detector noise in the time domain as a discrete stochastic process that is assumed to be Gaussian and stationary [316]. Similarly, the point-wise likelihood for $\mathscr{H}_1$ is computed using the same expression, where we replace $d \to d - h_S(t;\vec{\theta})$. That is, the signal hypothesis states that the residual is pure noise.

We adopt two approaches in the injection of the scalar signal. First, we perform a zero-noise injection by setting $n(t) = 0$ in (4.49), in order to isolate possible biases due to realisation-specific effects of the noise in our analysis and disentangle them from potential systematic biases inherent to our model. Note, however, that since the likelihood is weighted by the noise PSDs of our GW detectors, the overall effect of the noise on the uncertainty of our measurements is still incorporated in our method. Second, we inject the scalar waveform into simulated noise and assess its effects on the parameter estimation. We have followed the standards of the LSC Algorithm Library (LAL) [2] to perform NR scalar waveform injections, for which we have used a modified version of `LALsuite` [318] to accommodate the construction of the scalar waveform (cf. Section 3.4).

We present results for the injection of the `BBH-12` binary configuration, which gives us the strongest scalar wave signal. We place the source along one of the arms of the detector, as described in Section 4.5.1, at a luminosity distance of $D_L = 100\,\text{Mpc}$, and choose a final mass of $M_{\text{fin}} = 500 M_\odot$. We choose to inject the two loudest modes $(lm) = (11)$ and $(lm) = (22)$ and further take maximally allowed values for the theory couplings β_0/m_1^2 and a_0 as described in Section 4.5.1, i.e. $\max(\beta_0/m_1^2) = 0.2$ and $a_0^{\max} = \sqrt{10^{-3}} \approx 0.0316$. The SNR value for the configuration involving the (11) mode is roughly 700 and for the (22) is around 100. We use Table 4.4.1 of Section 4.4 to determine which recovery model of Eqs. (4.41)–(4.42) to use for each of our injections. As such, for the (11) mode, we use the $N = 2$ fit with frequencies fixed to the fundamental and first overtone scalar Kerr QNMs, while for the (22) mode we use the $N = 1$ mode fit with the frequency fixed to the fundamental gravitational Kerr QNM.

4.6.2 Results

Using the two hypotheses, $\mathscr{H}_0$ and $\mathscr{H}_1$, as defined in Section 4.6.1, in Fig. 4.6.1, we present the results of the recovery of the (11) and (22) modes with zero-noise and coloured Gaussian noise injections in ET. The results suggest that the scalar-ringdown signal hypothesis $\mathscr{H}_1$ is favoured for both injections, i.e. the data contains a scalar-polarised GW present at the expected frequencies within the detector's sensitivity band. The Bayes factors for the zero-noise and Gaussian noise injections are $\log\mathscr{B}^{\text{S}}_{\text{N}} \sim 16771$ and $\log\mathscr{B}^{\text{S}}_{\text{N}} \sim 16127$, and $\log\mathscr{B}^{\text{S}}_{\text{N}} \sim 47$ and $\log\mathscr{B}^{\text{S}}_{\text{N}} \sim 15$ for the (11) and (22) modes respectively. Finally, in Fig. 4.6.2,

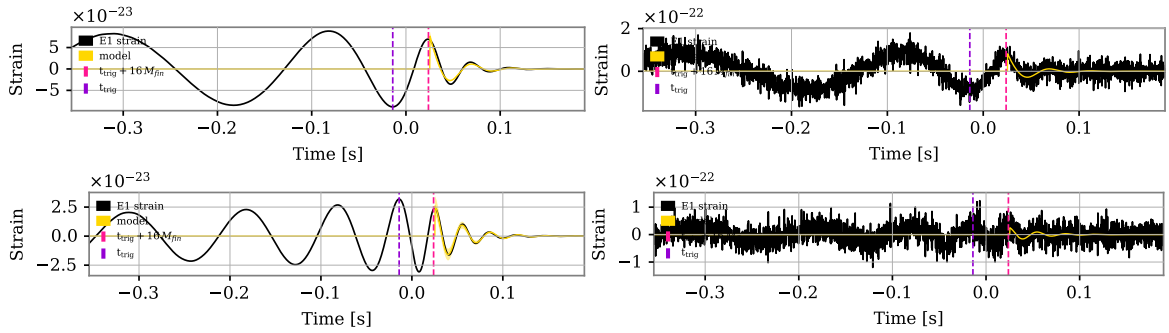


Fig. 4.6.1 Reconstructed waveforms for (11) (top) and (22) (bottom) modes for the scalar field for an injection into the Einstein Telescope. The left panel illustrates zero-noise injections and the right panel Gaussian-noise injections. The yellow line shows the recovered damped sinusoid model for each of the modes (see the main text for the details), the dashed purple and pink lines show the trigger-time (defined as the reference time in the reference detector) and ringdown start time respectively. For more discussion see Section 4.6.2.

we demonstrate the effect of Gaussian noise on the estimation of the modes' amplitudes and phases. Overall, with the source parameters of our choice we conclude that Gaussian noise does not compromise our ability to measure scalar polarisation, neither does it introduce significant biases in recovering the modes.

As we have seen in Section 4.5.1, for a fixed set of coupling parameters a_0 and β_0/m_1^2, larger total masses or more extreme mass ratios are needed to achieve higher SNRs at a given distance. From the observational point of view, the astrophysical population statistics for BBH systems allow for a rather faint probability of either placing stringent bounds on EsGB or making a direct detection, based on the scalar ringdown signal of a single BBH source, even with a 3G/XG detector. Having multiple detectors in the network and combining information from multiple BBH events across a wide mass range will improve our overall sensitivity to the consistent presence of such signals. As the rate of BBH events with SNR > 100 in the next-generation network is expected to reach $\mathcal{O}(10^2 - 10^3)$ per year [319], joint information from multiple events, even if they may be weak, will statistically improve the confidence of detecting a scalar signal as well as the precision of the inference by roughly a factor of $\sim \sqrt{n}$, n being the number of detected scalar signals [320]. While the presence of scalar polarisation in the ringdown spectrum will be a smoking gun effect (unlike the inspiral dephasing), indicating the existence of a fundamental scalar field, more care will be needed in disentangling this weak effect from noise artifacts and other systematics.

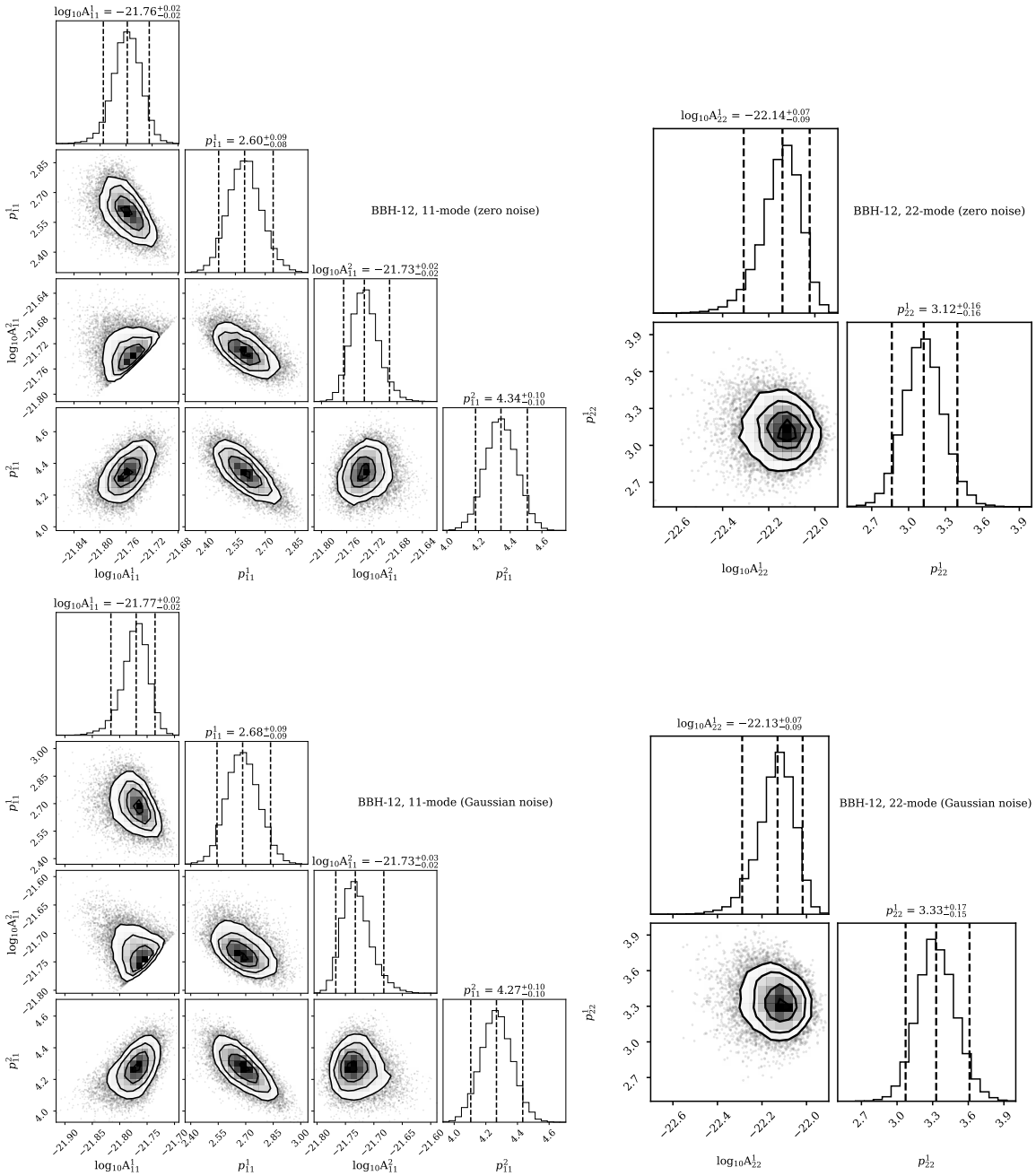


Fig. 4.6.2 Joint posterior distributions for the amplitudes and phases recovered for the (11) and (22) modes. The upper panel shows the parameters for the zero-noise injections and the lower panel for the Gaussian noise injections. The upper and lower limits on the estimated parameters lie within the 90% confidence interval. Parameter estimation from both injections clearly demonstrates that noise does not bias the recovered amplitudes and phases significantly. For more discussion see Section 4.6.2.

4.7 Conclusion

Through the presence of a conformal coupling to matter, black hole binaries in EsGB gravity emit gravitational waves that have a scalar polarisation. The family of theories we consider in this work is controlled by two coupling parameters: the Gauss-Bonnet coupling β_0 and the conformal coupling a_0, which both impact the strength of the scalar-polarised gravitational wave. We have studied the extent to which these couplings could be constrained through gravitational wave observations of the scalar polarisation during binary black hole ringdown. By exploring the parameter space in the range of validity of our couplings, and calculating respective signal-to-noise ratios, we conclude that the scalar polarisation has a low chance of being detected. There is a stronger possibility of detection with next generation detectors like the Einstein Telescope, targeting more asymmetric binary progenitors, given the observed amplification in the scalar polarisation amplitude for those systems in our NR simulations. Furthermore, future observations with LISA [321] may allow for more precise measurements of ringdown from extreme mass-ratio inspirals, although the much higher mass range that LISA will probe may not be favourable for sourcing sufficiently strong scalar modes in theories like the ones studied here. The SNR is greatly dependent on the value of the dimensionless EsGB parameter, β_0/m_1^2. Even at the largest allowed theoretical value for the dimensionless coupling ($\beta_0/m_1^2 \sim 0.2$), one would need to have a total mass of roughly $\gtrsim 50M_\odot$ and a fairly asymmetric mass ratio ($q \sim 1/2$) in order for there to be a detection with a future generation GW detector. For smaller values of β_0/m_1^2, the strength of the signal drops below the detectability threshold for any inspiral scenario we have considered, even for the Einstein Telescope. Given the present observational constraint of $\sqrt{\beta_0} \lesssim 1.18$km, and that $M_\odot \sim 1.5$km in geometrised units, detecting a scalar polarisation in a $50M_\odot$ event requires the smaller mass black hole to have a mass of $\sim 2.5M_\odot$ in order for a competitive constraint on β_0 to be possible from a ringdown measurement with the Einstein Telescope.

The most stringent constraint on most modified theories of gravity comes from the inspiral, through measurements of the phase of the gravitational wave signal [226, 227]. This being said, a measurement of the inspiral phase does not completely determine the nature of a potential deviation from GR, as the dephasing could come from the emission of energy in other energy channels beyond (for example) that of a gravitational scalar field. Measuring the ringdown signal provides a complementary test to the measurement of the inspiral phase.

Apart from performing a targeted test on the GW data for signs of our EsGB model, the method that we propose here can be applied to a more general setting. EsGB with a conformal scalar coupling in its decoupling limit [322, 323] is a prime example of a well-motivated theory, in which the spin-0 QNMs of the Kerr metric are excited and observed via radiation of scalar GWs. Since back-reaction can be neglected in the limit of a small

coupling β_0/m_1^2, part of the scalar quasinormal mode spectrum is identical to that of the spectrum of a (massless) scalar around a Kerr black hole [256, 289]. More generally, any alternative theory featuring an additional scalar field that couples to the physical metric will also radiate spin-0 QNM frequencies, provided that the theory respects the "no-back-reaction" property (i.e. to leading order, the GR sector determines the background metric and is driving the dynamics). In short, the general strategy amounts to using the information from the observed tensorial QNM frequencies to measure the remnant BH parameters, fixing the spin-0 QNM frequencies, and subsequently searching for the presence of any residual scalar GW signal on those frequencies, while being agnostic about the amplitude of each mode. The mode amplitudes are sensitive to the details of a given theory, since the field equations will determine how strongly each mode is sourced from the initial perturbation. Therefore, following the detection of a scalar signal, measurements of the relative mode amplitudes, combined with measurements of the progenitor parameters, will narrow down the specifics of the theory and its couplings. A similar approach could also cover theories featuring a gravitational vector field. A thorough analysis of this strategy is beyond the scope of this thesis.

There are several more directions for future work. We have only considered the impact of the scalar polarisation on the ringdown; it would be interesting to see if stronger constraints could be placed on β_0 and a_0 from polarisation measurements of the inspiral waveform. We have solved for the equations of motion of EsGB gravity in the decoupling limit. While this approximation has been shown to be accurate for modeling the scalar waveform in EsGB gravity, at least at leading order and during the inspiral phase of evolution (and ignoring the effects of dephasing) [256], it would be interesting to compare it to full solutions to EsGB gravity [78, 92, 260]. It will also be important to extend our study to spinning progenitors and see whether the scalar mode amplitudes' dependence on spins follows a functional form similar to that of the tensorial modes [324, 325]. Finally, while we have argued that EsGB gravity with a conformal scalar coupling to the metric may give the largest scalar polarisation signal for black hole binaries among scalar-tensor gravity theories, it would be interesting to numerically model other modified theories of gravity featuring scalar or vector-polarised gravitational waves and devise similar targeted tests.

Appendix

Appendix 4.A Convergence testing and error estimation

4.A.1 Gravitational and scalar waveforms

In this Section we follow the methodology of Ref. [276]. We start with our results on the convergence of the code and the discretisation error due to finite resolution for simulation configuration `BBH-11`. We use $\Delta x_{\rm high} = 1/128M$, $\Delta x_{\rm med} = 1/96M$ and $\Delta x_{\rm low} = 1/80M$ on the finest level of high, medium and low resolution runs respectively. We note that that the results presented in the main text were obtained from evolving the higher resolution configuration. The order of convergence is estimated for the amplitude and the phase of Ψ_4

$$\Psi_{4,lm} = \Psi^A_{4,lm} e^{i\Psi^\phi_{4,lm}}. \tag{4.51}$$

In Fig. 4.A.1, where we have already multiplied the difference between medium and high resolutions by an appropriate factor, we plot the convergence order for the amplitude and the phase of Ψ_4. The convergence factor of order n for a given quantity τ is calculated by its difference at low/medium and medium/high resolutions

$$Q_n = \frac{\tau_{\rm low} - \tau_{\rm med}}{\tau_{\rm med} - \tau_{\rm high}}. \tag{4.52}$$

In the continuum limit the truncation error typically approaches zero as a power of the discretisation parameter Δx, that is for a given approximation error of order n

$$\lim_{\Delta x \to 0} \tau_{\Delta x} = \Delta x^n \times \text{const.} \tag{4.53}$$

Therefore, in the continuum limit the convergence factor reduces to

$$Q_n = \frac{\Delta x^n_{\rm low} - \Delta x^n_{\rm med}}{\Delta x^n_{\rm med} - \Delta x^n_{\rm high}}. \tag{4.54}$$

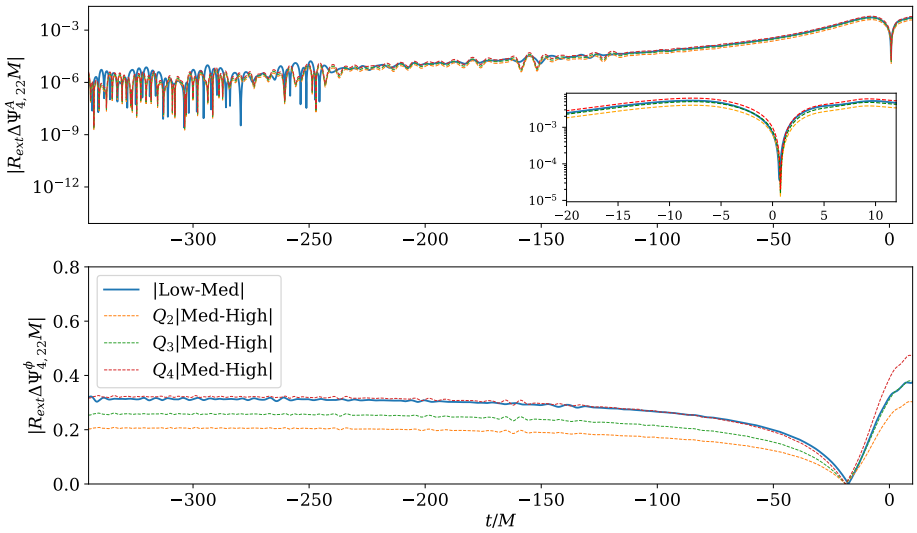


Fig. 4.A.1 Convergence of $\Psi_{4,22}$ extracted at $R_{\rm ext} = 110M$ for the BBH-11 configuration. *Top*: Convergence of the amplitude, $\Psi^A_{4,lm}$. The difference for medium/high resolutions is rescaled according to second and third orders of convergence. The inset shows an interval around the merger. *Bottom*: Convergence of the phase, $\Psi^\phi_{4,lm}$. The difference for medium/high resolutions is rescaled according to second, third and fourth orders of convergence.

For the amplitude of Ψ_4 we find the convergence order to be between second and third order in the inspiral, which then increases to between third and fourth in the late inspiral and merger. For the phase of Ψ_4 we find convergence consistent with fourth order dropping to third around merger. We perform a similar analysis for the amplitude of the scalar field amplitude and find the order of convergence fluctuating between second and third as indicated in the left panel of Fig. 4.A.2.

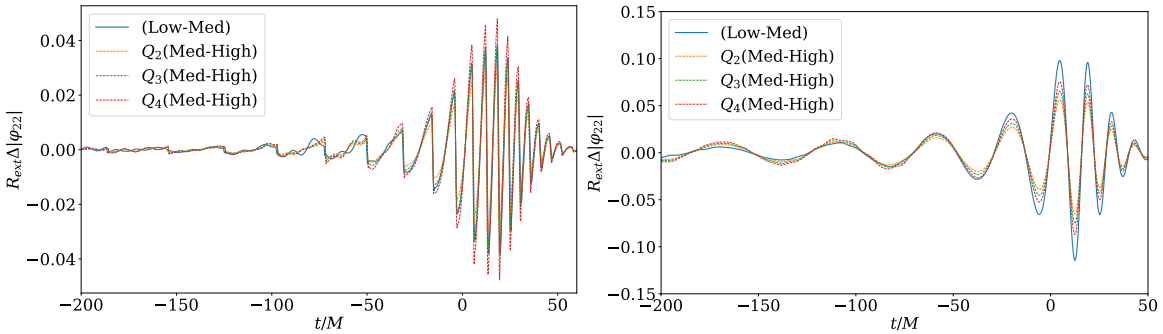


Fig. 4.A.2 *Left:* Convergence of the amplitude of φ_{22} extracted at $R_{\rm ext} = 110M$ for the BBH-11 configuration. The difference for medium/high resolutions is rescaled from second to fourth orders of convergence. *Right:* Same as left but for the BBH-12 configuration.

To estimate the discretisation error for the amplitude e_A, we measure the relative percentage error between the finest resolution result and Richardson extrapolation, while for the phase error e_ϕ we simply give it as the difference

$$e_A = \frac{|\Psi^A_{4,lm} - \Psi^{A,\text{Richardson}}_{4,lm}|}{\Psi^{A,\text{Richardson}}_{4,lm}} \times 100\%, \tag{4.55}$$

$$e_\phi = |\Psi^\phi_{4,lm} - \Psi^{\phi,\text{Richardson}}_{4,lm}|. \tag{4.56}$$

Finally, to estimate the error due to finite-radius extraction we compute a given radiated quantity at several finite extraction radii and extrapolate to infinity by fitting a polynomial in $1/r$. We use first order extrapolation of polynomial order $n = 1$

$$\Psi^{i,n=1}_{4,lm} = \Psi^i_{4,lm} + \frac{\text{const}}{r}. \tag{4.57}$$

We then compute the corresponding errors for the amplitude and phase as given in Eqs. (4.55) and (4.56), where Richardson extrapolated quantities are now replaced by the extrapolated quantities prescribed by Eq. (4.57).

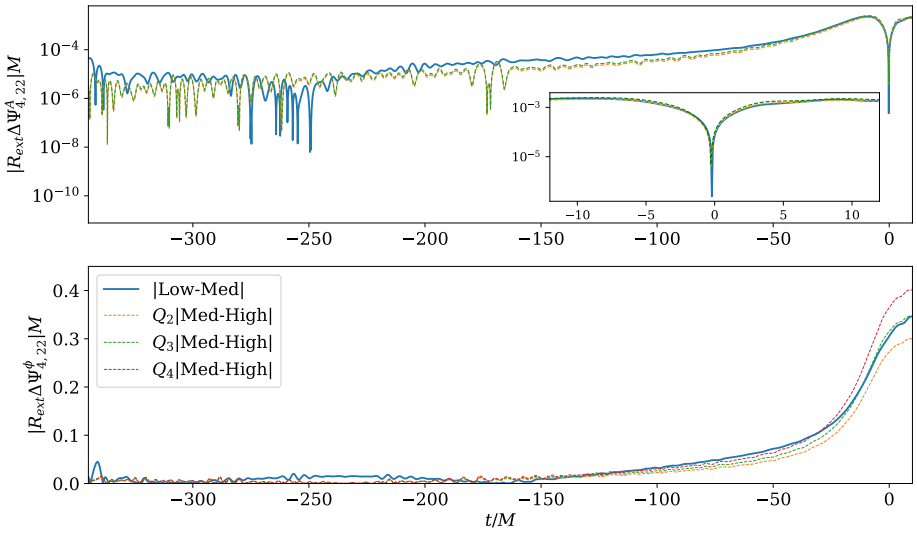


Fig. 4.A.3 Convergence of $\Psi_{4,22}$ extracted at $R_{\text{ext}} = 110M$ for the `BBH-12` configuration. *Top*: Convergence of the amplitude, $\Psi^A_{4,lm}$. *Bottom*: Convergence of the phase, $\Psi^\phi_{4,lm}$.

Additionally, we present convergence results for the `BBH-12` configuration, where we now use $\Delta x_{\text{high}} = 1/128M$, $\Delta x_{\text{med}} = 1/112M$ and $\Delta x_{\text{low}} = 1/96M$ on the finest level of high, medium and low resolution runs respectively. We present our results in Fig. 4.A.3 and the right panel of Fig. 4.A.2 for the gravitational (22) mode of Ψ_4 and the scalar field amplitude,

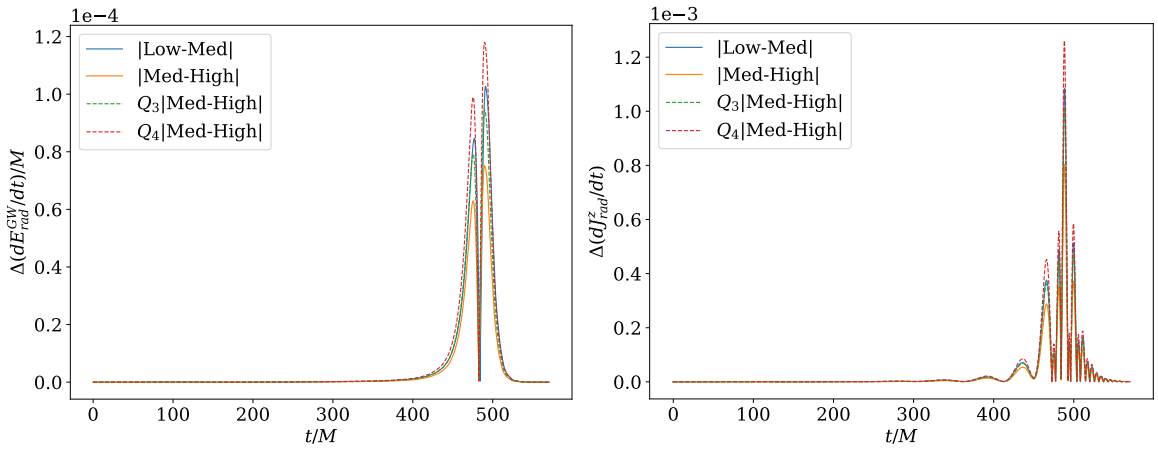


Fig. 4.A.4 *Left*: Convergence of the energy flux extracted at $R_{\rm ext} = 110M$ for `BBH-11`. The difference for medium/high resolutions is rescaled according to third and forth orders of convergence. *Right*: Same as left but the diagnostic quantity is the angular momentum flux in the z-direction extracted at $R_{\rm ext} = 110M$ for `BBH-11`.

respectively. We find similar results as for the `BBH-11` configuration. We observe between second and third order of convergence in the amplitude and between third and fourth order of convergence for the phase. The convergence order for the scalar field amplitude is second order in the inspiral and fourth order in the merger and ringdown.

4.A.2 GW Energy and angular momentum flux convergence

Finally, we present convergence plots for `BBH-11` of the GW energy flux and GW angular momentum flux computed with the use of Eqs. (4.32) and (4.33), respectively. We employ the same set of resolutions as in Section 4.A.1 and compute the total radiated energy and the total angular momentum flux, as described in Section 4.3.3 of the main text.

From Fig. 4.A.4, we conclude that both the energy flux and angular momentum flux have an order of convergence between third and fourth. By using third order Richardson extrapolation, we estimate the error of the final mass and spin to be 0.01% and 0.05%, respectively.

Appendix 4.B Code Validation

In this Section we address the tests on the implemented Gauss-Bonnet term in GRChombo. First of all, we perform a self-convergence test by evolving a scalar field on a Schwarzschild background. We use $\Delta x_{\rm high} = 1/48M$, $\Delta x_{\rm med} = 1/40M$ and $\Delta x_{\rm low} = 1/32M$ on the coarsest

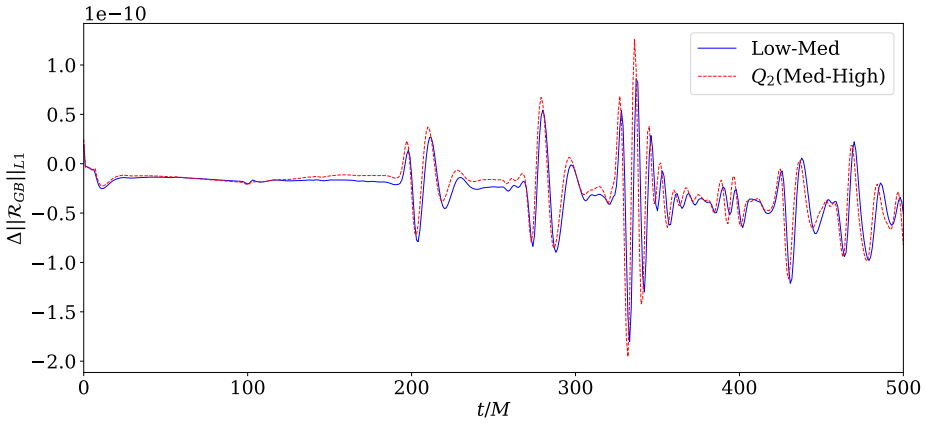


Fig. 4.B.1 Self convergence of the $L1$-norm normalised over the total volume for the Gauss-Bonnet term. The difference for medium/high resolutions is rescaled according to the second order convergence.

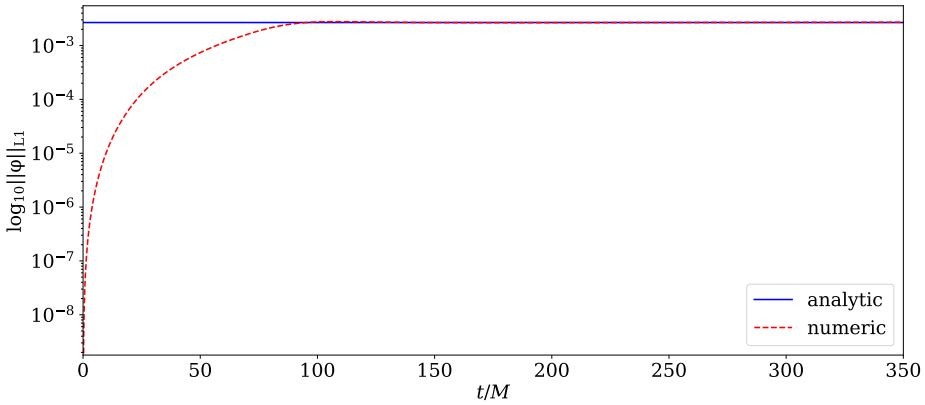


Fig. 4.B.2 Comparison of the $L1$-norm of the scalar field profile normalised over total volume for numeric and analytic solutions.

level of high, medium and low resolution runs, respectively. Figure 4.B.1 demonstrates our results and overall we find second-order convergence.

Finally, we compare our numerical result for a scalar field evolved on a Schwarzschild background to the analytic solution in Painlevè-Gullstrand (PG) coordinates. By starting with the scalar field equation

$$\Box\varphi + \beta_0 \mathscr{R}_{GB} = 0, \tag{4.58}$$

we impose regularity of $\partial_r\phi$ at the horizon $r = 2M$ and the fall-off of the scalar field at infinity, $\lim_{r\to\infty}\phi = 0$. We find an analytic solution given in terms of PG coordinates by

$$\varphi(x) = \frac{2\beta_0}{M}\left(\frac{1}{x} + \frac{1}{x^2} + \frac{4}{3x^3}\right), \qquad \text{where } x = \frac{r}{M}. \tag{4.59}$$

We then calculate the $L1$-norm for the analytic and numerical solutions and normalise it over the total volume. Figure 4.B.2 shows good agreement between solutions after $t \sim 100M$, when the scalar has grown and settled to a constant value.

Appendix 4.C Quasi-normal modes of a Kerr black hole in GR

In Section 4.4 and in particular Eqs. (4.41)-(4.42), we utilize QNMs of a Kerr black hole in GR to perform numerical fits to our data. In Table 4.C.1 we present the values of the frequencies (ω_{lmn}) and damping times (τ_{lmn}), of the gravitational quasinormal modes of the remnant black hole. These modes were computed using the QNM package [297].

Run	(lmn) mode	$\omega_{lmn}^{\text{Kerr,scalar}}$	$\tau_{lmn}^{\text{Kerr,scalar}}$	$\omega_{lmn}^{\text{Kerr,grav}}$	$\tau_{lmn}^{\text{Kerr,grav}}$
BBH-11	(220)	0.6526	11.3627	0.5291	12.3320
	(440)	1.2083	11.4250	1.1356	11.8200
BBH-23	(110)	0.3730	11.1043	–	–
	(111)	0.3570	3.6328	–	–
	(220)	0.6434	11.2444	0.5197	12.2165
	(330)	0.9159	11.2855	0.8246	11.8901
	(440)	1.1892	11.3026	1.11690	11.6904
BBH-12	(110)	0.3654	10.9405	–	–
	(111)	0.3485	3.5715	–	–
	(220)	0.6279	11.0667	0.5043	12.0431
	(330)	0.8923	11.10375	0.8016	11.6951
	(440)	1.1574	11.1192	1.0858	11.4945

Table 4.C.1 QNMs of the remnant Kerr BH in GR, used in the fitting procedure described in Section 4.4.

Chapter 5

Boson stars in general relativity

5.1 Introduction

Perhaps no concept is more central to modern physics than that of the field. Fields are building blocks of our universe and they play a key role in most paradigms of modern cosmology and theories that extend the Standard Model of particle physics. In recent years, in light of the discovery of the Higgs Boson, inflationary [326–328] and dark matter (DM) models [329, 330] have given an important role to scalar fields, which also naturally arise from string theory [331]. If given mass, scalar fields coupled to the gravitational field can theoretically form astrophysical, compact, star-like objects. One of the examples of such stars are *boson stars* (BSs) described by a complex, massive scalar field; see Refs. [96, 332] for a review. The constituents of a BS are bosonic particles, or bosons (hence, the name), whose mass in the range of $10^{-22} - 10^{-3}$eV has been considered in cosmological and astrophysical settings[1] [333, 334]. The formation channel of boson stars has been discussed in Ref. [335] through a mechanism referred as *gravitational cooling*, where starting from initial Gaussian distributions, the scalar field collapses and settles down to a bound state. Similar formation mechanisms have been discussed in the non-relativistic regime for Bose stars (packets of Bose-Einstein condensates bound by self-gravity) in Refs. [336–338], where the presence of dark matter bosons in the dark matter halos of the early Universe can lead to their *condensation* into self-gravitating compact objects. Finally, BSs may be seeded at early times due to large field fluctuations [339]. While the existence of fermionic compact objects – such as neutron stars or white dwarfs – is supported by a plethora of observational evidence (e.g. [173, 340, 341]), the search for localized solitons[2] made of bosons is still ongoing.

[1] Although bosonic fields with the mass $\leq 10^{-22}$eV may account only for some portion of the dark matter of the Universe [333].

[2] A soliton describes a wave packet solution that maintains its shape during propagation.

Due to their (potentially) very high compactness, BSs belong to the category of *exotic compact objects*, which we have reviewed in Section 1.3.2, and are even regarded as candidates for ultracompact BH mimickers in the sense of possessing a light ring [342, 343]. Despite BSs being called BH mimickers, it is important to note that they also have several distinct features, therefore presenting direct ways through which one may distinguish them from BHs. In particular, BSs (i) do not have a horizon; (ii) have a non-zero tidal deformability [344, 345]; and (iii) can have spins exceeding the Kerr bound [346]. The lack of the horizon may lead one to believe that BSs must be similar to neutron stars. However, this is not entirely true. Common to most stellar structures, like NSs, BSs have a maximum mass, however they do not have a surface; instead the scalar field extends to infinity and falls off exponentially. Furthermore, in a recent study [347], rotating BSs have been shown to possess a different universal relation between the moment of inertia, the dimensionless angular momentum and the quadrupole moment, than that of NSs. Therefore, thanks to their comparatively simple and mathematically regular nature but rich phenomenology, BSs are ideal proxies to study fundamental properties of compact objects and challenge our understanding of their nature. In this spirit, BSs are also intriguing probes in our search for evidence of extra degrees of freedom in theories of gravity extending general relativity (GR). From an observational viewpoint, BSs have been suggested as alternatives to primordial BHs [348] and supermassive BHs in the centres of galaxies [349]. Last but not least, BSs may contribute to the dark-matter sector of the universe and are an important target for gravitational-wave (GW) observations with the LIGO-Virgo-KAGRA (LVK) network [243, 344, 350–352], as well as future detectors like the Einstein Telescope and the Laser Interferometer Space Antenna [353, 354].

This Chapter is structured as follows. In Section 5.2 we review the recent progress made in the BS literature and in Section 5.3 we present their formulation. Next, we describe the methods used to construct spherically symmetric BS solutions in Section 5.4.1 and discuss various diagnostics we utilise to study these models in Section 5.5. We present some examples of BS solutions in Section 5.6 and finally in Section 5.7, we review the required conversion from areal to isotropic radius, which we employ later in binary simulations of boson-star mergers.

5.2 History of boson stars

In the absence of gravity, the closest cousins to BSs are the so-called *Q-ball* solutions [355] that can form in the early Universe and contribute to dark matter [356]. The first attempt at adding gravity and constructing self-gravitating fields was done by Wheeler, who proposed

the existence of *gravitational electromagnetic entities* or *geons* [357]; unfortunately they were soon found to be unstable. Only a decade later, Kaup's pioneering work [62] showed the existence of equilibrium solutions to the Einstein-Klein-Gordon equations. Instead of focusing on the electromagnetic field, Kaup proposed to minimally couple a massive complex scalar field to gravity, thus forming self-gravitating configurations, dubbed *Klein-Gordon geons*. Originally these configurations were devised for fundamental scalar (spin 0) fields [358, 359] and later on extended to vector (spin 1) fields (aka *Proca stars*) [63, 360–370] and high-spin fields [371, 372]. The nature of the scalar field can be real – resulting in potentially long lived but not strictly stable compact objects commonly referred to as *oscillatons* (OSs) [140, 373–375] – or complex for BSs. The first calculations of BSs employed non-interacting massive scalar fields, resulting in the so-called *mini boson-stars*. Extensive studies over the years, however, have uncovered a rich variety of other BS models, most notably through more elaborate scalar potential functions: self-interacting [376, 377], solitonic [71, 378], axionic potentials [334, 375, 379] and many more. The self-interaction terms lead to significantly more compact BSs, comfortably exceeding the compactness of neutron stars, and also increase the maximum mass BSs may acquire in dynamic scenarios without forming a black hole (BH) [376, 380]. Further BS models include charged stars [381, 382], BSs comprised of multi-fields [383, 384] and rotating models [385, 386] where the nature of the spin is quantised. The stability of various bosonic configurations has been addressed in Refs. [387–391] and confirmed by numerous numerical relativity (NR) simulations [142, 374, 392, 393].

5.3 Formulation

Mathematically, boson stars (BSs) are localized, soliton-like solutions of the coupled system of the Einstein and general relativistic Klein-Gordon equations for a complex scalar field φ. In this Chapter from now on, we set $\hbar = c = 1$. The action is then given by the Einstein-Hilbert term for four-dimensional gravity and a minimally coupled complex scalar field,

$$S = \int \sqrt{-g} \left\{ \frac{1}{16\pi G} R - \frac{1}{2} \left[g^{\mu\nu} \nabla_\mu \bar{\varphi} \nabla_\nu \varphi + V(\varphi) \right] \right\} d^4x, \tag{5.1}$$

where $V(\varphi)$ is the scalar potential. Varying this action, we recover the Einstein and matter evolution equations

$$G_{\alpha\beta} = 8\pi G T_{\alpha\beta}, \tag{5.2}$$

$$\nabla^\mu \nabla_\mu \varphi = \frac{\mathrm{d}V}{\mathrm{d}|\varphi|^2} \varphi, \tag{5.3}$$

and the energy-momentum tensor reads

$$T_{\alpha\beta} = \partial_{(\alpha}\bar{\varphi}\partial_{\beta)}\varphi - \frac{1}{2}g_{\alpha\beta}\left[g^{\mu\nu}\partial_\mu\bar{\varphi}\partial_\nu\varphi + V(\varphi)\right]. \tag{5.4}$$

The simplest potential one can consider, and the one that has been studied in the original work by Kaup, is that of a mini BS

$$V_{\rm mini}(|\varphi|) = \mu^2|\varphi|^2, \tag{5.5}$$

where μ is the mass of the bosonic scalar field. One can then proceed to add higher order terms with powers of $|\varphi|^2$. Following this logic we arrive at *repulsive* [394] and *solitonic* [380] potentials respectively

$$V_{\rm rep}(|\varphi|) = \mu^2|\varphi|^2 + \lambda_4|\varphi|^4, \tag{5.6}$$

$$V_{\rm sol}(|\varphi|) = \mu^2|\varphi|^2\left(1 - 2\frac{|\varphi|^2}{\sigma_0^2}\right)^2, \tag{5.7}$$

where λ_4 and σ_0 are self-interaction terms of the two individual potentials[3]. The name of the repulsive potential requires further explanations. Typically repulsive potentials are those with a positive first correction beyond the mass-term, which in the context of a binary system means that increasing nonlinear self-interactions increases the potential energy. This effect is the opposite for attractive potentials, such as the solitonic one. Note that both repulsive and solitonic potential functions include the case of *mini BSs* in the respective limits $\lambda_4 \to 0$ and $\sigma_0 \to \infty$. Furthermore, note that the solitonic potential has multiple roots in $|\varphi|$: $|\varphi| = 0$, which corresponds to the true vacuum state and $|\varphi| = \sigma_0/\sqrt{2}$, which represents a "false" or "degenerate" vacuum state. We graphically illustrate the features of these three potentials in Fig. 5.3.1 for two solitonic potentials with $\sigma_0 = 0.2$ and $\sigma_0 = 0.4$, the case of mini BSs and a repulsive potential with $\lambda_4 = 50$ over the range $A := |\varphi| \in [0, 0.2]$. We clearly see the false vacuum states for $\sigma_0 = 0.2$ and also note that in this range of $|\varphi|$, the potential values systematically increase in the order $\sigma_0 = 0.2$, $\sigma_0 = 0.4$, the mini BS limit and $\lambda_4 = 50$.

The solitonic potential in Eq. (5.7) can result in highly compact stars and produces some particularly interesting solutions; for example, in the case of $\varphi \sim \sigma_0/\sqrt{2}$ thin-wall configurations have been found for sufficiently small σ_0, where the scalar field profile acquires a shape almost like a Heaviside function [395]. The resulting soliton profile is then split into three different regions: the interior solution where $\varphi \sim \sigma_0/\sqrt{2}$ (i.e. a false vacuum

[3] In natural units, λ_4 is dimensionless, whilst σ_0 has units of the Planck mass, $M_{\rm pl}$.

state), a transition region with a sharp drop from $\varphi \sim \sigma_0/\sqrt{2}$ to $\varphi = 0$ and the exterior true vacuum state $\varphi = 0$.

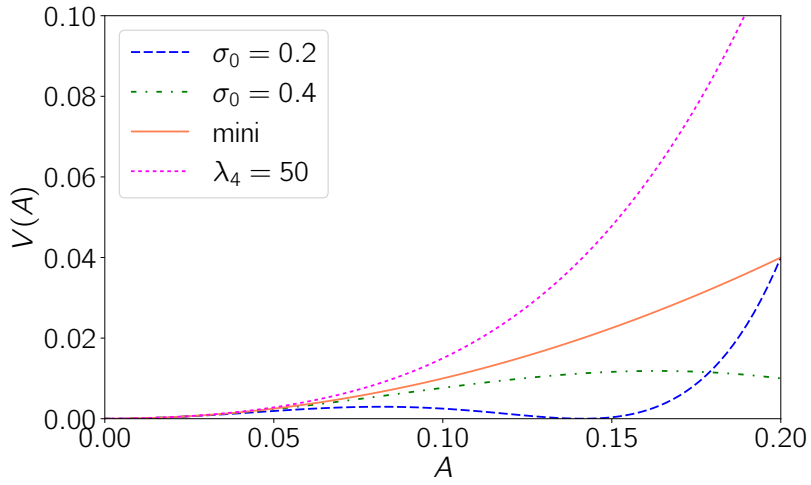


Fig. 5.3.1 Four example cases of the BS scalar potential function $V(A)$, where $A := |\varphi|$, defined in Eqs. (5.5–5.7). Here we set $\mu = 1$ for simplicity, however the BS solution can be rescaled appropriately for any value of μ following scaling arguments of Eqs. (5.17) and (5.20). The non-interacting potential for mini BSs is recovered for $\sigma_0 \to \infty$ or $\lambda_4 = 0$. Note the false vacuum state for solitonic potentials and the systematic increase of $V(A)$ from small σ_0 to the mini-BS limit and larger λ_4.

5.4 Equilibrium, Spherically Symmetric Solutions

5.4.1 Equations of motions

In this Section we describe how we model single BSs as stationary solutions in spherical symmetry. First, we decompose the scalar field into its amplitude $A(r)$ and constant frequency ω, so that

$$\varphi = A(r)e^{i\omega t}. \tag{5.8}$$

Using polar slicing and radial gauge, we write the line element as

$$ds^2 = -\alpha^2 dt^2 + X^2 dr^2 + r^2 d\Omega^2, \tag{5.9}$$

where α and X are both functions of r. Plugging the line-element into Eq. (5.3), we arrive at the following equations

$$\frac{\partial_r \alpha}{\alpha} = \frac{X^2-1}{2r} + 2\pi G r \left[(\partial_r A)^2 + \frac{X^2}{\alpha^2}\omega^2 A^2 - X^2 V \right], \tag{5.10}$$

$$\frac{\partial_r X}{X} = -\frac{X^2-1}{2r} + 2\pi G r \left[(\partial_r A)^2 + \frac{X^2}{\alpha^2}\omega^2 A^2 + X^2 V \right], \tag{5.11}$$

$$\partial_r^2 A = -\frac{X^2\omega^2}{\alpha^2}A + \frac{\partial_r X}{X}\partial_r A - \frac{\partial_r \alpha}{\alpha}\partial_r A - 2\frac{\partial_r A}{r} + X^2 \frac{\mathrm{dV}}{\mathrm{d}|\varphi|^2} A. \tag{5.12}$$

Now let us introduce the following auxiliary variables

$$m \coloneqq \frac{r}{2}\left(1 - \frac{1}{X^2}\right), \quad \Phi \coloneqq \ln(\alpha) \quad \text{and} \quad \eta \coloneqq \frac{\partial_{\mathrm{r}} \mathrm{A}}{\mathrm{X}}, \tag{5.13}$$

where m is the mass function as $X^2 = (1-2m/r)^{-1}$ (reminiscent of the Schwarzschild solution). The equations for the auxiliary variables are then found to be

$$\partial_r \Phi = \frac{X^2-1}{2r} + 2\pi G r \left[(\partial_r A)^2 + \frac{X^2}{\alpha^2}\omega^2 A^2 - X^2 V \right], \tag{5.14}$$

$$\partial_r m = 2\pi G r^2 \left[\frac{(\partial_r A)^2}{X^2} + \frac{\omega^2 A^2}{\alpha^2} + V \right], \tag{5.15}$$

$$\partial_r \eta = -2\frac{\eta}{r} - \eta \frac{\partial_r \alpha}{\alpha} + X\left(\frac{\mathrm{dV}}{\mathrm{d}|\varphi|^2} - \frac{\omega^2}{\alpha^2} \right) A. \tag{5.16}$$

Note that two scales are present in our equations of motion: the scalar field mass μ and the gravitational constant G. Using these constants, we rescale all our dimensional variables using

$$\hat{t} \coloneqq \mu t \quad \hat{r} \coloneqq \mu r, \quad \hat{m} \coloneqq \mu m, \quad \hat{A} \coloneqq \sqrt{G} A, \quad \hat{\omega} \coloneqq \frac{\omega}{\mu}, \quad \hat{\eta} = \frac{\sqrt{G}}{\mu}\eta. \tag{5.17}$$

These dimensionless variables can be converted back into SI units using

$$\hbar c = 1.97327 \times 10^{-10}\,\mathrm{eV\,km}, \tag{5.18}$$

so that

$$\frac{\mu}{\hbar c} = \frac{\mu}{1.97327 \times 10^{-10}\,\mathrm{eV\,km}}. \tag{5.19}$$

Hence, if we set $\hbar = 1 = c$, a rescaled radius $\hat{r} = \mu r$ and frequency $\hat{\omega} = \omega/\mu$ translate into SI units according to

$$\begin{aligned} r &= \frac{\hat{r}}{\mu} = \left(\frac{\mu}{\hbar c}\right)^{-1} \hat{r} = \hat{r} \left(\frac{\mu}{1.97327 \times 10^{-10}\,\mathrm{eV}}\right)^{-1} \mathrm{km}\,, \\ \omega &= \frac{\mu}{\hbar}\hat{\omega} = \hat{\omega}\,\frac{\mu}{6.58212 \times 10^{-16}\,\mathrm{eV}}\, s^{-1}\,, \end{aligned} \tag{5.20}$$

and likewise for the mass m and other dimensional quantities. In words, for a BS scalar mass $\mu = 1.97327 \times 10^{-10}\,\mathrm{eV}$, the numerical value of our radial coordinate gives the BS radius in km. For other scalar masses, the radius scales accordingly, becoming larger for smaller scalar masses and vice versa. The scalar field amplitude, in turn, is measured in units of the Planck mass, $A = \hat{A} M_{\mathrm{Pl}}$. From now on, we will work with dimensionless variables only and we will drop the caret in their notation for simplicity.

Our final equations of motion then become

$$\partial_r \Phi = \frac{X^2 - 1}{2r} + 2\pi r X^2 \left[\eta^2 + \omega^2 e^{-2\Phi} A^2 - V\right], \tag{5.21}$$

$$\frac{\partial_r X}{X} = -\frac{X^2 - 1}{2r} + 2\pi r X^2 \left[\eta^2 + \omega^2 e^{-2\Phi} A^2 + V\right], \tag{5.22}$$

$$\partial_r A = X\eta, \tag{5.23}$$

$$\partial_r \eta = -2\frac{\eta}{r} - \eta\,\partial_r \Phi + X\left(\frac{\mathrm{dV}}{\mathrm{d}|\varphi|^2} - \omega^2 e^{-2\Phi}\right) A. \tag{5.24}$$

5.4.2 Boundary conditions

To complete the system of equations given in Eqs. (5.21)–(5.24), we impose the following boundary conditions

$$A(0) = A_{\mathrm{ctr}}, \quad X(0) = 1, \quad \eta(0) = 0, \quad A(\infty) = 0, \quad \Phi(\infty) = 0, \tag{5.25}$$

where A_{ctr} is the central amplitude of the scalar field at the origin, $X(0) = 1$ ensures the spacetime has no conical singularity, $\eta(0) = 0$ – a finite density at the origin, $A(\infty) = 0$ – a regular solution and finally $\Phi(\infty) = 0$ compatible with asymptotic flatness. No boundary condition is imposed on the frequency ω, as in fact it remains constant and so our task simplifies to solving an eigenvalue problem given by Eqs. (5.21)–(5.24) with boundary conditions (5.25).

5.4.3 Asymptotic behaviour

The first step in our analysis of the asymptotic behaviour of the BS solutions is to translate all of the equations of motion into the compactified radial variable $y = 1/r$. This means that now the spatial infinity at $r = \infty$ will be represented by $y = 0$, around which we will be able to perform a series expansion. In the BS literature, the following asymptotic behaviour is usually quoted

$$A \sim \frac{e^{-\sqrt{1-\omega^2}r}}{r}, \tag{5.26}$$

which, however, is only valid in the flat-field regime. In this Section we will step-away from the flat-field limit and consider general curved spacetimes. Inspired by the flat-field form in Eq. (5.26), we propose to extend it to the following relation

$$A \sim y^{\varepsilon+1} e^{-k/y}, \tag{5.27}$$

where ε, k are as yet unspecified parameters and our goal will be to determine them. It is then convenient to re-scale our amplitude and its derivative so that the exponential behaviour is separated out in the following way

$$\sigma := \frac{e^{k/y}}{y^{\varepsilon}} A, \qquad \lambda := -\frac{e^{k/y}}{y^{\varepsilon}} \eta. \tag{5.28}$$

Our equations of motions in the newly re-scaled variables are

$$\partial_y \Phi = -\frac{X^2-1}{2y} - 2\pi \frac{X^2}{y^{3-2\varepsilon} e^{2k/y}} \left[\lambda^2 + \sigma^2 \left(\omega^2 e^{-2\Phi} - V\right)\right], \tag{5.29}$$

$$\frac{\partial_y X}{X} = \frac{X^2-1}{2y} - 2\pi \frac{X^2}{y^{3-2\varepsilon} e^{2k/y}} \left[\lambda^2 + \sigma^2 \left(\omega^2 e^{-2\Phi} + V\right)\right], \tag{5.30}$$

$$\partial_y \sigma = \frac{X\lambda - \sigma\left(k+\varepsilon y\right)}{y^2}, \tag{5.31}$$

$$\partial_y \lambda = \frac{(2-\varepsilon)\, y - k}{y^2} \lambda - \lambda \partial_y \Phi + \frac{X\sigma}{y^2} \left(\frac{\mathrm{dV}}{\mathrm{d}|\phi|^2} - \omega^2 e^{-2\Phi} \right). \tag{5.32}$$

This also translates into the following ordinary differential equation for the mass function

$$\partial_y m = -2\pi \frac{1}{y^{4-2\varepsilon} e^{2k/y}} \left[\lambda^2 + \sigma^2 \left(\omega^2 e^{-2\Phi} + V\right)\right]. \tag{5.33}$$

Note that the factor in Eq. (5.33) for $\partial_y m$ contains an exponential term. This term will go to infinity faster than any other polynomial, therefore any term in the expansion such that

$y^n, n > 1$ will vanish, leaving a series expansion of the mass containing only a constant,

$$m = M. \tag{5.34}$$

Now recalling that $X = (1-2m/r)^{-1/2}$ and imposing the condition $\alpha X = 1$ at infinity as for the Schwarzschild metric, we find that the series expansions for X, α, Φ are as follows

$$X(y) = 1 + My + \frac{3}{2}M^2y^2 + \frac{5}{2}M^3y^3 + ..., \tag{5.35}$$

$$\alpha(y) = 1 - My - \frac{1}{2}M^2y^2 - \frac{1}{2}M^3y^3 + ..., \tag{5.36}$$

$$\Phi(y) = -My - M^2y^2 - \frac{4}{3}M^3y^3 + ... \tag{5.37}$$

In similar fashion, we consider the following series expansions for other variables in Eqs. (5.29)–(5.32),

$$\sigma(y) = \sigma_1 y + \sigma_2 y^2 + ..., \tag{5.38}$$

$$\lambda(y) = \lambda_1 y + \lambda_2 y^2 + ... \tag{5.39}$$

Considering the first order, $\mathscr{O}(y^{-1})$, from Eq. (5.31) for $\partial_y \sigma$ and from Eq. (5.32) for $\partial_y \lambda$, we find

$$-\sigma_1 k + \lambda_1 = 0, \tag{5.40}$$

$$-\sigma_1 \omega^2 - \lambda_1 k + \sigma_1 = 0. \tag{5.41}$$

From above, we directly conclude that

$$\boxed{k^2 = 1 - \omega^2.} \tag{5.42}$$

Next, we consider the next leading order of y^0, where again from Eqs. (5.31) and (5.32), we find

$$(1+\varepsilon)\sigma_1 = M\lambda_1 + \lambda_2 - k\sigma_2, \tag{5.43}$$

$$(1-\varepsilon)\lambda_1 = k\lambda_2 - \sigma_2(1-\omega^2) + 3M\omega^2\sigma_1 - M\sigma_1. \tag{5.44}$$

Rearranging, we arrive at

$$\boxed{\varepsilon = \frac{M(1-2\omega^2)}{\sqrt{1-\omega^2}}.} \tag{5.45}$$

In summary, we find the following asymptotic behaviour of the BS amplitude,

$$\boxed{A \sim \frac{e^{-kr}}{r^{1+\varepsilon}}, \text{ where } \quad k = \sqrt{1-\omega^2}, \quad \varepsilon = \frac{M(1-2\omega^2)}{\sqrt{1-\omega^2}}.} \tag{5.46}$$

Finally, let us illustrate where and how the flat-field asymptotics of Eq. (5.26) go wrong, when used in the presence of gravity. Using the flat-field asymptotic behaviour (or, equivalently, setting $\varepsilon = 0$) leads to the following rescaled scalar variables

$$\sigma^{\text{flat}} := e^{k/y} A\,, \qquad\qquad \lambda^{\text{flat}} := -e^{k/y}\eta\,. \tag{5.47}$$

At $\mathscr{O}(y^{-1})$, the equation for $\partial_y \sigma^{\text{flat}}$ then gives the first ingredient of our result in Eq. (5.46), i.e. $k^2 = 1-\omega^2$. However, as we proceed to consider the next leading contributions at $\mathscr{O}(y^0)$ in the equations for $\partial_y \sigma^{\text{flat}}$ and $\partial_y \lambda^{\text{flat}}$, we arrive at

$$2M\sigma_1^{\text{flat}}(1-2\omega^2) = 0, \tag{5.48}$$

which can only be satisfied when $M = 0$ or when $\omega^2 = 1/2$ with $M \neq 0$. This analysis evidently results in a contradiction, as it postulates that BSs do not exist for frequencies $\omega^2 \neq 1/2$. The inclusion of the non-trivial parameter ε in Eqs. (5.28) avoids this contradiction.

5.4.4 Computing solutions

We use a shooting algorithm to compute single spherically-symmetric BS solutions. We will fix our central amplitude A_{ctr} and 'shoot' for ω until we obtain a regular solution[4]. Our algorithm is based on the observation that typically by starting with almost any ansatz on ω, our numerical integration soon leads to a diverging solution, i.e. $A \to \infty$ at a fixed radius. However, only for a countable number of eigenvalues ω_n, where $n = 0, 1, 2, ...\infty$, the BS solution is regular and the scalar amplitude satisfies the required condition $A(\infty) = 0$. The BS frequencies in fact satisfy the following monotonically increasing relation $\omega_1 < \omega_2 < ... < \omega_n$. The number n also marks the number of zero crossings in the amplitude $A(r)$. When $n = 0$,

[4]Note that an implementation where one fixes ω and shoots for the amplitude, A_{ctr}, is also possible.

the solution is referred to as the *ground* state, while all solutions with $n > 1$ are *excited* states. Below we describe our recipe for finding either of these states of the BS model:

1. Let us denote the true BS frequency by ω. We start by fixing the central amplitude $A_{\rm ctr}$ and initialising the frequency to some number, e.g. $\hat{\omega}_0 = 1$.

2. We use the 4th order Runge-Kutta method to compute the solution and our initial ansatz almost inevitably results in a diverging solution. However, we inspect how many zero crossings the amplitude $A(r)$ has. If there are more zero crossings than expected, from the monotonicity condition on ω_n we conclude that the frequency must be smaller and change our frequency ansatz to $\hat{\omega}_1 = \hat{\omega}_0/2$. Otherwise, we double our frequency ansatz, $\hat{\omega}_1 = 2\hat{\omega}_0$. We repeat this procedure, generating a sequence of $\{\hat{\omega}_i\}$ values. This allows us to construct the interval $[\hat{\omega}_{i-1}, \hat{\omega}_i]$ containing the frequency for which the solution has the desired number of zero-crossings.

3. Once we have the desired interval, we start to narrow it down by applying a bisection algorithm, i.e. we define $\hat{\omega}_{i+1} = (\hat{\omega}_i + \hat{\omega}_{i-1})/2$. If the BS solution has the desired number of zero-crossings, we pick the minimum bound of the new interval to be $\hat{\omega}_{i+1}$; if there are more zero-crossings than expected we set $\hat{\omega}_{i+1}$ to be the maximum of the new interval. We repeat this until the difference between the maximum and minimum frequencies in the interval is $\mathcal{O}(10^{-15})$ and denote the found BS frequency by $\hat{\omega}$.

4. We now recompute our solution with $\hat{\omega}$. Unfortunately, even with this improved BS frequency we will find that the amplitude diverges at large radii. To remedy this behaviour, we first search for the radius before which the amplitude starts to diverge and we find it convenient to use the radius at which $A(r)$ has a local minimum; we denote this radius by $r_{\rm min}$. We then match the integrated solution to the asymptotic behaviour given in Eq. (5.46), by defining our matching radius as 90% of $r_{\rm min}$.

5. The only boundary condition that is not satisfied in our shooting scheme is $\Phi(\infty) = 0$, as our grid does not extend to spatial infinity. Instead, we impose $\alpha^2 X^2 = 1$, a condition of the Schwarzschild spacetime in radial gauge and polar slicing, which we regard as accurate enough approximation. Inspecting Eqs. (5.10)–(5.12), we can see that α appears in a fraction with either its derivative or frequency ω. This means that if we rescale α, in order to preserve the equations, we must also rescale ω. Therefore, upon rescaling we must satisfy $\omega_{\rm original}/\alpha_{\rm original} = \omega_{\rm new}/\alpha_{\rm new}$. Now, condition $\alpha^2 X^2 = 1$ implies $\Phi_{\rm Schw} = -\ln(X_{\rm end})$, where $X_{\rm end} := X(r_{\rm end})$ and $r_{\rm end}$ is the end point of the grid (i.e. its total length). Imposing this condition necessitates a rescaling of the BS

frequency, so that $\omega = \hat{\omega}\exp(\Phi_{\rm Schw} - \Phi_{\rm end})$, where $\Phi_{\rm end} := \Phi(r_{\rm end})$. This completes our algorithm for finding the desired frequency ω as well as the BS solution.

5.5 Diagnostics

The mass of the BS directly follows from the definition of the mass function in Eq. (5.13) at infinite radius

$$M_{\rm BS} = \lim_{r\to\infty} m(r). \tag{5.49}$$

In practice, we never reach spatial infinity, so we usually approximate $M_{\rm BS} = m(r_{\rm end})$. Unlike neutron stars, BSs do not have a surface and therefore a well-defined notion of the radius – the scalar field instead extends to infinity and, as we already seen, falls off exponentially (cf. Eq.(5.46)). However, we can approximate the definition of the radius as the areal radius r_{99}, containing 99% of the BS's total mass. We also define the compactness, as the maximum ratio of the BS mass to its radius, $C = \max(m(r)/r)$. Note there exist many other ways of defining BS radius and compactness (see e.g. Ref.[395] for at least 5 alternative definitions of a BS radius). For thin-shell solutions, poorly defined radius of a BS can give misleading results, for example, allowing for very large compactness values in the absence of light rings [395]. However, the BS solutions we study in this work are outside of the thin-wall regime and we generally find our radius and compactness definitions sufficient and robust. Finally, we note that thanks to the $U(1)$ symmetry ($\varphi \to e^{i\varepsilon}\varphi$ and $\varphi^* \to e^{-i\varepsilon}\varphi^*$) of the Einstein-Hilbert action and a minimally coupled complex scalar field, BS solutions have a conserved *Noether* charge

$$Q_{\rm BS} = \int \sqrt{-g} J^0 {\rm d}^3x = \int r^2 \frac{4\pi|\varphi|^2\omega X}{\alpha} {\rm d}r, \tag{5.50}$$

where $J^\mu = i/2 g^{\mu\nu}(\varphi^*\nabla_\nu\varphi - \varphi\nabla_\nu\varphi^*)$ is the Noether current. Noether charge in quantum sense denotes the number of bosonic particles comprising the star.

5.6 Examples of boson-star solutions

In this Section, we discuss the properties of mini and solitonic boson-stars, using some examples illustrated in Fig. 5.6.1. In the Figure we present families of BS models for these potentials and consider ground and excited states. For most BS models computed in this thesis, we find it is sufficient to have a grid of length $r_{\rm end} = 1000 - 1200$ with around 10^6 points.

First, we note that excited states result in models of larger BS mass and frequencies (although the latter is not illustrated in the Figure). Excited states have been found to be unstable in Refs. [396, 397], and therefore in our subsequent investigations we will be focusing on the ground states only.

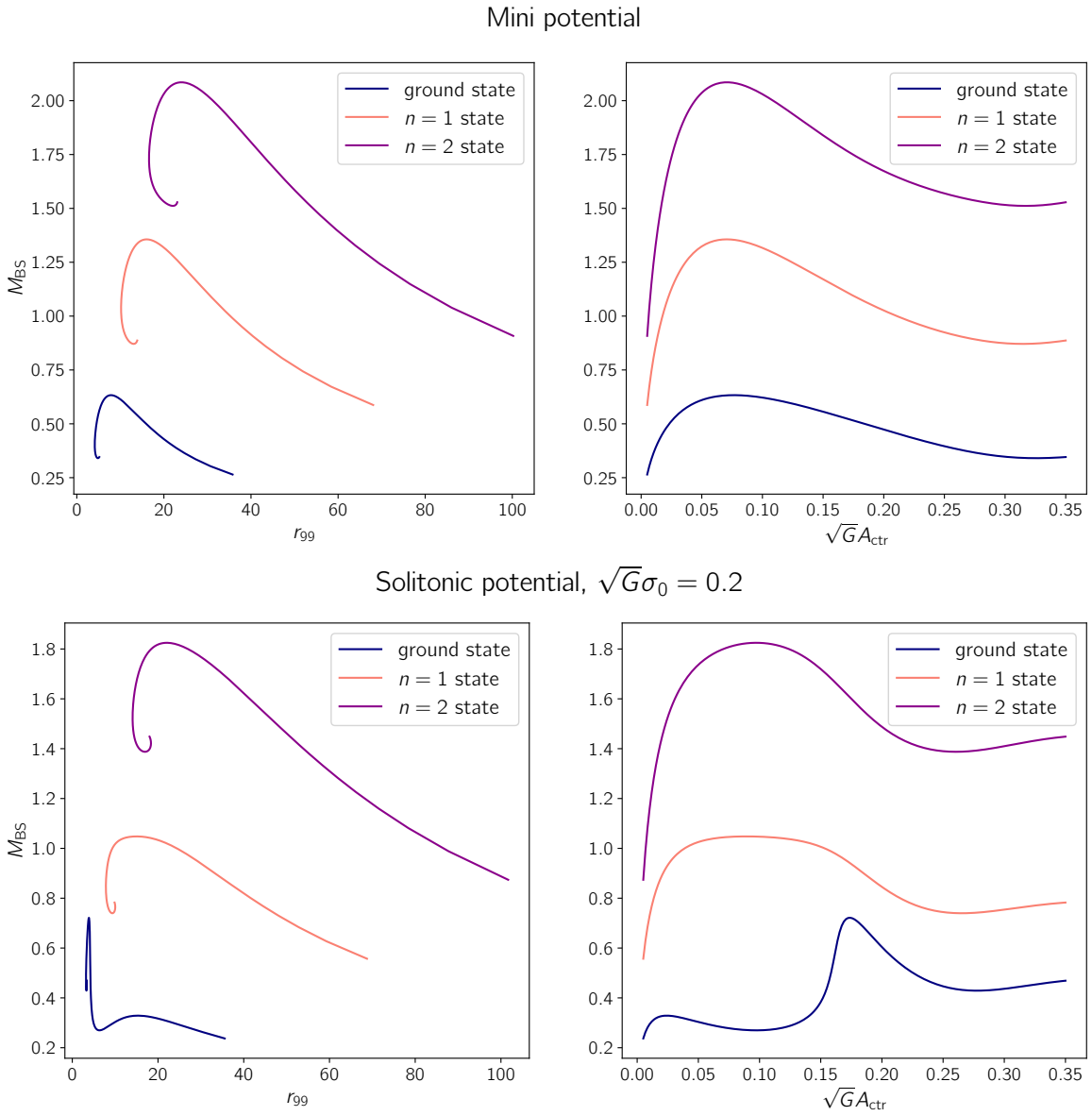


Fig. 5.6.1 Behaviour of BS models with the mini BS potential of Eq. (5.5) (top) and a solitonic potential (5.7) with $\sqrt{G}\sigma_0 = 0.2$ (bottom). In the left (right) figures we show families of BS models of ground ($n = 0$) and excited ($n = 1$ and $n = 2$) states in the mass-radius (mass-central-amplitude) planes.

A common feature of mass-over-radius plots, depicted in the left panels of Fig. 5.6.1, is the existence of a maximum mass. For the mini potential the maximum mass of the ground state, $M_{\rm BS} = 0.633$, is known as the *Kaup limit*. For BS models with the mini potential the maximum possible compactness of stable stars is therefore of $C \sim 0.12$. By incorporating self-interaction terms, like in the case of a solitonic potential, we are able to construct more massive models and the maximum allowed compactness almost doubles to $C \sim 0.2$.

The mass-over-central-amplitude plots in the right panels of Fig. 5.6.1 contain important information about the stability of the BS solutions. Let us focus on solutions with $\sqrt{G}A_{\rm ctr} \in [0.02, 0.3]$, which correspond to stars of low to moderate compactness values. In this case, spherically symmetric ground state configurations are known to typically consist of a stable and an unstable branch divided by the maximum mass [398]. This holds true for mini and repulsive potentials. However, the shape of the solitonic families of solutions is characterised by the two maxima, e.g for $\sqrt{G}\sigma_0 = 0.2$ we have the first maxima at the $\sqrt{G}A_{\rm ctr} \sim 0.237$ and the second at $\sqrt{G}A_{\rm ctr} \sim 0.172$. A typical way to judge the stability of these models is to consider the sign of the derivative of the mass as a function of the central amplitude: when $\mathrm{d}M_{\rm BS}/\mathrm{d}A_{\rm ctr} > 0$, the solutions are generally linearly stable, whilst when $\mathrm{d}M_{\rm BS}/\mathrm{d}A_{\rm ctr} < 0$ – they are unstable. For more details on the analyses of radial stability of BSs using perturbation and catastrophe theories we refer the interested readers to Refs. [387–389]. Taking the example of the ground state with $\sqrt{G}\sigma_0 = 0.2$ again, this means that up to $\sqrt{G}A_{\rm ctr} \lesssim 0.237$, BS models are stable against radial perturbations (these stars have low masses and large radii, and therefore comparatively low compactness values). Next, they are followed by unstable models up to the local minimum at $\sqrt{G}A_{\rm ctr} \sim 0.09$, where the derivative of $\mathrm{d}M_{\rm BS}/\mathrm{d}A_{\rm ctr}$ changes its sign again and BSs become stable. The stability continues from $\sqrt{G}A_{\rm ctr} \sim 0.09$ up to the maximum at $\sqrt{G}A_{\rm ctr} \sim 0.174$; after that all the models are unstable again.

5.7 Conversion to isotropic coordinates

In the binary evolutions of BSs, we will construct initial data using isotropic coordinates. In fact, it is possible to construct single BS solutions in isotropic coordinates from the start (see e.g. Section 2.2.2 of Ref. [399]). Here, however, we demonstrate how our areal radius r, defined in Eq. (5.9), is transformed into the isotropic radius R of the following line element

$$\mathrm{d}s^2 = \alpha^2 \mathrm{d}t^2 + \psi^4 \left(\mathrm{d}R^2 + R^2 \mathrm{d}\Omega^2\right), \tag{5.51}$$

where ψ is the inverse of the conformal factor we have previously encountered in Section 2.3 (i.e. here $\psi^4 = \chi^{-1}$). In the far region away from the BS, we have $\psi = 1 + m/(2R)$.

Directly comparing the areal line-element of Eq. (5.9) with the one in isotropic coordinates in Eq. (5.51), we find the following relation

$$\frac{\mathrm{d}P}{\mathrm{d}r} = \frac{P}{r}(X-1)\,, \tag{5.52}$$

where we have introduced a new variable denoting the ratio between the areal and isotropic radii, $P(r) \coloneqq \frac{R}{r}$. From the definition of X in Eq. (5.13), it follows that $X = 1 + \mathscr{O}(r^2)$ near the origin, so for sufficiently small r, $\mathrm{d}P/\mathrm{d}r = 0 \implies R \propto r$. Assuming a linear relation at the origin, where we use $P = 1$ as a preliminary boundary condition, we integrate Eq. (5.52) using 4th order Runge-Kutta method. We then correct the $P = 1$ condition through a linear scaling of r by requiring that it agrees with R at infinity. Assuming vacuum at infinity, we find the following relation

$$R \approx r - m - \frac{m^2}{4\,(r-m)}. \tag{5.53}$$

Chapter 6

Boson stars in massless and massive scalar-tensor gravity

The content presented in this Chapter contains material that appears in the co-authored publication Ref. [400] with R.Rosca-Mead, U.Sperhake and B.Brugmann. I implemented the code based on the shooting algorithm described in Appendix 6.B and used for the majority of the BS models in this Chapter. When the scalar-tensor theory parameters are set to zero, we recover the calculation of boson stars in general relativity, as described in Chapter 5. The exploration of the whole parameter space of boson star solutions in scalar-tensor theory was done jointly with the co-authors of the paper.

6.1 Introduction

BSs have been widely studied in the context of general relativity (GR), both as single BS spacetimes [332, 376, 377, 386, 391, 392, 396, 401–406], in terms of their formation [346, 390, 407] and as binary systems [141–143, 393, 408–414]; see also Refs. [96, 415–417] for reviews. Their understanding in modified theories of gravity, however, remains scarce. BSs in Brans-Dicke type theories with various couplings inspired from cosmology have been considered in Refs. [418–420], in Palatini $f(R)$ gravity in Refs. [421, 422] and in $f(T)$ extended theory of gravity in Ref. [423].

Scalar-tensor (ST) theories of gravity are one of the most natural and simplest extensions of GR that preserve the universality of a free fall [424]. The key ingredient of ST gravity is the presence of a scalar field non-minimally coupled to the metric such that gravity is not only mediated by a spin-2 graviton but also by the spin-0 scalar field. The inclusion of the scalar field is a common by-product of the compactification of higher dimensional

Kaluza-Klein type theories, like string theory, [425–427], making ST theories well-motivated gravity theories to study.

The theoretical implications of ST theories of gravity in various areas of fundamental physics are vast. For instance, on cosmological scales, ST theories have been proposed as models for dark energy, replacing the role of the cosmological constant [428, 429]. Furthermore, the additional scalar degree of freedom introduces a new channel of radiation emission in the form of scalar gravitational waves (GWs) also known as a "breathing mode". The perfect laboratories for tests and searches of these scalar waves are compact objects and binary systems composed thereof. In particular, it has been conjectured that in the process of *spontaneous scalarisation*, the scalar radiation can be detected with future gravitational wave detectors [31]. The phenomenon of spontaneous scalarisation is caused by a linear tachyonic instability inside the star that triggers the growth of the scalar field around it. Once the instability is quenched, the star becomes endowed with "scalar hair"; see Ref. [430] for a comprehensive review. This remarkable feature was first identified in the pioneering work of Damour and Esposito-Farèse [273, 431, 432], who studied spontaneous scalarisation of neutron stars in massless ST theory with a pair of parameters (α_0, β_0), inspired by Post-Newtonian (PN) theory and controlling the onset of scalarisation.

However, stringent constraints have been placed on massless ST theories by numerous observations, including the Cassini bound $\alpha_0 < 3.4 \times 10^{-3}$ [433] and pulsar–white dwarf binaries that rule out models with $\beta_0 \lesssim -5$ [434, 435]; for a summary of constraints on a broad range of modified theories of gravity obtained from gravitational-wave (GW) observations see also Ref. [224]. As a consequence, *massive* ST theories have acquired a great deal of attention, mainly for two reasons. First, the screening of the massive field maintains its compatibility with current observations and leaves a significant portion of the parameter space unconstrained. Second, because the mass term endows the scalar GW signal with a highly conspicuous long-lived, inverse chirp character [436–446]; see also Refs. [447–449] for studies of massive ST theory with self-interacting fields.

So far NSs have been extensively explored as ideal compact matter objects, in whose environment scalarisation can occur in this class of ST theories [93, 450, 451] (see also Ref. [452] on NSs in ST theory with quadratic conformal coupling). An intriguing extension is to investigate how the presence of a non-minimally coupled scalar field affects the phenomenology of other compact matter objects, such as BSs. The phenomena of spontaneous and induced scalarisation of BSs have been previously considered in Refs. [453–457]. In this Chapter we extend the study of BSs in scalar-tensor theories of gravity with Damour-Esposito-Farèse coupling [458] by focusing on the scalarisation of ground-state equilibrium

BSs for both massless and massive gravitational scalar fields as well as the stars' stability for various BS potentials.

This Chapter is structured as follows. In Section. 6.2, we present an overview of ST gravity with the specific Damour-Esposito-Farèse coupling function employed in our work, and formulate the system of first-order differential equations with the bosonic field in the matter sector. In Section 6.3, we present the results of our exploration of the parameter space and describe the main features of BS models in ST theory of gravity. We span the solution space for different parameters of the coupling function, mass values of the gravitational scalar field and BS potentials. In Section 6.4, we assess the stability of these models. Finally, we summarize our results together with an outlook on future research directions in Section 6.5. Unless specified otherwise, we employ units where the speed of light and Planck's constant satisfy $c = 1 = \hbar$, so that the Planck mass is given by $M_{\rm Pl} = 1/\sqrt{G}$.

6.2 Theory and formulation

6.2.1 Scalar-tensor action

We start by considering a general class of ST theories of gravity with a single, real-valued gravitational scalar field φ with potential $W(\varphi)$, whose action in the Einstein frame is given by [459],

$$\begin{aligned} S &= \int \mathrm{d}^4x \frac{\sqrt{-\bar{g}}}{16\pi}\left[\frac{\bar{R}}{G} - 2\bar{g}^{\mu\nu}\partial_\mu\varphi\,\partial_\nu\varphi - 4W(\varphi)\right] + S_{\rm M}\,, \\ S_{\rm M} &= \int \mathrm{d}^4x\sqrt{-g}\left\{-\frac{1}{2}[g^{\mu\nu}\nabla_\mu\psi^*\nabla_\nu\psi + V(\psi)]\right\}. \end{aligned} \tag{6.1}$$

Here, $\bar{g}_{\mu\nu}$ is a conformal metric, with corresponding Ricci scalar $\bar{R}$, related to the physical or Jordan-frame metric $g_{\mu\nu}$ by[1]

$$\bar{g}_{\mu\nu} = F(\varphi)g_{\mu\nu}, \tag{6.2}$$

where $F(\varphi)$ is the *coupling function*, which needs to be positive to ensure that the graviton carries positive energy [431]. For the matter sources, represented in Eq. (6.1) by the term $S_{\rm M}$, we consider a relativistic boson condensate, modelled as a massive complex scalar field $\psi = \psi_R + \mathrm{i}\psi_I$ with complex conjugate ψ^* and potential $V(\psi)$. Note that by Eq. (6.1) the matter moves according to the geometry of the *physical* metric $g_{\mu\nu}$; this is the price

[1] In our notation for the conformal factor we follow Salgado [459]; a common and equivalent alternative is to write Eq. (6.2) as $g_{\mu\nu} = a^2(\varphi)\bar{g}_{\mu\nu}$ where $a^2 = 1/F$.

tag for achieving the minimal coupling between the gravitational scalar and the conformal metric $\bar{g}_{\mu\nu}$ of the Einstein frame. Although the scalar field does not directly interact with the ordinary matter (which guarantees the weak equivalence principle), it affects the motion of test particles through its presence in Eq. (6.2). The appearance of two distinct scalar fields in our physical setup inevitably holds potential for confusion; whenever the meaning is not self-evident, we will therefore explicitly refer to the two fields as the *gravitational scalar* φ and the *BS scalar* ψ with amplitude $A := |\psi|$.

The covariant field equations are obtained from varying the action (6.1) with respect to $\bar{g}_{\mu\nu}$, φ and ψ. This leads to

$$\begin{aligned}
\frac{\bar{G}_{\alpha\beta}}{G} &= 2\partial_\alpha\varphi\partial_\beta\varphi - \bar{g}_{\alpha\beta}\bar{g}^{\mu\nu}\partial_\mu\varphi\,\partial_\nu\varphi - 2W\bar{g}_{\alpha\beta} + 8\pi\bar{T}_{\alpha\beta}\,,\\
\bar{\nabla}^\mu\bar{\nabla}_\mu\varphi &= 2\pi\frac{F_{,\varphi}}{F}\bar{T} + W_{,\varphi}\,,\\
\bar{\nabla}^\mu\bar{\nabla}_\mu\psi &= \frac{1}{2F}\left(\frac{\partial V}{\partial\psi_R} + \mathrm{i}\frac{\partial V}{\partial\psi_I}\right) + \bar{g}^{\mu\nu}\frac{\partial_\mu F}{F}\partial_\nu\psi\,,
\end{aligned} \tag{6.3}$$

where an overbar denotes tensors and operators in the Einstein frame; in particular, the energy-momentum tensor is given by

$$\begin{aligned}
\bar{T}_{\alpha\beta} &= \frac{2}{\sqrt{-\bar{g}}}\frac{\delta S_m}{\delta\bar{g}^{\alpha\beta}} = \frac{1}{F}T_{\alpha\beta} \\
&= \frac{1}{F}\left\{\partial_{(\alpha}\psi^*\partial_{\beta)}\psi - \frac{1}{2F}\bar{g}_{\alpha\beta}\left[F\bar{g}^{\mu\nu}\partial_\mu\psi^*\partial_\nu\psi + V(\psi)\right]\right\}.
\end{aligned} \tag{6.4}$$

6.2.2 Spherically symmetric solutions

In this Chapter, we consider stationary, spherically symmetric BS models and employ a metric ansatz using radial gauge and polar slicing. Specifically, we write

$$\begin{aligned}
\mathrm{d}\bar{s}^2 &= \bar{g}_{\mu\nu}dx^\mu dx^\nu \\
&= -F(\varphi)\alpha^2\mathrm{d}t^2 + F(\varphi)X^2\mathrm{d}r^2 + r^2\mathrm{d}\Omega^2\,,
\end{aligned} \tag{6.5}$$

where r is the areal radius in the Einstein frame and $\mathrm{d}\Omega^2 := \mathrm{d}\theta^2 + \sin^2\theta\mathrm{d}\phi^2$ is the standard angular line element. In spherical symmetry, it is convenient to express the complex BS

scalar field in terms of amplitude A and frequency ω

$$\psi = Ae^{i\omega t}\,. \tag{6.6}$$

At this point, we have three mass scales in our problem: the two scalar masses, μ_φ and μ for φ and ψ respectively, and the Planck mass $M_{\rm pl} = \sqrt{1/G}$ that appears in the Einstein equation (6.3). All dimensional quantities have units of some power of μ or $M_{\rm Pl}$ or a combination thereof. To see this explicitly, we still need to specify the potential functions $V(\psi)$ and $W(\varphi)$. The particular choices for these functions will be detailed in Section 6.2.4 below, but we note already at this stage that they will take the form $V(A) \sim \mu^2 A^2$ and $W(\varphi) \sim \mu_\varphi^2 \varphi^2$, hence acquiring units of $\mu^2 M_{\rm Pl}^2$. In similar spirit to Eq. (5.17), one can now eliminate all dimensional factors in the covariant equations (6.3) by introducing dimensionless variables according to

$$\hat{t} = \mu t, \quad \hat{r} = \mu r, \quad \hat{m} = \mu m, \quad \hat{\omega} = \frac{\omega}{\mu}, \tag{6.7}$$

$$\hat{\mu}_\varphi = \frac{\mu_\varphi}{\mu}, \quad \hat{\varphi} = \frac{\varphi}{M_{\rm Pl}}, \quad \hat{A} = \frac{A}{M_{\rm Pl}}\,. \tag{6.8}$$

These dimensionless variables can be converted back into SI units in the same way as in Section 5.4.1 and additionally noting that $\varphi = \hat{\varphi} M_{\rm Pl}$. From now on, we will work with dimensionless variables only and we will drop the caret in their notation for simplicity.

6.2.3 The field equations in spherical symmetry

Our physical system is completely described by φ, A, α and X, which are all functions of radius r. It is sometimes convenient to express the metric functions α and X in terms of the alternative variables

$$\Phi := \ln(F\sqrt{\alpha})\,, \qquad m := \frac{r}{2}\left(1 - \frac{1}{FX^2}\right)\,, \tag{6.9}$$

which, when combined with Eqs. (6.3)-(6.5), results in a set of ordinary differential equations (ODEs) that can be written as

$$\begin{aligned}
\partial_r \Phi &= \frac{FX^2-1}{2r} - rFX^2W + \frac{r}{2}\frac{X^2}{\alpha^2}\kappa^2 + \frac{2\pi r X^2}{F\alpha^2}\left(\omega^2A^2 - \alpha^2 V + F^2\theta^2\right), \\
\frac{\partial_r X}{X} &= -\frac{FX^2-1}{2r} + rFX^2W - \frac{X}{2\alpha}\frac{F'}{F}\kappa + \frac{r}{2}\frac{X^2}{\alpha^2}\kappa^2 + \frac{2\pi r X^2}{F\alpha^2}\left(\omega^2A^2 + \alpha^2 V + F^2\theta^2\right), \\
\partial_r \varphi &= \frac{X}{\alpha}\kappa, \\
\partial_r \kappa &= -2\frac{\kappa}{r} + 2\alpha XFW_{,\varphi^2}\varphi + 2\pi\frac{XF'}{\alpha F^2}\left(\omega^2A^2 - 2\alpha^2 V - F^2\theta^2\right), \\
\partial_r A &= \frac{XF}{\alpha}\theta, \\
\partial_r \theta &= -2\frac{\theta}{r} + \frac{X}{\alpha F}A\left(\alpha^2 V_{,A^2} - \omega^2\right).
\end{aligned} \tag{6.10}$$

Here, we have introduced the auxiliary variables κ and θ in order to write the two scalar-field equations in first-order form and used the notation

$$W_{,\varphi^2} \coloneqq \frac{\mathrm{d}W}{\mathrm{d}(\varphi^2)}, \qquad V_{,A^2} \coloneqq \frac{\mathrm{d}V}{\mathrm{d}(A^2)}. \tag{6.11}$$

The system (6.10) is complemented by the boundary conditions

$$\begin{aligned}
&X(0) = \frac{1}{\sqrt{F}}, \; A(0) = A_{\mathrm{ctr}}, \; \varphi(0) = \varphi_{\mathrm{ctr}}, \; \kappa(0) = 0, \\
&\theta(0) = 0, \; \Phi(\infty) = \Phi_0, \; A(\infty) = 0, \; \varphi(\infty) = 0.
\end{aligned} \tag{6.12}$$

The vanishing of the scalar fields at infinity can only be achieved for specific values of ω, A_{ctr} and φ_{ctr} which characterises Eq. (6.10) as an eigenvalue problem. More specifically, following a similar prescription to Section 5.4.3, one can show that the asymptotic behaviour with gravity is (cf. Appendix 6.A)

$$\varphi \sim \frac{e^{\pm hr}}{r^{1+\delta}}, \qquad A \sim \frac{e^{\pm kr}}{r^{1+\varepsilon}}, \tag{6.13}$$

where h, k, δ and ε are given in Eqs. (6.27) and (6.28) for a massive and massless φ, respectively.

The ground-state BS models, that we focus on in this study, are furthermore characterized by monotonic profiles $A(r)$ with no zero crossings except for their vanishing at infinity.

6.2.4 Choice of model

The field equations derived in the previous section hold for arbitrary potentials $W(\varphi)$, $V(\psi)$ and conformal function $F(\varphi)$. We now discuss the specific choices made in our work, starting with the conformal factor $F(\varphi)$. We consider the class of ST theories given by the Damour-Esposito-Farèse function [273],

$$F(\varphi) \;=\; e^{-2\alpha_0\varphi-\beta_0\varphi^2}, \tag{6.14}$$

with constants $\alpha_0 \geq 0$ and β_0. The choice of Damour and Esposito-Farèse is in part motivated by the fact that the modifications of gravity at first post-Newtonian order are completely determined by the asymptotic values of the first and second derivatives of $\ln F$ in the far-field limit [431, 432, 460]. In our notation, these derivatives are

$$\alpha_0 = -\frac{1}{2}\left.\frac{\mathrm{d}\ln F}{\mathrm{d}\varphi}\right|_{\varphi=0}, \qquad \beta_0 = -\frac{1}{2}\left.\frac{\mathrm{d}^2\ln F}{\mathrm{d}\varphi^2}\right|_{\varphi=0}. \tag{6.15}$$

In particular, this implies an effective Newtonian gravitational constant $\tilde{G} = G(1+\alpha_0^2)$. The parameters α_0, β_0 furthermore completely determine the Eddington parametrized post-Newtonian parameters β^{PPN} and γ^{PPN} [424, 461]; see also Eq. (3.7) and the surrounding discussion in Ref. [462]. For $\beta_0 = 0$, we recover Brans-Dicke theory [32], whereas Damour and Esposito-Farèse's inclusion of the quadratic term leads to the spontaneous-scalarisation phenomenon for sufficiently *negative* β_0.

The pioneering work on spontaneous scalarisation focused on massless ST gravity, which, however, has been constrained significantly by the Cassini mission and binary pulsar observations, not least because of the dramatic effect of the spontaneous scalarisation mechanism. This has resulted in an increasing amount of attention devoted to *massive* ST theories which, due to the screening effected by the mass term μ_φ, largely remain compatible with the observations. Roughly speaking, the Yukawa fall-off of a massive scalar suppresses the impact of the scalar sector on the binary pulsar dynamics for sufficiently large separations of the binary constituents; this leaves ST theories with $\mu_\varphi \gtrsim 10^{-15}\,\mathrm{eV}$ in agreement with present observations [436]. We note, however, that μ_φ may also be constrained through other types of observations. Specifically, a recent study on equilibrium neutron stars conjectures that the GW event 170817 is suggestive of a larger mass $\mu_\varphi \gtrsim 10^{-11}\,\mathrm{eV}$ [463] while the observation of highly spinning black holes, combined with their superradiant interaction

with surrounding massive fields, may exclude the mass range $10^{-13}\,\mathrm{eV} \lesssim \mu_\varphi \lesssim 10^{-11}\,\mathrm{eV}$ [464, 465]. Our analysis is largely motivated by theoretical considerations and the goal to obtain a comprehensive understanding of BS scalarisation. While bearing in mind the possible constraints above, we therefore consider a wide range of mass values $\mu_\varphi \geq 0$ as well as coupling parameters $\alpha_0,\ \beta_0$ with no further prejudice. In our theoretical formalism we include the gravitational scalar mass through a quadratic potential

$$W(\varphi) \;=\; \frac{1}{2}\mu_\varphi^2\varphi^2, \tag{6.16}$$

where $\mu_\varphi \geq 0$ measures the gravitational scalar mass in units of the BS scalar mass parameter μ. As we will see later both the massless and the massive cases will share common phenomenological features.

Finally, to describe the bosonic sector, we focus on repulsive and solitonic potentials,

$$\begin{aligned} V_{\mathrm{rep}} &= A^2 + \lambda_4 A^4\,, \\ V_{\mathrm{sol}} &= A^2\left(1 - 2\frac{A^2}{\sigma_0^2}\right)^2\,, \end{aligned} \tag{6.17}$$

where λ_4 and σ_0 are self-interaction parameters of the two individual potentials[2].

6.2.5 Numerics and Diagnostics

Accurately capturing the exponential behaviour of the scalars and determining the eigenvalues φ_{ctr} and ω is a non-trivial numerical challenge and we detail in Appendices 6.A and 6.B how we compute the solutions using shooting and relaxation techniques. The conceptual summary of our calculations is as follows.

1. Specify the ST theory through the parameters α_0, β_0 and μ_φ.
2. Specify the BS scalar potential by fixing σ_0 or λ_4.
3. Parametrize the sequence of BS solutions inside this framework by varying a *control parameter*, typically A_{ctr}, but sometimes also ω or $\Phi_{\mathrm{ctr}} \coloneqq \Phi(0)$.
4. For each value of this control parameter, we iteratively determine the eigenvalues φ_{ctr} and ω leading to a physical (i.e. asymptotically flat) BS solution. For some values of the control parameter, there exist multiple solutions with different degrees

[2]Note that both potential functions include the case of *mini BSs* in the respective limits $\lambda_4 \to 0$ and $\sigma_0 \to \infty$.

of gravitational scalarisation. In order to find all possible solutions, we perform the iterative procedure using different initial guesses for ω and $\varphi_{\rm ctr}$, usually obtained from neighbouring models with similar degrees of scalarisation.

The typical result of such a calculation for a given ST theory and potential function is a set of one-parameter branches of strongly and weakly scalarised BS solutions which can be displayed, for example, as curves in the mass-radius plane. Whereas the mass of a BS is well defined as the Arnowitt-Deser-Misner [103] or ADM mass, given in our formalism by $m(r\to\infty)$, the radius is not; BSs formally extend to infinity, albeit with exponentially decaying scalar amplitude A. In this work, we define the radius $R_{\rm J}$ of a BS as the Jordan frame radial coordinate $r/\sqrt{F}$ where the mass function m reaches 99 % of the ADM mass, i.e. where $m(r)=0.99\,m(\infty)$.

6.3 Scalarised boson stars

6.3.1 A prototypical example

We begin our discussion of the results with a representative family of BS models that illustrates the main features of their spontaneous scalarisation. This set of models is obtained for ST parameters $\mu_\varphi=0.05$, $\alpha_0=0$ and $\beta_0=-11$ as well as a solitonic potential $V_{\rm sol}$ (6.17) with $\sigma_0=0.2$ for the BS matter. The main diagnostic quantities we display for this family of models are the ADM mass $M_{\rm ADM}$, the radius $R_{\rm J}$, the central and maximal values $\varphi_{\rm ctr}$, $\varphi_{\rm max}$ of the gravitational scalar, the central magnitude of the complex BS scalar $A_{\rm ctr}$ and the frequency ω.

The resulting BS models are graphically illustrated in the form of mass-radius diagrams in Fig. 6.3.1 with the other diagnostic quantities encoded in colour. We note in this context that for $\alpha_0=0$ the BS models are invariant under the change $\varphi(r)\to-\varphi(r)$ and the profile $\varphi(r)$ has no zero crossings. Unless stated otherwise, we display in this Section the solutions with positive $\varphi=|\varphi|$. The breaking of this degeneracy for non-zero α_0 will be explored in Section 6.3.4 below. The main features visible in this Figure are as follows.

1. The BS models of GR are recovered as a one-parameter family with vanishing gravitational scalar φ; this set of models is conspicuous as the dark blue branch in the top right panel of Fig. 6.3.1. For the vanishing α_0 of our example, this branch exactly equals the BS models computed in GR as shown, for example, in the lower panel of Fig. 5.6.1 of Section 5 or Fig. 1 of Ref. [141] for the same σ_0.

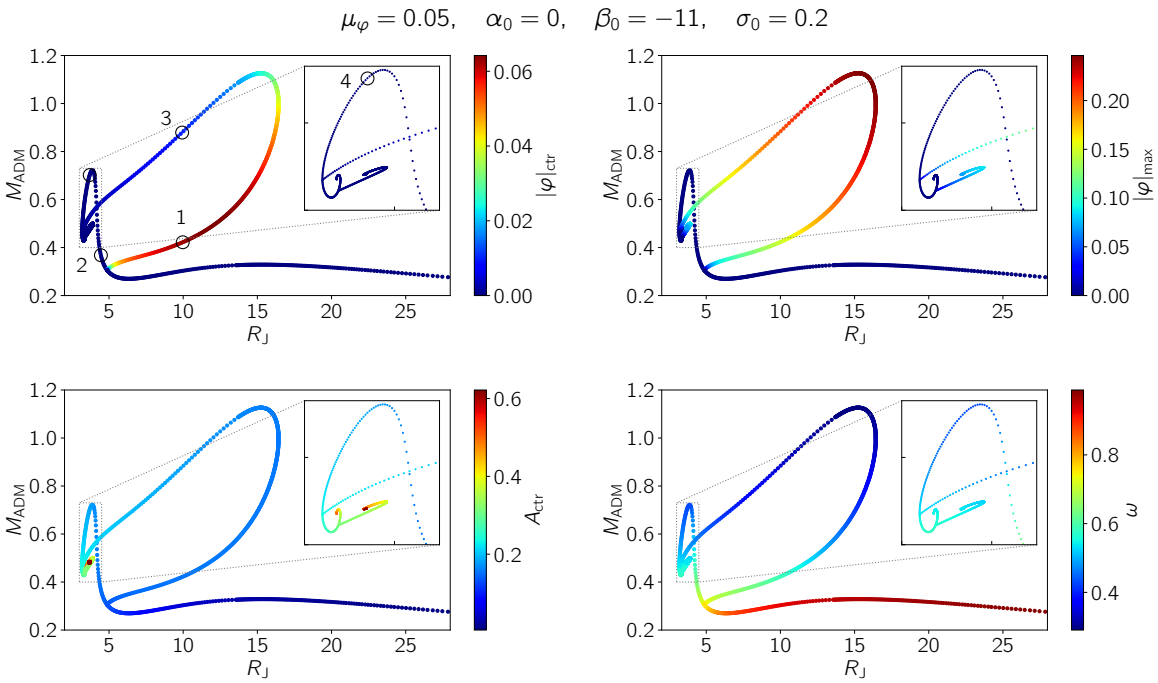


Fig. 6.3.1 BS models in ST gravity with $\mu_\varphi = 0.05$, $\alpha_0 = 0$ and $\beta_0 = -11$ for a solitonic potential with $\sigma_0 = 0.2$. Each point in these mass-radius diagrams represents a BS model. The location of the point represents the star's mass $M_{\rm ADM}$ and radius $R_{\rm J}$, and the colour coding in the respective panels displays the central gravitational scalar $|\varphi|_{\rm ctr}$, the maximum (over radius) gravitational scalar magnitude $|\varphi|_{\rm max}$, the central BS scalar amplitude $A_{\rm ctr}$ and the frequency ω. The four circles labeled 1 to 4 mark the models displayed in more detail in Fig. 6.3.2.

2. Scalarised models appear most prominently in the form of a second branch forming a loop starting from about a radius $R_{\rm J} \approx 5$ towards larger radii and masses and eventually reconnecting with the GR branch at $R_{\rm J} \approx 3$. As can be seen in the inset of the top right panel of Fig. 6.3.1, there exists a second segment of the scalarised branch extending to the right, a bit further down. As we will see in Section 6.3.2, the fine structure of the high-compactness (upper) end of the scalarised branch can change with β_0.

3. Bearing in mind our sign convention for φ, the upper two panels in Fig. 6.3.1 demonstrate that for many of the scalarised models, the gravitational scalar φ reaches its maximum away from the origin: $|\varphi|_{\rm ctr}$ is typically smaller than $|\varphi|_{\rm max}$.

4. As also observed for neutron stars [273, 466], the scalarised models can reach significantly larger masses and radii[3].

[3] Alternative definitions of BS radii exhibit the same qualitative behaviour in spite of quantitative differences.

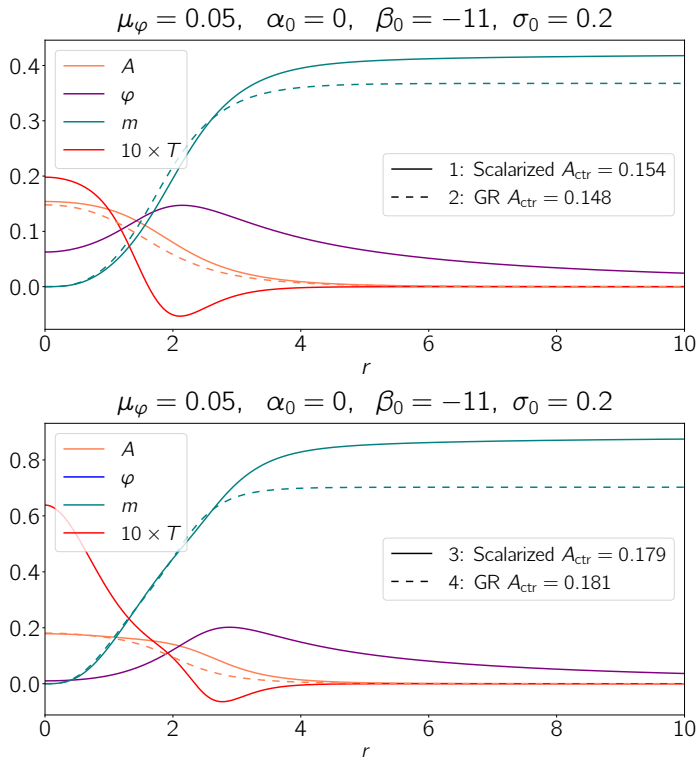


Fig. 6.3.2 Radial profiles of the BS scalar amplitude A, the gravitational scalar φ, the mass function m and the trace T of the energy momentum tensor for four selected models marked 1 to 4 in Fig. 6.3.1. The pair of models $1,2$ represents one scalarised and one GR star with equal compactness $C = 0.117$ and amplitudes $A_{\rm ctr}$ as indicated in the legend. Likewise, $3,4$ represent a scalarised and GR model with $C = 0.240$ each. As indicated by the dashed curves for GR and the solid lines for scalarised models, the scalarisation tends to push the BS scalar $A(r)$ towards larger radii and results in larger masses. In the region of strongest scalarisation in φ, the energy momentum tensor has negative trace T.

5. As the central BS scalar amplitude increases, the BS models become increasingly compact, as illustrated in the bottom left panel of Fig. 6.3.1.

6. As the BS compactness increases, the frequency ω generally decreases from $\lim_{A_{\rm ctr}\to 0}\omega = 1$. This trend is only mildly reversed at the extreme end for highly compact models; cf. the inset in the bottom right panel. The smallest frequencies are obtained in the high-mass regime of the scalarised branch.

In Fig. 6.3.2, we plot the BS scalar amplitude A, the gravitational scalar φ, the mass aspect m as well as the trace T of the physical energy momentum tensor as functions of radius r for four selected models marked by circles in Fig. 6.3.1. Here, models 1 and 3 are located on the scalarised branch with compactness $C := \max_{r\in\mathbb{R}} \frac{m(r)}{r} = 0.117$ and $C = 0.240$, respectively. The BSs marked 2 and 4 represent GR stars with respectively equal

compactness for comparison. The models exhibit quite similar main features despite their different locations in the mass-radius plane: (i) Whereas the BS scalar amplitude A is a monotonically decreasing function of r for all cases, the gravitational scalar of models 1 and 3 reaches its extremal value away from the origin. (ii) The mass function increases monotonically with radius, but levels off at relatively small radius due to the exponential decrease of A. (iii) The scalarisation tends to push the BS scalar profile $A(r)$ towards larger radii and results in larger total mass $M_{\rm ADM}$. (iv) The region of strongest scalarisation coincides with the region of a negative trace of the energy momentum tensor as expected for the onset of a tachyonic instability [436].

In the following Sections, we will explore in more detail the phenomenology of scalarised BS models in ST theory and will highlight how and when the main features illustrated by this prototype can alter for different potentials $V(A)$ and ST parameters.

6.3.2 Scalar mass and the onset of scalarisation

Having seen the main features of scalarised BSs in the previous Section, we next study how the mass μ_φ of the gravitational scalar affects the scalarisation phenomenon and, in particular, at which values of β_0 scalarisation sets in. For this purpose, we keep the BS potential function $V(A)$ fixed at its solitonic shape with $\sigma_0 = 0.2$; the effect of alternative potentials will be explored in Section 6.3.3 below.

The majority of spontaneously scalarised neutron-star models have been found below a threshold for $\beta_0 \lesssim \beta_{0,\rm thr} = -4.35$ where $\beta_{0,\rm thr}$ turns out to be remarkably robust against variations of other parameters such as the equation of state [436, 466–469]. One striking exception to this rule are the strongly scalarised solutions found by Mendes and collaborators [470–472] for positive β_0 provided the trace of the energy momentum tensor is positive in the GR limit; see also Ref. [436] where this effect is explained in terms of a tachyonic instability. For the BS models considered in this study, we focus on negative β_0, but we will see that the threshold value $\beta_{0,\rm thr}$ can differ from that for NSs and also depends more sensitively on the BS parameters. As a general observation we find that increasing the mass μ_φ weakens the effect of scalarisation. This is illustrated in Fig. 6.3.3 where we display solitonic BS families for $\alpha_0 = 0$, $\beta_0 = -12$ and $\sigma_0 = 0.2$, but varying μ_φ from 0 to 0.15. The top panel of this Figure demonstrates that the scalarised branches significantly reduce in terms of the BS radius and mass, getting closer to the GR branch for larger μ_φ. We note in this context that the rather large BS radii found for $\mu_\varphi = 0$ are a consequence of a slightly slower fall-off of $A(r)$, likely caused by its coupling to the now long-ranging φ. We investigate this effect in more detail in Section 6.3.5 below, but note that the outer regions even of BSs of radius

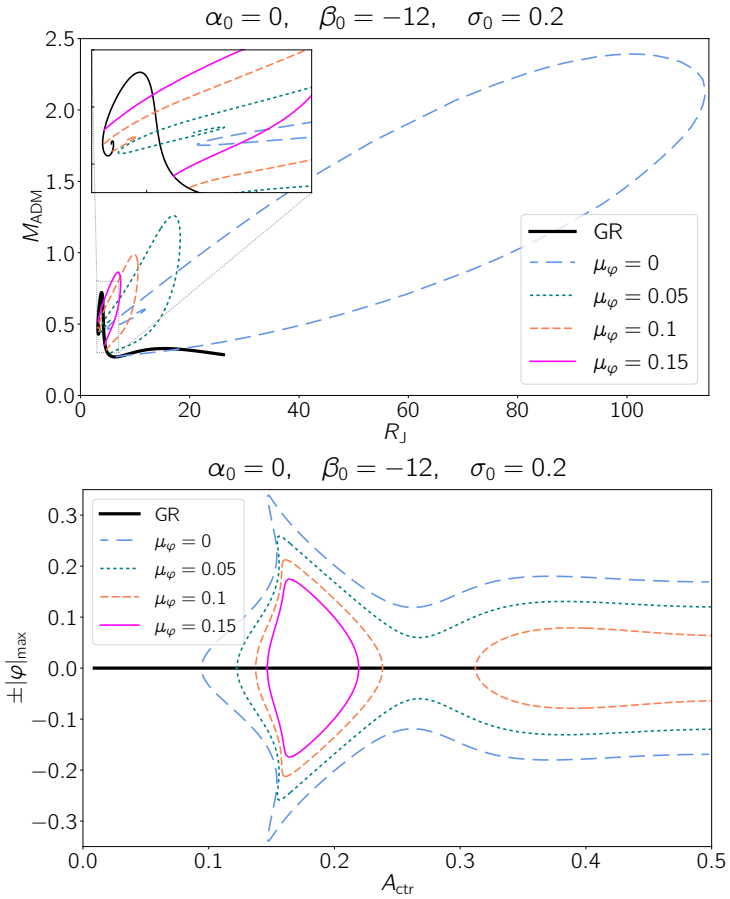


Fig. 6.3.3 *Top*: Mass radius diagram for four values of the scalar mass. The scalarised branches decrease in size for larger μ_φ. *Bottom*: The maximal value of the gravitational scalar, $|\varphi|_{\rm max}$, is shown as a function of the central BS scalar amplitude $A_{\rm ctr}$ for the same BS families. Note that for $\alpha_0 = 0$, the models for positive and negative φ are degenerate and we plot both extrema, $\pm|\varphi|_{\rm max}$, to illustrate the loop structure. Again the loops shrink for larger μ_φ, but we also notice a split into two separate loops at $\mu_\varphi = 0.1$. For $\mu_\varphi = 0.15$, the second loop containing highly compact models with large $A_{\rm ctr}$ is no longer present.

$R_{\rm J} \approx 100$ are tenuous with the small energy density merely amplified by the r^2 effect of the volume element.

The decrease in scalarisation becomes even more evident in the bottom panel of Fig. 6.3.3 where the same BS families are represented in the plane spanned by the central BS scalar amplitude $A_{\rm ctr}$ and the maximal value of $|\varphi(r)|$. Recalling that the BS models are identical under $\varphi \to -\varphi$, we display each BS in this Figure in terms of its two extrema $\pm|\varphi|_{\rm max}$ in order to illustrate more clearly the loop like structure of the branches. Clearly, the maximal scalarisation decreases for larger μ_φ, but we also notice two qualitative changes occurring between $0.05 < \mu_\varphi < 0.1$ and $0.1 < \mu_\varphi < 0.15$, respectively. First, the single loop (long-

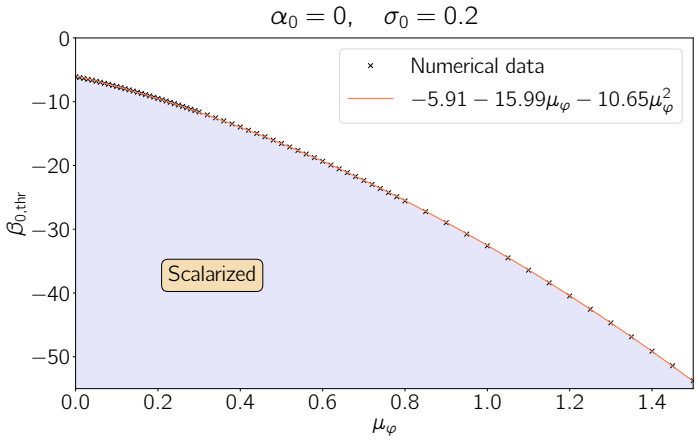


Fig. 6.3.4 The threshold value of β_0 for the onset of scalarisation; for $\beta_0 \leq \beta_{0,\mathrm{thr}}$, scalarised BS models exist.

dashed blue and dotted green) splits into two separate loops (dashed orange) leaving a finite range $0.25 \lesssim A_{\mathrm{ctr}} \lesssim 0.31$ where only GR models exist. For $\mu_\varphi = 0.15$, the second loop of highly compact (large A_{ctr}) models has disappeared; we cannot entirely rule out that it is shifted to very large A_{ctr}, but all our searches for scalarised models in this regime for $\mu_\varphi \geq 0.15$ have yielded no solutions. This behaviour is also reflected in the mass-radius diagram of the left panel, where for $\mu_\varphi = 0$ or 0.05 the scalarised branch connects to the GR branch only at the low mass end, but remains separate at the high-mass end as shown in the inset. For $\mu_\varphi = 0.1$, instead, we have two separate scalarised branch segments, both connected to GR models: note the small dashed orange branch in the inset near the end of the black GR branch. For $\mu_\varphi = 0.15$ (solid magenta), this small extra branch is no longer present.

The right panel of Fig. 6.3.3 resembles Fig. 3 of Ramanazoğlu and Pretorius [473] which shows $|\varphi|_{\max}$ obtained for scalarised neutron-stars. Their analysis of spontaneous scalarisation in terms of a tachyonic instability leads to an approximate criterion $\lambda_\varphi > \lambda_{\mathrm{eff,\,star}} \sim R_{\mathrm{J}}/\sqrt{C|\beta_0|}$ – their Eq. (6) – where C is an estimate of the star's compactness and λ_φ is the Compton wavelength associated with μ_φ. Translated into our variables, this relation becomes

$$|\beta_0| \gtrsim \frac{R_{\mathrm{J}}^2}{4\pi^2 C}\mu_\varphi^2\,, \tag{6.18}$$

and suggests an approximately quadratic relation between the threshold for scalarisation $\beta_{0,\mathrm{thr}}$ and the scalar mass μ_φ.

We have numerically computed the onset of scalarisation for the families of BS models with $\alpha_0 = 0$, $\sigma_0 = 0.2$ by starting for each fixed μ_φ with a sufficiently negative β_0 that admits scalarised models and then iteratively increasing β_0 towards 0 until scalarisation disappears.

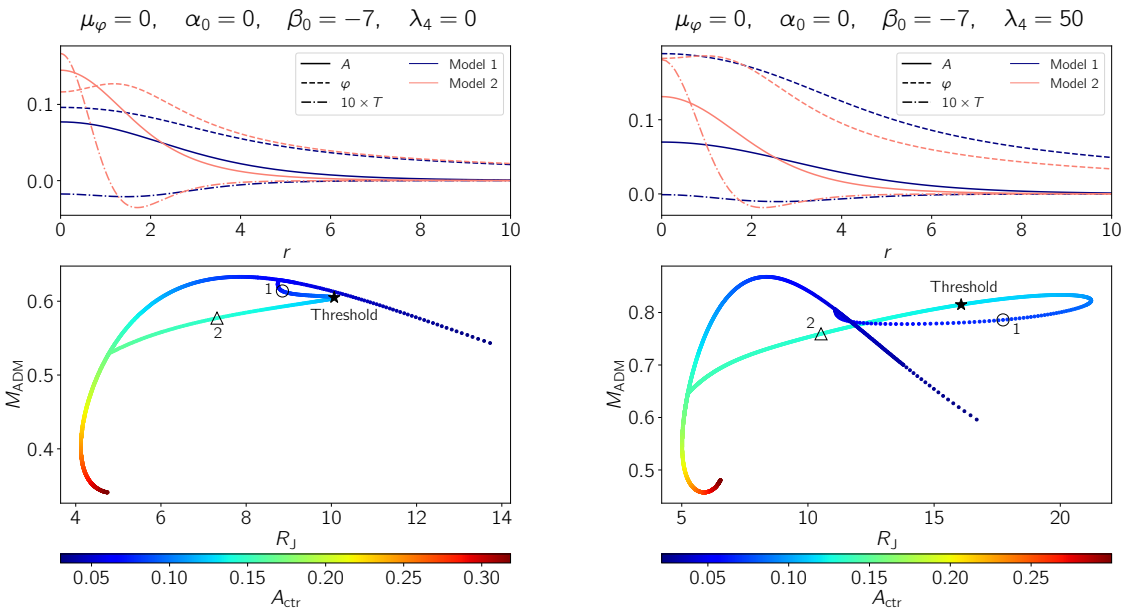


Fig. 6.3.5 *Upper panels*: Radial profiles of the BS scalar amplitude A, the gravitational scalar φ and the trace of the energy-momentum tensor T for the BS Models 1 and 2 indicated by a circle and a triangle, respectively, in the panels below. The models with $\lambda_4 = 0$ (left) have frequencies $\omega_1 = 0.8518$ and $\omega_2 = 0.7729$, whilst for models 1 and 2 with $\lambda_4 = 50$ (right) we have $\omega_1 = 0.8303$ and $\omega_2 = 0.7572$. Note that the trace of the energy-momentum tensor has been scaled for presentation purposes. As supported by the analysis in the main text, T becomes negative at small radii for models with a gravitational scalar peaking at the origin. *Lower panels*: Mass-radius plots with the colour bar indicating the central amplitude of the BS scalar field. The star marks the threshold at which the gravitational scalar starts to peak off centre; we ubiquitously observe that φ peaks at $r = 0$ for less compact stars ($A_{\rm ctr}$ is lower than for the threshold case, i.e. dark blue colour) and φ peaks off centre for more compact stars (large $A_{\rm ctr}$, i.e. cyan colour). We exemplify this with models 1 (less compact with φ peaking at $r = 0$) and 2 (more compact with φ peaking off-center) for each of the potentials (left with $\lambda_4 = 0$ and right with $\lambda_4 = 50$).

In practice, we have stopped this search at 4 significant digits in β_0 and verified that the result remains unchanged under a doubling or halving of the number of grid points. The resulting threshold $\beta_{0,\rm thr}$ is plotted as a function of μ_φ in Fig. 6.3.4 together with a quadratic fit. Typical values for radius and compactness of the BS models on the verge of scalarisation are $R_{\rm J} \sim 5$ and $C \sim 0.2$, resulting in a coefficient $R_{\rm J}^2/(4\pi^2 C) \sim 3$ in Eq. (6.18). Bearing in mind its approximate character, the tachyonic analysis captures the quadratic contribution of our fit rather well. The constant and linear contributions to our fit, in turn, are likely a direct consequence of a finite threshold for scalarisation in massless ST theory: using a series of self-gravity contributions, Damour and Esposito-Farèse conclude that the non-perturbative

amplification effect of spontaneous scalarisation can set in when $\beta_0 \lesssim -4$. For the massless case considered in their analysis, this remains a remarkably good estimate for BSs.

6.3.3 Dependence on the bosonic potential

In this Section, we consider the structure of BS solutions in ST theory of gravity for other potentials of the BS scalar field. We focus on models governed by the potentials given in Eq. (6.17), namely a solitonic one with $\sigma_0 \geq 0.2$ and a repulsive potential with $\lambda_4 \geq 0$. We find that the specific choices we consider here affect the structure of scalarised BS models, resulting in several differences to the prototypical example studied in Section 6.3.1. In particular, we find that the gravitational scalar changes its shape with stellar compactness and that strongly scalarised solutions may no longer have larger masses and radii than their GR counterparts. Similar to Alcubierre et. al. [456] we do not find self-interaction terms in the bosonic potential to be necessary for obtaining strong scalarisation. We analyse these features in more detail below.

Massless gravitational scalar field

Gravitational scalar profiles: Previously we noted that a solitonic potential with $\sigma_0 = 0.2$ leads to the distinct feature of a gravitational scalar field $\varphi(r)$ peaking off-centre; cf. Fig. 6.3.2. For repulsive ($\lambda_4 > 0$) and mini ($\lambda_4 = 0$) BS models, in contrast, the gravitational scalar more commonly reaches its global extremum exactly at the centre. We illustrate this in Fig. 6.3.5, where $\varphi(r)$ gradually changes its behaviour from peaking at $r = 0$ to peaking off-centre, as one moves to models with higher central amplitudes $A_{\rm ctr}$ of the BS scalar. The same behaviour has been observed for neutron stars of increasing compactness; cf. Fig. 7 in Ref. [466]. In Fig. 6.3.5 we mark by a star the threshold, where this transition occurs. We additionally plot in each of the upper panels the profiles $A(r)$ and $\varphi(r)$ for two models marked 1 and 2 in the mass-radius diagram. These models are located on either side of the threshold: for model 1 (less compact, i.e. smaller $A_{\rm ctr}$ than the threshold model) φ peaks at the centre $r = 0$ and for model 2 (more compact with larger $A_{\rm ctr}$) it peaks off centre.

We can qualitatively understand this behaviour as follows: the shape of the gravitational scalar field near the origin is controlled by Eq. (6.10) for κ, which denotes a re-scaled version of the radial derivative for the gravitational scalar field $\partial_r\varphi$. The overall sign of $\partial_r\kappa$ at small radii determines the concavity of φ near the origin, and, thus, whether it peaks off or at the centre. Without loss of generality, we assume that $\varphi_{\rm ctr} > 0$, then the sign of $\partial_r\kappa$ will be determined by the two terms: $2\alpha XFW_{,\varphi^2}\varphi$ and $\left(\omega^2A^2 - 2\alpha^2V - F^2\theta^2\right)$. The former is always positive or zero, whilst the latter can be negative, provided the magnitudes of the

potential and the lapse (i.e. $2\alpha^2 V$) are large enough to counteract the positive contribution of $\omega^2 A^2$. The last term $F^2\theta^2$ is negligible near the origin since $\theta(0) = 0$ by Eq. (6.12). The ingredients required to make $\partial_r \kappa$ negative, and thus cause the gravitational scalar φ to peak at the origin, are as follows:

1. **Large potential values** V: for typical values of $A_{\rm ctr} \in [0.1, 0.2]$ in the regime of scalarisation, the non-interacting and the repulsive potentials take on larger values compared to a solitonic potential with small σ_0; cf. Fig. 5.3.1.

2. **Small central amplitudes of the BS scalar**: models with small $A_{\rm ctr}$ result in less compact (or *fluffy*) stars. These fluffy configurations have shallower gravitational wells which manifest themselves in larger values of the lapse α near the origin[4]. Small $A_{\rm ctr}$ and the ensuing large α therefore are more likely to make the overall contribution to $\partial_r \kappa$ negative. Empirically, we find that mini and repulsive potentials, but rarely solitonic with $\sigma_0 \approx 0.2$, allow for scalarised BSs with small $A_{\rm ctr}$, i.e. low compactness; cf. Fig. 6.3.6.

This behaviour of the gravitational scalar can also be explained using the trace of the energy-momentum tensor which is obtained from Eq. (6.4)

$$T = g^{\alpha\beta} T_{\alpha\beta} = \frac{1}{F\alpha^2}\left(\omega^2 A^2 - 2\alpha^2 V - F^2\theta^2\right) . \tag{6.19}$$

Up to an overall factor, this expression equals the second source term of our above analysis that drives $\partial_r \kappa$ via Eq. (6.10). The sign of T can therefore be directly translated to the concavity of φ. Recalling that the tachyonic instability requires negative T, we expect strong scalarisation to occur in the region where $T < 0$. Fig. 6.3.5 illustrates exactly this effect: for less compact models with $T \lesssim 0$ at small r, φ peaks at the origin, and for compact models with a central $T \gtrsim 0$, φ peaks away from the origin; cf. also Fig. 6.3.2. The $\varphi(r)$ profile of particularly compact scalarised models is therefore more *shell*-like.

The onset and degree of scalarisation: The nature of the potential further determines the degree of scalarisation of BS solutions and the global properties of such models. Figure 6.3.5 illustrates one example of this for mini and repulsive potentials in the mass-radius plane, where all of the scalarised branch falls underneath the GR one for $\lambda_4 = 0$, but only part of it for $\lambda_4 = 50$. Similarly, we see in Fig. 6.C.1 in Appendix 6.C that many scalarised BSs for solitonic potentials with $\sigma \gtrsim 0.3$ have smaller masses than their GR counterparts with equal radius, very much in contrast to the solitonic $\sigma_0 = 0.2$ case of the prototypical example studied in Section 6.3.1.

[4] In our gauge, the lapse function α asymptotes to 1 at infinity and smaller values of the lapse function correspond to deeper gravitational wells and vice versa.

Table 6.3.1 Summary of threshold values of β_0 for the onset of scalarisation for different potentials in the massless case.

Potential	Coupling	$\beta_{0,\mathrm{thr}}$
Solitonic	$\sigma_0 = 0.2$	-6.079
Solitonic	$\sigma_0 = 0.3$	-7.282
Solitonic	$\sigma_0 = 0.5$	-6.641
Solitonic	$\sigma_0 = 1$	-6.219
Solitonic	$\sigma_0 = 2$	-6.128
Mini	$\lambda_4 = 0$	-6.098
Repulsive	$\lambda_4 = 50$	-5.272
Repulsive	$\lambda_4 = 100$	-4.961

Furthermore, the threshold for β_0 at which scalarisation starts to occur varies with the potential; we summarize this dependence in Table 6.3.1. Overall, we find that the repulsive potential requires less negative β_0 values for solutions to scalarise, which is then followed by the mini and solitonic potentials. For massless ST theory, the thresholds fall into a range $-7.5 \lesssim \beta_{0,\mathrm{thr}} \lesssim -4.96$, a bit below the threshold of -4.35 typically found for neutron stars.

Even though solutions are less strongly scalarised for the solitonic potential with $\sigma_0 \gtrsim 0.3$, there are some subtle features in the dependence of scalarisation on the self-interaction term as illustrated in Fig. 6.3.6. First, the degree of scalarisation varies non-monotonically with σ_0. Typically smaller values of $\sigma_0 \approx 0.2$ result in more strongly scalarised solutions than models with $\sigma_0 \approx 1$. On the other hand, larger σ_0 lead to a wider range of A_{ctr} for which scalarised solutions exist: in Fig. 6.3.6 the support of $|\varphi|_{\max}(A_{\mathrm{ctr}})$ significantly increases for models with $\sigma_0 \gtrsim 0.35$. As σ_0 increases, the scalarised branches slowly converge to the scalarised solutions of mini BSs, which can be seen by a close overlap of the $\sigma_0 = 2$ and $\lambda_4 = 0$ curves. We present a more detailed illustration of this transition in Appendix 6.C, where we compute families of solutions for a wider range of potentials. Finally, we find that for a fixed value of β_0, the strongest scalarisation occurs in the case of the repulsive potential with our largest $\lambda_4 = 100$.

Massive gravitational scalar field

Gravitational scalar profiles: We next turn to analysing the features of scalarised BS solutions with other bosonic potentials in the massive case. A systematic investigation of the global maximum of $|\varphi|$ across the parameter space confirms that for $\mu_\varphi > 0$, certain choices of the potential $V(A)$ still result in the gravitational scalar profiles peaking at the origin. However, we find that an increasing mass μ_φ tends to push the extremum of φ away from the origin. This effect can be explained using the same reasoning as in the massless case of Section 6.3.3

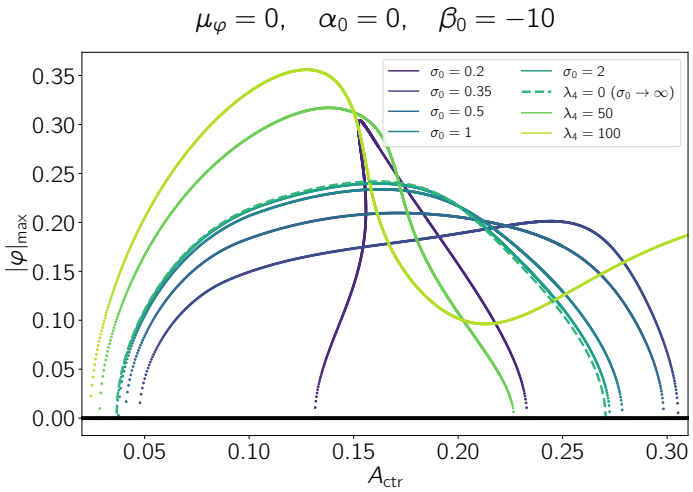


Fig. 6.3.6 Maximum of the gravitational scalar field as a function of the central bosonic amplitude for various potentials considered in this work. We remark that repulsive potentials result in more strongly scalarised solutions than any other potential considered here.

by assessing the sign of the right-hand-side of Eq. (6.10) for $\partial_r \kappa$. Assuming that $\varphi_{\rm ctr} > 0$, we conclude that $\mu_\varphi > 0$ increases the overall positive contribution from the $2\alpha X F W_{,\varphi^2} \varphi$ term and empirically we find it also increases ω. Therefore, larger values of the gravitational mass push $\partial_r \kappa$ towards positive values and the gravitational scalar φ tends to peak away from the origin.

It is possible however to push the gravitational scalar field maximum towards $r = 0$ by making β_0 negative enough. The impact of a more negative β_0 parameter is two-fold:

1. BS frequencies ω decrease,
2. The overall magnitude of $\frac{2\pi X F'}{\alpha F^2}(\omega^2 A^2 - 2\alpha^2 V)$ increases due to the larger F'/F^2 factor.

Table 6.3.2 The minimum value of σ_0 where we find BS models with a gravitational scalar peaking at $r = 0$ is listed for solitonic BS families with $\alpha_0 = 0$ as well as the specified values of μ_φ and β_0. A gravitational scalar φ reaching its global extremum at the origin is easier to obtain for smaller μ_φ and for larger β_0.

μ_φ	β_0	$\sigma_{0,\rm min}$
0	-10	0.25
0.1	-10	0.34
0.1	-14	0.24
0.3	-14	0.55

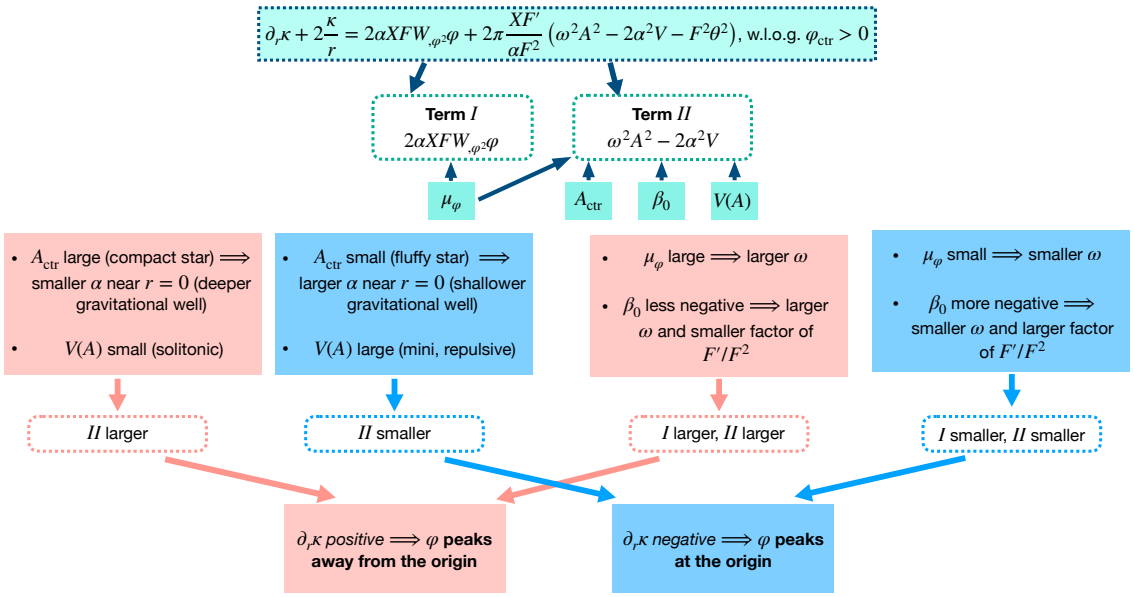


Fig. 6.3.7 Flow-chart showing the dependence of the gravitational scalar profile φ on the BS parameters, $A_{\rm ctr}$ and $V(A)$, and the ST parameters, μ_φ and β_0. As discussed in the main text, the sign of $\partial_r\kappa$ determines the behaviour of φ at the origin. If $\partial_r\kappa > 0$, φ peaks away from $r = 0$, whilst for $\partial_r\kappa < 0$, φ peaks at $r = 0$. The two source terms, denoted by I and II in the diagram, play the leading role in determining the sign of $\partial_r\kappa$ at $r = 0$. By the boxes' colours we mark how the ST and BS parameters tend to impact the φ profiles – blue for peaking at the origin and pink for peaking off centre.

The combined effect of a more negative β_0 is therefore to make the final term of the $\partial_r\kappa$ equation negative and large enough to counteract the non-zero positive contribution from $2\alpha XFW_{,\varphi^2}\varphi$ term. The sign of $\partial_r\kappa$ becomes negative and φ peaks at $r = 0$.

We quantitatively illustrate the effect of μ_φ and β_0 on the φ profile in Table 6.3.2 where we list for several combinations of (μ_φ, β_0) the minimal σ_0 values at which we find models with φ peaking at $r = 0$. Below the respective $\sigma_{0,\rm min}$, φ peaks off center for all scalarised BS models. As the Table suggests, it is easier to find φ profiles peaking at the origin for smaller gravitational masses μ_φ and more negative β_0. In Fig. 6.3.7 we summarize the dependence of the gravitational scalar profile on the BS and ST parameters. *The onset and degree of scalarisation*: Finally, we make a few remarks on the effect of $\mu_\varphi > 0$ on the scalarisation of BS solutions. As already seen in Fig. 6.3.4, the threshold $\beta_{0,\rm thr}$ for the onset of strong scalarisation for solitonic BSs with $\sigma_0 = 0.2$ is well described by a quadratic function of the mass parameter μ_φ for ST gravity with $\alpha_0 = 0$. In the upper panel of Fig. 6.3.8 we plot the onset of scalarisation for several other potential functions with parameters as listed in the legend. For all cases, the numerical data are in excellent agreement with a monotonically

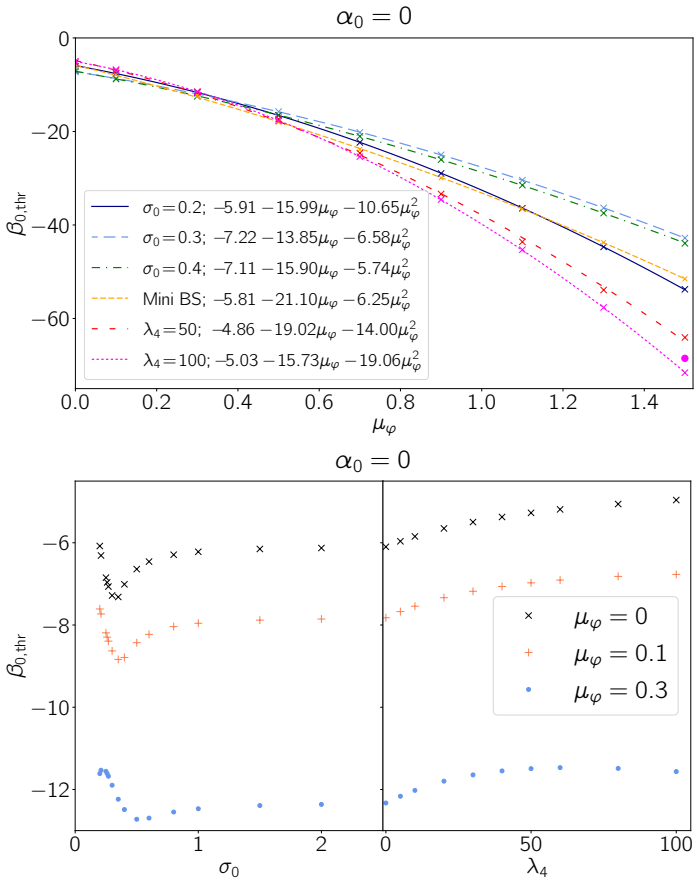


Fig. 6.3.8 *Top:* The threshold $\beta_{0,\mathrm{thr}}$ for the onset of scalarisation as a function of μ_φ for different BS potentials $V(A)$ as given in Eq. (6.17) with the indicated parameter values σ_0 and λ_4. The lines represent quadratic fits with the given coefficients. The case $\lambda_4 = 100$, $\mu_\varphi = 1.5$ exhibits one minor anomaly: here, the $\times$ symbol marks the disappearance of stable scalarised models, but extremely compact unstable BSs are still found up to the β_0 value marked by the filled circle. Only the former ($\times$) data point is used in the fit. *Bottom:* The threshold $\beta_{0,\mathrm{thr}}$ for the onset of strong scalarisation is shown for the different types of potentials and three values of the gravitational scalar mass $\mu_\varphi = 0,\ 0.1$ and 0.3. The horizontal axis represents σ_0 for the solitonic potential on the left and λ_4 for the repulsive potential on the right.

decreasing quadratic fit, which confirms our general observation that an increasing μ_φ weakens scalarisation. In order to assess in more detail how different potential functions affect the onset of scalarisation, we display in the bottom panel of Fig. 6.3.8 the threshold values $\beta_{0,\mathrm{thr}}$ as a function of the parameters σ_0 and λ_4 for three fixed values of the mass $\mu_\varphi = 0,\ 0.1$ and 0.3. We recall that mini BSs are obtained in both limits, $\sigma_0 \to \infty$ and $\lambda_4 = 0$, and can be regarded as the link between the solitonic and repulsive potential. The variation of $\beta_{0,\mathrm{thr}}$ in Fig. 6.3.8 shows that for $\mu_\varphi \lesssim 0.3$, similar to the massless case, BSs with a repulsive potential are more susceptible to scalarisation than solitonic and mini BSs, although not by a

huge amount. For $\mu_\varphi \gtrsim 0.3$, however this trend is reversed and solitonic BSs scalarise most easily.

6.3.4 Dependence on α_0

Previously we have considered ST theories with $\alpha_0 = 0$, where the solutions are degenerate under the transformation $\varphi \to -\varphi$. In the case, of $\alpha_0 \neq 0$ we acquire additional structure through the splitting of the scalarised branches. More specifically, we find[5]:

1. A larger branch (as viewed in the mass-radius plane), mostly with negative gravitational amplitudes $\varphi_{\rm ctr}$. At very high compactness (i.e. large $A_{\rm ctr}$) these models start to have $\varphi_{\rm ctr} > 0$ and the $\varphi(r)$ profiles have a zero-crossing.

2. A smaller closed loop, where we exclusively observe positive $\varphi_{\rm ctr}$.

These two branches contain strongly scalarised solutions, as well as weakly scalarised ones, in which case the BS models have similar mass and radius to their GR counterparts. This is illustrated in Fig. 6.3.9, where certain BS models of the $\alpha_0 > 0$ sequences closely resemble the GR solutions obtained for $\alpha_0 = 0$. For mild values of α_0, the closed loop intersects itself and acquires a shape similar to the ∞ symbol as in the case of $\alpha_0 = 0.01$. As we increase α_0, first the ∞-shape and then the entire loop slowly shrink and disappear (see e.g. $\alpha_0 = 0.1$). We note that certain values of α_0 we consider here are above the Cassini measurement constraint. This choice is made for visualization purposes: for smaller values of α_0 the two branches lie more closely to each other making their splitting less evident. Although here we discuss solitonic BSs, for other potentials we observe a qualitatively similar splitting of the solution branches.

The disappearance of one of the solution branches can be traced back to the conformal coupling function $F(\varphi) = \exp(-2\alpha_0\varphi - \beta_0\varphi^2)$. When $\alpha_0 = 0$, the value F is solely determined by the magnitude of β_0: a more negative β_0 leads to stronger scalarisation. A non-zero α_0, on the other hand, leads to a non-zero $-2\alpha_0\varphi$ contribution in the exponent of F. For $\varphi > 0$, this curbs the effect of β_0 and subsequent scalarisation whilst for $\varphi < 0$ the α_0 term strengthens it: for $\alpha_0 > 0$ we have $F(\varphi > 0) < F(\varphi < 0)$. This effect is further illustrated by the relative size of the scalarised branches in Fig. 6.3.9: the solution branches for $\varphi_{\rm ctr} > 0$ are systematically smaller in size than their $\varphi_{\rm ctr} < 0$ counterparts. For sufficiently large values of α_0 with fixed β_0, the solutions with $\varphi_{\rm ctr} > 0$ cease to exist and the branch disappears. Considering the case $\alpha_0 = 0.1$ and $\beta_0 = -7$, for example, we can easily support this by a back-of-the-envelope calculation: assuming $\varphi \sim 0.1$, the conformal coupling function is

[5]Recall that in our convention $\alpha_0 \geq 0$; for the opposite convention $\alpha_0 \leq 0$ the signs of φ would be reversed.

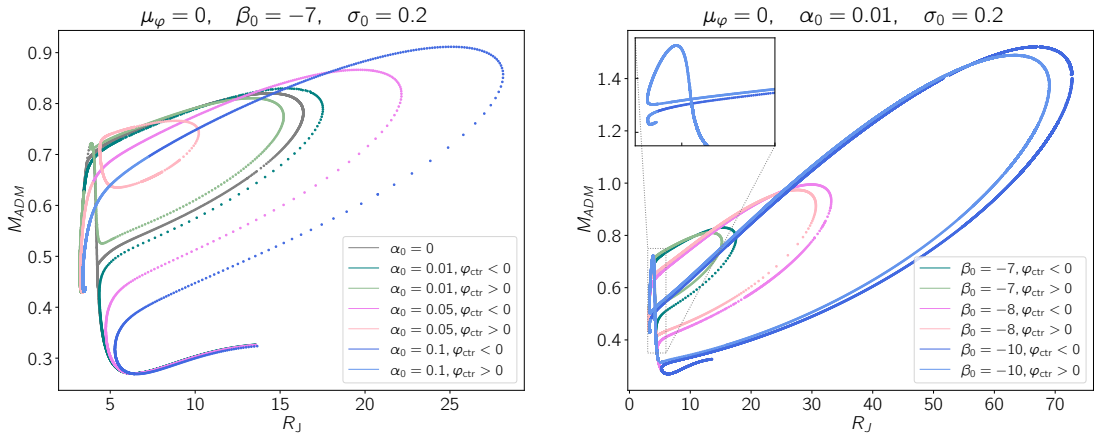


Fig. 6.3.9 *Left*: BS models in ST gravity with $\mu_\varphi = 0$, $\beta_0 = -7$ and varying α_0 for a solitonic potential with $\sigma_0 = 0.2$. The branches obtained for each value of α_0 are presented in different shades of one colour to differentiate between positive and negative central gravitational field amplitudes. For $\alpha_0 = 0.01$, for instance, dark green denotes models where $\varphi_{\rm ctr} < 0$ and light green those with $\varphi_{\rm ctr} > 0$. For reference, we also plot the solutions for $\alpha_0 = 0$ which are shown in grey. *Right*: Dependence of the BS solutions on β_0 for $\alpha_0 = 0.01$, $\mu_\varphi = 0$ and a solitonic potential with $\sigma_0 = 0.2$. The inset highlights the self-intersecting $\varphi_{\rm ctr} > 0$ branch with ∞ shape for the sequence of models with $\beta_0 = -10$.

$F(\varphi) \sim \exp(0.05)$, which is equivalent to setting $\alpha_0 = 0$ and $\beta_0 = -5$. As discussed in Section 6.3.2 (see also Fig. 6.3.4 and Table 6.3.1), however, the onset of scalarisation for $\mu_\varphi = 0$ and a solitonic potential with $\sigma_0 = 0.2$ occurs for $\beta_0 \gtrsim -6.1$. An effective $\beta_{0,\rm eff} \approx -5$ falls out of this range and is therefore compatible with the disappearance of positive solutions for $\alpha_0 = 0.1$.

Besides the branch splitting, BS solutions with $\alpha_0 > 0$ depend on β_0 and μ_φ in a way very similar to the $\alpha_0 = 0$ case discussed previously. In particular, a more negative β_0 results in stronger scalarisation of solutions, with larger mass $M_{\rm ADM}$ and radius $R_{\rm J}$ (cf. the right panel of Fig. 6.3.9). Increasing the mass parameter μ_φ, on the other hand, systematically reduces the scalarisation effect in the same way we have observed in Section 6.3.2 for $\alpha_0 = 0$.

6.3.5 Thin-shell models

In Ref. [395], Collodel and Doneva computed an intriguing type of BS solutions in GR dubbed *thin-shell* models (also see Ref. [71]). The main characteristics of these BSs are (i) an approximately constant scalar profile $A(r)$ extending out to rather large radius and (ii) a low frequency ω; see in particular their Fig. 6. As a consequence of these two features, the derivatives $\partial_t A$ and $\partial_r A$ become very small at small as well as very large radii, resulting in a nearly vanishing energy density except for a shell region where the scalar field eventually

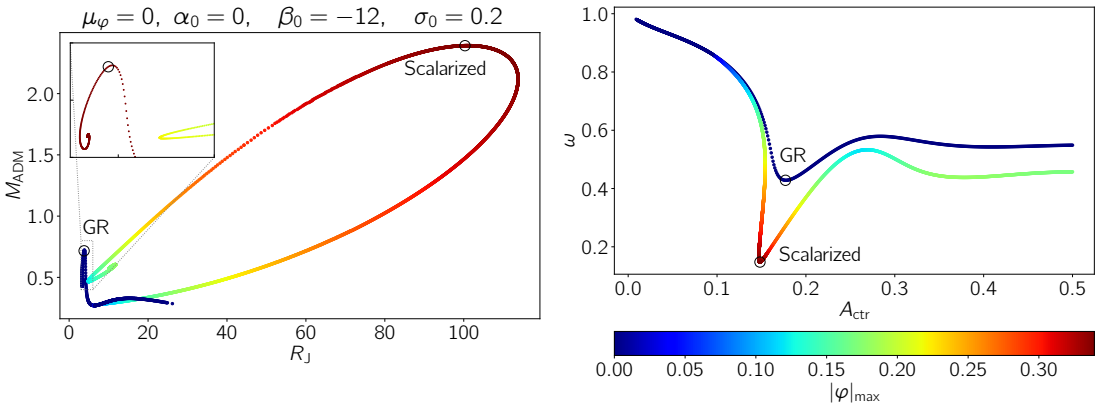


Fig. 6.3.10 *Left*: Mass-radius diagram for solitonic BS models with $\mu_\varphi = 0$, $\alpha_0 = 0$, $\beta_0 = -12$ and $\sigma_0 = 0.2$. *Right:* Frequency ω as a function of the central BS scalar amplitude $A_{\rm ctr}$ for the same family of models. The colour represents the maximal gravitational scalar in both panels.

drops to zero. In Fig. 6.3.1 for our prototypical BS family, we can see that the scalarised stars tend to have lower frequencies than their GR counterparts. We have found this behaviour systematically in our investigations of the BS and ST parameter space (see Fig. 6.C.4), suggesting that scalarisation can strengthen the thin-shell character of BSs.

We study this feature in more detail for the specific case of massless ST theory with $\alpha_0 = 0$ and $\beta_0 = -12$ for the solitonic potential with $\sigma_0 = 0.2$. Due to different conventions, our σ_0 is related to the parameter σ used by Collodel and Doneva by $\sigma = \sqrt{2\pi}\sigma_0$, so that our scenario corresponds to $\sigma \approx 0.5$ in Ref. [395], well above the regime where they encounter thin-shell stars. We likewise find no indication of shell-like structure on the GR branch of our scenario which yields a minimal frequency of about $\omega = 0.428$ in good agreement with Ref. [395]; this can be seen by comparing the right panel of our Fig. 6.3.10 with the left panel of their Fig. 2. Along the scalarised branch, however, we obtain BS models with much lower frequencies $\omega < 0.2$. As indicated in the left panel of Fig. 6.3.10, we also obtain significantly larger radii for these models, although we emphasize that this is largely due to the reduced fall-off of $A(r)$ rather than its behaviour in inner regions of the star. The radial profiles displayed in Fig. 6.3.11 for the strongly scalarised BS with minimal ω (marked by circles in Fig. 6.3.10), however, exhibit an approximately constant $A(r)$ out to $r \approx 7$. In contrast, the GR model with minimal ω displays a distinctly "ordinary" profile where $A(r)$ rapidly drops away from the origin.

A similar investigation of neighbouring models along the GR and scalarised branches yields very similar profiles and, as evident in Fig. 6.3.10, frequency values, and we observe qualitatively the same behaviour for other values of σ_0. Mathematically, we can explain this

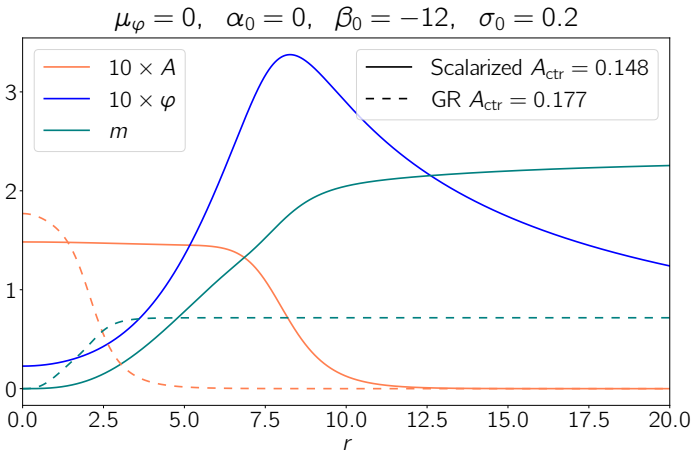


Fig. 6.3.11 Radial profiles of the scalar functions $A(r)$, $\varphi(r)$ and the mass $m(r)$ for a scalarised BS with $A_{\rm ctr} = 0.148$ and a GR model with $A_{\rm ctr} = 0.177$, corresponding to the minimal frequencies $\omega = 0.1476$ and $\omega = 0.4283$ and marked by circles in Fig. 6.3.10. For presentation purposes, the scalar fields A and φ have been amplified by a factor 10.

behaviour by considering Eq. (6.10) for $\partial_r A$ and $\partial_r \theta$. Thin-shell models can be regarded as a sequence of BSs that approach a uniformly constant scalar-field solution $A = \text{const}$ extending to larger and larger radii. In Eq. (6.10), this limiting (Minkowski) solution is obtained for a zero right-hand side of $\partial_r \theta$. Ignoring the geometric term $-2\theta/r$, which merely incorporates the r^2 behaviour of a 3D volume, the key mathematical origin of thin-shell stars is a nearly vanishing

$$\frac{X}{\alpha F}(\alpha^2 V_{,A^2} - \omega^2)\,. \tag{6.20}$$

For strongly scalarised BSs, $F(\varphi)$ is dominated by the quadratic contribution in the exponential (6.14) and therefore $F > 1$ which reduces the term (6.20) relative to its GR value and hence drives BSs in the direction of thin-shell models.

6.4 Stability

Depending on the ST parameters $(\mu_\varphi, \alpha_0, \beta_0)$ and the potential $V(A)$, there may exist up to seven (or even more for non-zero α_0) BS models with the same mass. This raises the question which of these models is energetically favoured. We assess this by using binding energy arguments for a wide range of BS solutions. More specifically, we define the binding energy

$$E_{\rm b} := M_{\rm ADM} - Q_{\rm BS}, \tag{6.21}$$

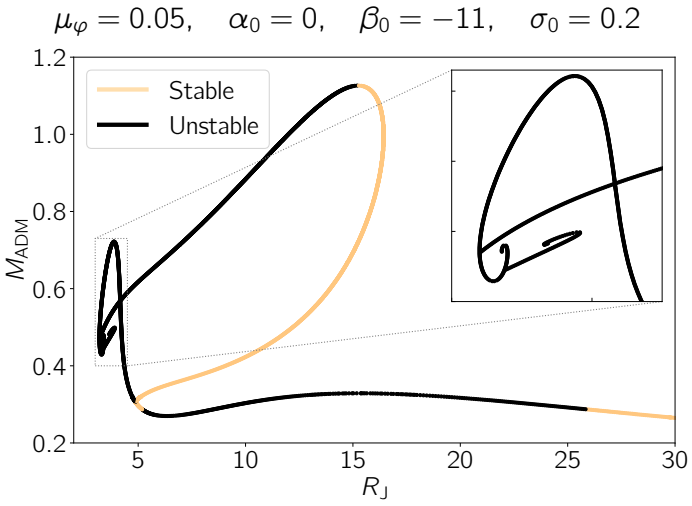


Fig. 6.4.1 Mass-radius diagram for BS solutions for $\mu_\varphi = 0.05,\ \alpha_0 = 0,\ \beta_0 = -11$ and a solitonic potential with $\sigma_0 = 0.2$. Stable models are determined by identifying among the set of all stars with equal Noether charge $Q_{\rm BS}$ the BS with the strongest binding energy $E_{\rm b} = M_{\rm ADM} - Q_{\rm BS}$. These stable models are displayed in light (copper) colour and the remaining unstable stars in dark (black).

where $Q_{\rm BS}$ denotes the conserved Noether charge, i.e. the number of bosonic particles making up the BS. It is defined as the spatial integral of the time component of the Noether current,

$$J^\alpha = \frac{\mathrm{i}}{2} g^{\alpha\beta} \left(\psi^* \nabla_\beta \psi - \psi \nabla_\beta \psi^* \right), \tag{6.22}$$

so that

$$Q_{\rm BS} = \int J^0 \sqrt{-g} \mathrm{d}x^3 = \int \frac{4\pi A^2 \omega X}{F\alpha} r^2 \mathrm{d}r. \tag{6.23}$$

For each set of BSs with equal Noether charge[6], the model with the strongest binding energy $E_{\rm b}$, i.e. the smallest mass $M_{\rm ADM}$, is taken as the stable, energetically favoured configuration. This does not necessarily imply that the other models are *perturbatively* unstable, but under sufficiently strong excitations, we expect them to either form a black hole, evaporate or migrate to a stable BS; we therefore refer to these other models as unstable in the following discussion.

We first apply this method to the prototypical example discussed in Section 6.3.1. This set of BS models is obtained for ST parameters $\mu_\varphi = 0.05,\ \alpha_0 = 0,\ \beta_0 = -11$ and a solitonic potential with $\sigma_0 = 0.2$. Figure 6.4.1 shows the same mass-radius diagram as Fig. 6.3.1 but now colour codes solutions in light (copper) for stable or dark (black) for unstable stars. We

[6]We remark that $Q_{\rm BS}$ in Eq. (6.23) is equal in both, Jordan and Einstein frames, making it a universal diagnostic.

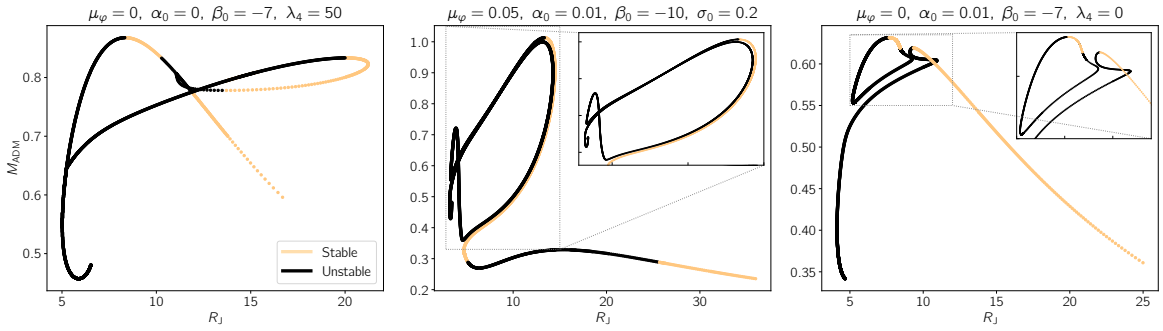


Fig. 6.4.2 Stability of other BS models considered in this work. From left to right: (i) repulsive potential with $\lambda_4 = 50$, massless φ, $\alpha_0 = 0$, $\beta_0 = -7$; (ii) solitonic potential with $\sigma_0 = 0.2$, massive φ with $\mu_\varphi = 0.05$, $\alpha_0 = 0.01$, $\beta_0 = -10$; (iii) mini potential with $\lambda_4 = 0$, massless φ, $\alpha_0 = 0$, $\beta_0 = -7$. As in Fig. 6.4.1, light (copper) colour denotes stable BS models and dark (black) unstable ones. Note that for $\alpha_0 \neq 0$ (center and right panels) we always have two separate scalarised branches, either of which may self-intersect: one closed loop and one open branch with two loose ends. For the mini BS in the right panel, these two branches almost touch, yet remain separate as shown in the inset.

clearly see that the scalarised branch from the low-mass bifurcation point all the way up to its maximal mass at about $(R_{\rm J} \approx 15, M_{\rm ADM} \approx 1.1)$ contains energetically favoured models. This set of stable BSs is completed by a small piece of the GR branch around $R_{\rm J} = 5$ which contains low-mass but comparatively compact BSs for whom no scalarised counterparts exist.

Repeating the same analysis in Fig.6.4.2 for other bosonic potentials and ST parameters, unravels a very similar pattern. For $\alpha_0 = 0$ scalarised BSs are commonly energetically favoured relative to their GR cousins with equal Noether charge. For non-zero α_0, where we commonly encounter multiple scalarised branches, we observe that strongly scalarised BSs with *larger* radius tend to be stable. We identify some exceptions to these rules, however: scalarised BSs with relatively small mass or radius may be energetically disfavoured relative to other scalarised solutions (see the left panel of Fig. 6.4.2) and, in some cases, even relative to GR models (see Fig. 6.C.5 in Appendix 6.C, where we explore a wider range of potentials V). In general, we observe that, similarly to BS models in GR, stable and unstable models in ST gravity are separated by the maximum-mass model.

6.5 Conclusions

In this Chapter we have performed a systematic study of the structure of strongly and weakly scalarised boson-star solutions in scalar-tensor theory of gravity with Damour-

Esposito-Farèse coupling. For this purpose we compute spherically symmetric ground-state BS models using shooting and relaxation algorithms. In order to control the challenging exponential behaviour of the scalar field solutions, we perform a comprehensive analysis of their asymptotic behaviour, identifying incompatibilities that arise from using the flat-field limit.

Our study suggests that there are many common features in the dependence of scalarised solutions on the ST parameters $(\mu_\varphi, \alpha_0, \beta_0)$ as compared to the neutron star case. In particular, we observe the following main features:

1. The scalarised solutions form additional branches in the mass-radius plane. These models can have larger mass and radius compared to their GR counterparts, although exceptions to this rule exist, depending on the potential and ST parameters.

2. A smaller gravitational scalar mass μ_φ and a more negative β_0 strengthen scalarisation, pushing the scalarised branch to larger radii; cf. Fig. 6.3.3 and the right panel of Fig. 6.3.9.

3. A non-zero α_0 splits the scalarised branches by breaking the $\varphi \to -\varphi$ degeneracy; cf. the left panel of Fig. 6.3.9. For sufficiently large values of α_0 one of the branches disappears.

4. Scalarised solutions are often energetically preferred (i.e. stable) when compared to their GR counterparts with the same Noether charge. We similarly find that a larger BS radius tends to favour stability.

Further to these main features, we summarize the specific traits inherent to scalarised BSs and their variation over the parameter space as follows.

Onset of scalarisation: Compared with neutron stars, we require more negative values of β_0 to obtain scalarised BSs. Our analysis suggests that BSs with repulsive potentials with large λ_4 are most susceptible to scalarisation in the massless case: the onset of scalarisation happens for $\beta_0 \lesssim -4.96$, compared to $\beta_0 \lesssim -4.35$ for NSs. Mini and solitonic BSs are less liable to scalarise and typically require more negative β_0. This trend also holds in the massive case up to $\mu_\varphi \approx 0.3$, beyond which solitonic BSs become more receptive to scalarisation. For all potentials, the threshold for scalarisation $\beta_{0,\mathrm{thr}}$ takes on a quadratic dependence on the mass term μ_φ; cf. Fig. 6.3.8.

Degree of scalarisation: The repulsive potential for large λ_4 results in the strongest scalarisation, both in magnitude and range of BS models. For solitonic potentials, in contrast, we observe a non-monotonic dependence of the degree of scalarisation on the self-interaction

parameter σ_0. In general small $\sigma_0 \approx 0.2$ leads to stronger scalarisation albeit over a narrower range of BS models than larger values $\sigma_0 \gtrsim 1$ and the mini BS limit $\sigma_0 \to \infty$; cf. Fig. 6.3.6.

Gravitational scalar behaviour: The potential not only determines the onset and degree of scalarisation, but also the resulting compactness of the star and the gravitational scalar behaviour near the origin; cf. Fig. 6.3.7. Generally, we find that less compact stars support a gravitational scalar whose radial profile peaks at the origin; this is most common for mini and repulsive potentials that result in less compact stars. As attractive self-interaction terms are included in the solitonic potential, the scalarised solutions become more compact and the gravitational scalar's extremum moves away from the origin. We also relate this behaviour to the trace of the energy-momentum tensor T, which needs to be negative in the regions of strong scalarisation. We systematically observe that less compact models achieve negative values of T near the origin; cf. Fig. 6.3.5. For more compact models, in contrast, T only becomes negative further away from $r = 0$ resulting in *shell*-like gravitational scalar profiles.

Thin-shell like models: Strong self-interactions in the solitonic potential (small σ_0) paired with strong scalarisation (small gravitational scalar mass μ_φ and/or very negative β_0) result in BS models akin to the *thin-shell* BS models found in GR [395]. These models correspond to highly massive BS solutions in their family and have a bosonic field amplitude $A(r)$ approximating the shape of a Heaviside function. In GR, typically small values of $\sigma_0 \lesssim 0.15$ are required to obtain such thin-shell like solutions. In ST theory, however, we easily find such models already for $\sigma_0 = 0.2$.

Our results demonstrate the rich structure of BSs in ST theory of gravity and open many opportunities for future work. A natural extension consists in further exploration of more extreme regions of the parameter space, as for example a thorough study of the onset of scalarisation for thin-shell models with $\sigma_0 < 0.2$. Furthermore, dynamical evolutions of our models would provide a robust picture of their stability complementary to our binding energy estimates. Finally, it will be intriguing to see how the peculiarities identified in the structure of single BSs for different ST parameters and/or BS potentials affect the gravitational-wave emission of binary systems including the scalar (breathing) polarisation mode.

Appendix

Appendix 6.A Asymptotic Behaviour

In this Appendix, we analyse the asymptotic behaviour of the BS and gravitational scalar fields in ST theory of gravity at infinity. Our discussion follows the asymptotic analysis of BSs in GR of Section 5.4.3, except we generalise it to the ST theory. We work in the compactified coordinate $y := 1/r$ and define re-scaled variables, separating the exponential behaviour in the following way,

$$\begin{aligned} \zeta &:= \frac{e^{k/y}}{y^{\varepsilon}} A\,, & \Pi &:= -\frac{e^{k/y}}{y^{\varepsilon}} \theta\,, \\ \rho &:= \frac{e^{h/y}}{y^{\delta}} \varphi\,, & \Lambda &:= -\frac{e^{h/y}}{y^{\delta}} \kappa\,, \end{aligned} \tag{6.24}$$

where the exponents $\varepsilon, k, h, \delta$ are as yet unspecified parameters and the goal of this section will be to determine them. As we will see below, their values will depend on the specifics of the BS model and ST parameters in question. The field equations for the re-scaled variables (6.24) are obtained by substituting them into Eqs. (6.10), which leads to

$$\begin{aligned} \partial_y \Phi &= -\frac{FX^2-1}{2y} + \frac{y^{2\delta-3}}{e^{2h/y}} X^2 \left(F\hat{W}\rho^2 - \frac{\Lambda^2}{2\alpha^2} \right) + 2\pi y^{2\varepsilon-3} \frac{X^2}{F\alpha^2} e^{-2k/y} \left(\alpha^2 \hat{V} \zeta^2 - \omega^2 \zeta^2 - F^2 \Pi^2 \right), \\ \partial_y m &= -\frac{y^{2\delta-4}}{e^{2h/y}} \left(\hat{W}\rho^2 + \frac{\Lambda^2}{2F\alpha^2} \right) - \frac{2\pi y^{2\varepsilon-4}}{F^2\alpha^2} e^{-2k/y} \left(\omega^2 \zeta^2 + \alpha^2 \hat{V} \zeta^2 + F^2 \Pi^2 \right), \\ \partial_y \rho &= \frac{X\Lambda/\alpha - (y\delta + h)\rho}{y^2}, \\ \partial_y \Lambda &= \frac{(2-\delta)y - h}{y^2} \Lambda + 2\frac{\alpha X F}{y^2} W_{,\varphi^2} \rho + \frac{2\pi}{y^{2+\delta-2\varepsilon}} e^{(h-2k)/y} \frac{X}{\alpha} \frac{F'}{F^2} \left(\omega^2 \zeta^2 - 2\alpha^2 \hat{V} \zeta^2 - F^2 \Pi^2 \right), \\ \partial_y \zeta &= \frac{FX\Pi/\alpha - (\varepsilon y + k)\zeta}{y^2}, \\ \partial_y \Pi &= \frac{(2-\varepsilon)y - k}{y^2} \Pi + \frac{X\zeta}{\alpha F y^2} \left(\alpha^2 V_{,A^2} - \omega^2 \right), \end{aligned} \tag{6.25}$$

where we denoted $\hat{W} := W/\varphi^2$ and $\hat{V} := V/A^2$. Note that the equation for $\partial_y\Lambda$ contains an exponential factor $\exp[(h-2k)/y]$ which diverges when $h > 2k$, resulting in unphysical spacetimes. We are thus left with two remaining possible scenarios: $h < 2k$ and $h = 2k$. All BS families studied in this work comfortably fall into the range $h < 2k$ which is the case we henceforth focus on.

Assuming that we recover a Schwarzschild metric at infinity, we propose the following ansätze around $y = 0$

$$\begin{aligned}
\Phi(y) &= \Phi_0 + \Phi_1 y + \Phi_2 y^2 + \Phi_3 y^3 + \Phi_4 y^4 + \dots, \\
m(y) &= M + m_1 y + m_2 y^2 + m_3 y^3 + m_4 y^4 + \dots, \\
\rho(y) &= \rho_1 y + \rho_2 y^2 + \rho_3 y^3 + \rho_4 y^4 + \dots, \\
\Lambda(y) &= \Lambda_1 y + \Lambda_2 y^2 + \Lambda_3 y^3 + \Lambda_4 y^4 + \dots, \\
\zeta(y) &= \zeta_1 y + \zeta_2 y^2 + \zeta_3 y^3 + \zeta_4 y^4 + \dots, \\
\Pi(y) &= \Pi_1 y + \Pi_2 y^2 + \Pi_3 y^3 + \Pi_4 y^4 + \dots.
\end{aligned} \tag{6.26}$$

Plugging these expansions into Eqs. (6.25) and considering terms order by order, we obtain a set of equations for the coefficients that leave[7] $\Phi_0, M, \zeta_1, \rho_1$ unspecified but uniquely determine all other coefficients in terms of the free parameters. The latter are eventually obtained by matching the exterior solution of Eqs. (6.25) to the interior solution of Eqs. (6.10) as described in more detail in Appendix 6.B.

Applying the series expansion for a massive gravitational scalar field, we arrive at the following relations for the free parameters in Eq. (6.24),

$$\boxed{k^2 = 1 - \frac{\omega^2}{e^{2\Phi_0}},\ \varepsilon = M\frac{2k^2-1}{k},\ \delta = Mh,\ h^2 = \mu_\varphi^2.} \tag{6.27}$$

Note that we obtain the asymptotic behaviour of BSs in GR by simply omitting the ρ and Λ coefficients intrinsic to ST gravity.

In the massless case $\mu_\varphi = 0$, we follow a similar procedure, except now there is no exponential fall-off for the gravitational scalar field, i.e. $h = 0$ and $\delta = 0$. Again, applying the asymptotic ansätze (6.26) and considering terms order by order in Eqs. (6.25), we arrive at

$$\boxed{k^2 = 1 - \frac{\omega^2}{e^{2\Phi_0}},\ \varepsilon = M\frac{2k^2-1}{k} + \frac{\alpha_0\rho_1}{k}.} \tag{6.28}$$

[7] The coefficient M turns out to equal the ADM mass, $M_{\rm ADM}$; for simplicity we use M in this discussion.

In summary, the re-scaled variables in Eq. (6.24) together with the series expansions in Eq. (6.26) imply that the bosonic and gravitational scalar fields have asymptotic behaviours given by,

$$\boxed{\varphi \sim e^{\pm h/y} y^{1+\delta} \quad \text{and} \quad A \sim e^{\pm k/y} y^{1+\varepsilon}}, \tag{6.29}$$

where h, k, δ and ε are determined by Eqs. (6.28) and (6.27) for massless and massive φ, respectively.

All frequencies we report in this work correspond to a unit lapse function at infinity, i.e. $\Phi_0 = 0$; even if a non-zero Φ_0 is used in the numerical calculation, this is straightforwardly achieved by an a-posteriori rescaling of ω. The frequencies thus obtained ubiquitously fall into the range $0 < \omega < 1$. The functional behaviour $k(\omega) = \sqrt{(1-\omega^2)}$ furthermore pushes k towards values rather close to unity in exactly the same way the Lorentz factor $\gamma = 1/\sqrt{1-v^2}$ reduces relativistic effects for all velocities but those close to the speed of light. This effect avoids extreme values of ε which we typically find to be in the range $-2 \lesssim \varepsilon \lesssim 3$. An unscalarised low-density mini BS with $M = 0.345$ and $\omega = 0.9785$, for instance, has $\varepsilon = -1.53$ whereas the strongly scalarised thin-shell BS with $M = 2.39$ and $\omega = 0.148$ of the $(\mu_\varphi = 0,\ \alpha_0 = 0,\ \beta_0 = -12,\ \sigma_0 = 0.2)$ family discussed in Section 6.3.5 has $\varepsilon = 2.31$. The exponential factor h for the asymptotic behaviour of the gravitational scalar, on the other hand, is directly given by the scalar mass μ_φ and the exponent δ merely acquires an extra factor of the BS mass M; δ vanishes in massless ST theory, but can reach values up to order unity for the BS sequences studied in this work. We similarly obtain values $\rho_1 = \mathcal{O}(1)$ for strongly scalarised stars.

Appendix 6.B Numerics

We have written three different codes for the numerical solution of the ODE system (6.10) with the boundary conditions (6.12). This slightly unusual approach was motivated by two main considerations. First, it was not entirely clear how the challenging asymptotic behaviour of the two scalar fields might be best controlled numerically. Second, in the absence of literature results for comparison, we wished to verify our results with independent means. Here, we briefly describe our schemes and assess the uncertainty of our results.

Numerical shooting: Our first code operates in a way similar to the BS shooting code developed for GR in Ref. [141]. Starting with $\Phi = 0$, $X = 1/\sqrt{F(\varphi)}$, $A = A_{\rm ctr}$, $\varphi = \varphi_{\rm ctr}$, $\kappa = 0$, $\theta = 0$ at $r = 0$ as well as an initial guess for the frequency eigenvalue ω, the system (6.10) is integrated outwards using a fourth-order Runge Kutta scheme. At some radius,

similar to the GR case, the scalar fields start to diverge and we deal with this divergence for each of the fields individually in the following way:

1. We find the radius where the scalar field modulus starts to exceed its central value by an order of magnitude (this usually happens sooner for A).

2. We terminate the integration at that point and search for the last local extremum of the scalar field.

3. As a buffer, we take 90% of the radius where that extremum occurs, which consequently determines our matching radius, $r_{\rm m}$.

4. At $r_{\rm m}$, we match the integrated solution to the asymptotics presented in Appendix 6.A.

In the massless case, we find that the gravitational scalar field can be integrated out, without any matching, as long as the BS scalar field is matched to its corresponding asymptotic expansion. In the massive case, in contrast, both fields have to be matched and this is done at radii $r_{{\rm m},A}$ and $r_{{\rm m},\varphi}$ which are not necessarily equal. Once the full solution is constructed, we assess the quality of the matching for both scalar fields. In the massive case, we do so by computing smoothness conditions at the matching radii:

$$C(\varphi) = \left| \varphi + \frac{\varphi'(r_{{\rm m},\varphi})}{1+\delta+r_{{\rm m},\varphi} m_\varphi} r_{{\rm m},\varphi} \right| , \tag{6.30}$$

$$C(A) = \left| A + \frac{A'(r_{\rm m,A})}{1+\varepsilon+r_{\rm m,A}\sqrt{1-\omega^2}} r_{\rm m,A} \right| , \tag{6.31}$$

where δ and ε are defined in Eq. (6.27). These conditions are obtained by translating the asymptotic expressions in Eq. (6.24) into relations between the scalar variables and their derivatives. In the massless case, we replace the $C(\varphi)$ criterion by an analytic condition that relates the vacuum solution at the stellar surface (shortly to be defined), $\varphi_{\rm s}$, to its asymptotic value, φ_0, at $r=\infty$ [273],

$$\varphi_{\rm s} = \varphi_0 - \frac{X_{\rm s}\eta_{\rm s}}{\sqrt{(\partial_r \Phi_{\rm s})^2 + X_{\rm s}\eta_{\rm s}}} \operatorname{artanh} \frac{\sqrt{(\partial_{\rm r}\Phi_{\rm s})^2 + {\rm X_s}\eta_{\rm s}}}{\partial_{\rm r}\Phi_{\rm s} + 1/{\rm r_s}} . \tag{6.32}$$

Here $\eta_s = \kappa_s/\alpha_s$ and, in our convention, $\varphi_0 = 0$. Since BSs do not have a surface, we compute the gravitational scalar field at the outer edge of the grid, $\varphi(r_{\rm end})$ (typically $r_{\rm end}=1200$), and evaluate the quality of the solution using a new criterion, $C(\varphi_{\rm massless}) = |\varphi(r_{\rm end}) - \varphi_{\rm s}|$. Improved guesses for $\varphi_{\rm ctr}$ and ω are then constructed through a standard Newton-Raphson

method [474], until the conditions $C(\varphi)$ and $C(A)$ are satisfied at the required threshold level, chosen to be 10^{-7} or smaller.

Two-way shooting: The second code operates with an inner region $r \in [0,2]$ where Eqs. (6.10) are integrated outward and an exterior region $y \in [0, \frac{1}{2}]$ where $y = 1/r$ and the BS equations (6.25) for the rescaled variables are integrated inwards from infinity to $y = 1/2$. Whereas integrating out of $r = 0$ is straightforwardly achieved by using the regularity of the variables, the integration out of $y = 0$ can result in numerical instabilities at very small y, likely due to the divisions by positive powers of y in several terms on the right-hand side of Eq. (6.25). We overcome these instabilities by using the asymptotic expansion (6.26) to a small but finite y, typically $y = 0.01$. We can reduce this value to arbitrarily small level by increasing the number of grid points in the exterior and employ this reduction in the uncertainty estimate through convergence analysis. A solution is obtained when the interior and exterior solutions thus obtained satisfy the 6 matching conditions (6.24) and (6.9) at $r = 2$ with a relative precision of 10^{-6} or better. In order to start the integrations at $r = 0$ and $y = 0$, we need to specify 7 parameters, $\varphi_{\rm ctr}$, $A_{\rm ctr}$ and $\Phi_{\rm ctr}$ at the origin, M, ζ_1 and ρ_1 at infinity as well as the frequency ω. With 7 free parameters for 6 matching conditions, we obtain one-parameter families of solutions, as expected. In practice, we choose one of the 7 free parameters to control the specific BS model, initialize the other 6 parameters with initial guesses typically obtained from neighbouring BSs, and solve the matching conditions with a Newton-Raphson iteration.

Relaxation: The third code uses a Newton-Raphson based relaxation scheme, implemented according to Chapter 17.3 of Ref. [474]. Here, we again operate with an inner and an outer region using the ODE system in the forms (6.10) and (6.25), respectively. The compactified grid and algorithm allows us to impose exact boundary conditions at spatial infinity. We also have the seven free parameters as in the two-way shooting code which now impose 6 boundary conditions needed in the relaxation scheme and leave one parameter free to control the specific model. The initial guess for the iterative procedure is either obtained from other BS solutions close by in parameter space, from the shooting code discussed at the start of this subsection or from outward integrated profiles starting with guesses for $A_{\rm ctr}$ and $\varphi_{\rm ctr}$ to which we append the exponentially decaying behaviour on the outer grid.

We have assessed the numerical uncertainties of our codes by verifying the respective convergence properties and by comparing the codes' results directly. For all our diagnostics this results in a relative error and agreement of 10^{-4} or better.

Appendix 6.C Boson-star families

In this appendix we illustrate the bulk properties of a wide range of BS solutions in the form of mass-radius diagrams for various potentials of the BS scalar. For this purpose, we have chosen a massless gravitational scalar, $\mu_\varphi = 0$, with vanishing α_0 (for non-zero α_0 the branches would exhibit the splitting discussed in Section 6.3.4), and $\beta_0 = -10$ which results in strongly scalarised models for all potentials considered. In each panel, the potential $V(A)$ is characterized by the corresponding values of σ_0 for solitonic BSs and λ_4 for massive BSs. The results shown in Fig. 6.C.1 demonstrate a rather complex variation of the branches with σ_0 for solitonic BSs, including even one case, $\sigma_0 = 0.35$, where all scalarised stars have a lower mass than their GR counterparts with equal radius. The parameter λ_4 for massive BSs, in contrast, has a relatively straightforward impact on the scalarised BSs' bulk properties, leading to systematically larger radii and masses as λ_4 is increased.

In Figs. 6.C.2-6.C.4, we display the same solutions but with $|\varphi|_{\rm ctr}$, $A_{\rm ctr}$ and ω encoded in colour. For solitonic potentials, the maximal value $|\varphi|_{\rm max}$ generally exceeds the central $|\varphi|_{\rm ctr}$, demonstrating that the gravitational scalar tends to peak away from the origin. For the mini BS case and repulsive potentials, on the other hand, $|\varphi|_{\rm max}$ and $|\varphi|_{\rm ctr}$ are much closer which illustrates the trend towards φ peaking near the origin. For all potentials, Fig. 6.C.4 exhibits lower frequency values along the scalarised branch as compared to the GR models, confirming the observation made in the bottom panel of Fig. 6.3.10 for thin-shell models. As exemplified by the solitonic potentials for $\sigma_0 \approx 0.35$, this is not simply a consequence of scalarised BSs being larger, but a more complex phenomenon.

Finally, we mark in Fig. 6.C.5 the stable and unstable models by light (copper) and dark (black) colour. The general trend is that scalarised models are energetically favoured as has also been observed for neutron stars. There are some exceptions to this rule, however. (i) Scalarised stars need to be sufficiently massive to become the stable member; cf. the cases $\sigma_0 = 0.35$ and 0.4 where scalarised BSs are mostly lighter than their GR counterparts and are *not* stable. (ii) At the very low-mass end, the GR models with very low compactness are favoured over their low-mass, high-compactness scalarised cousins. These features can result in rather chequered stability curves as for example in the case $\sigma_0 = 0.5$. Along both, GR and scalarised branches, the transition from stable to unstable BS models often occurs at local maxima in the mass viewed as a function of radius.

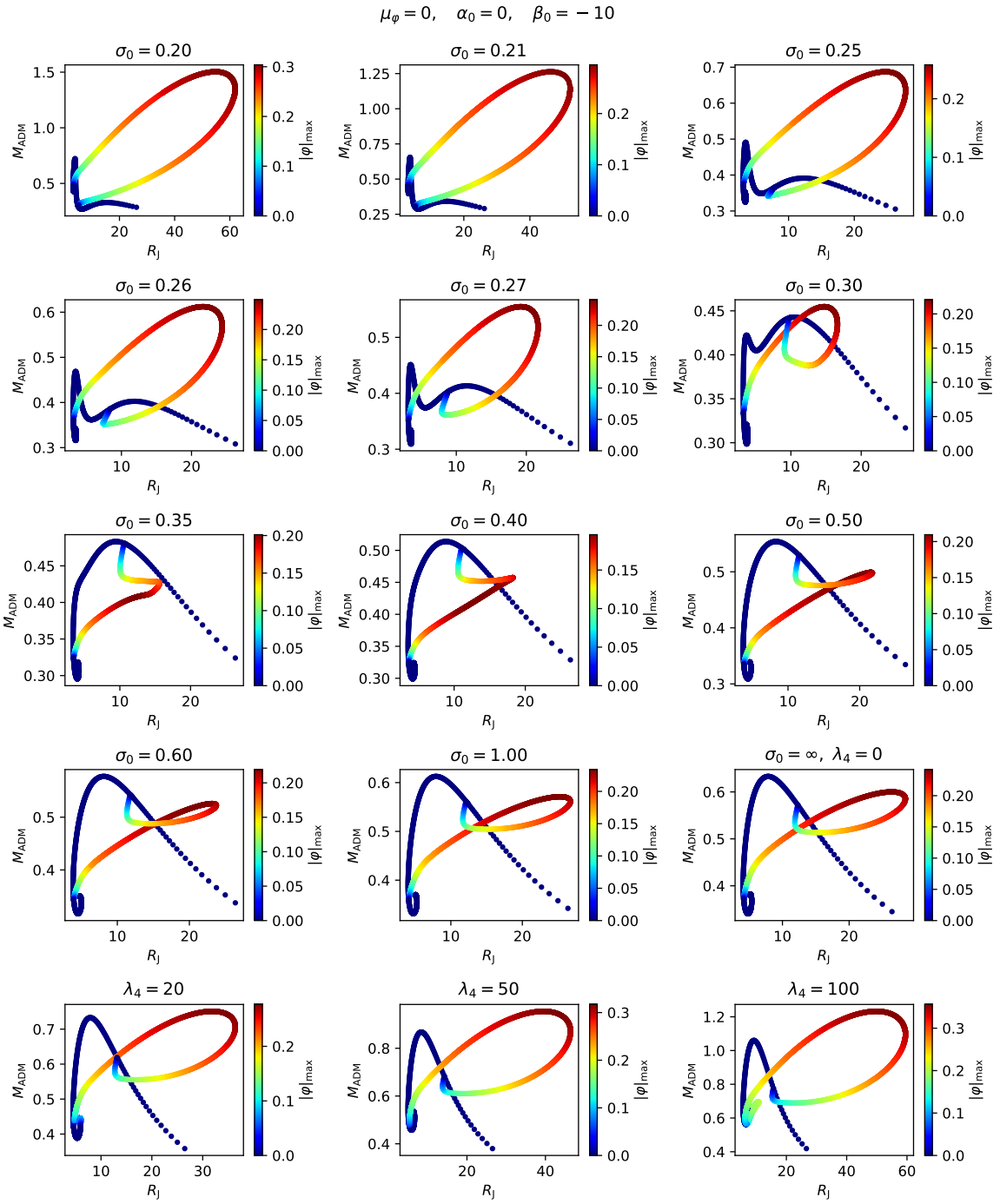


Fig. 6.C.1 Boson-star families in the mass-radius plane for fixed ST parameters $\alpha_0 = 0$, $\beta_0 = -10$, $\mu_\varphi = 0$ and BS potential functions $V(A)$ as given in Eq. (6.17). The parameters σ_0 or λ_4 are specified in each panel for the corresponding BS family. The mini-BS case is recovered in either of the limits $\sigma_0 \to \infty$ or $\lambda_4 = 0$. The colour bar marks the degree of scalarisation in terms of the maximum of $|\varphi(r)|$.

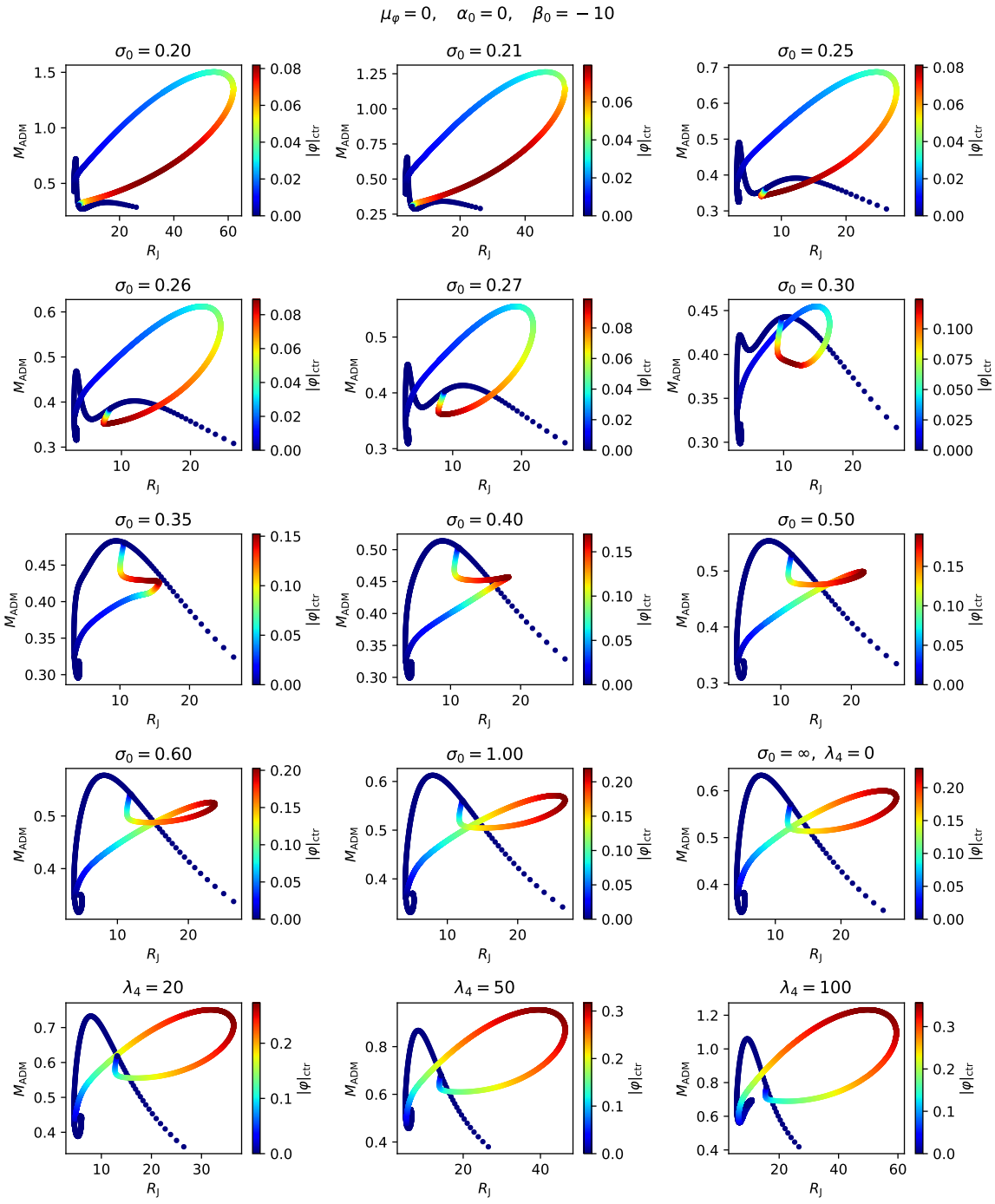


Fig. 6.C.2 Same as Fig. 6.C.1 but with $|\varphi|_{\rm ctr}$ colour coded.

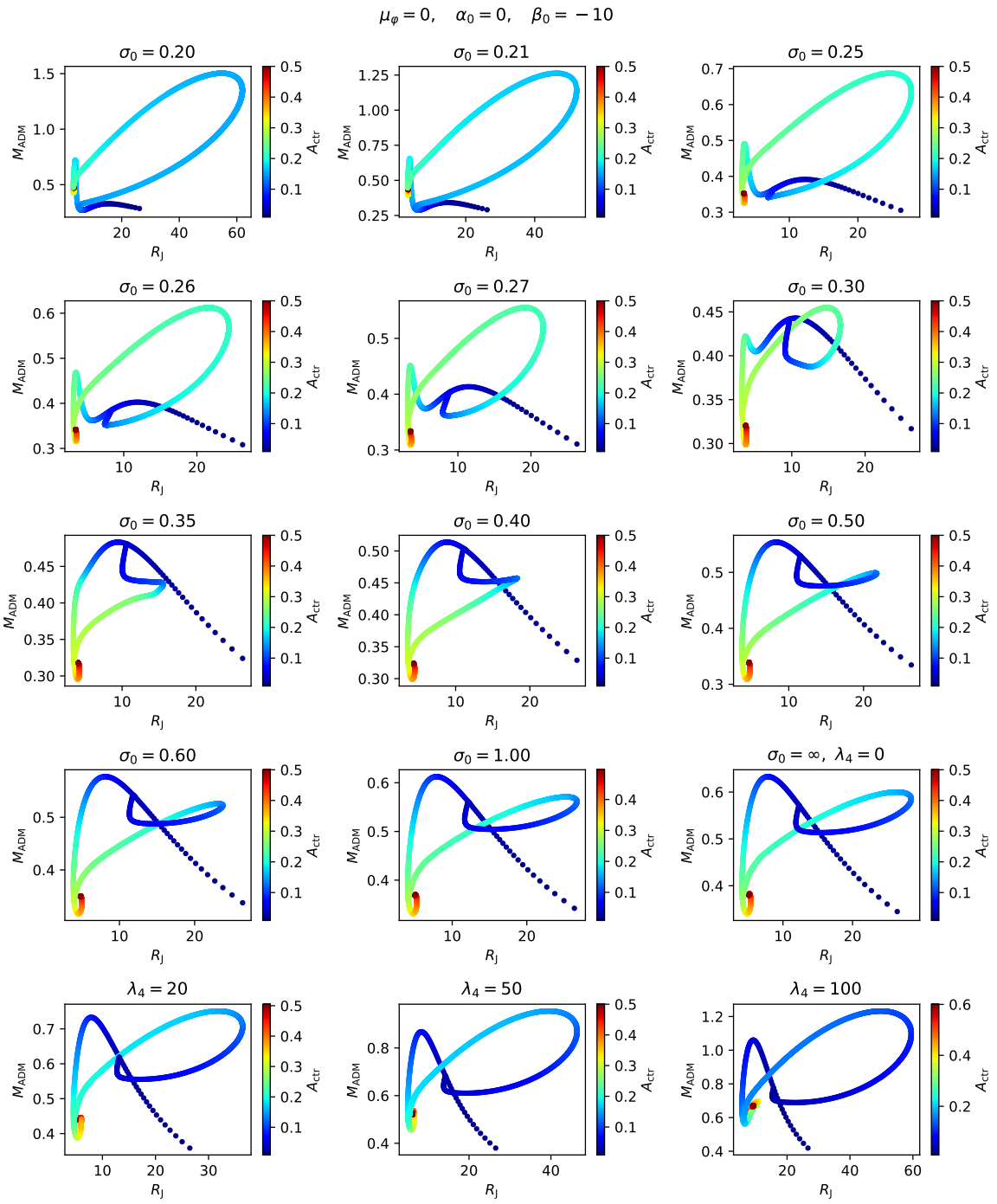


Fig. 6.C.3 Same as Fig. 6.C.1 but with $A_{\rm ctr}$ colour coded.

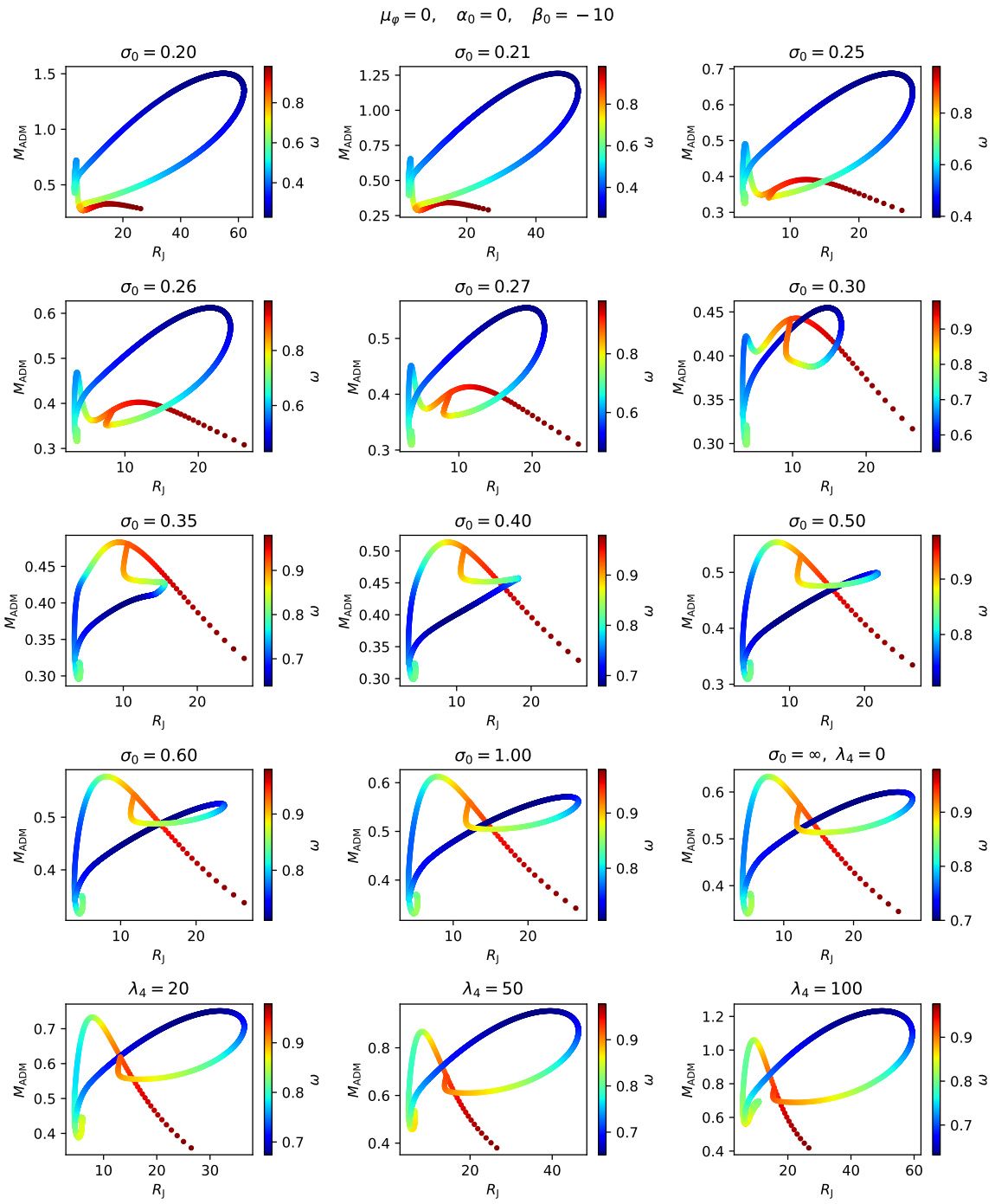


Fig. 6.C.4 Same as Fig. 6.C.1 but with ω colour coded.

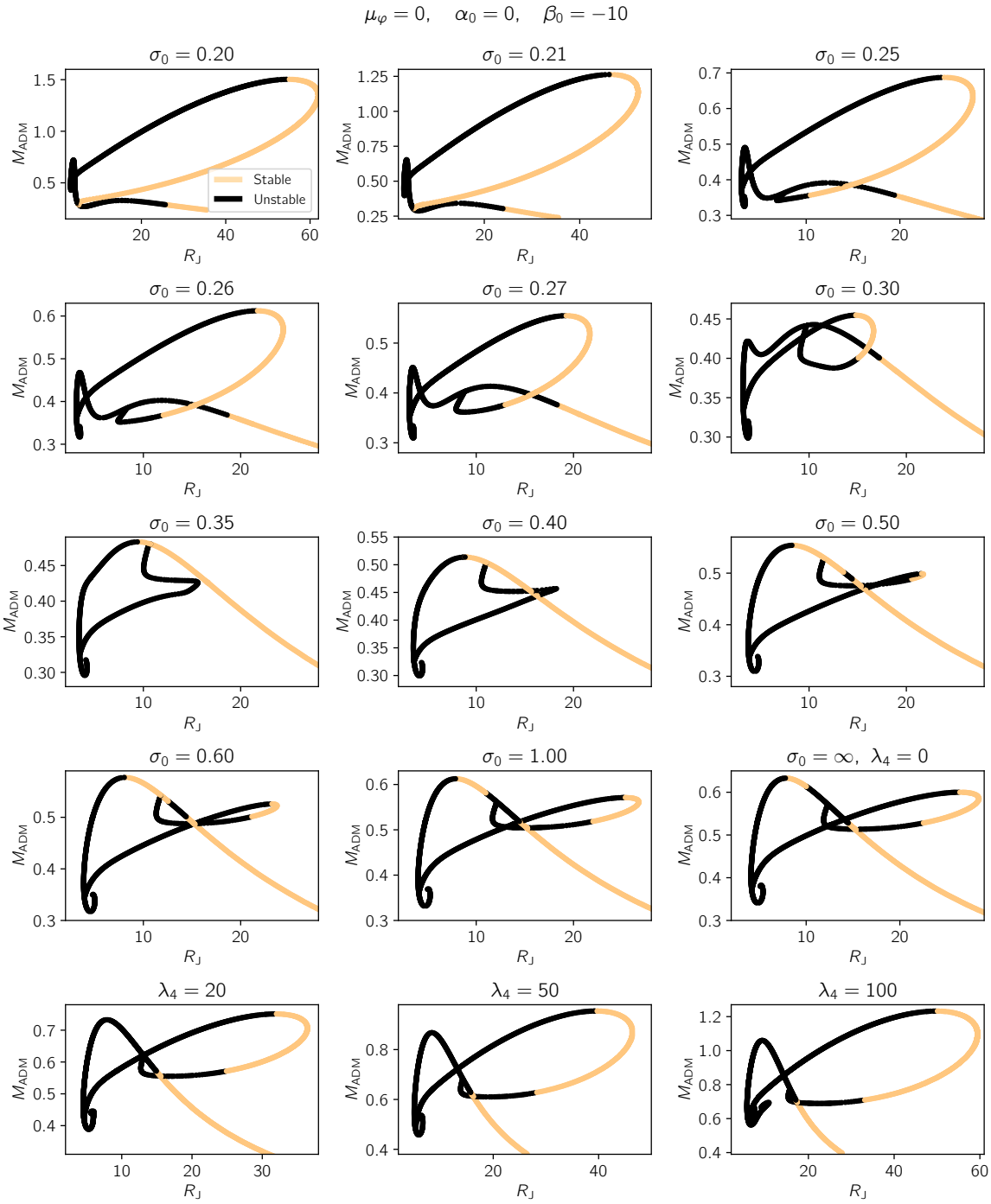


Fig. 6.C.5 Same as Fig. 6.C.1 but with the stability coded in colour, light (copper) for stable BSs and black for unstable models.

Chapter 7

Head-on collisions of boson stars

The content presented in this Chapter contains material that appears in the co-authored publication Ref. [143] with U.Sperhake, T.Helfer, R.Croft, M.Radia, B.Ge and E.A. Lim. The initial data construction for boson-star binaries of arbitrary mass ratio is my work. I have also performed all of the GRCHOMBO runs. The LEAN runs were performed by U.Sperhake. The analysis of the simulations was done jointly with the co-authors of the paper.

7.1 Introduction

In Chapter 5, we have explored single BS solutions in spherical symmetry and motivated why one may wish to study them. An important scenario to consider is that of a binary consisting of such BSs. The numerical modelling of binary systems can inform the searches for BS signatures with present and future gravitational-wave detectors. However, in order to achieve this we require accurate waveform models [475, 476] and therefore extensive high-precision numerical simulations. The numerical exploration of orbiting BS binary systems is still a relatively young field, but has already demonstrated the potentially rich phenomenology of the GW signals generated by these systems. To our knowledge, the first investigation dates back to Palenzuela *et al* [409] who find that the BSs' phase offset affects the merger stage more strongly than the inspiral. The GW signal generated by the merger remnant is furthermore mainly governed by the fundamental oscillation frequency of the remnant as it settles down into a non-spinning configuration[1] [410]. Quite remarkably, the GW signal from BS binary mergers can be exceptionally long-lived, resulting in a GW *afterglow* that decays at a much slower rate than the remnant's angular momentum [142]. The inspiral of unequal-mass BS binaries has been studied in Ref. [393] and can result in large kicks of

[1] Spinning remnants are also possible by-products of general mergers [346].

thousands of km/s which, however, is due to the asymmetric ejection of bosonic matter rather than that of GWs. So-called *dark boson-star binaries* with purely gravitational interaction have been found to generate GW signatures distinguishable from other astrophysical objects like black holes, neutron stars and even "normal" BSs [477]. Further simulations of compact binaries involving BSs include the piercing of bosonic clouds by a BH [412] and the inspiral of neutron stars with bosonic dark cores [478].

In spite of the tremendous progress made in these numerical explorations, our understanding of the GW emission across the BS binary parameter space remains very limited, both in terms of coverage and precision. One key ingredient indispensable for the systematic construction of GW waveforms forms the central focus of this Chapter: the generation of accurate initial data representing plausible physical configurations with negligible violations of the Einstein constraint equations. The importance of initial data for binary BS star evolutions in the equal-mass case has been previously addressed by Helfer et al. [139, 141], who demonstrate how inaccurate initial superposition of boson stars can lead to substantial spurious features in the resulting gravitational waveforms; to overcome these issues they further propose a new binary superposition that we dub the *equal-mass fix*. This binary initial data is also applied to the case of equal-mass binary *neutron star* initial data in the FUKA code [479]. We see here an example how BS studies serve as a valuable proxy well beyond the immediate scope of BS physics. A key limitation of the above cure, however, is its restriction to equal-mass binaries. In this work, we develop a generalised version of this method that achieves the same benefits for binaries with arbitrary mass ratios and contains the equal-mass fix as a limiting case in the choice of two free parameters. The proposed methodology can be applied to head-on collisions as well as systems with angular momentum, as for example in Ref. [142]. Here we employ this improved initial data construction in the simulation of equal- and unequal-mass BS binary head-on collisions studying systematically the impact of the BSs' phase offset on the collision dynamics and resulting GW signals.

The outline of this Chapter is as follows. We start by introducing the theoretical framework and the BS model of interest in Section 7.2. In Section 7.3 we summarise the $3+1$ split of our equations of motion and the code infrastructures used for our simulations. Section 7.5 opens with a brief review of the improved construction of initial data in the equal-mass case and proceeds with the generalisation to unequal mass ratios. We explore the parameter space of this initial data construction in Section 7.6. The results from our exploration of the BSs' phase parameter are presented in Section 7.7 and we conclude in Section 7.8. Throughout this Chapter, we set $\hbar = c = 1$ and use M to denote the total mass of the binary. We label spacetime indices by Greek letters running from 0 to 3 and spatial indices by Latin indices running from 1 to 3.

7.2 Theoretical framework

Mathematically, boson stars (BSs) are localised, soliton-like[2] solutions of the coupled system of the Einstein and general relativistic Klein-Gordon equations for a complex scalar field φ. From Chapter 5, we recall that the action is given by the Einstein-Hilbert term for four-dimensional gravity and a minimally coupled complex scalar field

$$S = \int \sqrt{-g} \left\{ \frac{1}{16\pi G} R - \frac{1}{2} \left[g^{\mu\nu} \nabla_\mu \bar{\varphi} \nabla_\nu \varphi + V(\varphi) \right] \right\} d^4x, \tag{7.1}$$

where we choose the scalar potential $V(\varphi)$ to be of solitonic nature [480]

$$V_{\text{sol}} = \mu^2 |\varphi|^2 \left(1 - 2\frac{|\varphi|^2}{\sigma_0^2} \right)^2. \tag{7.2}$$

Here we focus on time evolutions of head-on BS collisions. In general, the outcome of the collision is a non-spinning boson star or a black hole. However, a scenario where the two BSs "pass through" each other [481] is also possible. In our head-on collisions, the resulting remnant is always a BH. We model single BSs as stationary solutions in spherical symmetry, where our ansatz splits the complex solution into amplitude $A(r)$, constant frequency $\omega \in \mathbb{R}$ and phase-offset $\delta\phi \in [0, 2\pi)$

$$\varphi(r,t) = A(r) e^{i(\omega t + \delta\phi)}. \tag{7.3}$$

With this ansatz we construct single equilibrium BS solutions using the shooting algorithm described in Section 5.4.4.

7.3 The 3+1 decomposition and boosted stars

We utilise the 3+1 decomposition, reviewed in Chapter 2, to numerically evolve the BS binary. We remind the reader that the spacetime metric is decomposed into the spatial metric γ_{ij}, the shift vector β^i and the lapse function α in adapted coordinates $x^\alpha = (t, x^i)$ according to

$$\mathrm{d}s^2 = g_{\mu\nu} \mathrm{d}x^\mu \mathrm{d}x^\nu = -\alpha^2 \mathrm{d}t^2 + \gamma_{mn} (\mathrm{d}x^m + \beta^m \mathrm{d}t)(\mathrm{d}x^n + \beta^n \mathrm{d}t), \tag{7.4}$$

and the extrinsic curvature is given by the spatial projection of the covariant derivative of the time like unit normal n_α of the foliation, $K_{\alpha\beta} = -(\delta^\mu{}_\beta + n^\mu n_\beta) \nabla_\mu n_\alpha$. In analogy to the

[2] A soliton describes a wave packet solution that maintains its shape during propagation.

extrinsic curvature, we additionally define a time derivative for the scalar field[3]

$$\Pi := -\frac{1}{2\alpha}(\partial_t \varphi - \beta^m \partial_m \varphi)\,, \tag{7.5}$$

so that the energy density, momentum density and stress-tensor can be written as

$$\begin{aligned} \rho &= 2\Pi\bar{\Pi} + \frac{1}{2}\partial^m \bar{\varphi}\,\partial_m \varphi + \frac{1}{2}V\,, \\ j_i &= \bar{\Pi}\partial_i \varphi + \Pi \partial_i \bar{\varphi}\,, \\ S_{ij} &= \partial_{(i}\bar{\varphi}\partial_{j)}\varphi - \frac{1}{2}\gamma_{ij}(\gamma^{mn}\partial_m \bar{\varphi}\,\partial_n \varphi - 4\bar{\Pi}\Pi + V)\,. \end{aligned} \tag{7.6}$$

These sources appear on the right-hand side of the Einstein equations as given in full detail in Section 2.A (cf. also Eqs. (8)–(12) of Ref. [141]), and the time evolution of the scalar field is given by the first-order-in-time system of equations

$$\partial_t \varphi = \beta^m \partial_m \varphi - 2\alpha\Pi, \tag{7.7}$$

$$\partial_t \Pi = \beta^m \partial_m \Pi + \alpha\left[\Pi K + \frac{1}{2}V'\varphi + \frac{1}{4}\tilde{\gamma}^{mn}\left(\partial_m \varphi \partial_n \chi - 2\chi \tilde{D}_m \tilde{D}_n \varphi\right)\right] - \frac{1}{2}\chi\tilde{\gamma}^{mn}\partial_m \varphi \partial_n \alpha, \tag{7.8}$$

where $V' = \mathrm{d}V/\mathrm{d}\left(|\varphi|^2\right)$. Besides the evolution equations, Einstein's equations imply the Hamiltonian, $\mathscr{H}$, and momentum, $\mathscr{M}_i$, constraints given by

$$\mathscr{H} := \mathscr{R} + K^2 - K^{mn}K_{mn} - 16\pi\rho = 0, \tag{7.9}$$

$$\mathscr{M}_i := D_i K - D_m K_i^m - 8\pi j_i = 0. \tag{7.10}$$

In order to prescribe linear momentum to the two stars, we boost them towards each other using a Lorentz transformation following Section 2.3 of Ref. [141]. We now review the main steps. Our task is to establish the relationship between two frames: a frame of a single BS at rest, denoted by O with coordinates $x^\alpha = (t, x^k)$, and a frame $\tilde{O}$ with $\tilde{x}^{\tilde{\alpha}} = (\tilde{t}, \tilde{x}^k)$ moving with velocity v^i. The latter frame will model our boosted star in the z-direction. The transformation between the two frames is facilitated by the Lorentz transformation matrix

$$\Lambda_\mu{}^{\tilde{\alpha}} = \begin{pmatrix} \gamma & 0 & 0 & -\gamma v \\ 0 & 1 & 0 & 0 \\ 0 & 0 & 1 & 0 \\ -\gamma v & 0 & 0 & \gamma \end{pmatrix}, \tag{7.11}$$

[3]Equation (7.5) is given in the conventions of the LEAN code, whilst in GRCHOMBO the time derivative for the scalar field is defined via $\Pi_{\mathrm{GRChombo}} = 2\Pi$.

and its inverse

$$\Lambda_{\tilde{\alpha}}{}^{\mu} = \begin{pmatrix} \gamma & 0 & 0 & \gamma v \\ 0 & 1 & 0 & 0 \\ 0 & 0 & 1 & 0 \\ \gamma v & 0 & 0 & \gamma \end{pmatrix}, \tag{7.12}$$

where $\gamma = (1-v^2)^{-1/2}$ is the Lorentz factor.

First, the coordinate systems are related via

$$\tilde{x}^{\tilde{\alpha}} = \Lambda^{\tilde{\alpha}}{}_{\mu} x^{\mu} \quad \text{and} \quad x^{\mu} = \Lambda^{\mu}{}_{\tilde{\alpha}} \tilde{x}^{\alpha}. \tag{7.13}$$

Next, the metric variables of the frames are related by

$$\tilde{g}_{\tilde{\alpha}\tilde{\beta}} = \Lambda^{\mu}{}_{\tilde{\alpha}} \Lambda^{\nu}{}_{\tilde{\beta}} g_{\mu\nu}, \quad \partial_{\tilde{\gamma}} \tilde{g}_{\tilde{\alpha}\tilde{\beta}} = \Lambda^{\lambda}{}_{\tilde{\gamma}} \Lambda^{\mu}{}_{\tilde{\alpha}} \Lambda^{\nu}{}_{\tilde{\beta}} \partial_{\lambda} g_{\mu\nu} \tag{7.14}$$

$$\tilde{\gamma}_{\tilde{k}\tilde{l}} = \tilde{g}_{\tilde{k}\tilde{l}}, \quad \tilde{\partial}_{\tilde{0}} \tilde{\gamma}_{\tilde{k}\tilde{l}} = \tilde{\partial}_{\tilde{0}} \tilde{g}_{\tilde{k}\tilde{l}}, \quad \tilde{\partial}_{\tilde{m}} \tilde{\gamma}_{\tilde{k}\tilde{l}} = \tilde{\partial}_{\tilde{m}} \tilde{g}_{\tilde{k}\tilde{l}}, \tag{7.15}$$

$$\tilde{K}_{\tilde{k}\tilde{l}} = -\frac{1}{2\tilde{\alpha}} \left(\tilde{\partial}_0 \tilde{\gamma}_{\tilde{k}\tilde{l}} - \tilde{\beta}^{\tilde{m}} \tilde{\partial}_{\tilde{m}} \tilde{\gamma}_{\tilde{k}\tilde{l}} - \tilde{\gamma}_{\tilde{m}\tilde{l}} \tilde{\partial}_{\tilde{k}} \tilde{\beta}^{\tilde{m}} - \tilde{\gamma}_{\tilde{k}\tilde{m}} \tilde{\partial}_{\tilde{l}} \tilde{\beta}^{\tilde{m}} \right), \tag{7.16}$$

along with the scalar field transformations

$$\tilde{\varphi}(\tilde{x}^{\alpha}) = \varphi(x^{\mu}), \quad \partial_{\tilde{\alpha}} \tilde{\varphi} = \Lambda^{\mu}{}_{\tilde{\alpha}} \partial_{\mu} \varphi, \quad \text{and} \quad \tilde{\Pi} = -\frac{1}{2\tilde{\alpha}} \left(\partial_{\tilde{0}} \tilde{\varphi} - \tilde{\beta}^{\tilde{m}} \partial_{\tilde{m}} \tilde{\varphi} \right). \tag{7.17}$$

Finally the lapse and shift directly follow from

$$\tilde{\beta}_{\tilde{k}} = \tilde{g}_{\tilde{0}\tilde{k}}, \quad \tilde{\alpha} = \sqrt{-\tilde{g}^{\tilde{0}\tilde{0}}}^{-1}, \quad \tilde{\gamma}_{\tilde{k}\tilde{l}} = \tilde{g}_{\tilde{k}\tilde{l}}. \tag{7.18}$$

7.4 Computational infrastructure

The simulations of BS collisions in this work have been performed with two independent numerical relativity codes, GRCHOMBO, reviewed in Section 2.7, and LEAN [482]. Both codes evolve lapse α and shift β^i according to the *moving puncture* gauge [483, 484], i.e. using 1+log slicing and the Γ driver condition outlined in Sections 2.5.1-2.5.2. Some key ingredients of the codes differ in evolving the Einstein equations, so we summarise them in the following Sections and list the grid setups employed for our runs.

7.4.1 Lean

The LEAN code is based on the CACTUS computational toolkit [156] and employs mesh refinement in the form of moving boxes as provided by CARPET [157]. The code evolves the Einstein equations using the Baumgarte-Shapiro-Shibata-Nakamura-Oohara-Kojima (BSSNOK) formulation [110–112] (cf. Section 2.3 for more details). The computational domain for all LEAN simulations consists of 7 nested refinement levels: 4 outer levels centered on the origin and 3 inner levels, each consisting of 2 boxes centered on the two BSs. The box (edge) size decreases from each outer level inwards by a factor of 2 except for level 4 to 5 where it decreases by a factor of 8. The grid spacing dx decreases by a factor 2 on each consecutive inner level. We can thus describe a grid in terms of two numbers, the edge L_1 and grid spacing dx_1 of the outermost level. For the LEAN simulations of this paper we use[4] $L_1 \approx 1024\,M$, d$x_1 \approx 2.67\,M$ which implies boxes of size $L_7 \approx 4\,M$ with spacing d$x_7 \approx M/24$ on the innermost level.

7.4.2 GRChombo

The GRCHOMBO code evolves the Einstein equations using the covariant and conformal Z4 (CCZ4) formulation [116] (cf. Section 2.4). We set up a grid of length $L_1 \approx 512\,M$ with 7 additional AMR levels such that on the finest level, the spatial grid spacing is d$x_7 \approx M/32$. Finally, we use a tagging criterion based on second derivatives of the complex scalar field and the conformal factor (see Section 2.7.3 for more details on grid variable tagging).

7.4.3 Convergence testing

The full details of the convergence testing are provided in Appendix 7.C. In summary, the total error budget, including finite radius extraction and discretisation errors, is 2% for LEAN and 3.7% for GRCHOMBO. All of the results reported here use extraction radius $R_{\rm ex}^{\rm Lean} \approx 200\,M$ for LEAN and $R_{\rm ex}^{\rm GRChombo} \approx 120\,M$ for GRCHOMBO.

7.5 Boson-star binary initial data construction

The construction of binary initial data is a challenging task in GR, mainly due to the non-linearity of the Einstein equations and the gauge dependence of the variables describing the spacetime. For boson stars, we encounter two additional challenges not present for neutron stars or black holes: (i) exponentially growing modes of single-star solutions and (ii) the lack

[4] We use approximate equality here, as the total mass in our simulations is roughly one but not exactly.

of a consistent framework for binary initial data that are conformally flat; cf. for example the great simplification afforded by Bowen-York data [107, 125]. In this Section, we present an ansatz for computing BS-binary initial data that significantly reduce constraint violations relative to the superposition methods used in the literature, and that we also expect to be a valuable preconditioner reducing unphysical features in a full constraint solving process.

7.5.1 Revisiting the initial data construction for equal-mass binaries

Before describing our proposed methodology, we briefly outline the equal-mass initial data construction proposed in Ref. [139], which our method then generalises to the unequal mass case. In the remainder of this Chapter, the initial set-up of our BS binary configurations is as follows. We start off with two BS stars, star A and star B, initially located at $x^i_{\rm A}$ and $x^i_{\rm B}$, and therefore separated by an initial distance $d = ||x^i_{\rm A} - x^i_{\rm B}||$. We then boost the stars through Lorentz transformations with initial velocities $v^i_{\rm A}$ and $v^i_{\rm B}$ towards each other. The details of the $3+1$ variables with the Lorentz boost can be found in Ref. [141]. We note that the initial positions $x^i_{\rm A}$, $x^i_{\rm B}$ and initial boost velocities $v^i_{\rm A}$, $v^i_{\rm B}$ are chosen such that the BSs are initially located in the centre of mass frame; these values will be given in our specification of the simulations in Table 7.6.2.

The most common procedure for constructing binary initial data is to superpose individual star solutions in a point-wise fashion. In terms of the $3+1$ ADM variables this is written as

$$\gamma_{ij} = \gamma^{\rm A}_{ij} + \gamma^{\rm B}_{ij} - \delta_{ij}, \tag{7.19}$$

$$\varphi = \varphi_{\rm A} + \varphi_{\rm B}, \tag{7.20}$$

$$\Pi = \Pi_{\rm A} + \Pi_{\rm B}, \tag{7.21}$$

$$K_{ij} = \gamma_{m(i}\left[K^{\rm A}_{j)n}\gamma^{mn}_{\rm A} + K^{\rm B}_{j)n}\gamma^{nm}_{\rm B}\right]. \tag{7.22}$$

This method and, in particular, Eq. (7.19) will henceforth be referred to as the method of *plain superposition*; here the value of Kronecker delta function, δ_{ij}, is subtracted from the two superposed individual metrics to ensure the Minkowski metric is recovered in the far-field limit. Whilst the asymptotic flatness condition is thus satisfied, it has been shown in Refs. [139, 141] that plain superposition can induce large deviations from the equilibrium values of the volume element, $\sqrt{\det(\gamma)}$, at the centres of the stars. This effect arises from the fact that our binary system no longer contains isolated stars and simply superposing metric solutions induces a change in the volume element near the center of each BS due to the influence of its companion (see Appendix A1 of Ref. [139] for more details). To account for such a change in the volume element for the equal-mass binary stars, Ref. [139] proposes to

modify the plain superposition by replacing Eq. (7.19) with

$$\gamma_{ij} = \gamma^{\mathrm{A}}_{ij} + \gamma^{\mathrm{B}}_{ij} - \gamma^{\mathrm{B}}_{ij}(x^i_{\mathrm{A}}) = \gamma^{\mathrm{A}}_{ij} + \gamma^{\mathrm{B}}_{ij} - \gamma^{\mathrm{A}}_{ij}(x^i_{\mathrm{B}}). \tag{7.23}$$

This modification recovers the equilibrium volume element at the centres of stars A and B as in the case of isolated stars and from now on we will refer to Eq. (7.23) as the *equal-mass fix*. The equal-mass fix has been shown to significantly reduce constraint violations at the centres of the stars relative to the plain superposition procedure and also mitigate spurious physical features such as premature collapse of the stars to a BH and/or altered GW signals [141]. We stress, however, that Eq. (7.23) is only applicable for equal-mass binaries, since in that case $\gamma^{\mathrm{B}}_{ij}(x^i_{\mathrm{A}}) = \gamma^{\mathrm{A}}_{ij}(x^i_{\mathrm{B}})$. In the unequal-mass case, this no longer holds true: the volume element change invoked by each star on its companion will no longer be the same for both stars.

7.5.2 Construction of the generalised unequal-mass initial data

Now, the question arises how to generalise the proposed modification in Eq. (7.23) to unequal-mass BS binaries. In the spirit of Eq. (7.23), we have to meet only two conditions: fix the volume element at the centres of each of the stars, x^i_{A} and x^i_{B}. One way to do so is to work with the 3-metric components γ_{ij} directly and introduce spatially varying corrections that recover the required volume element at the centres of the stars. However, this leads to an under-determined problem, since each metric has 6 components, whilst we have only 2 conditions to satisfy. Instead, we choose to work with the conformal factor, which is a scalar density and thus makes it possible to satisfy both conditions at x^i_{A} and x^i_{B} using only 2 parameters.

We start with the plainly superposed metric (7.19) and conformally decompose it with a conformal factor λ defined by

$$\tilde{\gamma}_{ij} = \lambda^{-1}\gamma_{ij} \quad \text{with} \quad \lambda = \gamma^{1/3}, \tag{7.24}$$

where $\det\tilde{\gamma}_{ij} = 1$ by construction. We note that the conformal factor λ is related to the standard BSSN/CCZ4 variable χ by $\lambda^{-1} = \chi$. Appendix 7.A discusses more general choices for the conformal factor and illustrates why the exponent of $1/3$ in Eq. (7.24) is a particularly convenient choice. In our procedure, we leave the conformally rescaled metric $\tilde{\gamma}_{ij}$ unchanged at the values it takes on in the plain superposition. So far this construction does not remedy the main error inherited from the plain superposition consisting in the change of the volume element at the centres of the stars and the resulting perturbation in their central energy densities. However, we can control the volume element by adjusting the

superposed conformal factor λ with a correction $\delta\lambda$, such that we recover the equilibrium volume element at both stars' centres. At the centers of the stars this correction must satisfy

$$\lambda_{\rm new}(x^i_{\rm A}) = \lambda(x^i_{\rm A}) + \delta\lambda(x^i_{\rm A}) = \lambda_{\rm A}(x^i_{\rm A}), \tag{7.25}$$
$$\lambda_{\rm new}(x^i_{\rm B}) = \lambda(x^i_{\rm B}) + \delta\lambda(x^i_{\rm B}) = \lambda_{\rm B}(x^i_{\rm B}), \tag{7.26}$$

where λ_A and λ_B are the unperturbed conformal factors for stars A and B. In contrast to the equal-mass case, this approach necessitates a spatially varying correction to the conformal factor. For this purpose, we construct weight functions $w_{\rm A}(x^i)$ and $w_{\rm B}(x^i)$ around the centres of the stars, which will be specified later in this Section. We then propose the following ansatz for the new conformal factor on the entire initial hypersurface

$$\lambda_{\rm new}(x^i) = \lambda(x^i) + w_{\rm A}(x^i)h_{\rm A} + w_{\rm B}(x^i)h_{\rm B}\,. \tag{7.27}$$

Here $h_{\rm A}$ and $h_{\rm B}$ are determined by imposing our target conditions in Eqs. (7.25)–(7.26), which reduce to a (2×2) system of linear equations. The required values of $h_{\rm A}$ and $h_{\rm B}$ are then found to be

$$h_{\rm A} = \frac{-w_{\rm B}(x^i_{\rm A})\delta\lambda(x^i_{\rm B}) + w_{\rm B}(x^i_{\rm B})\delta\lambda(x^i_{\rm A})}{w_{\rm A}(x^i_{\rm A})w_{\rm B}(x^i_{\rm B}) - w_{\rm A}(x^i_{\rm B})w_{\rm B}(x^i_{\rm A})}, \qquad h_{\rm B} = \frac{w_{\rm A}(x^i_{\rm A})\delta\lambda(x^i_{\rm B}) - w_{\rm A}(x^i_{\rm B})\delta\lambda(x^i_{\rm A})}{w_{\rm A}(x^i_{\rm A})w_{\rm B}(x^i_{\rm B}) - w_{\rm A}(x^i_{\rm B})w_{\rm B}(x^i_{\rm A})}\,. \tag{7.28}$$

For these constants $h_{\rm A}$ and $h_{\rm B}$ the newly corrected conformal factor $\lambda_{\rm new}$ allows us to recover the desired volume element at the centres of the stars, as if they were isolated. This can be seen by considering the newly re-scaled metric

$$\gamma^{\rm new}_{ij} = \left(\frac{\lambda_{\rm new}}{\lambda}\right)\gamma_{ij} = \frac{\lambda_{\rm new}}{\gamma^{1/3}}\gamma_{ij}, \tag{7.29}$$

where $\gamma^{-1/3}\gamma_{ij}$ has unit determinant by construction and therefore ensures that $\gamma^{\rm new}(x^i_{\rm A}) = \gamma^{\rm A}(x^i_{\rm A})$ and likewise for star B.

We are now left to choose what weight functions to use around the stars in Eq. (7.27). Focusing here on asymptotically flat spacetimes, we wish to obtain metric corrections that fall off $\propto 1/r$. To guarantee such behaviour we construct the following weight functions

$$w_{\rm J}(x^i) = \frac{1}{\sqrt{R^2_{\rm J} + r^2_{\rm J}}}, \tag{7.30}$$

where ${\rm J}\in\{{\rm A},{\rm B}\}$, $r_{\rm J} := ||x^i - x^i_{\rm J}||$ and $R_{\rm J}$ are freely specifiable constants that control the width of the functions. Our initial data method therefore consists of the following main steps:

Model	$\sqrt{G}A(0)$	$\mu M_{\rm BS}$	ω/μ	μr_{99}	$\max(m(r)/r)$
S-170	0.17	0.7134	0.4392	3.97	0.222
S-160	0.16	0.5368	0.5375	4.18	0.166
S-147	0.147	0.3606	0.6784	4.48	0.115
S-100	0.1	0.2701	0.8506	6.21	0.070

Table 7.6.1 Solitonic BS models with $\sqrt{G}\sigma_0 = 0.2$ considered in this work. $A(0)$ denotes the central scalar field amplitude, $M_{\rm BS}$ the mass of the BS, ω the frequency of the ground state solution, r_{99} the areal radius containing 99% of the BS mass, and $\max(m(r)/r)$ our measure of compactness. Note that for this potential the maximum mass of a BS is $\mu M_{BS} = 0.7212$.

1. Construct the plainly superposed metric γ_{ij} according to Eq. (7.19).
2. Construct the conformal factor λ from a plainly superposed metric according to Eq. (7.24).
3. Choose a suitable parameter pair $(R_{\rm A}, R_{\rm B})$.
4. Compute corrections at the stars' centres, $\delta\lambda(x_{\rm A})$ and $\delta\lambda(x_{\rm B})$, according to Eqs. (7.25)-(7.26) required for calculation of constant $h_{\rm A}$ and $h_{\rm B}$ in Eq. (7.28).
5. Correct the conformal factor λ to $\lambda_{\rm new}$ in Eq. (7.27) to recover the equilibrium volume element at the stars' centres.

The choice of the two parameters, $R_{\rm A}$ and $R_{\rm B}$, in step (2) will be explored in more detail through our numerical simulations in the next Section.

7.6 Set-up and exploration of the parameter space

In this Section, we start by listing the BS models we study in this work in Table 7.6.1. We focus on the solitonic BSs, with $\sqrt{G}\sigma_0 = 0.2$, which allows us to access a variety of mass ratios, including heavy and relatively compact BSs. To construct binary systems of various mass ratios $q = M_{\rm A}/M_{\rm B}$, where $M_{\rm A} < M_{\rm B}$, we superpose combinations of the BS models from Table 7.6.1. The resulting binary configurations are detailed in Table 7.6.2.

7.6.1 Equal-mass binaries

For equal-mass binaries, the equal-mass fix (7.23) has been shown to remedy the spurious effects of plain superposition [141]. It is therefore important to verify that our method recovers these improvements in the equal-mass limit. First, we recall that our method

Run	Model for star A	Model for star B	$v_x^{\rm A}(0)$	$v_x^{\rm B}(0)$	d/M	q	Code
`q1-dX-pX`	`S-170`	`S-170`	-0.1	0.1	$11.2, 22.3, 33.5, 44.6$	1	both
`q075-dX-pX`	`S-160`	`S-170`	-0.1141	0.0859	$12.7, 25.5, 38.2, 50.9$	0.75	GRCHOMBO
`q05-dX-pX`	`S-147`	`S-170`	-0.1328	0.0672	$14.8, 29.7, 44.5, 59.3$	0.5	LEAN
`q038-dX-pX`	`S-100`	`S-170`	-0.1451	0.0549	$16.2, 32.4, 48.6, 64.8$	0.38	both

Table 7.6.2 Binary initial data configurations considered in this work. Each run has a suffix `dX-pX`, where `dX` is a wildcard for the initial separation and `pX` is a wildcard for the off-phase parameter in degrees, $\frac{180^\circ}{\pi}\delta\phi \in [0^\circ, 360^\circ)$. In our convention, the off-phase parameter, $\delta\phi$, is added to star A, whilst for star B it remains zero. Here $v_x^{\rm J}$ for ${\rm J} \in \{{\rm A}, {\rm B}\}$ denote the initial boost velocities with associated Lorentz factors $\gamma_{\rm J}$, $d = ||x^i_{\rm A} - x^i_{\rm B}||$ is the initial separation and $M = \gamma_{\rm A} M^{\rm A}_{\rm BS} + \gamma_{\rm B} M^{\rm B}_{\rm BS}$ is the total mass of the binary.

requires the choice of free parameters $(R_{\rm A}, R_{\rm B})$. As shown in more detail in Appendix 7.B, we can recover both, plain superposition and the equal-mass fix, as limiting cases of this choice. Specifically, in the limit $R_{\rm A}, R_{\rm B} \to 0$, our initial data reconstruction recovers plain superposition, whilst for the equal-mass case and in the limit $R_{\rm A}, R_{\rm B} \to \infty$, we recover exactly the equal-mass fix (7.23). Our method thus provides a direct generalization for constructing BS binary initial data with arbitrary mass ratios that includes plain superposition and the equal-mass fix as limiting cases. We next verify this claim empirically by evolving in time the binary configuration `q1-d11-p000` using four types of superposition: plain, the equal-mass fix and our generalised method using very small and very large $(R_{\rm A}, R_{\rm B})$, namely $R_{\rm A} = R_{\rm B} = 0.1$ and 1000. Figure 7.6.1 shows the gravitational waveforms and the central scalar field value as functions of time obtained for these four cases. The Figure demonstrates excellent agreement of our proposed method with plain superposition and the equal-mass fix, respectively, for $R_{\rm A} = R_{\rm B} = 0.01$ and $R_{\rm A} = R_{\rm B} = 1000$.

7.6.2 Unequal-mass binaries

In the unequal-mass case, the choice of radial parameters $(R_{\rm A}, R_{\rm B})$ is more complex. Changing the profile shape of the radial functions affects the extent to which the corrections are applied to the conformal factor in Eq. (7.27) around the centres of the stars: very small $(R_{\rm A}, R_{\rm B})$ will result in smaller corrections around the stars and vice versa. As such, there exists a region of suitable radial parameters, which we find numerically by calculating the $L2$-norm of the Hamiltonian constraint (7.9) in the parameter space of $(R_{\rm A}, R_{\rm B})$. Figure 7.6.2 demonstrates the dependence of the $L2$-norm of the Hamiltonian constraint violations on the choice of radial parameters for a binary configuration with $q = 0.75$. We show the corresponding "heat-maps" for other mass ratios in Appendix 7.D. It is important to note that

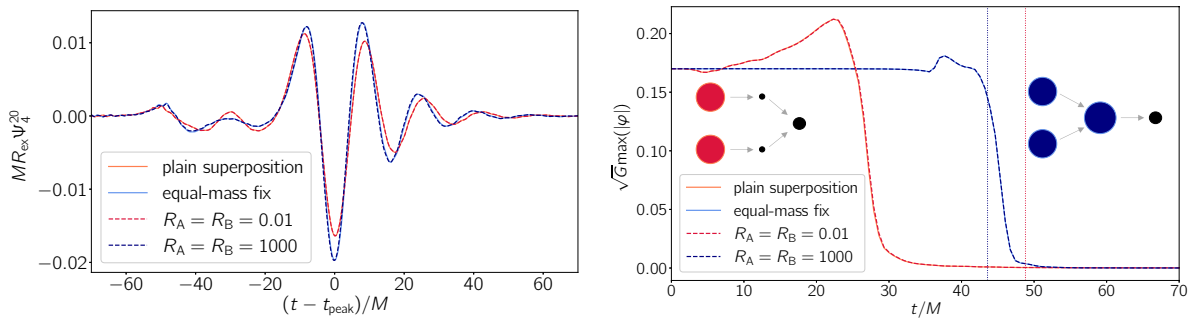


Fig. 7.6.1 *Left:* Real parts of the (20)-mode of the Newman-Penrose scalar Ψ_4 for binary sequence `q1-d11-p000`, obtained for plain superposition, the equal-mass fix and our improved method. The waveforms have been shifted by $t_{\rm peak}$, the time at which the maximum GW amplitude is reached. *Right:* Maximum of the scalar field amplitude for the same binary configuration. Notably, plain superposition leads to formation of a BH well before the equal-mass fix, therefore resulting in an altered gravitational waveform. Here we indicate the merger time by the vertical lines.

there are regions in the parameter space, where the initial constraint violations become very large – these regions are indicated by the grey shaded area for readability. The diverging behaviour of the constraints for certain pairs of $(R_{\rm A}, R_{\rm B})$ can be attributed to a zero crossing of $\lambda_{\rm new}$ away from the stars' centers, which results in a singular 3-metric. Regions in the parameter space where this happens are evidently not suitable for time evolutions.

In the following, we base our specific choices for radial parameters $(R_{\rm A}, R_{\rm B})$ on two criteria. First, the pair has to result in reduced constraint violations relative to plain superposition, and second, they should remedy spurious oscillations in the time evolutions of the scalar field profiles that result from plainly superposed initial data[5]. In this Section we focus on constraint violations, whilst we discuss the scalar field profiles in more detail in Section 7.7.3. For unequal-mass BS binaries, we find that radii $R_{\rm A} = 10 - 100$ (light BS) and $R_{\rm B} = 1 - 100$ (heavy BS) work generally well. For smaller mass ratios $q \lesssim 0.5$ we find that $(R_{\rm A}, R_{\rm B})$ differing by at most one order of magnitude are optimal. We note that different pairs $(R_{\rm A}, R_{\rm B})$ can result in small global time-shifts in the GW signals due to gauge effects; besides this time shift, however, the phase and amplitude of the waveforms remain unaffected. We summarise our choices of radial parameters in Table 7.6.3 for all unequal-mass binary configurations studied here.

For the radial parameters thus chosen, we observe a particularly pronounced reduction in the constraint violations at the centres of the stars relative to plain superposition. This

[5]Note that these two criteria are not the same; it is for instance possible to choose $(R_{\rm A}, R_{\rm B})$ that reduce the constraint violations without satisfactorily reducing scalar field oscillations.

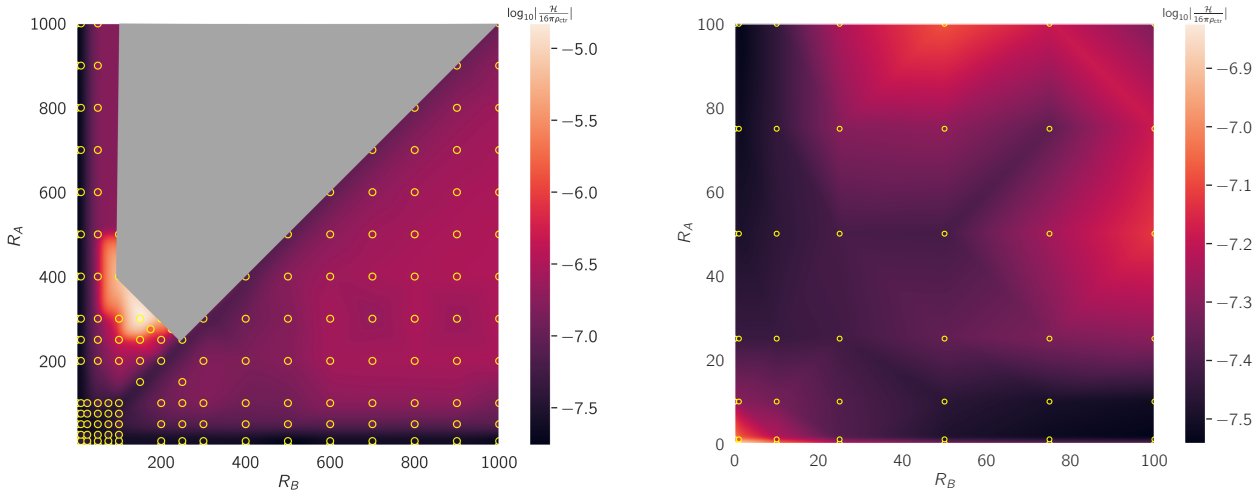


Fig. 7.6.2 *Left:* Log plot of the $L2$-norm of the Hamiltonian constraint violations (normalised by the central energy density $16\pi\rho_{\rm ctr}$ of the heavier star) across the simulation grid for the binary configuration `q075-d12-p000`. The grey region indicates the parameter space of $(R_{\rm A}, R_{\rm B})$ where constraint violations diverge. The values of constraint violations have been interpolated onto the full domain using the runs performed indicated by the yellow circles. *Right:* A zoom-in on the region $(R_{\rm A}, R_{\rm B}) \in [(0,100)\times(0,100)]$. Asymmetries in the constraint violations are visible across the diagonal $R_{\rm A} = R_{\rm B}$, demonstrating the non-trivial dependence of the constraints on the choice of radial parameters. In the equal-mass case, we have verified that the constraint violations are symmetric under exchange A $\leftrightarrow$ B, as expected. The results for the remaining mass ratios are displayed in Figure 7.D.1.

Run	$R_{\rm A}$	$R_{\rm B}$
`q075-dX-pX`	100	1
`q05-dX-pX`	10	100
`q038-dX-pX`	10	100

Table 7.6.3 Choice of radial parameters $(R_{\rm A}, R_{\rm B})$ for the unequal-mass binaries considered in this work.

is as desired by construction of our method, since the correction to the volume element is imposed exactly at the stars' centres. As for the equal-mass fix studied in Ref. [141], we find this effect to be particularly pronounced in the Hamiltonian constraint. This is illustrated in Figure 7.6.3, which shows the constraint violations along the collision axis (x-axis) for the binary `q05-d15-p000`. Other binary configurations result in qualitatively similar constraint violation profiles.

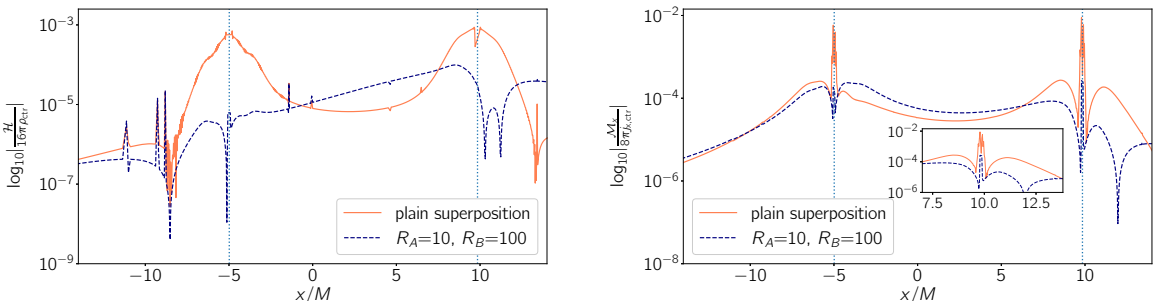


Fig. 7.6.3 Log-scaled Hamiltonian constraint $\mathscr{H}$ (normalised by the central energy density $16\pi\rho_{\mathrm{ctr}}$ of the heavier star) and the x-component of the momentum constraint $\mathscr{M}_x$ (normalised by the central momentum density $8\pi j_{x,\mathrm{ctr}}$ of the heavier star) computed along the collision axis of the binary of mass ratio $q = 0.5$ and initial separation $d/M = 14.8$.

7.7 Results: time evolutions of off-phase BS binaries

7.7.1 Equal-mass collisions

We begin the discussion of our results with the simplest case of equal-mass collisions simulated using plain superposition and the equal-mass fix. It has been shown in Ref. [141] that for $q = 1$ binaries with $\delta\phi = 0$, plain superposition results in two crucial spurious features:

1. premature BH formation as indicated by a sudden drop in the scalar-field amplitude at the BS center and AH formation; i.e. the two BSs collapse to a BH prior to merger (cf. Figure 9 of Ref. [141]), which can be attributed to the spurious oscillations of the scalar field's central amplitude,

2. energy dependence on the initial separation, which was found to be less pronounced for solitonic BSs.

Extending the argument of Ref. [141] to the case of arbitrary $\delta\phi$, we span the dephasing parameter space over the range[6] $\delta\phi \in [0,\pi]$. Similar to Ref. [141], we find that plain superposition results in premature BH formation regardless of the dephasing parameter $\delta\phi$. Therefore, in case of plain superposition, the radiated energy becomes independent of the dephasing angle, as is demonstrated in the left panel of Figure 7.7.1. In contrast, the equal-mass fix avoids premature BH formation for all choices of $\delta\phi$ and the radiated energy takes on a non-trivial dependence on the dephasing parameter as displayed in the right panel of Fig. 7.7.1. This panel furthermore demonstrates that for large $\delta\phi$ the second observation

[6]The range $\delta\phi \in (\pi, 2\pi]$ is automatically covered by symmetry.

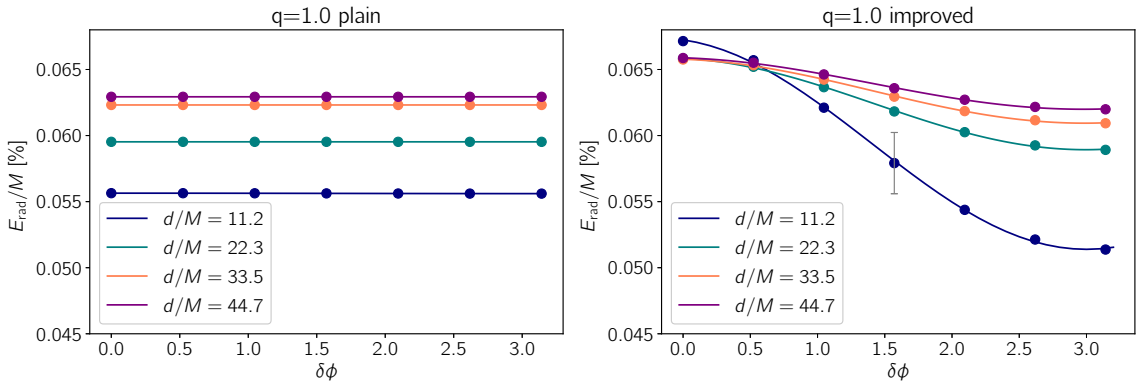


Fig. 7.7.1 Radiated energy $E_{\rm rad}$ as a function of the phase off-set parameter $\delta\phi$ for equal-mass BS binary head-on collisions `q1-dX-pX` of Table 7.6.2 starting from different separations d/M using plain superposition (left panel) and the equal-mass fix (right panel). The single error bar displayed at $\delta\phi = \pi/2$ in the right panel indicates our numerical uncertainty which is very similar for all data points.

in the above list no longer holds: for $\delta\phi \gtrsim 1$, the radiated energy *does* vary significantly with initial separation. As we will discuss in more detail below, the choice of the dephasing parameter can significantly affect the dynamics and GW energy emission for equal as well as for unequal-mass BS binaries.

The role of the phase offset has been studied before in the context of head-on collisions of Proca stars and was found to significantly affect the GW emission and mode structure of the stars [485]. Similarly, in Ref. [486] the phase parameter was found to impact the merger dynamics of real-scalar-field solitons, aka oscillatons (OSs). In particular, over a considerable range of compactness values they find anti-phase ($\delta\phi = \pi$) OS head-on collisions to bounce whereas equal-phase ($\delta\phi = 0$) collisions result in dispersal of the scalar field; cf. their Fig. 1. A similar repulsive effect has been found for $\delta\phi = \pi$ in BS head-on collisions in Refs. [408, 487], where in particular Appendix B of Ref. [408] gives an explanation in terms of an effective interaction potential. This feature may be connected to the fact that anti-phase collisions produce destructive interference, as shown in the case of Newtonian gravity in Ref. [488]. Our collision sequences `q1-dX-pX` involve highly compact solitonic stars, and so a BH forms post-collision. We therefore do not observe bounces in the anti-phase collisions, but the scalar field's repulsive character still manifests itself in a weaker signal and reduced radiated energy. Equal-phase configurations form a BH most 'efficiently' and result in the largest energy burst.

The energy dependence on the phase off-set is most naturally modelled as a single sinusoidal function[7]; cf. Eq. (16) in Ref. [488]. This is confirmed by our numerical results in Figure 7.7.1, which are well fitted by

$$E_{\rm fit} = A_1 \sin(f_1 \delta\phi + p_1) + s, \tag{7.31}$$

where amplitude A_1, frequency f_1, phase p_1 and shift s are determined using a least-squares algorithm. From the right panel of Figure 7.7.1, it is clear that in the evolutions starting from the equal-mass fix, some energy discrepancy occurs between various separations. Whereas for $\delta\phi \lesssim 1$ the radiated energy varies only mildly with d/M, it increases significantly with initial separation for larger dephasing parameters. In all cases, however, we observe a gradual convergence of the energy for large d/M, albeit at distinct rates for different $\delta\phi$. These effects can be attributed to the increase in the collision velocity that results from larger separations and enhances the merger dynamics. We can likewise attribute the decrease of $E_{\rm rad}$ for larger $\delta\phi$ to the off-phase scalar fields' repulsion and a consequential weakening of the merger dynamics. However, a higher collision velocity (equivalent to larger initial separation) appears to 'break down' the repulsive nature of the scalar field, thus narrowing the energy discrepancy as $d \to \infty$. For the collisions starting from plain superposition, we also observe convergence of the radiated energy in the limit of large separations, but here the energy is a constant function of $\delta\phi$ for each given d.

The increase of energy with separation due to higher collision velocity is a plausible interpretation, supporting our results. But is it correct? We quantitatively test the hypothesis as follows. Using the Newtonian approximation, we estimate that in the evolution starting from initial separation $d/M = 22.3$ and initial boost velocity $v = 0.1$, a velocity $v = 0.18$ is reached at distance $d/M = 11.2$. BS collisions with $d/M = 11.2$ and this larger velocity $v = 0.18$ would then be expected to result in energy values comparable to those obtained for the $d/M = 22.3$, $v = 0.1$ sequence. Likewise, BS collisions starting with $d/M = 11.2$ and $v = 0.199$ (0.208) should reproduce the coral (purple) curves for $d/M = 33.5$ $(d/M = 44.7)$ in Fig. 7.7.1.

In simple terms, we should obtain a transition of the dark blue curve for $d/M = 11.2$ in Fig. 7.7.1 into the teal coloured one for $d/M = 22.3$ by fixing $d/M = 11.2$ and increasing the initial velocity from $v = 0.1$ to $v = 0.18$. The left panel of Fig. 7.7.2 illustrates this transition by displaying the energy obtained for equal-mass collisions with initial separation $d/M = 11.2$ and varying the initial boost velocity in the range $v \in [0.1, 0.18]$. For $\delta\phi \gtrsim 1$

[7]Note that in the equal-mass collisions the two stars oscillate at the same frequency. For $\delta\phi = 0$ they therefore have identical phases throughout the entire infall. By perturbing the phase of one of the stars with $\delta\phi$, we change the phase difference at merger $\delta\phi_{\rm merger}$ by the same amount, i.e. $\delta\phi_{\rm merger} = \delta\phi$.

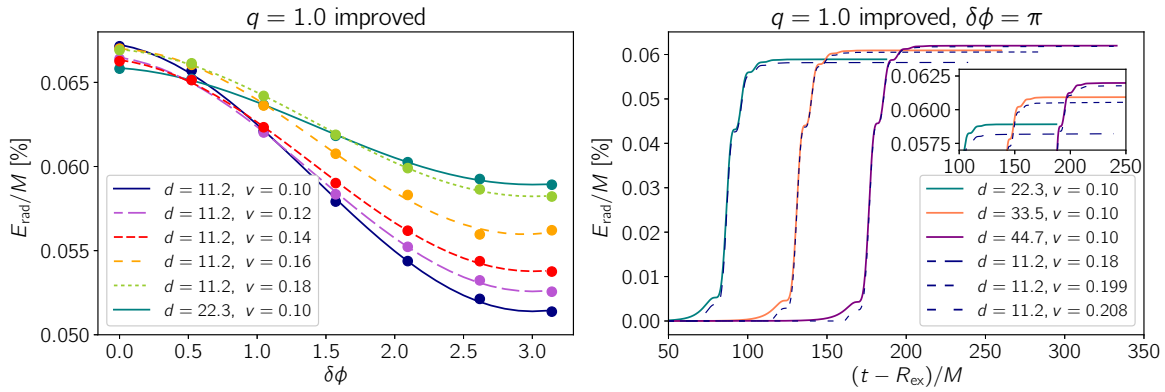


Fig. 7.7.2 *Left:* The radiated energy $E_{\rm rad}$ is shown as a function of the phase offset parameter $\delta\phi$ as in Fig. 7.7.1, but now for BS binary configurations starting from initial separation $d/M = 11.2$ with different velocities. For $v = 0.18$, the radiated energy closely matches the teal coloured curve of the $d/M = 22.3$, $v = 0.1$ binary as predicted by a Newtonian calculation of the infall velocity. *Right:* The radiated energy is shown as a function of time for BS binaries with a phase offset $\delta\phi = \pi$. Again, starting a BS binary from $d/M = 11.2$ with a larger velocity, as obtained from a Newtonian calculation, the energy functions for $v = 0.1$ but larger initial separation are recovered. The initial separation d is given in units of M, even though this factor has been omitted in the legends for presentation purposes.

we observe a gradual increase in the energy with rising initial boost velocity. This increase is most pronounced for the anti-phase sequence whereas the velocity change has almost no effect on the radiated energy for in-phase binaries. Over the entire range $\delta\phi \in [0, \pi]$, however, we recover with high accuracy the radiated energies of the $d/M = 22.3$ binaries by starting from $d/M = 11.2$ with larger velocity $v = 0.18$ as predicted by the Newtonian calculation. We are likewise able to recover comparable energies for separations of $d/M = 33.5$ and $d/M = 44.7$ by starting the sequence with $d/M = 11.2$ with yet higher initial boost velocities; see the right panel of Fig. 7.7.2.

7.7.2 Unequal-mass collisions

In the remainder of this Section, we focus on the unequal-mass binary simulations and present a direct comparison between the results obtained for plain superposition (7.19) and our improved method for $q \neq 1$ binaries developed in Section 7.5.2. There are two limits, in which we would expect the two methods to give comparable results:

1. With decreasing mass ratio, the metric of the lighter star will approach Minkowski, hence the volume factor change induced by it on the heavier star will be negligible. For plainly superposed data, overall constraint violations will be reduced, however, the

volume factor change induced on the lighter star by its heavier companion would be inevitable, resulting in spurious star excitations.

2. In the limit of infinite separation ($d \to \infty$), both stars will be isolated and therefore even start in their 'equilibrium' state for plain superposition.

In practice, we are limited to finite mass ratios and initial separations, and as we will see later, the regimes, where plain superposition can give comparable results to our method require very large initial separations, often impractical due to the ensuing computational costs.

For this comparison, it is important to realise that in the unequal-mass case, the initial dephasing parameter $\delta\phi$ no longer represents the dephasing at merger, $\delta\phi_{\text{merger}}$. This is a consequence of the two stars' different oscillation frequencies which introduce a "natural" time-dependent phase offset. Introducing a constant phase offset parameter $\delta\phi$ to one of the stars adds a constant phase difference to this time dependent dephasing in a controlled manner. Using multiple values of the initial dephasing parameter $\delta\phi$ for otherwise identical configurations allows us to cover a complete range of dephasing at merger, $\delta\phi_{\text{merger}} \in [0, 2\pi)$.

As will be shown in the following analysis, the key effects of varying the off-set parameter $\delta\phi$ for a given BS binary configuration are as follows:

1. a change in the infall time (Fig. 7.7.5, $\delta\phi = 60^\circ, 150^\circ$),

2. a change in the GW amplitude and the radiated energy (Figs. 7.7.4 and 7.7.6),

3. a relative enhancement of higher-order multipoles in the GW signal, indicating significant tidal deformation of the lighter star (Fig. 7.7.5, $\delta\phi = 60^\circ, 90^\circ$).

First, however, we test our improved initial data construction by exploring the time evolution of the BSs' central scalar field amplitude.

7.7.3 Scalar field profiles

The deficiencies of the plain-superposition procedure are diagnosed most directly in the time evolution of the scalar-field amplitude at the centres of the two BSs. For equal mass head-on collisions of BSs and OSs, respectively, this has been shown in Fig. 9 of Ref. [141] and Fig. 7 of Ref. [139]. A closer analysis of the scalar-field evolutions we obtain from our equal-mass BS collisions of Section 7.7.1 confirms this picture for all values of the dephasing parameter $\delta\phi$. In this Section, we demonstrate that for sufficiently compact BSs plain superposition results in the same spurious effects in the unequal-mass BS collisions, namely spurious oscillations of the two stars' central scalar amplitudes around their equilibrium values that subsequently trigger premature collapse to a BH.

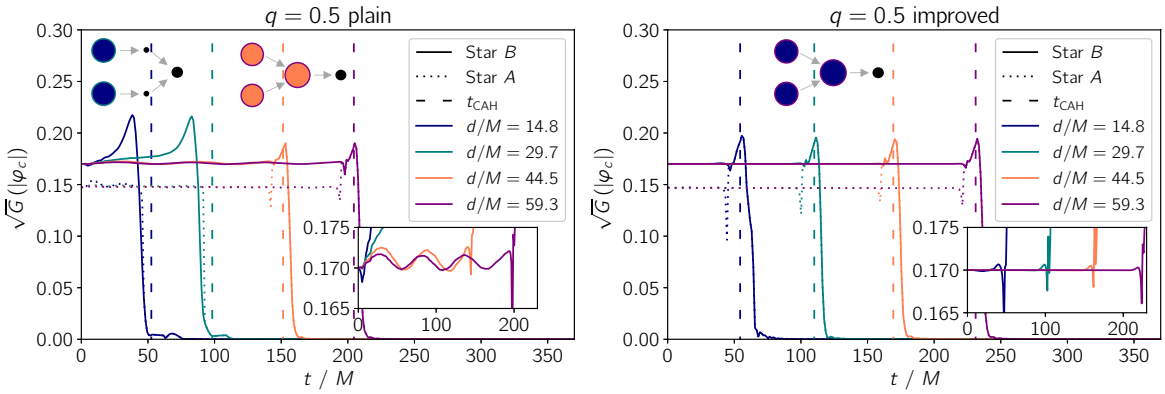


Fig. 7.7.3 Evolution of the central scalar field $|\varphi_c|$ of the two BSs for the mass ratio $q = 0.5$ using plain superposition (left) and the improved method (right). The results for the heavy star B are shown as solid and those for the light star A as dotted curves, and the colour encodes the initial separation. For each configuration, the phase offset $\delta\phi$ has been chosen to maximise the GW radiation; cf. Table 7.7.1. The vertical dashed lines mark the time of formation of a common apparent horizon. The inset shows the early evolution of $|\varphi_c|$ for the heavy star B up to the point of divergence; plain superposition results in significant oscillations of $|\varphi_c|$. For $d/M = 14.8$ and 29.7, these oscillations trigger a premature collapse of the heavy star into a BH (signalled by the rapid drop of $|\varphi_c|$ to zero) well before a common apparent horizon forms.

d/M	14.8	29.7	44.5	59.3
$\delta\phi$ (plain)	330°	60°	60°	30°
$\delta\phi$ (improved)	240°	210°	120°	0°

Table 7.7.1 Choices of dephasing parameters $\delta\phi$ maximising the GW energy for `q05-dX-pX` binary configuration.

In this analysis of unequal-mass collisions, we encounter one minor difficulty, the *a-priori* unknown dephasing at merger. To ensure that our comparison of binaries starting from different initial separations is not adversely affected by possible variations in the dephasing at merger, we choose for each separation the initial phase-parameter that maximises the radiated GW energy (cf. Fig. 7.7.6 below). For the mass ratio $q = 0.5$ and our two superposition types the specific values of the dephasing parameter can be found in Table 7.7.1.

The resulting time evolutions $|\varphi_c(t)|$ are shown for all four initial separations and both superposition methods in Fig. 7.7.3 and exhibit the same features as mentioned above: plain superposition (left panel) results in significant unphysical oscillations of $|\varphi_c|$ which for $d/M = 14.8$ and $d/M = 29.7$ also cause a collapse of the heavier star B into a BH well before a common horizon forms as marked by the vertical dashed lines. For the larger separations $d/M = 44.5$ and $d/M = 59.3$, the premature BH formation is avoided, but

plain superposition still results in significant pulsations of the BSs. In contrast, the scalar-field amplitude of both BSs remains very close to its equilibrium value for our improved superposition method throughout the infall as demonstrated in the right panel of Fig. 7.7.3. As expected, significant dynamics in the scalar field, including the eventual collapse to a single BH, are only encountered around merger: the local maximum in the scalar field coincides with common horizon formation for small and large initial separations alike.

We have repeated this analysis for different mass ratios and different choices of the dephasing parameter. As it turns out, the dephasing parameter has no significant effect on the results shown in Fig. 7.7.3 and our above concern about choosing $\delta\phi$ appropriately has been unnecessary. The mass ratio, however, does affect the results to some extent. The spurious effects of plain superposition are even more pronounced for $q = 0.75$ (where premature BH formation occurs for all but the largest d/M) and less pronounced for $q = 0.38$ (where only the smallest initial separation results in premature BH formation). This q dependence is fully consistent with the above observation (i) in Section 7.7.2 that plain superposition becomes viable for $q \to 0$.

7.7.4 Gravitational waveforms

As we have seen in Section 7.7.1 and, in particular, in Fig. 7.7.1, the initial binary separation d can have a significant effect on the magnitude of the GW signal due to the corresponding differences in the collision velocity around merger. This variation arises additionally due to the choice of the initial dephasing parameter $\delta\phi$. We can still check the consistency of our evolutions, however, in the limit of large separation d and simultaneously selecting $\delta\phi$ such that it maximises the GW energy. Specifically, we show the resulting GW signals in Fig. 7.7.4 for the `q075-dX-pX` binaries with initial separation from $d/M = 12.7$ to $d/M = 50.9$ and the `q038-dX-pX` binaries with $d/M = 16.2$ to $d/M = 64.8$. The dephasing parameters $\delta\phi$ maximising the GW energy for these configurations are shown in Table 7.7.2.

	$q = 0.75$				$q = 0.38$			
d/M	12.7	25.5	38.2	50.9	16.2	32.4	48.6	64.8
$\delta\phi$ (plain)	300°	330°	330°	270°	330°	150°	180°	180°
$\delta\phi$ (improved)	180°	240°	270°	270°	180°	330°	300°	210°

Table 7.7.2 Choices of dephasing parameters $\delta\phi$ maximising the GW energy for `q075-dX-pX` and `q038-dX-pX` binary configurations.

The Figure clearly demonstrates that for mass ratio $q = 0.75$ ($q = 0.38$), our improved superposition method results in comparable GW amplitudes for initial separations $d/M \gtrsim 25.5$

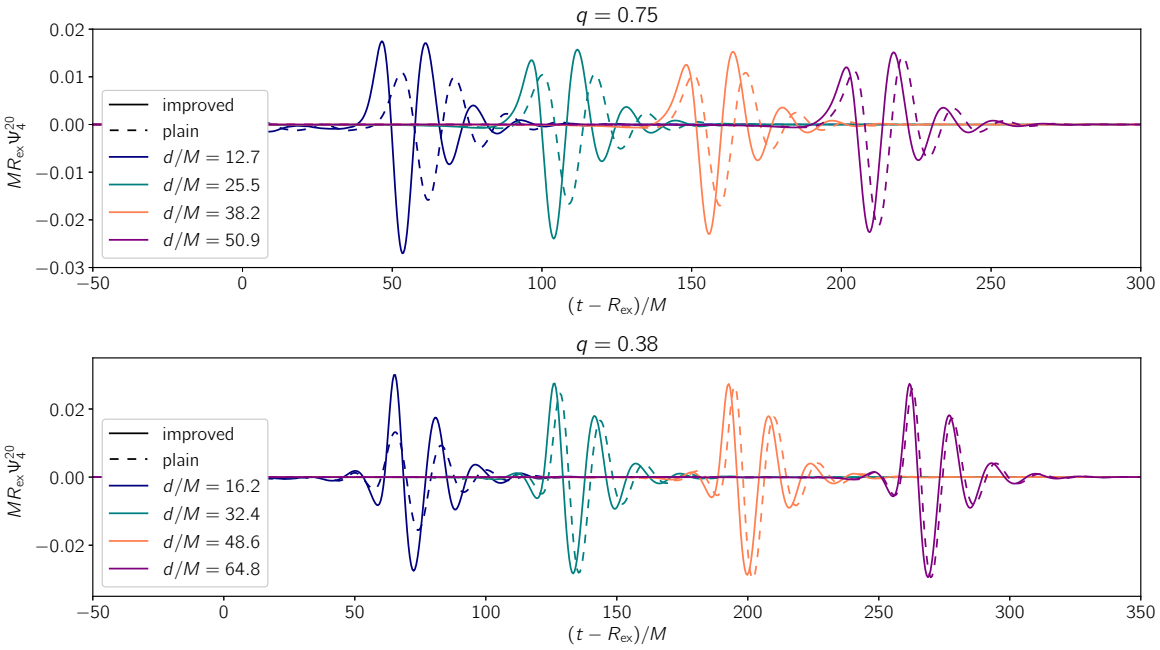


Fig. 7.7.4 20-modes of the Newman-Penrose scalar Ψ_4 of binary configurations with $q = 0.75$ (upper) and $q = 0.38$ (lower) with varying initial separation, d. For each mass ratio, initial separation and superposition method, we choose the phase off-set parameter that maximises the GW energy; cf. Table 7.7.2. The straight line shows the waveform obtained for our improved method, whilst the dashed line shows that for plain superposition. As we increase the separation, both superpositions give comparable results. This is most notable in the case of smaller mass ratio $q = 0.38$, where good agreement is already reached at smaller distances $d/M \gtrsim 32.4$.

$(d/M \gtrsim 32.4)$. This convergence in the GW signal (maximised over $\delta\phi$) is as expected for large initial separations. In contrast, plain superposition only achieves this convergence for much larger initial separations, namely $d/M \gtrsim 50.9$ $(d/M \gtrsim 32.4)$. For small initial separations, plain superposition systematically results in weaker GW amplitude when compared to our improved superposition method. In fact, this is a distinct feature of premature BH formation that occurs precisely for these plainly superposed configurations; cf. Section 7.7.3. As expected, the agreement in the GW amplitude between the two superposition methods improves as we increase the separation and/or decrease the mass ratio, i.e. the very limits described in items (i) and (ii) of Section 7.7.2.

Quite remarkably, we obtain the largest GW amplitudes for the smallest mass ratio $q = 0.38$. This mass ratio also exhibits the most interesting waveforms. For a wide range of the dephasing angle $\delta\phi$, we find the GW radiation to be quadrupole dominated with a merger pulse reminiscent of BH head-on collisions; see e.g. Fig. 8 of Ref. [482]. However, certain phase off-set parameters result in fainter and aberrant GW signals with signatures of

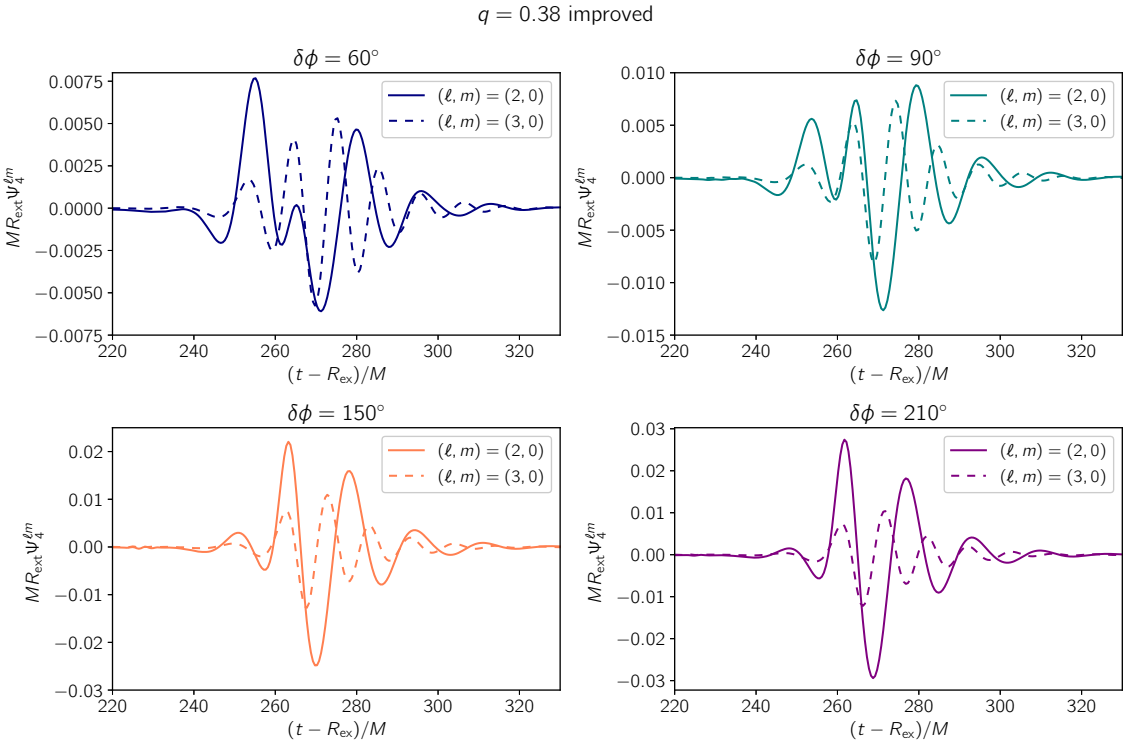


Fig. 7.7.5 20-modes and 30-modes of the Newman-Penrose scalar Ψ_4 for the improved binary configuration $q = 0.38$ with initial separation $d/M = 64.8$ and different phase off-set parameters $\delta\phi$. The prominent feature of certain off-set parameters (e.g. $\delta\phi = 60°, 90°$) is that they result in fainter GW signals with more complex structure and $\ell = 3$ modes become comparable in amplitude to the $\ell = 2$ ones. This is unlike the head-on BH case of the same mass ratio, where $\ell = 3$ mode is roughly 5 times smaller than the $\ell = 2$ mode [3].

tidal deformation of the binary constituents. We attribute this more complex shape of the fainter signals to the lighter BS in the binary becoming more prone to tidal effects from its more compact and heavier companion. For a given self-interaction constant σ_0 and with decreasing mass, it has been shown that tidal deformability of the star increases [344], and as a result the gravitational waveform can significantly depart from the BH-like form [489]. We illustrate this phenomenon in more detail in Fig. 7.7.5, which shows the $q = 0.38$ waveforms for phase off-set parameters $\delta\phi = 60°, 90°, 150°, 210°$. The former two give the smallest GW amplitude and exhibit significant deformation, whilst the latter two show a clear, 'black hole' like signal. In the case of fainter GW signals, the importance of higher modes becomes more prominent: as indicated in the same Figure, $\ell = 3$ modes become almost comparable in amplitude to the $\ell = 2$ modes for binaries with $\delta\phi = 60°, 90°$.

7.7.5 Energy radiated by unequal-mass binaries

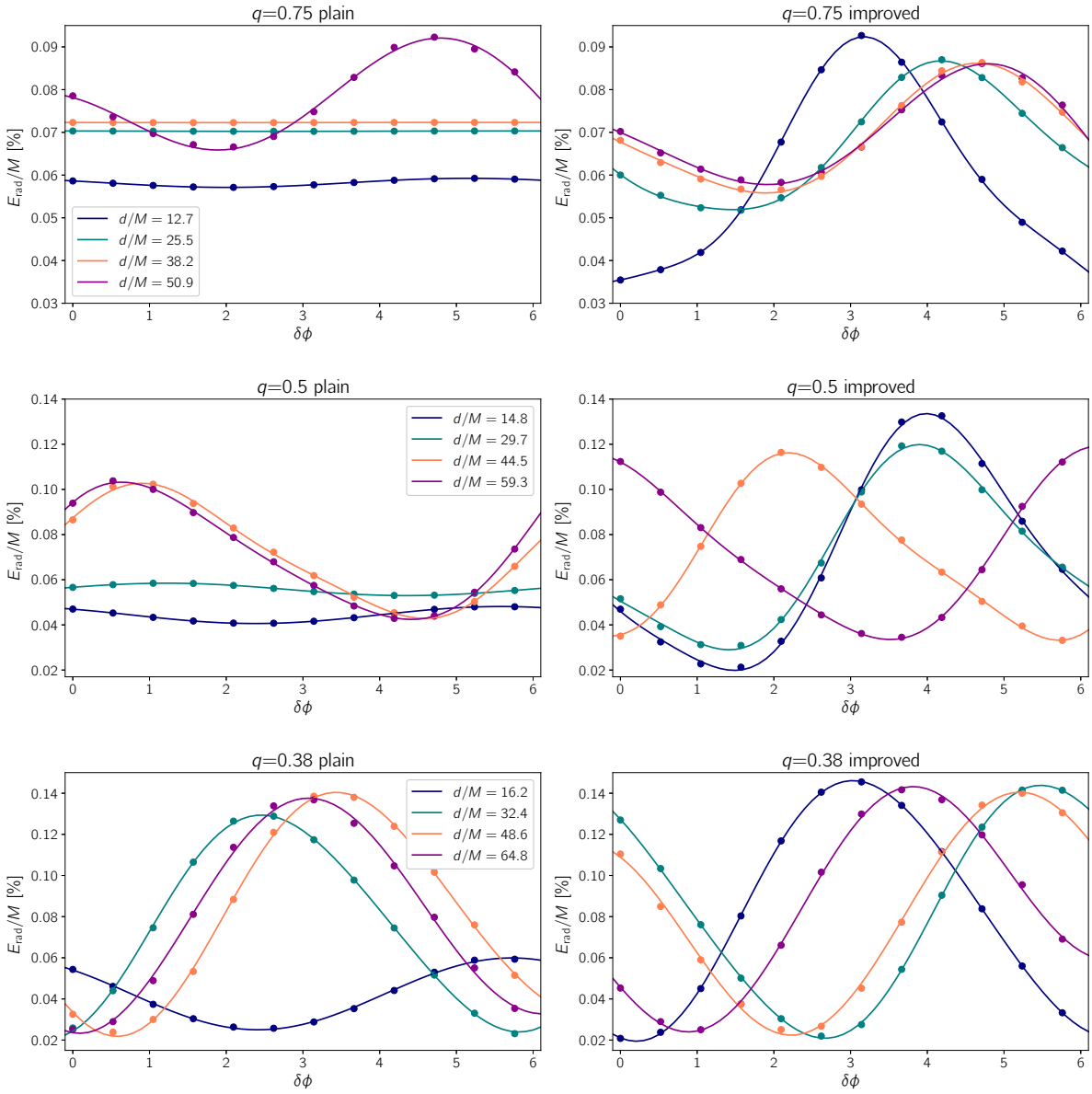


Fig. 7.7.6 Radiated energy as a function of the phase off-set parameter $\delta\phi$ for binary collisions of $q = 0.75, 0.5, 0.38$. The left panels show the results for plain superposition (7.27) and the right panels those for our improved superposition.

Similar to the equal-mass binaries, in the unequal-mass case we also observe some discrepancy in the GW energy with varying initial separation and dephasing parameter. We recall that these effects (see Fig. 7.7.1) have been attributed to the differences in the collision velocity and the degree of the repulsive nature of the scalar field. However, in the

unequal-mass case the dependency of the energy on the dephasing parameter and separation becomes even more complex. This is due to the fact that the phase difference at merger for unequal-mass binaries is no longer the initial dephasing $\delta\phi$ we apply to one of the BSs and as we vary the initial separation d we further change the phase difference at merger.

In Fig. 7.7.6, we illustrate this dependence of the radiated energy on the dephasing parameter, $E_{\rm rad}(\delta\phi)$, for varying initial separations and all the mass ratios considered here. As shown in the left column, plain superposition results in flat energy profiles for smaller separations. We see here once again a manifestation of premature BH formation which largely eliminates the effect of the scalar field's dephasing on the merger dynamics. This is unlike the energy profiles of our improved superposition displayed in the right column of Fig. 7.7.6. Here the energy dependence on the dephasing parameter takes on an approximately sinusoidal shape for all separations d. The distinct horizontal shift between these profiles can be attributed to the infall-time dependent contribution to the dephasing $\delta\phi$. Except for the smallest separation and modulo the horizontal shift, the energy profiles exhibit comparable maxima and minima as we change the initial separation. However, similar to the equal-mass case, the results for the smallest separation differ significantly, presumably due to differing collision velocity as illustrated in Fig. 7.7.2.

Since the dependence of the radiated energy on $\delta\phi$ is time-dependent in the unequal-mass case, $E_{\rm rad}(\delta\phi)$ is no longer described by a single sinusoidal fit (7.31). In fact, we find that a two-mode sinusoidal fit

$$E_{\rm fit} = \sum_{i=1}^{2} A_i \sin(f_i \delta\phi + p_i) + s \tag{7.32}$$

well approximates the data. This two-mode fit applies to all configurations using the improved initial data construction and the data of plain superposition at larger initial separations. Only in the case of small initial separations, where plain superposition results in premature BH formation, the energy is well fitted with the one-mode fit (7.31); here the BH formation eliminates the overall effect of the dephasing as well as any complications arising from its time dependence during the merger stage. In summary, our results demonstrate that plain superposition not only results in quantitative changes in the emitted GW signals, but also leads to a significant over-simplification of the merger dynamics.

7.8 Conclusion

In this Chapter, we have extended previous studies of boson-star (BS) binaries in two principle directions: (i) we have generalised the initial data construction for equal-mass BS binaries of

Ref. [141] to the unequal-mass case, (ii) we have systematically explored the effect of the scalar field's dephasing $\delta\phi$ on the merger dynamics and GW emission.

For all mass ratios and dephasing parameters, we have shown how plainly superposed initial data can result in spurious physical effects, such as increased constraint violations, oscillations of the scalar fields' central amplitudes and premature BH formation. The key drawback of plain superposition that leads to these spurious effects is its failure to recover equilibrium values of the volume element at the stars' centres. By appropriately correcting the conformal factor of the spatial metric, our method exactly recovers the equilibrium volume element at the centres of the stars and thus circumvents the spurious features of plainly superposed data for all mass ratios and $\delta\phi$. Notably, our improved method explicitly incorporates the equal-mass fix and plain superposition as limiting cases.

Similar to previous studies (e.g. Refs. [410, 486, 487]), we find that the choice of the dephasing parameter significantly affects the merger dynamics of BS binaries, most notably through the repulsive character of merging scalar-field solitons with large phase differences. Crucially, for unequal-mass binaries, this phase difference is not equal to the initial dephasing parameter $\delta\phi$ but also acquires a time-dependent contribution due to the individual BSs' different oscillation frequencies.

To leading order, we find that the radiated energy and, hence, GW amplitude depends approximately sinusoidally on the dephasing parameter.

More specifically, we find equal-mass collisions to result in the strongest GW signals (and maximal energy) for $\delta\phi = 0$, i.e. configurations with equal phase at merger. As the dephasing $\delta\phi$ is increased towards π, the energy and GW amplitude decrease monotonically. For unequal-mass binaries, we observe the same behaviour, accompanied, however, by a constant offset in $\delta\phi$ due to the differing oscillation frequencies and the subsequent additional phase offset at merger; cf. Figs. 7.7.1 and 7.7.6.

In general, the BSs' phase offset introduces considerable complexity to the merger dynamics and GW emission. In the equal-mass case, this manifests itself most prominently in a significant variation of the GW energy from off-phase BS binaries as we change the initial separation; cf. Fig. 7.7.1. We attribute this variation to differences in the binaries' binding energies and the corresponding differences in the collision velocities as shown in Fig. 7.7.2. We observe the same phenomenon for unequal-mass binaries but with maximal and minimal radiation occurring for shifted values of $\delta\phi$ which we ascribe to the time dependent nature of the dephasing. The extent of the energy discrepancy depends on the dephasing parameter. This may be connected to complex interactions between the collision velocity and the scalar fields' repulsion, which we leave for future study.

Additionally our unequal-mass collisions exhibit several distinct features which we summarise as follows.

1. As shown in Fig. 7.7.6, smaller mass ratios produce larger GW energy than the equal-mass case. This is in contrast to the BH case, where $E_{\rm rad} \sim \eta^2 := q^2/(1+q)^4$ [287], where η is a monotonically decreasing function of q.

2. As shown in Fig. 7.7.5, certain dephasing parameters result in weaker GW signals with signatures of tidal deformation. For these configurations, higher modes, such as $\ell = 3$, exhibit almost comparable magnitude as their quadrupolar counterparts, especially in the case of binaries with $q = 0.38$. This is unlike the black hole case, where the $\ell = 3$ mode is 5 times smaller than the $\ell = 2$ mode [3].

3. The numerical data of the radiated energy $E_{\rm rad}(\delta\phi)$ in Fig. 7.7.6 displays some deviation from the pure sinusoidal fit of (7.31) and is better described by the two-mode sinusoidal fit (7.32). We believe this is a feature of the time-dependent phase difference *during* the merger.

Appendix

Appendix 7.A Choice of conformal factor

In Eq. (7.24), rewritten here as

$$\gamma_{ij} = \lambda\,\tilde{\gamma}_{ij} \quad \Leftrightarrow \quad \tilde{\gamma}_{ij} = \lambda^{-1}\gamma_{ij} \quad \text{with} \quad \lambda = \gamma^{1/3}\,,$$

we have expressed the conformal factor in terms of the variable $\lambda = \gamma^{1/3}$. The exponent $1/3$ is, of course, a free choice in this equation and we will now explore the implications of choosing a different exponent and why $1/3$ turns out to work particularly well in our practical applications. Let us start with the conformal factor motivated by the Schwarzschild metric in (Cartesian) isotropic coordinates,

$$\mathrm{d}s^2 = -\left(\frac{2r-M}{2r+M}\right)^2 \mathrm{d}t^2 + \left(1+\frac{M}{2r}\right)^4 \delta_{ij}\mathrm{d}x^i\,\mathrm{d}x^j \tag{7.33}$$

$$= -\left(\frac{2r-M}{2r+M}\right)^2 \mathrm{d}t^2 + \psi^4\delta_{ij}\mathrm{d}x^i\,\mathrm{d}x^j\,. \tag{7.34}$$

Note that the spatial metric is now written as

$$\gamma_{ij} = \psi^4\delta_{ij}\,, \tag{7.35}$$

which is Eq. (7.24) – for the special case of conformal flatness – written in terms of the alternative variable ψ and an exponent 4. We generalise this freedom of writing the conformal factor by introducing the variable

$$\Lambda = \psi^n = \gamma^{n/12} \quad \text{with} \quad \gamma := \det\gamma_{ij}\,, \tag{7.36}$$

Name	Variable	Relation to $\tilde{\gamma}_{ij}$
Standard notation for isotropic Schwarzschild	ψ	$\gamma_{ij} = \psi^4 \tilde{\gamma}_{ij} = \psi^4 \delta_{ij}$
General conformal function	$\Lambda = \psi^n$	$\gamma_{ij} = \Lambda^{4/n} \tilde{\gamma}_{ij}$
BSSN/CCZ4 conformal factor	χ	$\gamma_{ij} = \chi^{-1} \tilde{\gamma}_{ij}$
Conformal variable for $n = 4$ (our preferred choice)	λ	$\gamma_{ij} = \lambda \tilde{\gamma}_{ij}$

Table 7.A.1 A list of the conformal factor functions used in our discussion of binary initial-data construction. Note that in the main text we fix $n = 4$ in the newly defined conformal factor, so that $\gamma_{ij} = \lambda_{\rm new} \tilde{\gamma}_{ij}$.

where[8] $n \in \mathbb{Z}$. For $n = -4$, for example, we recover the customary BSSN/CCZ4 conformal function $\Lambda = \chi$, whilst for the choice of $n = 4$ we recover the conformal factor $\Lambda = \lambda = \gamma^{1/3}$ of Eq. (7.24). In the general case, we conformally decompose the spatial metric according to

$$\gamma_{ij} = \gamma^{1/3} \tilde{\gamma}_{ij} = \Lambda^{4/n} \tilde{\gamma}_{ij} \quad \text{with} \quad \det \tilde{\gamma}_{ij} = 1 \,. \tag{7.37}$$

In our construction of BS binary initial data, we start with the spatial metric γ_{ij} obtained from plain superposition and then conformally rescale this metric in order to correct the volume element at the individual BSs' centers. This correction gives us a new spatial metric

$$\gamma_{ij}^{\rm new} = \left(\frac{\Lambda_{\rm new}}{\Lambda} \right)^{4/n} \gamma_{ij} = \frac{\Lambda_{\rm new}^{4/n}}{\gamma^{1/3}} \gamma_{ij} = \Lambda_{\rm new}^{4/n} \tilde{\gamma}_{ij} . \tag{7.38}$$

By construction, this correction will recover the correct volume element at the centers of both BSs for *any* choice of n. The metric corrections thus introduced *in the neighbourhood* of the BS centers, however, will differ for different choices of n. And we see in Eq. (7.38) that the conformal rescaling is a linear function of our conformal variable only for $n = 4$. If we Taylor expand the rescaling factor $\Lambda_{\rm new}/\Lambda$ around either BS center (where, we recall, it gives us the exact correction), then any choice $n \neq 4$ will result in complicated additional terms in the Taylor expansion of the factor $(\Lambda_{\rm new}/\Lambda)^{4/n}$. We cannot rigorously prove that this non-linearity in Eq. (7.38) inevitably leads to a significant deterioration of our initial data construction, but this is exactly what we observe in all our numerical experiments; choices $n \neq 4$ systematically result in significantly larger constraint violations compared to those of Fig. 7.6.3 and generally more so the further n deviates from 4.

As a summary, we list in Table 7.A.1 the different variables for the conformal factor discussed in our initial data construction.

[8] In principle we could allow for any $n \in \mathbb{R}$ here, but for practical reasons have performed numerical tests only for integer n.

Appendix 7.B Improved superposition in the limits $R_{\rm A}, R_{\rm B} \to 0$ or $R_{\rm A}, R_{\rm B} \to \infty$

In Section 7.6.2 we have demonstrated that in the equal mass case our improved superposition (7.29) with $R_A, R_B \to 0$ results in the same gravitational waveform as obtained with plain superposition, whilst with $R_A, R_B \to \infty$ we recover the waveform from the equal mass fix of Refs. [139, 141]. Here we derive analytically that our proposed method indeed reduces to plain superposition and the equal-mass fix in the respective limits.

7.B.1 The limit $R_{\rm A}, R_{\rm B} \to 0$

In the limit $R_{\rm A}, R_{\rm B} \to 0$, the weight functions of Eq. (7.30) become

$$w_{\rm A}(x^i) = \frac{1}{r_{\rm A}}, \qquad w_{\rm B}(x^i) = \frac{1}{r_{\rm B}}, \tag{7.39}$$

where $r_{\rm A} = ||x^i - x^i_{\rm A}||$ and $r_{\rm B} = ||x^i - x^i_{\rm B}||$. This implies, in particular, that in Eq. (7.28) the terms $w_{\rm A}(x^i_{\rm A}) \to \infty$ and $w_{\rm B}(x^i_{\rm B}) \to \infty$ diverge at the respective stars' centres, whereas $w_{\rm A}(x^i_{\rm B})$ and $w_{\rm B}(x^i_{\rm A})$ remain finite, so that

$$h_{\rm A} \to \frac{w_{\rm B}(x^i_{\rm B})\delta\lambda(x^i_{\rm A})}{w_{\rm A}(x^i_{\rm A})w_{\rm B}(x^i_{\rm B})} = \frac{\delta\lambda(x^i_{\rm A})}{w_{\rm A}(x^i_{\rm A})}, \qquad h_{\rm B} \to \frac{w_{\rm A}(x^i_{\rm A})\delta\lambda(x^i_{\rm B})}{w_{\rm A}(x^i_{\rm A})w_{\rm B}(x^i_{\rm B})} = \frac{\delta\lambda(x^i_{\rm B})}{w_{\rm B}(x^i_{\rm B})}. \tag{7.40}$$

The correction $\delta\lambda(x^i)$ applied to the conformal factor in Eq. (7.27) then becomes

$$\delta\lambda(x^i) = w_{\rm A}(x^i)h_{\rm A} + w_{\rm B}(x^i)h_{\rm B} = \begin{cases} \delta\lambda(x^i_{\rm A}) & \text{for } x^i = x^i_{\rm A}, \\ \delta\lambda(x^i_{\rm B}) & \text{for } x^i = x^i_{\rm B}, \\ 0 & \text{otherwise.} \end{cases} \tag{7.41}$$

We thus recover $\delta\lambda = 0$, i.e. plain superposition, everywhere except at the isolated points $x^i_{\rm A}$ and $x^i_{\rm B}$. The Dirac δ function like correction at $x^i_{\rm A}$ and $x^i_{\rm B}$ is a consequence of our condition (7.26) but is lost in numerical evolutions due to finite resolution, so that for $R_{\rm A}, R_{\rm B} \to 0$ we expect to obtain the same results as for plain superposition.

7.B.2 The limit $R_{\rm A}, R_{\rm B} \to \infty$

For $R_{\rm A}, R_{\rm B} \to \infty$, we can write the weight functions (7.30) as

$$w_{\rm J}(x^i) = \frac{1}{\sqrt{R_{\rm J}^2 + r_{\rm J}^2}} = \frac{1}{R_{\rm J}} \left(1 + \frac{r_{\rm J}^2}{R_{\rm J}^2}\right)^{-1/2} \approx \frac{1}{R_{\rm J}} \left(1 - \frac{r_{\rm J}^2}{2R_{\rm J}^2}\right), \tag{7.42}$$

where ${\rm J} = {\rm A}, {\rm B}$ and we have Taylor expanded to first order in $\frac{r_{\rm J}^2}{R_{\rm J}^2}$. Bearing in mind that $r_{\rm A}(x^i_{\rm A}) = r_{\rm B}(x^i_{\rm B}) = 0$ and $r_{\rm A}(x^i_{\rm B}) = ||x^i_{\rm B} - x^i_{\rm A}|| = r_{\rm B}(x^i_{\rm A})$ is simply the separation d of the two BSs, we obtain, again to leading order,

$$\begin{aligned} w_{\rm A}(x^i_{\rm A}) w_{\rm B}(x^i_{\rm B}) - w_{\rm A}(x^i_{\rm B}) w_{\rm B}(x^i_{\rm A}) &\approx \frac{1}{R_{\rm A} R_{\rm B}} - \frac{1}{R_{\rm A} R_{\rm B}} \left(1 - \frac{d^2}{2R_{\rm A}^2}\right) \left(1 - \frac{d^2}{2R_{\rm B}^2}\right) \\ &\approx \frac{1}{R_{\rm A} R_{\rm B}} \left(\frac{d^2}{2R_{\rm A}^2} + \frac{d^2}{2R_{\rm B}^2}\right). \end{aligned} \tag{7.43}$$

We likewise expand, to leading order in $\frac{r_{\rm J}^2}{R_{\rm J}^2}$, the coefficients $h_{\rm A}$, $h_{\rm B}$ in the form of their linear combination in Eq. (7.27),

$$\begin{aligned} & w_{\rm A}(x^i) h_{\rm A} + w_{\rm B}(x^i) h_{\rm B} \\ &\approx \frac{\left[-\frac{1}{R_{\rm B}} \left(1 - \frac{d^2}{2R_{\rm B}^2}\right) \delta\lambda(x^i_{\rm B}) + \frac{1}{R_{\rm B}} \delta\lambda(x^i_{\rm A})\right] \frac{1}{R_{\rm A}} + \left[\frac{1}{R_{\rm A}} \delta\lambda(x^i_{\rm B}) - \frac{1}{R_{\rm A}} \left(1 - \frac{d^2}{2R_{\rm A}^2}\right) \delta\lambda(x^i_{\rm A})\right] \frac{1}{R_{\rm B}}}{w_{\rm A}(x^i_{\rm A}) w_{\rm B}(x^i_{\rm B}) - w_{\rm A}(x^i_{\rm B}) w_{\rm B}(x^i_{\rm A})} \\ &= \frac{-\left(1 - \frac{d^2}{2R_{\rm B}^2}\right) \delta\lambda(x^i_{\rm B}) + \delta\lambda(x^i_{\rm A}) + \delta\lambda(x^i_{\rm B}) - \left(1 - \frac{d^2}{2R_{\rm A}^2}\right) \delta\lambda(x^i_{\rm A})}{\frac{d^2}{2R_{\rm A}^2} + \frac{d^2}{2R_{\rm B}^2}} \\ &= \frac{\frac{d^2}{2R_{\rm B}^2} \delta\lambda(x^i_{\rm B}) + \frac{d^2}{2R_{\rm A}^2} \delta\lambda(x^i_{\rm A})}{\frac{d^2}{2R_{\rm A}^2} + \frac{d^2}{2R_{\rm B}^2}}. \end{aligned} \tag{7.44}$$

In the equal-mass case, the corrections at the BSs' centers are the same, $\delta\lambda(x^i_{\rm A}) = \delta\lambda(x^i_{\rm B})$, so that

$$w_{\rm A}(x^i) h_{\rm A} + w_{\rm B}(x^i) h_{\rm B} = \delta\lambda(x^i_{\rm A}) = \delta\lambda(x^i_{\rm B}), \tag{7.45}$$

which, after multiplication with $\tilde{\gamma}_{ij}$, is the equal mass fix (7.22).

Appendix 7.C Gravitational radiation and numerical uncertainties

In this Section, we calibrate the accuracy of our numerical simulations by studying the convergence of two BS binary configurations, one obtained with GRCHOMBO and one with the LEAN code.

7.C.1 Extraction of physical quantities

In our convergence studies for both codes we use the radiated energy. For this purpose, we extract the GW signal in the form of the Newman-Penrose [279, 280] scalar Ψ_4 for outgoing radiation as described in Section 2.7.5. We then compute the radiated energy via

$$E_{\rm rad}(t) = \lim_{r\to\infty} \frac{r^2}{16\pi} \int_{t_0}^{t} dt' \oint_{S^2} d\Omega\, \mathbf{e}_r \left| \int_{-\infty}^{t'} dt'' \Psi_4 \right|^2 , \tag{7.46}$$

where $\mathbf{e}_r$ is the unit radial vector of a sphere.

7.C.2 LEAN code

The first case we study is the binary configuration `q05_d29_p000` of Table 7.6.2. In terms of the notation of Section 7.4.1, the grid setup for these runs is given by a domain size $L_1 = 1024$ with grid spacing (on the innermost refinement level) $\mathrm{d}x_7 = 1/20$, $1/24$ and $1/32$, respectively, for a total mass $M = 1.0787$. In Fig. 7.C.1, we show the resulting convergence analysis for the energy $E_{\rm rad}$ radiated in GWs. We see from the upper panel of the Figure that the total radiated energy converges at about fourth order. The early part of the signal, which is dominated by the high-frequency contributions from the spurious "junk" radiation converges at lower order, approximately first, but does not significantly affect the total radiated energy. Through comparison with the Richardson extrapolated values, we estimate the discretisation in the radiated energy to be about 0.6 % at medium resolution $\mathrm{d}x_7 = 1/24$ which is the resolution used in our LEAN production runs.

The second main uncertainty in our results arises from the extraction of the GW signal at finite radius. We determine this error by extrapolating the GW signals computed at seven equidistant extraction radii in the range $R_{\rm ex} = 120$ to 240 using a first order fit in $1/R_{\rm ex}$ as described in Section 4.13 of Ref. [133] and obtain a numerical uncertainty of 1.4 % for the radiated energy. Combined with the discretisation error, this gives us a numerical error budget of 2 %.

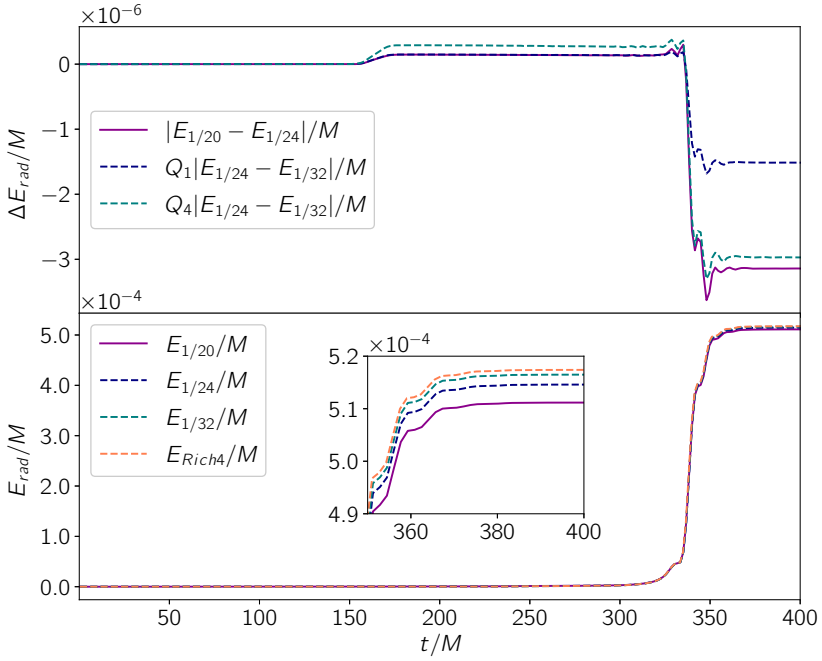


Fig. 7.C.1 Convergence analysis of the GW energy computed with the LEAN code for the collision and merger of the BS binary `q05_d29_p000` of Table 7.6.2. The upper panel shows the differences in the energy results obtained for different resolutions, measured here in terms of the grid spacing on the innermost refinement level. The high-resolution difference has been rescaled by $Q_1 = 0.8$ and $Q_4 = 1.57$ corresponding to first and fourth-order convergence. While the small contribution due to noisy junk radiation converges only at first order, the total radiated energy exhibits convergence close to fourth order. The bottom panel displays the radiated energy as a function of time for the three resolutions as well as a fourth-order Richardson extrapolation.

We have analysed in the same way the quadrupole of the Newman-Penrose scalar Ψ_4 and observe the same order of convergence but find a total error about twice as large, 4 % in the GW amplitude.

7.C.3 GRCHOMBO code

Here we study the binary configuration `q075_d12_p000` of Table 7.6.2. We use the same grid set-up as described in the main section with $\mathrm{d}x = 1/32$, $\mathrm{d}x = 1/40$ and $\mathrm{d}x = 1/48$ on the finest refinement level for low, medium and high resolutions respectively; here the total mass is $M = 1.2558$. The results shown in Fig. 7.C.2 demonstrate overall second-order convergence.

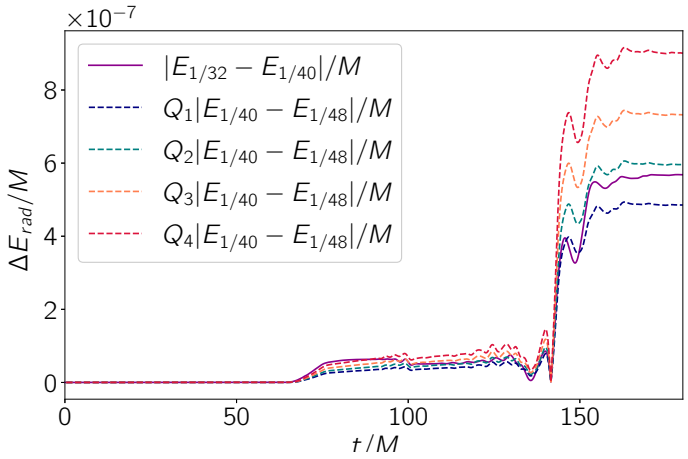


Fig. 7.C.2 Convergence analysis of the GW energy computed with at $R_{ex} = 120$ for the GRCHOMBO simulation of BS binary `q075_d12_p000` of Table 7.6.2. The difference between high and medium resolutions has been rescaled by factors Q_1 to Q_4 corresponding to convergence of first to fourth order. At early times, the order of convergence fluctuates between second and third, whilst at later times it settles to just below second order of convergence.

By comparison with the Richardson extrapolated results, we obtain a discretisation error of around 1.1% for the low resolution, on which the results of the main text are based on.

We estimate the error due to the finite extraction radius by extrapolating the GW signals computed at six equidistant radii in the range $R_{ex} = 60 - 120$ and find an uncertainty of 2.6%. This thus gives us a total error budget for GRCHOMBO of 3.7%.

Appendix 7.D Constraint violations in the (R_A, R_B) parameter space

In Fig. 7.6.2 of Section 7.6.2, we have shown the behaviour of the $L2$ norm of Hamiltonian constraint over the parameter space (R_A, R_B) for $q = 0.75$. In this Appendix we attach results for the other unequal-mass binary configurations with $q = 0.5$ and $q = 0.38$.

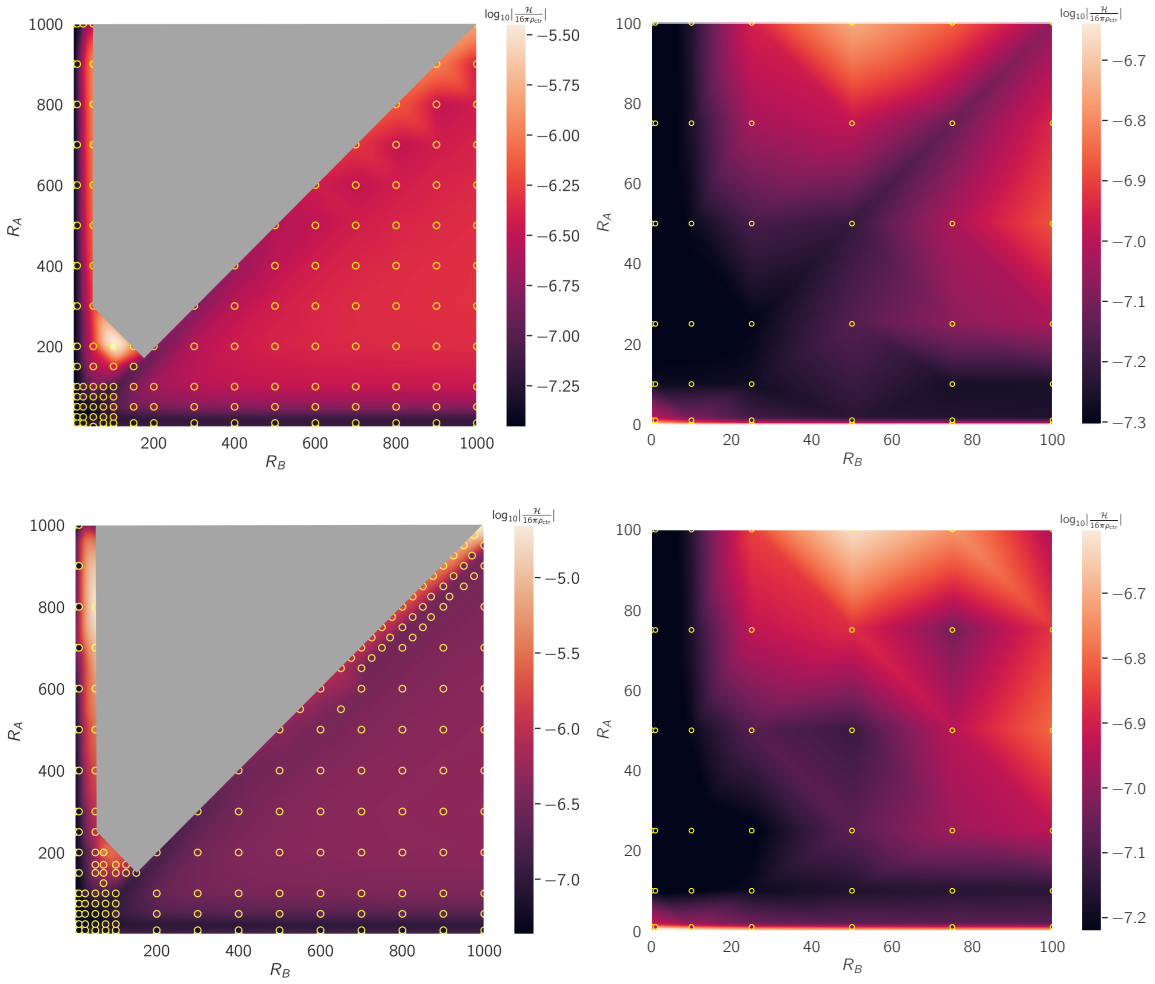


Fig. 7.D.1 The logarithm of the $L2$-norm of the Hamiltonian constraint violations is shown for the binary configurations `q05-d14-p000` (upper) and `q038-d16-p000` (lower panels). For each case, the right panel shows a zoom-in on the region $(R_{\rm A}, R_{\rm B}) = [(0,100)\times(0,100)]$. The grey region indicates the parameter space of $(R_{\rm A}, R_{\rm B})$, where constraint violations are too large; note that this region increases in size for smaller mass ratios.

Chapter 8

Gravitational-wave data analysis with high-precision numerical relativity simulations of boson star mergers

The content presented in this Chapter contains material that appears in the co-authored publication Ref. [490] with U.Sperhake, I.Romero-Shaw, M.Agathos. I have performed all of the GRCHOMBO simulations. Simulations in LEAN were performed by U.Sperhake. I led the data analysis, the injections and developed the necessary scripts. The interpretation of the results was performed jointly with the co-authors of the paper.

8.1 Introduction

You may already be wondering where this boson-star saga of Chapters 5-7 leads to... We have repeatedly motivated how the ever-increasing ensemble of GW events observed by the Laser Interferometer Gravitational-Wave Observatory (LIGO) and Virgo provides ample opportunities to explore some of the deepest mysteries of the cosmos and test the nature of compact objects: black holes (BHs), neutron stars (NSs) and exotic compact objects (ECOs) [19]. In this Chapter we will finally bring together our numerical relativity simulations of binary boson-star systems with predictions from present GW analysis pipelines and detectors.

A research programme targeting tests of the nature of compact objects[1], in general, faces several crucial challenges: (i) Given a candidate class of ECOs, can we generate gravitational waveforms of sufficient longevity and accuracy? (ii) Supposing ECO coalescences occur

[1]The same modelling challenges are faced by tests of GR using modified theories of gravity. Here however we focus on boson stars.

in the Universe, can we detect them with our current search pipelines? (iii) If yes, can we distinguish them from traditional binary BH (BBH) or NS events? (iv) Can we generate comprehensive GW template banks suitable as alternatives to BH and NS approximants for parameter estimation (PE)? The main goal of this Chapter is to explore the answers to these questions for the case of scalar-field boson stars (BSs) – the self-gravitating equilibrium solutions to the Einstein-Klein-Gordon equations [62, 96, 358] we have extensively reviewed in Chapter 5. Despite numerical studies of BS binaries making tremendous progress in the last decade, focusing in particular on the merger remnants [142, 346, 393, 410, 414, 491], and analytic approximations for performing PE of BS binary signals [492–494] (see also Refs. [352, 495] for searches of Proca-star head-on collisions in GW data), we are yet to achieve a modelling of binary BS systems with the precision obtained for BHs. We take the first steps towards this goal and numerically compute the first high-precision ~ 20 orbit inspiral-merger-ringdown (IMR) waveforms for quasi-circular BS binaries and inject them into LIGO detector noise. We perform PE using Bayesian inference using BILBY [199] and assess the ability of present BBH and binary NS waveform templates to recover the injected signals.

We start with a brief review of the theoretical framework in Section 8.2. Next, we outline the numerical set-up of our simulations in Section 8.3 and the parameter estimation set-up in Section 8.4. We present our main parameter estimation results in Sections 8.5-8.6 and, finally, conclude in Section 8.7. Throughout this Chapter, we use natural units $c = 1 = \hbar$, i.e. $G = M_{\rm Pl}^{-2}$. Our data and animations are publicly available in Refs. [496–498].

8.2 Theory

By now you probably know the action of BSs in general relativity by heart, but for completeness let us re-iterate it below

$$S = \int \frac{\sqrt{-g}}{2}\left\{\frac{R}{8\pi G} - \left[g^{\mu\nu}\nabla_\mu\bar{\varphi}\nabla_\nu\varphi + V(\varphi)\right]\right\}\mathrm{d}^4x, \tag{8.1}$$

where $V(\varphi)$ is the potential, which in this Chapter we choose to be of solitonic type [380, 499]

$$V_{\rm sol} = \mu^2|\varphi|^2\left(1 - 2\frac{|\varphi|^2}{\sigma_0^2}\right)^2, \tag{8.2}$$

with $\sigma_0 = 0.2$. Through appropriate re-scaling of the variables as discussed in Section 5.4.1, the mass of the scalar can be set to $\mu = 1$ which, henceforth, sets the length scale of our units. Varying the action (8.1) yields the Einstein-Klein-Gordon equations and spherically

Model	$\sqrt{G}A_{\rm ctr}$	μm	ω/μ	μr_{99}	C
A17	0.17	0.7134	0.4392	3.97	0.222
A147	0.147	0.3606	0.6784	4.48	0.115

Table 8.2.1 Summary of the solitonic BS models considered in this Chapter. We start by listing the central amplitude $A_{\rm ctr}$, the mass of the BS m, the frequency of the ground state solution ω, the areal radius containing 99% of the BS mass r_{99} and the compactness C.

symmetric solutions are obtained by decomposing the scalar field into amplitude A and frequency ω,

$$\varphi(t,r) = A(r)e^{{\rm i}(\varepsilon\omega t+\delta\phi)}. \tag{8.3}$$

Here we introduce the parameter $\varepsilon = \pm 1$, determining the rotation of the scalar field in the complex plane, and the phase offset $\delta\phi$ we have previously encountered in Chapter 7. Our primary BS always has $\varepsilon = 1,\ \delta\phi = 0$ and we refer to configurations with secondary parameters $(\delta\phi = 0,\ \varepsilon = 1)$, $(\delta\phi = \frac{\pi}{2},\ \varepsilon = 1)$, $(\delta\phi = \pi,\ \varepsilon = 1)$, $(\delta\phi = 0,\ \varepsilon = -1)$ as *in-phase*, *dephased*, *anti-phase* and *anti-BS* binaries respectively. Given the central amplitude $A_{\rm ctr} = A(0)$, we obtain a BS solution via the shooting algorithm described in Section 5.4.4 and consider two BS models: a compact "A17" star with $\sqrt{G}A_{\rm ctr} = 0.17$, and a less compact "A147" star with $\sqrt{G}A_{\rm ctr} = 0.147$. In Table 8.2.1, we summarise the properties of these models.

An intriguing property of BSs, distinguishing them from BHs and making them similar to NSs, is their tidal deformability, which characterises the stars' tidal interaction – the higher Λ, the more susceptible the BS is to tidal deformations. When the binary orbital radius becomes comparable to the radius of BSs, tides lead to a change in the GW phase and an accelerated late inspiral, therefore posing a potential channel for unique GW signatures. We estimate the tidal deformability of our BS models using Ref. [344]. We find that the compact model A17 has dimensionless tidal deformability $\Lambda \sim 10$ [344], whilst the less compact model A147 has $\Lambda \sim 1000$[2].

8.3 NR Simulations

8.3.1 Numerical set-up

We focus on equal-mass non-spinning BS binaries of total mass $M = 2m$, listed in Table 8.3.1. Similar to the spirit of Chapter 7, our simulations have been performed using two codes,

[2]Depending on the equation of state and the mass, neutron stars can achieve similar tidal deformability values, see e.g. Fig.1 of Ref. [500].

Simulation	$v_{x,\mathrm{ini}}$	b/M	d/M	$E_{l=2}/M$
`A17-d12`	0.1671	12.283	0.2243	0.0333
`A17-d12-p180`	0.1671	12.283	0.2243	0.0353
`A17-d12-e1`	0.1671	12.283	0.2243	0.0299
`A17-d14`	0.1533	14.017	0.2102	0.0346
`A17-d15`	0.14625	15.087	0.2033	0.0367
`A17-d15-p090`	0.14625	15.087	0.2033	0.0377
`A17-d15-p180`	0.14625	15.087	0.2033	0.0387
`A17-d15-e1`	0.14625	15.087	0.2033	0.0352
`A147-d17`	0.1389	16.639	0.0693	0.0589
`A147-d19`	0.1256	19.412	0.1109	0.0691

Table 8.3.1 Summary of the BS binaries evolved in the centre-of-mass frame with initial boost velocity $v_{x,\mathrm{ini}}$ in the x-direction, impact parameter b in the y-direction and separation d in the x-direction. The dephased, anti-phase and anti-BS binaries are labelled as `p090`, `p180`, `e1`. $E_{l=2}$ is the GW energy contained in the $l=2$ modes.

GRCHOMBO [130, 153, 501] and LEAN [482]. In our set-up, both codes evolve the Einstein equations through fourth-order finite-differencing of the CCZ4 formulation [116] (cf. also Section 2.4) and employ the moving puncture gauge [483, 484] (cf. Sections 2.5.1-2.5.2 for further details). In GRCHOMBO we utilise the power of adaptive-mesh-refinement: (i) for `A17` configurations we use a tagging criterion based on second derivatives of the complex scalar field and the conformal factor (cf. Section 2.7.3 for more details on grid variable tagging), (ii) for `A147` configurations we employ a tagging replicating the moving-boxes approach as prescribed in Section 2.7.3. We find that the binary evolution of a less compact model is more susceptible to numerical artefacts arising from asymmetric grids and interpolation errors[3] at the refinement boundaries, which can result in unphysical behaviour if the tagging criterion or AMR parameters are not properly set. Imposing more symmetric refinement using moving boxes approach for the `A147` BBS allows us to circumvent the eventual accumulation of numerical errors and spoiled inspiral of the binary. We discuss in more detail the problems that arise in Appendix 8.A, however, here we emphasise that choosing an appropriate tagging criterion plays a crucial role in this work. The LEAN code on the other hand utilises mesh refinement using the moving-boxes approach for both BS configurations.

In both codes we use a computational domain of length $L = 1024$ with bitant symmetry, 8 nested refinement levels with resolutions $\Delta x = 1/40$ to $1/48$ on the innermost level and extract GWs at $R_{\mathrm{ex}} \in [140, 240]$.

[3] In GRCHOMBO we interpolate from the finer to coarser levels (i.e. restrict) using simple averaging, which is only second-order accurate.

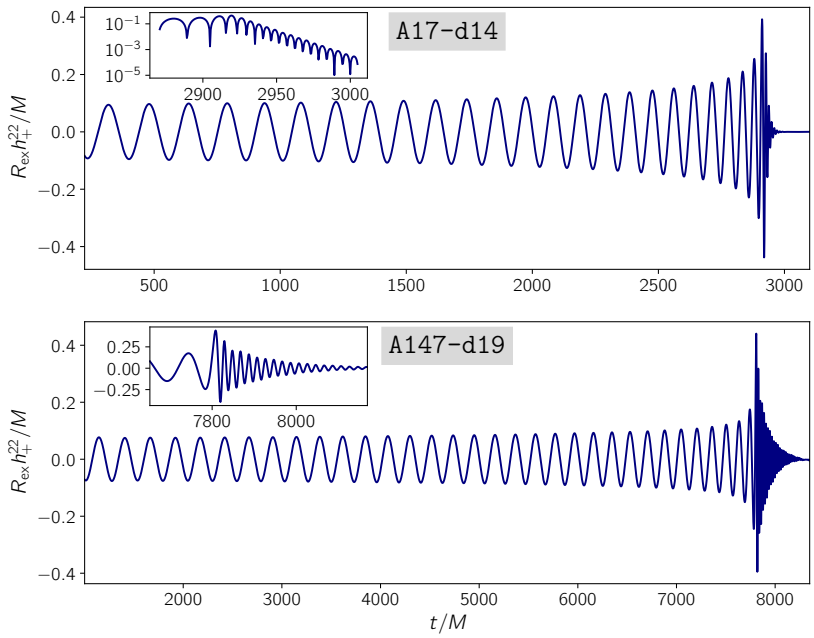


Fig. 8.3.1 Plus polarizations of the 22 IMR mode for the `A17-d14` and `A147-d19` binaries of Table 8.3.1.

Our initial data is constructed as in Refs. [141, 143] (cf. Chapter 7). By tuning the initial velocities, we reduce their orbital eccentricity, estimated according to Eq. (17) of Ref. [278], as $0.002-0.005$. By verifying convergence of the `A17` and `A147` BS binaries and extrapolating GW signals to infinity, we obtain an error budget of $(0.1,\ 4\,\%)$ for the GW phase and amplitude for `A17` binaries and $(0.2,\ 4\,\%)$ for `A147` binaries, similar to finite differencing production runs for BH inspirals reported in Ref. [502]; see Appendix 8.B for more details.

8.3.2 Waveforms

In Fig. 8.3.1 we present the typical GW signals that result from compact `A17` and fluffy (less compact) `A147` BS models. In physical terms, the most conspicuous difference between these binary families is their ultimate fate. The compact `A17` coalescences ubiquitously result in the formation of a BH remnant with dimensionless final spin $a_{\rm fin}\sim 0.7$, similar to the end-product of non-spinning equal-mass BH mergers (cf. e.g. Table 4.3.1). By eye, the resulting GW form looks indistinguishable from a BH signal; cf. Fig. 8.3.1. In contrast, the "fluffy" `A147` binaries merge into a more compact, highly distorted BS remnant with an oscillating central amplitude $0.156\leq\sqrt{G}A_{\rm ctr}\leq 0.164$. The GW signal emitted by these

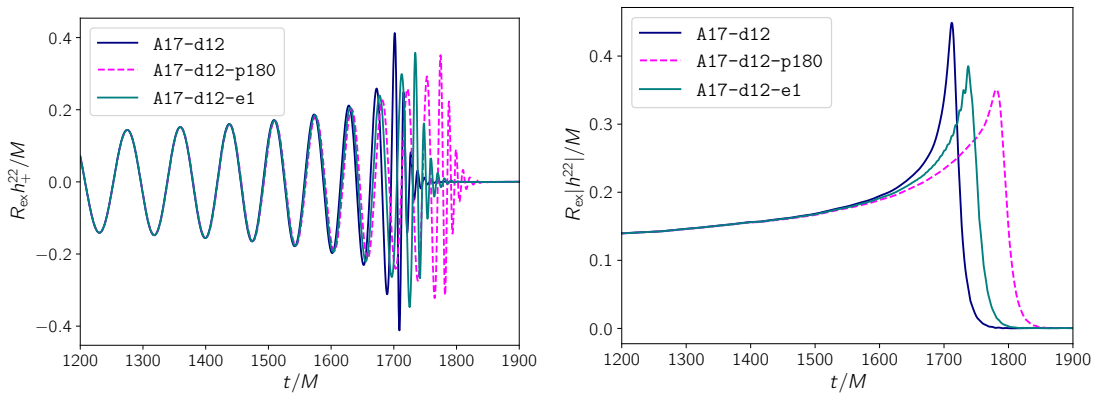


Fig. 8.3.2 *Left*: Comparison of the plus polarizations of the 22 IMR mode for the `A17-d12`, `A17-d12-p180` and `A17-d12-e1` binaries of Table 8.3.1. *Right*: The same as the left panel but showing the amplitude of the strain. Note the difference in the strength of the chirp across all of the runs.

fluffy binaries is characterised by a lower-amplitude inspiral followed by an immense GW burst at merger and a prolonged, rapidly pulsating ringdown.

For the `A17` family of stars we consider additional configurations with non-zero phase-offsets, $\delta\phi = \pi/2, \pi$ and anti-BS binaries. All `A17` binaries produce identical signals in the early inspiral, but as the BSs get closer, the scalar-field interaction [408, 485] leads to delayed mergers for $\delta\phi \neq 0$, $\varepsilon = -1$ and, especially, for $\delta\phi = \pi$. We illustrate this effect for the `A17-d12` family of runs in Fig. 8.3.2.

A comparison with BH waveforms [153] furthermore suggests that the `A17` anti-BS signal resembles most closely that from a non-spinning, equal-mass BH binary in terms of the GW amplitude in the late inspiral and its phase evolution close to merger; cf. Fig.8.C.1 in Appendix 8.C.

8.4 Parameter Estimation

8.4.1 Set-up

Injections

We inject our numerically computed GW signals into Gaussian noise coloured by the O4 design sensitivities of the LIGO Hanford (H1) and Livingston (L1) detectors [13]. We utilise LALSUITE [318, 503] to perform reconstruction of our NR signals (cf. also Chapter 3). Prior to injecting, we remove junk radiation at the beginning of our waveforms and prepare the NR data in line with the Format 1 standards of LIGO Algorithms Library injections [2].

We focus on the dominant $l = 2$ modes and consider systems of total masses $M_{\rm tot}^{\rm inj} \in [5, 105]\, M_\odot$ in the source frame[4], corresponding to scalar-field masses $\mu \in [10^{-13}, 10^{-12}]\,\mathrm{eV}$. We report the mass values in the source frame; quantities in the detector frame will be denoted by 'det'. Finally, we choose luminosity distances $d_{\rm L}$ corresponding to (zero-noise) optimal injected signal-to-noise ratios (SNRs) $\rho^{\rm H1} \in [15, 60]$, $\rho^{\rm L1} \in [10, 45]$. Unless otherwise stated all of our injections use the same extrinsic parameters. In particular, we use a right ascension $\alpha = 1.375$, declination $\delta = -1.2108$, inclination angle $\iota = \frac{\pi}{3} = 60^\circ$ and polarisation angle $\psi = \frac{\pi}{2} = 90^\circ$.

Parameter estimation

We perform Bayesian inference using the parameter estimation pipeline BILBY [199, 504]. In all analyses, we use a sampling frequency of 4096 Hz, a reference frequency of 50 Hz and a minimum frequency set by the starting frequency of our NR waveforms. When the starting frequency of our injected waveforms drops below 20 Hz, we set the minimum frequency to 20 Hz. The NR signals are injected into the Hanford and Livingston detectors, assuming noise curves from the 4th observing run (O4) [13]. For all of the PE runs reported here, we initialise the sampler with 1000 points and marginalise over time and luminosity distance. For approximants including only the (22)-mode, we additionally marginalise over the phase. We have used a range of nested samplers, such as `dynesty` [207], `cpnest` [208] and `nessai` [213, 214, 505], and have found good agreement between them. The sampling space is determined by BILBY's default BBH and BNS priors (cf. Tables 1 and 2 of Ref. [199]). However, we increase the spin magnitude (a_1, a_2) upper limits to 0.99. When using non-precessing models, the prior on the spin magnitudes is a uniform distribution $\chi_1, \chi_2 \in [-1, 1]$, where χ_1, χ_2 denote the dimensionless spin projections onto the orbital angular momentum. This range includes binaries with anti-aligned spins. For BNS models, we additionally increase the upper limits in the prior of the dimensionless tidal deformability parameters (Λ_1, Λ_2) to 20000. We find this choice necessary for injections of the less compact `A147` family in order to circumvent one of the tidal deformability numbers railing against the upper prior bound. We perform our inference using two sets of BBH-like spin priors: (i) we fix the spins in the recovery templates to their zero injected values; (ii) we explore the complete spin prior with all parameters being free.

[4]The source frame takes into account the redshift effects so that the relation between the mass in the source frame, $m^{\rm s}$, to the mass in the detector frame, $m^{\rm d}$, is given by: $m^{\rm s} = m^{\rm d}/(1+z)$, where z is the redshift for a given luminosity distance. The total binary masses $M_{\rm tot}^{\rm inj} \in [5, 105] M_\odot$ in the source frame considered in this Chapter correspond to $M_{\rm tot}^{\rm det} \in [5, 120] M_\odot$ in the detector frame.

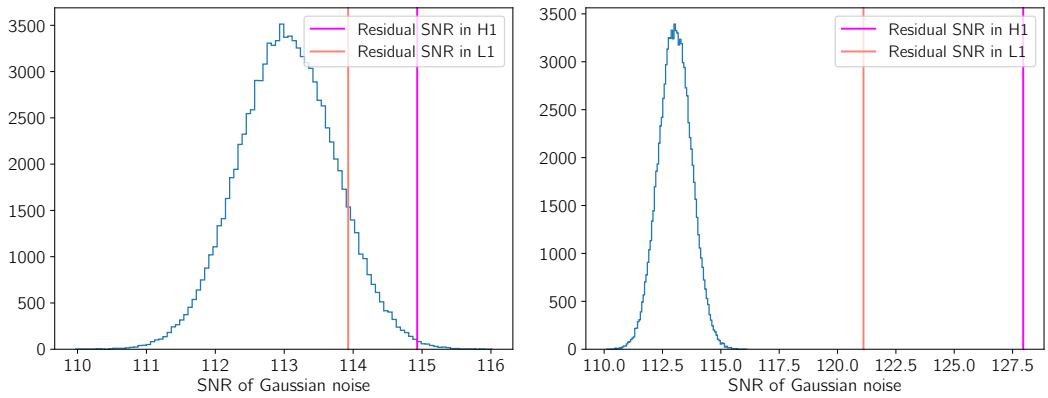


Fig. 8.4.1 Null distribution of the SNR of Gaussian noise and the residual SNR in the Hanford (H1) and Livingston (L1) detectors, computed from the `IMRPhenomXP` approximant evaluated at the source parameters of the maximum of the joint log-likelihood. *Left*: Example of a Gaussian residual for a `A147-d19` binary of $M_{\rm tot}^{\rm inj} = 72.4 M_\odot$ at $d_{\rm L} = 500$Mpc. *Right*: Example of a *non*-Gaussian residual for a `A147-d19` binary of $M_{\rm tot}^{\rm inj} = 75.8 M_\odot$ at $d_{\rm L} = 250$Mpc.

We have also performed parameter estimation using injections from different resolutions and extraction radii, and have found consistent results.

Waveform approximants

We recover injected BS signals using standard waveform approximants: the aligned-spin model `IMRPhenomD` [506, 507]; models including the effects of spin-induced precession, `IMRPhenomPv3` [508] and `IMRPhenomXP`; one model including spin-precession plus higher-order modes `IMRPhenomXPHM` [509]; one inspiral-only aligned-spin tidal model `TaylorF2` [510]; one full IMR aligned-spin waveform with tidal effects, `TEOBResumS` [511] and one full IMR waveform with precession and tidal effects `IMRPhenomPv2_NRTidal` [512, 513]. We obtain comparable results for the various approximants, as reviewed in more detail in Appendix 8.D, and focus the following discussion on `IMRPhenomXP` and `IMRPhenomPv2_NRTidal`.

8.4.2 Diagnostics

During our analysis, for each detector we compute the strength of the recovered (injected) signal using the optimal SNR ρ defined via

$$\rho^2 = 4 \int_0^\infty \frac{|\tilde{h}(f)|^2}{S_n(f)} df, \tag{8.4}$$

where $\tilde{h}(f)$ is a recovered (injected) waveform in the frequency domain and $S_n(f)$ is the detector's noise power-spectral density (PSD). We also compute the network SNR given by $\rho_{\rm net} = \sum_j \rho_j^2$, where ρ_j is the SNR of a single detector. For each recovery we compute the Bayes factor $\mathscr{B}^{\rm S}_{\rm N}$, quantifying the evidence ratio between a signal being present in the data relative to the hypothesis of pure Gaussian noise. To asses the quality of the recovery we additionally compute the residual $r := d - h_{\rm max}$ from the data stream d and the approximant's strain $h_{\rm max}$ evaluated at the maximum-joint-log-likelihood source parameters across H1/L1. Specifically, we construct a null distribution of the white-noise optimal SNR for a signal duration D by generating random noise realizations via

$$n_{\rm w} := \frac{\tilde{n}(f)}{\sqrt{S_n(f)}} \sim \mathscr{N}\left(0, \tfrac{1}{2}\sqrt{D}\right), \tag{8.5}$$

If the residual's SNR falls above the 99th percentile of the noise SNR, we regard the residual as incompatible with Gaussian noise. In Fig. 8.4.1 we show a typical result of Gaussian and non-Gaussian residuals, resulting from injections of `A147-d19` binary system and recoveries with the `IMRPhenomXP` waveform template.

8.5 Results: `A17` families

For the compact `A17` binaries, which form a BH post-merger, all waveform approximants enable confident recovery of the signals with a residual compatible with Gaussian noise, regardless of the analysis type; see Table 8.5.1 for a representative set of examples and Figure 8.5.1 for comparison of PE results from different priors. Approximants including tidal effects furthermore infer tidal deformability parameters consistent with the injected $\Lambda_{1,2} \sim \mathscr{O}(10)$, albeit with poor constraints on Λ_2 (cf. the right panel of Fig. 8.5.2). This corresponds to a well measured tidal deformability $\delta\tilde{\Lambda}$ of the binary, but a poorly constrained $\tilde{\Lambda}$ [514]. All waveform approximants, however, fail to correctly infer some other injected parameters (component masses, spins and/or luminosity distance) within the 90% credible region; cf. Fig. 8.5.2 for a typical example. Provided the inspiral contributes significantly to the SNR, i.e. for $M^{\rm inj}_{\rm tot} \lesssim 80\,M_\odot$ in our case, however, these deviations are not random but exhibit clear systematics which we illustrate in Fig. 8.5.3 for a wide range of injections and now discuss in more detail.

Run	$\log(\mathscr{B}^{\mathrm{S}}_{\mathrm{N}})$	$\rho^{\mathrm{inj}}_{\mathrm{net}}$	$\rho^{\mathrm{rec}}_{\mathrm{net}}$	$\mathscr{M}^{\mathrm{rec}}_{\mathrm{c}}/M_\odot$	q^{rec}
$M^{\mathrm{inj}}_{\mathrm{tot}} = 72.4M_\odot, \quad \mathscr{M}^{\mathrm{inj}}_{\mathrm{c}} = 31.5M_\odot, \quad d^{\mathrm{inj}}_L = 500\,\mathrm{Mpc}$					
A17-d12	717	40.37	38.63	26.60	0.32
A17-d15-p090	1019	45.17	46.74	31.63	0.65
A17-d12-p180	792	43.84	36.62	25.07	0.97
A17-d12-e1	820	41.12	41.91	27.13	0.71
A17-d14	678	41.41	38.26	26.72	0.30
A147-d19	555	57.75	32.16	40.02	1.00
$M^{\mathrm{inj}}_{\mathrm{tot}} = 9.9M_\odot, \quad \mathscr{M}^{\mathrm{inj}}_{\mathrm{c}} = 4.3M_\odot, \quad d^{\mathrm{inj}}_L = 62.5\,\mathrm{Mpc}$					
A17-d12	406	29.69	30.60	3.89	0.39
A17-d15-p090	698	39.15	38.73	4.07	0.93
A17-d12-p180	328	30.91	28.28	3.94	1.00
A17-d12-e1	407	30.13	29.07	4.03	0.92
A17-d14	536	34.13	34.24	3.92	0.40
A147-d19	286	37.73	24.45	4.41	0.13

Table 8.5.1 Recovery results for a range of BS injections from Table 8.3.1 using the IMRPhenomXP approximant with spins fixed to zero. We contrast the injected ($\rho^{\mathrm{inj}}_{\mathrm{net}}$) and recovered ($\rho^{\mathrm{rec}}_{\mathrm{net}}$) network SNRs and report the recovered chirp-masses $\mathscr{M}^{\mathrm{rec}}_{\mathrm{c}}$, mass-ratios q^{rec} at maximum-joint-log-likelihood.

8.5.1 A17 ($\delta\phi = 0$, $\varepsilon = 1$)

We obtain consistent results for using either of the three waveform lengths employed, d17, d20 and d21, indicating that they are sufficiently long for the mass range considered. In general, the recovered luminosity distance is overestimated, likely compensating for amplitude effects arising from biases in the other parameters (e.g. like the inclination angle, which has a well-known degeneracy with the luminosity distance [515, 516]). Next, the posteriors from BH approximants employed with spins fixed to zero systematically peak at total mass values within $\sim 10\,\%$ of the injected $M^{\mathrm{inj}}_{\mathrm{tot}}$. For $M^{\mathrm{inj}}_{\mathrm{tot}} \lesssim 80M_\odot$, mass ratios are recovered with peaks in the range $0.3 \lesssim q := m_2/m_1 \lesssim 0.7$, with no posteriors supporting the injected $q = 1$ at $90\,\%$ confidence. This picture changes considerably when we allow the spins to be sampled over in the prior. Then we obtain more accurate estimates for the primary mass m_1, often supporting the injected mass inside the $90\,\%$ confidence interval, and larger mass ratios $0.5 \lesssim q \lesssim 0.85$, albeit still well below the injected $q = 1$. We furthermore infer significant spin magnitudes peaking at $0.3 \leq a_{1,2} \leq 0.98$ with clear preference for negatively aligned spins, i.e. $\chi_{\mathrm{eff}} < 0$.

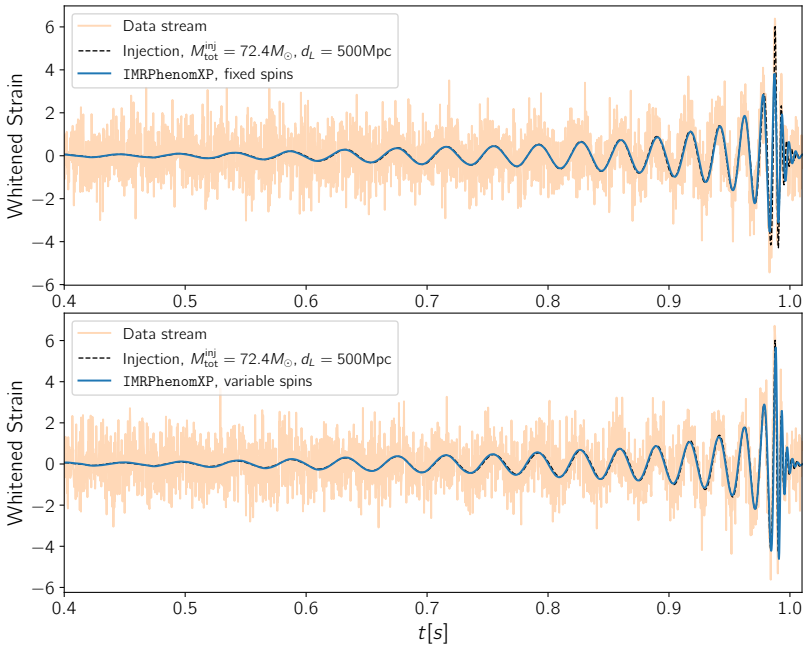


Fig. 8.5.1 Injection of an A17-d12 binary of $M_{\rm inj}^{\rm tot} = 72.4 M_\odot$ at $d_{\rm L} = 500$Mpc and its recovery using the IMRPhenomXP waveform approximant with fixed (variable) spins in the top (bottom) panels. As expected, the inference with variable spins is able to match the injected GW signal better, especially in the merger and the ringdown. This is in particular manifested in the increase of the recovered SNR, e.g. in Hanford we find a SNR of 32.7 for variable spins and 31.4 for fixed. Note the SNR of the injection in Hanford is 32.9.

8.5.2 A17-p180 ($\delta\phi = \pi, \varepsilon = 1$)

As for $\delta\phi = 0$, the recovered luminosity distance is often overestimated. Quite remarkably, however, these anti-phase binaries result in nearly opposite behaviour in PE results in every other regard. For $M_{\rm tot}^{\rm inj} \lesssim 80 M_\odot$, we obtain good estimates for the primary mass m_1 and large mass ratios $q \geq 0.8$ when the spins are *fixed* to their injected values. Allowing the spins to vary, now results in significant overestimates of m_1 and more unequal mass ratios $0.3 \leq q \leq 0.8$. We typically obtain large spin magnitudes $a_{1,2} \geq 0.5$ but preferably exhibiting partial alignment with the orbital angular momentum, $0.1 \leq \chi_{\rm eff} \leq 0.5$.

8.5.3 A17-d090 ($\delta\phi = \pi/2, \varepsilon = 1$)

This family of BS injections yields qualitatively similar behaviour as A17-p180, but with generally smaller departure from the injected parameters.

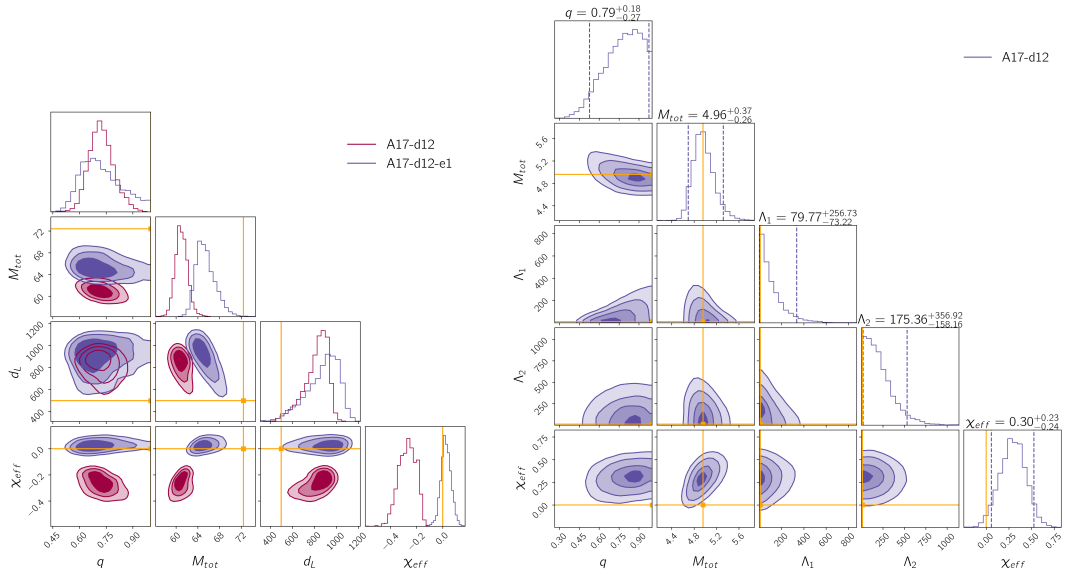


Fig. 8.5.2 *Left:* Comparison of key PE results for `A17-d12` and `A17-d12-e1` injections. We use `IMRPhenomXP` for recovery of a BS binary with $M_{\rm tot}^{\rm inj} = 72.4 M_\odot$, $d_{\rm L} = 500$Mpc and allow all binary parameters to be sampled over. The 1, 1.5, 2-sigma contours are shown. *Right*: PE results for an `A17-d12` injection with $M_{\rm tot}^{\rm inj} = 4.96 M_\odot$, $d_{\rm L} = 31.25$Mpc and recovery with `IMRPhenomPv2_NRTidal` with all parameters being sampled over. The dotted vertical lines show the 90% confidence interval. We note that the 90% confidence interval, within which the recovered tidal deformability Λ_2 is contained, is wider than that of the Λ_1 parameter.

8.5.4 `A17-e1` ($\delta\phi = 0, \varepsilon = -1$)

The anti-BS family is the best recovered of all our injections, supporting our conjecture that these binaries most closely resemble waveforms from non-spinning BHs. We typically obtain mass ratios $q \gtrsim 0.75$, where the primary mass m_1 is either contained inside the 90% confidence interval or close by, and, for $M_{\rm tot}^{\rm inj} \gtrsim 20 M_\odot$, spin values close to zero. We illustrate this behaviour by comparing in Fig. 8.5.2 a representative $M_{\rm tot}^{\rm inj} = 72.4 M_\odot$ example of this family with its less accurately recovered `A17-d12` counterpart.

8.5.5 Interpretation

The most pronounced difference between $\delta\phi = 0$ BS binary signals, compared to their anti-phase counterparts, is the steep increase of the GW amplitude in the late inspiral and merger whereas for $\delta\phi = \pi$, this *chirp* is shallower; cf. the right panel of Fig. 8.3.1 and Fig. 8.C.1 in Appendix 8.C. A closer inspection of GW signals from non-spinning BH binaries in the frequency domain similarly yields a steeper increase in the GW amplitude close to merger for unequal masses relative to $q = 1$. Unequal-mass BH chirps therefore resemble more

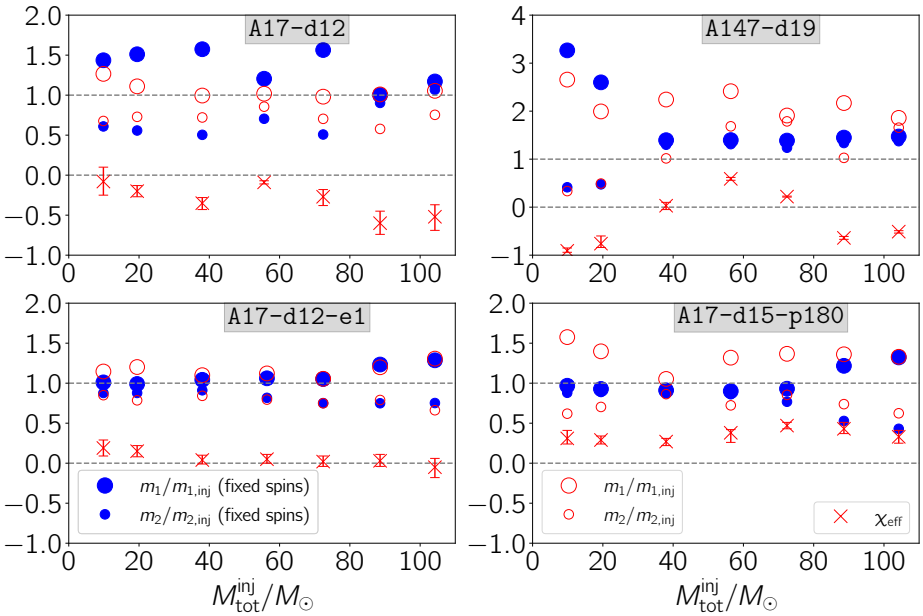


Fig. 8.5.3 PE results obtained for four BS families and injections with total mass $M^{\mathrm{inj}}_{\mathrm{tot}} \in [5,105]M_\odot$ and luminosity distance $d_L = (M^{\mathrm{det}}_{\mathrm{tot}}/80M_\odot)500\,\mathrm{Mpc}$. For each injection, we display the median values of the recovered component masses m_1, m_2 normalised by their injected values (large and small circles) and the effective spin (crosses with 90 % confidence interval). The recoveries are obtained for fixed (blue) or variable spins (red symbols). The dashed lines mark the injected values, 1 for the masses and 0 for χ_{eff}. The recovered parameters deviate from these values non-randomly; cf. the main text. By repeating selected injections with different d_{L}, we have verified that the displayed trends are robust under variations of the SNR.

closely those from $\delta\phi = 0$ BS binaries while $\delta\phi = \pi$ BS chirps are better approximated by equal-mass BH binaries.

The inclusion of spins allows for an additional adjustment of the chirp's steepness, typically boosting $\log(\mathscr{B}^{\mathrm{S}}_{\mathrm{N}})$ by $\sim 10\,\%$. BH binaries with aligned spins have an enhanced yet shallower inspiral than those with anti-aligned spins; see e.g. Figs. 1 and 3 in Ref. [517]. The shallow inspiral-merger transition of $\delta\phi = \pi$ binaries, therefore, favours the "hang-up" of aligned spins whereas the more abrupt transition of $\delta\phi = 0$ BS binaries favours partially anti-aligned spins. This effect also sheds light on the mass-ratio drifts when we allow the spins to vary. For spins fixed at zero, the steep chirp of $\delta\phi = 0$ BS binaries can *only* be reproduced through an unequal mass ratio in the BBH approximant. For variable spins, in contrast, it can at least partly be accommodated through anti-aligned spins (the anti-hang-up effect); statistically we then expect a drift towards $q = 1$. For $\delta\phi = \pi$ BS binaries, in turn, the inclusion of spins enables BILBY to reproduce the shallow chirp in the BS signal through

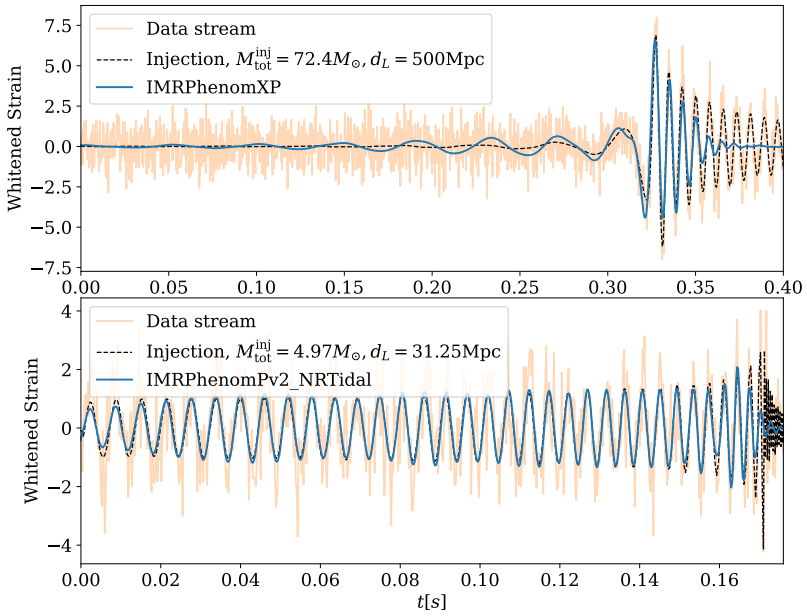


Fig. 8.5.4 *Top:* The recovery of a high-mass `A147-d19` binary injection using `IMRPhenomXP` results in $m_1 \sim 70M_\odot$, $m_2 \sim 65M_\odot$, $a_1 \sim 0.98$ and $a_2 \sim 0.60$. *Bottom:* The recovery of a low-mass `A147-d19` binary injection using `IMRPhenomPv2_NRTidal` yields maximum-joint-log-likelihood estimates $m_1 \sim 3.7M_\odot$, $m_2 \sim 1.3M_\odot$, $a_1 \sim 0.96$, $a_2 \sim 0.63$, $\Lambda_1 \sim 3000$ and $\Lambda_2 \sim 11000$.

aligned spins rather than resorting *exclusively* to a high ($q \approx 1$) mass ratio; this results in a drift towards smaller q.

8.6 Results: `A147` family

As illustrated in Fig. 8.3.1, GW signals from our less compact `A147` family of BS binaries differ more pronouncedly from BH waveforms, especially around merger and ringdown. These differences manifest themselves not only in the form of PE biases, but also an incomplete recovery of the injected signals. In particular, for high (low) total mass $M_{\rm tot}^{\rm inj}$, the approximants are able to match the merger (inspiral) part of the signals but never both and never the ringdown; cf. Fig. 8.5.4. Overall, this leads to a reduction in the recovered optimal SNR compared to the injection; cf. Table 8.5.1. For injections with $\rho_{\rm inj} \lesssim 30$, the residual is still consistent with noise but for $\rho_{\rm inj} \gtrsim 30$ we often obtain significant residuals.

Furthermore, the late inspiral of less compact BS binaries occurs at lower frequencies than that of compact ones, so that BBH approximants systematically overestimate the total mass; cf. Fig. 8.5.3. The addition of tidal effects improves the approximant's ability to capture features in the inspiral portion of the signal for small $M_{\rm tot}^{\rm inj}$; we thus obtain large tidal

parameters $\Lambda_{1,2} \sim 10^3$ to 10^4 consistent with the BS binary, albeit with large uncertainties in Λ_2. Similar to the compact BS injections, overall the inclusion of tidal effects does not improve the estimation of other injection parameters.

8.7 Conclusions

By performing high-precision NR simulations of inspiralling and merging BS binaries, we have investigated the capability of current waveform models to recover BS GW signals with the following key results. (i) Most BS systems considered here are detectable with current GW analysis pipelines although current waveform templates systematically infer incorrect source parameters. (ii) BS binaries can be numerically modelled with accuracy comparable to BH binaries. (iii) BSs are excellent candidate sources for constructing GW template banks alternative to BHs and NSs.

Our study suggests that, from the viewpoint of current GW detectors, BS signals exhibit significant degeneracy with BBH waveforms obstructing the distinction between BS binaries, especially those forming a BH upon merger, and NS or BH systems. The most notable exception from this degeneracy consists in the exceptionally strong inspiral-merger transition and a long-lived ringdown in binaries forming a BS post-merger; both these features are generally poorly matched by present approximants leaving behind non-Gaussian residuals.

With the improvement of detector sensitivity and the detection of increasingly loud events, however, we can expect any features pertinent to BS binaries, that cannot be reproduced within the manifold of BBH signals, to become increasingly pronounced. Such features may be identified by data analysis methods that are specifically build to search for signs of deviations from the GR and Kerr-BBH model hypothesis. This will be the subject of future work.

Appendix

Appendix 8.A Tagging criterion and adaptive-mesh-refinement parameters

In this Section we will discuss the challenges faced by GRCHOMBO in evolving the 'fluffy' `A147-d17` binary configuration. We note that the results reported here are specific to the GRCHOMBO code and are empirical, based on our extended experimentation. Let us, however, first highlight that following common practice of most AMR codes, we typically use tagging using grid variables, including second derivatives of the complex scalar field and the conformal factor. With this tagging we are able to successfully and accurately evolve BS head-on collisions in Chapter 7 and the compact inspiralling BS binary `A17` of this Chapter (cf. Appendix 8.B below for a convergence analysis). Despite this success, we found evolution of the fluffy binary `A147` with this tagging problematic.

In Fig. 8.A.1 we illustrate the problems we encounter: the left panels show the typical results we obtain by using grid-variable based tagging for the `A147` binary, whilst the right panels show the results using 'moving boxes' tagging approach. We note that here we use slightly different initial boost and impact parameters (namely the parameters prior to eccentricity reduction) compared to those in Table 8.3.1. Nevertheless eccentricity is small here and does not affect the overall unphysical behaviour we observe in this example. In the following we discuss Fig. 8.A.1 in more detail:

- The GW signal of the run using grid-variable tagging displays significant signatures of amplitude variations. This is most notable in the inset of the left panel. Direct comparison of the waveforms obtained for grid-variable tagging and moving-boxes tagging suggests that in the former case the stars merge later and start to accumulate a phase difference already at $t/M \sim 800$. The spurious artifacts we observe later in the inspiral are likely to be the by-product of accumulated numerical errors (as discussed below).

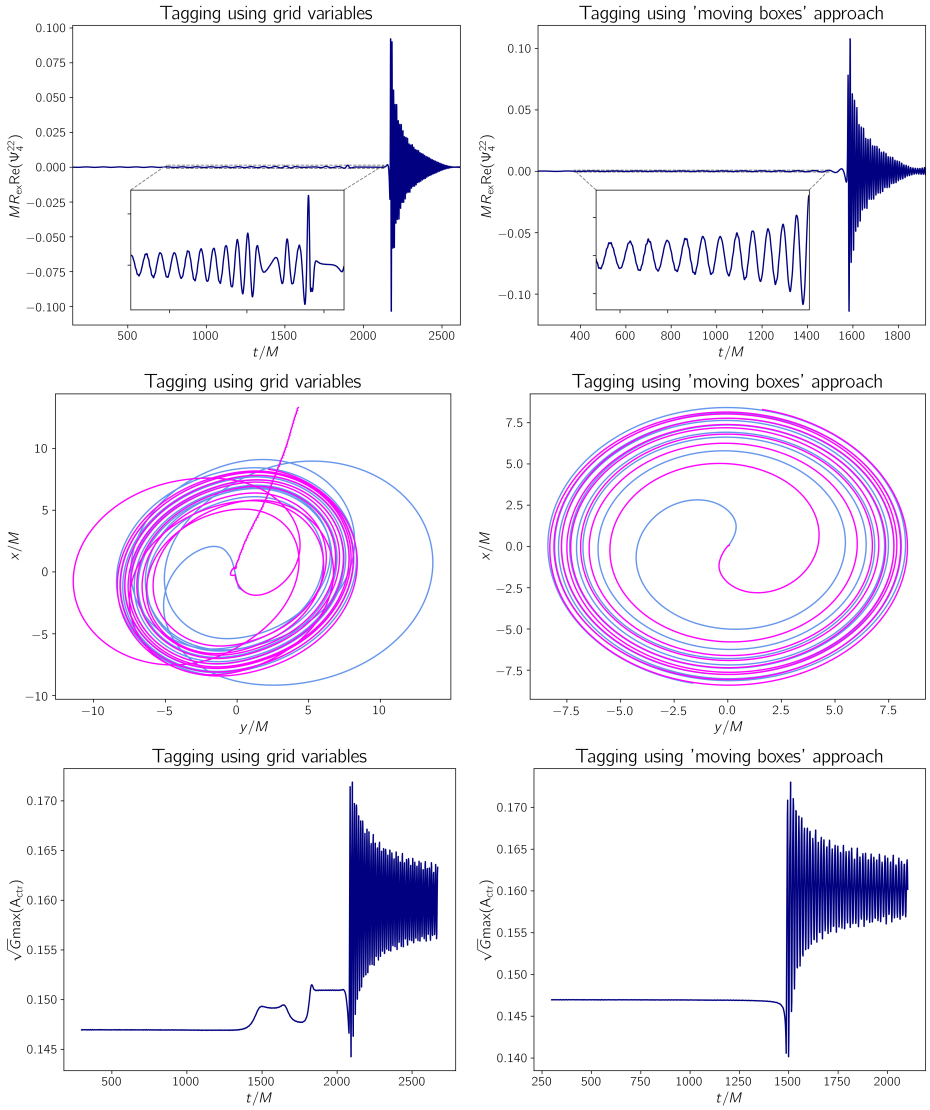


Fig. 8.A.1 We compare results of `A147-d17` binary evolutions with tagging using grid variables (left) and tagging using a 'moving-boxes' approach (right). From top to bottom we show the real part of the (22)-mode of Ψ_4, the positions of the stars and the maximum of the central amplitude of the scalar field.

- This peculiar effect in the GW signal is in fact a result of the two stars 'repelling' each other. From the second row of the Figure it can be clearly seen that the symmetry of the system (being an equal-mass binary) is broken. Unlike the run with grid variable tagging, tagging using moving boxes results in normal behaviour, where the stars proceed to follow their orbits and inspiral into merger.

- The symmetry breaking can also be traced out through the behaviour of the scalar field at the centres of the stars (cf. the third row). Tagging using grid variables conspicuously

results in a sudden oscillation of the central amplitude, $A_{\rm ctr}$, starting at $t/M \sim 1550$. 2D visualisation suggests that during inspiral the two stars in fact exchange their scalar matter with each other. One of the stars becomes more compact than the other, and so the binary is no longer of strictly equal mass – our symmetry is broken.

Having analysed the key differences in the evolutions using grid variable tagging and moving boxes approach, let us now comment on why we think the tagging using moving boxes approach is more suitable and correctly evolves this binary system. Firstly, we note that the fluffy `A147` stars are less compact and therefore may be more susceptible to numerical noise and/or errors. The behaviour we see in the left panels of Fig. 8.A.1 is likely *not* physical, as there are no theoretical considerations under which we may expect that the symmetry of the binary is broken. Furthermore, a direct comparison with the LEAN code demonstrates excellent agreement with the results of the right panels, and therefore does not support a spurious repulsion of the stars. Secondly, we consider several factors that may lead to numerical noise due to AMR and regridding: (i) insufficient separation between the refinement levels and subsequent reflection of noise off the refinement boundaries, (ii) insufficient accuracy of the interpolation at the refinement boundaries, and (iii) insufficient resolution of the physics using AMR grids[5]. The latter point is more easily controlled via a moving boxes approach, where one can specify the size of the AMR grids used in the tagging. Next, the first two effects can be regarded as equivalent to each other, however we find that increasing the number of cells in the buffer region to $n_{\rm B} = 64$ (cf. Section 2.7.2) does not remedy the spurious behaviour of the run with grid variable tagging. Having said that, we notice less constraint violations on lower refinement boundaries with larger buffer regions, and so we always use $n_{\rm B} = 64$. The interpolation errors also depend on the accuracy of the used scheme. In GRCHOMBO a particularly relevant source of errors arises from the interpolation of data from finer to coarser levels, where the implemented method simply averages the values. The accuracy of this method is only of second order. Robust tests among different interpolation methods are required to confidently conclude whether this is the leading issue in the unphysical behaviour. Finally, tagging using grid variables often leads to AMR grids with many corners and edges (cf. Section 2.7.3 and Fig. 2.3), which, during the evolution, often become asymmetric due to the Berger-Rigoutsos partitioning algorithm. These effects together with the noise from interpolation can cause eventual accumulation of numerical errors and, thus, the spurious evolution of the binary that we observe. The sharp edges present in the AMR grids and the unphysical behaviour of tagging with grid variables may be cured by increasing the fill-ratio to $\varepsilon_{\rm FR} = 1$, however this significantly increases the

[5]Frequent regridding can also lead to numerical noise, however by lowering the frequency of our regridding in evolutions of BS binaries we did not find it leading to much improvement.

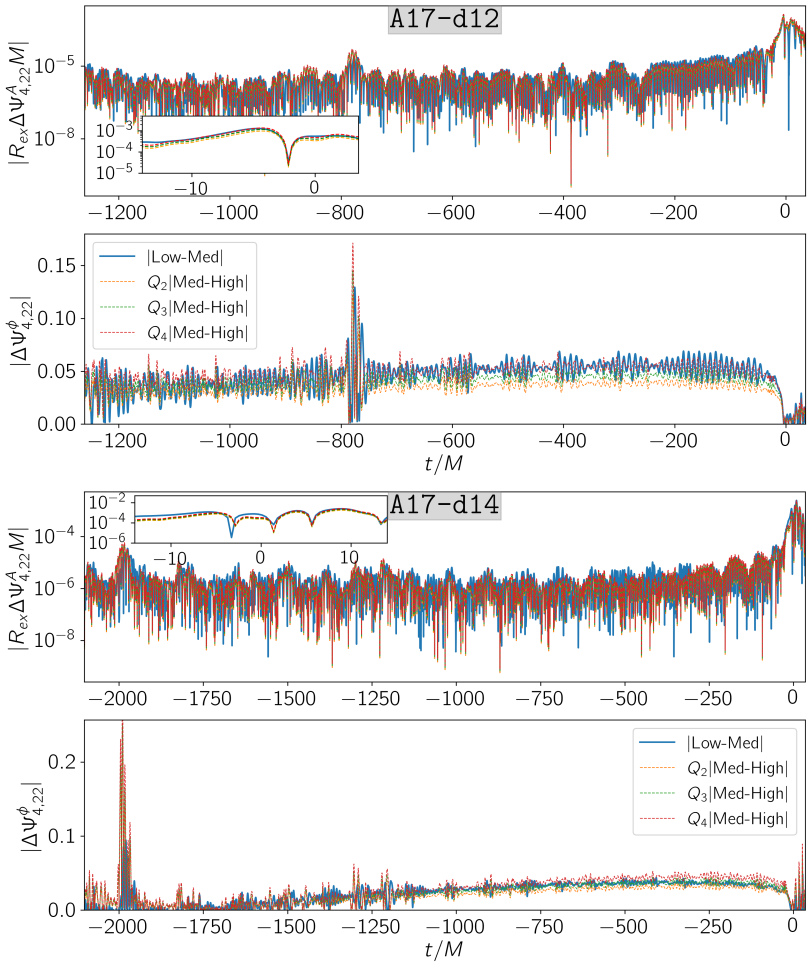


Fig. 8.B.1 Convergence test of the compact configurations `A17-d12` and `A17-d14` of Table 8.3.1. The difference between high and medium resolutions has been re-scaled by factors Q_2 to Q_4, corresponding to convergence of second to fourth order.

computational time and resources required for the runs with higher resolutions. Alternatively, the tagging using moving boxes approach results in a similar 'fix', and so we use it for our subsequent evolutions of the `A147` binary system.

Appendix 8.B Convergence tests

To evaluate the numerical error incurred in our simulations, we analyse their convergence properties for three representative configurations. We start with the GRCHOMBO simulations of binaries from the compact families `A17-d12` and `A17-d14`. Here we use $\Delta x_{\rm low} = 1/28$, $\Delta x_{\rm med} = 1/32$, $\Delta x_{\rm high} = 1/40$ for the low, medium and high resolutions, respectively. The resulting convergence analysis for the GW signals extracted at $R_{\rm ex} = 140$ is shown in

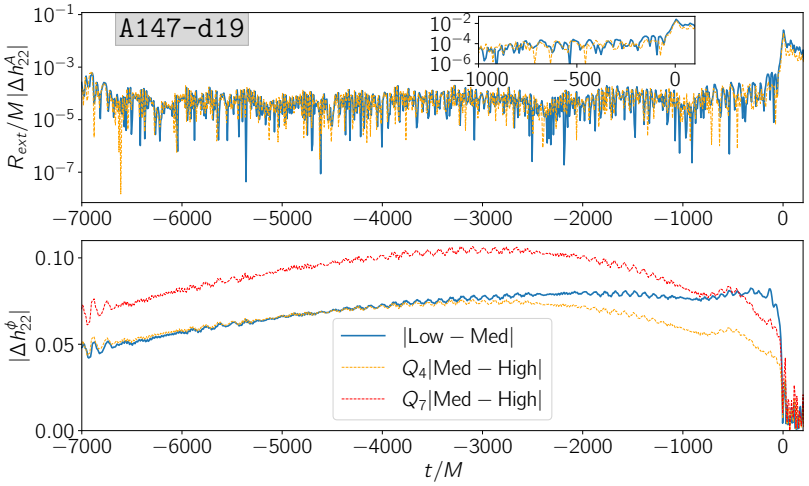


Fig. 8.B.2 Convergence test of the configuration `A147-d19` of Table II in the main document for the GW strain (upper) and phase (lower panel). The difference between high and medium resolutions has been scaled by factors Q_4 and Q_7, corresponding to fourth- and seventh-order convergence.

Fig. 8.B.1 and yields convergence between third and fourth order. For the shorter `A17-d12` configuration, Richardson extrapolation yields an amplitude error of 2.5% and a phase error of 0.03 while we obtain 3% in the amplitude and 0.04 in the phase for the longer `A17-d14` binary. We quantify the error due to finite radius extraction through extrapolation to infinity and thus find a phase error of 0.06 and an amplitude error of 1%. Overall, this brings the total numerical error budget for the `A17` family of runs to 4% in the amplitude and 0.1 in the phase.

For the less compact `A147-d19` configuration, we display in Fig. 8.B.2 the convergence properties obtained with the LEAN code for the GW multipole h_{22} extracted at $R_{\rm ex} = 240$ for resolutions $\Delta x_{\rm low} = 1/32$, $\Delta x_{\rm med} = 1/36$ and $\Delta x_{\rm high} = 1/40$. We obtain fourth-order convergence for the amplitude and, during most of the inspiral, for the phase. In the late inspiral and merger, the phase evolution exhibits over convergence up to about seventh order, likely due to fortuitous cancellations of different error contributions. We conservatively estimate the numerical uncertainties for this configuration assuming exclusively fourth-order convergence. For the amplitude, we obtain 0.5% in the early inspiral slowly increasing to about 3% around merger. The phase error peaks at about 0.09 during the mid inspiral. The uncertainty due to finite extraction radius is about 0.15 or less in the GW phase and decreases from 4% (in the early inspiral) to 1% (around merger) in the amplitude. This results in an overall error budget of 0.2 in the phase and 4% in the amplitude.

Appendix 8.C Black-hole and boson-star signals

In this Section, we compare the IMR signals of our BS families with those from equal-mass non-spinning BH binaries and discuss the varying degrees of deviation from the BH case which we observe. We start this discussion by exploring first what behaviour we would expect theoretically. For this purpose, we follow the analysis of the scalar-field interaction outlined in Appendix B of Ref. [408] and in particular consider the energy density of a scalar field φ in the flat-space limit,

$$\rho = \frac{1}{2}\left[|\Pi|^2 + |\partial_i \varphi|^2 + V(\varphi)\right]. \tag{8.6}$$

During the plunge and merger phase of a binary the two BSs' scalar fields overlap and we can approximate the resulting field and its time derivative as a superposition given by $\varphi = \varphi_1 + \varphi_2$ and $\Pi = \Pi_1 + \Pi_2$. This results in a combined energy density

$$\rho = \rho_1 + \rho_2 + \Delta, \tag{8.7}$$

where ρ_1, ρ_2 are the individual energy densities of the stars as in Eq. (8.6) and Δ is the interaction potential; cf. Eq.(B3) of Ref [408]. This interaction term is composed of mixed products of the scalar field, such as $\varphi_1 \bar{\varphi}_2$ or $\Pi_1 \bar{\Pi}_2$, and therefore vanishes in the limit of large separations. We next recall that the two BS scalar fields' phase offset and relative rotation in the complex plane are determined by the parameters $\delta\phi$ and ε, respectively. For an equal-mass binary system, the scalar field profiles of the two stars forming a binary thus acquire the following forms,

$$\varphi_1 = A(t,r)e^{i\omega t}, \tag{8.8}$$

$$\varphi_2 = A(t,r)e^{i(\varepsilon\omega t + \delta\phi)}. \tag{8.9}$$

We assume that the scalar field amplitude is a slowly varying function of time so that the dynamical part is dominated by the exponential factor $e^{i\omega t}$. Evaluating the interaction potential Δ for the equal-mass (i) $\varepsilon = 1$, $\delta\phi = 0$ (in-phase), (ii) $\varepsilon = 1$, $\delta\phi = \pi/2$ (dephased), (iii) $\varepsilon = 1$, $\delta\phi = \pi$ (anti-phase), and (iv) $\varepsilon = -1$, $\delta\phi = 0$ (anti-BS) configurations, we then

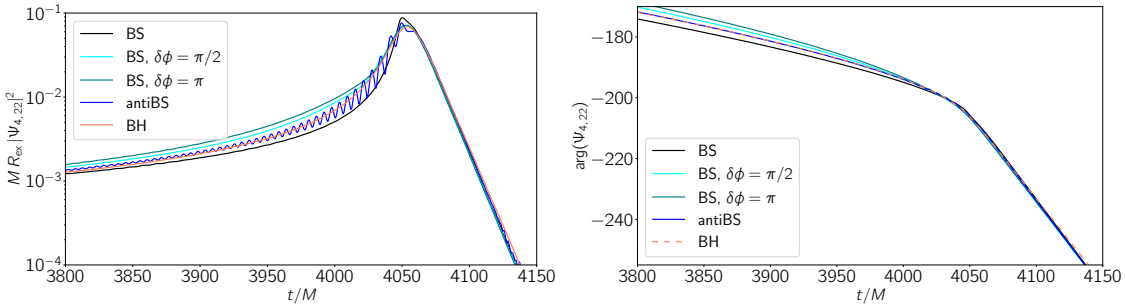


Fig. 8.C.1 Comparison of amplitude (left) and phase (right) of the dominant (22)-modes obtained for the in-phase BS (`A17-d15`), dephased (`A17-d15-p090`), anti-phase (`A17-d15-p180`), anti-BS (`A17-d15-e1`) and BH binaries. Both amplitude and phase have been aligned such that the peak amplitudes coincide in time. The anti-BS signal exhibits the best agreement with the BH waveform, whereas the in-phase and anti-phase configurations result in the largest deviations from the BH signal.

find

$$\Delta_{\rm BS} = \Delta_0, \tag{8.10}$$

$$\Delta_{\delta\phi=\frac{\pi}{2}} = 0, \tag{8.11}$$

$$\Delta_{\delta\phi=\pi} = -\Delta_0, \tag{8.12}$$

$$\Delta_{\rm anti-BS} = \Delta_0 \cos(2\omega t), \tag{8.13}$$

where Δ_0 is strictly non-negative. Note that the anti-BS configuration results in an interaction potential with explicitly harmonic time dependence that oscillates between the Δ values of the in-phase and anti-phase binaries. If the time-scale of the late inspiral and plunge is much longer than the scalar oscillation period of individual BSs, the interaction contribution to the energy density averages out to zero. The interaction potential for the $\delta\phi = \pi/2$ binary, in turn, vanishes completely without any oscillating behaviour. Therefore, we may expect that the anti-BS and $\delta\phi = \pi/2$ configurations will bear closest resemblance to the BH case, where scalar self-interactions are absent by construction. As we will see next, this expectation is largely, but not completely, borne out by the empirical results. For testing this hypothesis, we compare in Fig. 8.C.1 the aligned GW amplitude and phase obtained for the different BS configurations with those obtained in Ref. [153] for an equal-mass non-spinning BH binary. In accordance with our above discussion, the anti-BS binary exhibits excellent agreement with the BH results and displays an oscillatory pattern in the GW amplitude commensurate with the expected oscillation of the interaction term $\Delta_{\rm anti-BS}$. Its amplitude and phase furthermore fall into the range between the in-phase and anti-phase binaries. The $\delta\phi = \pi/2$ binary, however, does not quite fulfil the expectations from our theoretical

analysis; even though its amplitude and phase match the BH signal better than the in-phase and anti-phase binaries do, its deviations exceed those of the (averaged) anti-BS signal. This feature may simply mark the limitations of the above flat-space analysis; and yet there remains the question why the prediction works so well for the anti-BS configuration but not for the $\delta\phi = \pi/2$ case. At present, we do not have a fully satisfactory answer to this question. A more comprehensive exploration of the BS model parameter space may shed more light on this puzzle.

Appendix 8.D Injections

We present in Table 8.D.1 a list of injections of boson-star (BS) waveforms together with the recovered parameters and consistency checks of the recovered signals. We sort this table by the different families of non-spinning BS binaries listed in Table 8.3.1 of the main text. The varying injected parameters, namely the component masses m_1, m_2 in the source frame and the luminosity distance $d_{\rm L}$, are listed along with the resulting injected optimal SNR values for the Hanford and Livingston detectors, $\rho^{\rm H1}$ and $\rho^{\rm L1}$. Each injection is analysed using a waveform approximant abbreviated as follows.

`D`	=	`IMRPhenomD`
`F2`	=	`TaylorF2`
`Pv2T`	=	`IMRPhenomPv2_NRTidal`
`Pv3`	=	`IMRPhenomPv3`
`TEOB`	=	`TEOBResumS`
`XP`	=	`IMRPhenomXP`
`XPHM`	=	`IMRPhenomXPHM`

The recovery is performed using the listed samplers with N_s points. Next, we report the recovered parameters which are obtained from the posterior distributions with 90 % confidence intervals: the component masses m_1 and m_2, the luminosity distance d_L, the dimensionless spins[6] a_1 and a_2, the effective spin $\chi_{\rm eff}$, the precession spin parameter χ_p and the tidal deformation parameters Λ_1 and Λ_2. The recovered SNR is given for the two detectors as $\rho^{\rm H1}$ and $\rho^{\rm L1}$ and calculated from the inferred parameters maximising the joint-log-likelihood. We flag with ticks or crosses whether the residual is compatible with Gaussian noise and quantify the significance of a detection with the Bayes factor $\log(\mathscr{B}^{\rm S}_{\rm N})$.

[6]For non-precessing models, we report projections of the dimensionless spins onto the orbital angular momentum, χ_1, χ_2, which are allowed to be negative.

Table 8.D.1 List of all our injections for the BS families listed in Table 8.3.1. We report the injected component masses, m_1 and m_2, luminosity distance d_L and the corresponding SNR values for the H1 and L1 detectors. The recovery is performed using the specified approximants and samplers initialised with N_s sampling points. The recovered values for the masses, luminosity distance, the dimensionless spins a_1 and a_2, the effective and precession spin parameters $\chi_{\rm eff}$, $\chi_{\rm p}$ and the tidal deformability parameters Λ_1, Λ_2 are given in the form of median values with 90% confidence intervals. We additionally list the recovered optimal SNR and Bayes evidence factors $\log(\mathscr{B}^{\rm S}_{\rm N})$ and mark residuals consistent (inconsistent) with Gaussian noise by a ✓(✗) symbol.

	Injection					Analysis			Recovery										Consistency	
Family	$\frac{m_1}{M_\odot}$	$\frac{m_2}{M_\odot}$	$\frac{d_L}{\rm Mpc}$	$\rho^{\rm H1}$	$\rho^{\rm L1}$	Appr.	Sampler	N_s	$\frac{m_1}{M_\odot}$	$\frac{m_2}{M_\odot}$	$\frac{d_L}{\rm Mpc}$	a_1	a_2	$\chi_{\rm eff}$	$\chi_{\rm p}$	Λ_1	Λ_2	$\rho^{\rm H1}$	$\rho^{\rm L1}$	Res.(H,L)	$\log(\mathscr{B}^{\rm S}_{\rm N})$
A147-d19	2.48	2.48	30	24.5	17.4	Pv2T	nessai	1000	$3.70^{+0.12}_{-0.10}$	$1.75^{+0.05}_{-0.06}$	$51.2^{+24.3}_{-16.9}$	–	–	–	–	10407^{+1915}_{-1795}	10002^{+8973}_{-8897}	21.7	14.7	(✗,✗)	316
A147-d19	2.48	2.48	30	24.5	17.4	Pv2T	nessai	1000	$3.64^{+0.15}_{-0.13}$	$1.70^{+0.15}_{-0.21}$	$49.8^{+9.9}_{-11.3}$	$0.78^{+0.18}_{-0.29}$	$0.47^{+0.44}_{-0.41}$	$-0.33^{+0.27}_{-0.28}$	$0.53^{+0.26}_{-0.20}$	6102^{+2519}_{-2352}	10302^{+8602}_{-8881}	22.1	17.0	(✓,✓)	341
A147-d19	2.48	2.48	31.25	23.8	17.1	Pv2T	nessai	1000	$3.57^{+0.20}_{-0.11}$	$1.59^{+0.16}_{-0.19}$	$54.3^{+8.6}_{-13.1}$	$0.79^{+0.18}_{-0.38}$	$0.52^{+0.42}_{-0.46}$	$-0.40^{+0.34}_{-0.25}$	$0.47^{+0.30}_{-0.22}$	7894^{+2791}_{-3089}	9998^{+8902}_{-8867}	22.5	16.0	(✓,✓)	350
A147-d19	2.48	2.48	31.25	23.8	17.1	XP	nessai	1000	$6.92^{+0.56}_{-0.33}$	$1.07^{+0.07}_{-0.08}$	$74.0^{+23.9}_{-28.5}$	–	–	–	–	–	–	17.2	12.6	(✓,✓)	214
A147-d19	2.48	2.48	31.25	23.8	17.1	XP	nessai	1000	$5.31^{+1.23}_{-0.72}$	$1.37^{+0.18}_{-0.21}$	432^{+63}_{-368}	$0.69^{+0.16}_{-0.16}$	$0.80^{+0.17}_{-0.51}$	$0.00^{+0.14}_{-0.12}$	$0.68^{+0.13}_{-0.16}$	–	–	3.14	1.66	(✗,✗)	237
A147-d19	4.98	4.98	20	96.2	68.1	XP	nessai	1000	$13.7^{+0.05}_{-0.06}$	$1.72^{+0.01}_{-0.01}$	$26.0^{+0.96}_{-0.84}$	$0.86^{+0.01}_{-0.01}$	$0.98^{+0.01}_{-0.05}$	$-0.74^{+0.02}_{-0.02}$	$0.46^{+0.01}_{-0.01}$	–	–	75.6	51.6	(✗,✗)	4221
A147-d19	4.94	4.94	50	38.5	27.2	XP	nessai	1000	$15.0^{+0.2}_{-0.4}$	$1.90^{+0.06}_{-0.02}$	$56.1^{+8.2}_{-3.8}$	$0.90^{+0.04}_{-0.02}$	$0.87^{+0.11}_{-0.39}$	$-0.57^{+0.05}_{-0.03}$	$0.71^{+0.03}_{-0.02}$	–	–	26.6	17.3	(✓,✓)	674
A147-d19	4.93	4.93	62.5	30.8	21.8	XP	nessai	1000	$15.8^{+0.2}_{-0.2}$	$1.99^{+0.03}_{-0.02}$	140^{+35}_{-68}	–	–	–	–	–	–	19.9	14.2	(✓,✓)	286
A147-d19	4.93	4.93	62.5	30.8	21.8	XP	nessai	1000	$16.1^{+0.2}_{-0.7}$	$2.04^{+0.04}_{-0.07}$	110^{+190}_{-47}	–	–	–	–	–	–	18.8	14.1	(✓,✓)	253
A147-d19	4.93	4.93	62.5	30.8	21.8	XP	nessai	1000	$13.1^{+0.1}_{-0.1}$	$1.65^{+0.02}_{-0.02}$	$75.4^{+17.3}_{-10.0}$	$0.99^{+0.00}_{-0.01}$	$0.87^{+0.11}_{-0.39}$	$-0.91^{+0.06}_{-0.03}$	$0.32^{+0.05}_{-0.08}$	–	–	25.2	14.7	(✓,✓)	378
A147-d19	4.93	4.93	62.5	30.8	21.8	F2	nessai	1000	$9.83^{+3.11}_{-1.13}$	$2.06^{+0.23}_{-0.29}$	171^{+42}_{-59}	$-0.83^{+0.31}_{-0.11}$	$-0.05^{+0.41}_{-0.52}$	$-0.69^{+0.23}_{-0.11}$	–	511^{+235}_{-279}	2544^{+2136}_{-2221}	21.4	15.6	(✓,✓)	342
A147-d19	4.93	4.93	62.5	30.8	21.8	TEOB	nessai	1000	$12.9^{+0.14}_{-0.13}$	$1.62^{+0.02}_{-0.02}$	$98.4^{+37.2}_{-40.6}$	$-0.98^{+0.02}_{-0.01}$	$-0.84^{+0.27}_{-0.12}$	$-0.96^{+0.03}_{-0.02}$	–	–	–	21.0	14.1	(✓,✓)	337
A147-d19	4.89	4.89	100	19.2	13.6	F2	nessai	1000	$13.2^{+1.0}_{-1.3}$	$1.93^{+0.20}_{-0.15}$	273^{+113}_{-101}	–	–	–	–	1666^{+601}_{-344}	2514^{+2161}_{-2201}	14.1	11.6	(✓,✓)	111
A147-d19	4.89	4.89	100	19.2	13.6	F2	nessai	1000	$10.2^{+2.9}_{-2.3}$	$2.18^{+0.50}_{-0.39}$	294^{+89}_{-110}	$-0.61^{+0.22}_{-0.25}$	$-0.03^{+0.39}_{-0.50}$	$-0.51^{+0.16}_{-0.17}$	–	688^{+724}_{-356}	2518^{+2186}_{-2192}	14.8	10.6	(✓,✓)	114
A147-d19	9.73	9.73	125	38.7	27.2	XPHM	cpnest	1000	$23.6^{+0.8}_{-1.0}$	$4.60^{+0.41}_{-0.11}$	477^{+112}_{-166}	–	–	–	–	–	–	18.0	12.1	(✗,✓)	193
A147-d19	9.73	9.73	125	38.7	27.2	XPHM	cpnest	1000	$20.3^{+1.4}_{-3.6}$	$4.97^{+0.86}_{-0.20}$	227^{+32}_{-31}	$0.70^{+0.25}_{-0.14}$	$0.63^{+0.34}_{-0.56}$	$-0.55^{+0.15}_{-0.22}$	$0.37^{+0.11}_{-0.06}$	–	–	22.6	15.1	(✗,✗)	318
A147-d19	9.73	9.73	125	38.7	27.2	XP	nessai	1000	$25.3^{+1.8}_{-0.9}$	$4.62^{+0.20}_{-0.15}$	473^{+156}_{-184}	–	–	–	–	–	–	18.6	11.6	(✓,✓)	181
A147-d19	9.73	9.73	125	38.7	27.2	XP	nessai	1000	$19.4^{+0.8}_{-3.1}$	$4.79^{+1.31}_{-0.06}$	247^{+28}_{-46}	$0.96^{+0.03}_{-0.21}$	$0.84^{+0.14}_{-0.37}$	$-0.76^{+0.16}_{-0.08}$	$0.38^{+0.10}_{-0.06}$	–	–	22.6	16.1	(✗,✓)	340
A147-d19	19.0	19.0	250	43.4	30.4	XP	nessai	1000	$26.5^{+2.5}_{-1.6}$	$24.7^{+2.1}_{-1.7}$	1119^{+324}_{-463}	–	–	–	–	–	–	21.0	15.1	(✗,✓)	284
A147-d19	19.0	19.0	250	43.4	30.4	XP	nessai	1000	$42.6^{+1.3}_{-1.3}$	$19.3^{+0.7}_{-0.7}$	101^{+4}_{-1}	$0.33^{+0.05}_{-0.05}$	$0.66^{+0.15}_{-0.12}$	$0.03^{+0.07}_{-0.08}$	$0.06^{+0.01}_{-0.01}$	–	–	32.3	19.7	(✓,✓)	660
A147-d19	28.2	28.2	300	57.0	39.9	XP	nessai	1000	$39.4^{+3.0}_{-2.5}$	$37.0^{+2.7}_{-2.8}$	889^{+376}_{-362}	–	–	–	–	–	–	30.2	21.2	(✗,✗)	642
A147-d19	28.2	28.2	300	57.0	39.9	XP	nessai	1000	$68.1^{+2.7}_{-2.4}$	$47.5^{+1.1}_{-1.7}$	103^{+9}_{-3}	$0.96^{+0.02}_{-0.07}$	$0.65^{+0.05}_{-0.04}$	$0.59^{+0.03}_{-0.03}$	$0.42^{+0.03}_{-0.03}$	–	–	42.8	25.4	(✓,✓)	1243
A147-d19	37.9	37.9	250	94.7	66.2	XP	nessai	1000	$53.9^{+3.4}_{-2.4}$	$51.4^{+3.2}_{-2.6}$	721^{+198}_{-300}	–	–	–	–	–	–	52.6	35.7	(✗,✗)	2002
A147-d19	37.9	37.9	250	94.7	66.2	XP	nessai	1000	$67.4^{+0.42}_{-0.38}$	$60.2^{+0.35}_{-0.33}$	124^{+5}_{-6}	$0.83^{+0.00}_{-0.01}$	$0.99^{+0.00}_{-0.01}$	$-0.02^{+0.00}_{-0.00}$	$0.71^{+0.01}_{-0.01}$	–	–	78.0	44.9	(✗,✗)	4041
A147-d19	36.9	36.9	400	61.0	42.3	XPHM	cpnest	500	$83.9^{+3.5}_{-2.7}$	$57.6^{+4.2}_{-3.5}$	103^{+10}_{-2}	$0.57^{+0.10}_{-0.09}$	$0.98^{+0.01}_{-0.02}$	$0.49^{+0.06}_{-0.05}$	$0.47^{+0.06}_{-0.05}$	–	–	47.6	26.8	(✓,✓)	1560
A147-d19	36.2	36.2	500	47.3	33.1	XP	nessai	1000	$50.2^{+5.6}_{-3.9}$	$44.8^{+4.6}_{-4.8}$	1350^{+373}_{-533}	–	–	–	–	–	–	26.5	18.2	(✗,✓)	457
A147-d19	36.2	36.2	500	47.3	33.1	XP	nessai	1000	$69.1^{+0.8}_{-0.9}$	$64.7^{+0.8}_{-0.9}$	116^{+15}_{-12}	$0.97^{+0.02}_{-0.05}$	$0.59^{+0.02}_{-0.03}$	$0.22^{+0.01}_{-0.01}$	$0.80^{+0.04}_{-0.05}$	–	–	38.1	23.7	(✓,✓)	919
A147-d19	36.2	36.2	500	47.3	33.1	D	nessai	1000	$45.6^{+3.3}_{-2.3}$	$43.2^{+3.0}_{-2.4}$	826^{+245}_{-358}	$-0.97^{+0.03}_{-0.01}$	$-0.97^{+0.03}_{-0.02}$	$-0.97^{+0.02}_{-0.01}$	–	–	–	31.5	19.8	(✓,✓)	671
A147-d19	36.2	36.2	500	47.3	33.1	XPHM	cpnest	1000	$64.7^{+1.0}_{-1.0}$	$36.8^{+1.7}_{-1.6}$	247^{+35}_{-36}	$0.98^{+0.01}_{-0.02}$	$0.96^{+0.02}_{-0.08}$	$-0.42^{+0.04}_{-0.05}$	$0.41^{+0.06}_{-0.06}$	–	–	41.0	21.7	(✓,✓)	955
A147-d19	44.3	44.3	625	48.4	33.8	XP	nessai	1000	$64.2^{+6.4}_{-5.0}$	$59.2^{+5.6}_{-5.2}$	1345^{+509}_{-539}	–	–	–	–	–	–	30.5	21.0	(✓,✓)	644
A147-d19	44.3	44.3	625	48.4	33.8	XP	nessai	1000	$96.1^{+1.4}_{-2.4}$	$45.5^{+2.4}_{-1.8}$	106^{+13}_{-6}	$0.98^{+0.01}_{-0.04}$	$0.96^{+0.02}_{-0.07}$	$-0.64^{0.03}_{-0.03}$	$0.53^{+0.06}_{-0.06}$	–	–	41.0	20.7	(✓,✓)	1017
A147-d19	52.1	52.1	750	48.6	34.0	XP	nessai	1000	$76.7^{+6.6}_{-5.8}$	$71.6^{+6.3}_{-5.6}$	1305^{+560}_{-492}	–	–	–	–	–	–	33.1	23.0	(✓,✓)	753
A147-d19	52.1	52.1	750	48.6	34.0	XP	nessai	1000	$96.9^{+0.8}_{-1.3}$	$86.3^{+1.1}_{-1.3}$	102^{+6}_{-2}	$0.98^{+0.01}_{-0.04}$	$0.97^{+0.02}_{-0.04}$	$-0.51^{0.02}_{-0.03}$	$0.85^{+0.02}_{-0.03}$	–	–	40.5	24.1	(✓,✓)	1047

	Injection					Analysis			Recovery									Consistency	
Family	$\frac{m_1}{M_\odot}$	$\frac{m_2}{M_\odot}$	$\frac{d_L}{\mathrm{Mpc}}$	ρ^{H1}	ρ^{L1}	Appr.	Sampler	N_s	$\frac{m_1}{M_\odot}$	$\frac{m_2}{M_\odot}$	$\frac{d_L}{\mathrm{Mpc}}$	a_1	a_2	χ_{eff}	χ_{p}	Λ_1	Λ_2	ρ^{H1}	ρ^{L1}	Res.(H,L)	$\log(\mathscr{B}^{\mathrm{S}}_{\mathrm{N}})$
A17-d12	2.48	2.48	31.25	16.5	11.8	Pv2T	nessai	1000	$2.75^{+0.67}_{-0.31}$	$2.19^{+0.25}_{-0.41}$	$55.0^{+20.2}_{-21.6}$	$0.57^{+0.37}_{-0.48}$	$0.53^{+0.41}_{-0.47}$	$0.30^{+0.23}_{-0.24}$	$0.44^{+0.34}_{-0.29}$	$79.8^{+257}_{-73.2}$	175^{+357}_{-158}	16.3	12.9	(✓,✓)	154
A17-d12	2.48	2.48	31.25	16.3	11.5	XP	nessai	1000	$2.80^{+0.70}_{-0.39}$	$1.98^{+0.35}_{-0.46}$	$52.2^{+17.0}_{-22.2}$	–	–	–	–	–	–	16.4	11.2	(✓,✓)	151
A17-d12	2.48	2.48	31.25	16.3	11.5	XP	nessai	1000	$3.33^{+1.48}_{-0.85}$	$1.76^{+0.58}_{-0.49}$	$48.2^{+19.4}_{-16.9}$	$0.52^{+0.41}_{-0.43}$	$0.52^{+0.42}_{-0.45}$	$0.13^{+0.22}_{-0.20}$	$0.49^{+0.41}_{-0.34}$	–	–	15.2	10.4	(✓,✓)	153
A17-d12	4.93	4.93	62.5	24.2	17.2	F2	nessai	1000	$10.7^{+3.0}_{-4.9}$	$2.44^{+2.01}_{-0.56}$	126^{+35}_{-41}	$0.41^{+0.17}_{-0.09}$	$0.04^{+0.54}_{-0.45}$	$0.35^{+0.07}_{-0.06}$	–	$0.80^{+11.3}_{-0.75}$	$94.0^{+618}_{-88.2}$	22.3	17.7	(✓,✓)	357
A17-d12	4.93	4.93	62.5	24.2	17.2	XP	nessai	1000	$7.08^{+0.59}_{-0.79}$	$3.00^{+0.48}_{-0.31}$	$98.7^{+24.4}_{-38.8}$	–	–	–	–	–	–	24.6	18.2	(✓,✓)	406
A17-d12	4.93	4.93	62.5	24.2	17.2	XP	nessai	1000	$6.24^{+1.84}_{-1.55}$	$3.34^{+0.95}_{-0.69}$	$103.6^{+19.9}_{-33.7}$	$0.21^{+0.38}_{-0.19}$	$0.42^{+0.46}_{-0.37}$	$-0.08^{+0.18}_{-0.17}$	$0.23^{+0.32}_{-0.17}$	–	–	21.6	16.2	(✓,✓)	406
A17-d12	9.73	9.73	125	31.0	22.0	XP	nessai	1000	$14.7^{+0.9}_{-0.9}$	$5.43^{+0.49}_{-0.42}$	197^{+45}_{-74}	–	–	–	–	–	–	31.7	22.2	(✓,✓)	685
A17-d12	9.73	9.73	125	31.0	22.0	XP	nessai	1000	$10.8^{+1.0}_{-1.2}$	$7.09^{+0.84}_{-0.59}$	125^{+84}_{-40}	$0.51^{+0.26}_{-0.22}$	$0.57^{+0.26}_{-0.36}$	$-0.20^{+0.07}_{-0.07}$	$0.40^{+0.18}_{-0.16}$	–	–	33.1	21.4	(✓,✓)	697
A17-d12	19.0	19.0	250	35.0	24.8	TEOB	nessai	1000	$17.7^{+2.3}_{-1.5}$	$14.8^{+1.3}_{-1.8}$	376^{+95}_{-166}	$-0.41^{+0.41}_{-0.36}$	$-0.31^{+0.41}_{-0.51}$	$-0.37^{+0.06}_{-0.06}$	–	–	–	34.1	22.8	(✓,✓)	806
A17-d12	19.0	19.0	250	35.0	24.8	D	nessai	1000	$17.7^{+2.5}_{-1.6}$	$14.5^{+1.4}_{-1.8}$	373^{+101}_{-168}	$-0.41^{+0.37}_{-0.37}$	$-0.39^{+0.43}_{-0.44}$	$-0.40^{+0.06}_{-0.06}$	–	–	–	33.5	22.3	(✓,✓)	792
A17-d12	19.0	19.0	250	35.0	24.8	F2	nessai	1000	$50.9^{+3.1}_{-4.6}$	$6.86^{+0.64}_{-0.37}$	523^{+152}_{-243}	$0.39^{+0.04}_{-0.03}$	$-0.01^{+0.46}_{-0.48}$	$0.34^{+0.03}_{-0.03}$	–	$0.20^{+0.35}_{-0.18}$	203^{+401}_{-180}	34.1	22.5	(✓,✓)	765
A17-d12	19.0	19.0	250	35.0	24.8	XP	nessai	1000	$29.9^{+1.9}_{-4.1}$	$9.57^{+0.92}_{-1.34}$	410^{+917}_{-213}	–	–	–	–	–	–	32.2	21.7	(✓,✓)	762
A17-d12	19.0	19.0	250	35.0	24.8	XP	nessai	1000	$18.9^{+2.04}_{-5.85}$	$13.7^{+1.5}_{-4.4}$	302^{+3203}_{-125}	$0.56^{+0.28}_{-0.24}$	$0.56^{+0.28}_{-0.33}$	$-0.35^{+0.07}_{-0.08}$	$0.35^{+0.16}_{-0.15}$	–	–	33.5	23.5	(✓,✓)	796
A17-d12	29.5	29.5	75	171.6	122.0	XPHM	dynesty	500	$30.5^{+0.06}_{-0.07}$	$26.4^{+0.08}_{-0.05}$	$58.9^{+2.9}_{-2.7}$	$0.63^{+0.01}_{-0.01}$	$0.98^{+0.01}_{-0.02}$	$-0.12^{+0.00}_{-0.00}$	$0.15^{+0.01}_{-0.01}$	–	–	170.0	115.9	(✓,✓)	21637
A17-d12	29.0	29.0	150	85.8	61.0	XP	nessai	1000	$30.2^{+0.13}_{-0.14}$	$26.0^{+0.14}_{-0.09}$	116^{+11}_{-10}	$0.61^{+0.02}_{-0.02}$	$0.97^{+0.02}_{-0.04}$	$-0.12^{+0.01}_{-0.01}$	$0.15^{+0.02}_{-0.01}$	–	–	86.2	60.5	(✓,✓)	5413
A17-d12	28.7	28.7	200	64.3	45.7	XP	nessai	1000	$30.0^{+0.24}_{-0.23}$	$25.9^{+0.25}_{-0.18}$	147^{+25}_{-23}	$0.61^{+0.02}_{-0.03}$	$0.96^{+0.02}_{-0.06}$	$-0.12^{+0.01}_{-0.01}$	$0.15^{+0.02}_{-0.02}$	–	–	64.0	45.2	(✓,✓)	3032
A17-d12	27.8	27.8	375	34.3	24.4	XP	nessai	1000	$33.5^{+1.9}_{-3.5}$	$19.6^{+2.9}_{-1.0}$	665^{+159}_{-237}	–	–	–	–	–	–	32.9	23.7	(✓,✓)	794
A17-d12	27.8	27.8	375	34.3	24.4	XP	nessai	1000	$28.3^{+1.1}_{-0.9}$	$23.8^{+0.87}_{-1.02}$	525^{+185}_{-128}	$0.81^{+0.15}_{-0.19}$	$0.91^{+0.07}_{-0.17}$	$-0.09^{+0.02}_{-0.02}$	$0.74^{+0.12}_{-0.11}$	–	–	33.8	24.4	(✓,✓)	834
A17-d12	27.8	27.8	375	34.3	24.4	XPHM	dynesty	500	$32.8^{+1.5}_{-2.2}$	$19.8^{+2.2}_{-1.2}$	690^{+122}_{-154}	–	–	–	–	–	–	32.5	23.2	(✓,✓)	794
A17-d12	27.8	27.8	375	34.3	24.4	XPHM	dynesty	500	$28.8^{+0.8}_{-0.8}$	$24.5^{+0.8}_{-0.8}$	403^{+117}_{-84}	$0.86^{+0.12}_{-0.21}$	$0.89^{+0.09}_{-0.19}$	$-0.12^{+0.03}_{-0.03}$	$0.70^{+0.13}_{-0.13}$	–	–	32.3	23.2	(✓,✓)	738
A17-d12	27.2	27.2	500	25.7	18.3	XP	nessai	1000	$27.9^{+1.5}_{-1.5}$	$23.4^{+1.3}_{-1.4}$	633^{+304}_{-224}	$0.72^{+0.23}_{-0.18}$	$0.89^{+0.09}_{-0.26}$	$-0.09^{+0.04}_{-0.03}$	$0.61^{+0.26}_{-0.39}$	–	–	24.7	17.4	(✓,✓)	459
A17-d12	26.2	26.2	700	18.4	13.1	XP	nessai	1000	$26.1^{+3.6}_{-2.2}$	$22.3^{+2.1}_{-2.6}$	985^{+435}_{-310}	$0.67^{+0.29}_{-0.54}$	$0.61^{+0.34}_{-0.51}$	$-0.07^{+0.05}_{-0.04}$	$0.67^{+0.25}_{-0.35}$	–	–	19.4	15.1	(✓,✓)	224
A17-d12	25.8	25.8	800	16.1	11.4	XP	nessai	1000	$25.5^{+3.9}_{-3.0}$	$21.7^{+2.2}_{-3.4}$	1176^{+719}_{-381}	$0.61^{+0.34}_{-0.51}$	$0.52^{+0.41}_{-0.46}$	$-0.07^{+0.06}_{-0.05}$	$0.64^{+0.28}_{-0.36}$	–	–	15.6	11.2	(✓,✓)	167
A17-d12	36.2	36.2	500	32.9	23.4	XPHM	cpnest	1000	$53.2^{+5.1}_{-8.7}$	$19.1^{+6.4}_{-2.6}$	896^{+138}_{-123}	–	–	–	–	–	–	28.7	20.8	(✓,✓)	692
A17-d12	36.2	36.2	500	32.9	23.4	XPHM	cpnest	500	$34.3^{+3.6}_{-4.5}$	$24.5^{+3.9}_{-3.3}$	692^{+142}_{-290}	$0.77^{+0.20}_{-0.34}$	$0.64^{+0.32}_{-0.53}$	$-0.53^{+0.12}_{-0.13}$	$0.37^{+0.25}_{-0.24}$	–	–	32.8	24.0	(✓,✓)	764
A17-d12	36.2	36.2	500	32.9	23.4	XP	nessai	1000	$56.6^{+3.9}_{-3.8}$	$18.4^{+1.9}_{-1.4}$	740^{+188}_{-281}	–	–	–	–	–	–	31.4	22.5	(✓,✓)	717
A17-d12	36.2	36.2	500	32.9	23.4	XP	nessai	1000	$35.5^{+2.3}_{-3.0}$	$25.5^{+2.0}_{-2.0}$	838^{+113}_{-240}	$0.33^{+0.26}_{-0.18}$	$0.78^{+0.14}_{-0.24}$	$-0.27^{+0.09}_{-0.11}$	$0.46^{+0.15}_{-0.18}$	–	–	32.7	22.5	(✓,✓)	792
A17-d12	36.2	36.2	500	32.9	23.4	Pv3	nessai	1000	$58.3^{+3.9}_{-3.7}$	$17.8^{+1.7}_{-1.4}$	736^{+185}_{-284}	–	–	–	–	–	–	31.4	21.9	(✓,✓)	706
A17-d12	36.2	36.2	500	32.9	23.4	Pv3	nessai	1000	$35.3^{+2.8}_{-2.5}$	$26.3^{+2.1}_{-2.0}$	811^{+119}_{-214}	$0.29^{+0.22}_{-0.14}$	$0.42^{+0.38}_{-0.25}$	$-0.21^{+0.07}_{-0.14}$	$0.27^{+0.23}_{-0.17}$	–	–	34.8	24.1	(✓,✓)	792
A17-d12	44.3	44.3	625	30.9	22.1	XP	nessai	1000	$44.3^{+4.7}_{-3.1}$	$40.0^{+3.6}_{-3.8}$	1192^{+303}_{-469}	–	–	–	–	–	–	27.2	19.6	(✓,✓)	625
A17-d12	44.3	44.3	625	30.9	22.1	XP	nessai	1000	$44.7^{+3.9}_{-5.3}$	$25.6^{+7.2}_{-4.1}$	780^{+199}_{-250}	$0.88^{+0.10}_{-0.29}$	$0.60^{+0.37}_{-0.54}$	$-0.60^{+0.15}_{-0.14}$	$0.26^{+0.34}_{-0.18}$	–	–	29.2	22.2	(✓,✓)	680
A17-d12	44.3	44.3	625	30.9	22.1	XPHM	dynesty	500	$50.4^{+3.5}_{-3.6}$	$35.5^{+3.5}_{-3.2}$	1041^{+253}_{-257}	–	–	–	–	–	–	27.2	19.6	(✓,✓)	633
A17-d12	44.3	44.3	625	30.9	22.1	XPHM	dynesty	500	$44.3^{+3.3}_{-3.1}$	$26.1^{+4.0}_{-2.9}$	830^{+146}_{-152}	$0.88^{+0.10}_{-0.22}$	$0.33^{+0.59}_{-0.30}$	$-0.56^{+0.11}_{-0.11}$	$0.28^{+0.32}_{-0.19}$	–	–	28.8	20.4	(✓,✓)	681
A17-d12	52.1	52.1	750	29.3	20.9	XP	nessai	1000	$61.0^{+4.6}_{-2.9}$	$55.6^{+2.8}_{-4.8}$	398^{+79}_{-81}	–	–	–	–	–	–	28.1	21.7	(✓,✓)	543
A17-d12	52.1	52.1	750	29.3	20.9	XP	nessai	1000	$54.9^{+5.6}_{-6.0}$	$39.3^{+6.6}_{-7.5}$	260^{+61}_{-56}	$0.81^{+0.16}_{-0.37}$	$0.45^{+0.41}_{-0.38}$	$-0.52^{+0.15}_{-0.17}$	$0.26^{+0.23}_{-0.17}$	–	–	28.4	22.4	(✓,✓)	592
A17-d14	2.48	2.48	31.25	19.6	13.9	Pv2T	nessai	1000	$2.68^{+0.73}_{-0.31}$	$2.05^{+0.27}_{-0.42}$	$54.3^{+15.0}_{-17.7}$	$0.44^{+0.45}_{-0.39}$	$0.52^{+0.41}_{-0.46}$	$0.12^{+0.19}_{-0.17}$	$0.48^{+0.36}_{-0.30}$	$84.8^{+296}_{-78.9}$	233^{+482}_{-210}	17.9	13.4	(✓,✓)	205
A17-d14	4.93	4.93	62.5	27.8	19.8	F2	nessai	1000	$11.2^{+1.7}_{-3.3}$	$2.27^{+0.88}_{-0.29}$	111^{+31}_{-34}	$0.38^{+0.06}_{-0.07}$	$0.02^{+0.50}_{-0.43}$	$0.32^{+0.05}_{-0.06}$	–	$0.39^{+1.28}_{-0.35}$	$74.9^{+239.9}_{-70.4}$	26.1	21.4	(✓,✓)	528
A17-d14	4.93	4.93	62.5	27.8	19.8	XP	nessai	1000	$7.19^{+0.42}_{-0.44}$	$2.98^{+0.24}_{-0.21}$	$95.9^{+23.5}_{-33.6}$	–	–	–	–	–	–	27.5	20.4	(✓,✓)	536
A17-d14	4.93	4.93	62.5	27.8	19.8	XP	nessai	1000	$5.00^{+1.45}_{-0.30}$	$4.15^{+0.20}_{-0.89}$	$97.0^{+27.7}_{-22.6}$	$0.61^{+0.30}_{-0.47}$	$0.83^{+0.15}_{-0.71}$	$-0.19^{+0.12}_{-0.07}$	$0.66^{+0.16}_{-0.51}$	–	–	22.0	17.7	(✓,✓)	532
A17-d14	19.0	19.0	250	37.8	27.0	F2	nessai	1000	$49.1^{+2.4}_{-2.1}$	$7.09^{+0.34}_{-0.35}$	479^{+109}_{-146}	$0.37^{+0.04}_{-0.04}$	$0.01^{+0.55}_{-0.51}$	$0.32^{+0.04}_{-0.03}$	–	$0.03^{+0.05}_{-0.03}$	$21.0^{+48.2}_{-18.7}$	36.7	27.5	(✓,✓)	1004
A17-d14	19.0	19.0	250	37.8	27.0	XP	nessai	1000	$29.8^{+1.1}_{-1.1}$	$10.1^{+0.5}_{-0.4}$	362^{+85}_{-120}	–	–	–	–	–	–	34.5	26.7	(✓,✓)	994
A17-d14	19.0	19.0	250	37.8	27.0	XP	nessai	1000	$18.3^{+1.0}_{-2.4}$	$15.4^{+2.0}_{-0.8}$	415^{+48}_{-61}	$0.33^{+0.30}_{-0.16}$	$0.65^{+0.27}_{-0.32}$	$-0.20^{+0.04}_{-0.08}$	$0.49^{+0.24}_{-0.24}$	–	–	36.8	28.0	(✓,✓)	1038
A17-d14	36.2	36.2	500	33.6	24.2	XPHM	dynesty	750	$51.2^{+3.9}_{-3.8}$	$21.0^{+2.6}_{-2.3}$	884^{+100}_{-113}	–	–	–	–	–	–	32.5	22.7	(✓,✓)	737
A17-d14	36.2	36.2	500	33.6	24.2	XPHM	dynesty	750	$37.0^{+2.9}_{-2.6}$	$22.3^{+2.8}_{-2.3}$	698^{+85}_{-100}	$0.88^{+0.10}_{-0.20}$	$0.53^{+0.44}_{-0.49}$	$-0.53^{+0.10}_{-0.09}$	$0.33^{+0.24}_{-0.23}$	–	–	34.3	24.1	(✓,✓)	805
A17-d14	36.2	36.2	500	33.6	24.2	XP	nessai	1000	$58.8^{+4.9}_{-8.1}$	$17.8^{+4.2}_{-2.0}$	710^{+208}_{-255}	–	–	–	–	–	–	30.5	23.1	(✓,✓)	678
A17-d14	36.2	36.2	500	33.6	24.2	XP	nessai	1000	$35.3^{+2.3}_{-2.7}$	$25.7^{+2.3}_{-1.9}$	727^{+116}_{-218}	$0.5^{+0.24}_{-0.21}$	$0.72^{+0.23}_{-0.30}$	$-0.33^{+0.08}_{-0.13}$	$0.47^{+0.18}_{-0.21}$	–	–	34.1	24.2	(✓,✓)	866
A17-d14	36.2	36.2	500	33.9	23.7	TEOB	nessai	1000	$35.6^{+3.3}_{-3.9}$	$24.0^{+3.5}_{-2.3}$	662^{+150}_{-235}	$-0.73^{+0.36}_{-0.19}$	$-0.24^{+0.29}_{-0.56}$	$-0.53^{+0.06}_{-0.05}$	–	–	–	34.1	24.2	(✓,✓)	808

	Injection					Analysis			Recovery									Consistency	
Family	$\frac{m_1}{M_\odot}$	$\frac{m_2}{M_\odot}$	$\frac{d_L}{\mathrm{Mpc}}$	ρ^{H1}	ρ^{L1}	Appr.	Sampler	N_s	$\frac{m_1}{M_\odot}$	$\frac{m_2}{M_\odot}$	$\frac{d_L}{\mathrm{Mpc}}$	a_1	a_2	χ_{eff}	χ_{p}	Λ_1	Λ_2	ρ^{H1}	ρ^{L1}	Res.(H,L)	$\log(\mathscr{B}^{\mathrm{S}}_{\mathrm{N}})$
A17-d15	4.94	4.94	50	39.2	27.8	F2	nessai	1000	$4.76^{+0.33}_{-0.15}$	$4.44^{+0.15}_{-0.29}$	$71.9^{+34.6}_{-23.5}$	–	–	–	–	$1.77^{+17.93}_{-1.63}$	$2.20^{+26.27}_{-2.02}$	36.6	29.2	(✓,✓)	1023
A17-d15	4.94	4.94	50	38.0	27.8	F2	nessai	1000	$13.8^{+0.2}_{-0.5}$	$1.77^{+0.07}_{-0.03}$	$95.5^{+18.1}_{-31.2}$	$0.36^{+0.04}_{-0.03}$	$-0.04^{+0.47}_{-0.56}$	$0.31^{+0.03}_{-0.03}$	–	$0.10^{+0.26}_{-0.09}$	107^{+302}_{-99}	37.4	26.4	(✓,✓)	977
A17-d15	4.89	4.89	100	19.6	13.9	F2	dynesty	500	$4.65^{+0.17}_{-0.17}$	$4.30^{+0.17}_{-0.15}$	158^{+63}_{-57}	–	–	–	–	168^{+153}_{-151}	208^{+206}_{-186}	20.1	13.1	(✓,✓)	235
A17-d15	4.89	4.89	100	19.6	13.9	F2	dynesty	500	$11.7^{+1.8}_{-6.0}$	$1.96^{+1.70}_{-0.24}$	182^{+44}_{-66}	$0.34^{+0.06}_{-0.25}$	$0.01^{+0.48}_{-0.45}$	$0.29^{+0.06}_{-0.20}$	–	$1.29^{+5.97}_{-1.17}$	352^{+1581}_{-340}	19.4	14.0	(✓,✓)	235
A17-d15	4.89	4.89	100	19.6	13.9	F2	nessai	1000	$4.80^{+0.68}_{-0.29}$	$4.18^{+0.28}_{-0.53}$	171^{+55}_{-65}	–	–	–	–	$11.4^{+50.9}_{-10.5}$	$19.6^{+86.6}_{-18.0}$	18.3	14.8	(✓,✓)	225
A17-d15	19.0	19.0	250	40.8	28.9	XPHM	cpnest	500	$17.9^{+2.4}_{-1.5}$	$14.4^{+1.5}_{-1.8}$	342^{+82}_{-118}	$0.75^{+0.21}_{-0.45}$	$0.51^{+0.44}_{-0.44}$	$-0.45^{+0.08}_{-0.06}$	$0.34^{+0.33}_{-0.21}$	–	–	38.8	28.5	(✓,✓)	1103
A17-d15	39.1	39.1	100	172	123	XPHM	cpnest	1000	$38.9^{+1.2}_{-1.3}$	$25.4^{+1.6}_{-1.2}$	135^{+7}_{-10}	$0.97^{+0.02}_{-0.10}$	$0.94^{+0.05}_{-0.88}$	$-0.62^{+0.04}_{-0.03}$	$0.52^{+0.12}_{-0.46}$	–	–	172	123	(✓,✓)	22229
A17-d15	38.3	38.3	200	86.1	61.6	XPHM	cpnest	1000	$37.8^{+1.1}_{-1.1}$	$25.4^{+1.1}_{-1.2}$	236^{+23}_{-22}	$0.95^{+0.03}_{-0.13}$	$0.13^{+0.72}_{-0.12}$	$-0.59^{+0.04}_{-0.05}$	$0.14^{+0.32}_{-0.08}$	–	–	83.1	64.0	(✓,✓)	5392
A17-d15	37.6	37.6	300	57.4	41.1	XPHM	cpnest	1000	$36.5^{+2.1}_{-1.8}$	$26.3^{+3.5}_{-2.2}$	393^{+48}_{-52}	$0.87^{+0.10}_{-0.23}$	$0.57^{+0.39}_{-0.50}$	$-0.51^{+0.12}_{-0.08}$	$0.46^{+0.33}_{-0.29}$	–	–	54.2	42.7	(✓,✓)	2356
A17-d15	36.9	36.9	400	43.0	30.8	XPHM	cpnest	500	$35.6^{+3.3}_{-3.4}$	$24.7^{+3.5}_{-2.9}$	515^{+90}_{-127}	$0.86^{+0.12}_{-0.30}$	$0.55^{+0.39}_{-0.51}$	$-0.57^{+0.09}_{-0.11}$	$0.33^{+0.27}_{-0.22}$	–	–	42.9	31.3	(✓,✓)	1294
A17-d15	36.9	36.9	400	43.0	30.8	XPHM	cpnest	1000	$36.8^{+1.9}_{-2.1}$	$23.9^{+2.4}_{-1.9}$	473^{+62}_{-93}	$0.90^{+0.08}_{-0.21}$	$0.45^{+0.49}_{-0.41}$	$-0.60^{+0.08}_{-0.09}$	$0.25^{+0.30}_{-0.18}$	–	–	43.8	30.3	(✓,✓)	1402
A17-d15	36.2	36.2	500	35.6	25.1	XPHM	cpnest	500	$35.1^{+2.9}_{-2.9}$	$26.0^{+3.5}_{-3.4}$	538^{+207}_{-172}	$0.77^{+0.19}_{-0.35}$	$0.57^{+0.37}_{-0.50}$	$-0.54^{+0.10}_{-0.10}$	$0.32^{+0.30}_{-0.21}$	–	–	34.7	25.7	(✓,✓)	896
A17-d15	36.2	36.2	500	35.6	25.1	XPHM	cpnest	1000	$37.7^{+4.2}_{-3.5}$	$26.2^{+4.4}_{-5.2}$	507^{+215}_{-229}	$0.80^{+0.17}_{-0.29}$	$0.56^{+0.40}_{-0.50}$	$-0.44^{+0.11}_{-0.14}$	$0.43^{+0.35}_{-0.27}$	–	–	37.3	27.5	(✓,✓)	895
A17-d15	29.3	29.3	2000	8.61	6.16	XPHM	cpnest	1000	$31.1^{+12.9}_{-5.8}$	$22.8^{+6.0}_{-7.6}$	2689^{+1372}_{-1247}	$0.50^{+0.44}_{-0.45}$	$0.52^{+0.42}_{-0.47}$	$-0.15^{+0.23}_{-0.31}$	$0.48^{+0.40}_{-0.36}$	–	–	8.44	7.66	(✓,✓)	32
A17-d12-p180	2.48	2.48	31.25	16.8	11.8	Pv2T	nessai	1000	$2.68^{+0.77}_{-0.30}$	$2.14^{+0.24}_{-0.41}$	$63.0^{+19.1}_{-25.1}$	$0.74^{+0.23}_{-0.50}$	$0.65^{+0.31}_{-0.55}$	$0.45^{+0.23}_{-0.25}$	$0.48^{+0.32}_{-0.30}$	109^{+397}_{-101}	283^{+574}_{-255}	17.9	11.1	(✓,✓)	146
A17-d12-p180	4.93	4.93	62.5	24.1	17.7	F2	nessai	1000	$14.3^{+1.0}_{-3.0}$	$2.07^{+0.57}_{-0.15}$	125^{+30}_{-42}	$0.55^{+0.10}_{-0.05}$	$0.00^{+0.49}_{-0.52}$	$0.48^{+0.06}_{-0.04}$	–	$1.22^{+1.20}_{-1.05}$	632^{+1211}_{-577}	22.6	17.0	(✓,✓)	450
A17-d12-p180	4.93	4.93	62.5	25.2	17.9	XP	nessai	1000	$4.73^{+0.39}_{-0.18}$	$4.35^{+0.17}_{-0.35}$	$85.1^{+15.7}_{-26.9}$	–	–	–	–	–	–	22.6	17.0	(✓,✓)	328
A17-d12-p180	4.93	4.93	62.5	25.2	17.9	XP	nessai	1000	$7.43^{+1.82}_{-0.99}$	$4.11^{+0.62}_{-0.76}$	$76.3^{+20.5}_{-24.6}$	$0.87^{+0.10}_{-0.14}$	$0.86^{+0.12}_{-0.29}$	$0.68^{+0.07}_{-0.07}$	$0.45^{+0.18}_{-0.20}$	–	–	24.5	17.9	(✓,✓)	405
A17-d12-p180	36.2	36.2	500	35.8	25.3	XP	nessai	1000	$31.6^{+3.2}_{-1.9}$	$28.3^{+2.1}_{-2.6}$	756^{+195}_{-300}	–	–	–	–	–	–	29.2	22.1	(✓,✓)	792
A17-d12-p180	36.2	36.2	500	35.8	25.3	XP	nessai	1000	$45.3^{+7.0}_{-4.9}$	$29.4^{+4.4}_{-5.2}$	808^{+272}_{-257}	$0.81^{+0.16}_{-0.25}$	$0.75^{+0.21}_{-0.51}$	$0.51^{+0.06}_{-0.06}$	$0.44^{+0.20}_{-0.27}$	–	–	34.5	25.2	(✓,✓)	906
A17-d12-p180	36.2	36.2	500	35.8	25.3	XPHM	dynesty	500	$32.9^{+2.5}_{-2.7}$	$28.8^{+2.0}_{-2.6}$	623^{+325}_{-239}	–	–	–	–	–	–	29.9	21.9	(✓,✓)	744
A17-d12-p180	36.2	36.2	500	35.8	25.3	XPHM	dynesty	500	$46.7^{+4.2}_{-4.7}$	$24.8^{+3.7}_{-2.2}$	1168^{+119}_{-154}	$0.65^{+0.17}_{-0.21}$	$0.63^{+0.33}_{-0.55}$	$0.48^{+0.06}_{-0.06}$	$0.32^{+0.21}_{-0.19}$	–	–	33.6	24.8	(✓,✓)	885
A17-d15-p180	2.48	2.48	30	23.7	16.8	XP	nessai	1000	$2.52^{+0.38}_{-0.20}$	$2.11^{+0.18}_{-0.29}$	$42.6^{+7.0}_{-14.8}$	–	–	–	–	–	–	21.9	16.4	(✓,✓)	348
A17-d15-p180	2.48	2.48	30	23.7	16.8	XP	nessai	1000	$2.94^{+0.83}_{-0.52}$	$1.86^{+0.36}_{-0.35}$	$41.7^{+7.9}_{-13.4}$	$0.27^{+0.28}_{-0.23}$	$0.55^{+0.39}_{-0.48}$	$0.09^{+0.15}_{-0.11}$	$0.32^{+0.27}_{-0.23}$	–	–	23.9	14.4	(✓,✓)	347
A17-d15-p180	4.93	4.93	60	33.3	23.6	XP	nessai	1000	$4.77^{+0.40}_{-0.20}$	$4.34^{+0.19}_{-0.35}$	$97.6^{+22.1}_{-38.5}$	–	–	–	–	–	–	31.9	21.1	(✓,✓)	697
A17-d15-p180	4.93	4.93	60	33.3	23.6	XP	nessai	1000	$7.77^{+1.72}_{-0.92}$	$3.05^{+0.36}_{-0.44}$	$95.8^{+13.0}_{-26.3}$	$0.75^{+0.16}_{-0.12}$	$0.84^{+0.14}_{-0.43}$	$0.31^{+0.10}_{-0.07}$	$0.55^{+0.24}_{-0.21}$	–	–	31.6	24.5	(✓,✓)	800
A17-d15-p180	9.73	9.73	125	39.5	28.0	XP	nessai	1000	$9.03^{+0.41}_{-0.20}$	$8.66^{+0.21}_{-0.36}$	201^{+43}_{-73}	–	–	–	–	–	–	36.8	28.3	(✓,✓)	949
A17-d15-p180	9.73	9.73	125	39.5	28.0	XP	nessai	1000	$13.6^{+1.8}_{-2.0}$	$6.84^{+1.08}_{-0.90}$	127^{+81}_{-14}	$0.60^{+0.17}_{-0.18}$	$0.30^{+0.55}_{-0.26}$	$0.29^{+0.05}_{-0.05}$	$0.40^{+0.22}_{-0.19}$	–	–	36.9	28.4	(✓,✓)	1070
A17-d15-p180	19.0	19.0	250	42.3	30.0	XP	nessai	1000	$17.3^{+0.7}_{-0.5}$	$16.6^{+0.6}_{-0.6}$	406^{+87}_{-166}	–	–	–	–	–	–	39.3	26.3	(✓,✓)	1054
A17-d15-p180	19.0	19.0	250	42.3	30.0	XP	nessai	1000	$20.0^{+0.5}_{-0.4}$	$16.4^{+0.5}_{-0.6}$	452^{+38}_{-54}	$0.97^{+0.02}_{-0.08}$	$0.88^{+0.10}_{-0.21}$	$0.27^{+0.04}_{-0.05}$	$0.72^{+0.15}_{-0.15}$	–	–	43.6	30.6	(✓,✓)	1322
A17-d15-p180	28.2	28.2	300	50.4	35.8	XP	nessai	1000	$25.4^{+1.2}_{-0.8}$	$24.3^{+1.0}_{-1.0}$	474^{+103}_{-187}	–	–	–	–	–	–	45.6	33.5	(✓,✓)	1523
A17-d15-p180	28.2	28.2	300	50.4	35.8	XP	nessai	1000	$37.2^{+2.4}_{-2.6}$	$20.4^{+1.9}_{-1.8}$	589^{+44}_{-122}	$0.68^{+0.15}_{-0.13}$	$0.42^{+0.52}_{-0.37}$	$0.38^{+0.04}_{-0.12}$	$0.22^{+0.21}_{-0.13}$	–	–	50.2	35.1	(✓,✓)	1860
A17-d15-p180	36.2	36.2	500	37.6	26.7	XP	nessai	1000	$33.7^{+4.2}_{-3.1}$	$27.8^{+2.9}_{-3.2}$	718^{+212}_{-298}	–	–	–	–	–	–	34.2	23.9	(✓,✓)	850
A17-d15-p180	36.2	36.2	500	37.6	26.7	XP	nessai	1000	$49.5^{+3.6}_{-3.8}$	$30.9^{+2.7}_{-2.5}$	446^{+193}_{-101}	$0.91^{+0.07}_{-0.13}$	$0.73^{+0.22}_{-0.26}$	$0.47^{+0.04}_{-0.04}$	$0.41^{+0.14}_{-0.13}$	–	–	38.9	28.0	(✓,✓)	1045
A17-d15-p180	44.3	44.3	625	35.5	25.2	XP	nessai	1000	$53.9^{+3.7}_{-3.1}$	$23.4^{+2.0}_{-1.6}$	762^{+180}_{-295}	–	–	–	–	–	–	34.5	24.2	(✓,✓)	870
A17-d15-p180	44.3	44.3	625	35.5	25.2	XP	nessai	1000	$60.3^{+5.4}_{-6.7}$	$32.7^{+5.8}_{-3.4}$	875^{+307}_{-242}	$0.71^{+0.17}_{-0.17}$	$0.83^{+0.15}_{-0.41}$	$0.43^{+0.08}_{-0.06}$	$0.39^{+0.17}_{-0.19}$	–	–	37.1	22.8	(✓,✓)	940
A17-d15-p180	52.1	52.1	750	33.7	24.0	XP	nessai	1000	$68.9^{+4.9}_{-4.1}$	$22.4^{+2.0}_{-1.7}$	808^{+203}_{-326}	–	–	–	–	–	–	32.6	23.1	(✓,✓)	758
A17-d15-p180	52.1	52.1	750	33.7	24.0	XP	nessai	1000	$69.3^{+5.7}_{-5.7}$	$32.5^{+4.9}_{-3.6}$	1112^{+238}_{-358}	$0.49^{+0.18}_{-0.20}$	$0.57^{+0.37}_{-0.48}$	$0.33^{+0.08}_{-0.08}$	$0.27^{+0.19}_{-0.17}$	–	–	34.8	25.1	(✓,✓)	884

	Injection					Analysis			Recovery								Consistency	
Family	$\frac{m_1}{M_\odot}$	$\frac{m_2}{M_\odot}$	$\frac{d_L}{\mathrm{Mpc}}$	ρ^{H1}	ρ^{L1}	Appr.	Sampler	N_s	$\frac{m_1}{M_\odot}$	$\frac{m_2}{M_\odot}$	$\frac{d_L}{\mathrm{Mpc}}$	a_1	a_2	χ_{eff}	χ_{p}	Λ_1	Λ_2	ρ^{H1}	ρ^{L1}	Res.(H,L)	$\log(\mathscr{B}^{\mathrm{S}}_{\mathrm{N}})$
A17-d15-p090	2.48	2.48	30	23.8	16.9	XP	nessai	1000	$2.69^{+0.47}_{-0.33}$	$2.00^{+0.29}_{-0.32}$	$43.3^{+6.5}_{-14.3}$	–	–	$0.06^{+0.10}_{-0.10}$	$0.45^{+0.14}_{-0.28}$	–	–	22.3	15.7	(✓,✓)	342
A17-d15-p090	2.48	2.48	30	23.8	16.9	XP	nessai	1000	$3.00^{+0.57}_{-0.39}$	$1.82^{+0.16}_{-0.16}$	$33.6^{+12.3}_{-12.3}$	$0.43^{+0.14}_{-0.33}$	$0.79^{+0.17}_{-0.33}$	–	–	—	—	22.9	18.1	(✓,✓)	420
A17-d15-p090	2.48	2.48	31.25	22.8	16.2	Pv2T	nessai	1000	$2.53^{+0.29}_{-0.15}$	$2.21^{+0.25}_{-0.31}$	$53.6^{+15.0}_{-19.2}$	$0.40^{+0.36}_{-0.36}$	$0.48^{+0.33}_{-0.42}$	$0.22^{+0.35}_{-0.18}$	$0.40^{+0.45}_{-0.27}$	114^{+288}_{-110}	190^{+366}_{-175}	21.6	16.7	(✓,✓)	342
A17-d15-p090	4.93	4.93	60	33.2	23.6	XP	nessai	1000	$4.77^{+0.33}_{-0.16}$	$4.41^{+0.16}_{-0.29}$	$96.1^{+21.6}_{-34.9}$	–	–	–	–	–	–	31.6	22.4	(✓,✓)	722
A17-d15-p090	4.93	4.93	60	33.2	23.6	XP	nessai	1000	$5.04^{+1.38}_{-0.11}$	$4.28^{+0.09}_{-0.09}$	$99.6^{+17.1}_{-24.3}$	–	$0.92^{+0.07}_{-0.44}$	$0.04^{+0.06}_{-0.05}$	$0.83^{+0.12}_{-0.37}$	–	–	32.4	22.3	(✓,✓)	750
A17-d15-p090	4.93	4.93	62.5	31.9	22.7	F2	nessai	1000	$14.1^{+6.2}_{-0.6}$	$1.82^{+0.08}_{-0.21}$	104^{+22}_{-25}	$0.42^{+0.03}_{-0.03}$	$-0.04^{+0.44}_{-0.57}$	$0.37^{+0.03}_{-0.03}$	–	$0.13^{+0.29}_{-0.12}$	146^{+338}_{-131}	31.0	24.3	(✓,✓)	730
A17-d15-p090	4.93	4.93	62.5	31.9	22.7	XP	nessai	1000	$4.82^{+0.42}_{-0.21}$	$4.35^{+0.21}_{-0.36}$	100^{+25}_{-36}	–	–	–	–	–	–	31.6	22.4	. (✓,✓)	698
A17-d15-p090	9.73	9.73	125	39.1	27.8	XP	nessai	1000	$9.26^{+0.57}_{-0.31}$	$8.66^{+0.31}_{-0.50}$	208^{+46}_{-85}	–	–	. –	–	–	–	38.6	26.4	(✓,✓)	1037
A17-d15-p090	9.73	9.73	125	39.1	27.8	XP	nessai	1000	$9.87^{+2.56}_{-0.28}$	$8.45^{+0.28}_{-0.26}$	206^{+26}_{-26}	$0.76^{+0.14}_{-0.25}$	$0.77^{+0.18}_{-0.33}$	$0.09^{+0.06}_{-0.03}$	$0.74^{+0.15}_{-0.29}$	–	–	38.6	29.5	(✓,✓)	1174
A17-d15-p090	19.0	19.0	250	41.8	29.7	XP	nessai	1000	$17.9^{+1.26}_{-0.7}$	$16.7^{+0.8}_{-1.0}$	387^{+96}_{-174}	–	–	–	–	–	–	41.0	28.0	(✓,✓)	1200
A17-d15-p090	19.0	19.0	250	41.8	29.7	XP	nessai	1000	$24.4^{+1.9}_{-2.3}$	$13.0^{+1.4}_{-0.9}$	389^{+93}_{-115}	$0.38^{+0.28}_{-0.19}$	$0.56^{+0.37}_{-0.45}$	$0.12^{+0.05}_{-0.05}$	$0.32^{+0.25}_{-0.17}$	–	–	39.8	31.6	(✓,✓)	1309
A17-d15-p090	28.2	28.2	300	49.3	35.0	XP	nessai	1000	$26.4^{+1.7}_{-1.7}$	$24.7^{+1.2}_{-1.7}$	445^{+115}_{-131}	–	–	–	–	–	–	48.5	34.9	(✓,✓)	1698
A17-d15-p090	28.2	28.2	300	49.3	35.0	XP	nessai	1000	$38.3^{+2.9}_{-3.1}$	$18.0^{+1.4}_{-1.4}$	529^{+131}_{-156}	$0.28^{+0.19}_{-0.19}$	$0.63^{+0.32}_{-0.52}$	$0.19^{+0.05}_{-0.05}$	$0.26^{+0.16}_{-0.15}$	–	–	46.0	34.2	(✓,✓)	1599
A17-d15-p090	36.2	36.2	500	36.8	26.2	XP	nessai	1000	$39.1^{+3.4}_{-3.4}$	$26.3^{+3.7}_{-2.3}$	710^{+156}_{-291}	–	–	–	–	–	–	37.8	27.5	(✓,✓)	1019
A17-d15-p090	36.2	36.2	500	36.8	26.2	XP	nessai	1000	$40.6^{+5.4}_{-5.4}$	$30.1^{+4.6}_{-4.0}$	935^{+111}_{-205}	$0.47^{+0.32}_{-0.38}$	$0.49^{+0.42}_{-0.43}$	$0.29^{+0.05}_{-0.05}$	$0.34^{+0.31}_{-0.21}$	–	–	37.4	27.6	(✓,✓)	1010
A17-d15-p090	36.2	36.2	500	36.8	26.2	XPHM	cpnest	500	$38.9^{+3.1}_{-5.9}$	$33.2^{+3.6}_{-4.6}$	851^{+382}_{-382}	$0.43^{+0.37}_{-0.39}$	$0.55^{+0.38}_{-0.48}$	$0.30^{+0.06}_{-0.06}$	$0.34^{+0.30}_{-0.20}$	–	–	34.6	23.9	(✓,✓)	952
A17-d15-p090	36.2	36.2	500	36.8	26.2	XPHM	cpnest	1000	$41.2^{+7.0}_{-5.8}$	$29.0^{+6.4}_{-5.4}$	818^{+215}_{-285}	$0.41^{+0.36}_{-0.35}$	$0.54^{+0.38}_{-0.42}$	$0.24^{+0.09}_{-0.08}$	$0.36^{+0.30}_{-0.23}$	–	–	39.5	29.7	(✓,✓)	1047
A17-d15-p090	44.3	44.3	625	34.7	24.7	XP	nessai	1000	$54.0^{+4.1}_{-4.9}$	$26.1^{+2.6}_{-3.1}$	824^{+202}_{-307}	–	–	–	–	–	–	34.0	23.2	(✓,✓)	802
A17-d15-p090	44.3	44.3	625	34.7	24.7	XP	nessai	1000	$50.0^{+6.3}_{-4.9}$	$37.3^{+5.2}_{-5.4}$	932^{+225}_{-325}	$0.54^{+0.32}_{-0.39}$	$0.56^{+0.37}_{-0.46}$	$0.27^{+0.07}_{-0.07}$	$0.43^{+0.29}_{-0.26}$	–	–	34.7	25.8	(✓,✓)	936
A17-d15-p090	52.1	52.1	750	33.0	23.5	XP	nessai	1000	$69.1^{+4.9}_{-3.9}$	$26.0^{+2.4}_{-2.0}$	844^{+203}_{-323}	–	–	–	–	–	–	33.8	24.2	(✓,✓)	817
A17-d15-p090	52.1	52.1	750	33.0	23.5	XP	nessai	1000	$59.1^{+7.1}_{-8.5}$	$36.5^{+9.1}_{-6.0}$	1230^{+269}_{-423}	$0.40^{+0.34}_{-0.32}$	$0.47^{+0.44}_{-0.42}$	$0.21^{+0.09}_{-0.10}$	$0.32^{+0.31}_{-0.21}$	–	–	32.2	24.3	(✓,✓)	759
A17-d12-e1	2.48	2.48	31.25	16.4	11.6	Pv2T	nessai	1000	$2.62^{+0.56}_{-0.18}$	$2.32^{+0.18}_{-0.29}$	61.0^{+14}_{-14}	$0.47^{+0.43}_{-0.33}$	$0.49^{+0.43}_{-0.42}$	$0.26^{+0.18}_{-0.19}$	$0.41^{+0.37}_{-0.28}$	$25.1^{+76.0}_{-23.0}$	$39.1^{+100.0}_{-35.4}$	16.9	11.1	(✓,✓)	177
A17-d12-e1	2.49	2.49	17.0	30.2	21.4	XP	nessai	1000	$3.28^{+0.75}_{-0.65}$	$1.94^{+0.49}_{-0.43}$	$30.3^{+7.0}_{-10.2}$	$0.60^{+0.31}_{-0.37}$	$0.63^{+0.31}_{-0.51}$	$0.30^{+0.15}_{-0.13}$	$0.49^{+0.28}_{-0.25}$	–	–	30.1	21.7	(✓,✓)	646
A17-d12-e1	2.48	2.48	31.25	16.4	11.6	XP	nessai	1000	$2.66^{+0.49}_{-0.26}$	$2.07^{+0.23}_{-0.35}$	$49.0^{+15.6}_{-21.2}$	–	–	–	–	–	–	16.5	11.9	(✓,✓)	174
A17-d12-e1	2.48	2.48	31.25	16.4	11.6	XP	nessai	1000	$3.32^{+2.24}_{-0.79}$	$1.88^{+0.52}_{-0.62}$	$54.5^{+14.5}_{-19.8}$	$0.68^{+0.27}_{-0.51}$	$0.52^{+0.42}_{-0.45}$	$0.29^{+0.24}_{-0.23}$	$0.52^{+0.34}_{-0.31}$	–	–	17.1	12.1	(✓,✓)	177
A17-d12-e1	4.93	4.93	62.5	24.6	17.4	F2	nessai	1000	$13.4^{+2.2}_{-2.2}$	$1.95^{+0.19}_{-0.14}$	118^{+44}_{-44}	$0.43^{+0.29}_{-0.04}$	$0.00^{+0.53}_{-0.52}$	$0.37^{+0.04}_{-0.04}$	–	$0.31^{+0.60}_{-0.28}$	205^{+593}_{-187}	23.4	18.1	(✓,✓)	376
A17-d12-e1	4.93	4.93	62.5	24.6	17.4	XP	nessai	1000	$4.98^{+0.65}_{-0.53}$	$4.33^{+0.28}_{-0.53}$	$81.8^{+16.4}_{-29.0}$	–	–	–	–	–	–	24.4	15.8	(✓,✓)	407
A17-d12-e1	4.93	4.93	62.5	24.6	17.4	XP	nessai	1000	$5.65^{+1.46}_{-0.30}$	$4.19^{+0.60}_{-0.82}$	117^{+22}_{-47}	$0.49^{+0.40}_{-0.39}$	$0.48^{+0.44}_{-0.42}$	$0.19^{+0.10}_{-0.10}$	$0.44^{+0.41}_{-0.29}$	–	–	24.8	15.6	(✓,✓)	409
A17-d12-e1	9.73	9.73	125	31.6	22.4	XP	nessai	1000	$9.63^{+1.04}_{-0.71}$	$8.54^{+0.89}_{-0.89}$	202^{+55}_{-55}	–	–	–	–	–	–	31.7	23.5	(✓,✓)	724
A17-d12-e1	9.73	9.73	125	31.6	22.4	XP	nessai	1000	$11.7^{+1.5}_{-1.8}$	$7.65^{+1.28}_{-0.89}$	178^{+64}_{-86}	$0.36^{+0.24}_{-0.20}$	$0.48^{+0.37}_{-0.40}$	$0.15^{+0.07}_{-0.07}$	$0.34^{+0.24}_{-0.17}$	–	–	32.9	24.0	(✓,✓)	729
A17-d12-e1	19.0	19.0	250	35.9	25.5	XP	nessai	1000	$19.8^{+2.1}_{-1.1}$	$17.3^{+1.1}_{-1.8}$	$87.8^{+10.8}_{-16.1}$	–	–	–	–	–	–	37.7	23.8	(✓,✓)	915
A17-d12-e1	19.0	19.0	250	35.9	25.5	XP	nessai	1000	$20.9^{+2.3}_{-1.9}$	$16.0^{+1.9}_{-1.7}$	180^{+47}_{-69}	$0.17^{+0.25}_{-0.15}$	$0.23^{+0.39}_{-0.21}$	$0.04^{+0.06}_{-0.05}$	$0.16^{+0.24}_{-0.13}$	–	–	36.6	22.8	(✓,✓)	914
A17-d12-e1	27.8	27.8	375	35.6	25.2	XP	nessai	1000	$29.5^{+3.3}_{-3.0}$	$22.7^{+2.7}_{-2.5}$	431^{+69}_{-117}	–	–	–	–	–	–	36.8	26.9	(✓,✓)	957
A17-d12-e1	27.8	27.8	375	35.6	25.2	XP	nessai	1000	$31.2^{+3.0}_{-3.9}$	$22.1^{+3.12}_{-2.01}$	422^{+70}_{-98}	$0.20^{+0.40}_{-0.18}$	$0.28^{+0.55}_{-0.25}$	$0.05^{+0.06}_{-0.05}$	$0.21^{+0.37}_{-0.16}$	–	–	32.1	21.6	(✓,✓)	955
A17-d12-e1	36.2	36.2	500	33.6	23.7	XPHM	dynesty	500	$35.8^{+4.8}_{-3.5}$	$27.8^{+4.4}_{-4.8}$	971^{+156}_{-307}	–	–	–	–	–	–	32.4	23.3	(✓,✓)	817
A17-d12-e1	36.2	36.2	500	33.6	23.7	XPHM	dynesty	1000	$37.1^{+4.1}_{-4.1}$	$27.2^{+3.9}_{-4.8}$	999^{+247}_{-204}	$0.21^{+0.43}_{-0.19}$	$0.31^{+0.56}_{-0.28}$	$0.04^{+0.07}_{-0.07}$	$0.26^{+0.36}_{-0.21}$	–	–	33.1	24.8	(✓,✓)	816
A17-d12-e1	36.2	36.2	500	33.6	23.7	XP	nessai	1000	$38.1^{+4.39}_{-5.02}$	$27.2^{+4.38}_{-3.14}$	826^{+306}_{-317}	–	–	–	–	–	–	34.0	24.5	(✓,✓)	820
A17-d12-e1	36.2	36.2	500	33.2	23.8	XP	nessai	500	$38.2^{+4.54}_{-4.86}$	$27.1^{+4.4}_{-3.3}$	901^{+168}_{-317}	$0.15^{+0.32}_{-0.13}$	$0.23^{+0.51}_{-0.20}$	$0.02^{+0.07}_{-0.06}$	$0.19^{+0.32}_{-0.15}$	–	–	33.1	24.8	(✓,✓)	817
A17-d12-e1	44.3	44.3	625	31.7	22.3	XP	nessai	1000	$54.6^{+4.6}_{-3.5}$	$33.2^{+3.5}_{-3.6}$	411^{+107}_{-227}	–	–	–	–	–	–	31.3	23.1	(✓,✓)	725
A17-d12-e1	44.3	44.3	625	31.7	22.3	XP	nessai	500	$53.1^{+5.4}_{-6.6}$	$35.0^{+7.0}_{-5.0}$	434^{+60}_{-119}	$0.13^{+0.27}_{-0.11}$	$0.23^{+0.42}_{-0.20}$	$0.03^{+0.08}_{-0.07}$	$0.16^{+0.27}_{-0.11}$	–	–	30.6	23.4	(✓,✓)	722
A17-d12-e1	52.1	52.1	750	30.0	21.2	XP	nessai	1000	$67.0^{+6.0}_{-8.6}$	$39.2^{+8.2}_{-4.8}$	449^{+47}_{-155}	–	–	–	–	–	–	29.9	21.6	(✓,✓)	652
A17-d12-e1	52.1	52.1	750	30.0	21.2	XP	nessai	500	$68.1^{+5.3}_{-6.2}$	$34.5^{+8.3}_{-6.5}$	455^{+40}_{-109}	$0.16^{+0.26}_{-0.14}$	$0.27^{+0.48}_{-0.24}$	$-0.05^{+0.11}_{-0.13}$	$0.17^{+0.22}_{-0.12}$	–	–	30.1	22.3	(✓,✓)	652

Chapter 9

Conclusions and outlook

In this thesis we have presented various examples of how numerical relativity can be used for modelling gravitational waves (GWs) coming from binary black holes (BHs) in modified theories of gravity and exotic compact objects. Whilst much of this thesis was driven by numerics, we have demonstrated in many instances how data analysis techniques can be employed in assessing the measurability of the new physics and translating the features of the simulated GWs into observable effects that may be constrained by gravitational-wave detectors. Our conclusions are therefore two-fold and we first discuss our numerical results.

At first, we focused on binary black holes in the so-called Einstein-scalar-Gauss-Bonnet (EsGB) theory, where using an order reduction scheme, we have simulated their dynamics to leading order. The resulting GW content contains an additional scalar polarisation that we have extracted numerically for various multipole modes. Next, we have moved to the study of boson stars (BSs) in general relativity. The numerical modelling of gravitational waves from binary BSs is a relatively new field, with constraint satisfying initial data being in particular challenging to obtain without a robust elliptic solver and a good initial guess. We have studied the issue of initial data in the context of head-on collisions of boson stars of various mass ratios and devised an improved initial data superposition that results in reduced constraint violations and avoids spurious effects that arise from conventional initial data superpositions used in the literature. By applying our new initial data, we have investigated the effects of the dephasing of boson stars, uncovering a sinusoidal dependence of the GW energy on the initial phase offset and even non-BH like signatures in the GW signals. Further, leveraging the power of our initial data construction and numerical set-up, we have performed the first long and high-precision evolutions of inspiralling boson stars. By focusing on equal-mass systems, we were able to extract GW signals of low eccentricity and high accuracy, comparable to the quality of BH simulations. Finally, we have performed a detailed study of BSs in massless and massive scalar-tensor theory, finding that BSs are prone to spontaneous scalarasation,

however less so when compared to neutron stars (NSs). By considering various bosonic potentials and couplings of the scalar-tensor theory, we have assessed the phenomenological features of spherically symmetric solutions and found that scalarised BS solutions are often energetically preferred (i.e. stable) over their GR counterparts.

From the data analysis perspective, we have devised a model-fit of our simulated scalar ringdown resulting from a binary BH merger in EsGB gravity and inferred its amplitudes using the Markov chain Monte Carlo sampling. We have also demonstrated the ability of a time-domain ringdown pipeline to utilise our model-fit in the search for a scalar polarised signal of EsGB theory. By considering binary BH sources of various total masses and at different luminosity distances, we have demonstrated that given current stringent constraints on the theory couplings, the scalar ringdown is highly unlikely to be detected with present or future GW detectors. Finally, we have also applied data analysis techniques to our high-precision BS signals, by mainly focusing on injections of our numerically simulated signals into the detector noise of present GW detectors. By utilising various binary BH and NS approximants, our aim was to investigate the biases of standard parameter estimation pipelines if a boson-star signal were present in the detector band. On the one hand, we find strong degenaracies between BH waveform approximants and BS signals in some regimes (however with incorrectly inferred source parameters), suggesting that BS mergers can truly be BH mimickers. On the other hand, GW signals from mergers forming a BS remnant pose modelling challenges to standard waveform approximants, thereby presenting an example of exotic physics poorly captured by current waveform templates.

The future avenues and opportunities are ample in this field. Although for EsGB gravity with a massless scalar field the prospects of detecting scalar polsarisation from binary black hole mergers of moderate mass ratios ($q \gtrsim 1/2$) are very slim, understanding the deviations in the inspiral, merger and ringdown of tensor polarised waves using full numerical simulations with backreaction is necessary to draw concrete conclusions on the possibility of distinguishing EsGB gravity from GR. As the effects from the coupling are the strongest for systems of lower masses (but high compactness), NSs are likely to be more suitable laboratories for looking for potential deviations. However, small deviations in the phase and amplitude of the tensor modes in EsGB gravity [518] are likely to be the main challenges leading to degeneracies with GR parameters and preventing us from confidently inferring a deviation from GR. Such degeneracies and small effects are expected to be bottlenecks for most modified theories of gravity inspired from effective field theory arguments and lacking observable smoking-gun effects. An important step in understanding this problem would be construction of several concrete sets of NR waveforms from a modified theory of gravity (or even exotic compact objects) that results in 'small' effects in the GW signals. For example,

mergers of compact BSs that form a BH post-merger, resulting in GW waveforms alike to BH signals, would be intriguing probes for assessing how well in principle present tests of GR perform, and if they can pick up small effects present in the numerical data. We leave this investigation to future work. Inspiral-merger-ringdown (IMR) consistency checks would be particularly interesting in this case, as these tests may uncover inconsistencies across the source parameters inferred from different parts of the signals and become indispensable in breaking potential degeneracies.

On the other hand, smoking-gun effects (such as GW signals from BS mergers forming a BS post-merger) can present more direct ways for testing our theories[1], especially in the high SNR regime. The study of matter fields (e.g. NSs or BSs) in *massive* scalar-tensor theory, which has not been as extensively constrained yet, provides another instance where we may expect to see smoking-gun effects in the form of scalar polarised GWs. Extending our study of BSs in this theory to numerical simulations of their collapse or binaries therefore represents intriguing directions for future work.

Numerical modelling of BSs in GR equally poses many possibilities for further explorations, such as extensions of our work to inspiralling unequal-mass and spinning progenitors. The development of an initial data solver for BSs would constitute an important step towards more accurate modelling of their dynamics and assessing the magnitude of numerical errors introduced by employing various initial data superpositions. Expanding the parameter space spanned by our NR waveforms and solving for initial data would be of paramount importance for constructing the first phenomenological model for exotic compact objects, which may be utilised in future analyses of GW signals, complementary to standard binary BH and NS approximants. Whilst BSs may not exist in nature, they are great proxies for studying new physics. As we have seen before, they offer a rich phenomenology, where the features of their GW signals may be reminiscent of binary BH signals in modified theories of gravity or present smoking-gun effects. Thanks to their amenability to numerical modelling, boson stars are great candidates for studying concrete deviations from GR and SM paradigm and informing future agnostic tests.

With future GW detectors and their increased sensitivity, we will enter the next phase of tests of GR and the BH paradigm and we will have to be prepared together as a community for the challenges that await us.

[1] However, there is no evidence for believing that deviations from GR or the BH paradigm should be smoking-gun effects, they may indeed be just small deviations.

References

[1] L. Smarr and J. W. York, Jr. Kinematical conditions in the construction of spacetime. *Phys. Rev. D*, 17:2529–2551, 1978. doi: 10.1103/PhysRevD.17.2529.

[2] P. Schmidt, I. W. Harry, and H. P. Pfeiffer. Numerical Relativity Injection Infrastructure. 2017. URL https://doi.org/10.48550/arXiv.1703.01076. arXiv.1703.01076 [gr-qc].

[3] U. Sperhake, V. Cardoso, C. D. Ott, E. Schnetter, and H. Witek. Extreme black hole simulations: collisions of unequal mass black holes and the point particle limit. *Phys. Rev. D*, 84:084038, 2011. doi: 10.1103/PhysRevD.84.084038. arXiv:1105.5391 [gr-qc].

[4] A. Einstein. The foundation of the general theory of relativity. *Annalen Phys.*, 49(7): 769–822, 1916. doi: 10.1002/andp.19163540702.

[5] J. Eisenstaedt. *The Curious History of Relativity : How Einstein's Theory of Gravity Was Lost and Found Again / Jean Eisenstaedt.* 2018. ISBN 9780691186757.

[6] F. W. Dyson, A. S. Eddington, and C. Davidson. A Determination of the Deflection of Light by the Sun's Gravitational Field, from Observations Made at the Total Eclipse of May 29, 1919. *Phil. Trans. Roy. Soc. Lond. A*, 220:291–333, 1920. doi: 10.1098/rsta.1920.0009.

[7] G. Gilmore and G. Tausch-Pebody. The 1919 eclipse results that verified general relativity and their later detractors: a story re-told. *Notes and Records: the Royal Society Journal of the History of Science*, 76(1):155–180, 2022. doi: 10.1098/rsnr.2020.0040. URL https://royalsocietypublishing.org/doi/abs/10.1098/rsnr.2020.0040.

[8] Irwin I. Shapiro. Fourth Test of General Relativity. *Phys. Rev. Lett.*, 13:789–791, 1964. doi: 10.1103/PhysRevLett.13.789.

[9] Irwin I. Shapiro, Gordon H. Pettengill, Michael E. Ash, Melvin L. Stone, William B. Smith, Richard P. Ingalls, and Richard A. Brockelman. Fourth Test of General Relativity: Preliminary Results. *Phys. Rev. Lett.*, 20:1265–1269, 1968. doi: 10.1103/PhysRevLett.20.1265.

[10] Suvodip Mukherjee, Benjamin D. Wandelt, and Joseph Silk. Probing the theory of gravity with gravitational lensing of gravitational waves and galaxy surveys. *Mon. Not. Roy. Astron. Soc.*, 494(2):1956–1970, 2020. doi: 10.1093/mnras/staa827.

[11] G. Damour, T.and Esposito-Farese. Testing gravity to second post Newtonian order: A Field theory approach. *Phys. Rev. D*, 53:5541–5578, 1996. doi: 10.1103/PhysRevD.53.5541.

[12] B. P. Abbott et al. Observation of Gravitational Waves from a Binary Black Hole Merger. *Phys. Rev. Lett.*, 116(6):061102, 2016. doi: 10.1103/PhysRevLett.116.061102.

[13] B. P. Abbott et al. Prospects for Observing and Localizing Gravitational-Wave Transients with Advanced LIGO, Advanced Virgo and KAGRA. *Living Rev. Rel.*, 21(1):3, 2018. doi: 10.1007/s41114-018-0012-9,10.1007/lrr-2016-1.

[14] R. Abbott et al. GWTC-3: Compact Binary Coalescences Observed by LIGO and Virgo during the Second Part of the Third Observing Run. *Phys. Rev. X*, 13(4):041039, 2023. doi: 10.1103/PhysRevX.13.041039.

[15] B. P. Abbott et al. Tests of General Relativity with GW170817. *Phys. Rev. Lett.*, 123 (1):011102, 2019. doi: 10.1103/PhysRevLett.123.011102.

[16] B.P. Abbott et al. Tests of General Relativity with the Binary Black Hole Signals from the LIGO-Virgo Catalog GWTC-1. *Phys. Rev. D*, 100(10):104036, 2019. doi: 10.1103/PhysRevD.100.104036.

[17] B. P. Abbott et al. Tests of general relativity with GW150914. *Phys. Rev. Lett.*, 116 (22):221101, 2016. doi: 10.1103/PhysRevLett.116.221101.

[18] R. Abbott et al. Tests of general relativity with binary black holes from the second LIGO-Virgo gravitational-wave transient catalog. *Phys. Rev. D*, 103(12):122002, 2021. doi: 10.1103/PhysRevD.103.122002.

[19] V. Cardoso and P. Pani. Testing the nature of dark compact objects: a status report. *Living Rev. Rel.*, 22(1):4, 2019. doi: 10.1007/s41114-019-0020-4.

[20] A. Shomer. A Pedagogical explanation for the non-renormalizability of gravity. 9 2007. URL https://doi.org/10.48550/arXiv.0709.3555. arXiv.0709.3555 [hep-th].

[21] G. Esposito. An Introduction to quantum gravity. 8 2011. URL https://doi.org/10.48550/arXiv.1108.3269. arXiv.1108.3269 [hep-th].

[22] M. Tegmark et al. Cosmological Constraints from the SDSS Luminous Red Galaxies. *Phys. Rev. D*, 74:123507, 2006. doi: 10.1103/PhysRevD.74.123507.

[23] A. G. Riess et al. Observational evidence from supernovae for an accelerating universe and a cosmological constant. *Astron. J.*, 116:1009–1038, 1998. doi: 10.1086/300499.

[24] P. Bull et al. Beyond ΛCDM: Problems, solutions, and the road ahead. *Phys. Dark Univ.*, 12:56–99, 2016. doi: 10.1016/j.dark.2016.02.001.

[25] B.P. Abbott et al. Multi-messenger Observations of a Binary Neutron Star Merger. *Astrophys. J. Lett.*, 848(2):L12, 2017. doi: 10.3847/2041-8213/aa91c9.

[26] Jose María Ezquiaga and Miguel Zumalacárregui. Dark Energy After GW170817: Dead Ends and the Road Ahead. *Phys. Rev. Lett.*, 119(25):251304, 2017. doi: 10.1103/PhysRevLett.119.251304.

[27] Jeremy Sakstein and Bhuvnesh Jain. Implications of the Neutron Star Merger GW170817 for Cosmological Scalar-Tensor Theories. *Phys. Rev. Lett.*, 119(25): 251303, 2017. doi: 10.1103/PhysRevLett.119.251303.

[28] S. E. Rugh and H. Zinkernagel. The Quantum vacuum and the cosmological constant problem. *Stud. Hist. Phil. Sci. B*, 33:663–705, 2002. doi: 10.1016/S1355-2198(02)00033-3.

[29] D. Lovelock. The Einstein tensor and its generalizations. *J. Math. Phys.*, 12:498–501, 1971. doi: 10.1063/1.1665613.

[30] T. Clifton, P. G. Ferreira, A. Padilla, and C. Skordis. Modified Gravity and Cosmology. *Phys. Rept.*, 513:1–189, 2012. doi: 10.1016/j.physrep.2012.01.001. arXiv:1106.2476 [astro-ph].

[31] E. Berti et al. Testing General Relativity with Present and Future Astrophysical Observations. *Class. Quant. Grav.*, 32:243001, 2015. doi: 10.1088/0264-9381/32/24/243001.

[32] C. Brans and R.H. Dicke. Mach's principle and a relativistic theory of gravitation. *Phys.Rev.*, 124:925–935, 1961. doi: 10.1103/PhysRev.124.925.

[33] P. G. Bergmann. Comments on the scalar tensor theory. *Int. J. Theor. Phys.*, 1:25–36, 1968. doi: 10.1007/BF00668828.

[34] G. W. Horndeski. Second-order scalar-tensor field equations in a four-dimensional space. *Int. J. Theor. Phys.*, 10:363–384, 1974. doi: 10.1007/BF01807638.

[35] M. A. Vasiliev. Consistent equation for interacting gauge fields of all spins in (3+1)-dimensions. *Phys. Lett. B*, 243:378–382, 1990. doi: 10.1016/0370-2693(90)91400-6.

[36] L. Heisenberg. Scalar-Vector-Tensor Gravity Theories. *JCAP*, 10:054, 2018. doi: 10.1088/1475-7516/2018/10/054.

[37] M. Ostrogradsky. Mémoires sur les équations différentielles, relatives au problème des isopérimètres. *Mem. Acad. St. Petersbourg*, 6(4):385–517, 1850.

[38] S. Nojiri and S.D. Odintsov. Introduction to modified gravity and gravitational alternative for dark energy. *eConf*, C0602061:06, 2006. doi: 10.1142/S0219887807001928.

[39] A. Starobinsky. Disappearing cosmological constant in f(R) gravity. *JETP Lett.*, 86: 157–163, 2007. doi: 10.1134/S0021364007150027.

[40] W. Hu and I. Sawicki. Models of f(R) Cosmic Acceleration that Evade Solar-System Tests. *Phys. Rev. D*, 76:064004, 2007. doi: 10.1103/PhysRevD.76.064004.

[41] S. A. Appleby and R. A. Battye. Do consistent $F(R)$ models mimic General Relativity plus Λ? *Phys. Lett. B*, 654:7–12, 2007. doi: 10.1016/j.physletb.2007.08.037.

[42] A. Starobinsky. A New Type of Isotropic Cosmological Models Without Singularity. *Phys. Lett. B*, 91:99–102, 1980. doi: 10.1016/0370-2693(80)90670-X.

[43] T. P. Sotiriou and V. Faraoni. f(R) Theories Of Gravity. *Rev. Mod. Phys.*, 82:451–497, 2010. doi: 10.1103/RevModPhys.82.451. arXiv:0805.1726 [gr-qc].

[44] R. Cayuso and L. Lehner. Nonlinear, noniterative treatment of EFT-motivated gravity. *Phys. Rev. D*, 102(8):084008, 2020. doi: 10.1103/PhysRevD.102.084008.

[45] G. Allwright and L. Lehner. Towards the nonlinear regime in extensions to GR: assessing possible options. *Class. Quant. Grav.*, 36(8):084001, 2019. doi: 10.1088/1361-6382/ab0ee1.

[46] Pau Figueras, Aaron Held, and Áron D. Kovács. Well-posed initial value formulation of general effective field theories of gravity. 7 2024.

[47] T. Kaluza. Zum Unitätsproblem der Physik. *Sitzungsber. Preuss. Akad. Wiss. Berlin (Math. Phys.)*, 1921:966–972, 1921.

[48] R. H. Brandenberger. Challenges for string gas cosmology. In *59th Yamada Conference on Inflating Horizon of Particle Astrophysics and Cosmology*, 9 2005.

[49] K. Akama. An Early Proposal of 'Brane World'. *Lect. Notes Phys.*, 176:267–271, 1982.

[50] S. Bahamonde, K. F. Dialektopoulos, C. Escamilla-Rivera, G. Farrugia, V. Gakis, M. Hendry, M. Hohmann, J. Levi Said, J. Mifsud, and E. Di Valentino. Teleparallel gravity: from theory to cosmology. *Rept. Prog. Phys.*, 86(2):026901, 2023. doi: 10.1088/1361-6633/ac9cef.

[51] P. Aschieri, M. Dimitrijevic, F. Meyer, and J. Wess. Noncommutative geometry and gravity. *Class. Quant. Grav.*, 23:1883–1912, 2006. doi: 10.1088/0264-9381/23/6/005.

[52] V. Faraoni and E. Gunzig. Einstein frame or Jordan frame? *Int. J. Theor. Phys.*, 38: 217–225, 1999. doi: 10.1023/A:1026645510351.

[53] M. Postma and M. Volponi. Equivalence of the Einstein and Jordan frames. *Phys. Rev. D*, 90(10):103516, 2014. doi: 10.1103/PhysRevD.90.103516.

[54] K. S. Stelle. Renormalization of Higher Derivative Quantum Gravity. *Phys. Rev. D*, 16:953–969, 1977. doi: 10.1103/PhysRevD.16.953.

[55] C. de Rham, J. Francfort, and J. Zhang. Black Hole Gravitational Waves in the Effective Field Theory of Gravity. *Phys. Rev. D*, 102(2):024079, 2020. doi: 10.1103/PhysRevD.102.024079.

[56] V. Cardoso, M. Kimura, A. Maselli, and L. Senatore. Black Holes in an Effective Field Theory Extension of General Relativity. *Phys. Rev. Lett.*, 121(25):251105, 2018. doi: 10.1103/PhysRevLett.121.251105.

[57] S. Endlich, V. Gorbenko, J. Huang, and L. Senatore. An effective formalism for testing extensions to General Relativity with gravitational waves. *JHEP*, 09:122, 2017. doi: 10.1007/JHEP09(2017)122.

[58] John F. Donoghue. General relativity as an effective field theory: The leading quantum corrections. *Phys. Rev. D*, 50:3874–3888, 1994. doi: 10.1103/PhysRevD.50.3874.

[59] S. Weinberg. Effective Field Theory for Inflation. *Phys. Rev. D*, 77:123541, 2008. doi: 10.1103/PhysRevD.77.123541.

[60] S. Alexander and N. Yunes. Chern-Simons Modified General Relativity. *Phys. Rept.*, 480:1–55, 2009. doi: 10.1016/j.physrep.2009.07.002.

[61] V. Cardoso, L. C. B. Crispino, C. F. B. Macedo, H. Okawa, and P. Pani. Light rings as observational evidence for event horizons: long-lived modes, ergoregions and nonlinear instabilities of ultracompact objects. *Phys. Rev. D*, 90(4):044069, 2014. doi: 10.1103/PhysRevD.90.044069.

[62] D. J. Kaup. Klein-Gordon Geon. *Phys. Rev.*, 172:1331–1342, 1968. doi: 10.1103/PhysRev.172.1331.

[63] R. Brito, V. Cardoso, C. A. R. Herdeiro, and E. Radu. Proca stars: Gravitating Bose–Einstein condensates of massive spin 1 particles. *Phys. Lett.*, B752:291–295, 2016. doi: 10.1016/j.physletb.2015.11.051.

[64] P. O. Mazur and E. Mottola. Gravitational vacuum condensate stars. *Proc. Nat. Acad. Sci.*, 101:9545–9550, 2004. doi: 10.1073/pnas.0402717101.

[65] P. O. Mazur and E. Mottola. Gravitational Condensate Stars: An Alternative to Black Holes. *Universe*, 9(2):88, 2023. doi: 10.3390/universe9020088.

[66] H. A. Buchdahl. General Relativistic Fluid Spheres. *Phys. Rev.*, 116:1027, 1959. doi: 10.1103/PhysRev.116.1027.

[67] A. Urbano and H. Veermäe. On gravitational echoes from ultracompact exotic stars. *JCAP*, 04:011, 2019. doi: 10.1088/1475-7516/2019/04/011.

[68] Celine Cattoen, Tristan Faber, and Matt Visser. Gravastars must have anisotropic pressures. *Class. Quant. Grav.*, 22:4189–4202, 2005. doi: 10.1088/0264-9381/22/20/002.

[69] Samir D. Mathur. The Fuzzball proposal for black holes: An Elementary review. *Fortsch. Phys.*, 53:793–827, 2005. doi: 10.1002/prop.200410203.

[70] Samir D. Mathur. GIAN course on the black hole information paradox. URL https://www.asc.ohio-state.edu/mathur.16/gian/gianintro.html.

[71] M. Bošković and E. Barausse. Soliton boson stars, Q-balls and the causal Buchdahl bound. 11 2021.

[72] J. B. Hartle. *Solar System Tests of General Relativity*, page 219–233. Cambridge University Press, 2021.

[73] W. Del Pozzo and A. Vecchio. On tests of general relativity with binary radio pulsars. *Mon. Not. Roy. Astron. Soc.*, 462(1):L21–L25, 2016. doi: 10.1093/mnrasl/slw116.

[74] Y. Choquet-Bruhat and J. W. York, Jr. Geometrical well posed systems for the Einstein equations. *Compt. Rend. Acad. Sci. Ser. I Math.*, 321(8):1089–1095, 1995.

[75] Y. Choquet-Bruhat and J. W. York, Jr. Well posed reduced systems for the Einstein equations. 6 1996.

[76] Á. D. Kovács and H. S. Reall. Well-posed formulation of Lovelock and Horndeski theories. *Phys. Rev. D*, 101(12):124003, 2020. doi: 10.1103/PhysRevD.101.124003.

[77] I. Davies and H. S. Reall. Well-posed formulation of Einstein-Maxwell effective field theory. *Phys. Rev. D*, 106(10):104019, 2022. doi: 10.1103/PhysRevD.106.104019.

[78] L. Aresté Saló, K. Clough, and P. Figueras. Well-posedness of the four-derivative scalar-tensor theory of gravity in singularity avoiding coordinates. 8 2022.

[79] O. Sarbach and M. Tiglio. Continuum and Discrete Initial-Boundary-Value Problems and Einstein's Field Equations. *Living Reviews in Relativity*, 15:9, 2012. arXiv:1203.6443 [gr-qc].

[80] R. Abbott et al. Tests of General Relativity with GWTC-3. 12 2021. URL https://doi.org/10.48550/arXiv.2112.06861. arXiv..2112.06861 [gr-qc].

[81] L. Blanchet, T. Damour, and B. R. Iyer. Gravitational waves from inspiralling compact binaries: Energy loss and waveform to second-post-Newtonian order. *Phys. Rev. D*, 51:5360–5386, 1995. doi: 10.1103/PhysRevD.51.5360,10.1103/PhysRevD.54.1860. gr-qc/9501029.

[82] L. Blanchet, T. Damour, and G. Schaefer. Postnewtonian hydrodynamics and postnewtonian gravitational wave generation for numerical relativity. *Mon. Not. Roy. Astron. Soc.*, 242:289–305, 1990.

[83] L. Barack and A. Pound. Self-force and radiation reaction in general relativity. *Rept. Prog. Phys.*, 82(1):016904, 2019. doi: 10.1088/1361-6633/aae552.

[84] Adam Pound, Barry Wardell, Niels Warburton, and Jeremy Miller. Second-Order Self-Force Calculation of Gravitational Binding Energy in Compact Binaries. *Phys. Rev. Lett.*, 124(2):021101, 2020. doi: 10.1103/PhysRevLett.124.021101.

[85] N. Yunes and X. Siemens. Gravitational-Wave Tests of General Relativity with Ground-Based Detectors and Pulsar Timing-Arrays. *Living Reviews in Relativity*, 16: 9, 2013. doi: 10.12942/lrr-2013-9. arXiv:1304.3473 [gr-qc].

[86] V. Varma, S.E. Field, M.A. Scheel, J. Blackman, L.E. Kidder, and H.P. Pfeiffer. Surrogate model of hybridized numerical relativity binary black hole waveforms. *Phys. Rev. D*, 99(6):064045, 2019. doi: 10.1103/PhysRevD.99.064045.

[87] S. G. Hahn and R. W. Lindquist. The two body problem in geometrodynamics. *Ann. Phys.*, 29:304–331, 1964.

[88] F. Pretorius. Evolution of Binary Black-Hole Spacetimes. *Phys. Rev. Lett.*, 95:121101, 2005. doi: 10.1103/PhysRevLett.95.121101. gr-qc/0507014.

[89] M. Campanelli, C. O. Lousto, P. Marronetti, and Y. Zlochower. Accurate evolutions of orbiting black-hole binaries without excision. *Phys. Rev. Lett.*, 96:111101, 2006. doi: 10.1103/PhysRevLett.96.111101.

[90] J.G. Baker, J. Centrella, D. Choi, M. Koppitz, and J. van Meter. Gravitational wave extraction from an inspiraling configuration of merging black holes. *Phys. Rev. Lett.*, 96:111102, 2006. doi: 10.1103/PhysRevLett.96.111102.

[91] M. Boyle et al. The SXS Collaboration catalog of binary black hole simulations. *Class. Quant. Grav.*, 36(19):195006, 2019. doi: 10.1088/1361-6382/ab34e2.

[92] W.E. East and J.L. Ripley. Evolution of Einstein-scalar-Gauss-Bonnet gravity using a modified harmonic formulation. *Phys. Rev. D*, 103(4):044040, 2021. doi: 10.1103/PhysRevD.103.044040.

[93] S. Ma, V. Varma, L.C. Stein, F. Foucart, M.D. Duez, L.E. Kidder, H.P. Pfeiffer, and M.A. Scheel. Numerical simulations of black hole-neutron star mergers in scalar-tensor gravity. *Phys. Rev. D*, 107(12):124051, 2023. doi: 10.1103/PhysRevD.107.124051.

[94] Z. Cao, P. Galaviz, and L. Li. Binary black hole mergers in $f(R)$ theory. *Phys. Rev. D*, 87(10):104029, 2013. doi: 10.1103/PhysRevD.87.104029.

[95] D. Doneva, L.G. Collodel, C.J. Krüger, and S.S. Yazadjiev. Spin-induced scalarization of Kerr black holes with a massive scalar field. *Eur. Phys. J. C*, 80(12):1205, 2020. doi: 10.1140/epjc/s10052-020-08765-3.

[96] S.L. Liebling and C. Palenzuela. Dynamical Boson Stars. *Living Rev. Rel.*, 15:6, 2012. doi: 10.12942/lrr-2012-6.

[97] L. Lehner and F. Pretorius. Black Strings, Low Viscosity Fluids, and Violation of Cosmic Censorship. *Phys. Rev. Lett.*, 105:101102, 2010. doi: 10.1103/PhysRevLett.105.101102. arXiv:1006.5960 [hep-th].

[98] P. Figueras, T. França, C. Gu, and T. Andrade. Endpoint of the Gregory-Laflamme instability of black strings revisited. *Phys. Rev. D*, 107(4):044028, 2023. doi: 10.1103/PhysRevD.107.044028.

[99] U. Sperhake, W. Cook, and D. Wang. The high-energy collision of black holes in higher dimensions. *Phys. Rev. D*, 100(10):104046, 2020. doi: 10.1103/PhysRevD.100.104046.

[100] W. G. Cook, U. Sperhake, E. Berti, and V. Cardoso. Black-hole head-on collisions in higher dimensions. *Phys. Rev. D*, 96(12):124006, 2017. doi: 10.1103/PhysRevD.96.124006.

[101] T. Helfer, J.C. Aurrekoetxea, and E.A. Lim. Cosmic String Loop Collapse in Full General Relativity. *Phys. Rev. D*, 99(10):104028, 2019. doi: 10.1103/PhysRevD.99.104028.

[102] K. Kiuchi, S. Fujibayashi, K. Hayashi, K. Kyutoku, Y. Sekiguchi, and M. Shibata. Self-Consistent Picture of the Mass Ejection from a One Second Long Binary Neutron Star Merger Leaving a Short-Lived Remnant in a General-Relativistic Neutrino-Radiation Magnetohydrodynamic Simulation. *Phys. Rev. Lett.*, 131(1):011401, 2023. doi: 10.1103/PhysRevLett.131.011401.

[103] R. Arnowitt, S. Deser, and C. W. Misner. The dynamics of general relativity. In L. Witten, editor, *Gravitation an introduction to current research*, pages 227–265. John Wiley, New York, 1962.

[104] J. W. York, Jr. Kinematics and dynamics of general relativity. In *Sources of Gravitational Radiation*, pages 83–126. Cambridge University Press, Cambridge, 1979.

[105] L. Lindblom, M. A. Scheel, L. E. Kidder, R. Owen, and O. Rinne. A New Generalized Harmonic Evolution System. *Class. Quant. Grav.*, 23:S447–S462, 2006. doi: 10.1088/0264-9381/23/16/S09. gr-qc/0512093.

[106] D. Garfinkle. Harmonic coordinate method for simulating generic singularities. *Phys. Rev. D*, 65:044029, 2002. doi: 10.1103/PhysRevD.65.044029. gr-qc/0110013.

[107] J. M. Bowen and J. W. York, Jr. Time-asymmetric initial data for black holes and black-hole collisions. *Phys. Rev. D*, 21:2047–2056, 1980. doi: 10.1103/PhysRevD.21.2047.

[108] E. Gourgoulhon. *3+1 Formalism and Bases of Numerical Relativity*. Springer, New York, 2012. gr-qc/0703035.

[109] C. Palenzuela. Introduction to Numerical Relativity. *Frontiers in Astronomy and Space Sciences*, 7:58, 2020. doi: 10.3389/fspas.2020.00058. URL https://www.frontiersin.org/article/10.3389/fspas.2020.00058.

[110] T. W. Baumgarte and S. L. Shapiro. On the Numerical integration of Einstein's field equations. *Phys. Rev. D*, 59:024007, 1998. doi: 10.1103/PhysRevD.59.024007. gr-qc/9810065.

[111] M. Shibata and T. Nakamura. Evolution of three-dimensional gravitational waves: Harmonic slicing case. *Phys. Rev. D*, 52:5428–5444, 1995. doi: 10.1103/PhysRevD.52.5428.

[112] T. Nakamura, K. Oohara, and Y. Kojima. General Relativistic Collapse To Black Holes And Gravitational Waves From Black Holes. *Prog. Theor. Phys. Suppl.*, 90:1–218, 1987. doi: 10.1143/PTPS.90.1.

[113] M. Alcubierre, G. Allen, B. Brügmann, E. Seidel, and W.-M. Suen. Towards an understanding of the stability properties of the 3+1 evolution equations in general relativity. *Phys. Rev. D*, 62:124011, 2000. doi: 10.1103/PhysRevD.62.124011. gr-qc/9908079.

[114] M. Alcubierre, G. Allen, B. Brügmann, T. Dramlitsch, J. A. Font, P. Papadopoulos, E. Seidel, N. Stergioulas, and R. Takahashi. Towards a stable numerical evolution of strongly gravitating systems in general relativity: The conformal treatments. *Phys. Rev. D*, 62:044034, 2000. doi: 10.1103/PhysRevD.62.044034. gr-qc/0003071.

[115] C. Bona, T. Ledvinka, C. Palenzuela, and M. Žáček. General-covariant evolution formalism for numerical relativity. *Phys. Rev. D*, 67:104005, 2003. doi: 10.1103/PhysRevD.67.104005. gr-qc/0302083.

[116] D. Alic, C. Bona-Casas, C. Bona, L. Rezzolla, and C. Palenzuela. Conformal and covariant formulation of the Z4 system with constraint-violation damping. *Phys. Rev. D*, 85:064040, 2012. doi: 10.1103/PhysRevD.85.064040. arXiv:1106.2254 [gr-qc].

[117] C. Gundlach, G. Calabrese, I. Hinder, and J. M. Martín-García. Constraint damping in the Z4 formulation and harmonic gauge. *Class. Quantum Grav.*, 22:3767–3773, 2005. doi: 10.1088/0264-9381/22/17/025.

[118] D. Alic, W. Kastaun, and L. Rezzolla. Constraint damping of the conformal and covariant formulation of the Z4 system in simulations of binary neutron stars. *Phys. Rev. D*, 88(6):064049, 2013. doi: 10.1103/PhysRevD.88.064049.

[119] C. Bona, J. Massó, E. Seidel, and J. Stela. A New Formalism for Numerical Relativity. *Phys. Rev. Lett.*, 75:600–603, 1995. doi: 10.1103/PhysRevLett.75.600. gr-qc/9412071.

[120] M. Alcubierre and B. Brügmann. Simple excision of a black hole in 3 + 1 numerical relativity. *Phys. Rev. D*, 63:104006, 2001. doi: 10.1103/PhysRevD.63.104006. gr-qc/0008067.

[121] J.C. Aurrekoetxea, K. Clough, and E.A. Lim. CTTK: a new method to solve the initial data constraints in numerical relativity. *Class. Quant. Grav.*, 40(7):075003, 2023. doi: 10.1088/1361-6382/acb883.

[122] H.P. Pfeiffer and J.W. York. Extrinsic curvature and the Einstein constraints. *Phys. Rev. D*, 67:044022, 2003. doi: 10.1103/PhysRevD.67.044022.

[123] W.E. East, F.M. Ramazanoglu, and F. Pretorius. Conformal Thin-Sandwich Solver for Generic Initial Data. *Phys. Rev. D*, 86:104053, 2012. doi: 10.1103/PhysRevD.86.104053.

[124] M. Alcubierre. *Introduction to 3+1 Numerical Relativity*. Oxford University Press, Oxford, 2008.

[125] S. Brandt and B. Brügmann. A Simple construction of initial data for multiple black holes. *Phys. Rev. Lett.*, 78:3606–3609, 1997. doi: 10.1103/PhysRevLett.78.3606. gr-qc/9703066.

[126] M. Ansorg, B. Brügmann, and W. Tichy. A single-domain spectral method for black hole puncture data. *Phys. Rev. D*, 70:064011, 2004. doi: 10.1103/PhysRevD.70.064011. gr-qc/0404056.

[127] R.J. Gleiser, C.O. Nicasio, R.H. Price, and J. Pullin. Evolving the Bowen-York initial data for spinning black holes. *Phys. Rev. D*, 57:3401–3407, 1998. doi: 10.1103/PhysRevD.57.3401.

[128] A. Garat and R.H. Price. Nonexistence of conformally flat slices of the Kerr space-time. *Phys. Rev. D*, 61:124011, 2000. doi: 10.1103/PhysRevD.61.124011.

[129] Adams M. et al. Tech. Report No. LBNL-6616E, 2019.

[130] K. Clough, P. Figueras, H. Finkel, M. Kunesch, E. A. Lim, and S. Tunyasuvunakool. GRChombo : Numerical Relativity with Adaptive Mesh Refinement. *Class. Quant. Grav.*, 32(24):245011, 2015. doi: 10.1088/0264-9381/32/24/245011. arXiv:1503.03436 [gr-qc].

[131] M.R. Radia. *Numerical modelling of gravitational wave sources in general relativity*. PhD thesis, Department of Applied Mathematics And Theoretical Physics, Cambridge U., University of Cambridge, 1 2023.

[132] T. França. *Binary Black Holes in Modified Gravity*. PhD thesis, Queen Mary, U. of London (main), 2023.

[133] M. Radia, U. Sperhake, E. Berti, and R. Croft. Anomalies in the gravitational recoil of eccentric black-hole mergers with unequal mass ratios. *Phys. Rev. D*, 103(10):104006, 1 2021. doi: 10.1103/PhysRevD.103.104006.

[134] L. Aresté Saló, K. Clough, and P. Figueras. Puncture gauge formulation for Einstein-Gauss-Bonnet gravity and four-derivative scalar-tensor theories in d+1 spacetime dimensions. *Phys. Rev. D*, 108(8):084018, 2023. doi: 10.1103/PhysRevD.108.084018.

[135] P. Figueras and T. França. Black hole binaries in cubic Horndeski theories. *Phys. Rev. D*, 105(12):124004, 2022. doi: 10.1103/PhysRevD.105.124004.

[136] R. Cayuso, P. Figueras, T. França, and L. Lehner. Modelling self-consistently beyond General Relativity. *Phys. Rev. Lett.*, 131:111403, 3 2023.

[137] J. Bamber, J.C. Aurrekoetxea, K. Clough, and P.G. Ferreira. Black hole merger simulations in wave dark matter environments. *Phys. Rev. D*, 107(2):024035, 2023. doi: 10.1103/PhysRevD.107.024035.

[138] L. Chung-Jukko, E.A. Lim, and D.J.E. Marsh. Multimessenger signals from compact axion star mergers. 3 2024. URL https://doi.org/10.48550/arXiv.2403.03774. arXiv.2403.03774 [astro-ph.CO].

[139] T. Helfer, E. A. Lim, M. A. G. Garcia, and M. A. Amin. Gravitational Wave Emission from Collisions of Compact Scalar Solitons. *Phys. Rev. D*, 99(4):044046, 2019. doi: 10.1103/PhysRevD.99.044046.

[140] T. Helfer, D. J. E. Marsh, K. Clough, M. Fairbairn, E. A. Lim, and R. Becerril. Black hole formation from axion stars. *JCAP*, 1703(03):055, 2017. doi: 10.1088/1475-7516/2017/03/055.

[141] T. Helfer, U. Sperhake, R. Croft, M. Radia, B.-X. Ge, and E. A. Lim. Malaise and remedy of binary boson-star initial data. *Class. Quant. Grav.*, 39(7):074001, 2022. doi: 10.1088/1361-6382/ac53b7.

[142] R. Croft, T. Helfer, B. Ge, M. Radia, T. Evstafyeva, E.A. Lim, U. Sperhake, and K. Clough. The gravitational afterglow of boson stars. *Class. Quant. Grav.*, 40(6):065001, 2023. doi: 10.1088/1361-6382/acace4.

[143] Tamara Evstafyeva, Ulrich Sperhake, Thomas Helfer, Robin Croft, Miren Radia, Bo-Xuan Ge, and Eugene A. Lim. Unequal-mass boson-star binaries: initial data and merger dynamics. *Class. Quant. Grav.*, 40(8):085009, 2023. doi: 10.1088/1361-6382/acc2a8.

[144] Z. Wang, T. Helfer, and M.A. Amin. General relativistic polarized Proca stars. *Phys. Rev. D*, 109(2):024019, 2024. doi: 10.1103/PhysRevD.109.024019.

[145] Z. Wang, T. Helfer, K. Clough, and E. Berti. Superradiance in massive vector fields with spatially varying mass. *Phys. Rev. D*, 105(10):104055, 2022. doi: 10.1103/PhysRevD.105.104055.

[146] Matthew Elley, Josu C. Aurrekoetxea, Katy Clough, Raphael Flauger, Panagiotis Giannadakis, and Eugene A. Lim. Robustness of inflation to kinetic inhomogeneities. 5 2024. URL https://doi.org/10.48550/arXiv.2405.03490. arXiv.2405.03490 [astro-ph.CO].

[147] J.C. Aurrekoetxea, K. Clough, and F. Muia. Oscillon formation during inflationary preheating with general relativity. *Phys. Rev. D*, 108(2):023501, 2023. doi: 10.1103/PhysRevD.108.023501.

[148] J.C. Aurrekoetxea, K. Clough, J. Bamber, and P.G. Ferreira. Effect of Wave Dark Matter on Equal Mass Black Hole Mergers. *Phys. Rev. Lett.*, 132(21):211401, 2024. doi: 10.1103/PhysRevLett.132.211401.

[149] A. Drew and E.P.S. Shellard. Radiation from Global Topological Strings using Adaptive Mesh Refinement: Methodology and Massless Modes. 10 2019.

[150] A. Drew and E. P. S. Shellard. Radiation from global topological strings using adaptive mesh refinement: Massive modes. *Phys. Rev. D*, 107(4):043507, 2023. doi: 10.1103/PhysRevD.107.043507.

[151] K. Clough, T. Dietrich, and S. Khan. What no one has seen before: gravitational waveforms from warp drive collapse. 6 2024. URL https://doi.org/10.48550/arXiv.2406.02466. arXiv.2406.02466 [gr-qc].

[152] K. Clough. *Scalar Fields in Numerical General Relativity: Inhomogeneous inflation and asymmetric bubble collapse*. PhD thesis, King's Coll. London, Cham, 2017.

[153] M. Radia, U. Sperhake, A. Drew, K. Clough, P. Figueras, E. A. Lim, J. L. Ripley, J. C. Aurrekoetxea, T. França, and T. Helfer. Lessons for adaptive mesh refinement in numerical relativity. *Class. Quant. Grav.*, 39(13):135006, 2022. doi: 10.1088/1361-6382/ac6fa9.

[154] L. Aresté Saló, S.E. Brady, K. Clough, D. Doneva, T. Evstafyeva, T. Figueras, P.and França, L. Rossi, and S. Yao. GRFolres: A code for modified gravity simulations in strong gravity. *J. Open Source Softw.*, 9:98, 2024. doi: 10.21105/joss.06369.

[155] J.C. Aurrekoetxea, J. Bamber, S.E. Brady, K. Clough, T. Helfer, J. Marsden, M. Radia, D. Traykova, and Z. Wang. GRDzhadzha: A code for evolving relativistic matter on analytic metric backgrounds. *J. Open Source Softw.*, 9(96):5956, 2024. doi: 10.21105/joss.05956.

[156] Allen, G. and Goodale, T. and Massó, J. and Seidel, E. The Cactus Computational Toolkit and Using Distributed Computing to Collide Neutron Stars. In *Proceedings of Eighth IEEE International Symposium on High Performance Distributed Computing, HPDC-8, Redondo Beach, 1999*, , 1999. IEEE Press.

[157] E. Schnetter, S. H. Hawley, and I. Hawke. Evolutions in 3-D numerical relativity using fixed mesh refinement. *Class. Quant. Grav.*, 21:1465–1488, 2004. doi: 10.1088/0264-9381/21/6/014. gr-qc/0310042.

[158] M. Berger and I. Rigoutsos. An algorithm for point clustering and grid generation. *IEEE Transactions on Systems, Man, and Cybernetics*, 21(5):1278–1286, 1991. doi: 10.1109/21.120081.

[159] O. Sarbach. Absorbing boundary conditions for Einstein's field equations. *J. Phys. Conf. Ser.*, 91:012005, 2007. doi: 10.1088/1742-6596/91/1/012005.

[160] L.T. Buchman, M.D. Duez, M. Morales, M.A. Scheel, T.M. Kostersitz, and A.M. Evans. Numerical Relativity Multimodal Waveforms using Absorbing Boundary Conditions. 2 2024. URL https://doi.org/10.48550/arXiv.2402.12544. arXiv.2402.12544 [gr-qc].

[161] M. Maggiore. *Gravitational Waves. Vol. 1: Theory and Experiments*. Oxford Master Series in Physics. Oxford University Press, 2007. ISBN 978-0-19-857074-5, 978-0-19-852074-0.

[162] M. Maggiore. *Gravitational Waves. Vol. 2: Astrophysics and Cosmology*. Oxford University Press, 3 2018. ISBN 978-0-19-857089-9.

[163] Clifford M. Will. *Gravity: Newtonian, Post-Newtonian, and General Relativistic*, pages 9–72. 2016. doi: 10.1007/978-3-319-20224-2_2.

[164] S.M. Carroll. *Spacetime and Geometry: An Introduction to General Relativity*. Cambridge University Press, 7 2019. ISBN 978-0-8053-8732-2, 978-1-108-48839-6, 978-1-108-77555-7. doi: 10.1017/9781108770385.

[165] D. M. Eardley, D. L. Lee, and A. P. Lightman. Gravitational-wave observations as a tool for testing relativistic gravity. *Phys. Rev. D*, 8:3308–3321, 1973. doi: 10.1103/PhysRevD.8.3308.

[166] M. Campanelli, B. J. Kelly, and C. O. Lousto. The Lazarus project. II. Space-like extraction with the quasi-Kinnersley tetrad. *Phys. Rev. D*, 73:064005, 2006. doi: 10.1103/PhysRevD.73.064005. gr-qc/0510122.

[167] R. Geroch. Asymptotic Structure of Space-Time. In *Symposium on Asymptotic Structure of Space-Time*, 1977. doi: 10.1007/978-1-4684-2343-3_1.

[168] I. Hinder, B. Wardell, and E. Bentivegna. Falloff of the Weyl scalars in binary black hole spacetimes. *Phys. Rev. D*, 84:024036, 2011. doi: 10.1103/PhysRevD.84.024036.

[169] E. T. Newman and R. Penrose. Note on the Bondi-Metzner-Sachs group. *J. Math. Phys.*, 7:863–870, 1966. doi: 10.1063/1.1931221.

[170] C. Reisswig and D. Pollney. Notes on the integration of numerical relativity waveforms. *Class. Quant. Grav.*, 28:195015, 2011. doi: 10.1088/0264-9381/28/19/195015. arXiv:1006.1632 [gr-qc].

[171] D. J. A. McKechan, C. Robinson, and B. S. Sathyaprakash. A tapering window for time-domain templates and simulated signals in the detection of gravitational waves from coalescing compact binaries. *Class. Quant. Grav.*, 27:084020, 2010. doi: 10.1088/0264-9381/27/8/084020.

[172] L. Santamaria *et al.* Matching post-newtonian and numerical relativity waveforms: systematic errors and a new phenomenological model for non-precessing black hole binaries. *Phys. Rev. D*, 82:064016, 2010. doi: 10.1103/PhysRevD.82.064016. arXiv:1005.3306.

[173] R. Abbott et al. Observation of Gravitational Waves from Two Neutron Star–Black Hole Coalescences. *Astrophys. J. Lett.*, 915(1):L5, 2021. doi: 10.3847/2041-8213/ac082e.

[174] Benjamin P Abbott et al. A guide to LIGO}textendashVirgo detector noise and extraction of transient gravitational-wave signals. *Class. Quant. Grav.*, 37(5):055002, 2020. doi: 10.1088/1361-6382/ab685e.

[175] T.T. Lyons, M.W. Regehr, and F.J. Raab. Shot Noise in Gravitational-Wave Detectors with Fabry Perot Arms. , 39(36):6761–6770, dec 2000. doi: 10.1364/AO.39.006761.

[176] M. Saleem et al. The science case for LIGO-India. *Class. Quant. Grav.*, 39(2):025004, 2022. doi: 10.1088/1361-6382/ac3b99.

[177] D. Reitze et al. Cosmic Explorer: The U.S. Contribution to Gravitational-Wave Astronomy beyond LIGO. *Bull. Am. Astron. Soc.*, 51(7):035, 2019.

[178] M. Evans et al. A Horizon Study for Cosmic Explorer: Science, Observatories, and Community. 9 2021.

[179] M. Punturo et al. The Einstein Telescope: A third-generation gravitational wave observatory. *Class. Quant. Grav.*, 27:194002, 2010. doi: 10.1088/0264-9381/27/19/194002.

[180] N. Afshordi et al. Waveform Modelling for the Laser Interferometer Space Antenna. 11 2023. URL https://doi.org/10.48550/arXiv.2311.01300. arXiv.2311.01300 [gr-qc].

[181] S. Babak, J. Gair, A. Sesana, E. Barausse, C.F. Sopuerta, C.P. L. Berry, E. Berti, P. Amaro-Seoane, A. Petiteau, and A. Klein. Science with the space-based interferometer LISA. V: Extreme mass-ratio inspirals. *Phys. Rev. D*, 95(10):103012, 2017. doi: 10.1103/PhysRevD.95.103012.

[182] N. Bartolo et al. Science with the space-based interferometer LISA. IV: Probing inflation with gravitational waves. *JCAP*, 12:026, 2016. doi: 10.1088/1475-7516/2016/12/026.

[183] H. Audley et al. LISA Pathfinder. In *28th International Symposium on Lepton Photon Interactions at High Energies*, pages 185–204, Singapur, 2020. WSP. doi: 10.1142/9789811207402_0013.

[184] S. Kawamura et al. Current status of space gravitational wave antenna DECIGO and B-DECIGO. *PTEP*, 2021(5):05A105, 2021. doi: 10.1093/ptep/ptab019.

[185] M. Isi, M. Pitkin, and A.J. Weinstein. Probing Dynamical Gravity with the Polarization of Continuous Gravitational Waves. *Phys. Rev. D*, 96(4):042001, 2017. doi: 10.1103/PhysRevD.96.042001.

[186] Maximiliano Isi and Alan J. Weinstein. Probing gravitational wave polarizations with signals from compact binary coalescences. 10 2017. URL https://doi.org/10.48550/arXiv.1710.03794. arXiv.1710.03794 [gr-qc].

[187] Y. Hagihara, N. Era, D. Iikawa, and H. Asada. Probing gravitational wave polarizations with Advanced LIGO, Advanced Virgo and KAGRA. *Phys. Rev. D*, 98(6):064035, 2018. doi: 10.1103/PhysRevD.98.064035.

[188] A. Nishizawa, A. Taruya, K. Hayama, S. Kawamura, and M. Sakagami. Probing non-tensorial polarizations of stochastic gravitational-wave backgrounds with ground-based laser interferometers. *Phys. Rev. D*, 79:082002, 2009. doi: 10.1103/PhysRevD.79.082002.

[189] M. Drago et al. Coherent WaveBurst, a pipeline for unmodeled gravitational-wave data analysis. 6 2020.

[190] S. Klimenko, I. Yakushin, A. Mercer, and Guenakh Mitselmakher. Coherent method for detection of gravitational wave bursts. *Class. Quant. Grav.*, 25:114029, 2008. doi: 10.1088/0264-9381/25/11/114029.

[191] Carl L. Rodriguez, Michael Zevin, Chris Pankow, Vasilliki Kalogera, and Frederic A. Rasio. Illuminating Black Hole Binary Formation Channels with Spins in Advanced LIGO. *Astrophys. J. Lett.*, 832(1):L2, 2016. doi: 10.3847/2041-8205/832/1/L2.

[192] S. Vitale, D. Gerosa, C. Haster, K. Chatziioannou, and A. Zimmerman. Impact of Bayesian Priors on the Characterization of Binary Black Hole Coalescences. *Phys. Rev. Lett.*, 119(25):251103, 2017. doi: 10.1103/PhysRevLett.119.251103.

[193] B. Farr et al. Parameter estimation on gravitational waves from neutron-star binaries with spinning components. *Astrophys. J.*, 825(2):116, 2016. doi: 10.3847/0004-637X/825/2/116.

[194] N. Metropolis, A.W. Rosenbluth, M.N. Rosenbluth, A.H. Teller, and E. Teller. Equation of State Calculations by Fast Computing Machines. *The Journal of Chemical Physics*, 21(6):1087–1092, 06 1953. ISSN 0021-9606. doi: 10.1063/1.1699114. URL https://doi.org/10.1063/1.1699114.

[195] J. Skilling. Nested Sampling. In Rainer Fischer, Roland Preuss, and Udo Von Toussaint, editors, *Bayesian Inference and Maximum Entropy Methods in Science and Engineering: 24th International Workshop on Bayesian Inference and Maximum*

Entropy Methods in Science and Engineering, volume 735 of *American Institute of Physics Conference Series*, pages 395–405, November 2004. doi: 10.1063/1.1835238.

[196] S. Sharma. Markov chain monte carlo methods for bayesian data analysis in astronomy. *Annual Review of Astronomy and Astrophysics*, 55(1):213–259, August 2017. ISSN 1545-4282. doi: 10.1146/annurev-astro-082214-122339. URL http://dx.doi.org/10.1146/annurev-astro-082214-122339.

[197] G. Ashton et al. Nested sampling for physical scientists. *Nature*, 2, 2022. doi: 10.1038/s43586-022-00121-x.

[198] J. Veitch et al. Parameter estimation for compact binaries with ground-based gravitational-wave observations using the LALInference software library. *Phys. Rev. D*, 91(4):042003, 2015. doi: 10.1103/PhysRevD.91.042003.

[199] G. Ashton et al. BILBY: A user-friendly Bayesian inference library for gravitational-wave astronomy. *Astrophys. J. Suppl.*, 241(2):27, 2019. doi: 10.3847/1538-4365/ab06fc.

[200] W. K. Hastings. Monte Carlo Sampling Methods Using Markov Chains and Their Applications. *Biometrika*, 57:97–109, 1970. doi: 10.1093/biomet/57.1.97.

[201] P.M. Goggans and Y. Chi. Using Thermodynamic Integration to Calculate the Posterior Probability in Bayesian Model Selection Problems. In Gary J. Erickson and Yuxiang Zhai, editors, *Bayesian Inference and Maximum Entropy Methods in Science and Engineering*, volume 707 of *American Institute of Physics Conference Series*, pages 59–66. AIP, April 2004. doi: 10.1063/1.1751356.

[202] Nial Friel and Jason Wyse. Estimating the evidence – a review. *Statistica Neerlandica*, 66(3):288–308, 2012. doi: https://doi.org/10.1111/j.1467-9574.2011.00515.x. URL https://onlinelibrary.wiley.com/doi/abs/10.1111/j.1467-9574.2011.00515.x.

[203] D. Foreman-Mackey, D. W. Hogg, D. Lang, and J. Goodman. Emcee: The MCMC Hammer. *PASP*, 125:306–312, 2013. doi: 10.1086/670067.

[204] G. Ashton and C. Talbot. Bilby-MCMC: an MCMC sampler for gravitational-wave inference. *Mon. Not. Roy. Astron. Soc.*, 507(2):2037–2051, 2021. doi: 10.1093/mnras/stab2236.

[205] W. D. Vousden, W. M. Farr, and I. Mandel. Dynamic temperature selection for parallel tempering in markov chain monte carlo simulations. *Monthly Notices of the Royal Astronomical Society*, 455(2):1919–1937, November 2015. ISSN 1365-2966. doi: 10.1093/mnras/stv2422. URL http://dx.doi.org/10.1093/mnras/stv2422.

[206] E. Higson, W. Handley, M. Hobson, and A. Lasenby. Dynamic nested sampling: an improved algorithm for parameter estimation and evidence calculation. *Statistics and Computing*, 29(5):891–913, December 2018. ISSN 1573-1375. doi: 10.1007/s11222-018-9844-0. URL http://dx.doi.org/10.1007/s11222-018-9844-0.

[207] J.S Speagle. Dynesty: a dynamic nested sampling package for estimating bayesian posteriors and evidences. *Monthly Notices of the Royal Astronomical Society*, 493 (3):3132–3158, February 2020. ISSN 1365-2966. doi: 10.1093/mnras/staa278. URL http://dx.doi.org/10.1093/mnras/staa278.

[208] W. Del Pozzo and J. Veitch. CPNest: Parallel nested sampling. Astrophysics Source Code Library, record ascl:2205.021, May 2022. URL https://ui.adsabs.harvard.edu/abs/2022ascl.soft05021D.

[209] F. Feroz, M. P. Hobson, and M. Bridges. MultiNest: an efficient and robust Bayesian inference tool for cosmology and particle physics. *Mon. Not. Roy. Astron. Soc.*, 398: 1601–1614, 2009. doi: 10.1111/j.1365-2966.2009.14548.x.

[210] D.J. Rezende and S. Mohamed. Variational inference with normalizing flows. In *Proceedings of the 32nd International Conference on International Conference on Machine Learning - Volume 37*, ICML'15, page 1530–1538. JMLR.org, 2015.

[211] E.G. Tabak and E. Vanden-Eijnden. Density estimation by dual ascent of the log-likelihood. *Communications in Mathematical Sciences*, 8(1):217 – 233, 2010.

[212] L. Dinh, D. Krueger, and Y. Bengio. Nice: Non-linear independent components estimation, 2015. URL https://doi.org/10.48550/arXiv.1410.8516. arXiv.1410.8516.

[213] M.J. Williams, J. Veitch, and C. Messenger. Nested sampling with normalizing flows for gravitational-wave inference. *Phys. Rev. D*, 103(10):103006, 2021. doi: 10.1103/PhysRevD.103.103006.

[214] M.J. Williams, J. Veitch, and C. Messenger. Importance nested sampling with normalising flows. *Mach. Learn. Sci. Tech.*, 4(3):035011, 2023. doi: 10.1088/2632-2153/acd5aa.

[215] K.W. Wong, M. Gabrié, and D. Foreman-Mackey. flowMC: Normalizing flow enhanced sampling package for probabilistic inference in JAX. *The Journal of Open Source Software*, 8(83):5021, March 2023. doi: 10.21105/joss.05021.

[216] M. Dax, S.R. Green, J. Gair, J.H. Macke, A. Buonanno, and B. Schölkopf. Real-Time Gravitational Wave Science with Neural Posterior Estimation. *Phys. Rev. Lett.*, 127 (24):241103, 2021. doi: 10.1103/PhysRevLett.127.241103.

[217] U. Bhardwaj, J. Alvey, B.K. Miller, S. Nissanke, and C. Weniger. Sequential simulation-based inference for gravitational wave signals. *Phys. Rev. D*, 108(4): 042004, 2023. doi: 10.1103/PhysRevD.108.042004.

[218] D. Brown, S. Fairhurst, B. Krishnan, R. A. Mercer, R. K. Kopparapu, K. Santamaria, and J. T. Whelan. Data formats for numerical relativity waves. 2007. arXiv:0709.0093 [gr-qc].

[219] T. Evstafyeva, M. Agathos, and J.L. Ripley. Measuring the ringdown scalar polarization of gravitational waves in Einstein-scalar-Gauss-Bonnet gravity. *Phys. Rev. D*, 107 (12):124010, 2023. doi: 10.1103/PhysRevD.107.124010.

[220] C.M. Will. The Confrontation between General Relativity and Experiment. *Living Rev. Rel.*, 17:4, 2014. doi: 10.12942/lrr-2014-4.

[221] M. Ishak. Testing General Relativity in Cosmology. *Living Rev. Rel.*, 22(1):1, 2019. doi: 10.1007/s41114-018-0017-4.

[222] J. Aasi et al. Advanced LIGO. *Class. Quant. Grav.*, 32:074001, 2015. doi: 10.1088/0264-9381/32/7/074001.

[223] F. Acernese et al. Advanced Virgo: a second-generation interferometric gravitational wave detector. *Class. Quant. Grav.*, 32(2):024001, 2015. doi: 10.1088/0264-9381/32/2/024001.

[224] N. Yunes, K. Yagi, and F. Pretorius. Theoretical Physics Implications of the Binary Black-Hole Mergers GW150914 and GW151226. *Phys. Rev. D*, 94(8):084002, 2016. doi: 10.1103/PhysRevD.94.084002.

[225] T. Baker, E. Bellini, P. G. Ferreira, M. Lagos, J. Noller, and I. Sawicki. Strong constraints on cosmological gravity from GW170817 and GRB 170817A. *Phys. Rev. Lett.*, 119(25):251301, 2017. doi: 10.1103/PhysRevLett.119.251301.

[226] Z. Lyu, N. Jiang, and K. Yagi. Constraints on Einstein-dilation-Gauss-Bonnet gravity from black hole-neutron star gravitational wave events. *Phys. Rev. D*, 105(6):064001, 2022. doi: 10.1103/PhysRevD.105.064001.

[227] S.E. Perkins, R. Nair, H.O. Silva, and N. Yunes. Improved gravitational-wave constraints on higher-order curvature theories of gravity. *Phys. Rev. D*, 104(2):024060, 2021. doi: 10.1103/PhysRevD.104.024060.

[228] M. Okounkova, W.M. Farr, M. Isi, and L.C. Stein. Constraining gravitational wave amplitude birefringence and Chern-Simons gravity with GWTC-2. *Phys. Rev. D*, 106 (4):044067, 2022. doi: 10.1103/PhysRevD.106.044067.

[229] Á. D. Kovács and H. S. Reall. Well-Posed Formulation of Scalar-Tensor Effective Field Theory. *Phys. Rev. Lett.*, 124(22):221101, 2020. doi: 10.1103/PhysRevLett.124.221101.

[230] D.J. Gross and J.H. Sloan. The Quartic Effective Action for the Heterotic String. *Nucl. Phys. B*, 291:41–89, 1987. doi: 10.1016/0550-3213(87)90465-2.

[231] B. Zwiebach. Curvature Squared Terms and String Theories. *Phys. Lett. B*, 156: 315–317, 1985. doi: 10.1016/0370-2693(85)91616-8.

[232] P.A. Cano and A. Ruipérez. String gravity in D=4. *Phys. Rev. D*, 105(4):044022, 2022. doi: 10.1103/PhysRevD.105.044022.

[233] P. Kanti, N. E. Mavromatos, J. Rizos, K. Tamvakis, and E. Winstanley. Dilatonic black holes in higher curvature string gravity. *Phys. Rev. D*, 54:5049–5058, 1996. doi: 10.1103/PhysRevD.54.5049.

[234] T.P. Sotiriou and S. Zhou. Black hole hair in generalized scalar-tensor gravity: An explicit example. *Phys. Rev. D*, 90:124063, 2014. doi: 10.1103/PhysRevD.90.124063.

[235] C.A.R. Herdeiro and E. Radu. Asymptotically flat black holes with scalar hair: A review. *Int. J. Mod. Phys. D*, 24(09):1542014, 2015. doi: 10.1142/S0218271815420146.

[236] K. Yagi, L.C. Stein, N. Yunes, and T. Tanaka. Post-Newtonian, Quasi-Circular Binary Inspirals in Quadratic Modified Gravity. *Phys. Rev. D*, 85:064022, 2012. doi: 10.1103/PhysRevD.85.064022. [Erratum: Phys.Rev.D 93, 029902 (2016)].

[237] T. Kobayashi. Horndeski theory and beyond: A review. *Rept. Prog. Phys.*, 82(8): 086901, 2019. doi: 10.1088/1361-6633/ab2429.

[238] W.E. East and F. Pretorius. Binary neutron star mergers in Einstein-scalar-Gauss-Bonnet gravity. *Phys. Rev. D*, 106(10):104055, 2022. doi: 10.1103/PhysRevD.106.104055.

[239] J.L. Ripley. Numerical relativity for Horndeski gravity. *Int. J. Mod. Phys. D*, 31(13): 2230017, 2022. doi: 10.1142/S0218271822300178.

[240] J.L. Ripley and F. Pretorius. Hyperbolicity in Spherical Gravitational Collapse in a Horndeski Theory. *Phys. Rev. D*, 99(8):084014, 2019. doi: 10.1103/PhysRevD.99.084014.

[241] J.L. Ripley and F. Pretorius. Gravitational collapse in Einstein dilaton-Gauss-Bonnet gravity. *Class. Quant. Grav.*, 36(13):134001, 2019. doi: 10.1088/1361-6382/ab2416.

[242] A.H.K. R., J.L. Ripley, and N. Yunes. Where and why does Einstein-Scalar-Gauss-Bonnet theory break down? 11 2022.

[243] E. Berti, K. Yagi, and N. Yunes. Extreme Gravity Tests with Gravitational Waves from Compact Binary Coalescences: (I) Inspiral-Merger. *Gen. Rel. Grav.*, 50(4):46, 2018. doi: 10.1007/s10714-018-2362-8.

[244] E. Berti, K. Yagi, H. Yang, and N. Yunes. Extreme Gravity Tests with Gravitational Waves from Compact Binary Coalescences: (II Ringdown. *Gen. Rel. Grav.*, 50(5):49, 2018. doi: 10.1007/s10714-018-2372-6.

[245] Banafsheh Shiralilou, Tanja Hinderer, Samaya Nissanke, Néstor Ortiz, and Helvi Witek. Nonlinear curvature effects in gravitational waves from inspiralling black hole binaries. *Phys. Rev. D*, 103(12):L121503, 2021. doi: 10.1103/PhysRevD.103.L121503.

[246] P. Wagle, Al. Saffer, and N. Yunes. Polarization modes of gravitational waves in quadratic gravity. *Physical Review D*, 100(12), Dec 2019. ISSN 2470-0029. doi: 10.1103/physrevd.100.124007. URL http://dx.doi.org/10.1103/PhysRevD.100.124007.

[247] M. Isi, A.J. Weinstein, C. Mead, and M. Pitkin. Detecting Beyond-Einstein Polarizations of Continuous Gravitational Waves. *Phys. Rev. D*, 91(8):082002, 2015. doi: 10.1103/PhysRevD.91.082002.

[248] Maximiliano Isi. Parametrizing gravitational-wave polarizations. *Class. Quant. Grav.*, 40(20):203001, 2023. doi: 10.1088/1361-6382/acf28c.

[249] M. Isi and L.C. Stein. Measuring stochastic gravitational-wave energy beyond general relativity. *Phys. Rev. D*, 98(10):104025, 2018. doi: 10.1103/PhysRevD.98.104025.

[250] A. Joyce, B. Jain, J. Khoury, and M. Trodden. Beyond the Cosmological Standard Model. *Phys. Rept.*, 568:1–98, 2015. doi: 10.1016/j.physrep.2014.12.002.

[251] T. Damour and G. Esposito-Farèse. Tensor-scalar gravity and binary-pulsar experiments. *Phys. Rev. D*, 54:1474–1491, Jul 1996. doi: 10.1103/PhysRevD.54.1474. URL https://link.aps.org/doi/10.1103/PhysRevD.54.1474.

[252] K. Chatziioannou, N. Yunes, and N. Cornish. Model-Independent Test of General Relativity: An Extended post-Einsteinian Framework with Complete Polarization Content. *Phys. Rev. D*, 86:022004, 2012. doi: 10.1103/PhysRevD.86.022004. [Erratum: Phys.Rev.D 95, 129901 (2017)].

[253] S. Hou, Y. Gong, and Y. Liu. Polarizations of gravitational waves in Horndeski theory. *The European Physical Journal C*, 78(5), May 2018. ISSN 1434-6052. doi: 10.1140/epjc/s10052-018-5869-y. URL http://dx.doi.org/10.1140/epjc/s10052-018-5869-y.

[254] D.L. Lee. Conservation laws, gravitational waves, and mass losses in the Dicke-Brans-Jordan theory of gravity. *Phys. Rev. D*, 10:2374–2383, Oct 1974. doi: 10.1103/PhysRevD.10.2374. URL https://link.aps.org/doi/10.1103/PhysRevD.10.2374.

[255] M. Okounkova, L. C. Stein, M. A. Scheel, and D. A. Hemberger. Numerical binary black hole mergers in dynamical Chern-Simons gravity: Scalar field. *Phys. Rev. D*, 96 (4):044020, 2017. doi: 10.1103/PhysRevD.96.044020.

[256] H. Witek, L. Gualtieri, P. Pani, and T. P. Sotiriou. Black holes and binary mergers in scalar Gauss-Bonnet gravity: scalar field dynamics. *Phys. Rev. D*, 99(6):064035, 2019. doi: 10.1103/PhysRevD.99.064035.

[257] S. W. Hawking. Black holes in the Brans-Dicke theory of gravitation. *Communications in Mathematical Physics*, 25(2):167 – 171, 1972. doi: cmp/1103857885. URL https://doi.org/.

[258] B. P. Abbott et al. Gravitational Waves and Gamma-rays from a Binary Neutron Star Merger: GW170817 and GRB 170817A. *Astrophys. J. Lett.*, 848(2):L13, 2017. doi: 10.3847/2041-8213/aa920c.

[259] M. Okounkova. Numerical relativity simulation of GW150914 in Einstein dilaton Gauss-Bonnet gravity. *Phys. Rev. D*, 102(8):084046, 2020. doi: 10.1103/PhysRevD.102.084046.

[260] M. Corman, J.L. Ripley, and W.E. East. Nonlinear studies of binary black hole mergers in Einstein-scalar-Gauss-Bonnet gravity. *Phys. Rev. D*, 107(2):024014, 2023. doi: 10.1103/PhysRevD.107.024014.

[261] J.L. Ripley and F. Pretorius. Scalarized Black Hole dynamics in Einstein dilaton Gauss-Bonnet Gravity. *Phys. Rev. D*, 101(4):044015, 2020. doi: 10.1103/PhysRevD.101.044015.

[262] L. Amendola, C. Charmousis, and S.C. Davis. Solar System Constraints on Gauss-Bonnet Mediated Dark Energy. *JCAP*, 10:004, 2007. doi: 10.1088/1475-7516/2007/10/004.

[263] R. D. Reasenberg, I. I. Shapiro, P. E. MacNeil, R. B. Goldstein, J. C. Breidenthal, J. P. Brenkle, D. L. Cain, T. M. Kaufman, T. A. Komarek, and A. I. Zygielbaum. Viking relativity experiment - Verification of signal retardation by solar gravity. *ApJl*, 234: L219–L221, December 1979. doi: 10.1086/183144.

[264] B. Bertotti, L. Iess, and P. Tortora. A test of general relativity using radio links with the Cassini spacecraft. *Nature*, 425:374–376, 2003. doi: 10.1038/nature01997.

[265] H. Wang, S. Tang, P. Li, M. Han, and Y. Fan. Tight constraints on Einstein-dilation-Gauss-Bonnet gravity from GW190412 and GW190814. *Phys. Rev. D*, 104(2):024015, 2021. doi: 10.1103/PhysRevD.104.024015.

[266] S. Tahura, K. Yagi, and Z. Carson. Testing gravity with gravitational waves from binary black hole mergers: Contributions from amplitude corrections. *Phys. Rev. D*, 100:104001, Nov 2019. doi: 10.1103/PhysRevD.100.104001. URL https://link.aps.org/doi/10.1103/PhysRevD.100.104001.

[267] G. Carullo. Enhancing modified gravity detection from gravitational-wave observations using the parametrized ringdown spin expansion coeffcients formalism. *Phys. Rev. D*, 103(12):124043, 2021. doi: 10.1103/PhysRevD.103.124043.

[268] H.O. Silva, A. Ghosh, and A. Buonanno. Black-hole ringdown as a probe of higher-curvature gravity theories. *Phys. Rev. D*, 107(4):044030, 2023. doi: 10.1103/PhysRevD.107.044030.

[269] K. Yagi. New constraint on scalar Gauss-Bonnet gravity and a possible explanation for the excess of the orbital decay rate in a low-mass X-ray binary. *Phys. Rev. D*, 86: 081504, Oct 2012. doi: 10.1103/PhysRevD.86.081504. URL https://link.aps.org/doi/10.1103/PhysRevD.86.081504.

[270] L.C. Stein and K. Yagi. Parametrizing and constraining scalar corrections to general relativity. *Phys. Rev. D*, 89:044026, Feb 2014. doi: 10.1103/PhysRevD.89.044026. URL https://link.aps.org/doi/10.1103/PhysRevD.89.044026.

[271] P. Pani, E. Berti, V. Cardoso, and J. Read. Compact stars in alternative theories of gravity: Einstein-Dilaton-Gauss-Bonnet gravity. *Phys. Rev. D*, 84:104035, Nov 2011. doi: 10.1103/PhysRevD.84.104035. URL https://link.aps.org/doi/10.1103/PhysRevD.84.104035.

[272] H. Witek, P. Gualtieri, L.and Pani, and T.P. Sotiriou. Black holes and binary mergers in scalar Gauss-Bonnet gravity: Scalar field dynamics. *Phys. Rev. D*, 99:064035, Mar 2019. doi: 10.1103/PhysRevD.99.064035. URL https://link.aps.org/doi/10.1103/PhysRevD.99.064035.

[273] T. Damour and G. Esposito-Farèse. Nonperturbative strong field effects in tensor - scalar theories of gravitation. *Phys. Rev. Lett.*, 70:2220–2223, 1993. doi: 10.1103/PhysRevLett.70.2220.

[274] S. S. Shapiro, J. L. Davis, D. E. Lebach, and J. S. Gregory. Measurement of the Solar Gravitational Deflection of Radio Waves using Geodetic Very-Long-Baseline Interferometry Data, 1979-1999. *Phys. Rev. Lett.*, 92:121101, 2004. doi: 10.1103/PhysRevLett.92.121101.

[275] Tomas A. et al. GRChombo: An adaptable numerical relativity code for fundamental physics. *Journal of Open Source Software*, 6(68):3703, 2021. doi: 10.21105/joss.03703. URL https://doi.org/10.21105/joss.03703.

[276] M. Radia, U. Sperhake, A. Drew, K. Clough, P. Figueras, E.A. Lim, J.L. Ripley, J.C. Aurrekoetxea, T. França, and T. Helfer. Lessons for adaptive mesh refinement in numerical relativity. *Class. Quant. Grav.*, 39(13):135006, 2022. doi: 10.1088/1361-6382/ac6fa9.

[277] T.W. Baumgarte and S.L. Shapiro. On the numerical integration of Einstein's field equations. *Phys. Rev. D*, 59:024007, 1998. doi: 10.1103/PhysRevD.59.024007.

[278] A. H. Mroue, H. P. Pfeiffer, L. E. Kidder, and S. A. Teukolsky. Measuring orbital eccentricity and periastron advance in quasi-circular black hole simulations. *Phys. Rev. D*, 82:124016, 2010. doi: 10.1103/PhysRevD.82.124016. arXiv:1004.4697 [gr-qc].

[279] E. Newman and R. Penrose. An Approach to gravitational radiation by a method of spin coefficients. *J. Math. Phys.*, 3:566–578, 1962. doi: 10.1063/1.1724257.

[280] N. T. Bishop and L. Rezzolla. Extraction of gravitational waves in numerical relativity. *Living Reviews in Relativity*, 20(1):1, 2016. doi: 10.1007/s41114-016-0001-9. arXiv:1606.02532 [gr-qc].

[281] B. Bruegmann, J.A. Gonzalez, M. Hannam, S. Husa, U. Sperhake, and W. Tichy. Calibration of Moving Puncture Simulations. *Phys. Rev. D*, 77:024027, 2008. doi: 10.1103/PhysRevD.77.024027.

[282] Y. Wiaux, L. Jacques, and P. Vandergheynst. Fast spin ± 2 spherical harmonics transforms. *J. Comput. Phys.*, 226:2359–2371, 2007. doi: 10.1016/j.jcp.2007.07.005.

[283] Helvi Witek, Vitor Cardoso, Carlos Herdeiro, Andrea Nerozzi, Ulrich Sperhake, and Miguel Zilhao. Black holes in a box: Towards the numerical evolution of black holes in AdS. *Phys. Rev. D*, 82:104037, 2010. doi: 10.1103/PhysRevD.82.104037.

[284] M. Campanelli and C.O. Lousto. Second order gauge invariant gravitational perturbations of a Kerr black hole. *Phys. Rev. D*, 59:124022, May 1999. doi: 10.1103/PhysRevD.59.124022. URL https://link.aps.org/doi/10.1103/PhysRevD.59.124022.

[285] C.O. Lousto and Y. Zlochower. Practical formula for the radiated angular momentum. *Phys. Rev. D*, 76:041502, Aug 2007. doi: 10.1103/PhysRevD.76.041502. URL https://link.aps.org/doi/10.1103/PhysRevD.76.041502.

[286] B. Shiralilou, T. Hinderer, S. Nissanke, N. Ortiz, and H. Witek. Post-Newtonian Gravitational and Scalar Waves in Scalar-Gauss-Bonnet Gravity. 5 2021.

[287] E. Berti, V. Cardoso, J. A. González, U. Sperhake, M. D. Hannam, S. Husa, and B. Brügmann. Inspiral, merger and ringdown of unequal mass black hole binaries: a multipolar analysis. *Phys. Rev. D*, 76:064034, 2007. doi: 10.1103/PhysRevD.76.064034. gr-qc/0703053.

[288] W.H. Press. Long Wave Trains of Gravitational Waves from a Vibrating Black Hole. *Astrophys. J. Lett.*, 170:L105–L108, 1971. doi: 10.1086/180849.

[289] E. Berti, V. Cardoso, and A. O. Starinets. Quasinormal modes of black holes and black branes. *Class. Quantum Grav.*, 26:163001, 2009. doi: 10.1088/0264-9381/26/16/163001. arXiv:0905.2975 [gr-qc].

[290] S.A. Teukolsky. Perturbations of a rotating black hole. 1. Fundamental equations for gravitational electromagnetic and neutrino field perturbations. *Astrophys. J.*, 185:635–647, 1973. doi: 10.1086/152444.

[291] R. A. Konoplya and A. F. Zinhailo. Quasinormal modes, stability and shadows of a black hole in the 4D Einstein–Gauss–Bonnet gravity. *Eur. Phys. J. C*, 80(11):1049, 2020. doi: 10.1140/epjc/s10052-020-08639-8.

[292] A. Bryant, H.O. Silva, K. Yagi, and K. Glampedakis. Eikonal quasinormal modes of black holes beyond general relativity. III. Scalar Gauss-Bonnet gravity. *Phys. Rev. D*, 104(4):044051, 2021. doi: 10.1103/PhysRevD.104.044051.

[293] L. Pierini and L. Gualtieri. Quasinormal modes of rotating black holes in Einstein-dilaton Gauss-Bonnet gravity: The first order in rotation. *Physical Review D*, 103 (12), Jun 2021. ISSN 2470-0029. doi: 10.1103/physrevd.103.124017. URL http://dx.doi.org/10.1103/PhysRevD.103.124017.

[294] Lorenzo Pierini and Leonardo Gualtieri. Quasi-normal modes of rotating black holes in Einstein-dilaton Gauss-Bonnet gravity: The second order in rotation. 7 2022.

[295] D. Li, P. Wagle, Y. Chen, and N. Yunes. Perturbations of spinning black holes beyond General Relativity: Modified Teukolsky equation. 6 2022.

[296] M. Okounkova, L.C. Stein, M.A. Scheel, and S.A. Teukolsky. Numerical binary black hole collisions in dynamical Chern-Simons gravity. *Phys. Rev. D*, 100(10):104026, 2019. doi: 10.1103/PhysRevD.100.104026.

[297] L.C. Stein. Qnm: A Python package for calculating Kerr quasinormal modes, separation constants, and spherical-spheroidal mixing coefficients. *J. Open Source Softw.*, 4 (42):1683, 2019. doi: 10.21105/joss.01683.

[298] S. Bhagwat, M. Okounkova, S.W. Ballmer, D.A. Brown, M. Giesler, M.A. Scheel, and S.A. Teukolsky. On choosing the start time of binary black hole ringdowns. *Phys. Rev. D*, 97(10):104065, 2018. doi: 10.1103/PhysRevD.97.104065.

[299] C.D. Capano, M. Cabero, J. Westerweck, J. Abedi, S. Kastha, A.H. Nitz, Y. Wang, A.B. Nielsen, and B. Krishnan. Observation of a multimode quasi-normal spectrum from a perturbed black hole. 5 2021.

[300] D. London, L.and Shoemaker and J. Healy. Modeling ringdown: Beyond the fundamental quasinormal modes. *Phys. Rev. D*, 90(12):124032, 2014. doi: 10.1103/PhysRevD.90.124032. [Erratum: Phys.Rev.D 94, 069902 (2016)].

[301] M. Giesler, M. Isi, M.A. Scheel, and S. Teukolsky. Black Hole Ringdown: The Importance of Overtones. *Phys. Rev. X*, 9(4):041060, 2019. doi: 10.1103/PhysRevX.9.041060.

[302] X. Jiménez Forteza, S. Bhagwat, P. Pani, and V. Ferrari. Spectroscopy of binary black hole ringdown using overtones and angular modes. *Phys. Rev. D*, 102(4):044053, 2020. doi: 10.1103/PhysRevD.102.044053.

[303] L. Magaña Zertuche et al. High Precision Ringdown Modeling: Multimode Fits and BMS Frames. *Phys. Rev. D*, 105:104015, 2022. doi: 10.1103/PhysRevD.105.104015.

[304] Maximiliano Isi and Will M. Farr. Analyzing black-hole ringdowns. 7 2021. URL https://doi.org/10.48550/arXiv.2107.05609. arXiv.2107.05609 [gr-qc].

[305] R. Cotesta, G. Carullo, E. Berti, and V. Cardoso. Analysis of Ringdown Overtones in GW150914. *Phys. Rev. Lett.*, 129(11):111102, 2022. doi: 10.1103/PhysRevLett.129.111102.

[306] Mark Ho-Yeuk Cheung et al. Nonlinear Effects in Black Hole Ringdown. *Phys. Rev. Lett.*, 130(8):081401, 2023. doi: 10.1103/PhysRevLett.130.081401.

[307] Keefe Mitman et al. Nonlinearities in Black Hole Ringdowns. *Phys. Rev. Lett.*, 130 (8):081402, 2023. doi: 10.1103/PhysRevLett.130.081402.

[308] J. Aasi et al. Advanced LIGO. *Class. Quant. Grav.*, 32:074001, 2015. doi: 10.1088/0264-9381/32/7/074001.

[309] B. P. Abbott et al. Prospects for observing and localizing gravitational-wave transients with Advanced LIGO, Advanced Virgo and KAGRA. *Living Rev. Rel.*, 21(1):3, 2018. doi: 10.1007/s41114-020-00026-9.

[310] M. Punturo et al. The Einstein Telescope: A third-generation gravitational wave observatory. *Class. Quant. Grav.*, 27:194002, 2010. doi: 10.1088/0264-9381/27/19/194002.

[311] S. Hild et al. Sensitivity Studies for Third-Generation Gravitational Wave Observatories. *Class. Quant. Grav.*, 28:094013, 2011. doi: 10.1088/0264-9381/28/9/094013.

[312] B.P. Abbott et al. Search for intermediate mass black hole binaries in the first observing run of Advanced 'LIGO. *Phys. Rev. D*, 96(2):022001, 2017. doi: 10.1103/PhysRevD.96.022001.

[313] F. Iacovelli, M. Mancarella, S. Foffa, and M. Maggiore. Forecasting the detection capabilities of third-generation gravitational-wave detectors using `GWFAST`. 7 2022.

[314] B. P. Abbott and et.al. GW151226:Observation of gravitational waves from a 22-solar-mass binary black hole coalescence. *Phys. Rev. Lett.*, 116:241103, Jun 2016. doi: 10.1103/PhysRevLett.116.241103. URL https://link.aps.org/doi/10.1103/PhysRevLett.116.241103.

[315] R. Abbott et al. GWTC-2: Compact Binary Coalescences Observed by LIGO and Virgo During the First Half of the Third Observing Run. *Phys. Rev. X*, 11:021053, 2021. doi: 10.1103/PhysRevX.11.021053.

[316] G. Carullo, W. Del Pozzo, and J. Veitch. Observational Black Hole Spectroscopy: A time-domain multimode analysis of GW150914. *Phys. Rev. D*, 99(12):123029, 2019. doi: 10.1103/PhysRevD.99.123029. [Erratum: Phys.Rev.D 100, 089903 (2019)].

[317] M. Isi, M. Giesler, W.M. Farr, M.A. Scheel, and S.A. Teukolsky. Testing the no-hair theorem with GW150914. *Phys. Rev. Lett.*, 123(11):111102, 2019. doi: 10.1103/PhysRevLett.123.111102.

[318] LIGO Scientific Collaboration. LIGO Algorithm Library - LALSuite. free software (GPL), 2018.

[319] S. Borhanian and B. S. Sathyaprakash. Listening to the Universe with Next Generation Ground-Based Gravitational-Wave Detectors. 2 2022.

[320] A. Zimmerman, C. Haster, and K. Chatziioannou. On combining information from multiple gravitational wave sources. *Phys. Rev. D*, 99:124044, Jun 2019. doi: 10.1103/PhysRevD.99.124044. URL https://link.aps.org/doi/10.1103/PhysRevD.99.124044.

[321] Pau Amaro-Seoane et al. Laser Interferometer Space Antenna. 2 2017. URL https://doi.org/10.48550/arXiv.1702.00786. arXiv.1702.00786 [astro-ph.IM].

[322] R. Benkel, T.P. Sotiriou, and H. Witek. Dynamical scalar hair formation around a Schwarzschild black hole. *Phys. Rev. D*, 94(12):121503, 2016. doi: 10.1103/PhysRevD.94.121503.

[323] H.O. Silva, H. Witek, M. Elley, and N. Yunes. Dynamical Descalarization in Binary Black Hole Mergers. *Phys. Rev. Lett.*, 127(3):031101, 2021. doi: 10.1103/PhysRevLett.127.031101.

[324] I. Kamaretsos, M. Hannam, and B. Sathyaprakash. Is black-hole ringdown a memory of its progenitor? *Phys. Rev. Lett.*, 109:141102, 2012. doi: 10.1103/PhysRevLett.109.141102.

[325] L. T. London. Modeling ringdown. II. Aligned-spin binary black holes, implications for data analysis and fundamental theory. *Phys. Rev. D*, 102(8):084052, 2020. doi: 10.1103/PhysRevD.102.084052.

[326] M. A. Amin, I. Banik, C. Negreanu, and I-S. Yang. Ultrarelativistic oscillon collisions. *Phys. Rev. D*, 90(8):085024, 2014. doi: 10.1103/PhysRevD.90.085024.

[327] M. A. Amin, R. Easther, H. Finkel, R. Flauger, and M. P. Hertzberg. Oscillons After Inflation. *Phys. Rev. Lett.*, 108:241302, 2012. doi: 10.1103/PhysRevLett.108.241302.

[328] M. A. Amin, R. Easther, and H. Finkel. Inflaton Fragmentation and Oscillon Formation in Three Dimensions. *JCAP*, 12:001, 2010. doi: 10.1088/1475-7516/2010/12/001.

[329] S. Borsanyi, M. Dierigl, Z. Fodor, S. D. Katz, S. W. Mages, D. Nogradi, J. Redondo, A. Ringwald, and K. K. Szabo. Axion cosmology, lattice QCD and the dilute instanton gas. *Phys. Lett. B*, 752:175–181, 2016. doi: 10.1016/j.physletb.2015.11.020.

[330] D. J. E. Marsh and A.-R. Pop. Axion dark matter, solitons and the cusp–core problem. *Mon. Not. Roy. Astron. Soc.*, 451(3):2479–2492, 2015. doi: 10.1093/mnras/stv1050. arXiv:1502.03456 [astro-ph].

[331] P. Svrcek and E. Witten. Axions In String Theory. *JHEP*, 06:051, 2006. doi: 10.1088/1126-6708/2006/06/051.

[332] F. E. Schunck and E. W. Mielke. General relativistic boson stars. *Class. Quant. Grav.*, 20:R301–R356, 2003. doi: 10.1088/0264-9381/20/20/201.

[333] D. J. E. Marsh. Axion Cosmology. *Phys. Rept.*, 643:1–79, 2016. doi: 10.1016/j.physrep.2016.06.005.

[334] F. Di Giovanni, D. Guerra, S. Albanesi, M. Miravet-Tenés, and D. Tseneklidou. Fermion-axion stars: static solutions and dynamical stability. 7 2022.

[335] E. Seidel and W.-M. Suen. Formation of solitonic stars through gravitational cooling. *Phys. Rev. Lett.*, 72:2516–2519, 1994. doi: 10.1103/PhysRevLett.72.2516. gr-qc/9309015.

[336] D. G. Levkov, A. G. Panin, and I. I. Tkachev. Gravitational Bose-Einstein condensation in the kinetic regime. *Phys. Rev. Lett.*, 121(15):151301, 2018. doi: 10.1103/PhysRevLett.121.151301.

[337] Jiajun Chen, Xiaolong Du, Erik W. Lentz, David J. E. Marsh, and Jens C. Niemeyer. New insights into the formation and growth of boson stars in dark matter halos. *Phys. Rev. D*, 104(8):083022, 2021. doi: 10.1103/PhysRevD.104.083022.

[338] Jan Veltmaat, Jens C. Niemeyer, and Bodo Schwabe. Formation and structure of ultralight bosonic dark matter halos. *Phys. Rev. D*, 98(4):043509, 2018. doi: 10.1103/PhysRevD.98.043509.

[339] C. J. Hogan and M. J. Rees. AXION MINICLUSTERS. *Phys. Lett. B*, 205:228–230, 1988. doi: 10.1016/0370-2693(88)91655-3.

[340] I. S. Shklovsky. On the nature of the source of X-ray emission of Sco XR-1. *Astrophys. J.*, 148:L1–L4, 1967.

[341] Harvey B. Richer et al. White dwarfs in globular clusters: hst observations of m4. *Astrophys. J.*, 484:741–760, 1997. doi: 10.1086/304379.

[342] V. Cardoso, E. Franzin, and P. Pani. Is the gravitational-wave ringdown a probe of the event horizon? *Phys. Rev. Lett.*, 116(17):171101, 2016. doi: 10.1103/PhysRevLett.117.089902,10.1103/PhysRevLett.116.171101. [Erratum: Phys. Rev. Lett.117,no.8,089902(2016)].

[343] E. Maggio, P. Pani, and G. Raposo. Testing the nature of dark compact objects with gravitational waves. 5 2021. doi: 10.1007/978-981-15-4702-7_29-1.

[344] N. Sennett, T. Hinderer, J. Steinhoff, A. Buonanno, and S. Ossokine. Distinguishing Boson Stars from Black Holes and Neutron Stars from Tidal Interactions in Inspiraling Binary Systems. *Phys. Rev. D*, 96(2):024002, 2017. doi: 10.1103/PhysRevD.96.024002.

[345] C.A.R. Herdeiro, G. Panotopoulos, and E. Radu. Tidal Love numbers of Proca stars. *JCAP*, 08:029, 2020. doi: 10.1088/1475-7516/2020/08/029.

[346] N. Siemonsen and W. E. East. Binary boson stars: Merger dynamics and formation of rotating remnant stars. *Phys. Rev. D*, 107(12):124018, 2023. doi: 10.1103/PhysRevD.107.124018.

[347] C. Adam, J. Castelo, A. García Martín-Caro, M. Huidobro, R. Vázquez, and A. Wereszczynski. Universal relations for rotating boson stars. *Phys. Rev. D*, 106(12):123022, 2022. doi: 10.1103/PhysRevD.106.123022.

[348] E.W. Mielke and F.E. Schunck. Boson stars: Alternatives to primordial black holes? *Nucl. Phys. B*, 564:185–203, 2000. doi: 10.1016/S0550-3213(99)00492-7.

[349] D.F. Torres, S. Capozziello, and G. Lambiase. Supermassive boson star at the galactic center? *Phys. Rev. D*, 62:104012, Oct 2000. doi: 10.1103/PhysRevD.62.104012. URL https://link.aps.org/doi/10.1103/PhysRevD.62.104012.

[350] V. Cardoso and P. Pani. Tests for the existence of black holes through gravitational wave echoes. *Nature Astron.*, 1(9):586–591, 2017. doi: 10.1038/s41550-017-0225-y.

[351] J. C. Bustillo, N. Sanchis-Gual, A. Torres-Forné, J. A. Font, A. Vajpeyi, R. Smith, C. Herdeiro, E. Radu, and S. H. W. Leong. GW190521 as a Merger of Proca Stars: A Potential New Vector Boson of 8.7×10^{-13} eV. *Phys. Rev. Lett.*, 126(8):081101, 2021. doi: 10.1103/PhysRevLett.126.081101.

[352] J. Calderon Bustillo, N. Sanchis-Gual, S. H. W. Leong, K. Chandra, A. Torres-Forne, J. A. Font, C. Herdeiro, E. Radu, I. C. F. Wong, and T. G. F. Li. Searching for vector boson-star mergers within LIGO-Virgo intermediate-mass black-hole merger candidates. 6 2022.

[353] D. A. Shaddock. Space-based gravitational wave detection with LISA. *Class. Quant. Grav.*, 25:114012, 2008. doi: 10.1088/0264-9381/25/11/114012.

[354] M. Maggiore et al. Science Case for the Einstein Telescope. *JCAP*, 03:050, 2020. doi: 10.1088/1475-7516/2020/03/050.

[355] S. R. Coleman. Q-balls. *Nucl. Phys. B*, 262(2):263, 1985. doi: 10.1016/0550-3213(86)90520-1. [Addendum: Nucl.Phys.B 269, 744 (1986)].

[356] A. Kusenko and M. E. Shaposhnikov. Supersymmetric Q balls as dark matter. *Phys. Lett. B*, 418:46–54, 1998. doi: 10.1016/S0370-2693(97)01375-0.

[357] J. A. Wheeler. Geons. *Phys. Rev.*, 97:511–536, 1955. doi: 10.1103/PhysRev.97.511.

[358] R. Ruffini and S. Bonazzola. Systems of selfgravitating particles in general relativity and the concept of an equation of state. *Phys. Rev.*, 187:1767–1783, 1969. doi: 10.1103/PhysRev.187.1767.

[359] D.A. Feinblum and W.A. McKinley. Stable States of a Scalar Particle in Its Own Gravational Field. *Phys. Rev.*, 168(5):1445, 1968. doi: 10.1103/PhysRev.168.1445.

[360] M. Minamitsuji. Vector boson star solutions with a quartic order self-interaction. *Phys. Rev. D*, 97(10):104023, 2018. doi: 10.1103/PhysRevD.97.104023.

[361] R. Brito, V. Cardoso, and H. Okawa. Accretion of dark matter by stars. *Phys. Rev. Lett.*, 115(11):111301, 2015. doi: 10.1103/PhysRevLett.115.111301. arXiv:1508.04773 [gr-qc].

[362] H.-Y. Zhang, M. Jain, and M. A. Amin. Polarized vector oscillons. *Phys. Rev. D*, 105 (9):096037, 2022. doi: 10.1103/PhysRevD.105.096037.

[363] J. March-Russell and J. G. Rosa. Micro-Bose/Proca dark matter stars from black hole superradiance. 5 2022. URL https://doi.org/10.48550/arXiv.2205.15277. arXiv.2205.15277 [gr-qc].

[364] Marco Gorghetto, Edward Hardy, John March-Russell, Ningqiang Song, and Stephen M. West. Dark photon stars: formation and role as dark matter substructure. *JCAP*, 08(08):018, 2022. doi: 10.1088/1475-7516/2022/08/018.

[365] C. A. R. Herdeiro, A. M. Pombo, E. Radu, P. V. P. Cunha, and N. Sanchis-Gual. The imitation game: Proca stars that can mimic the Schwarzschild shadow. *JCAP*, 04:051, 2021. doi: 10.1088/1475-7516/2021/04/051.

[366] M. Minamitsuji. Proca stars with nonminimal coupling to the Einstein tensor. *Phys. Rev. D*, 96(4):044017, 2017. doi: 10.1103/PhysRevD.96.044017.

[367] N. Sanchis-Gual, C. Herdeiro, E. Radu, J. C. Degollado, and J. A. Font. Numerical evolutions of spherical Proca stars. *Phys. Rev. D*, 95(10):104028, 2017. doi: 10.1103/PhysRevD.95.104028.

[368] M. Duarte and R. Brito. Asymptotically anti-de Sitter Proca Stars. *Phys. Rev. D*, 94 (6):064055, 2016. doi: 10.1103/PhysRevD.94.064055.

[369] I. Salazar Landea and F. García. Charged Proca Stars. *Phys. Rev. D*, 94(10):104006, 2016. doi: 10.1103/PhysRevD.94.104006.

[370] M. Zilhão, H. Witek, and V. Cardoso. Nonlinear interactions between black holes and Proca fields. *Class. Quant. Grav.*, 32:234003, 2015. doi: 10.1088/0264-9381/32/23/234003.

[371] Mudit Jain and Mustafa A. Amin. Polarized solitons in higher-spin wave dark matter. *Phys. Rev. D*, 105(5):056019, 2022. doi: 10.1103/PhysRevD.105.056019.

[372] Mudit Jain. Soliton stars in yang-mills-higgs theories. *Physical Review D*, 106 (8), October 2022. ISSN 2470-0029. doi: 10.1103/physrevd.106.085011. URL http://dx.doi.org/10.1103/PhysRevD.106.085011.

[373] S. H. Hawley and M. W. Choptuik. Numerical evidence for 'multi - scalar stars'. *Phys. Rev. D*, 67:024010, 2003. doi: 10.1103/PhysRevD.67.024010.

[374] F. Muia, M. Cicoli, K. Clough, F. Pedro, F. Quevedo, and G. P. Vacca. The Fate of Dense Scalar Stars. *JCAP*, 07:044, 2019. doi: 10.1088/1475-7516/2019/07/044.

[375] L. A. Urena-Lopez, S. Valdez-Alvarado, and R. Becerril. Evolution and stability phi**4 oscillatons. *Class. Quant. Grav.*, 29:065021, 2012. doi: 10.1088/0264-9381/29/6/065021.

[376] M. Colpi, S. L. Shapiro, and I. Wasserman. Boson Stars: Gravitational Equilibria of Selfinteracting Scalar Fields. *Phys. Rev. Lett.*, 57:2485–2488, 1986. doi: 10.1103/PhysRevLett.57.2485.

[377] F.E. Schunck and D.F. Torres. Boson stars with generic selfinteractions. *Int. J. Mod. Phys. D*, 9:601–618, 2000. doi: 10.1142/S0218271800000608.

[378] R. Friedberg, T. D. Lee, and Y. Pang. Scalar Soliton Stars and Black Holes. *Phys. Rev. D*, 35:3658, 1987. doi: 10.1103/PhysRevD.35.3658.

[379] D. Guerra, C. F. B. Macedo, and P. Pani. Axion boson stars. *JCAP*, 09(09):061, 2019. doi: 10.1088/1475-7516/2019/09/061. [Erratum: JCAP 06, E01 (2020)].

[380] T. D. Lee. Soliton Stars and the Critical Masses of Black Holes. *Phys. Rev. D*, 35: 3637, 1987. doi: 10.1103/PhysRevD.35.3637.

[381] P. Jetzer and J. J. van der Bij. CHARGED BOSON STARS. *Phys. Lett. B*, 227: 341–346, 1989. doi: 10.1016/0370-2693(89)90941-6.

[382] D. Pugliese, H. Quevedo, J. A. Rueda H., and R. Ruffini. On charged boson stars. *Phys. Rev. D*, 88:024053, 2013. doi: 10.1103/PhysRevD.88.024053.

[383] M. Alcubierre, J. Barranco, A. Bernal, J. C. Degollado, A. Diez-Tejedor, M. Megevand, D. Nunez, and O. Sarbach. ℓ-Boson stars. *Class. Quant. Grav.*, 35(19):19LT01, 2018. doi: 10.1088/1361-6382/aadcb6.

[384] M. Alcubierre, J. Barranco, A. Bernal, J. C. Degollado, A. Diez-Tejedor, V. Jaramillo, M. Megevand, D. Núñez, and O. Sarbach. Extreme ℓ-boson stars. 12 2021.

[385] B. Kleihaus, J. Kunz, and M. List. Rotating boson stars and Q-balls. *Phys. Rev. D*, 72: 064002, 2005. doi: 10.1103/PhysRevD.72.064002.

[386] F. E. Schunck and E. W. Mielke. Rotating boson star as an effective mass torus in general relativity. *Phys. Lett.*, A249:389–394, 1998. doi: 10.1016/S0375-9601(98)00778-6.

[387] M. Gleiser and R. Watkins. Gravitational Stability of Scalar Matter. *Nucl. Phys. B*, 319:733–746, 1989. doi: 10.1016/0550-3213(89)90627-5.

[388] F.V. Kusmartsev, E.W. Mielke, and F.E. Schunck. Gravitational stability of boson stars. *Phys. Rev. D*, 43:3895–3901, 1991. doi: 10.1103/PhysRevD.43.3895.

[389] B. Kleihaus, J. Kunz, and S. Schneider. Stable Phases of Boson Stars. *Phys. Rev. D*, 85:024045, 2012. doi: 10.1103/PhysRevD.85.024045.

[390] N. Sanchis-Gual, F. Di Giovanni, M. Zilhão, C. Herdeiro, P. Cerdá-Durán, J. A. Font, and E. Radu. Nonlinear Dynamics of Spinning Bosonic Stars: Formation and Stability. *Phys. Rev. Lett.*, 123(22):221101, 2019. doi: 10.1103/PhysRevLett.123.221101.

[391] Nils Siemonsen and William E. East. Stability of rotating scalar boson stars with nonlinear interactions. *Phys. Rev. D*, 103(4):044022, 2021. doi: 10.1103/PhysRevD.103.044022.

[392] Jayashree Balakrishna, Ruxandra Bondarescu, Gregory Daues, and Mihai Bondarescu. Numerical Simulations of Oscillating Soliton Stars: Excited States in Spherical Symmetry and Ground State Evolutions in 3D. *Phys. Rev. D*, 77:024028, 2008. doi: 10.1103/PhysRevD.77.024028.

[393] M. Bezares, M. Bošković, S. Liebling, C. Palenzuela, P. Pani, and E. Barausse. Gravitational waves and kicks from the merger of unequal mass, highly compact boson stars. *Phys. Rev. D*, 105(6):064067, 2022. doi: 10.1103/PhysRevD.105.064067.

[394] R. Friedberg, T. D. Lee, and Y. Pang. MINI - SOLITON STARS. *Phys. Rev. D*, 35: 3640, 1987. doi: 10.1103/PhysRevD.35.3640.

[395] L. G. Collodel and D. D. Doneva. Solitonic Boson Stars: Numerical solutions beyond the thin-wall approximation. 3 2022.

[396] J. Balakrishna, E. Seidel, and W.-M. Suen. Dynamical evolution of boson stars. 2. Excited states and selfinteracting fields. *Phys. Rev. D*, 58:104004, 1998. doi: 10.1103/PhysRevD.58.104004.

[397] T. D. Lee and Yang Pang. Stability of Mini - Boson Stars. *Nucl. Phys. B*, 315:477, 1989. doi: 10.1016/0550-3213(89)90365-9.

[398] Marcelo Gleiser. Stability of Boson Stars. *Phys. Rev. D*, 38:2376, 1988. doi: 10.1103/PhysRevD.38.2376. [Erratum: Phys.Rev.D 39, 1257 (1989)].

[399] Robin Croft. *Numerical Modelling of the Dynamics and Gravitational Radiation of Compact Binaries in General Relativity*. PhD thesis, Cambridge U., DAMTP, 10 2022.

[400] Tamara Evstafyeva, Roxana Rosca-Mead, Ulrich Sperhake, and Bernd Brugmann. Boson stars in massless and massive scalar-tensor gravity. *Phys. Rev. D*, 108(10): 104064, 2023. doi: 10.1103/PhysRevD.108.104064.

[401] Edward Seidel and Wai-Mo Suen. Dynamical Evolution of Boson Stars. 1. Perturbing the Ground State. *Phys. Rev. D*, 42:384–403, 1990. doi: 10.1103/PhysRevD.42.384.

[402] Y. Kobayashi, M. Kasai, and T. Futamase. Does a boson star rotate? *Phys. Rev. D*, 50: 7721–7724, 1994. doi: 10.1103/PhysRevD.50.7721.

[403] Fintan D. Ryan. Spinning boson stars with large selfinteraction. *Phys. Rev. D*, 55: 6081–6091, 1997. doi: 10.1103/PhysRevD.55.6081.

[404] Shijun Yoshida and Yoshiharu Eriguchi. Rotating boson stars in general relativity. *Phys. Rev. D*, 56:762–771, 1997. doi: 10.1103/PhysRevD.56.762.

[405] Jayashree Balakrishna, Ruxandra Bondarescu, Gregory Daues, F. Siddhartha Guzman, and Edward Seidel. Evolution of 3-D boson stars with waveform extraction. *Class. Quant. Grav.*, 23:2631–2652, 2006. doi: 10.1088/0264-9381/23/7/024.

[406] Betti Hartmann, Burkhard Kleihaus, Jutta Kunz, and Isabell Schaffer. Compact Boson Stars. *Phys. Lett. B*, 714:120–126, 2012. doi: 10.1016/j.physletb.2012.06.067.

[407] F. E. Schunck and E. W. Mielke. Boson stars: Rotation, formation, and evolution. *Gen. Rel. Grav.*, 31:787, 1999. doi: 10.1023/A:1026673918588.

[408] C. Palenzuela, I. Olabarrieta, L. Lehner, and S. L. Liebling. Head-on collisions of boson stars. *Phys. Rev. D*, 75:064005, 2007. doi: 10.1103/PhysRevD.75.064005.

[409] C. Palenzuela, L. Lehner, and S. L. Liebling. Orbital Dynamics of Binary Boson Star Systems. *Phys. Rev. D*, 77:044036, 2008. doi: 10.1103/PhysRevD.77.044036.

[410] C. Palenzuela, P. Pani, M. Bezares, V. Cardoso, L. Lehner, and S. Liebling. Gravitational Wave Signatures of Highly Compact Boson Star Binaries. *Phys. Rev. D*, 96(10): 104058, 2017. doi: 10.1103/PhysRevD.96.104058.

[411] Nicolas Sanchis-Gual, Miguel Zilhão, Carlos Herdeiro, Fabrizio Di Giovanni, José A. Font, and Eugen Radu. Synchronized gravitational atoms from mergers of bosonic stars. *Phys. Rev. D*, 102(10):101504, 2020. doi: 10.1103/PhysRevD.102.101504.

[412] Vitor Cardoso, Taishi Ikeda, Zhen Zhong, and Miguel Zilhão. Piercing of a boson star by a black hole. *Phys. Rev. D*, 106(4):044030, 2022. doi: 10.1103/PhysRevD.106.044030.

[413] Nicolas Sanchis-Gual, Miguel Zilhão, and Vitor Cardoso. Electromagnetic emission from axionic boson star collisions. *Phys. Rev. D*, 106(6):064034, 2022. doi: 10.1103/PhysRevD.106.064034.

[414] Nils Siemonsen and William E. East. Generic initial data for binary boson stars. *Phys. Rev. D*, 108(12):124015, 2023. doi: 10.1103/PhysRevD.108.124015.

[415] Philippe Jetzer. Boson stars. *Phys. Rept.*, 220:163–227, 1992. doi: 10.1016/0370-1573(92)90123-H.

[416] E. W. Mielke and F. E. Schunck. Boson stars: Early history and recent prospects. In *Recent developments in theoretical and experimental general relativity, gravitation, and relativistic field theories. Proceedings, 8th Marcel Grossmann meeting, MG8, Jerusalem, Israel, June 22-27, 1997. Pts. A, B*, pages 1607–1626, 1997.

[417] Luca Visinelli. Boson stars and oscillatons: A review. *Int. J. Mod. Phys. D*, 30(15): 2130006, 2021. doi: 10.1142/S0218271821300068.

[418] Diego F. Torres. Boson stars in general scalar - tensor gravitation: Equilibrium configurations. *Phys. Rev. D*, 56:3478–3484, 1997. doi: 10.1103/PhysRevD.56.3478.

[419] J. Balakrishna and H.-a. Shinkai. Dynamical evolution of boson stars in Brans-Dicke theory. *Phys. Rev. D*, 58:044016, 1998. doi: 10.1103/PhysRevD.58.044016.

[420] G. L. Comer and Hisa-aki Shinkai. Generation of scalar - tensor gravity effects in equilibrium state boson stars. *Class. Quant. Grav.*, 15:669–688, 1998. doi: 10.1088/0264-9381/15/3/016.

[421] Andreu Masó-Ferrando, Nicolas Sanchis-Gual, José A. Font, and Gonzalo J. Olmo. Boson stars in Palatini gravity. *Class. Quant. Grav.*, 38(19):194003, 2021. doi: 10.1088/1361-6382/ac1fd0.

[422] Andreu Masó-Ferrando, Nicolas Sanchis-Gual, José A. Font, and Gonzalo J. Olmo. Birth of baby universes from gravitational collapse in a modified-gravity scenario. *JCAP*, 06:028, 2023. doi: 10.1088/1475-7516/2023/06/028.

[423] Saša Ilijić and Marko Sossich. Boson stars in $f(T)$ extended theory of gravity. *Phys. Rev. D*, 102(8):084019, 2020. doi: 10.1103/PhysRevD.102.084019.

[424] C. M. Will. *Theory and Experiment in Gravitational Physics*. Cambridge University Press, Cambridge, 1993.

[425] T. R. Taylor and G. Veneziano. Dilaton Couplings at Large Distances. *Phys. Lett. B*, 213:450–454, 1988. doi: 10.1016/0370-2693(88)91290-7.

[426] Kei-Ichi Maeda. On Time Variation of Fundamental Constants in Superstring Theories. *Modern Physics Letters A*, 3(3):243–249, January 1988. doi: 10.1142/S0217732388000295.

[427] T. Damour and Alexander M. Polyakov. The String dilaton and a least coupling principle. *Nucl. Phys. B*, 423:532–558, 1994. doi: 10.1016/0550-3213(94)90143-0.

[428] Alain Riazuelo and Jean-Philippe Uzan. Cosmological observations in scalar - tensor quintessence. *Phys. Rev. D*, 66:023525, 2002. doi: 10.1103/PhysRevD.66.023525.

[429] Carlo Schimd, Jean-Philippe Uzan, and Alain Riazuelo. Weak lensing in scalar-tensor theories of gravity. *Phys. Rev. D*, 71:083512, 2005. doi: 10.1103/PhysRevD.71.083512.

[430] Daniela D. Doneva, Fethi M. Ramazanoğlu, Hector O. Silva, Thomas P. Sotiriou, and Stoytcho S. Yazadjiev. Spontaneous scalarization. *Rev. Mod. Phys.*, 96(1):015004, 2024. doi: 10.1103/RevModPhys.96.015004.

[431] T. Damour and G. Esposito-Farése. Tensor multiscalar theories of gravitation. *Class. Quant. Grav.*, 9:2093–2176, 1992. doi: 10.1088/0264-9381/9/9/015.

[432] T. Damour and G. Esposito-Farése. Tensor - scalar gravity and binary pulsar experiments. *Phys. Rev. D*, 54:1474–1491, 1996. doi: 10.1103/PhysRevD.54.1474.

[433] B. Bertotti, L. Iess, and P. Tortora. A test of general relativity using radio links with the Cassini spacecraft. , 425:374–376, September 2003. doi: 10.1038/nature01997.

[434] P. C. C. Freire *et al.* The relativistic pulsar-white dwarf binary PSR J1738+0333 II. The most stringent test of scalar-tensor gravity. *Mon. Not. Roy. Astron. Soc.*, 423:3328, 2012. doi: 10.1111/j.1365-2966.2012.21253.x. arXiv:1205.1450 [astro-ph].

[435] J. Antoniadis *et al.* A Massive Pulsar in a Compact Relativistic Binary. *Science*, 340:6131, 2013. doi: 10.1126/science.1233232. arXiv:1304.6875 [qstro-ph].

[436] F. M. Ramazanoglu and F. Pretorius. Spontaneous Scalarization with Massive Fields. *Phys. Rev. D*, 93(6):064005, 2016. doi: 10.1103/PhysRevD.93.064005.

[437] U. Sperhake, C. J. Moore, R. Rosca, M. Agathos, D. Gerosa, and C. D. Ott. Long-Lived Inverse Chirp Signals from Core-Collapse in Massive Scalar-Tensor Gravity. *Phys. Rev. Lett.*, 119(20):201103, November 2017. doi: 10.1103/PhysRevLett.119.201103.

[438] Roxana Rosca-Mead, Ulrich Sperhake, Christopher J. Moore, Michalis Agathos, Davide Gerosa, and Christian D. Ott. Core collapse in massive scalar-tensor gravity. , 102(4):044010, August 2020. doi: 10.1103/PhysRevD.102.044010.

[439] J. C. Aurrekoetxea, P.G. Ferreira, K. Clough, E. A. Lim, and O. J. Tattersall. Where is the ringdown: Reconstructing quasinormal modes from dispers+ive waves. *Phys. Rev. D*, 106(10):104002, 2022. doi: 10.1103/PhysRevD.106.104002.

[440] J. L. Blázquez-Salcedo, F. S. Khoo, J. Kunz, and V. Preut. Polar Quasinormal Modes of Neutron Stars in Massive Scalar-Tensor Theories. *Front. in Phys.*, 9:741427, 2021. doi: 10.3389/fphy.2021.741427.

[441] H.-J. Kuan, A. G. Suvorov, D. D. Doneva, and S. S+. Yazadjiev. Gravitational Waves from Accretion-Induced Descalarization in Massive Scalar-Tensor Theory. *Phys. Rev. Lett.*, 129(12):121104, 2022. doi: 10.1103/PhysRevLett.129.121104.

[442] R. Rosca-Mead, M. Agathos, C. J. Moore, and U. Sperhake. Stochastic gravitational wave background from supernovae in massive scalar-tensor gravity. *Phys. Rev. D*, 107 (12):124040, 2023. doi: 10.1103/PhysRevD.107.124040.

[443] T. Kuroda and M. Shibata. Spontaneous scalarization as a new core-collapse supernova mechanism and its multimessenger signals. *Phys. Rev. D*, 107(10):103025, 2023. doi: 10.1103/PhysRevD.107.103025.

[444] S. S. Yazadjiev, D. D. Doneva, and D. Popchev. Slowly rotating neutron stars in scalar-tensor theories with a massive scalar field. *Phys. Rev. D*, 93(8):084038, 2016. doi: 10.1103/PhysRevD.93.084038.

[445] Soichiro Morisaki and Teruaki Suyama. Spontaneous scalarization with an extremely massive field and heavy neutron stars. *Phys. Rev. D*, 96(8):084026, 2017. doi: 10.1103/PhysRevD.96.084026.

[446] Fethi M. Ramazanoğlu and Frans Pretorius. Spontaneous scalarization with massive fields. *Phys. Rev. D*, 93:064005, Mar 2016. doi: 10.1103/PhysRevD.93.064005. URL https://link.aps.org/doi/10.1103/PhysRevD.93.064005.

[447] R. Rosca-Mead, C. J. Moore, M. Agathos, and U. Sperhake. Inverse-chirp signals and spontaneous scalarisation with self-interacting potentials in stellar collapse. *Class. Quant. Grav.*, 36(13):134003, 2019. doi: 10.1088/1361-6382/ab256f.

[448] D. Huang, C.-Q. Geng, and H.-J. Kuan. Scalar gravitational wave signals from core collapse in massive scalar–tensor gravity with triple-scalar interactions. *Class. Quant. Grav.*, 38(24):245006, 2021. doi: 10.1088/1361-6382/ac35ab.

[449] N. Asakawa and Y. Sekiguchi. Constraining self-interactions of a massive scalar field using scalar gravitational waves from stellar core collapse. *Phys. Rev. D*, 108(4): 044060, 2023. doi: 10.1103/PhysRevD.108.044060.

[450] Kent Yagi and Michael Stepniczka. Neutron stars in scalar-tensor theories: Analytic scalar charges and universal relations. *Phys. Rev. D*, 104(4):044017, 2021. doi: 10.1103/PhysRevD.104.044017.

[451] E. Barausse, C. Palenzuela, M. Ponce, and L. Lehner. Neutron-star mergers in scalar-tensor theories of gravity. *Phys. Rev. D*, 87:081506, 2013. doi: 10.1103/PhysRevD.87.081506.

[452] S. D. Odintsov and V. K. Oikonomou. Neutron stars in scalar–tensor gravity with quartic order scalar potential. *Annals Phys.*, 440:168839, 2022. doi: 10.1016/j.aop.2022.168839.

[453] A. W. Whinnett and Diego F. Torres. Charged scalar tensor boson stars: Equilibrium, stability and evolution. *Phys. Rev. D*, 60:104050, 1999. doi: 10.1103/PhysRevD.60.104050.

[454] A. W. Whinnett. Spontaneous scalarization and boson stars. *Phys. Rev. D*, 61:124014, 2000. doi: 10.1103/PhysRevD.61.124014.

[455] Milton Ruiz, Juan Carlos Degollado, Miguel Alcubierre, Dario Nunez, and Marcelo Salgado. Induced scalarization in boson stars and scalar gravitational radiation. *Phys. Rev. D*, 86:104044, 2012. doi: 10.1103/PhysRevD.86.104044.

[456] Miguel Alcubierre, Juan C. Degollado, Dario Nunez, Milton Ruiz, and Marcelo Salgado. Dynamic transition to spontaneous scalarization in boson stars. *Phys. Rev. D*, 81:124018, 2010. doi: 10.1103/PhysRevD.81.124018.

[457] Yves Brihaye and Betti Hartmann. Spontaneous scalarization of boson stars. *JHEP*, 09:049, 2019. doi: 10.1007/JHEP09(2019)049.

[458] Thibault Damour and Gilles Esposito-Farèse. Nonperturbative strong-field effects in tensor-scalar theories of gravitation. *Phys. Rev. Lett.*, 70:2220–2223, Apr 1993. doi: 10.1103/PhysRevLett.70.2220. URL https://link.aps.org/doi/10.1103/PhysRevLett.70.2220.

[459] M. Salgado. The cauchy problem of scalar-tensor theories of gravity. *Class. Quantum Grav.*, 23:4719–4741, 2006. doi: 10.1088/0264-9381/23/14/010.

[460] Takeshi Chiba, Tomohiro Harada, and Ken-ichi Nakao. Gravitational physics in scalar tensor theories: Tests of strong field gravity. *Prog. Theor. Phys. Suppl.*, 128:335–372, 1997. doi: 10.1143/PTPS.128.335.

[461] A. S. Faraoni. *The Mathematical Theory of Relativity*. Cambridge University Press, Cambridge, 1923.

[462] D. Gerosa, U. Sperhake, and C. D. Ott. Numerical simulations of stellar collapse in scalar-tensor theories of gravity. *Class. Quant. Grav.*, 33(13):135002, 2016. doi: 10.1088/0264-9381/33/13/135002.

[463] H.-J. Kuan, K. Van Aelst, A.T.-L. Lam, and M. Shibata. Binary neutron star mergers in massive scalar-tensor theory: Quasi-equilibrium states and dynamical enhancement of the scalarization. 9 2023.

[464] Ramesh Narayan and Jeffrey E. McClintock. Observational Evidence for Black Holes. 12 2013. URL https://doi.org/10.48550/arXiv.1312.6698. arXiv.1312.6698 [astro-ph.HE].

[465] Richard Brito, Vitor Cardoso, and Paolo Pani. Superradiance. *Lect. Notes Phys.*, 906: pp.1–237, 2015. doi: 10.1007/978-3-319-19000-6.

[466] Roxana Rosca-Mead, Christopher J. Moore, Ulrich Sperhake, Michalis Agathos, and Davide Gerosa. Structure of neutron stars in massive scalar-tensor gravity. *Symmetry*, 12:9, 7 2020. doi: 10.3390/sym12091384.

[467] J. Novak. Spherical neutron star collapse toward a black hole in a tensor-scalar theory of gravity. *Phys. Rev. D*, 57:4789–4801, 1998. doi: 10.1103/PhysRevD.57.4789.

[468] J. Novak. Neutron star transition to strong scalar field state in tensor scalar gravity. *Phys. Rev. D*, 58:064019, 1998. doi: 10.1103/PhysRevD.58.064019.

[469] P. Pani and E. Berti. Slowly rotating neutron stars in scalar-tensor theories. *Phys. Rev. D*, 90(2):024025, 2014. doi: 10.1103/PhysRevD.90.024025.

[470] R. F. P. Mendes, G. E. A. Matsas, and D. A. T. Vanzella. Instability of nonminimally coupled scalar fields in the spacetime of slowly rotating compact objects. *Phys. Rev. D*, 90(4):044053, 2014. doi: 10.1103/PhysRevD.90.044053.

[471] R. F. P. Mendes. Possibility of setting a new constraint to scalar-tensor theories. *Phys. Rev. D*, 91(6):064024, 2015. doi: 10.1103/PhysRevD.91.064024.

[472] R. F.P. Mendes and N. Ortiz. Highly compact neutron stars in scalar-tensor theories of gravity: Spontaneous scalarization versus gravitational collapse. *Phys. Rev. D*, 93(12): 124035, 2016. doi: 10.1103/PhysRevD.93.124035.

[473] F. M. Ramazanoğlu. Spontaneous growth of vector fields in gravity. *Phys. Rev. D*, 96 (6):064009, 2017. doi: 10.1103/PhysRevD.96.064009.

[474] Press, William H. and Teukolsky, Saul A. and Vetterling, William T. and Flannery, Brian P. *Numerical recipes in C (2nd ed.): the art of scientific computing*. Cambridge University Press, New York, NY, USA, 1992. ISBN 0-521-43108-5.

[475] H. S. Chia and T. D. P. Edwards. Searching for General Binary Inspirals with Gravitational Waves. *JCAP*, 11:033, 2020. doi: 10.1088/1475-7516/2020/11/033.

[476] Alexandre Toubiana, Stanislav Babak, Enrico Barausse, and Luis Lehner. Modeling gravitational waves from exotic compact objects. *Phys. Rev. D*, 103(6):064042, 2021. doi: 10.1103/PhysRevD.103.064042.

[477] M. Bezares and C. Palenzuela. Gravitational Waves from Dark Boson Star binary mergers. *Class. Quant. Grav.*, 35(23):234002, 2018. doi: 10.1088/1361-6382/aae87c.

[478] M. Bezares, D. Viganò, and C. Palenzuela. Gravitational wave signatures of dark matter cores in binary neutron star mergers by using numerical simulations. *Phys. Rev. D*, 100(4):044049, 2019. doi: 10.1103/PhysRevD.100.044049.

[479] L. J. Papenfort, S. D. Tootle, P. Grandclément, E. R. Most, and L. Rezzolla. New public code for initial data of unequal-mass, spinning compact-object binaries. *Phys. Rev. D*, 104(2):024057, 2021. doi: 10.1103/PhysRevD.104.024057.

[480] T. D. Lee and Y. Pang. Fermion Soliton Stars and Black Holes. *Phys. Rev. D*, 35:3678, 1987. doi: 10.1103/PhysRevD.35.3678.

[481] D. I. Choi, K. C. W. Lai, M. W. Choptuik, E. W. Hirschmann, S. L. Liebling, and F. Pretorius. Dynamics of axisymmetric (head-on) mini-boson star collisions. 2009.

[482] U. Sperhake. Binary black-hole evolutions of excision and puncture data. *Phys. Rev. D*, 76:104015, 2007. doi: 10.1103/PhysRevD.76.104015. gr-qc/0606079.

[483] M. Campanelli, C. O. Lousto, P. Marronetti, and Y. Zlochower. Accurate Evolutions of Orbiting Black-Hole Binaries without Excision. *Phys. Rev. Lett.*, 96:111101, 2006. doi: 10.1103/PhysRevLett.96.111101. gr-qc/0511048.

[484] J. G. Baker, J. Centrella, D.-I. Choi, M. Koppitz, and J. van Meter. Gravitational-Wave Extraction from an inspiraling Configuration of Merging Black Holes. *Phys. Rev. Lett.*, 96:111102, 2006. doi: 10.1103/PhysRevLett.96.111102. gr-qc/0511103.

[485] N. Sanchis-Gual, J. Calderón Bustillo, C. Herdeiro, E. Radu, J. A. Font, S. H. W. Leong, and A. Torres-Forné. Impact of the wavelike nature of Proca stars on their gravitational-wave emission. *Phys. Rev. D*, 106(12):124011, 2022. doi: 10.1103/PhysRevD.106.124011.

[486] J. Y. Widdicombe, T. Helfer, and Eugene A. Lim. Black hole formation in relativistic Oscillaton collisions. *JCAP*, 2001(01):027, 2020. doi: 10.1088/1475-7516/2020/01/027.

[487] Miguel Bezares, Carlos Palenzuela, and Carles Bona. Final fate of compact boson star mergers. *Phys. Rev. D*, 95(12):124005, 2017. doi: 10.1103/PhysRevD.95.124005.

[488] B. Schwabe, J. C. Niemeyer, and J. F. Engels. Simulations of solitonic core mergers in ultralight axion dark matter cosmologies. *Phys. Rev. D*, 94(4):043513, 2016. doi: 10.1103/PhysRevD.94.043513.

[489] N. K. Johnson-Mcdaniel, A. Mukherjee, R. Kashyap, P. Ajith, W. Del Pozzo, and S. Vitale. Constraining black hole mimickers with gravitational wave observations. *Phys. Rev. D*, 102:123010, 2020. doi: 10.1103/PhysRevD.102.123010.

[490] Tamara Evstafyeva, Ulrich Sperhake, Isobel Romero-Shaw, and Michalis Agathos. Gravitational-wave data analysis with high-precision numerical relativity simulations of boson star mergers. *Phys. Rev. Lett.*, 6 2024. doi: 10.1103/PhysRevLett.133.131401. URL https://doi.org/10.48550/arXiv.2406.02715. arXiv.2406.02715 [gr-qc].

[491] Nils Siemonsen. Nonlinear Treatment of a Black Hole Mimicker Ringdown. *Phys. Rev. Lett.*, 133(3):031401, 2024. doi: 10.1103/PhysRevLett.133.031401.

[492] C. Pacilio, M. Vaglio, A. Maselli, and P. Pani. Gravitational-wave detectors as particle-physics laboratories: Constraining scalar interactions with a coherent inspiral model of boson-star binaries. *Phys. Rev. D*, 102(8):083002, 2020. doi: 10.1103/PhysRevD.102.083002.

[493] M. Vaglio, C. Pacilio, A. Maselli, and P. Pani. Bayesian parameter estimation on boson-star binary signals with a coherent inspiral template and spin-dependent quadrupolar corrections. *Phys. Rev. D*, 108(2):023021, 2023. doi: 10.1103/PhysRevD.108.023021.

[494] Huai-Ke Guo, Kuver Sinha, and Chen Sun. Probing Boson Stars with Extreme Mass Ratio Inspirals. *JCAP*, 09:032, 2019. doi: 10.1088/1475-7516/2019/09/032.

[495] Juan Calderón Bustillo, Nicolas Sanchis-Gual, Alejandro Torres-Forné, José A. Font, Avi Vajpeyi, Rory Smith, Carlos Herdeiro, Eugen Radu, and Samson H. W. Leong. GW190521 as a Merger of Proca Stars: A Potential New Vector Boson of 8.7×10^{-13} eV. *Phys. Rev. Lett.*, 126(8):081101, 2021. doi: 10.1103/PhysRevLett.126.081101.

[496] Tamara Evstafyeva and Ulrich Sperhake. Boson star waveforms, 2024. URL https://github.com/tamaraevst/Boson-star-waveforms.

[497] Tamara Evstafyeva, Ulrich Sperhake, Isobel Romero-Shaw, and Michalis Agathos. Inspiral and merger of equal-mass boson star binary forming a black hole post-merger, 2024. URL https://www.youtube.com/watch?v=QrbJKKAOerY.

[498] Tamara Evstafyeva, Ulrich Sperhake, Isobel Romero-Shaw, and Michalis Agathos. Inspiral and merger of equal-mass boson star binary forming a boson star post-merger, 2024. URL https://www.youtube.com/watch?v=hj1WzNPpeS0.

[499] T. D. Lee and Y. Pang. Nontopological solitons. *Phys. Rept.*, 221:251–350, 1992. doi: 10.1016/0370-1573(92)90064-7.

[500] Katerina Chatziioannou. Neutron star tidal deformability and equation of state constraints. *Gen. Rel. Grav.*, 52(11):109, 2020. doi: 10.1007/s10714-020-02754-3.

[501] T. Andrade et al. GRChombo: An adaptable numerical relativity code for fundamental physics. *J. Open Source Softw.*, 6:3703, 2021. doi: 10.21105/joss.03703.

[502] I. Hinder et al. Error-analysis and comparison to analytical models of numerical waveforms produced by the NRAR Collaboration. *Class. Quant. Grav.*, 31:025012, 2014. doi: 10.1088/0264-9381/31/2/025012. arXiv:1307.5307 [gr-qc].

[503] Karl Wette. SWIGLAL: Python and Octave interfaces to the LALSuite gravitational-wave data analysis libraries. *SoftwareX*, 12:100634, 2020. doi: 10.1016/j.softx.2020.100634.

[504] I.M. Romero-Shaw et al. Bayesian inference for compact binary coalescences with bilby: validation and application to the first LIGO–Virgo gravitational-wave transient catalogue. *Mon. Not. Roy. Astron. Soc.*, 499(3):3295–3319, 2020. doi: 10.1093/mnras/staa2850.

[505] Michael J. Williams. Nessai: Nested sampling with artificial intelligence, February 2021. URL https://doi.org/10.5281/zenodo.4550693.

[506] Sascha Husa, Sebastian Khan, Mark Hannam, Michael Pürrer, Frank Ohme, Xisco Jiménez Forteza, and Alejandro Bohé. Frequency-domain gravitational waves from nonprecessing black-hole binaries. I. New numerical waveforms and anatomy of the signal. *Phys. Rev. D*, 93(4):044006, 2016. doi: 10.1103/PhysRevD.93.044006.

[507] S. Khan et al. Frequency-domain gravitational waves from non-precessing black-hole binaries. II. A phenomenological model for the advanced detector era. *Phys. Rev. D*, 93:044007, 2016. doi: 10.1103/PhysRevD.93.044007. arXiv:1508.07253 [gr-qc].

[508] Sebastian Khan, Katerina Chatziioannou, Mark Hannam, and Frank Ohme. Phenomenological model for the gravitational-wave signal from precessing binary black holes with two-spin effects. *Phys. Rev. D*, 100(2):024059, 2019. doi: 10.1103/PhysRevD.100.024059.

[509] Geraint Pratten et al. Computationally efficient models for the dominant and subdominant harmonic modes of precessing binary black holes. *Phys. Rev. D*, 103(10):104056, 2021. doi: 10.1103/PhysRevD.103.104056.

[510] Francesco Messina and Alessandro Nagar. Parametrized-4.5PN TaylorF2 approximants and tail effects to quartic nonlinear order from the effective one body formalism. *Phys. Rev. D*, 95(12):124001, 2017. doi: 10.1103/PhysRevD.95.124001. [Erratum: Phys.Rev.D 96, 049907(E) (2017)].

[511] Alessandro Nagar et al. Time-domain effective-one-body gravitational waveforms for coalescing compact binaries with nonprecessing spins, tides and self-spin effects. *Phys. Rev. D*, 98(10):104052, 2018. doi: 10.1103/PhysRevD.98.104052.

[512] Tim Dietrich, Sebastiano Bernuzzi, and Wolfgang Tichy. Closed-form tidal approximants for binary neutron star gravitational waveforms constructed from high-resolution numerical relativity simulations. *Phys. Rev. D*, 96(12):121501(R), 2017. doi: 10.1103/PhysRevD.96.121501.

[513] Tim Dietrich, Anuradha Samajdar, Sebastian Khan, Nathan K. Johnson-McDaniel, Reetika Dudi, and Wolfgang Tichy. Improving the NRTidal model for binary neutron star systems. *Phys. Rev. D*, 100(4):044003, 2019. doi: 10.1103/PhysRevD.100.044003.

[514] Leslie Wade, Jolien D. E. Creighton, Evan Ochsner, Benjamin D. Lackey, Benjamin F. Farr, Tyson B. Littenberg, and Vivien Raymond. Systematic and statistical errors in a bayesian approach to the estimation of the neutron-star equation of state using advanced gravitational wave detectors. *Phys. Rev. D*, 89(10):103012, 2014. doi: 10.1103/PhysRevD.89.103012.

[515] Samantha A. Usman, Joseph C. Mills, and Stephen Fairhurst. Constraining the Inclinations of Binary Mergers from Gravitational-wave Observations. *Astrophys. J.*, 877(2):82, 2019. doi: 10.3847/1538-4357/ab0b3e.

[516] Yiqi Xie, Deep Chatterjee, Gilbert Holder, Daniel E. Holz, Scott Perkins, Kent Yagi, and Nicolás Yunes. Breaking bad degeneracies with Love relations: Improving gravitational-wave measurements through universal relations. *Phys. Rev. D*, 107(4): 043010, 2023. doi: 10.1103/PhysRevD.107.043010.

[517] M. Campanelli, C. O. Lousto, and Y. Zlochower. Spinning-black-hole binaries: The orbital hang up. *Phys. Rev. D*, 74:041501, 2006. doi: 10.1103/PhysRevD.74.041501. gr-qc/0604012.

[518] Maxence Corman and William E. East. Black hole-neutron star mergers in Einstein-scalar-Gauss-Bonnet gravity. 5 2024.